Parallel Adaptive Simulation of Multi-dimensional Detonation Structures

Von der Fakultät für Mathematik, Naturwissenschaften und Informatik
der Brandenburgischen Technischen Universität Cottbus

zur Erlangung des akademischen Grades

Doktor der Naturwissenschaften
Dr. rer. nat.

genehmigte Dissertation

vorgelegt von

Diplom-Mathematiker

Ralf Deiterding

geboren am 30. August 1971 in Osterode am Harz

Gutachter: Prof. Dr. rer. nat. habil. Georg Bader

Gutachter: Prof. Dr. rer. nat. habil. Dietmar Kröner

Gutachter: Prof. Dr. rer. nat. habil. Ulrich Maas

Tag der mündlichen Prüfung: 10. September 2003

Abstract

The approximation of transient detonation waves requires numerical methods that are able to resolve a wide range of different scales. Especially the accurate consideration of detailed chemical kinetics is extremely demanding. This thesis describes an efficient solution strategy for the Euler equations of gas dynamics for mixtures of thermally perfect species with detailed, non-equilibrium reaction that tackles the problem of source term stiffness by temporal and spatial dynamic mesh adaptation. All gas dynamically relevant scales are sufficiently resolved.

The blockstructured adaptive mesh refinement technique of Berger and Colella is utilized to supply the required resolution locally on the basis of hydrodynamic refinement criteria. This adaptive method is tailored especially for time-explicit finite volume schemes and uses a hierarchy of spatially refined subgrids which are integrated recursively with reduced time steps. A parallelization strategy for distributed memory machines is developed and implemented. It follows a rigorous domain decomposition approach and partitions the entire grid hierarchy.

A time-operator splitting technique is employed to decouple hydrodynamic transport and chemical reaction. It allows the separate numerical integration of the homogeneous Euler equations with time-explicit finite volume methods and the usage of an time-implicit discretization only for the stiff reaction terms. High-resolution shock capturing schemes are constructed for the homogeneous Euler equations with complex equation of state. In particular, a reliable hybrid Roe-solver-based method is derived. The scheme avoids unphysical values due to the Roe linearization and utilizes additional numerical viscosity to stabilize the approximation of strong shocks that inherently appear at the head of detonation waves. In different test configurations it is shown that this hybrid Roe-type method is superior for detonation simulation to any other method considered.

Large-scale simulations of unstable detonation structures of hydrogen-oxygen detonations run on recent Beowulf clusters demonstrate the efficiency of the entire approach. In particular, computations of regular cellular structures in two and three space dimensions and their development under transient conditions, e.g. Mach reflection and diffraction, are presented. The achieved resolutions go far beyond previously published results and provide new reference solutions.

Parallele Adaptive Simulation Mehrdimensionaler Detonationsstrukturen

Die Approximation transienter Detonationswellen erfordert numerische Verfahren, die über die Fähigkeit verfügen, einen großen Bereich verschiedener Skalen aufzulösen. Insbesondere die Berücksichtigung detaillierter Reaktionskinetik ist außerordentlich schwierig. In dieser Dissertation wird eine effiziente Lösungsstrategie für die Eulergleichungen der Gasdynamik für Mischungen thermisch perfekter Spezies mit detaillierter Nichtgleichgewichtschemie vorgeschlagen, die das Problem numerisch steifer Quellterme mittels dynamischer zeitlicher und örtlicher Gitteradaption angeht. Alle gasdynamisch relevanten Skalen werden hinreichend aufgelöst.

Die blockstrukturierte Gitteradaptionstechnik nach Berger und Collela wird verwendet, um die lokal erforderliche Auflösung anhand hydrodynamischer Verfeinerungskriterien bereitzustellen. Diese Adaptionsmethodik ist insbesondere auf zeitexplizite Finite-Volumen-Verfahren zugeschnitten und verwendet eine Hierarchie örtlich verfeinerter Untergitter, die in rekursiver Art und Weise mit verfeinerten Zeitschritten integriert werden. Eine Parallelisierungsstrategie für Maschinen mit verteiltem Speicher wird entwickelt und umgesetzt. Die Strategie basiert auf einem rigorosen Gebietszerlegungsansatz, der zu einer Aufteilung der gesamten Hierarchie führt.

Die Zwischenschrittmethode wird verwendet, um die hydrodynamischen Transportvorgänge von der chemischen Reaktion abzukoppeln. Die Methode erlaubt die separate numerische Integration der homogenen Eulergleichungen mit zeitexpliziten Finite-Volumen-Verfahren und die Verwendung einer zeitimpliziten Diskretisierung für die steifen Reaktionsterme. Für die Eulergleichungen mit komplexer Zustandsgleichung werden hochauflösende Shock-Capturing-Schemata konstruiert. Im Besonderen wird ein hybrides Roe-Löser-basiertes Schema hergeleitet. Das Verfahren vermeidet unphysikalische Werte aufgrund der Roe-Linearisierung und verwendet zusätzliche numerische Viskosität zur Stabilisierung der Approximation starker Schocks, welche Detonationenwellen zwangsläufig vorausgehen. In verschieden Testkonfigurationen wird die Überlegenheit des hybriden Roe-Verfahren für Detonationsprobleme gegenüber anderen Verfahren aufgezeigt.

Umfangreiche Simulationen instabiler Detonationstrukturen von Wasserstoff-Sauerstoff-Detonationen, die auf aktuell gebräuchlichen Beowulf-Clustern gerechnet wurden, demonstrieren die Effizienz des gesamten Ansatzes. Im Besonderen werden Berechnungen regulärer zellularer Strukturen in zwei und drei Raumrichtungen, sowie ihre Veränderung unter veränderlichen Bedingungen, z.B. Machsche Reflexion und Diffusor, präsentiert. Die erzielten Auflösungen gehen wesentlich über bisher veröffentlichte Resultate hinaus und lieferen neue Referenzlösungen.

Acknowledgments

I want to thank my thesis advisor Prof. Dr. Georg Bader for his continuing interest and support of my work. His generosity to share his ideas with me was the starting point for the work of this thesis. After pushing things forward he gave me the opportunity to develop an independent research. He provided me with the necessary computational resources and never rested in assuring a modern parallel working environment even under difficult circumstances.

I would like to express my special thanks to Prof. Dr. Rolf Rannacher for supporting my usage of the HEidelberg LInux Cluster System, one of the world-fastest Linux Beowulf-clusters. The large-scale simulations in this thesis would not have been possible without the access to this competitive system.

I am grateful to Dr. Klaus Schenk who prepared the project 'Analysis and Simulation of Flows for Multicomponent Gas-Mixtures' within the DFG-priority research program 'Analysis and Numerics of Conservation Laws' that supported me during my entire work. This thesis is based mainly on results of this long-term project and applies them to the important problem class of detonation waves. Only the support of the ANumE program gave me the opportunity to present parts of my work on international meetings.

Finally, I thank Dr. Guntram Berti for reading a draft version of the whole manuscript and his helpful comments.

This work was supported by DFG grants No. Ba 840/3-1,2,3 in the high-priority research program ANumE.

Contents

Chapter 1

Introduction

Reacting flows have been a topic of on-going research since more than hundred years. The interaction between hydrodynamic flow and chemical kinetics can be extremely complex and even today many phenomena are not very well understood. One of these phenomena is the propagation of detonation waves in gaseous media. While the classical Chapman-Jouguet theory [41, 98] predicts the average propagation velocity almost correctly, no theory exists up to now, which describes the internal flow structure satisfactory. The famous ZND theory, proposed independently by Zel'dovich [209], von Neumann [200] and Döring [57], is widely believed to describe the one-dimensional detonation structure correctly, but already early experiments [55, 199, 181] uncovered that the reduction to one space dimension is not even justified in long tubes. It was found that detonation waves usually exhibit instationary multi-dimensional sub-structures and do not remain planar. But the experimental analysis of these transient sub-structures is difficult. Numerical simulation of the governing equations can be an alternative here. Recent high performance computers allow direct simulations of detonations that provide detailed insight into the flow field far beyond previous experimental results.

1.1 Detonation Structure

A detonation is characterized by a configuration of a discontinuous hydrodynamic shock wave followed by a smooth region of decaying combustion. The shock causes an adiabatic compression, which rises the temperature of the combustible mixture above the ignition limit. After the ignition, it takes an induction time of a few microseconds, until the reactants start to react rapidly to the constant equilibrium state. The chemical reaction results in an energy release that drives the shock wave forward. In a self-sustaining detonation, shock and reaction zone propagate essentially with an identical wave speed, which is approximately equal to the Chapman-Jouguet (CJ) velocity. The CJ value is the minimal velocity of a discontinuous wave separating reactants and equilibrium products and can be calculated from the Chapman-Jouguet theory in advance. The CJ value is approximately the limit of

convergence in unconfinement. In the CJ point, shock and reaction front would be in perfect thermo- and hydrodynamic balance. But smallest transverse oscillations are sufficient to destroy the equilibrium. In the multi-dimensional case, inherently unstable modes do exist and minor disturbances are enough to trigger the breaking of the planar structure. These instabilities lead to the creation of instationary shock waves propagating perpendicular to the detonation front. A complex flow pattern is formed around each point, where the detonation front is intersected by a transverse shock. In the vicinity of such triple points, the chemical reaction is enhanced drastically giving rise to an enormous local energy release. For some particular configurations very regular triple point patterns, so-called detonations cells, have been observed. The accurate representation of triple points is essential for safety analysis, but also in technical applications, where shock-induced combustion leads to the formation of detonation waves, e.g. in the pulse detonation engine.

1.2 Detonation Simulation

The governing equations of detonation waves in premixed inviscid gases are the multi-component Euler equations with chemically reactive source terms. These equations can be written as an inhomogeneous conservation law of hyperbolic type. The appropriate discretization technique for discontinuous solutions like they typically occur in detonation simulation is the finite volume (FV) approach. Only FV methods satisfy the essential property of discrete conservation in the homogeneous case and are guaranteed to converge toward weak solutions. Only the FV approach is capable to approximate the propagation velocity of the shock at the head of a detonation wave correctly. But the reaction in a detonation wave introduces additional temporal and spatial scales into the Euler equations. While a detonation propagates with a supersonic velocity between 1000 m/s and 2000 m/s, the distance between leading shock and reaction front is typically in the millimetre range. Source terms that involve significantly shorter scales than the homogeneous equations are often said to be stiff [92, 134, 15]. They require meshes with an extraordinarily high resolution. If a mesh is too coarse to represent the influence of the source term correctly, every reasonable FV scheme will produce a physically meaningful approximation, but unfortunately it is not the sought weak entropy solution of the original inhomogeneous equations, but of the same conservation law with a different source. Some researchers, e.g. Bao and Jin [15] or Helzel [92], have proposed *underresolved* schemes that approximate the correct detonation speed on relatively coarse meshes, but these approaches use special assumptions and are restricted to simplified reaction models (compare Sec. 3.1.1).

In particular, the shock of a detonation wave with detailed chemical reaction can be very sensitive to changes of the reaction behind, and if the mesh does not resolve all reaction details accurately, the Riemann Problem at the detonation front is changed remarkably leading to an incorrect detonation speed [51]. We make a simple discretization test in order to illustrate, how fine computational grids for

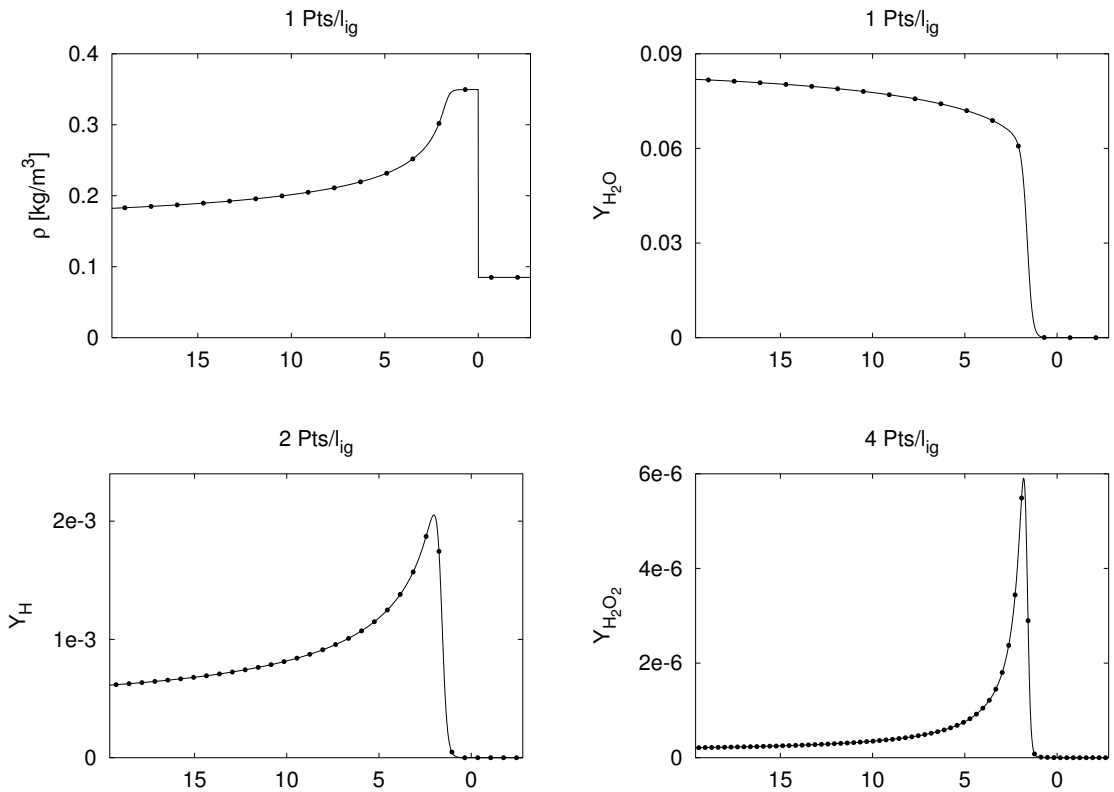

Figure 1.1: Representation of characteristic quantities of the self-sustaining hydrogen-oxygen detonation of Fig. 3.4 on grids with different mesh widths. The dots represent the values in the middle of a finite volume. The abscissae display the distance behind the detonation front in mm.

detonation simulations with detailed non-equilibrium chemistry in fact have to be. Fig. 1.1 displays the *exact* solution of a one-dimensional CJ detonation discretized with different FV grids. The chemical reaction in this example is modeled with the non-equilibrium reaction mechanism for hydrogen-oxygen combustion tabulated on page 225. Beside H_2, O_2 and H_2O the mechanism considers the species H, O, OH, HO_2 and H_2O_2. The inert gas argon is only a diluent. As characteristic length scale we utilize the induction length l_{ig}, the distance between leading shock and measurable reaction.

The upper row of Fig. 1.1 shows the discretizations of total density ρ and mass fraction $Y_{\mathrm{H_2O}} := \rho_{\mathrm{H_2O}}/\rho$, which is the quotient between the partial density of H_2O and ρ, for a mesh width of 1 finite volume per induction length ($1\,\mathrm{Pts}/l_{ig}$). Both functions are in principle correctly reproduced, but the maxima in the graphs of the highly reactive radicals H, O can not be captured even with a twice as fine resolution (compare left picture in lower row). This requires at least $4\,\mathrm{Pts}/l_{ig}$, but even with such a fine grid the maximum of the intermediate product H_2O_2 is not correct. Approximately 5 to $6\,\mathrm{Pts}/l_{ig}$ are necessary to discretize all quantities of the

detonation wave in agreement with the exact solution. As numerical methods naturally introduce additional errors, it can be expected that the correct approximation of this detonation requires a resolution of at least 7 to $8\,\mathrm{Pts}/l_{ig}$. If a time-explicit FV shock-capturing scheme would be used to approximate the described detonation wave on a grid of $8\,\mathrm{Pts}/l_{ig}$, the maximal time step due to numerical stability would be approximately $0.06\,\mu$s. This is above a reasonable time step for the evaluation of the reaction terms. The numerical approximation of the source terms in this example with a sufficient accuracy (compare Sec. 4.10.2) requires at least at the reaction front a time step between 0.01 and $0.02\,\mu$s. In a triple point significantly smaller values can be expected.

The discretization of typical combustion devices with a length of several metres with such fine uniform grids can easily require more than 10^7 FV cells for two-dimensional simulations and more than 10^9 cells in the three-dimensional case. As multi-dimensional detonations are intrinsically unstable, numerical simulations have to be instationary and usually would involve several ten thousand time steps. Consequently, uniform meshes are far too expensive and multi-dimensional detonation simulations necessarily have to employ sophisticated dynamically adaptive mesh refinement techniques [79, 78, 59].

1.3 Contents of this Thesis

In this thesis, we describe an efficient solution strategy for the Euler equations for mixtures of thermally perfect gases with detailed reaction terms that tackles the problem of source term stiffness by temporal and spatial dynamic mesh adaptation. Reliable high resolution shock-capturing schemes are applied as an elementary ingredient to reduce the number of FV cells to the minimum. A time-operator splitting technique [96, 175] with local time step adjustment (sub-cycling) is utilized to account for temporal scales in the source term that do not influence the hydrodynamic flow remarkably, but need to be resolved due to the local temporal stiffness. The operator splitting approach allows the derivation of various time-explicit FV methods for the homogeneous generalized Euler equations separately and to incorporate the reaction terms as ordinary differential equations (ODEs) subsequently. As the numerical integration of ODEs with automatic time step adjustment is a standard task today [56, 85, 106] our focus lies especially on the shock-capturing methods for the hydrodynamic flow. Special emphasis is put on the Roe approximate Riemann solver [156, 158] and the prevention of its various inaccuracies and failures. In particular, a hybrid Roe-solver-based method is constructed that allows the reliable simulation of detonation waves. Based on different test configurations it is shown, that this hybrid method is superior to all other schemes considered, especially in the multi-dimensional case.

The blockstructured adaptive mesh refinement (AMR) algorithm of Berger and Collela [21] is applied to construct non-uniform meshes dynamically and to achieve

the required high resolution of the hydrodynamic flow. The adaptation is based on hydrodynamic refinement criteria, e.g. scaled gradients and a heuristic error estimation for the entire splitting scheme. The AMR algorithm is tailored for time-explicit FV methods and utilizes a hierarchy of spatially refined subgrids that are integrated recursively with reduced hydrodynamic time steps. The AMR approach requires only logically rectangular data structures and allows various technical optimizations on super-scalar processors. A dynamic parallelization strategy tailored for distributed memory machines is developed [145]. We describe our own implementation AMROC [53], which was the basis for the large-scale computations throughout this thesis.

Instationary multi-dimensional detonation structure computations for hydrogen-oxygen mixtures diluted with argon demonstrate the efficiency of the entire approach in practice. In particular, simulations of regular cellular detonation structures in two and three space dimensions and their development under transient conditions are presented. The achieved resolutions go far beyond previously published results [138, 59, 78] and provide new reference solutions.

Detailed Summary of the Chapters

We start with a detailed introduction of the governing equations of detonation calculation in Chap. 2. The appropriate equations are the Euler equations for mixtures of thermally perfect gases with reaction terms in conservation-law form [73, 204]. In the first part of the chapter, the most important theoretical facts on conservation laws are briefly recalled. Emphasis is put on a condensed presentation of the results of the highly developed analysis of the one-dimensional Riemann Problem for the homogeneous case [171, 82, 117]. Throughout the rest of the chapter we discuss the multi-component Euler equations with complex equations of state from a mathematical point of view. We give a comprehensive description of the multi-component model and discuss the equation of state and its solvability in detail. We prove various mathematical properties, like hyperbolicity or rotational invariance for the generalized equations and obtain various results necessary for the construction of numerical methods by the way. We analyze the solution of the homogeneous Riemann Problem for generalized Euler equations and find its structure to be in principle identical to the standard case [109, 108]. The profound understanding of the one-dimensional Riemann Problem provides the theoretical basis for the construction of a reliable approximate Riemann solver as a key ingredient for detonation simulation.

In Chap. 3 we derive exact stationary one-dimensional solutions of the inhomogeneous Euler equations under the assumptions of the classical ZND detonation model [209, 200, 57]. We start with the derivation of the solution of the simplest model-problem with just one single irreversible reaction between two calorically perfect gases. The results are then extended to an arbitrary number of thermally perfect gases with detailed reaction mechanism. The exact one-dimensional solutions provide reference data and will be utilized as reproducible initial conditions in

the Chaps. 6 and 7. In the last part of the chapter we give an introduction into the inherently unstable nature of detonation waves in multiple space dimensions. We explain the hydrodynamic structure of multi-dimensional detonation waves, how it is known from experiments [176, 178]. As multi-dimensional detonation waves are intrinsically unstable, this basic flow structure is the core of the physical interpretation of the numerical results in the Chaps. 6 and 7.

The basic numerical methods are developed in Chap. 4. We derive different FV discretizations for inhomogeneous conservation laws on Cartesian grids and discuss their applicability to detonation wave simulation. We introduce our basic solution method, the operator splitting technique or method of fractional steps. Then we derive one-dimensional time-explicit high resolution FV methods for the homogeneous case. After an introduction to upwinding we present the Flux-Vector Splitting and the Flux-Difference Splitting approach in general and explain briefly two possible higher-order extensions: The MUSCL variable extrapolation of Van Leer [191, 195] and the Wave Propagation Method of LeVeque as a fully multi-dimensional scheme [119, 107].

The majority of Chap. 4 is concerned with the application of the different shock-capturing approaches to multi-component Euler equations for thermally perfect gases. After a discussion of discrete boundary conditions and the practical solution of the complex equation of state, the split fluxes of Steger-Warming- and Van Leer-type are presented [169, 127, 109, 84]. We construct the difficult Roe linearization in detail and present possible entropy corrections [87, 89]. Finally, the Harten-Lax-Van Leer (HLL) method [91, 62] is introduced. We discuss the application of the two higher-order methods to multiple thermally perfect components and develop a suitable variable reconstruction. Then an overview on the various problems and failures, which can arise in shock-capturing schemes, is given. Most of the problems are associated to the Roe method and have to be cured in a reliable Roe solver for detonation simulation. We demonstrate that artificial oscillations at strong shock waves [154, 9], that typically would appear at the head of detonation waves [150, 14], can be moderated (or in case of the carbuncle phenomenon avoided completely) by utilizing an entropy correction, which adds artificial viscosity and by modifying the amount of viscosity appropriately [160]. Further on, we describe how unphysical total and energy densities due to the Roe linearization [62] can be circumvented by switching to the robust HLL scheme. Finally, we present a flux modification based upon the properties of the exact solution that ensures the positivity of the partial densities of a Godunov-type method in the multi-component case without an additional scheme [108]. All corrections are combined in a complex hybrid Roe-type method that is shown to be superior for detonation simulations to all tested upwind methods in Chap. 6. The last part of the chapter discusses briefly the numerical integration of stiff reaction terms from a practical point of view.

The dynamically adaptive algorithm is developed in Chap. 5. After an overview on adaptive mesh refinement in general, the blockstructured AMR algorithm of Berger and Collela is derived [21]. We start with a detailed explanation of the AMR method on a single-processor machine and extend it to parallel distributed

machines subsequently. The presentation is topologically oriented and allows the exact derivation of the parallel algorithm from the serial one under the chosen domain decomposition strategy. In our parallelization approach the entire AMR hierarchy is separated and higher-level subgrids are associated to the same node as the underlying base grid. This strategy reduces the communication overhead and simplifies the implementation [145].

A topological notation is employed in order to allow a condensed formulation of the AMR sub-routines in pseudo-code. The exactness of the formulation ensures that the presentation could be used as a guide-line for practical implementations. In particular, the parallelization of the flux correction at hanging nodes, which is indispensable for FV methods, and the setting of internal ghost cell values are presented in detail. Load-balancing techniques based on generalized space-filling curves [145, 159], standard refinement criteria [21] and the combination of flagged cells to rectangular subgrids are briefly described [19]. We explain the object-oriented design of our own AMR code AMROC [53] and contrast it with other implementations. Finally, two highly adaptive examples for standard Euler equations are presented. Intentionally, a Mach reflection and a shock wave diffraction have been chosen to introduce these hydrodynamic flow structures in the non-reactive case. Both setups provide basic understanding for the physical interpretation of detonation waves under similar conditions that are studied in the last section of Chap. 7. Benchmark computations are carried out allowing a rough estimation of the high efficiency of the AMROC code.

In Chap. 6 all hydrodynamic transport schemes are very thoroughly tested within the operator splitting for the simplified detonation model of Chap. 3. We start with the validation of the different first-order upwind schemes within the splitting approach in one space dimension. A stable and an unstable test configuration near the limit of absolute stability are considered. It is demonstrated that artificial oscillations can corrupt the solution significantly, if accurate Riemann solvers are employed. The behavior is analogously to that already observed in Chap. 4 at strong shock waves and it is shown that the problem can be cured within the Roe scheme by adding numerical viscosity via the entropy fix. We demonstrate the enormous resolution improvements by second-order reconstruction and by utilizing quasi-stationary detonation configurations, whenever possible. Two-dimensional cellular structure simulations show the superiority of the hybrid Roe-type method especially in the multi-dimensional case. In the last section of the chapter, we employ our most efficient FV scheme to verify the parallel AMR algorithm with large-scale computations of three-dimensional cellular structure.

We apply the entire framework to simulate two- and three-dimensional unstable cellular detonation structures with detailed chemistry in Chap. 7. All simulations have been carried out with dynamically adaptive meshes with two to five refinement levels on recent parallel machines of moderate size, e.g. clusters of standard personal computer hardware. The regular cellular structure of a self-sustaining CJ detonation for $H_2 : O_2 : Ar$ with molar ratios $2 : 1 : 7$ at $T_0 = 298\,\mathrm{K}$ and $p_0 = 6.67\,\mathrm{kPa}$ in two- and three-dimension is simulated. The configuration is identical to the one

used in the test of Fig. 1.1 and a resolution study (11 to 45 Pts/l_{ig}) in the two-dimensional case verifies the estimation for the minimal necessary resolution. A reference solution with 45 Pts/l_{ig} is presented. This resolution is remarkably finer than any previously published results [138, 59, 78] and allows the detailed analysis of the reinitiation process at the end of a detonation cell. In particular, an unreacted region is formed. Its burning sends out hydrodynamic shock waves that influence the wave patterns around the triple points almost for 2/3 of the detonation cell. The given wave analysis is the most detailed one that has been presented so far [113, 138]. Further on, the CJ detonation is extended to three space dimensions. To our best knowledge, this computation (17 Pts/l_{ig}) is the only successful simulation of three-dimensional cellular detonation structure with detailed chemistry up to now. Finally, two complex two-dimensional problems are tackled with highly adaptive setups: the Mach reflection of a CJ detonation wave at a wall and its diffraction when propagating out of a rectangular tube into an unconfined region. Except an initial pressure of $p_0 = 10.0$ kPa the configuration in the unreacted gas is identical to the one previously used. All simulations are sufficiently resolved (20 to 25 Pts/l_{ig}) to display the development of the cellular structure under transient conditions. The numerical results are in perfect qualitative agreement with experimental observations [7, 163] and provide detailed insight into the complex thermo- and hydrodynamic combustion processes. In particular, the experimentally measured critical tube width of approximately 10 detonation cells in rectangular channels is reproduced in the diffraction simulations. Conclusions and an outlook on possible future work in the last chapter close the presentation.

Chapter 2

Governing Equations

Before we consider the chemically reactive Euler equations for mixtures of thermally perfect gases in Sec. 2.3, we recall briefly some elementary facts of the theory of hyperbolic conservation laws that is presented more in detail for instance in the text books of Godlewski and Raviart [82], Smoller [171], LeVeque [117] and Kröner [105]. Sec. 2.1 introduces generalized weak solutions and the concept of entropy. Sec. 2.2 summarizes the analysis of the one-dimensional Riemann Problem (RP) for the general homogeneous case. The exact solution of the linear RP in Sec. 2.2.1 is the basis of the linearized Riemann solver of Roe-type in Sec. 4.6.1.

Sec. 2.3 presents the reactive Euler equations in conservation-law form. In contrast to typical combustion text books, e.g. Williams [204] or Fickett and Davis [73], we discuss the equations from a mathematical point of view. We specify the space of admissible states and formulate typical boundary conditions. Sec. 2.3.2 gives a comprehensive description of the multi-component model. In Sec. 2.3.3 we introduce the implicit equation of state for mixtures of thermally perfect species and discuss its mathematical solvability in detail. The frozen speed of sound for the gas-mixture is derived in Sec. 2.3.4. Utilizing the deduced mixture quantities we prove the hyperbolicity and the rotational invariance of the generalized Euler equations in Sec. 2.3.5. The proof of hyperbolicity requires the Jacobians of the flux functions and the corresponding matrices of right eigenvalues and their inverses. These matrices, which are required for the construction of most upwind schemes in Chap. 4, are notated in appendix A.1. In Sec. 2.3.6 we analyze the homogeneous RP for generalized Euler equations for mixtures of thermally perfect gases[1]. Although its solution structure is in principle identical to the standard case of Euler equations for a single polytropic gas, no complete set of Riemann invariants can be derived [109, 108].

The source terms of detailed chemical reaction are introduced in Sec. 2.3.7. The last subsection mentions alternative formulations of the Euler equations and discusses briefly their equivalence with the chosen conservation-law form.

[1]The specific heats $c_{pi}(T)$, $c_{vi}(T)$ of thermally perfect gases are temperature-dependent.

2.1 Hyperbolic Conservation Laws with Source Terms

We consider systems of time-dependent nonlinear partial differential equations (PDEs) of first order that take the following structure:

$$\frac{\partial}{\partial t}\mathbf{q}(\mathbf{x},t) + \sum_{n=1}^{d} \frac{\partial}{\partial x_n}\mathbf{f}_n(\mathbf{q}(\mathbf{x},t)) = \mathbf{s}(\mathbf{q}(\mathbf{x},t))\,, \quad \mathbf{x} \in \mathbb{R}^d\,, \quad t > 0\,. \tag{2.1}$$

Herein, $t \in \mathbb{R}_0^+$ denotes the time and $\mathbf{x} = (x_1, \ldots, x_d)^T \in \mathbb{R}^d$ denotes a point in Cartesian coordinates. The vector-valued mapping $\mathbf{q} = \mathbf{q}(\mathbf{x}, t)$ from $D := \{(\mathbf{x}, t) \in \mathbb{R}^d \times \mathbb{R}_0^+\}$ into the space of *admissible* states $S \subset \mathbb{R}^M$ is called *vector of state*. The components of the vector of states are physical meaningful quantities, like mass, momentum or energy, that have to be conserved because of fundamental physical principles. The space of admissible states for generalized Euler equations will be discussed in detail in Sec. 2.3.

The vector-valued functions $\mathbf{f}_n(\mathbf{q}(\mathbf{x},t))$, $n = 1, \ldots, d$ and $\mathbf{s}(\mathbf{q}(\mathbf{x},t))$ are assumed to be continuously differentiable, i.e. $\mathbf{f}_n(\mathbf{q}), \mathbf{s}(\mathbf{q}) \in \mathrm{C}^1(S, \mathbb{R}^M)$. The functions $\mathbf{f}_n(\mathbf{q})$ are called *flux functions*, $\mathbf{s}(\mathbf{q})$ is a *source term*.

Definition 1 (Hyperbolicity). *Let $\mathbf{A}_n(\mathbf{q}) = \partial\mathbf{f}_n(\mathbf{q})/\partial\mathbf{q}$ denote the Jacobian matrix of flux function $\mathbf{f}_n(\mathbf{q})$. System (2.1) is called hyperbolic, if the matrix $\mathbf{A}(\mathbf{q},\nu) = \nu_1\mathbf{A}_1(\mathbf{q}) + \cdots + \nu_d\mathbf{A}_d(\mathbf{q})$ has M real eigenvalues $\lambda_1(\mathbf{q},\nu) \leq \ldots \leq \lambda_M(\mathbf{q},\nu)$ and M linear independent right eigenvectors $\mathbf{r}_m(\mathbf{q},\nu)$, $m = 1, \ldots, M$ defined by $\mathbf{A}(\mathbf{q},\nu)\,\mathbf{r}_m(\mathbf{q},\nu) = \lambda_m(\mathbf{q},\nu)\,\mathbf{r}_m(\mathbf{q},\nu)$ for all admissible states $\mathbf{q} \in S$ and $\nu = (\nu_1, \ldots, \nu_d) \in \mathbb{R}^d$ with $|\nu_1| + \cdots + |\nu_d| > 0$.*

In order to achieve unique solutions the hyperbolic system (2.1) must be augmented with initial conditions and appropriate boundary conditions, if the solution has to be restricted to a bounded subset $\Omega \subset \mathbb{R}^d$. The simplest problem is the Cauchy Problem, for which (2.1) holds true and initial conditions are specified by

$$\mathbf{q}(\mathbf{x}, 0) = \mathbf{q}_0(\mathbf{x})\,, \quad \mathbf{x} \in \mathbb{R}^d\,. \tag{2.2}$$

From the theory of hyperbolic conservation laws it is well-known that in the general case of nonlinear flux functions $\mathbf{f}_n(\mathbf{q})$ classical solutions, i.e. $\mathbf{q}(\mathbf{x},t) \in \mathrm{C}^1(D, S)$, of the Cauchy Problem (2.1), (2.2) exist only for small times, even for continuously differentiable initial data $\mathbf{q}_0(\mathbf{x}) \in \mathrm{C}^1(\mathbb{R}^d, S)$ [130, 105]. It is the inherent behavior of nonlinear hyperbolic conservation laws that smooth initial data may be steepened to discontinuities (see for instance [130] or [117] for scalar one-dimensional examples with $s \equiv \mathbf{0}$). Beyond the point of "wave breaking" classical solutions do not exist anymore and a more general formulation with less differentiability is required instead of (2.1).

2.1.1 Weak Solutions

The basic idea in order to define generalized weak solutions of (2.1), (2.2) is to multiply (2.1) by an appropriate test function $\varphi = \varphi(\mathbf{x}, t)$ and to integrate the result over the entire domain D.

Definition 2 (Weak solutions). *Let* $\mathbf{q}_0 \in \mathrm{L}^\infty_{loc}(\mathbb{R}^d, S)$. *A function* $\mathbf{q} \in \mathrm{L}^\infty_{loc}(D, S)$ *is called a weak solution of the Cauchy Problem (2.1), (2.2) if* $\mathbf{q}$ *satisfies*

$$\int_0^\infty \int_{\mathbb{R}^d} \left[\frac{\partial \varphi}{\partial t} \cdot \mathbf{q} + \sum_{n=1}^d \frac{\partial \varphi}{\partial x_n} \cdot \mathbf{f}_n(\mathbf{q}) - \varphi \cdot \mathbf{s}(\mathbf{q}) \right] d\mathbf{x}\, dt + \int_{\mathbb{R}^d} \varphi(\mathbf{x}, 0) \cdot \mathbf{q}_0(\mathbf{x})\, d\mathbf{x} = 0 \quad (2.3)$$

for any function $\varphi \in \mathrm{C}^1_0(D, S)$.

In Def. 2 L^∞_{loc} denotes the space of *locally* bounded measurable functions and C^1_0 is the space of continuously differentiable functions with compact support. See [82] for further explanations. Another integral form of (2.1) that may also be utilized to define weak solutions is

$$\int_\Omega \mathbf{q}(\mathbf{x}, t + \Delta t)\, d\mathbf{x} - \int_\Omega \mathbf{q}(\mathbf{x}, t)\, d\mathbf{x} + \sum_{n=1}^d \int_t^{t+\Delta t} \int_{\partial\Omega} \mathbf{f}_n(\mathbf{q}(\mathbf{o}, t))\, \sigma_n(\mathbf{o})\, d\mathbf{o}\, dt = \int_t^{t+\Delta t} \int_\Omega \mathbf{s}(\mathbf{q}(\mathbf{x}, t))\, d\mathbf{x}\,, \quad (2.4)$$

cf. [172]. Herein, σ_n denotes the n-th component of $\mathbf{n}$, the outward unit normal vector of $\partial\Omega$, the boundary of the problem domain Ω. Eq. (2.4) may be derived from expression (2.3) by utilizing

$$\bar{\varphi}(\mathbf{x}, t) = \begin{cases} \mathbf{1}\,, & (\mathbf{x}, t) \in \Omega \times [t, t + \Delta t]\,, \\ \mathbf{0}\,, & \text{otherwise} \end{cases}$$

as test function in (2.3). Formally, Def. 2 rules out $\bar{\varphi}$ as a valid test function, but note that $\bar{\varphi}$ may be approximated arbitrarily well by smooth functions satisfying $\varphi \in \mathrm{C}^1_0(D, S)$.

2.1.2 Entropy Solutions

The class of weak solutions of (2.1), (2.2) is in general to large to guarantee uniqueness (see [82] for an example). On the other hand, only one solution can be physically correct and this particular solution must be the limit $\lim_{\varepsilon \to 0} \mathbf{q}_\varepsilon = \mathbf{q}$ almost everywhere in D of the extended viscous system

$$\frac{\partial \mathbf{q}_\varepsilon}{\partial t} + \sum_{n=1}^d \frac{\partial \mathbf{f}_n(\mathbf{q}_\varepsilon)}{\partial x_n} - \varepsilon \sum_{n=1}^d \frac{\partial^2 \mathbf{q}_\varepsilon}{\partial x_n^2} = \mathbf{s}(\mathbf{q}_\varepsilon)\,, \quad \mathbf{x} \in \mathbb{R}^d\,, \quad t > 0 \quad (2.5)$$

with Cauchy initial data $\mathbf{q}_\varepsilon(\mathbf{x},0) = \mathbf{q}_{0\varepsilon}(\mathbf{x})$ for $\lim_{\varepsilon\to 0}\mathbf{q}_{0\varepsilon} = \mathbf{q}_0(\mathbf{x})$. System (2.5) is parabolic and we assume that a classical unique solution $\mathbf{q}_\varepsilon$ exists that is a C^2 function of $\mathbf{x}$ in $\mathbb{R}^d$ and a C^1 function of t in $\mathbb{R}^+$ for each $\varepsilon > 0$. Note, that for particular hyperbolic systems viscous extensions might exist which are physically more meaningful than Eq. (2.5). In particular for gas dynamics elaborated viscous extensions have been proposed. A brief overview of possible viscous extensions of the Euler equations oriented along the Navier-Stokes equations and their equivalence with (2.5) can be found in [82].

The definition of the physically relevant weak solution as the *vanishing viscosity limit* is appropriate for theoretical purposes, but it is inadequate for the construction of numerical methods. In practice, we want schemes that approximate the correct solution with minimal computational expense and do not reproduce the limiting process $\varepsilon \to 0$ numerically. The mathematical concept of entropy has been introduced to obtain criteria that ensure the approximation of the physically correct solution without any auxiliary viscous problems.

Definition 3 (Entropy). *Assume that S is convex. A twice continously differentiable convex function $\eta \in \mathrm{C}^2(S,\mathbb{R})$ is called an entropy of (2.1), if there exist continously differentiable entropy fluxes $\psi_n \in \mathrm{C}^1(S,\mathbb{R})$ that satisfy*

$$\frac{\partial\eta(\mathbf{q})}{\partial\mathbf{q}}^T \cdot \frac{\partial\mathbf{f}_n(\mathbf{q})}{\partial\mathbf{q}} = \frac{\partial\psi_n(\mathbf{q})}{\partial\mathbf{q}}^T, \quad n = 1,\dots,d \tag{2.6}$$

for all $\mathbf{q} \in S$.

Multiplying (2.1) by $(\partial\eta(\mathbf{q})/\partial\mathbf{q})^T$ and applying (2.6) yields the additional scalar conservation law

$$\frac{\partial\eta(\mathbf{q})}{\partial t} + \sum_{n=1}^{d}\frac{\partial\psi_n(\mathbf{q})}{\partial x_n} = \frac{\partial\eta(\mathbf{q})}{\partial\mathbf{q}}^T \cdot \mathbf{s}(\mathbf{q})\,. \tag{2.7}$$

From this equation a criterion separating the physically relevant solution from all weak solutions of (2.1) can be derived:

Theorem 1 (Entropy condition). *Assume that (2.1) admits an entropy $\eta(\mathbf{q})$ and entropy fluxes $\psi_n(\mathbf{q}), n = 1,\dots,d$. Let $\mathbf{q}$ be the limit of a sequence $(\mathbf{q}_\varepsilon)_\varepsilon$ of classical solutions of (2.5) almost everywhere in D, i.e. $\mathbf{q}_\varepsilon \to \mathbf{q}$ as $\varepsilon \to 0$ a.e. in D, where all $\mathbf{q}_\varepsilon$ are bounded by a constant $C > 0$ independent of ε by $\|\mathbf{q}_\varepsilon\|_{\mathrm{L}^\infty(D)} \le C$. Then $\mathbf{q}$ is a weak solution of (2.1), (2.2) and satisfies the entropy condition*

$$\frac{\partial\eta(\mathbf{q})}{\partial t} + \sum_{n=1}^{d}\frac{\partial\psi_n(\mathbf{q})}{\partial x_n} \le \frac{\partial\eta(\mathbf{q})}{\partial\mathbf{q}}^T \cdot \mathbf{s}(\mathbf{q}) \tag{2.8}$$

in the sense of distributions on $\mathbb{R}^d \times \mathbb{R}^+$.

Proof. [82].

Multiplying Eq. (2.8) by an appropriate test function φ and integration over D yields the supplementary condition (2.9) that admits an appropriate extension of Def. 2:

Definition 4 (Entropy solutions). *A weak solution* $\mathbf{q}$ *of the Cauchy Problem (2.1), (2.2) is called an entropy solution, if* $\mathbf{q}$ *satisfies*

$$\int_0^\infty \int_{\mathbb{R}^d} \left[\frac{\partial \varphi}{\partial t} \eta(\mathbf{q}) + \sum_{n=1}^d \frac{\partial \varphi}{\partial x_n} \psi_n(\mathbf{q}) - \varphi \, \frac{\partial \eta(\mathbf{q})}{\partial \mathbf{q}}^T \cdot \mathbf{s}(\mathbf{q}) \right] d\mathbf{x}\, dt + \int_{\mathbb{R}^d} \varphi(\mathbf{x}, 0)\, \eta(\mathbf{q}_0(\mathbf{x}))\, d\mathbf{x} \geq 0 \tag{2.9}$$

for all entropy functions $\eta(\mathbf{q})$ *and all scalar test functions* $\varphi \in \mathrm{C}_0^1(D, \mathbb{R}_0^+)$, $\varphi \geq 0$.

2.1.3 Jump Conditions

The most important subset of entropy solutions of the Cauchy Problem (2.1), (2.2) are solutions in the sense of distributions that are piecewise continuously differentiable and have discontinuous jumps along a finite number of smooth orientable surfaces Ξ in the $(\mathbf{x}, t)$-space. If the one-sided limits of $\mathbf{q}$ on both sides of Ξ are defined by $\mathbf{q}^\pm(\mathbf{x}, t) := \lim_{\bar{\varepsilon} \to 0, \bar{\varepsilon} > 0} \mathbf{q}((\mathbf{x}, t) \pm \bar{\varepsilon}\, \bar{\mathbf{n}})$ with $\bar{\mathbf{n}} := (\sigma_1, \ldots, \sigma_d, \sigma_t)^T$ denoting the outward unit normal to Ξ, the following important theorem can be derived:

Theorem 2 (Piecewise C^1 solutions and jump conditions). *Let* $\mathbf{q} : D \to S$ *be a piecewise* C^1 *function (in the above sense) and let there exist an entropy* $\eta \in \mathrm{C}^2(S, \mathbb{R})$ *and corresponding entropy fluxes* $\psi_n \in \mathrm{C}^1(S, \mathbb{R})$. *Then* $\mathbf{q}$ *is an entropy solution in the sense of distributions, if and only if* $\mathbf{q}$ *is a classical solution of (2.1) in the domains where* $\mathbf{q} \in \mathrm{C}^1(D,S)$ *that fulfills (2.2) almost everywhere and satisfies the Rankine-Hugoniot (RH) jump condition*

$$(\mathbf{q}^+ - \mathbf{q}^-)\, \sigma_t + \sum_{n=1}^d \left(\mathbf{f}_n(\mathbf{q}^+) - \mathbf{f}_n(\mathbf{q}^-) \right) \sigma_n = \mathbf{0} \tag{2.10}$$

and the jump inequality

$$(\eta(\mathbf{q}^+) - \eta(\mathbf{q}^-))\, \sigma_t + \sum_{n=1}^d \left(\psi_n(\mathbf{q}^+) - \psi_n(\mathbf{q}^-) \right) \sigma_n \leq 0 \tag{2.11}$$

along the surfaces of discontinuity.

Proof. [82].

2.1.4 Rotational Invariance

Some special systems, e.g. the Euler equations in Cartesian coordinates, are invariant under rotation in multiple space dimensions. This means that for each unit normal vector in space $\mathbf{n} := (\sigma_1, \ldots, \sigma_d)^T$ a rotation matrix $\mathbf{T} = \mathbf{T}(\sigma_1, \ldots, \sigma_d)$ exists such that

$$\sum_{n=1}^d \mathbf{f}_n(\mathbf{q})\, \sigma_n = \mathbf{T}^{-1} \mathbf{f}_1(\mathbf{T}\mathbf{q}) \tag{2.12}$$

holds true. If we denote the axis in the direction of $(\sigma_1, \ldots, \sigma_d)^T$ by $\tilde{x}$ and the rotated vector of state by $\tilde{\mathbf{q}} = \mathbf{T}\mathbf{q}$ and assume the source term to be invariant under rotation, i.e. $\mathbf{s}(\mathbf{q}) \equiv \mathbf{s}(\tilde{\mathbf{q}}) \equiv \mathbf{T}\mathbf{s}(\mathbf{q})$, then it is a straight-forward task to show by inserting (2.12) into (2.4) that the conservation law in the rotated coordinate system simplifies to

$$\frac{\partial}{\partial t}\tilde{\mathbf{q}}(\tilde{\mathbf{x}}, t) + \frac{\partial}{\partial \tilde{x}}\mathbf{f}_1(\tilde{\mathbf{q}}(\tilde{\mathbf{x}}, t)) = \mathbf{s}(\tilde{\mathbf{q}}(\tilde{\mathbf{x}}, t))\,, \quad \tilde{\mathbf{x}} \in \mathbb{R}^d\,, \quad t > 0\,. \tag{2.13}$$

If we further assume a rotational invariant entropy $\eta(\mathbf{q}) \equiv \eta(\mathbf{T}\mathbf{q})$, we can easily transform (2.7) into the rotated coordinate system. By comparing the result to (2.7) we obtain the relation

$$\sum_{n=1}^{d} \psi_n(\mathbf{q})\,\sigma_n = \psi_1(\mathbf{T}\mathbf{q}) \tag{2.14}$$

for the entropy fluxes.

2.2 The Homogeneous Riemann Problem

We consider the Riemann Problem (RP) for Eq. (2.1) with $\mathbf{s} \equiv \mathbf{0}$. A Riemann Problem is a Cauchy Problem for (2.1) with initial data that is discontinuous along a d-dimensional hyper plane, i.e.

$$\tilde{\mathbf{q}}_0(\tilde{\mathbf{x}}) = \begin{cases} \tilde{\mathbf{q}}_L\,, & \tilde{x}_1 < 0 \\ \tilde{\mathbf{q}}_R\,, & \tilde{x}_1 > 0 \end{cases}\,, \tag{2.15}$$

where $\tilde{x}_1$ denotes the axis in a rotated Cartesian coordinate system that is orthogonal to the surface of discontinuity. We assume the validity of the rotational invariance property and restrict our attention to systems of the form

$$\frac{\partial}{\partial t}\tilde{\mathbf{q}}(\tilde{\mathbf{x}}, t) + \frac{\partial}{\partial \tilde{x}_1}\mathbf{f}_1(\tilde{\mathbf{q}}(\tilde{\mathbf{x}}, t)) = \mathbf{0}\,, \quad \tilde{\mathbf{x}} \in \mathbb{R}^d\,, \quad t > 0\,. \tag{2.16}$$

As the solution of (2.16), (2.15) is quasi-one-dimensional and depends only on $\tilde{x}_1$ and t, it obviously suffices to study the RP for general one-dimensional hyperbolic conservation-laws, which we write in short as

$$\frac{\partial}{\partial t}\mathbf{q}(x, t) + \frac{\partial}{\partial x}\mathbf{f}(\mathbf{q}(x, t)) = \mathbf{0}\,, \quad x \in \mathbb{R}, \quad t > 0\,. \tag{2.17}$$

The solution structure of the RP in one space dimension for nonlinear hyperbolic conservation laws without source terms is very well understood. In the following, some of the most important results will be reviewed. Detailed analysis can be found for instance in [171] or in [82].

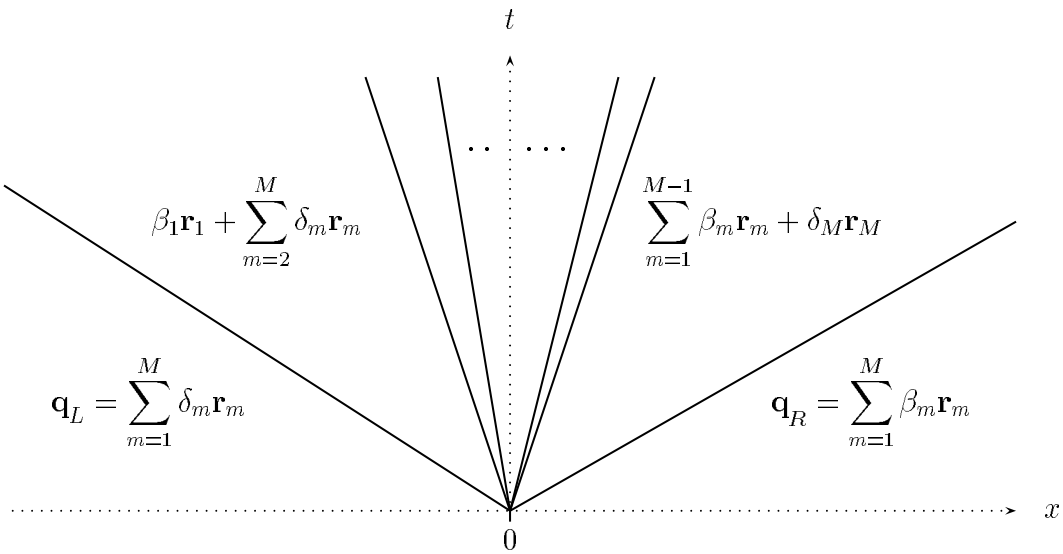

Figure 2.1: Solution $\mathbf{q}(x,t)$ of the linear Riemann Problem in the x-t plane [117].

2.2.1 Linear Systems

As an introduction we consider the RP for the linear hyperbolic equation

$$\frac{\partial}{\partial t}\mathbf{q}(x,t) + \mathbf{A}\frac{\partial}{\partial x}\mathbf{q}(x,t) = \mathbf{0}\,, \quad x \in \mathbb{R}\,, \quad t > 0 \tag{2.18}$$

for systems with $\mathbf{q} : \mathbb{R} \times \mathbb{R}^+ \mapsto \mathbb{R}^M$. $\mathbf{A}$ is a constant matrix and for simplicity we assume that $\mathbf{A}$ has M *distinct* real eigenvalues $\lambda_1 < \cdots < \lambda_M$ with M linear independent right eigenvectors $\mathbf{r}_m$, $m = 1, \ldots, M$. If the left state $\mathbf{q}_L$ and the right state $\mathbf{q}_R$ are decomposed in terms of the right eigenvectors by

$$\mathbf{q}_L = \sum_{m=1}^{M} \delta_m \mathbf{r}_m\,, \; \mathbf{q}_R = \sum_{m=1}^{M} \beta_m \mathbf{r}_m \Rightarrow \mathbf{q}_R - \mathbf{q}_L = \sum_{m=1}^{M} (\beta_m - \delta_m)\mathbf{r}_m = \sum_{m=1}^{M} a_m \mathbf{r}_m\,, \tag{2.19}$$

the exact solution of the RP reads

$$\mathbf{q}(x,t) = \mathbf{q}_L + \sum_{\lambda_m < x/t} a_m \mathbf{r}_m = \mathbf{q}_R - \sum_{\lambda_m \geq x/t} a_m \mathbf{r}_m = \sum_{\lambda_m \geq x/t} \delta_m \mathbf{r}_m + \sum_{\lambda_m < x/t} \beta_m \mathbf{r}_m\,. \tag{2.20}$$

The complete derivation can be found for instance in [117]. The solution structure is displayed in Fig. 2.1. The initial discontinuity breaks up into M discontinuities that separate $M+1$ regions of constant state. The discontinuities lie on characteristic lines that are given by the ordinary differential equations

$$\frac{dx}{dt} = \lambda_m\,, \quad x(0) = 0\,, \quad m = 1, \ldots, M\,.$$

Each characteristic separates two constant states differing exactly by a scalar multiple of the corresponding right eigenvector $\mathbf{r}_m$. We call the change over the mth characteristic field the m-simple wave. The m-simple wave becomes the weak solution of the entire RP for (2.18), if the two constant values abutting the mth characteristic are used as initial data. In this case, the solution simply would be

$$\mathbf{q}^s(\mathbf{x}, t) = \begin{cases} \mathbf{q}_L\,, & x < \sigma t\,, \\ \mathbf{q}_R\,, & x > \sigma t\,, \end{cases} \tag{2.21}$$

with $\sigma = \lambda_m$. All simple wave solutions (2.21) satisfy the Rankine-Hugoniot condition (2.10), which we now express in one space dimension by employing the notations $\Delta\mathbf{q} := \mathbf{q}_R - \mathbf{q}_L$, $\Delta\mathbf{f}(\mathbf{q}) := \mathbf{f}(\mathbf{q}_R) - \mathbf{f}(\mathbf{q}_L)$ as

$$\sigma\Delta\mathbf{q} = \Delta\mathbf{f}(\mathbf{q})\,. \tag{2.22}$$

2.2.2 Nonlinear Systems

Like in the linear case, weak solutions of the RP for Eq. (2.17) are self-similar, i.e. a function $\mathbf{v}$ exists, such that $\mathbf{q}(x,t) \equiv \mathbf{v}(x/t)$. But the characteristic lines

$$\frac{dx}{dt} = \lambda_m(\mathbf{q}(x,t))\,, \quad x(0) = 0\,, \quad m = 1, \ldots, M$$

now depend on the solution $\mathbf{q}$ and simple wave solutions need not be discontinuous.

Definition 5 (Characterization of the characteristic fields). *The mth characteristic field is said to be genuinely nonlinear, if the mth eigenvalue $\lambda_m(\mathbf{q})$ and its corresponding right eigenvector $\mathbf{r}_m(\mathbf{q})$ satisfy*

$$\frac{\partial\lambda_m(\mathbf{q})}{\partial\mathbf{q}}^T \cdot \mathbf{r}_m(\mathbf{q}) \neq 0\,,$$

and it is said to be linearly degenerate, if they satisfy

$$\frac{\partial\lambda_m(\mathbf{q})}{\partial\mathbf{q}}^T \cdot \mathbf{r}_m(\mathbf{q}) = 0$$

for all admissible states $\mathbf{q} \in S$.

The only simple wave solution in a linearly degenerate field is a *contact discontinuity*. The solution is of the form (2.21) and satisfies (2.22) across the discontinuity with

$$\sigma = \lambda_m(\mathbf{q}_L) = \lambda_m(\mathbf{q}_R)\,.$$

A genuinely nonlinear field admits discontinuous *shock waves* and smooth *rarefaction waves*. The simple wave solution of a shock wave is also of the form (2.21) and

satisfies (2.22) along the discontinuity, but the value $\sigma = \lambda_m(\mathbf{q}^s)$ now depends on the solution. The simple wave solution of a rarefaction wave is

$$\mathbf{q}^s(\mathbf{x},t) = \begin{cases} \mathbf{q}_L\,, & x < \lambda_m(\mathbf{q}_L)\,t\,, \\ \mathbf{v}(x/t)\,, & \lambda_m(\mathbf{q}_L)\,t \le x \le \lambda_m(\mathbf{q}_R)\,t\,, \\ \mathbf{q}_R\,, & x > \lambda_m(\mathbf{q}_R)\,t\,, \end{cases} \tag{2.23}$$

with $\mathbf{v}(\lambda_m(\mathbf{q}_L)) = \mathbf{q}_L$ and $\mathbf{v}(\lambda_m(\mathbf{q}_R)) = \mathbf{q}_R$. The decision, which of these two different weak solutions is the physically correct entropy solution can be taken by checking whether the shock wave satisfies the jump inequality (2.11). Analogously to (2.22) Eq. (2.11) reduces in one space dimension to

$$\sigma\Delta\eta(\mathbf{q}) \ge \Delta\psi(\mathbf{q})\,. \tag{2.24}$$

A shock wave satisfying (2.24) is called admissible. Unfortunately, Eq. (2.24) is not applicable in many practical cases, because it requires the explicit knowledge of an entropy function. A convenient alternative here are the Lax entropy conditions:

Definition 6 (Lax entropy conditions). *A discontinuity in the mth characteristic field satisfies the Lax entropy conditions, if either*

$$\begin{cases} \lambda_m(\mathbf{q}_R) < \sigma < \lambda_{m+1}(\mathbf{q}_R) \\ \lambda_{m-1}(\mathbf{q}_L) < \sigma < \lambda_m(\mathbf{q}_L) \end{cases}\,, \tag{2.25}$$

if the mth field is genuinely nonlinear, or

$$\lambda_m(\mathbf{q}_L) = \sigma = \lambda_m(\mathbf{q}_R) \tag{2.26}$$

if the mth field is linearly degenerate, is satisfied.

For sufficiently small discontinuous jumps $\Delta\mathbf{q}$ the Lax entropy conditions can be shown to be equivalent to (2.24). See [82] for the proof. For shock waves Liu's entropy condition

$$\lambda_m(\mathbf{q}_R) < \sigma < \lambda_m(\mathbf{q}_L) \tag{2.27}$$

can be shown to be equivalent to (2.25).

The following theorem describes the structure of entropy solutions of the general nonlinear RP just as a composition of the three different simple waves:

Theorem 3 (Solution of the RP). *For all admissible states $\mathbf{q}_L \in S$ there exists a neighborhood ϑ of $\mathbf{q}_L$ in S with the following property: If $\mathbf{q}_R$ belongs to ϑ, the RP for the nonlinear system (2.17) has an entropy solution that consists of constant states separated by rarefaction waves, admissible shock waves or contact discontinuities.*

Proof. [82].

Important for the practical solution of the RP is the knowledge of equation-specific functions that are called Riemann invariants.

Definition 7 (Riemann invariants). *A smooth function $\varpi : S \to \mathbb{R}$ is called a m-Riemann invariant, if it satisfies*

$$\frac{\partial \varpi(\mathbf{q})}{\partial \mathbf{q}}^T \cdot \mathbf{r}_m(\mathbf{q}) = 0 \tag{2.28}$$

for all admissible states $\mathbf{q} \in S$.

A Riemann invariant is constant along the integral curves of $\mathbf{r}_m$

$$\frac{d\mathbf{v}(\xi)}{d\xi} = \mathbf{r}_m(\mathbf{v}(\xi)) \ ,$$

because the necessary condition

$$\frac{d}{d\xi}\varpi(\mathbf{v}(\xi)) = \frac{\partial \varpi(\mathbf{q})}{\partial \mathbf{q}}^T \cdot \frac{dv(\xi)}{d\xi} = 0$$

follows directly from the definition (2.28). In the solution of the general nonlinear RP an m-Riemann invariant remains constant across the mth simple wave solution, because the simple wave solutions are integral curves of the corresponding eigenvector $\mathbf{r}_m$ and satisfy $\mathbf{q}_m(x,t) = \mathbf{v}_m(\xi)$ with $\xi = x/t$ (see [82] for details).

2.3 Reactive Multi-Component Euler Equations

We now consider the Euler equations for a mixture of K different thermally perfect gaseous species with chemically reactive source terms. These equations can be written as a system of hyperbolic conservation laws of the form of Eq. (2.1).[2] For a detailed derivation of the equations from physical conservation principles we refer to the book of Williams [204]. We specify the space of physically admissible states and derive various important mixture properties. The complex equation of state for thermally perfect gas-mixtures is introduced.

Vector of State

In d space dimensions the vector of state of conserved quantities $\mathbf{q} = \mathbf{q}(\mathbf{x}, t)$ of the multi-component Euler equations with K species has $K + d + 1$ components. We choose the following form for $\mathbf{q}$:

$$\mathbf{q}(\mathbf{x}, t) = (\rho_1, \ldots, \rho_K, m_1, \ldots, m_d, \bar{E})^T = (\rho_1, \ldots, \rho_K, \rho u_1, \ldots, \rho u_d, \rho E)^T \tag{2.29}$$

The partial density of each species is denoted by ρ_i. The sum of partial densities

$$\rho = \sum_{i=1}^{K} \rho_i \tag{2.30}$$

[2]Other formulations are possible. Note, that conservative and non-conservative formulations are equivalent only for classical solutions (compare Sec. 2.3.8).

is called the total density of the mixture. It follows from the physical principle of mass conservation that ρ is a conserved quantity, too. While some of the partial densities $\rho_i \in \mathbb{R}_0^+$ are allowed to vanish, a first restriction on $\mathbf{q}(\mathbf{x}, t)$ to be admissible is $\rho \in \mathbb{R}^+$. The products of the velocities in the three coordinate directions $u_n \in \mathbb{R}$ and the total density ρ are called the momentum densities $m_n \in \mathbb{R}$. The total energy density is denoted by $\bar{E} \in \mathbb{R}^+$. It may never vanish imposing the further restriction $E \in \mathbb{R}^+$ on the total energy per unit mass. The total energy is the sum of internal and kinetic energy, i.e.

$$E = e + \frac{1}{2}\sum_{n=1}^{d} u_n^2 = e + \frac{\mathbf{u}^2}{2} \tag{2.31}$$

or in terms of the conserved quantities

$$\bar{E} = \rho e + \frac{1}{2\rho}\sum_{n=1}^{d} m_n^2 = \rho e + \frac{\mathbf{m}^2}{2\rho} \ .$$

Since Eq. (2.31) has to be valid for all admissible states, it follows immediately that the internal energy per unit mass e has to be positive and real, too.

Flux Functions

In terms of the conserved quantities ρ_i, $m_n = \rho u_n$ and $\bar{E} = \rho E$ the multi-component Euler equations are a system of PDEs in the form Eq. (2.1). The flux functions are

$$\mathbf{f}_n(\mathbf{q}) = (\rho_1 u_n, \ldots, \rho_K u_n, \rho u_1 u_n + \delta_{1n} p, \ldots, \rho u_d u_n + \delta_{dn} p, u_n(\rho E + p))^T \tag{2.32}$$

for $n = 1, \ldots, d$. Herein, p denotes the hydrostatic pressure. The function $p = p(\mathbf{q}) : S \mapsto \mathbb{R}^+$ is called the equation of state. Note, that the Kronecker-Symbol δ_{jn} is defined as $\delta_{jn} = 1$ for $j = n$ and $\delta_{jn} = 0$ for $j \neq n$. The basic thermodynamic relation

$$\rho h = \rho e + p \tag{2.33}$$

defines the internal enthalpy per unit mass $h \in \mathbb{R}^+$. By inserting (2.31) into Eq. (2.33), i.e.

$$\rho E + p = \rho e + \frac{\mathbf{m}^2}{2\rho} + p = \rho h + \frac{\mathbf{m}^2}{2\rho} = \rho H \ ,$$

the total enthalpy per unit mass $H \in \mathbb{R}^+$ is introduced. The last component of $\mathbf{f}_n(\mathbf{q})$ may also be expressed in terms of this quantity as $u_n \rho H$.

2.3.1 Boundary Conditions

The solution of the reactive Euler equations on bounded domains $\Omega \in \mathbb{R}^d$ requires appropriate boundary conditions on $\partial\Omega$. In practice, four different types of boundary conditions can occur.

Symmetry Planes or Impermeable Walls

Many flow problems are symmetric with respect to one or more planes. Along a symmetry plane the component of the velocity vector normal to the boundary is required to vanish, i.e.

$$\mathbf{u} \cdot \mathbf{n} = 0 \; . \tag{2.34}$$

If we use condition (2.34) to simplify the component of the flux vector $(\mathbf{f}_1, \ldots, \mathbf{f}_d)^T$ normal to the boundary [172], we obtain for the boundary flux

$$(\mathbf{f}_1, \ldots, \mathbf{f}_d)^T \cdot \mathbf{n} = \sum_{n=1}^{d} \mathbf{f}_n(\mathbf{q})\, \sigma_n = (0, \ldots, 0, p\,\sigma_1, \ldots, p\,\sigma_d, 0)^T \; . \tag{2.35}$$

Since the Euler equations describe the motion of *inviscid* fluid flow, the boundary condition at an impermeable wall is identical to (2.34). For this reason, wall and symmetry boundaries are often said to be *reflective* in the context of Euler equations.

Inlet and Outlet

Finite computational domains require in- and outflow boundaries. Unfortunately, their accurate mathematical treatment is quite difficult. Up to now, it is unclear in general, which in- and outflow boundary conditions lead to well-posed problems for Euler equations [172].

In practice, Dirichlet boundary conditions are usually applied at an inlet, while the von Neumann boundary condition

$$\frac{\partial \mathbf{q}}{\partial \mathbf{n}} = \mathbf{0} \tag{2.36}$$

should be satisfied at an outlet. Outflow boundaries are also called *transparent* or *transmissive*.

2.3.2 Mixture Properties

We assume that the multi-component gaseous flow is in thermal equilibrium, which means that the same absolute temperature $T \in \mathbb{R}^+$ can be used for all K species. Each species is treated as an ideal gases and for each partial pressure $p_i \in \mathbb{R}_0^+$ the ideal gas law

$$p_i = \rho_i \frac{\mathcal{R}}{W_i} T = \rho_i\, R_i\, T \tag{2.37}$$

applies. Note, that the universal gas constant is denoted by $\mathcal{R}$, while R_i and $W_i \in \mathbb{R}^+$ are the specific gas constant and the specific molecular weight of a single species. According to Dalton's law the mixture itself has the physical properties of an ideal gas and the total hydrostatic pressure p is given by

$$p = \sum_{i=1}^{K} p_i \; . \tag{2.38}$$

Every physical quantity that can be evaluated for a single species consequently has a multi-component analogue. In the following, we introduce the appropriate algebraic model that allows the computation of all mixture properties without physical contradictions. Similar comprehensive descriptions have been given for example by Williams [204] and by Fedkiw et al. [71].

Mass and Mole Fractions

The ratio of the partial densities with respect to the density of the mixture

$$Y_i := \frac{\rho_i}{\rho} \tag{2.39}$$

are the mass fractions. For the mass fractions the equation $\sum_{i=1}^{K} Y_i = 1$ holds true. Further important quantities are the species molar concentrations per unit volume C_i. They are evaluated directly from the partial densities as

$$C_i = \frac{\rho_i}{W_i} = \rho \frac{Y_i}{W_i} \tag{2.40}$$

and are often utilized to evaluate chemical production rates. The concentrations are used to define mole fractions X_i as

$$X_i := \frac{C_i}{\sum_{j=1}^{K} C_j} \ . \tag{2.41}$$

For the sum of the mole fractions $\sum_{i=1}^{K} X_i = 1$ holds true. With definition (2.41) the mean molecular weight for the mixture W is easily found to be

$$W = \sum_{i=1}^{K} X_i \, W_i \ . \tag{2.42}$$

Replacing X_i in (2.42) with (2.41) and inserting (2.40) leads to the further expression

$$W = \left(\sum_{i=1}^{K} Y_i \, W_i \right)^{-1} \ . \tag{2.43}$$

If we insert expression (2.40) into (2.41) and apply relation (2.43), we obtain the elementary relation

$$X_i = Y_i \frac{W}{W_i} \ . \tag{2.44}$$

Enthalpy and Internal Energy

Each gaseous species is assumed to be a *thermally perfect* gas. In this case, the specific heats at constant pressure and volume, $c_{pi} = c_{pi}(T)$ and $c_{vi} = c_{vi}(T)$, are

functions of the temperature only. The enthalpies and internal energies per unit mass are written as

$$h_i(T) = h_i^0 + \int_{T^0}^{T} c_{pi}(s)ds\,, \qquad e_i(T) = h_i^0 + \int_{T^0}^{T} c_{vi}(s)ds \tag{2.45}$$

with h_i^0 called the *heat of formation* at the reference temperature T^0. The functions $c_{pi}(T)$, $c_{vi}(T)$ are usually approximated by polynomials of degree 4 of the form

$$c_{pi}(T) = \frac{\mathcal{R}}{W_i}\left(a_{1i} + a_{2i}T + a_{3i}T^2 + a_{4i}T^3 + a_{5i}T^4\right) \tag{2.46}$$

that are valid within a restricted temperature range, e.g. from 300 K to 5000 K. The constants a_{ji} and h_i^0 can be taken from various thermodynamic data bases [183, 103]. For specific enthalpy and internal energy of the mixture the relations

$$h(Y_1,\ldots,Y_K,T) = \sum_{i=1}^{K} Y_i\, h_i(T)\,, \quad e(Y_1,\ldots,Y_K,T) = \sum_{i=1}^{K} Y_i\, e_i(T) \tag{2.47}$$

hold true. Employing (2.45) and (2.47) the specific heats for the mixture are found to be

$$c_p(Y_1,\ldots,Y_K,T) = \frac{\partial h}{\partial T} = \sum_{i=1}^{K} Y_i\, c_{pi}(T)\,, \quad c_v(Y_1,\ldots,Y_K,T) = \frac{\partial e}{\partial T} = \sum_{i=1}^{K} Y_i\, c_{vi}(T)\,. \tag{2.48}$$

Since e and h have to be positive and non-zero, the inequalities $e_i(T) > 0$ and $h_i(T) > 0$ always have to be satisfied.

Specific Gas Constant and Adiabatic Exponent

With the specific heats for the mixture (2.48) the ideal-gas relations

$$R_i = \frac{\mathcal{R}}{W_i} = c_{pi}(T) - c_{vi}(T)\,, \qquad \gamma_i(T) = \frac{c_{pi}(T)}{c_{vi}(T)} \tag{2.49}$$

that apply to the specific gas constant R_i and the adiabatic exponent $\gamma_i(T)$ of a single species, carry over directly to the corresponding properties for the mixture as

$$R(Y_1,\ldots,Y_K) = \frac{\mathcal{R}}{W(Y_1,\ldots,Y_K)} = c_p(Y_1,\ldots,Y_K,T) - c_v(Y_1,\ldots,Y_K,T) \tag{2.50}$$

and

$$\gamma(Y_1,\ldots,Y_K,T) = \frac{c_p(Y_1,\ldots,Y_K,T)}{c_v(Y_1,\ldots,Y_K,T)}\,. \tag{2.51}$$

Note, that the inequality $c_{pi} > c_{vi} > 0$, which results for ideal gases from thermodynamical stability considerations, also applies to the mixture as $c_p > c_v > 0$. Like for each species, the relations $R > 0$ and $\gamma > 1$ are satisfied for all admissible states of the mixture. A useful relation for the adiabatic exponents is

$$\gamma - 1 = \left(\sum_{i=1}^{K} \frac{X_i}{\gamma_i - 1}\right)^{-1}\,. \tag{2.52}$$

2.3.3 Equation of State

We assume the existence of a C^1 mapping $\psi : S \mapsto \mathbb{R}$, such that the relation $\psi(\mathbf{q}) = T$ holds true for all admissible states $\mathbf{q}$. Such a mapping allows the evaluation of the unknown temperature T from the conserved quantities, and the total hydrodynamic pressure $p = \acute{p}(\rho_1, \ldots, \rho_K, T) \in \mathbb{R}^+$ could be evaluated easily from (2.38) as sum of all partial pressures $p_i = p_i(\rho_i, T) \in \mathbb{R}_0^+$ given by Eq. (2.37), i.e.

$$p = \acute{p}(\rho_1, \ldots, \rho_K, T) = \sum_{i=1}^{K} p_i(\rho_i, T) = \sum_{i=1}^{K} \rho_i \, R_i \, T = \mathcal{R}T \sum_{i=1}^{K} \frac{\rho_i}{W_i} = \rho \frac{\mathcal{R}}{W} T = \rho \, R \, T \; . \tag{2.53}$$

Relation (2.53) is called *thermal* equation of state. Obviously, it is the proposed ideal-gas law for the mixture. To make use of (2.53), the existence of the mapping ψ has to be proven.

Evaluation of the Temperature

Inserting the total specific enthalpy from (2.47) into the basic thermodynamic relation $p = \rho h - \rho e$ gives the following equation for the hydrostatic pressure:

$$p = \check{p}(\rho_1, \ldots, \rho_K, e, T) = \sum_{i=1}^{K} \rho_i \, h_i(T) - \rho e \tag{2.54}$$

We insert Eq. (2.31) into Eq. (2.54) and express it in terms of the conserved variables as

$$p = \check{p}(\rho_1, \ldots, \rho_K, m_1, \ldots, m_d, \bar{E}, T) = \sum_{i=1}^{K} \rho_i \, h_i(T) - \bar{E} + \frac{\mathbf{m}^2}{2\rho} \; . \tag{2.55}$$

By setting (2.53) equal to (2.55) the implicit equation

$$\varphi(\mathbf{q}, T) := \sum_{i=1}^{K} \rho_i \, h_i(T) - \bar{E} + \frac{\mathbf{m}^2}{2\rho} - \mathcal{R}T \sum_{i=1}^{K} \frac{\rho_i}{W_i} = 0 \; . \tag{2.56}$$

is derived. It allows the computation of the temperature T from the vector of conserved quantities $\mathbf{q}$.

Proposition 1 (Solvability of the implicit temperature-equation). *A mapping $\psi \in C^1(S, \mathbb{R})$ exists, such that $\psi(\mathbf{q}) = T$ solves the Eq. $\varphi(\mathbf{q}, T) = 0$ on $S \times \mathbb{R}$ with $\varphi : S \times \mathbb{R} \mapsto \mathbb{R}$ defined in Eq. (2.56).*

Proof. The proof of the proposition is a direct application of the inverse mapping theorem (see for instance [60]). Obviously $\varphi : S \mapsto \mathbb{R}$ is a C^1 mapping. The derivative of $\varphi(\mathbf{q}, T)$ with respect to T reads

$$\varphi'(\mathbf{q}, T) = \frac{\partial \varphi(\mathbf{q}, T)}{\partial T} = \sum_{i=1}^{K} \rho_i \, c_{pi} - \mathcal{R} \sum_{i=1}^{K} \frac{\rho_i}{W_i} = \rho \sum_{i=1}^{K} Y_i \, (c_{pi} - R_i) = \rho \sum_{i=1}^{K} Y_i \left(\frac{R_i}{\gamma_i - 1} \right) \tag{2.57}$$

Replacing Y_i with X_i according to (2.44) and applying relation (2.52) simplifies the final expression of (2.57) to

$$\varphi'(\mathbf{q}, T) = \frac{\rho R}{\gamma - 1} \,. \tag{2.58}$$

As seen in the preceding section, the adiabatic exponent of the mixture γ is always greater than 1 and therefore $\varphi'(\mathbf{q}, T) > 0$ always holds true. Hence, $\varphi'(\mathbf{q}, T)$ is non-singular for all admissible states and the inverse mapping theorem ensures the proposed existence of the C^1 mapping $\psi : S \mapsto \mathbb{R}$ that solves $\psi(\mathbf{q}) = T$. ■

Proposition 1 allows us to drop $T = \psi(\rho_1, \ldots, \rho_K, m_1, \ldots, m_d, \bar{E})$ from the list of arguments of (2.55). Nevertheless, the computation of T utilizing the implicit equation (2.56) is unavoidable in our model, whenever the hydrostatic pressure p is not known. Prop. 1 only states the existence of the mapping $\psi(\mathbf{q}) = T$, but due to the temperature-dependency of the specific heats $c_{pi}(T)$, $c_{vi}(T)$ this mapping is not known explicitly in general. Only in the special case of *calorically perfect* gases, for which c_{pi}, c_{vi} are constant, the mapping $\psi(\mathbf{q}) = T$ can be found and the explicit equation of state

$$p = (\gamma(Y_1, \ldots, Y_K) - 1) \left(\bar{E} - \frac{\mathbf{m}^2}{2\rho} - \sum_{i=1}^{K} \rho_i h_i^0 \right) \tag{2.59}$$

can be derived. A calorically perfect gas with zero heat of formation h_i^0 is often said to be *polytropic*. For a single polytropic gas Eq. (2.59) simplifies to the well-known equation of state $p = (\gamma - 1)(\bar{E} - \mathbf{m}^2/(2\rho))$. This is the standard case, which is discussed in detail for the Euler equations in multiple text books (see for instance [171, 82, 187]).

Derivatives of the Hydrostatic Pressure

The partial derivatives of the hydrostatic pressure p with respect to the conserved variables $\rho_1, \ldots, \rho_K, m_1, \ldots, m_d, \bar{E}$ are necessary for the derivation of the speed of sound and for computation of the Jacobians of the flux functions. The partial derivative of p with respect to Y_i has to be known to evaluate the thermicity in the primitive variable formulation of Sec. 2.3.8. Since the temperature $T = T(\rho_1, \ldots, \rho_K, m_1, \ldots, m_d, \bar{E})$ itself is a function of the conserved quantities, the thermal equation of state (2.53) and Eq. (2.55) have to be utilized together to eliminate unwanted partial derivatives of T. The partial derivatives of $p = \acute{p}(\rho_1, \ldots, \rho_K, T)$ and $p = \check{p}(\rho_1, \ldots, \rho_K, m_1, \ldots, m_d, \bar{E})$ are

$$\begin{aligned}
\frac{\partial \acute{p}}{\partial \rho_i} &= R_i T + \rho R \frac{\partial T}{\partial \rho_i} \,, & \frac{\partial \check{p}}{\partial \rho_i} &= h_i + \rho c_p \frac{\partial T}{\partial \rho_i} - \frac{\mathbf{u}^2}{2} \,, \\
\frac{\partial \acute{p}}{\partial m_n} &= \rho R \frac{\partial T}{\partial m_n} \,, & \frac{\partial \check{p}}{\partial m_n} &= \frac{m_n}{\rho} + \rho c_p \frac{\partial T}{\partial m_n} \,, \\
\frac{\partial \acute{p}}{\partial \bar{E}} &= \rho R \frac{\partial T}{\partial \bar{E}} \,, & \frac{\partial \check{p}}{\partial \bar{E}} &= \frac{c_p}{R} \frac{\partial T}{\partial \bar{E}} - 1 \,,
\end{aligned}$$

$$\frac{\partial \acute{p}}{\partial Y_i} = \rho R_i T + \rho R \frac{\partial T}{\partial Y_i} , \qquad \frac{\partial \check{p}}{\partial Y_i} = \rho h_i + \rho c_p \frac{\partial T}{\partial Y_i} .$$

Combination of these relations allows the elimination of the partial derivatives of T. Useful partial derivatives of p with respect to the conserved quantities $\rho_1, \ldots, \rho_K$, $m_1, \ldots, m_d$, $\bar{E}$ and with respect to Y_i are found to be

$$\frac{\partial p}{\partial \rho_i} = \frac{R}{R - c_p}\left(h_i - \frac{\mathbf{u}^2}{2}\right) - \frac{c_p}{R - c_p} R_i T = \bar{\gamma}\left(\frac{\mathbf{u}^2}{2} - h_i\right) + \gamma R_i T =: \phi_i , \tag{2.60}$$

$$\frac{\partial p}{\partial m_n} = -\bar{\gamma}\frac{m_n}{\rho} = -\bar{\gamma} u_n , \quad \frac{\partial p}{\partial \bar{E}} = \gamma - 1 =: \bar{\gamma} , \quad \frac{\partial p}{\partial Y_i} = \gamma \rho R \left(\frac{WT}{W_i} - \frac{h_i}{c_p}\right) . \tag{2.61}$$

Derivatives of the Temperature

If we replace the partial derivatives of $\acute{p}$ with respect to the conserved quantities by the expressions of (2.60) and (2.61), we derive the following partial derivatives of the temperature T:

$$\frac{\partial T}{\partial \rho_i} = \frac{\phi_i - R_i T}{\rho R} , \quad \frac{\partial T}{\partial m_n} = -\frac{\bar{\gamma} u_n}{\rho R} , \quad \frac{\partial T}{\partial \bar{E}} = \frac{\bar{\gamma}}{\rho R} . \tag{2.62}$$

2.3.4 Speed of Sound

The appropriate speed of sound for the described model is the *frozen* speed of sound. It is derived by assuming a fixed composition with $Y_i = const$. In this case, the specific internal energy is written as

$$e = e(\rho_1, \ldots, \rho_K, p) = e(\rho, p)_{Y_1,\ldots,Y_K}$$

and the equations of state (2.53) and (2.54) take the form

$$p = \check{p}(\rho_1, \ldots, \rho_K, e) = \check{p}(\rho, e)_{Y_1,\ldots,Y_K} , \qquad p = \acute{p}(\rho_1, \ldots, \rho_K, T) = \acute{p}(\rho, T)_{Y_1,\ldots,Y_K} .$$

Application of First and Second Law of Thermodynamics to the frozen mixture gives the relation

$$T \, \mathrm{d}s = \mathrm{d}e + p \, \mathrm{d}\left(\frac{1}{\rho}\right) \tag{2.63}$$

that introduces the new variable $s \in \mathbb{R}^+$, the entropy. The internal energy may be expressed in terms of (2.63) by

$$e = e(\rho, s)_{Y_1,\ldots,Y_K} ,$$

and the caloric equation of state may written as

$$p = p(\rho, s)_{Y_1,\ldots,Y_K} . \tag{2.64}$$

From (2.64) the differential dp for the frozen mixture is evaluated as

$$\mathrm{d}p = \left(\frac{\partial p}{\partial \rho}\right)_{s,Y_1,\ldots,Y_K} \mathrm{d}\rho + \left(\frac{\partial p}{\partial s}\right)_{\rho,Y_1,\ldots,Y_K} \mathrm{d}s \ . \tag{2.65}$$

The speed of sound c now is introduced by assuming unconstrained thermodynamic equilibrium, i.e. by setting $\mathrm{d}s = 0$ in (2.65), and by defining

$$c = \sqrt{\left(\frac{\partial p}{\partial \rho}\right)_{s,Y_1,\ldots,Y_K}} \ . \tag{2.66}$$

On the other hand, dp may also be derived from (2.55) as

$$\mathrm{d}p = \sum_{i=1}^{K} \frac{\partial \check{p}}{\partial \rho_i} \mathrm{d}\rho_i + \sum_{n=1}^{d} \frac{\partial \check{p}}{\partial m_n} \mathrm{d}m_n + \frac{\partial \check{p}}{\partial \bar{E}} \mathrm{d}\bar{E} \ . \tag{2.67}$$

By differentiation of (2.31) it is found that the differential d$\bar{E}$ can be expressed as

$$\mathrm{d}\bar{E} = E\,\mathrm{d}\rho + \rho\,\mathrm{d}e \ .$$

Inserting (2.63) into this expression and setting $\mathrm{d}s = 0$ yields the simple relation

$$\mathrm{d}\bar{E} = \left(E + \frac{p}{\rho}\right) \mathrm{d}\rho = H\,\mathrm{d}\rho \ .$$

For the case of constant entropy expression (2.67) therefore simplifies to

$$\mathrm{d}p = \sum_{i=1}^{K} \frac{\partial \check{p}}{\partial \rho_i} \mathrm{d}\rho_i + \sum_{n=1}^{d} \frac{\partial \check{p}}{\partial m_n} \mathrm{d}m_n + \frac{\partial \check{p}}{\partial \bar{E}} H\,\mathrm{d}\rho \tag{2.68}$$

and the frozen speed of sound may be evaluated by applying Eq. (2.65) with $\mathrm{d}s = 0$ and by inserting the already derived relations (2.61) as

$$c^2 = \left(\frac{\partial p}{\partial \rho}\right)_{s,Y_1,\ldots,Y_K} = \sum_{i=1}^{K} Y_i\,\phi_i - \bar{\gamma}\mathbf{u}^2 + \bar{\gamma}H \ . \tag{2.69}$$

Replacing ϕ_i with the relation (2.60) simplifies Eq. (2.69) to

$$c^2 = \bar{\gamma}\left[H - \mathbf{u}^2 + \sum_{i=1}^{K} Y_i \left(\frac{\mathbf{u}^2}{2} - h_i + \frac{\gamma\,R_i\,T}{\bar{\gamma}}\right)\right] = \gamma \sum_{i=1}^{K} Y_i\,R_i\,T = \gamma\frac{p}{\rho} \ , \tag{2.70}$$

which is the same simple expression as in the standard case of a single polytropic gas.

Derivatives of the Speed of Sound

The partial derivatives of the frozen speed of sound c with respect to the conserved variables $\rho_1, \ldots, \rho_K, m_1, \ldots, m_d, \bar{E}$ are mandatory to determine the type of the characteristic fields in Prop. 5. We express c as

$$c = (\gamma R T)^{1/2} = \left(\gamma\, T \sum_{i=1}^{K} \frac{\rho_i}{\rho} R_i \right)^{1/2}$$

and obtain for instance for the partial derivative with respect to ρ_i

$$\frac{\partial c}{\partial \rho_i} = \frac{1}{2c} \left(R T \frac{\partial \gamma}{\partial T} \frac{\partial T}{\partial \rho_i} + \gamma \frac{\partial (RT)}{\partial \rho_i} \right) ,$$

because the temperature $T = T(\rho_1, \ldots, \rho_K, m_1, \ldots, m_d, \bar{E})$ itself is a function of the conserved quantities. Utilizing the partial derivatives of the temperature (2.62) we find

$$\frac{\partial (RT)}{\partial \rho_i} = \frac{\partial}{\partial \rho_i} (T \sum_{i=1}^{K} \frac{\rho_i}{\rho} R_i) = \frac{\phi_i - RT}{\rho} , \quad \frac{\partial (RT)}{\partial m_n} = -\frac{\bar{\gamma} u_n}{\rho} , \quad \frac{\partial (RT)}{\partial \bar{E}} = \frac{\bar{\gamma}}{\rho} .$$

If we use these expressions and (2.62) together, we obtain as partial derivatives of c

$$\frac{\partial c}{\partial \rho_i} = \varrho \phi_i - \frac{T}{2c\rho} \left(R_i T \frac{\partial \gamma}{\partial T} + \gamma R \right) , \quad \frac{\partial c}{\partial m_n} = -\varrho \bar{\gamma} u_n , \quad \frac{\partial c}{\partial \bar{E}} = \varrho \bar{\gamma} , \tag{2.71}$$

where ϱ is defined by

$$\varrho := \frac{1}{2c\rho} \left(\gamma + T \frac{\partial \gamma}{\partial T} \right) . \tag{2.72}$$

2.3.5 Hyperbolicity

We prove the hyperbolicity of the multi-component Euler equations in two and three space dimensions by employing the rotational invariance property (2.12). The validity of property (2.12) is also important from a practical point of view, because its application allows the direct extension of all finite volume discretization, that are presented in this thesis on Cartesian structured grids, to unstructured triangulations.

Proposition 2 (Rotational invariance). *The three-dimensional partial differential equation (2.1) with vector of state (2.29) and flux functions (2.32) is rotationally invariant, that is it satisfies*

$$\cos\theta^y \cos\theta^z \; \mathbf{f}_1(\mathbf{q}) + \cos\theta^y \sin\theta^z \; \mathbf{f}_2(\mathbf{q}) + \sin\theta^y \; \mathbf{f}_3(\mathbf{q}) = \mathbf{T}^{-1} \; \mathbf{f}_1(\mathbf{T}\; \mathbf{q})$$

for all angles θ^y, θ^z and all admissible states $\mathbf{q} \in S$. The rotational matrix $\mathbf{T} = \mathbf{T}(\theta^y, \theta^z)$ is

$$\mathbf{T} = \begin{bmatrix} 1 & 0 & & & & \dots & 0 \\ 0 & \ddots & & & & & \vdots \\ & & 1 & & & & \\ & & & \cos\theta^y \cos\theta^z & \cos\theta^y \sin\theta^z & \sin\theta^y & 0 \\ \vdots & & & -\sin\theta^z & \cos\theta^z & 0 & 0 \\ & & & -\sin\theta^y \cos\theta^z & -\sin\theta^y \sin\theta^z & \cos\theta^y & 0 \\ 0 & & \dots & 0 & 0 & 0 & 1 \end{bmatrix}.$$

Proof. The proof of property (2.12) for the Euler equations for mixtures of thermally perfect gases is analogous to the standard case of a single polytropic gas. Hence, we omit the tedious algebraic calculations and refer to the book of Toro [187] instead, where the detailed proof for the standard case can be found. Essential for the proof are the rotational invariance of the temperature T calculated from Eq. (2.56) and of the hydrostatic pressure p evaluated by Eq. (2.37). ■

Proposition 3 (Rotational invariance). *The two-dimensional partial differential equation (2.1) with vector of state (2.29) and flux functions (2.32) is rotationally invariant, that is it satisfies*

$$\cos\theta\, \mathbf{f}_1(\mathbf{q}) + \sin\theta\, \mathbf{f}_2(\mathbf{q}) = \mathbf{T}^{-1}\, \mathbf{f}_1(\mathbf{T}\, \mathbf{q})$$

for all angles θ and all admissible states $\mathbf{q} \in S$. The rotational matrix $\mathbf{T} = \mathbf{T}(\theta)$ is

$$\mathbf{T} = \begin{bmatrix} 1 & 0 & & & \dots & 0 \\ 0 & \ddots & & & & \vdots \\ & & 1 & & & \\ & & & \cos\theta & \sin\theta & 0 \\ \vdots & & & -\sin\theta & \cos\theta & 0 \\ 0 & & \dots & 0 & 0 & 1 \end{bmatrix}.$$

Proof. With $\theta^y \equiv 0$, $\theta^z \equiv \theta$ the proof follows immediately from the proof of Prop. 2. ■

Proposition 4 (Hyperbolicity). *The partial differential equation (2.1) with vector of state (2.29) and flux functions (2.32) is hyperbolic (see Def. 1).*

Proof. For $d = 1$ the proposition is identical to Prop. 10. In the multi-dimensional case we apply the Props. 2 and 3. We only consider the three-dimensional case in detail and notice that the formulas below carry over immediately to the two-dimensional case for $\theta^y \equiv 0$, $\theta^z \equiv \theta$. In polar coordinates the three-dimensional vector of coefficients reads

$$(\nu_1, \nu_2, \nu_3)^T = (r\cos\theta^y \cos\theta^z, r\cos\theta^y \sin\theta^z, r\sin\theta^y)^T$$

with $r = (\nu_1^2 + \nu_2^2 + \nu_3^2)^{1/2}$. We express the vector of coefficients in polar coordinates and obtain by applying Prop. 2

$$\begin{aligned}\mathbf{A} &= \frac{\partial}{\partial \mathbf{q}} \left(\sum_{n=1}^{3} \nu_n \, \mathbf{f}_n \right) \\ &= r \, \frac{\partial}{\partial \mathbf{q}} \left(\cos\theta^y \cos\theta^z \, \mathbf{f}_1 + \cos\theta^y \sin\theta^z \, \mathbf{f}_2 + \sin\theta^y \, \mathbf{f}_3 \right) = r \, \frac{\partial}{\partial \mathbf{q}} \left(\mathbf{T}^{-1} \, \mathbf{f}_1(\mathbf{T}\mathbf{q}) \right) \; .\end{aligned}$$

We differentiate the result by $\mathbf{q}$ and apply Prop. 10, where it has been proved that $\mathbf{A}_1(\mathbf{q})$ is diagonalizable for all admissible states. We obtain

$$\begin{aligned} r \, \mathbf{T}^{-1} \, \frac{\partial}{\partial \mathbf{q}} \left(\mathbf{f}_1(\mathbf{T}\mathbf{q}) \right) &= r \mathbf{T}^{-1} \, \mathbf{A}_1(\mathbf{T}\mathbf{q}) \, \mathbf{T} = r \mathbf{T}^{-1} \, \mathbf{R}_1(\mathbf{T}\mathbf{q}) \, \mathbf{\Lambda}_1(\mathbf{T}\mathbf{q}) \, \mathbf{R}_1^{-1}(\mathbf{T}\mathbf{q}) \, \mathbf{T} \\ &= \mathbf{T}^{-1} \, \mathbf{R}_1(\mathbf{T}\mathbf{q}) \, r \mathbf{\Lambda}_1(\mathbf{T}\mathbf{q}) \left(\mathbf{T}^{-1} \, \mathbf{R}_1(\mathbf{T}\mathbf{q}) \right)^{-1} \; . \end{aligned}$$

Hence, $\mathbf{A}$ is diagonalizable for all admissible states. The diagonal matrix of eigenvalues is $r\mathbf{\Lambda}_1(\mathbf{T}\mathbf{q})$, the matrix of right eigenvectors reads $\mathbf{T}^{-1} \, \mathbf{R}_1(\mathbf{T}\mathbf{q})$. ■

2.3.6 The Non-reactive Riemann Problem

In this section, we discuss the solution structure of the RP (2.15) for Eq. (2.1) with vector of state (2.29) and flux functions (2.32) for the important case $\mathbf{s} \equiv \mathbf{0}$. As Props. 2 and 3 state the validity of the rotational invariance property, the solution is quasi-one-dimensional and we can restrict our attention to the one-dimensional equation (2.17) with $\mathbf{f} \equiv \mathbf{f_1}$. For this particular case, the solution structure of the RP has already been discussed in Sec. 2.2.

Proposition 5 (Types of characteristic fields). *The characteristic fields of the partial differential equation (2.17) with vector of state (2.29) and flux function* $\mathbf{f} \equiv \mathbf{f_1}$ *according to (2.32) are linearly degenerate for* $m = 2, \ldots, K + d$*, while they are genuinely nonlinear for* $m = 1$ *and* $m = K + d + 1$*, iff the condition*

$$\frac{\gamma(\gamma + 1)}{(1 - \gamma)T} \neq \frac{\partial \gamma}{\partial T} \tag{2.73}$$

is satisfied for all admissible states $\mathbf{q} \in S$*.*

Proof. The eigenvalues of the Jacobian of $\mathbf{f_1}$ follow from Prop. 9 as $\lambda_1 = u_1 - c$, $\lambda_{K+d+1} = u_1 + c$ and $\lambda_m = u_1$ for $m = 2, \ldots, K + d$. Their gradients with respect to $\mathbf{q} = (\rho_1, ..., \rho_K, m_1, ..., m_d, \bar{E})^T$ are

$$\frac{\partial \lambda_{2,\ldots,K+d}(\mathbf{q})}{\partial \mathbf{q}}^T = \frac{\partial}{\partial \mathbf{q}} \left(\frac{m_1}{\rho} \right)^T = \left(-\frac{u_1}{\rho}, \ldots, -\frac{u_1}{\rho}, \frac{1}{\rho}, 0, \ldots, 0 \right)^T \tag{2.74}$$

and

$$\frac{\partial \lambda_{1/K+d+1}(\mathbf{q})}{\partial \mathbf{q}}^T = \frac{\partial}{\partial \mathbf{q}}\left(\frac{m_1}{\rho} \mp c\right)^T$$
$$= \left(-\frac{u_1}{\rho} \mp \frac{\partial c}{\partial \rho_1}, \ldots, -\frac{u_1}{\rho} \mp \frac{\partial c}{\partial \rho_K}, \frac{1}{\rho} \mp \frac{\partial c}{\partial m_1}, \ldots, \mp\frac{\partial c}{\partial m_d}, \mp\frac{\partial c}{\partial \bar{E}}\right)^T . \quad (2.75)$$

The matrix of right eigenvectors $\mathbf{R}_1(\mathbf{q}) = (\mathbf{r}_1|\ldots|\mathbf{r}_{K+d+1})$ follows from Prop. 10. For $m = 2\ldots, K+d$ we get

$$\frac{\partial \lambda_m}{\partial \mathbf{q}}^T \cdot \mathbf{r}_m = 0 \ , \quad (2.76)$$

which proves that the fields for $m = 2, \ldots, K+d$ are linearly degenerate. For $m = 1, K+d+1$ we have to insert the partial derivatives of the frozen speed of sound from (2.71) into the gradient (2.75) and obtain

$$\frac{\partial \lambda_{1/K+d+1}}{\partial \mathbf{q}}^T \cdot \mathbf{r}_{1/K+d+1} = \mp\varrho\left[\sum_{i=1}^{K} Y_i\phi_i - \bar{\gamma}\mathbf{u}^2 + \bar{\gamma}H\right] \mp \frac{c}{\rho} \pm \sum_{i=1}^{K} Y_i\left(\frac{T}{2\rho c}R_iT\frac{\partial\gamma}{\partial T} + \gamma R\right).$$

By inserting the relation for the frozen speed of sound (2.69) and by applying $R = \sum Y_iR_i$ we derive with ϱ defined in (2.72) from the last expression

$$\frac{\partial \lambda_{1/K+d+1}}{\partial \mathbf{q}}^T \cdot \mathbf{r}_{1/K+d+1} = \mp(\varrho c^2 + \frac{c}{\rho} - \varrho RT) = \mp\left[\frac{(\gamma+1)c}{2\rho} - \frac{c(1-\gamma)T}{2\gamma\rho}\frac{\partial\gamma}{\partial T}\right]$$
$$= \mp\frac{c}{2\gamma\rho}\left[\gamma(\gamma+1) - (1-\gamma)T\frac{\partial\gamma}{\partial T}\right] .$$

From the final parenthesis it is easy to see, that the fields with $m = 1, K+d+1$ are genuinely nonlinear if and only if (2.73) is satisfied for all $\mathbf{q} \in S$. ■

In the following, we *assume* that the inequality (2.73) is satisfied for all $\mathbf{q} \in S$. Utilizing the results of Sec. 2.2 and especially Theorem 3, we know from Prop. 5 that the solution structure of the RP for the multi-component Euler equations is in principle identical to the standard case of a single polytropic gas, which is discussed in detail for instance in the books of Smoller [171], Godelewski and Raviart [82] and Toro [187]. The first and last characteristic fields with eigenvalues $u_1 - c$ and $u_1 + c$ admit admissible shocks and rarefaction waves, while all other characteristic fields sum up to a single contact discontinuity associated to the eigenvalue u_1.

Proposition 6 (Riemann invariants). *The mass fractions Y_i, $i = 1, \ldots, K$ are $1-$ and $K+d+1$-Riemann invariants of equation (2.17) with vector of state (2.29) and flux function (2.32) $\mathbf{f} \equiv \mathbf{f_1}$. The velocity u_1 and the hydrodynamic pressure p are Riemann invariants of the characteristic fields $2, \ldots, K+d$.*

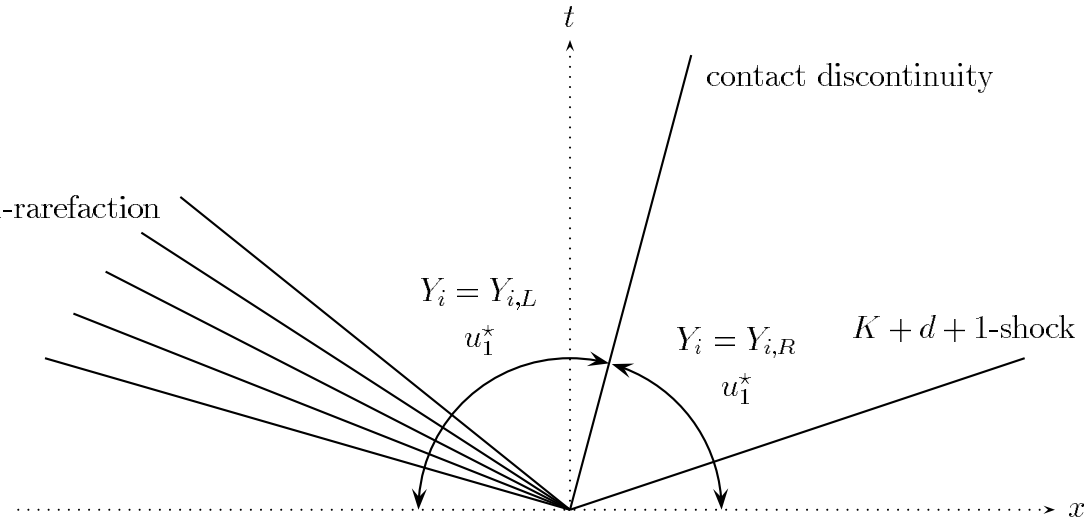

Figure 2.2: Solution $\mathbf{q}(x,t)$ of the Riemann Problem for the quasi-one-dimensional multi-component Euler equations in the x-t plane [109, 108].

Proof. To prove the first part of the proposition, we have to verify that the functions $Y_i(\mathbf{q}) = \rho_i/\rho$, $i = 1, \ldots, K$ satisfy condition (2.28) with $\mathbf{r}_1(\mathbf{q})$ and $\mathbf{r}_{K+d+1}(\mathbf{q})$ according to Prop. 10 for all $\mathbf{q} \in S$. With the gradient

$$\frac{\partial}{\partial \mathbf{q}} \left(\frac{\rho_i}{\rho}\right)^T = \left(-\frac{Y_i}{\rho}, \ldots, -\frac{Y_i}{\rho}, \frac{1}{\rho} - \frac{Y_i}{\rho}, -\frac{Y_i}{\rho}, \ldots, -\frac{Y_i}{\rho}, 0, 0, 0, 0\right)^T ,$$

which has $\frac{1}{\rho} - \frac{Y_i}{\rho}$ at the ith column, we immediately get the desired result for the mass fractions:

$$\frac{\partial}{\partial \mathbf{q}} \left(\frac{\rho_i}{\rho}\right)^T \cdot \mathbf{r}_{1/K+d+1} = -\frac{Y_i}{\rho} + \frac{Y_i}{\rho} = 0$$

The proof, that $u_1(\mathbf{q}) = m_1/\rho$ is a Riemann invariant of the linearly degenerate fields, is trivial, because condition (2.28) is exactly Eq. (2.76) for the gradient (2.74). Inserting the partial derivatives of the pressure (2.60), (2.61) the gradient of $p(\mathbf{q})$ is

$$\frac{\partial p(\mathbf{q})}{\partial \mathbf{q}}^T = (\phi_1, \ldots, \phi_K, -\bar{\gamma} u_1, \cdots - \bar{\gamma} u_d, \bar{\gamma})^T$$

and we obtain the required results

$$\frac{\partial p(\mathbf{q})}{\partial \mathbf{q}}^T \cdot \mathbf{r}_m = \begin{cases} \phi_m - \bar{\gamma}\mathbf{u}^2 + \bar{\gamma}\left(\mathbf{u}^2 - \phi_m/\bar{\gamma}\right) = 0 & \text{for } m = 2, \ldots, K+1 , \\ 0 & \text{for } K+2 \leq m \leq K+d . \end{cases} \qquad \blacksquare$$

Like in the standard case of a single polytropic gas (compare [171, 82, 187]), the pressure p is constant over the contact discontinuity. Further on, Prop. 6 proves that the mass fractions Y_i remain constant over admissible shocks and rarefaction waves. Fig. 2.2 displays the self-similar solution structure of the RP $\mathbf{q}(x,t) = \mathbf{v}(\xi) =$

$(\rho_1(\xi), \ldots, \rho_K(\xi), m_1(\xi), \ldots, m_d(\xi), \bar{E}(\xi))^T$ with $\xi = x/t$, how it is now known from Props. 5 and 6. It is obvious, that $\mathbf{v}(\xi)$ satisfies the relation

$$Y_i(\mathbf{v}(0)) = \begin{cases} Y_{i,L}\,, & u_1^\star > 0\,, \\ Y_{i,R}\,, & u_1^\star < 0\,, \end{cases}$$

which can be utilized to evaluate the exact fluxes of all partial densities ρ_i, $i = 1, \ldots, K$ as

$$\mathbf{f}_i(\mathbf{v}(0)) = m_1(0) \times \begin{cases} Y_{i,L}\,, & u_1^\star > 0\,, \\ Y_{i,R}\,, & u_1^\star < 0\,. \end{cases}$$

Larrouturou proves in [108] that the last expression is equivalent to

$$\mathbf{f}_i(\mathbf{v}(0)) = \mathbf{f}_\rho(\mathbf{v}(0)) \times \begin{cases} Y_{i,L}\,, & \mathbf{f}_\rho(\mathbf{v}(0)) > 0\,, \\ Y_{i,R}\,, & \mathbf{f}_\rho(\mathbf{v}(0)) < 0 \end{cases} \tag{2.77}$$

with $\mathbf{f}_\rho(\mathbf{v}(\xi)) = m_1(\xi)$ denoting the exact flux of the total density ρ.

2.3.7 Reactive Source Terms

We write the chemical production of a single species as product of its chemical production rate in molar concentration per unit volume $\dot{\omega}_i = \dot{\omega}_i(\mathbf{q}) \in C^1(S, \mathbb{R})$ and its constant molecular weight W_i. External body forces are not considered and the source term $\mathbf{s}(\mathbf{q})$ simply reads

$$\mathbf{s}(\mathbf{q}) = (W_1\,\dot{\omega}_1, \ldots, W_K\,\dot{\omega}_K, 0, \ldots, 0, 0)^T\ . \tag{2.78}$$

As the total density $\rho = \sum_{i=1}^K \rho_i$ has to be conserved, changes in the partial densities due to chemical reaction have to cancel, i.e.

$$\sum_{i=1}^K W_i\,\dot{\omega}_i = 0\ . \tag{2.79}$$

Reaction Mechanisms

The chemical production rates $\dot{\omega}_i(\rho_1, \ldots, \rho_K, T)$ are derived from a reaction mechanism that consists of J chemical reactions

$$\sum_{i=1}^K \nu_{ji}^f S_i \rightleftharpoons \sum_{i=1}^K \nu_{ji}^r S_i\ , \quad j = 1, \ldots, J\ , \tag{2.80}$$

where ν_{ji}^f and ν_{ji}^r are the stoichiometric coefficients of species S_i appearing as a reactant and as a product. Note, that especially for a large number of species the majority of the coefficients ν_{ji}^f, ν_{ji}^r is usually zero in most reactions. The entire molar production rate of species S_i per unit volume is then given by

$$\dot{\omega}_i(C_1, \ldots, C_K, T) = \sum_{j=1}^J (\nu_{ji}^r - \nu_{ji}^f)\left[k_j^f \prod_{l=1}^K C_l^{\nu_{jl}^f} - k_j^r \prod_{l=1}^K C_l^{\nu_{jl}^r}\right], \quad i = 1, \ldots, K\ , \tag{2.81}$$

with $k_j^f(T)$ and $k_j^r(T)$ denoting the forward and backward reaction rate of each chemical reaction. The reaction rates are calculated by the Arrhenius law

$$k_j^{f/r}(T) = A_j^{f/r} T^{\beta_j^{f/r}} \exp(-E_j^{f/r}/\mathcal{R}T) \,. \tag{2.82}$$

The parameters of some backward reaction rates might be derived by assuming the corresponding chemical reaction to be in chemical equilibrium.[3] But especially simulations of detonation phenomena usually require mechanisms that utilize non-equilibrium backward reaction rates at least for some of the reactions.

A chemical kinetics package (e.g. Chemkin [102] or LARKIN [13]) is usually utilized to evaluate (2.81), (2.82) according to the particular reaction mechanism and given thermodynamic data.

2.3.8 Alternative Formulations

Primitive Variable Formulation

In primitive variables the reactive multi-component Euler equations with chemical reaction read

$$\frac{\partial \rho}{\partial t} + \sum_{n=1}^{d} u_n \frac{\partial \rho}{\partial x_n} + \rho \sum_{n=1}^{d} \frac{\partial u_n}{\partial x_n} = 0 \,, \tag{2.83}$$

$$\frac{\partial u_m}{\partial t} + \sum_{n=1}^{d} u_n \frac{\partial u_m}{\partial x_n} + \frac{1}{\rho} \frac{\partial p}{\partial x_m} = 0 \,, \qquad m = 1, \ldots, d \,, \tag{2.84}$$

$$\frac{\partial p}{\partial t} + \sum_{n=1}^{d} u_n \frac{\partial p}{\partial x_n} + \rho c^2 \sum_{n=1}^{d} \frac{\partial u_n}{\partial x_n} = \rho c^2 \dot{\varsigma} \,, \tag{2.85}$$

$$\frac{\partial Y_i}{\partial t} + \sum_{n=1}^{d} u_n \frac{\partial Y_i}{\partial x_n} = \frac{W_i \, \dot{\omega}_i}{\rho} \,, \quad i = 1, \ldots, K-1 \,. \tag{2.86}$$

The difference to the standard case without reaction [187] is the occurrence of the term on the right side of the pressure equation (2.85) and the $K-1$ quasi-linear equations for Y_i that follow directly from (2.90). The term $\rho c^2 \dot{\varsigma}$ models the pressure change due to chemical reaction under adiabatic conditions. A detailed derivation of Eq. (2.85) can be found in the book of Fickett and Davis [73]. Herein, $\dot{\varsigma}$ denotes the thermicity, which is defined by

$$\dot{\varsigma} = \sum_{i=1}^{K} \varsigma_i \frac{W_i \, \dot{\omega}_i}{\rho} \quad \text{with} \quad \varsigma_i = \frac{1}{\rho c^2} \left(\frac{\partial p}{\partial Y_i} \right)_{e, \rho, Y_1, \ldots, Y_{i-1}, Y_{i+1}, \ldots, Y_K} \,. \tag{2.87}$$

[3] In chemical equilibrium the relation $k_j^r(T) = k_j^f(T)/K_j^c(T)$ holds true with $K_j^c(T)$ denoting the equilibrium constant. See [204] for further details.

If we insert $c^2 = \gamma RT$ and replace $\partial p/\partial Y_i$ by the expression given in (2.61), we can evaluate ς_i as

$$\varsigma_i = \frac{W}{W_i} - \frac{h_i}{c_p T} = \frac{1}{\gamma}\left(\frac{W}{W_i} - \frac{e_i}{c_v T}\right) . \tag{2.88}$$

The Eqs. (2.83) to (2.86) and the conservative Euler equations introduced at the beginning of Sec. 2.3 are equivalent for classical solutions only. They are not equivalent for non-classical weak solutions like they have been introduced in Sec. 2.1, because weak solutions of (2.83) to (2.86) can not be found simply by integration. In particular, the Eqs. (2.83) to (2.86) are not conservative for vanishing source terms and numerical methods utilizing (2.83) to (2.86) do not satisfy the Lax-Wendroff theorem (see Sec. 4.1.2). Schemes built upon (2.83) to (2.86) do not approximate weak solution of the Euler equations correctly, but they can be an alternative for the calculation of classical solutions [187].

Overall Continuity Equation

The K species equations

$$\frac{\partial \rho_i}{\partial t} + \sum_{n=1}^{d} \frac{\partial}{\partial x_n}\left(Y_i\, \rho u_n\right) = W_i\, \dot{\omega}_i \ , \quad i = 1, \ldots, K \ , \tag{2.89}$$

can be replaced by an overall continuity equation and $K-1$ species equations

$$\frac{\partial \rho}{\partial t} + \sum_{n=1}^{d} \frac{\partial}{\partial x_n}\left(\rho u_n\right) = 0 \ , \qquad \frac{\partial \rho_i}{\partial t} + \sum_{n=1}^{d} \frac{\partial}{\partial x_n}\left(Y_i\, \rho u_n\right) = W_i\, \dot{\omega}_i \ , \quad i = 1, \ldots, K-1 \ . \tag{2.90}$$

Both formulations are equivalent from the point of view of the exact solution and – beside round-off errors – for the corresponding numerical approximation, because (2.90) is derived from (2.89) by simple linear combination and by applying (2.79).

Chapter 3

Detonation Theory

In this chapter we recall briefly the theory of detonations as it can be found for instance in the text books of Fickett and Davis [73] and Williams [204]. In Sec. 3.1 we introduce the classical one-dimensional detonation model, which has been proposed independently by Zel'dovich [209], von Neumann [200] and Döring [57] (ZND). We focus mainly on the derivation of the exact solution, because its knowledge is essential in order to obtain reliable and reproducible initial data and to quantify the deviation of numerical approximations exactly in terms of error norms (compare Chap. 6). In Sec. 3.1 we consider the frequently used model of a single irreversible reaction between two calorically perfect gases [92, 26, 162]. The results are extended to an arbitrary number of thermally perfect species with detailed chemical reaction in Sec. 3.1.2. In the Secs. 3.2 and 3.3 we give an introduction into the oscillatory behavior of self-sustaining detonation waves. Emphasis is put on the description of the hydrodynamic flow pattern in multiple space dimensions. The basic wave pattern has been verified by numerous experiments [176, 178] and is the core of the physical interpretation of the numerical results in the Chaps. 6 and 7.

3.1 Planar Detonation Structure

For the one-dimensional reactive multi-component Euler equations with overall continuity equation as presented in Sec. 2.3.8 we introduce the classical ZND detonation model. The basic assumption of this model is that a detonation wave consists of a leading hydrodynamic shock followed by a region of decaying continuous reaction (compare Fig. 3.4). The shock causes an enormous pressure increase rising the temperature above the ignition limit. After a characteristic *ignition delay* time a shock-induced high-speed combustion toward the chemical equilibrium state occurs. Since the detonation propagates forward with a supersonic velocity, the leading shock front and the beginning of the combustion zone appear to be spatially separated by the *induction distance*. The chemical reaction throughout the combustion zone is continuous and is similar to the reaction in low-speed, subsonic *deflagrations* (see [204] for a detailed explanation).

We start our considerations with the simple chemical model of a single irreversible reaction that has been discussed frequently in the literature. Detailed derivations of the exact solution in this simplified case are given for instance by Fickett and Davis [73] and by Williams [204]. Condensed presentations can be found for instance in [92, 26, 162].

3.1.1 Simplified Reaction Model

We assume that the reaction mechanism consists just of one exothermic reaction $A \longrightarrow B$ with an energy release $h_A^0 - h_B^0 =: \Delta h^0 > 0$ and a forward reaction rate $k^f(T) = k\exp(-E_A/\mathcal{R}T)$. The mass production rates $W_A\dot{\omega}_A$, $W_B\,\dot{\omega}_B$ therefore read

$$W_A\dot{\omega}_A = -k\rho_A\exp(-E_A/\mathcal{R}T)\ , \quad W_B\,\dot{\omega}_B = -W_A\dot{\omega}_A\ .$$

Further, we assume that the species A and B are calorically perfect gases with $\gamma = \gamma_A = \gamma_B$. In this case, the hydrodynamic pressure is evaluated from Eq. (2.59) and with Z denoting the mass fraction of B we obtain the expression

$$p = (\gamma - 1)(\rho e - \rho(1-Z)h_A^0 - \rho Z h_B^0)\ .$$

Under the additional assumption $h_B^0 = 0$ we set $q_0 := \Delta h^0 = h_A^0$ and derive the equation of state for the simplified ZND-model

$$p = (\gamma - 1)(\rho e - \rho(1-Z)\,q_0)\ , \tag{3.1}$$

from which we derive the expression

$$e = \frac{p}{\rho(\gamma-1)} + (1-Z)\,q_0 \tag{3.2}$$

for the internal energy e. Together with (3.1) the governing equations of the simplified ZND-model are

$$\frac{\partial\rho}{\partial t} + \frac{\partial}{\partial x}(\rho u) = 0\ , \tag{3.3}$$

$$\frac{\partial}{\partial t}(\rho u) + \frac{\partial}{\partial x}(\rho u^2 + p) = 0\ , \tag{3.4}$$

$$\frac{\partial}{\partial t}(\rho E) + \frac{\partial}{\partial x}(u(\rho E + p)) = 0\ , \tag{3.5}$$

$$\frac{\partial}{\partial t}(\rho Z) + \frac{\partial}{\partial x}(\rho Z u) = k\rho(1-Z)\exp(-E_A^\star\,\rho/p) \tag{3.6}$$

with $-E_A^\star = E_A/W_A$. [1]

[1] An equivalent model can be derived by assuming $h_A^0 = 0$ and setting $q_0 := \Delta h^0 = -h_B^0$. In this case, the equation of state takes the modified form $p = (\gamma-1)(\rho e^\star + \rho Z q_0)$, while the Eqs. (3.3)-(3.6) remain unchanged. Only E in (3.5) has to replaced by $E^\star = e^\star + u^2/2$. All flow variables are identical in both models, only the specific internal and total energy differ by an additive constant q_0, i.e. $e^\star = e - q_0$ and $E^\star = E - q_0$. The following formulas are valid for both models, because the only step where the equation of state is inserted, from Eq. (3.15) to (3.16), is identical in both cases (compare [73]).

We now consider the special situation of a stationary reaction front propagating with constant speed $d^\star$ into a region of unburned gas with values $\rho_0, p_0, u_0 = 0, Z_0 = 0$. Under this assumption all derivatives with respect to t in the Eqs. (3.3) to (3.6) drop out and under the Galilean transformation $\grave{x} = t\, d^\star - x$ these equations become

$$\frac{\partial}{\partial \grave{x}}(\rho \grave{u}) = 0 \ , \tag{3.7}$$

$$\frac{\partial}{\partial \grave{x}}(\rho \grave{u}^2 + p) = 0 \ , \tag{3.8}$$

$$\frac{\partial}{\partial \grave{x}}(\grave{u}(\rho E + p)) = 0 \ , \tag{3.9}$$

$$\frac{\partial}{\partial \grave{x}}(\rho Z \grave{u}) = k\rho(1 - Z)\exp(-E_A^\star\, \rho/p) \tag{3.10}$$

with velocity $\grave{u} = d^\star - u$. If we integrate the Eqs. (3.7) to (3.9) between an arbitrary point $\grave{x}_0 < 0$ in the unburned gas region and an arbitrary point $\grave{x} \geq 0$, we obtain

$$\rho(\grave{x})\, \grave{u}(\grave{x}) = \rho_0 d^\star \ , \tag{3.11}$$

$$\rho(\grave{x})\, \grave{u}(\grave{x})^2 + p(\grave{x}) = \rho_0 (d^\star)^2 + p_0 \ , \tag{3.12}$$

$$\grave{u}(\grave{x})\, (\rho(\grave{x}) E(\grave{x}) + p(\grave{x})) = d^\star(\rho_0 E_0 + p_0) \ . \tag{3.13}$$

To simplify the notations we omit the dependency on $\grave{x}$ in the following formulas. Utilizing (3.11) and the specific volume $v := 1/\rho, v_0 := 1/\rho_0$, Eq. (3.12) can be transformed into the equation of the *Rayleigh line*

$$\frac{p - p_0}{v_0 - v} - \left(\frac{d^\star}{v_0}\right)^2 = 0 \ . \tag{3.14}$$

A similar calculation and the exchange of E with $e + \grave{u}^2/2$ and E_0 with $e_0 + (d^\star)^2/2$ transforms Eq. (3.13) into

$$e_0 - e + \frac{1}{2}(p + p_0)(v_0 - v) = 0 \ . \tag{3.15}$$

The explicit equation of state (3.1) allows the elimination of e, e_0 from the last relation and we obtain the expression

$$\frac{p_0 v_0 - pv}{\gamma - 1} + Z q_0 + \frac{1}{2}(p + p_0)(v_0 - v) = 0 \ , \tag{3.16}$$

which can be transformed with Eq. (3.14) into the equation of the *Hugoniot curve* for the ZND model

$$\left(\frac{p}{p_0} + \mu^2\right)\left(\frac{v}{v_0} - \mu^2\right) = 1 - \mu^4 + 2\mu^2 \frac{Z q_0}{p_0 v_0} \ , \tag{3.17}$$

where $\mu := (\gamma - 1)/(\gamma + 1)$.

Normalization

The PDEs (3.3) to (3.5) and the equation of state (3.1) are invariant under the normalization

$$P = \frac{p}{p_0}\ ,\quad V = \frac{v}{v_0}\ ,\quad \bar{\rho} = \frac{\rho}{\rho_0}\ ,\quad U, \grave{U}, D = \frac{u, \grave{u}, d^\star}{\sqrt{p_0 v_0}}\ , \tag{3.18}$$

$$\underline{E}, \bar{e} = \frac{E, e}{p_0 v_0}\ ,\quad Q_0 = \frac{q_0}{p_0 v_0}\ ,\quad E_0^\star = \frac{E_A^\star}{p_0 v_0}\ .$$

However, a further factor $(\sqrt{p_0 v_0})^{-1}$ appears on the right side of Eq. (3.6). Under the normalization (3.18) Eq. (3.6) becomes

$$\frac{\partial}{\partial t}(\bar{\rho} Z) + \frac{\partial}{\partial x}(\bar{\rho} Z U) = \bar{K}\bar{\rho}(1-Z)\exp\left(\frac{-E_0^\star}{PV}\right) \quad \text{with} \quad \bar{K} := \frac{k}{\sqrt{p_0 v_0}}\ ,$$

and we derive for our steady situation of interest the differential equation

$$\frac{\partial Z}{\partial \grave{x}} = \bar{K}\frac{(1-Z)}{\grave{U}}\exp\left(\frac{-E_0^\star}{PV}\right) = \bar{K}\frac{(1-Z)}{DV}\exp\left(\frac{-E_0^\star}{PV}\right) =: \bar{K} r(Z)\ . \tag{3.19}$$

Finally, we normalize the length scale by

$$\grave{X} = \frac{\grave{x}}{L_{1/2}/\bar{K}} \quad \text{with} \quad L_{1/2} := \int_0^{1/2} \frac{dZ}{r(Z)}\ , \tag{3.20}$$

since the frequency factor $\bar{K}$ can be eliminated under this specific choice and the rate equation of the reaction (3.19) simplifies to

$$\frac{\partial Z}{\partial \grave{X}} = L_{1/2}\, r(Z(\grave{X}))\ ,\quad \grave{X} > 0\ ,\quad Z(0) = 0 \tag{3.21}$$

with $Z(1) = 1/2$. The speed of sound in the unburned gas is $c_0 = \sqrt{\gamma p_0 v_0}$. In dimensionless variables according to (3.18) it reads $C_0 = \sqrt{\gamma}$.[2] In normalized quantities according to (3.18), (3.20) relation (3.11) becomes

$$\grave{U} = D - U = DV \tag{3.22}$$

and the relations (3.14), (3.17) read

$$\frac{P-1}{1-V} - D^2 = 0\ , \tag{3.23}$$

$$(P+\mu^2)(V-\mu^2) = 1 - \mu^4 + 2\mu^2 Z Q_0\ . \tag{3.24}$$

Stationary solutions of (3.7)-(3.10) have to satisfy both relations (3.23) and (3.24) for $\grave{X} \geq 0$ and all values $0 \leq Z(\grave{X}) \leq 1$.

[2] We have chosen this particular normalization for all computations, because it is most frequently used in the literature [204, 35, 34, 144]. But note, that some authors, e.g. Fickett and Davis [73], use c_0 to normalize all velocities ($C_0 = 1$) and therefore obtain slightly different expressions throughout the following analysis.

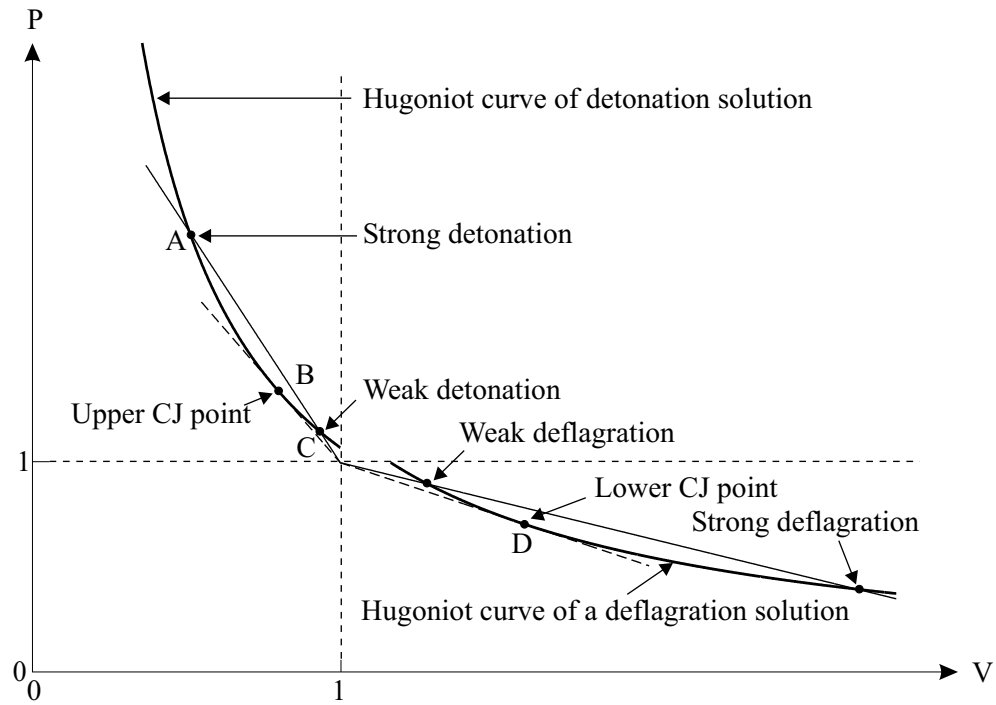

Figure 3.1: Typical Hugoniot curves of a detonation and a deflagration intersected by Rayleigh lines.

Equilibrium State and Chapman-Jouguet Point

We start our analysis of possible solutions of (3.23) and (3.24) with a discussion of the simplified situation in the final equilibrium state with $Z = 1$. In Fig. 3.1 both relations are visualized in a (P, V)-diagram for this particular case. Two different situations have to be considered (see also the detailed descriptions in [45] and [204]): If Rayleigh line and Hugoniot curve intersect in the upper branch for $P > 1, V < 1$, the reaction front is called a detonation; if they intersect in the lower branch with $P < 1, V > 1$, the reaction is a deflagration. A deflagration is characterized by a decrease of pressure, while only a detonation leads to a pressure increase in the equilibrium state. Hence, only intersections between Rayleigh line and Hugoniot curve in the upper branch are consistent with our basic assumptions.

For a fixed Hugoniot curve (3.24) with $Z = 1$ the parameter D determines the number of intersection points with (3.23). For $D > D_{CJ}$ we have two intersections. The upper point A is associated to a *strong* detonation wave, the lower point C corresponds to a *weak* detonation. Weak detonations are usually not observed in practice. For $D = D_{CJ}$ Rayleigh line and Hugoniot curve are tangential in the single point B with values (P_{CJ}, V_{CJ}), which is called *Chapman-Jouguet (CJ) point*, and for $D < D_{CJ}$ there is no intersection. In the CJ point both derivatives dP/dV derived from (3.23) and (3.24) have to be equal and after some algebraic manipulations we

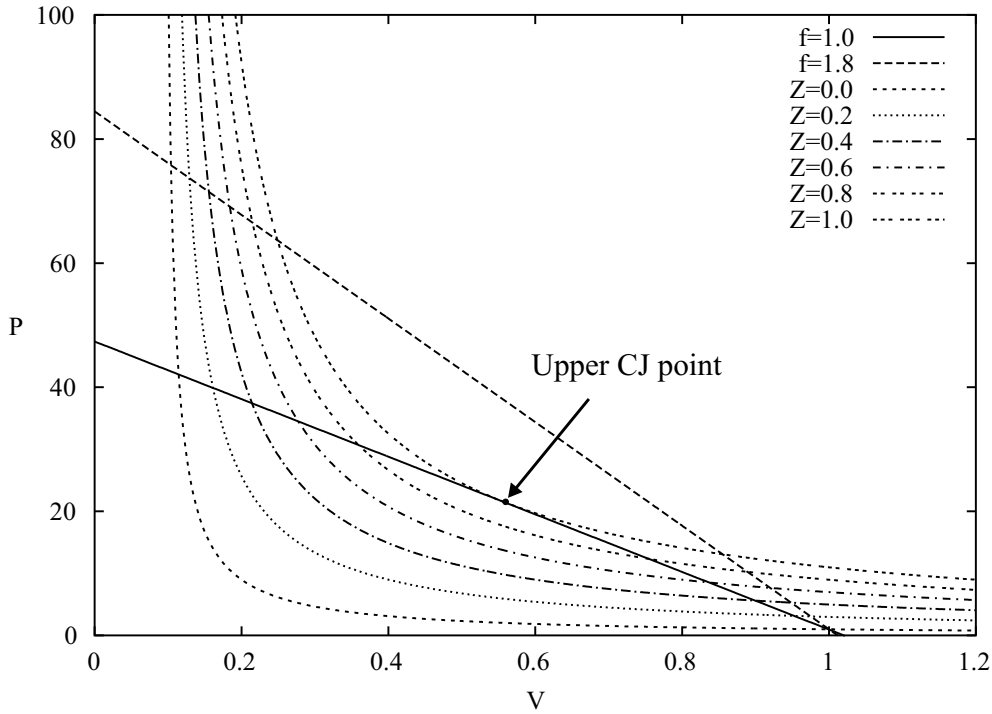

Figure 3.2: Hugoniot curves and Rayleigh lines for $\gamma = 1.2, Q_0 = 50, E_0^\star = 50$ in the detonation branch.

find

$$V_{CJ} = \frac{\gamma(1 + D_{CJ}^2)}{(\gamma + 1)D_{CJ}^2}\ , \quad P_{CJ} = \frac{1 + D_{CJ}^2}{\gamma + 1}\ . \tag{3.25}$$

In order to compute D_{CJ} these values are inserted into (3.24) for $Z = 1$:

$$D_{CJ} + \frac{\gamma}{D_{CJ}} = \sqrt{4\gamma + 2(\gamma^2 - 1)Q_0}$$

The last relation leads to a quadratic equation with the solutions

$$D_{CJ} = \sqrt{\frac{(\gamma^2 - 1)Q_0}{2} + \gamma} \pm \sqrt{\frac{(\gamma^2 - 1)Q_0}{2}}\ .$$

The plus sign corresponds to the sought upper CJ point B, while the minus denotes the lower CJ point D in the deflagration branch. It follows immediately from the relations of (3.25) that in both CJ points the equations

$$\grave{U}_{CJ} = D_{CJ}V_{CJ} = \frac{\gamma(1 + D_{CJ})}{(\gamma + 1)D_{CJ}} = \sqrt{\gamma P_{CJ}V_{CJ}} = C_{CJ}$$

hold true. Hence, the Mach number in the CJ point $\grave{M}_{CJ} = \grave{U}_{CJ}/C_{CJ}$ calculated in the frame of reference attached to the reaction front is equal to 1. The relation of

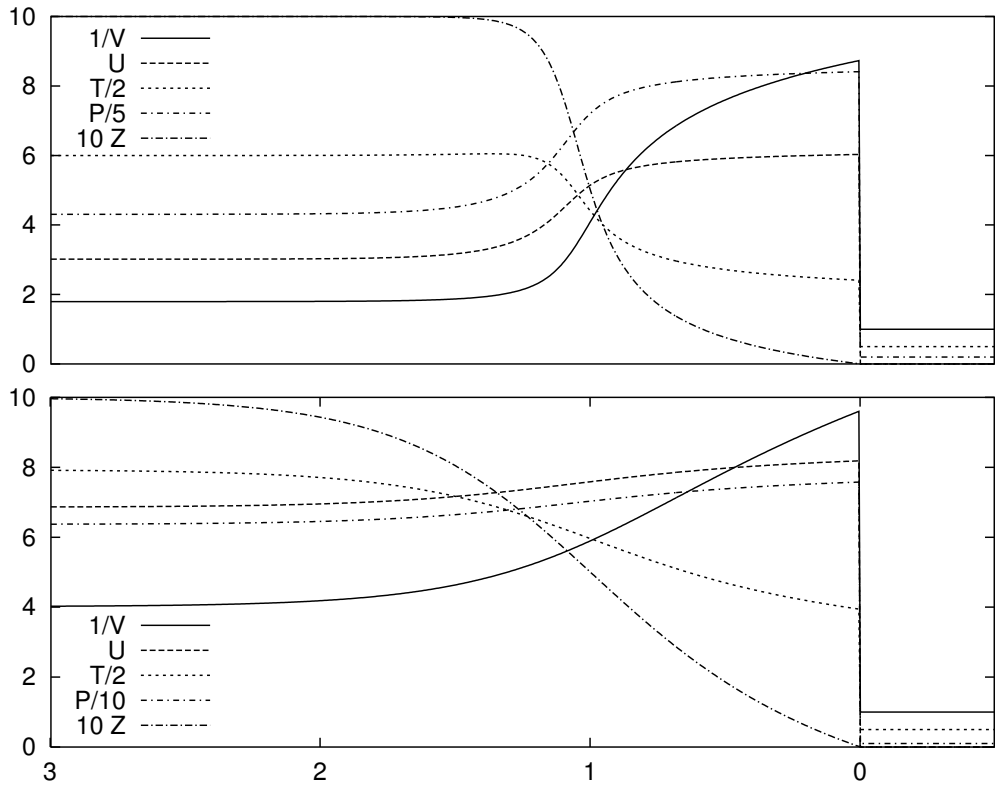

Figure 3.3: Stationary ZND solutions for $\gamma = 1.2, Q_0 = 50, E_0^\star = 50$. At the x-axis the normalized distance behind detonation front $\grave{X}$ is displayed. Top: $f = 1.0$, bottom: $f = 1.8$

a given detonation velocity $D, d^\star$ to the corresponding CJ value D_{CJ}, d_{CJ} is usually expressed in terms of the *overdrive parameter*

$$f := \left(\frac{D}{D_{CJ}}\right)^2 = \left(\frac{d^\star}{d_{CJ}}\right)^2 . \tag{3.26}$$

It is important to note, that the CJ point (P_{CJ}, V_{CJ}) denotes a particular equilibrium state with $Z = 1$. Fig. 3.2 clearly illustrates that even the Rayleigh line of a CJ detonation ($f = 1.0$) is intersected twice by all Hugoniot curves with $0 \leq Z < 1$. In case of an overdriven detonation ($f = 1.8$) also the final Hugoniot curve for $Z = 1$ has two intersections with the corresponding Rayleigh line.

General Solution

For arbitrary $D \geq D_{CJ}$ and arbitrary Z with $0 \leq Z \leq 1$ a tedious algebraic computation is necessary to evaluate the common points of Rayleigh line (3.14) and Hugoniot curve (3.17). The strong detonation solution is

$$V_S = V^\star(1 - \gamma^{-1}\xi) , \quad P_S = P^\star(1 + \xi) \tag{3.27}$$

with

$$V^\star = \frac{\gamma(1+D^2)}{(\gamma+1)D^2}\,, \quad P^\star = \frac{1+D^2}{\gamma+1}\,, \quad \xi = \frac{D^2-\gamma}{1+D^2}\sqrt{1-\frac{Z}{\tau}}\,, \quad \tau = \frac{(D^2-\gamma)^2}{2(\gamma^2-1)Q_0D^2}\,, \tag{3.28}$$

and the weak detonation solution reads

$$V_W = V^\star(1+\gamma^{-1}\xi)\,, \quad P_W = P^\star(1-\xi)\,.$$

Together with the ODE (3.21) with $r(Z)$ defined in (3.19) and the normalization parameter $L_{1/2}$ given in (3.20) and relation (3.22) the equations of (3.27), (3.28) specify the complete solution of a stationary strong detonation wave propagating with constant speed $D \geq D_{CJ}$. The solution of the ODE (3.21) and the parameter $L_{1/2}$ can only be calculated numerically. Note, that for V, P in (3.19) the values of the strong detonation solution V_S, P_S from (3.27), (3.28) have to used. Two solutions that have been computed with a standard explicit fourth-order Runge-Kutta method (compare Sec. 4.10.1) with different overdrive parameters f are displayed in Fig. 3.3. Unlike to detonations utilizing detailed non-equilibrium chemistry (compare Fig. 3.4) no clearly defined induction distance l_{ig} is visible in the graphs of Fig. 3.3. Hence, l_{ig} is no appropriate characteristic length scale for detonations with simplified chemistry and we utilize the normalization length $L_{1/2}$ in the following for this model instead.

3.1.2 Detailed Chemical Reaction

We extend the results of the previous section to the general case of thermally perfect gas-mixtures with detailed chemical reaction. Like in the simplified model of Sec. 3.1.1 we follow Zel'dovich's, von Neumann's and Döring's basic assumption and propose that the detonation consists of a planar shock followed by a region of decaying continuous combustion.

Once again, we consider a stationary reaction front under Galilean transformation with unburned gas values $\rho_0, p_0, T_0, u_0 = 0$ and initial mass fractions $Y_1^0, \ldots, Y_K^0$. Analogously to Eqs. (3.7) to (3.10) we obtain

$$\frac{\partial}{\partial \grave{x}}(\rho \grave{u}) = 0\,, \tag{3.29}$$

$$\frac{\partial}{\partial \grave{x}}(\rho \grave{u}^2 + p) = 0\,, \tag{3.30}$$

$$\frac{\partial}{\partial \grave{x}}(\grave{u}\rho H) = 0\,, \tag{3.31}$$

$$\frac{\partial}{\partial \grave{x}}(\rho Y_i \grave{u}) = W_i \dot{\omega}_i\left(\rho\tfrac{Y_1}{W_1}, \ldots, \rho\tfrac{Y_K}{W_K}, T\right)\,, \quad i = 1, \ldots, K-1\,, \tag{3.32}$$

where we have replaced $E + p/\rho$ by the total enthalpy H. Integration between a point $\grave{x}_0 < 0$ and a point $\grave{x} \geq 0$ gives Eq. (3.11) and after some manipulations we again deduce the equation for the Rayleigh line (3.14). From Eq. (3.31) we obtain

$$\rho H \grave{u} = \rho_0 H_0 d^\star\,.$$

By inserting $H = h(Y_1, \ldots, Y_K, T) + \grave{u}^2/2$ and $H_0 := h(Y_1^0, \ldots, Y_K^0, T_0) + (d^\star)^2/2$ we derive the relation for the Hugoniot curve in the general case

$$h(Y_1, \ldots, Y_K, T) + \frac{\grave{u}^2}{2} - h(Y_1^0, \ldots, Y_K^0, T_0) - \frac{(d^\star)^2}{2} = 0 \; . \tag{3.33}$$

With the new parameter $\zeta := \rho_0/\rho = v/v_0$ we derive from Eqs. (3.11) and (3.14) the explicit relations

$$\grave{u}(\zeta) = d^\star - u(\zeta) = \zeta d^\star \; , \tag{3.34}$$

$$p(\zeta) = p_0 + \rho_0 (d^\star)^2 (1 - \zeta) \tag{3.35}$$

and from (3.33) the implicit equation

$$h(Y_1, \ldots, Y_K, T(\zeta)) - h(Y_1^0, \ldots, Y_K^0, T_0) + \frac{(d^\star)^2}{2}(\zeta^2 - 1) = 0 \; . \tag{3.36}$$

Eq. (3.36) has only ζ as an unknown, because the temperature in the burned region $T(\zeta)$ can be evaluated from the ideal gas law (2.53) by employing (3.35) and $\rho(\zeta) = \rho_0/\zeta$ by

$$T(\zeta) = \frac{W p(\zeta)}{\mathcal{R}\rho(\zeta)} = \frac{W(p_0 + \rho_0 (d^\star)^2 (1-\zeta))\zeta}{\mathcal{R}\rho_0} = \frac{W}{\mathcal{R}} \left[\left(T_0 \frac{\mathcal{R}}{W_0} + (d^\star)^2 \right) \zeta - (d^\star \zeta)^2 \right] \tag{3.37}$$

where $p_0 = \rho_0 T_0 \mathcal{R}/W_0$ and $W = (\sum Y_i/W_i)^{-1}$, $W_0 = (\sum Y_i^0 W_i)^{-1}$.

A comparison of the obtained relations with those of the previous section shows that the parameter ζ is identical to the normalized specific volume V. Detonation solutions of (3.35), (3.36) are therefore possible only for $0 < \zeta < 1$. From the preceding section we know, that there will be no such solution for $d^\star < d_{CJ}$, one solution for $d^\star = d_{CJ}$ and two solutions for $d^\star > d_{CJ}$. Again, we are interested in strong detonations only and select the smallest value of ζ as the valid solution of (3.36). A robust numerical method to solve (3.36)+(3.37) for $d^\star \geq d_{CJ}$ can easily be implemented by first searching a solution ζ_1 in $]0, 1[$ and by searching for a possible smaller solution in the range $]0, \zeta_1[$ afterward. Supplemented with the ODE

$$\frac{\partial Y_i}{\partial \grave{x}} = \frac{W_i \dot{\omega}_i \left(\rho \frac{Y_1}{W_1}, \ldots, \rho \frac{Y_K}{W_K}, T(\zeta) \right)}{\rho(\zeta)\, \grave{u}(\zeta)} \; , \quad \grave{x} > 0 \; , \quad Y_i(0) = Y_i^0 \; , \quad i = 1, \ldots, K-1 \; , \tag{3.38}$$

the relations (3.34) to (3.37) allow the numerical computation of stationary detonations waves. The difference to the solution of the simplified ZND model is that the evaluation of the right side of (3.38) always requires the computation of the parameter ζ from (3.36)+(3.37). An example which has been calculated by utilizing the semi-implicit GRK4A method of Kaps and Rentrop [100] (compare Sec. 4.10.1) to integrate (3.38) and by applying an efficient root-finding algorithm to solve (3.36) that uses a combination of bisection and the secant rule [54] is shown in Fig. 3.4.

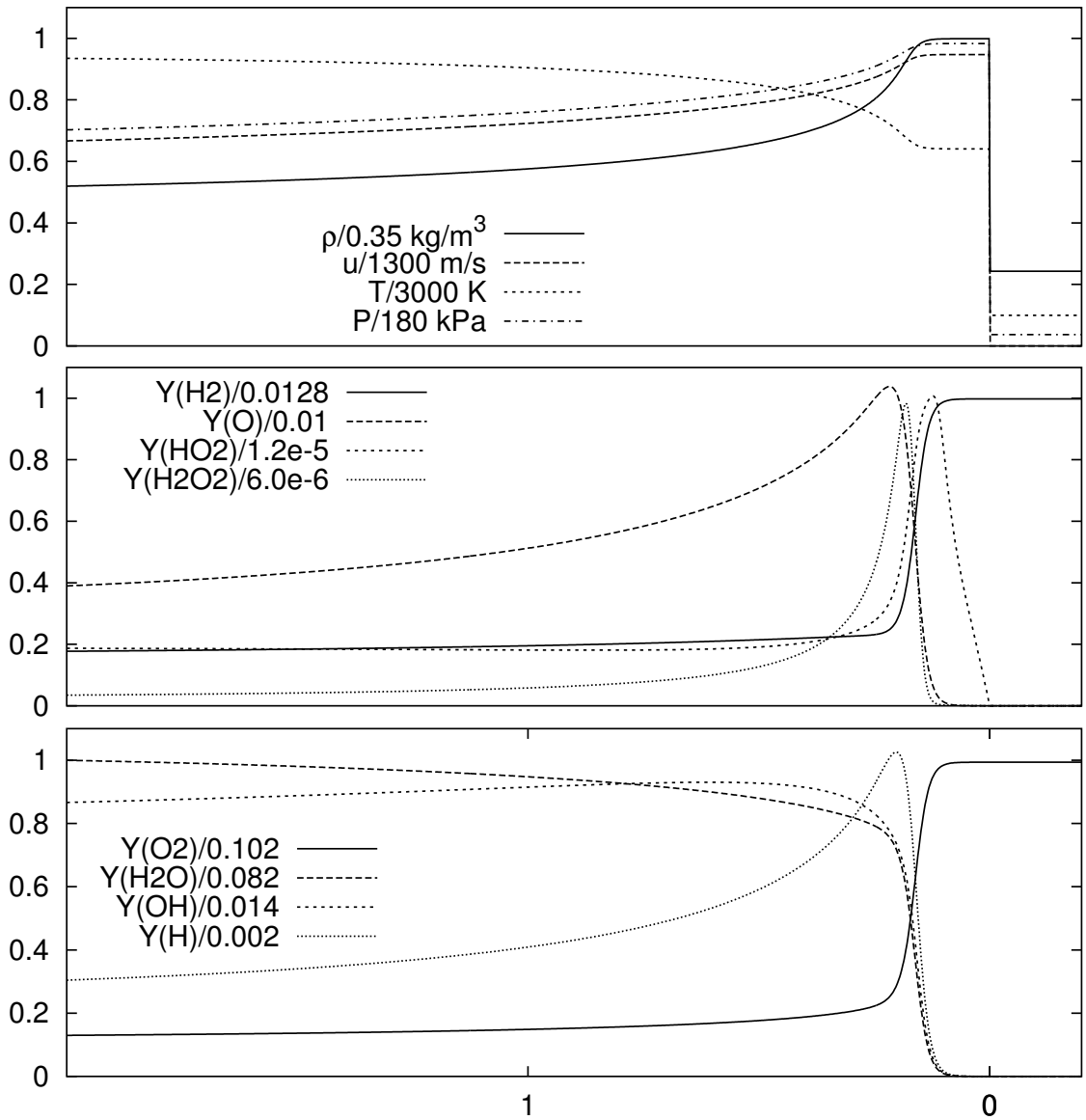

Figure 3.4: Detonation structure of a CJ detonation ($d_{CJ} \approx 1627\,\mathrm{m/s}$) of $H_2 : O_2 : Ar$ with molar ratios $2 : 1 : 7$ at $T_0 = 298\,\mathrm{K}$ and $p_0 = 6.67\,\mathrm{kPa}$. The abscissae display $\grave{x}\,[\mathrm{cm}]$, the distance behind the detonation front.

Direct Integration in Primitive Variables

Instead of calculating intersections of Rayleigh line and Hugoniot curve in order to find $\rho, p, \grave{u}$, it is also possible to solve the full system of stationary transport equations simultaneously. This approach is described especially by Fickett and Davis [73] and by Shepherd [167]. We apply the primitive variable formulation (2.83) to (2.86) for $d = 1$. For the stationary situation of interest we obtain under Galilean transformation

$$\grave{u}\frac{\partial \rho}{\partial \grave{x}} + \rho\frac{\partial \grave{u}}{\partial \grave{x}} = 0 \ , \quad \grave{u}\frac{\partial \grave{u}}{\partial \grave{x}} + \frac{1}{\rho}\frac{\partial p}{\partial \grave{x}} = 0 \ , \quad \grave{u}\frac{\partial p}{\partial \grave{x}} + \rho c^2\frac{\partial \grave{u}}{\partial \grave{x}} = \rho c^2 \dot{\varsigma} \ , \tag{3.39}$$

$$\grave{u}\frac{\partial Y_i}{\partial \grave{x}} = \frac{W_i\,\dot{\omega}_i}{\rho} \ , \ i = 1, .., K-1 \ ,$$

from which we easily derive the system of ODEs

$$\frac{\partial \rho}{\partial \grave{x}} = -\frac{\rho\dot{\varsigma}}{\xi\grave{u}} \ , \quad \frac{\partial p}{\partial \grave{x}} = -\frac{\rho\grave{u}\dot{\varsigma}}{\xi} \ , \quad \frac{\partial \grave{u}}{\partial \grave{x}} = \frac{\dot{\varsigma}}{\xi} \ , \quad \frac{\partial Y_i}{\partial \grave{x}} = \frac{W_i\,\dot{\omega}_i}{\rho\grave{u}} \ , \ i = 1, \ldots, K-1 \tag{3.40}$$

with

$$\xi = 1 - M^2 \ , \quad M = \frac{\grave{u}}{c} \ , \quad c = \sqrt{\gamma\frac{p}{\rho}} \ , \quad T = \frac{pW}{\rho\mathcal{R}} \ , \quad W = \left(\sum \frac{Y_i}{W_i}\right)^{-1} \ ,$$

which is valid for $\grave{x} > 0$. Initial conditions for (3.40) at $\grave{x} = 0$ are $\rho(0) = \rho_{vN}$, $\grave{u}(0) = \grave{u}_{vN}$, $p(0) = p_{vN}$ and $Y_i(0) = Y_i^0$ for $i = 1, \ldots, K-1$. Herein, ρ_{vN}, $\grave{u}_{vN}$ and p_{vN} denote the values at the head of the detonation front. The left limit of the leading discontinuity is called the von Neumann point and its values can be determined by applying the Rankine-Hugoniot jump conditions of Theorem 2 in the one-dimensional form (2.22) at $\grave{x} = 0$. As the RH jump conditions are only applicable to PDEs in conservation-law form (2.1) we have to use the Eqs. (3.3) to (3.5) instead of the primitive formulation (2.83) to (2.85) for this. Under Galilean transformation the discontinuity is at rest ($\sigma = 0$ in Eq. (2.22)) and by using $H = E + p/\rho$ we obtain

$$\Delta(\rho\grave{u}) = 0 \ , \quad \Delta(\rho\grave{u}^2 + p) \ , \quad \Delta(\rho\grave{u}H) = 0 \ .$$

If the values in the unburned gas and at the vN point are inserted, we derive

$$\rho_{vN}\,\grave{u}_{vN} = \rho_0 d^\star \ , \quad \rho_{vN}\,\grave{u}_{vN}^2 + p_{vN} = \rho_0\,(d^\star)_0^2 + p_0 \ , \quad \rho_{vN}\,H_{vN}\,\grave{u}_{vN} = \rho_0 H_0 d^\star \ .$$

Simple algebraic manipulations show, that the last equations are identical to (3.34) to (3.36) with $\zeta_{vN} := \rho_0/\rho_{vN}$. We solve (3.36) numerically to find ζ_{vN} as discussed before and calculate the values at the vN point by $\rho_{vN} = \rho_0/\zeta_{vN}$, $\grave{u}_{vN} = \zeta_{vN}\,d^\star$ and $p_{vN} = p(\zeta_{vN})$ from (3.35). Beside numerical round-off errors the direct integration method gives the same result as the algebraic method described in the preceding section.

Equilibrium State and Chapman-Jouguet Point

Like in the simplified ZND model of Sec. 3.1.1 the Mach number $\grave{M}_{CJ} = \grave{u}_{CJ}/c_{CJ}$ of the particular equilibrium state called the Chapman-Jouguet point with values $\rho_{CJ}, p_{CJ}, \grave{u}_{CJ}, Y_i^{CJ}$ can be shown to be equal to 1. A proof of this fact can be found in the book Williams [204]. Integration of (3.30) between a point $\grave{x}_0 < 0$ and $\grave{x} = \infty$ gives

$$\rho_{CJ}\grave{u}_{CJ}^2 + p_{CJ} = \rho_0 d_{CJ}^2 + p_0 \ .$$

Using $\grave{u}_{CJ} = c_{CJ} = \sqrt{\gamma_{CJ} p_{CJ}/\rho_{CJ}}$ we obtain from this expression

$$(\gamma_{CJ} + 1)p_{CJ} - p_0 - \rho_0 d_{CJ}^2 = 0 \ .$$

The last equation is only satisfied in the CJ point and can be employed to derive an estimate for the unknown detonation velocity d_{CJ}. All estimations of d_{CJ} in this thesis were calculated under the simplifying assumption of chemical equilibrium (see Sec. 2.3.7) with the program *Gaseq* of Morley [131].

Induction Length

Unlike the examples with simplified chemistry shown in Fig. 3.3 the CJ detonation with detailed chemistry in Fig. 3.4 has a clearly defined induction distance l_{ig}, where the hydrodynamic flow values of the von Neumann point are nearly preserved (compare Chap. 1). The induction distance l_{ig} is an appropriate characteristic length scale for detonations with detailed chemical reaction. It can be estimated to good accuracy by the simple expression

$$l_{ig} \approx t_{ig}\grave{u}_{vN} \ .$$

Herein, t_{ig} denotes the induction time between ignition and measurable chemical reaction. It depends especially on the induction temperature T_{vN} at the von Neumann point and can be calculated by purely chemical kinetics computations in advance. For the CJ detonation of Fig. 3.4 we have $t_{ig} \approx 3.55\,\mu$s[3] and with $\grave{u}_{vN} \approx 395.5\,$m/s follows an approximate induction length of $l_{ig} \approx 1.404\,$mm.

3.2 Instabilities in Detonation Waves

The classical ZND theory postulates that detonations are quasi-one-dimensional steady combustion waves. But already early experiments by Denisov and Troshin [55], Voisekhovsky et al. [199] and later by Strehlow [181] and his coworkers have shown that self-sustaining detonation waves in fact exhibit instationary multi-dimensional sub-structures and do not remain planar. For instance, it is a common belief that Chapman-Jouguet detonations ($f = 1.0$) never remain planar, because

[3]For all measurements of induction times throughout this thesis the criterion $T > T_{vN} + 20\,$K has been applied.

up to now, all such detonations in real combustible gas mixtures have been found to be unstable to certain non-planar disturbances [204]. In particular, the one-dimensional ZND solutions of the previous section and of Sec. 3.1.2 are instable even to planar disturbances by themselves. Usually the corresponding unstable modes are suppressed by stronger modes in the transverse directions, but *galloping* detonations with a dominant longitudinal oscillation also have been observed occasionally.

The hydrodynamic stability analysis for the ZND model with simplified reaction was pioneered by Erpenbeck [64, 65, 66, 68]. A review can be found in [67]. Fickett and Davis [73] also describe Erpenbeck's method in detail. In the linearized theory, the time-dependent equations of motions are linearized around the steady solution and it is analyzed, if arbitrary perturbations around the steady state will grow or decay. Following Erpenbeck [65], Bourlioux, Majda and Roytburd gave in [35] a detailed stability analysis in one space dimension for the frequently studied case $\gamma = 1.2$, $E_0^\star = 50$, $Q_0 = 50$ utilizing a numerical method by Lee and Stewart [111]. They found that the one-dimensional ZND detonation is stable for $f > f_0^\star = 1.73$. Further on, they found one unstable mode for $f_1^\star = 1.57 < f \leq f_0^\star$, two unstable modes for $f_2^\star = 1.39 < f \leq f_1^\star$ and three unstable modes for at least $1.3 < f \leq f_2^\star$. For $f = 1.2$ they discovered five unstable modes. In [34] Bourlioux and Majda extended the same linear stability method to two dimensions and were able to estimate the degree of instability with respect to the wavelength of transverse oscillations. Some more recent contributions to the topic of multi-dimensional linear stability analysis are [174, 173] and [168].

Linearized theories have the disadvantage that they do not provide much information about the flow pattern. In order to gain detailed insight into the hydrodynamic flow approximate nonlinear theories have been developed. Their idea is to replace the unstable steady solution by an oscillatory solution. Erpenbeck presented a method based on a Fourier series expansion, which is developed up to terms of second order, applicable to systems near the stability limit with only a single frequency of oscillation [66, 68]. A theory based on geometric acoustics has been developed by Strehlow and his coworkers [17, 16, 180, 179]. Tong and Abouseif derived a third method that does not consider the Arrhenius reaction rate $\exp(-E_0^\star/T)$, but the square wave model which follows from the Arrhenius law for $E_0^\star \longrightarrow \infty$ [4, 5]. The same model is studied by linear stability analysis by Buckmaster and his collaborators [39, 40, 37, 38].

All theoretical approaches clearly indicate that most ZND profiles are unstable to transverse oscillations [68] unless the heat release Q_0 and/or activation energy $E_0^\star$ are very small or the overdrive factor f is very large [34].

3.3 Transverse Detonation Structure

Systematic experiments to enlighten the multi-dimensional sub-structure of detonation waves were carried out for the first time by Strehlow and his coworkers [176, 182, 177, 178]. In contrast to previous experiments [55, 199] they utilized tubes with a rectangular cross-section to avoid the spinning of the detonation around the

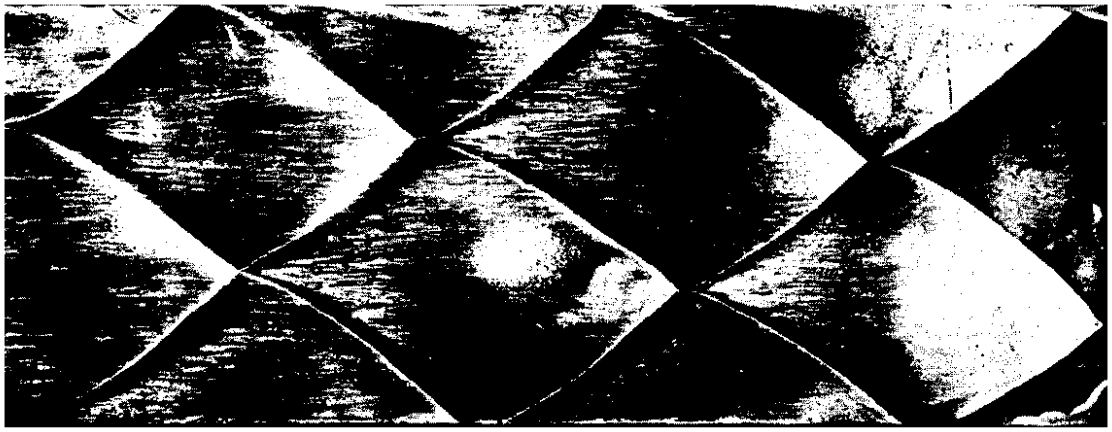

Figure 3.5: Regular smoke tracks for a $H_2 : O_2 : Ar$ detonation with molar ratios $2 : 1 : 7$ at $T_0 = 298\,\mathrm{K}$ and $p_0 = 6.67\,\mathrm{kPa}$ [176].

middle-axis. They coated the walls with soot and noticed that some particular detonation configurations left very regular patterns behind (see Fig. 3.5). For the first time, schlieren photographs were taken showing that transverse instabilities initiate instationary pressure waves perpendicular to the detonation front. A triple point is created where a transverse pressure wave hits the leading shock front. A shear layer (slip line) originates in each triple point and removes the soot from the walls. The observed "fish-scale" patterns (see left picture of Fig. 3.6) were the trajectories of these triple points. A closed cell between two trajectories is called a *detonation cell*.

The length L and the width λ of the detonation cells are important characteristic parameters for a detonation configuration. These parameters are determined by the ratio of the average propagation velocities of detonation front and transverse waves. Although the planar detonation is perturbed, it has been observed that the average velocity of a multi-dimensional Chapman-Jouguet detonation is still approximately d_{CJ}. On the other hand, the average propagation velocity of the transverse waves is only slightly above the speed of sound in the final equilibrium state c_{CJ}. The fixed ratio $c_{CJ}/d_{CJ} \approx 0.5$ is common for CJ detonations, which explains that CJ detonations with regular detonation cells all exhibit a nearly constant ratio $\lambda/L \approx 0.6$ [112, 197].

Shchelkin and Troshin [165] proposed a direct proportionality between λ and a characteristic length scale of the stationary one-dimensional ZND structure, e.g. l_{ig}. The linear equation

$$\lambda = C_R \, l_{ig} \tag{3.41}$$

with a reaction-dependent constant C_R does not consider any non-linearities and is only a rough estimation. Nevertheless, it predicts at least the order of the cell size correctly [166].

The left picture of Fig. 3.6 displays the hydrodynamic flow pattern of a detonation with regular cellular structure, how it is known since the early 1970th. The right picture shows the wave configuration in a triple point in detail. This particu-

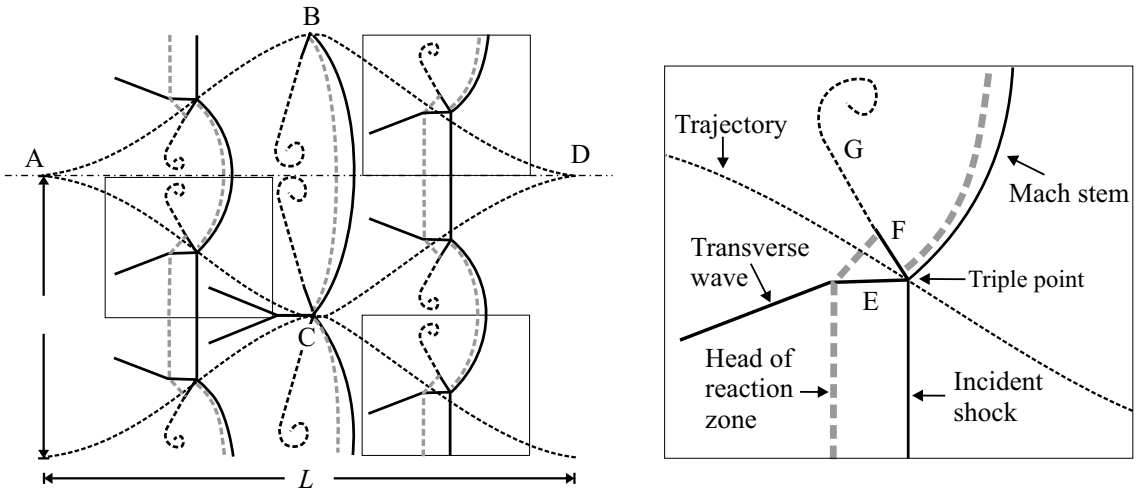

Figure 3.6: Left: regular detonation structure at three different time steps on triple point trajectories, right: enlargement of a periodical triple point configuration. E: reflected shock, F: slip line, G: diffusive extension of slip line with flow vertex.

lar situation is reproduced periodically in space and in time. It consists of a Mach reflection similar to the one observed in the non-reactive computation in Sec. 5.6.1. The undisturbed detonation front is the incident shock, while the transverse wave takes the role of the reflected shock. The triple point is driven forward by a strong shock wave, called Mach stem. Mach stem and reflected shock enclose the slip line, the contact discontinuity, which writes the soot tracks. Between these four discontinuities only those configurations are admissible that satisfy the Rankine-Hugoniot jump condition (2.10) at all four discontinuities. In a frame of reference attached to the triple point the coupled shock relations can be analyzed effectively (see for instance [204], [165] or [73]).

In self-sustaining detonations the Mach stem is always much stronger than the incident shock. While pressure and temperature behind the incident shock are below the von Neumann values of a plane ZND detonation, these quantities are drastically increased by the Mach stem. Consequently, the induction length separating shock and reaction zone is significantly shorter here than l_{ig}, while it is above l_{ig} behind the incident shock. The shock front inside the detonation cell travels as two Mach stems from point A to the line BC. In the point B and C the triple point configuration is inverted nearly instantaneously and the front in the cell becomes an incident shock. The change along the symmetry axis from A to D is smooth. From the beginning of the detonation cell at A to its end at D the pressure and therefore the temperature decrease continuously. At the end of the detonation cell the distance between the head of the reaction zone and the incident shock is maximal. The two triple points merge into one point exactly in position D. The incident shock vanishes completely and the stable situation displayed in the right picture of Fig. 3.6 does not exists anymore. The slip line, which was necessary for a stable triple point configuration between Mach stem and incident shock, is torn off the detonation front and remains

behind. Two new triple points with two new slip lines develop immediately after D.

Linear stability analysis of the growth rate of transverse oscillations for the simplified two-dimensional ZND model [34] shows that the cell spacing λ corresponds to the most unstable wavelength in the transverse direction. But it can not be expected that this spacing is reproduced exactly in combustion channels with finite width w'. In a finite channel only periodic regular cells satisfying the equation

$$w' = j\,\frac{\lambda}{2}\,, \quad j \in \mathbb{N}$$

can be produced. Especially a very thin channel can enforce a strong adaptation of the detonation to the geometry leading to measurements that do not represent the most unstable mode. But if the channel is wider or carefully chosen (in numerical simulations), we can expect to observe a cell size that is at least relatively near to the size that would occur in free space. The results of Bourlioux and Majda in [34] clearly show that the length with maximal instability is only the global maximum of a continuous function. In fact, this particular value is surrounded by wavelengths that are only slightly more stable. Hence, the detonation usually has some freedom in "choosing" an appropriate cell size and we can expect that at least the qualitative behavior is reproduced correctly. Nevertheless, minor inaccuracies in cell size measurements, that are regarded as natural in experiments, are also unavoidable in numerical simulations.

Chapter 4

Numerical Methods

In this chapter we derive methods for the numerical solution of the reactive Euler equations of Sec. 2.3. Our basic discretization is the finite volume (FV) approach, which is derived in detail on two-dimensional Cartesian grids in Sec. 4.1. In our presentation we focus especially on the numerical incorporation of the source term. In Sec. 4.1.3 we introduce the solution technique which is most appropriate for transient detonation waves: the operator splitting technique or method of fractional steps [96]. It allows a decoupled numerical integration of the homogeneous transport equations and the chemically reactive source term.

In Sec. 4.2 we describe the standard approaches in constructing first-order upwind schemes for the homogeneous equations. The MUSCL variable extrapolation technique [191, 195] and the Wave Propagation Method [119, 107] are introduced in Sec. 4.3 as two possible higher-order extensions. In the Secs. 4.4 to 4.7 we employ these methods to construct high resolution upwind schemes for mixtures of thermally perfect gases. After the notation of discrete boundary conditions and the description of an efficient iterative method for the evaluation of the complex equation of state in Sec. 4.4, we present in Sec. 4.5 the Flux-Vector Splittings of Steger-Warming and Van Leer-type [169, 127, 109, 84]. The approximative Riemann solvers of Roe and Harten-Lax-Van Leer (HLL) are derived in Sec. 4.6. Sec. 4.7 discusses the applicability of the two higher-order methods to mixtures of thermally perfect gases. Only the MUSCL variable extrapolation is reliable and we describe a robust reconstruction strategy.

The Secs. 4.8 and 4.9 summarize different known weaknesses of shock-capturing upwind schemes. While Sec. 4.8 recalls problems that are present already in the single-component case, Sec. 4.9 uncovers deficiencies associated to the multi-component model. The Roe scheme is the only FV method that suffers from all mentioned problems. We demonstrate that artificial oscillations at strong shock waves [154, 9], which typically would appear at the head of detonation waves [150, 14], can be moderated or even avoided completely within the Roe scheme by adding numerical viscosity to the flux approximation via the entropy correction [160]. Further on, we describe how unphysical total and energy densities due to the Roe linearization [62] can be circumvented by switching to the robust HLL scheme. Finally, we

present a modification the Roe flux that ensures the positivity of the mass fractions for all species [108]. All corrections are combined in Sec. 4.6.3 in a robust and reliable Roe-type method. In Chap. 6 we demonstrate that this corrected Roe-HLL scheme is superior for detonation simulations to all other tested upwind schemes. It has been employed for all computations with detailed chemistry in Chap. 7.

In the last section of this chapter we describe briefly the numerical integration of stiff reaction terms in the operator splitting approach and the practical choice of typical parameters of black-box integration routines.

4.1 Finite Volume Methods

Various publications on the construction of finite volume schemes for hyperbolic conservation laws are available today. Useful text books have been presented for instance by Godlewski and Raviart [82], LeVeque [117], Toro [187], Kröner [105] and Hirsch [94].

4.1.1 Generalities

Let us consider a Cauchy Problem in d space dimensions for the hyperbolic conservation law (2.1) with $\mathbf{s} \equiv 0$. Without loss of generality we set $d = 2$ in the following to simplify the notations. We assume that the Cauchy problem has an entropy solution $\mathbf{q}(\mathbf{x}, t)$ (compare Sec. 2.1). The computational domain D is discretized with a rectangular grid with mesh widths $\Delta x_1, \Delta x_2$ in each coordinate direction and a time step Δt. The discrete mesh points are defined by

$$(x_1^j, x_2^k) := \left(\left(j + \tfrac{1}{2}\right)\Delta x_1, \left(k + \tfrac{1}{2}\right)\Delta x_2\right) \ , \ j, k \in \mathbb{Z} \ . \tag{4.1}$$

Further on, it is useful to define

$$x_1^{j-1/2} := x_1^j - \frac{\Delta x_1}{2} \ , \ j \in \mathbb{Z} \quad \text{and} \quad x_2^{k-1/2} := x_2^k - \frac{\Delta x_2}{2} \ , \ k \in \mathbb{Z} \ . \tag{4.2}$$

Discrete time values are defined by $t_l := l\Delta t \ , \ l \in \mathbb{N}_0$. We denote the value in the discrete point (x_1^j, x_2^k, t_l) by $\mathbf{Q}_{jk}^l$ and define a piece-wise constant approximation $\mathbf{Q}(\mathbf{x}, t)$ to the exact solution $\mathbf{q}(\mathbf{x}, t)$ by

$$\mathbf{Q}(\mathbf{x}, t) = \mathbf{Q}_{jk}^l \ \text{ for } \ (x_1, x_2, t) \in [x_1^{j-1/2}, x_1^{j+1/2}[\times [x_2^{k-1/2}, x_2^{k+1/2}[\times [t_l, t_{l+1}[\ .$$

The solution is approximated by an explicit $(2s+1)^2$-point difference scheme of the form

$$\mathbf{Q}_{jk}^{l+1} = \mathcal{H}^{(\Delta t)}(\mathbf{Q}_{j-s,k-s}^l, \ldots, \mathbf{Q}_{j+s,k+s}^l) \ . \tag{4.3}$$

Definition 8 (Stability). *Scheme (4.3) is said to be stable, if for each time τ there is a constant C_S and a value $l_0 \in \mathbb{N}$ such that $\|\mathcal{H}^{(\Delta t)}(\mathbf{Q}^l)\| \leq C_S$ for all $l\Delta t \leq \tau$, $l < l_0$.*

Definition 9 (Consistency). *Scheme (4.3) is said to be consistent, if the local truncation error*

$$\mathcal{L}^{(\Delta t)}(\mathbf{x},t) := \frac{1}{\Delta t}\left[\mathbf{q}(\mathbf{x},t+\Delta t) - \mathcal{H}^{(\Delta t)}(\mathbf{q}(\cdot,t))\right]$$

satisfies $\|\mathcal{L}^{(\Delta t)}(\cdot,t)\| \to 0$ *as* $\Delta t \to 0$.

Definition 10 (Convergence). *Scheme (4.3) is said to be convergent, if the global error* $\mathcal{E}^{(\Delta t)}(\mathbf{x},t) := \mathbf{Q}(\mathbf{x},t) - \mathbf{q}(\mathbf{x},t)$ *satisfies* $\|\mathcal{E}^{(\Delta t)}(\cdot,t)\| \to 0$ *as* $\Delta t \to 0$ *for all admissible initial data* $\mathbf{q}_0(\mathbf{x})$.

Consistency and stability are necessary conditions for convergence of a finite volume method. But only in the linear case (compare Sec. 4.2.1) the Lax Equivalence Theorem states that these conditions are also sufficient [117].

Definition 11 (Order of accuracy). *Scheme (4.3) is said to be accurate of order o, if for all sufficiently smooth initial data* $\mathbf{q}_0(\mathbf{x})$*, there is a constant* C_L*, such that the local truncation error satisfies* $\|\mathcal{L}^{(\Delta t)}(\cdot,t)\| \le C_L \Delta t^o$ *for all* $\Delta t < \Delta t_0$ *,* $t \le \tau$.

For smooth solutions it can be proven that global and local truncation error are of the same order provided the method is stable [117]. Detailed descriptions of these classical notions can be found in the books of Kröner [105], Godlewski and Raviart [81] and LeVeque [117].

Definition 12 (Conservative form). *Scheme (4.3) is called conservative, if it can be written in the form*

$$\mathbf{Q}^{l+1}_{jk} = \mathbf{Q}^{l}_{jk} - \frac{\Delta t}{\Delta x_1}\left(\mathbf{F}^1_{j+\frac{1}{2},k} - \mathbf{F}^1_{j-\frac{1}{2},k}\right) - \frac{\Delta t}{\Delta x_2}\left(\mathbf{F}^2_{j,k+\frac{1}{2}} - \mathbf{F}^2_{j,k-\frac{1}{2}}\right) \tag{4.4}$$

with

$$\mathbf{F}^1_{j+\frac{1}{2},k} = \mathbf{F}^1(\mathbf{Q}^l_{j-s+1,k-s},\ldots,\mathbf{Q}^l_{j+s,k+s}) \ , \quad \mathbf{F}^1_{j-\frac{1}{2},k} = \mathbf{F}^1(\mathbf{Q}^l_{j-s,k-s},\ldots,\mathbf{Q}^l_{j+s-1,k+s}) \ ,$$
$$\mathbf{F}^2_{j,k+\frac{1}{2}} = \mathbf{F}^2(\mathbf{Q}^l_{j-s,k-s+1},\ldots,\mathbf{Q}^l_{j+s,k+s}) \ , \quad \mathbf{F}^2_{j,k-\frac{1}{2}} = \mathbf{F}^2(\mathbf{Q}^l_{j-s,k-s},\ldots,\mathbf{Q}^l_{j+s,k+s-1}) \ .$$

The functions $\mathbf{F}^n$ are called *numerical fluxes*. In the following, we write $\mathbf{F}^{1,\pm 1/2}_{jk}$ for $\mathbf{F}^1_{j\pm\frac{1}{2},k}$ and $\mathbf{F}^{2,\pm 1/2}_{jk}$ for $\mathbf{F}^2_{j,k\pm\frac{1}{2}}$. A conservative scheme satisfies the discrete conservation property

$$\sum_{j,k\in\mathbb{Z}} \mathbf{Q}^{l+1}_{jk} = \sum_{j,k\in\mathbb{Z}} \mathbf{Q}^{l}_{jk} \ . \tag{4.5}$$

Definition 13 (Consistency of a conservative method). *Scheme (4.4) is said to be consistent with (2.1), if the numerical fluxes satisfy* $\mathbf{F}^n(\mathbf{q},\ldots,\mathbf{q}) = \mathbf{f}_n(\mathbf{q})$ *for all* $\mathbf{q} \in S$.

The Definitions 8 to 11 require an appropriate norm $\|.\|$. The natural norm for conservative finite volume methods is the L^1-norm [117], which takes in our two-dimensional case the form

$$\|\mathbf{v}(\cdot,t)\|_1 = \int_{-\infty}^{\infty}\int_{-\infty}^{\infty} |\mathbf{v}(x_1,x_2,t)|\, dx_1 dx_2 \ . \tag{4.6}$$

4.1.2 Conservation Laws with Source Terms

As the Euler equations are a system of nonlinear hyperbolic conservation laws, non-classical weak solutions have to be considered (see Sec. 2.1). Finite difference discretizations that are obtained by discretizing the system of PDEs directly, for instance by replacing the derivatives in Eq. (2.1) simply by central differences, require differentiability and are therefore restricted to classical solutions. The appropriate alternative here is the finite volume (FV) approach that is based on the discretization of the integral form (2.4) and leads to numerical schemes that are conservative for $\mathbf{s} \equiv \mathbf{0}$. Lax and Wendroff proved in their famous theorem that the limit $\mathbf{q}(\mathbf{x}, t)$ of a converging conservative scheme is always a weak solution [110].

We define a rectangular computational cell C_{jk} around each mesh point (x_1^j, x_2^k). The domain of cell C_{jk} reads

$$I_{jk} = [x_1^{j-1/2}, x_1^{j+1/2}[\times [x_2^{k-1/2}, x_2^{k+1/2}[\ . \tag{4.7}$$

We use I_{jk} and the discrete time interval $[t_l, t_{l+1}[$ as integration domain in the integral form (2.4) and obtain

$$\int\limits_{I_{jk}} \mathbf{q}(\mathbf{x}, t_{l+1})\, d\mathbf{x} - \int\limits_{I_{jk}} \mathbf{q}(\mathbf{x}, t_l)\, d\mathbf{x} + \sum_{n=1}^{d} \int\limits_{t_l}^{t_{l+1}} \int\limits_{\partial I_{jk}} \mathbf{f}_n(\mathbf{q}(\mathbf{o}, t))\, \sigma_n(\mathbf{o})\, d\mathbf{o}\, dt = \int\limits_{t_l}^{t_{l+1}} \int\limits_{I_{jk}} \mathbf{s}(\mathbf{q}(\mathbf{x}, t))\, d\mathbf{x}\, dt \ . \tag{4.8}$$

Within each computational cell C_{jk} the value $\mathbf{Q}_{jk}(t)$ is an approximation to the exact cell average value

$$\mathbf{Q}_{jk}(t) \approx \frac{1}{|I_{jk}|} \int\limits_{I_{jk}} \mathbf{q}(\mathbf{x}, t)\, d\mathbf{x} \ . \tag{4.9}$$

By employing the approximated values $\mathbf{Q}_{jk}(t)$ instead of $\mathbf{q}(\mathbf{x}, t)$ as argument for $\mathbf{s}(\mathbf{q}(\mathbf{x}, t))$ a natural approximation to the cell average of the source term function is found immediately:

$$\mathbf{s}(\mathbf{Q}_{jk}(t)) \approx \frac{1}{|I_{jk}|} \int\limits_{I_{jk}} \mathbf{s}(\mathbf{q}(\mathbf{x}, t))\, d\mathbf{x} \tag{4.10}$$

Furthermore, we define numerical flux functions $\mathbf{F}^n$ at the sides of C_{jk} by

$$\mathbf{F}_{jk}^{1,+1/2}(\mathbf{Q}(t)) \approx \frac{1}{\Delta x_2} \int\limits_{x_2^{k-1/2}}^{x_2^{k+1/2}} \mathbf{f}_1(\mathbf{q}(x_1^{j+1/2}, x_2, t))\, dx_2 \ ,$$

$$\mathbf{F}_{jk}^{2,+1/2}\left(\mathbf{Q}(t)\right) \approx \frac{1}{\Delta x_1} \int\limits_{x_1^{j-1/2}}^{x_1^{j+1/2}} \mathbf{f}_2(\mathbf{q}(x_1, x_2^{k+1/2}, t))\, dx_1 \ .$$

We insert these approximations into (4.8) and divide by $|I_{jk}|$. We obtain

$$\mathbf{Q}_{jk}(t_{l+1}) = \mathbf{Q}_{jk}(t_l) - \sum_{n=1}^{d} \frac{1}{\Delta x_n} \int\limits_{t_l}^{t_{l+1}} \left(\mathbf{F}_{jk}^{n,+1/2}\left(\mathbf{Q}(t)\right) - \mathbf{F}_{jk}^{n,-1/2}\left(\mathbf{Q}(t)\right)\right) dt + \int\limits_{t_l}^{t_{l+1}} \mathbf{s}(\mathbf{Q}_{jk}(t))\, dt \ . \quad (4.11)$$

Explicit Schemes

If the Euler Method is used to approximate all time integrals of Eq. (4.11), the time-explicit scheme

$$\mathbf{Q}_{jk}^{l+1} = \mathbf{Q}_{jk}^{l} - \sum_{n=1}^{d} \frac{\Delta t}{\Delta x_n} \left(\mathbf{F}_{jk}^{n,+1/2}(\mathbf{Q}^l) - \mathbf{F}_{jk}^{n,-1/2}(\mathbf{Q}^l)\right) + \Delta t\, \mathbf{s}(\mathbf{Q}_{jk}^{l}) \quad (4.12)$$

is derived. For $\mathbf{s} \equiv 0$ the scheme is conservative. Although the Euler Method is only first-order accurate, higher-order accuracy can be achieved by the choice of proper numerical flux functions $\mathbf{F}^n$. Various *high resolution* methods have been developed for the case $\mathbf{s} \equiv 0$ that resolve discontinuities sharply and that are at least second-order accurate in smooth solution regions.[1] The MUSCL-Hancock variable extrapolation method that is employed throughout this thesis for this purpose is described in Sec. 4.3. In the following we assume a consistent and stable high resolution discretization of $\mathbf{F}^n$ that gives second-order accuracy on smooth solutions for the special case $\mathbf{s} \equiv 0$. Nevertheless, the accuracy of the entire scheme (4.12) will only be of first order, because the source term discretization is just first-order accurate in time. An explicit second-order alternative is

$$\mathbf{Q}_{jk}^{l+1} = \mathbf{Q}_{jk}^{l} - \sum_{n=1}^{d} \frac{\Delta t}{\Delta x_n} \left(\mathbf{F}_{jk}^{n,+1/2}(\mathbf{Q}^l) - \mathbf{F}_{jk}^{n,-1/2}(\mathbf{Q}^l)\right) + \frac{1}{2}\Delta t \left(\mathbf{s}(\mathbf{Q}_{jk}^{l}) + \mathbf{s}(\mathbf{Q}_{jk}^{l} + \Delta t \mathbf{s}(\mathbf{Q}_{jk}^{l}))\right) \quad (4.13)$$

that applies a two-stage Runge-Kutta method for the source term integral.

Mixed Explicit-Implicit Schemes

If all fluxes vanish, i.e. $\mathbf{f}_n \equiv 0$, Eq. (2.1) reduces to the ordinary differential equation (ODE)

$$\frac{\partial \mathbf{q}}{\partial t} = \mathbf{s}(\mathbf{q}(t)) \quad (4.14)$$

[1] Detailed presentations of different higher order reconstruction techniques can be found in the books of Toro [187], Hirsch [94] and LeVeque [117].

and our FV scheme (4.11) simplifies to the initial-value problem

$$\mathbf{Q}_{jk}^{l+1} = \int_{t_l}^{t_{l+1}} \mathbf{s}(\mathbf{Q}_{jk}(t))\, dt$$

that can be solved separately in every computational cell. The efficiency of the time-explicit schemes (4.12) and (4.13) can suffer significantly from the mathematical properties of the ODE (4.14). If the ODE is *stiff* (see Def. 17) the explicit schemes (4.12), (4.13) will undergo significant stability restrictions that reduce the maximal time step drastically [56, 106]. From the theory of ODEs it can be concluded that for instance scheme (4.12) can be guaranteed to be stable only, if the eigenvalues ξ_m of the Jacobian $\partial\mathbf{s}(\mathbf{q})/\partial\mathbf{q}$ satisfy the condition $|\xi_m + 1| < 1$ for all $m = 1, \ldots, M$.[2] Schemes for stiff ODEs should be time-implicit and in order to obtain a stable FV scheme we have to discretize a least the source term integral in (4.11) with a time-implicit method. Two alternatives with absolute stability and second-order accuracy on the source term integral are

$$\mathbf{Q}_{jk}^{l+1} = \mathbf{Q}_{jk}^{l} - \sum_{n=1}^{d} \frac{\Delta t}{\Delta x_n} \left(\mathbf{F}_{jk}^{n,+1/2}(\mathbf{Q}^l) - \mathbf{F}_{jk}^{n,-1/2}(\mathbf{Q}^l) \right) + \frac{1}{2}\Delta t \left(\mathbf{s}(\mathbf{Q}_{jk}^{l}) + \mathbf{s}(\mathbf{Q}_{jk}^{l+1}) \right) \tag{4.15}$$

that is based on the Trapezoidal Rule and

$$\mathbf{Q}_{jk}^{l+1} = \mathbf{Q}_{jk}^{l} - \sum_{n=1}^{d} \frac{\Delta t}{\Delta x_n} \left(\mathbf{F}_{jk}^{n,+1/2}(\mathbf{Q}^l) - \mathbf{F}_{jk}^{n,-1/2}(\mathbf{Q}^l) \right) + \Delta t\, \mathbf{s}\left(\frac{1}{2} \left(\mathbf{Q}_{jk}^{l} + \mathbf{Q}_{jk}^{l+1} \right) \right) \tag{4.16}$$

that utilizes the Mid-Point Rule. Both methods require the solution of a nonlinear equation for $\mathbf{Q}_{jk}^{l+1}$ in every cell. In practice, even mixed schemes like (4.15) or (4.16) are usually regarded to be too expensive. The accurate integration of a stiff source term (especially in the case of detailed non-equilibrium combustion) can involve time steps that are still significantly below a reasonable global time step Δt (compare Chap. 1). If the source term integration in only one single cell needs a time step $\Delta t_c \ll \Delta t$, Δt_c would have to be used as global time step, although the changes in the hydrodynamic flow during Δt_c might be negligible. A strict local phenomenon would determine the efficiency of the entire scheme. Therefore, we introduce in Sec. 4.1.3 a method that allows a more decoupled treatment of the time-implicit source term discretization and the time-explicit hydrodynamic transport scheme. This method is the operator splitting technique or method of fractional steps, which is most frequently used for time-dependent reactive flow computations [137]. It is the basic discretization throughout this thesis.

[2] See [56] for a detailed discussion of the region of *absolute stability* for the explicit Euler Method.

Implicit Schemes

Most schemes for hyperbolic conservation laws rely on a flux approximation only on the basis of t_l, but in principle the same implicit quadrature rule that is applied to the source term integral in (4.11) could also be used for the flux integrals. In this case the numerical fluxes $\mathbf{F}^n_{jk}$ do not only depend on $\mathbf{Q}^l$ but also on the unknown values $\mathbf{Q}^{l+1}$. The major advantage of fully or globally implicit discretizations is that the time step Δt is (theoretically) not restricted by any stability considerations.[3] Their principal disadvantage is, that they require the solution of a large coupled system of nonlinear algebraic equations for *all* cell values in each time step and become extraordinary expensive, if a large number of grid cells is unavoidable. Useful references on time-implicit high resolution methods are [206, 88].

A thorough comparison of globally implicit and mixed explicit-implicit schemes coupled by the method of fractional steps (compare Sec. 4.1.3) applied to time-dependent reactive flow problems, in particular to one-dimensional ZND detonations waves with simplified chemistry (compare Sec. 3.1.1), can be found in the work of Geßner [78]. He noticed that the usage of larger time steps in fully implicit schemes increases the numerical damping remarkably and that time-dependent results obtained with such schemes (although computationally more cumbersome) are usually less accurate in time than those of operator splitting methods. The fully implicit approach is particular well suited for stationary, non-time-dependent flow problems like they typically arise for instance in steady aerodynamics [207]. But it is inappropriate for the simulation of detonation waves, because detonations are characterized by an intrinsically instationary behavior (compare Sec. 3.2). Consequently, globally implicit schemes are not considered any further in this thesis.

4.1.3 The Method of Fractional Steps

The method of fractional steps is based on the idea of time-operator splitting that has been introduced by Janenko [96]. The homogeneous partial differential equation

$$\frac{\partial \mathbf{q}}{\partial t} + \sum_{n=1}^{d} \frac{\partial}{\partial x_n} \mathbf{f}_n(\mathbf{q}) = 0 \ , \quad \text{IC:} \ \ \mathbf{Q}^l \ \stackrel{\Delta t}{\Longrightarrow} \tilde{\mathbf{Q}}^{l+1} \tag{4.17}$$

and the ordinary differential equation

$$\frac{\partial \mathbf{q}}{\partial t} = \mathbf{s}(\mathbf{q}) \ , \quad \text{IC:} \ \ \tilde{\mathbf{Q}}^{l+1} \ \stackrel{\Delta t}{\Longrightarrow} \mathbf{Q}^{l+1} \tag{4.18}$$

[3] A special case are numerical methods that follow characteristics backward in time. They discretize the flux integrals with an implicit quadrature rule, but Δt is restricted by the standard CFL condition (compare Eqs. (4.29) and (4.42)) of time-explicit schemes. High resolution schemes of this type are for instance Colella's Piece-Wise Linear Method that uses the Trapezoidal Rule between the two discrete time points t_l and t_{l+1} and Ben Artzi's and Falcovic's Generalized Riemann Problem Method that applies the mid-point approximation at $t_l + \frac{1}{2}\Delta t$. See [187] for an introduction to both methods.

are solved successively with the result of the preceding step as initial condition (IC). In each computational cell the source term is integrated separately, the global coupling is achieved afterward by solving the homogeneous transport problem.

If we denote the discrete solution operator of (4.17) by $\mathcal{H}^{(\Delta t)}$ and the discrete operator of (4.18) by $\mathcal{S}^{(\Delta t)}$, the entire splitting scheme (4.17)+(4.18) reads

$$\mathbf{Q}^{l+1} = \mathcal{S}^{(\Delta t)}\mathcal{H}^{(\Delta t)}(\mathbf{Q}^l) \ . \tag{4.19}$$

Scheme (4.19) is called *Godunov splitting*. It is only first-order accurate in time, even if higher-order accurate operators $\mathcal{S}^{(\Delta t)}$ and $\mathcal{H}^{(\Delta t)}$ are employed [187]. A second-order accurate alternative is

$$\mathbf{Q}^{l+1} = \mathcal{S}^{(\frac{1}{2}\Delta t)}\mathcal{H}^{(\Delta t)}\mathcal{S}^{(\frac{1}{2}\Delta t)}(\mathbf{Q}^l) \tag{4.20}$$

that is called *Strang splitting* [175]. But in many practical cases nearly identical results are obtained with (4.19) and (4.20). Leaving the application of boundary conditions aside the successive application of Strang splitting reads

$$\mathcal{S}^{(\frac{1}{2}\Delta t)}\mathcal{H}^{(\Delta t)}\mathcal{S}^{(\Delta t)}\mathcal{H}^{(\Delta t)}\mathcal{S}^{(\Delta t)}\ldots\mathcal{S}^{(\Delta t)}\mathcal{H}^{(\Delta t)}\mathcal{S}^{(\frac{1}{2}\Delta t)}(\mathbf{Q}^0) \ ,$$

which is identical to Godunov splitting beside the first and the last step.

Local Sub-Cycling and Global Time Step Selection

The method of fractional steps decouples the physical processes of hydrodynamic transport and chemical reaction. Especially, it allows the integration of the source term with multiple time steps that can be chosen separately for each grid cell C_{jk} (sub-cycling). The local time steps Δt^{ν}_{jk} are chosen with respect to the local stiffness and required accuracy under the restriction

$$\Delta t = \sum_{\nu} \Delta t^{\nu}_{jk} \ .$$

A further advantage of the operator splitting approach with local sub-cycling is that the source term need not be considered in the derivation of high resolution FV schemes and existing implementations can be reused without modifications. On the other hand, sophisticated ODE methods of high accuracy with automatic time step adjustment and automatic switching between schemes for stiff and non-stiff ODEs can be incorporated as a "black-box" (compare Sec. 4.10).

In principle, the method of fractional steps with local sub-cycling would allow us to leave the source term integration completely aside when selecting the global time step Δt. But it has to be underlined that nevertheless all physical relevant phenomena have to be resolved by the transport scheme. Especially stiff reaction terms usually require a significant global time step reduction. Various heuristic criteria have been proposed to detect such cases [137, 43]. But stiff source terms also require a sufficiently fine spatial resolution that is able to represent the strong

local flow changes due to the source correctly. If the mesh widths Δx_n are too coarse, the unavoidable averaging in the cells can lead to utterly incorrect results [123].

In this thesis, we only present sufficiently resolved calculations. A fully adaptive mesh refinement approach (AMR) is utilized to supply the necessary local temporal *and* spatial resolution dynamically on the basis of hydrodynamic refinement criteria. The entire refinement strategy is described in detail in Chap. 5. In particular, the heuristic error estimation derived in Sec. 5.4.2 provides a natural criterion to recognize changes in the hydrodynamic flow caused by the source term. Consequently, no additional limiting strategy for the time steps on the different levels of the AMR hierarchy by an heuristic criterion derived from the source term had to be implemented. In all computations included in this thesis (even those with stiff non-equilibirum chemistry) a sufficient refinement was achieved by applying the criteria of Sec. 5.4 only.[4]

Dimensional Splitting

The idea of operator splitting can also be applied to the solution of (4.17), i.e. to the homogeneous operator $\mathcal{H}^{(\Delta t)}$. A simple dimensional splitting scheme in two space dimensions is

$$\begin{aligned} \frac{\partial \mathbf{q}}{\partial t} + \frac{\partial}{\partial x_1}\mathbf{f}_1(\mathbf{q}) = 0 \ , \quad & \text{IC: } \mathbf{Q}^l \quad \overset{\Delta t}{\Longrightarrow} \quad \tilde{\mathbf{Q}}^{1/2} \ , \\ \frac{\partial \mathbf{q}}{\partial t} + \frac{\partial}{\partial x_2}\mathbf{f}_2(\mathbf{q}) = 0 \ , \quad & \text{IC: } \tilde{\mathbf{Q}}^{1/2} \quad \overset{\Delta t}{\Longrightarrow} \quad \mathbf{Q}^{l+1} \ . \end{aligned} \tag{4.21}$$

By denoting the single dimensional steps by $\mathcal{X}_1^{(\Delta t)}$ and $\mathcal{X}_2^{(\Delta t)}$ scheme (4.21) is written in analogy to scheme (4.19) as

$$\mathbf{Q}^{l+1} = \mathcal{X}_2^{(\Delta t)}\mathcal{X}_1^{(\Delta t)}(\mathbf{Q}^l) \ . \tag{4.22}$$

The three-dimensional analogue simply reads $\mathbf{Q}^{l+1} = \mathcal{X}_3^{(\Delta t)}\mathcal{X}_2^{(\Delta t)}\mathcal{X}_1^{(\Delta t)}(\mathbf{Q}^l)$. Like the standard Godunov splitting (4.19) scheme (4.22) is first-order accurate in time, if the solution operators $\mathcal{X}_n^{(\Delta t)}$ are at least first-order accurate [187]. A second-order accurate scheme (supposed that the operators $\mathcal{X}_n^{(\Delta t)}$ are at least second-order) is

$$\mathbf{Q}^{l+1} = \mathcal{X}_1^{(\frac{1}{2}\Delta t)}\mathcal{X}_2^{(\Delta t)}\mathcal{X}_1^{(\frac{1}{2}\Delta t)}\mathbf{Q}^l) \tag{4.23}$$

or $\mathbf{Q}^{l+1} = \mathcal{X}_1^{(\frac{1}{2}\Delta t)}\mathcal{X}_2^{(\frac{1}{2}\Delta t)}\mathcal{X}_3^{(\Delta t)}\mathcal{X}_2^{(\frac{1}{2}\Delta t)}\mathcal{X}_1^{(\frac{1}{2}\Delta t)}(\mathbf{Q}^l)$ in three space dimensions. Dimensional splitting is a simple and efficient possibility of extending high resolution schemes that originally have been developed in one space dimension to multiple dimensions. Therefore, we restrict our presentation of numerical schemes for the hydrodynamic transport to the one-dimensional case.

[4] Geßner incorporated a sophisticated global time step limitation derived from local source term integration into a fully adaptive refinement strategy, but noticed no improvement compared to the fully adaptive approach alone for typical detonation problems with simplified chemistry [78].

4.2 Upwind Methods

All modern high resolution FV schemes are built upon first-order accurate upwind methods that utilize characteristic information. To introduce the idea of upwinding and to supply the basis of the Flux Difference Splitting methods (see Sec. 4.2.4), the upwind scheme for linear hyperbolic systems of conservation laws is derived.

4.2.1 Linear Upwind Scheme

In Sec. 2.2 we recalled the exact solution of the RP for the linear system (2.18). It was found that the solution is self-similar, i.e. $\mathbf{q}(x,t) \equiv \mathbf{v}(x/t)$. In particular, $\mathbf{q}(0,t) = const.$ holds true for $t \in \mathbb{R}^+$. Hence, the flux $\mathbf{F}(\mathbf{q}_L, \mathbf{q}_R) := \mathbf{f}(\mathbf{q}(0,t)) = \mathbf{A}\mathbf{q}(0,t)$ can easily be evaluated for all times t for the exact solution (2.20)

$$\begin{aligned}\mathbf{F}(\mathbf{q}_L, \mathbf{q}_R) &= \mathbf{A}\mathbf{q}_L + \sum_{\lambda_m<0} a_m \lambda_m \mathbf{r}_m = \mathbf{A}\mathbf{q}_R - \sum_{\lambda_m\geq 0} a_m \lambda_m \mathbf{r}_m \\ &= \sum_{\lambda_m\geq 0} \delta_m \lambda_m \mathbf{r}_m + \sum_{\lambda_m<0} \beta_m \lambda_m \mathbf{r}_m \ .\end{aligned} \tag{4.24}$$

We introduce the notations

$$\begin{aligned}\mathbf{\Lambda}^+ &:= \mathrm{diag}(\lambda_1^+, \ldots, \lambda_M^+), \quad \lambda_m^+ = \max(\lambda_m, 0) = \tfrac{1}{2}(\lambda_m + |\lambda_m|) \quad \text{for all } m = 1, ..., M\ , \\ \mathbf{\Lambda}^- &:= \mathrm{diag}(\lambda_1^-, \ldots, \lambda_M^-), \quad \lambda_m^- = \min(\lambda_m, 0) = \tfrac{1}{2}(\lambda_m - |\lambda_m|) \quad \text{for all } m = 1, ..., M\end{aligned}$$

and

$$\mathbf{A}^+ := \mathbf{R}\,\mathbf{\Lambda}^+\,\mathbf{R}^{-1}\,, \qquad \mathbf{A}^- := \mathbf{R}\,\mathbf{\Lambda}^-\,\mathbf{R}^{-1}$$

with

$$\mathbf{A} = \mathbf{A}^+ + \mathbf{A}^-\,, \qquad |\mathbf{A}| = \mathbf{A}^+ - \mathbf{A}^-$$

and express Eq. (4.24) with these definitions in short as

$$\mathbf{F}(\mathbf{q}_L, \mathbf{q}_R) = \mathbf{A}\mathbf{q}_L + \mathbf{A}^-\Delta\mathbf{q} = \mathbf{A}\mathbf{q}_R - \mathbf{A}^+\Delta\mathbf{q} = \mathbf{A}^+\mathbf{q}_L + \mathbf{A}^-\mathbf{q}_R\ . \tag{4.25}$$

Further on, summation yields the useful expression

$$\mathbf{F}(\mathbf{q}_L, \mathbf{q}_R) = \frac{1}{2}\left(\mathbf{A}\mathbf{q}_L + \mathbf{A}\mathbf{q}_R - |\mathbf{A}|\Delta\mathbf{q}\right)\ . \tag{4.26}$$

A numerical scheme for Eq. (2.18) that naturally considers the characteristic information can now be constructed by assuming a FV discretization as introduced in Sec. 4.1.2 with cell values $\mathbf{Q}_j^l, j \in \mathbb{Z}, l \in \mathbb{R}_0^+$ and by solving the Riemann initial-value problem between two neighboring cells in every time step. We choose $\mathbf{Q}_j^l$ as $\mathbf{q}_L$ and $\mathbf{Q}_{j+1}^l$ as $\mathbf{q}_R$ and introduce the notation $\Delta\mathbf{Q}_{j+1/2}^l = \mathbf{Q}_{j+1}^l - \mathbf{Q}_j^l$. The numerical flux function then reads

$$\mathbf{F}(\mathbf{Q}^l) = \mathbf{F}(\mathbf{Q}_j^l, \mathbf{Q}_{j+1}^l) = \mathbf{A}\mathbf{Q}_j^l + \mathbf{A}^+\Delta\mathbf{Q}_{j+1/2}^l = \mathbf{A}\mathbf{Q}_{j+1}^l - \mathbf{A}^-\Delta\mathbf{Q}_{j+1/2}^l\ .$$

We insert these numerical fluxes into (4.12) and obtain the FV upwind scheme for linear systems

$$\mathbf{Q}_j^{l+1} = \mathbf{Q}_j^l - \frac{\Delta t}{\Delta x}\left(\mathbf{F}(\mathbf{Q}_j^l, \mathbf{Q}_{j+1}^l) - \mathbf{F}(\mathbf{Q}_{j-1}^l, \mathbf{Q}_j^l)\right) \tag{4.27}$$

$$= \mathbf{Q}_j^l - \frac{\Delta t}{\Delta x}\left(\mathbf{A}^-\Delta\mathbf{Q}_{j+1/2}^l + \mathbf{A}^+\Delta\mathbf{Q}_{j-1/2}^l\right) \ . \tag{4.28}$$

Scheme (4.27) is *Godunov's Method* for Eq. (2.18), because the flux function $\mathbf{f}$ evaluated for the constant exact intermediate states $\mathbf{q}(x_{j+1/2}, t)$ is utilized as numerical flux. The scheme is first-order accurate [117]. Obviously, its numerical flux (4.26) is consistent. As scheme (4.27) is linear, only stability is required further to prove its convergence (compare Sec. 4.1.1).

CFL Condition

The linear upwind scheme (4.27) is stable under the Courant-Friedrichs-Levy (CFL) condition [117, 187, 82]

$$\frac{|\lambda_m|\Delta t}{\Delta x} \leq 1 \ , \quad \text{for all } m = 1, \ldots, M \ . \tag{4.29}$$

4.2.2 Nonlinear Equations

Godunov's Method requires the exact solution $\mathbf{q}(x,t)$ of the RP between $\mathbf{q}_L$ and $\mathbf{q}_R$ at least for $x = 0$. But the values $\mathbf{q}_L$, $\mathbf{q}_R$ are only approximations on a finite grid. Satisfying results can often be obtained, if the intermediate RPs by themselves are solved approximately. Schemes utilizing an approximative Riemann solver within Godunov's Method are said to be of *Godunov-type*.

In case of nonlinear hyperbolic systems even the approximate solution of the RP can be a very challenging task, especially for complex equations of state (compare Sec. 2.3.3). Therefore, methods for nonlinear systems usually avoid the evaluation of the intermediate state and try to approximate the flux at $x = 0$ directly on the basis of upwind directions of the neighboring values $\mathbf{q}_L$ and $\mathbf{q}_R$. Two different approaches here are *Flux-Vector Splitting* (FVS) and *Flux-Difference Splitting* (FDS). FDS methods are of Godunov-type. They utilize a suitable linearization of $\mathbf{f}(\mathbf{q})$ on the basis of $\mathbf{q}_L$ and $\mathbf{q}_R$ and solve the linear RP as described in Sec. 4.2.1. FVS methods are simpler and do not employ any RP. Consequently they are not of Godunov-type. Upwind directions are identified separately for $\mathbf{q}_L$ and $\mathbf{q}_R$.

4.2.3 Flux-Vector Splitting Approach

The FVS approach requires a splitting of $\mathbf{f}(\mathbf{q})$ into two components $\mathbf{f}^+(\mathbf{q})$ and $\mathbf{f}^-(\mathbf{q})$, such that the equation

$$\mathbf{f}(\mathbf{q}) = \mathbf{f}^+(\mathbf{q}) + \mathbf{f}^-(\mathbf{q}) \tag{4.30}$$

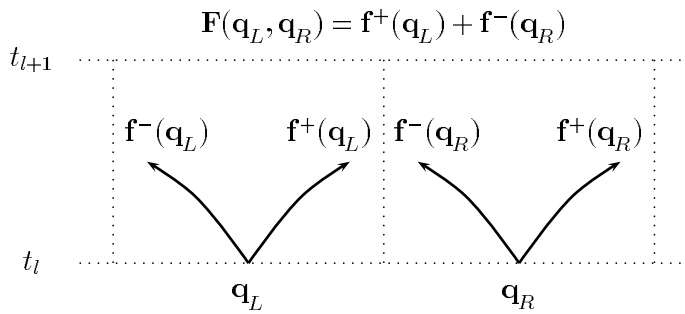

Figure 4.1: Splitting of the flux function within each computational cell at time t_l.

is satisfied under the restriction that the eigenvalues $\hat{\lambda}_m^+$ and $\hat{\lambda}_m^-$ of the split Jacobian matrices

$$\hat{\mathbf{A}}^+(\mathbf{q}) = \frac{\partial \mathbf{f}^+(\mathbf{q})}{\partial \mathbf{q}}\,, \quad \hat{\mathbf{A}}^-(\mathbf{q}) = \frac{\partial \mathbf{f}^-(\mathbf{q})}{\partial \mathbf{q}}$$

fulfill the conditions $\hat{\lambda}_m^+ \geq 0$ and $\hat{\lambda}_m^- \leq 0$ for all $m = 1, \ldots, M$. Further on, the splitting is required to reproduce regular upwinding, i.e.

$$\begin{array}{lllllllll} \mathbf{f}^+(\mathbf{q}) & = & \mathbf{f}(\mathbf{q})\,, & \mathbf{f}^-(\mathbf{q}) & = & \mathbf{0} & \text{if} & \lambda_m \geq 0 & \text{for all} \quad m = 1, \ldots, M\,, \\ \mathbf{f}^+(\mathbf{q}) & = & \mathbf{0}\,, & \mathbf{f}^-(\mathbf{q}) & = & \mathbf{f}(\mathbf{q}) & \text{if} & \lambda_m \leq 0 & \text{for all} \quad m = 1, \ldots, M\,. \end{array} \tag{4.31}$$

The FVS approach then approximates the unknown intermediate flux $\mathbf{F}(\mathbf{q}_L, \mathbf{q}_R)$ by

$$\mathbf{F}(\mathbf{q}_L, \mathbf{q}_R) = \mathbf{f}^+(\mathbf{q}_L) + \mathbf{f}^-(\mathbf{q}_R)\,. \tag{4.32}$$

The construction of the inter-cell numerical flux in the FVS method is shown in Fig. 4.1.

4.2.4 Flux-Difference Splitting Approach

The FDS approach uses an approximate Riemann solver to calculate an approximation to the unknown intermediate flux $\mathbf{F}(\mathbf{q}_L, \mathbf{q}_R)$. Instead of the RP between $\mathbf{q}_L$ and $\mathbf{q}_R$ for the nonlinear equation (2.17) a RP with the same initial data for the modified conservation law

$$\frac{\partial \bar{\mathbf{q}}}{\partial t} + \frac{\partial \bar{\mathbf{f}}(\bar{\mathbf{q}})}{\partial x} = \mathbf{0} \tag{4.33}$$

with a linear flux function $\bar{\mathbf{f}}(\bar{\mathbf{q}}) = \hat{\mathbf{A}}(\mathbf{q}_L, \mathbf{q}_R)\bar{\mathbf{q}}$ is solved. Herein, $\hat{\mathbf{A}}(\mathbf{q}_L, \mathbf{q}_R)$ denotes a suitable constant Jacobian chosen with respect to the initial data. The RP for this modified linear conservation law can easily be solved exactly (see Sec. 2.2.1), but care must be taken in the approximation of the intermediate flux $\mathbf{F}(\mathbf{q}_L, \mathbf{q}_R)$. The obvious choice $\bar{\mathbf{F}}(\mathbf{q}_L, \mathbf{q}_R)$ according to Eq. (4.24) leads to a scheme that is inconsistent with the original conservation law. The scheme would satisfy a different discrete conservation property than a scheme for the original conservation law and would converge toward the wrong weak solution.

Let S_R denote the largest eigenvalue of the original and of the modified RP. We evaluate the integral form (2.4) for both RPs over the domain $[0, S_R\Delta t] \times [0, \Delta t]$ and obtain for Eq. (2.17)

$$\int_0^{S_R\Delta t} \mathbf{q}(x, \Delta t)\, dx - S_R\Delta t\, \mathbf{q}_R + \Delta t \left[\mathbf{f}(\mathbf{q}_R) - \mathbf{F}(\mathbf{q}_L, \mathbf{q}_R)\right] = \mathbf{0} \tag{4.34}$$

and for Eq. (4.33)

$$\int_0^{S_R\Delta t} \bar{\mathbf{q}}(x, \Delta t)\, dx - S_R\Delta t\, \mathbf{q}_R + \Delta t \left[\bar{\mathbf{f}}(\mathbf{q}_R) - \bar{\mathbf{F}}(\mathbf{q}_L, \mathbf{q}_R)\right] = \mathbf{0}\ . \tag{4.35}$$

As the integrals in (4.34) and (4.35) must be equal, we immediately find the correct expression for the flux approximation for a scheme that internally utilizes a modified conservation law:

$$\mathbf{F}(\mathbf{q}_L, \mathbf{q}_R) = \bar{\mathbf{F}}(\mathbf{q}_L, \mathbf{q}_R) - \bar{\mathbf{f}}(\mathbf{q}_R) + \mathbf{f}(\mathbf{q}_R) \tag{4.36}$$

An analogous calculation for the smallest eigenvalue S_L and integration over $[S_L\Delta t, 0] \times [0, \Delta t]$ gives

$$\mathbf{F}(\mathbf{q}_L, \mathbf{q}_R) = \bar{\mathbf{F}}(\mathbf{q}_L, \mathbf{q}_R) - \bar{\mathbf{f}}(\mathbf{q}_L) + \mathbf{f}(\mathbf{q}_L)\ . \tag{4.37}$$

We insert for $\bar{\mathbf{F}}(\mathbf{q}_L, \mathbf{q}_R)$ and $\bar{\mathbf{f}}(\mathbf{q}_{L/R})$ the expressions from Eq. (4.24) and (2.19) and derive

$$\mathbf{F}(\mathbf{q}_L, \mathbf{q}_R) = \mathbf{f}(\mathbf{q}_L) + \sum_{\hat{\lambda}_m < 0} a_m \hat{\lambda}_m \hat{\mathbf{r}}_m = \mathbf{f}(\mathbf{q}_R) - \sum_{\hat{\lambda}_m \geq 0} a_m \hat{\lambda}_m \hat{\mathbf{r}}_m \tag{4.38}$$

or in terms of the notations of Sec. 4.2.1

$$\mathbf{F}(\mathbf{q}_L, \mathbf{q}_R) = \mathbf{f}(\mathbf{q}_L) + \hat{\mathbf{A}}^- \Delta\mathbf{q} = \mathbf{f}(\mathbf{q}_R) - \hat{\mathbf{A}}^+ \Delta\mathbf{q} \tag{4.39}$$

$$= \frac{1}{2}\left(\mathbf{f}(\mathbf{q}_L) + \mathbf{f}(\mathbf{q}_R) - |\hat{\mathbf{A}}|\Delta\mathbf{q}\right)\ . \tag{4.40}$$

If these flux approximations are used within a FV scheme, as it has been introduced in Sec. 4.2.1, the update formula simply reads

$$\mathbf{Q}_j^{l+1} = \mathbf{Q}_j^l - \frac{\Delta t}{\Delta x}\left(\hat{\mathbf{A}}^-(\mathbf{Q}_j^l, \mathbf{Q}_{j+1}^l)\Delta\mathbf{Q}_{j+\frac{1}{2}}^l + \hat{\mathbf{A}}^+(\mathbf{Q}_{j-1}^l, \mathbf{Q}_j^l)\Delta\mathbf{Q}_{j-\frac{1}{2}}^l\right)\ . \tag{4.41}$$

A necessary stability condition for scheme 4.41 is

$$\max_{j\in\mathbb{Z}} |\hat{\lambda}_{m,j+\frac{1}{2}}| \frac{\Delta t}{\Delta x} \leq 1\ , \quad \text{for all } m = 1, \ldots, M\ . \tag{4.42}$$

Note, that in the general nonlinear case condition (4.42) is only a necessary, but not a sufficient condition for stability [117].

Obviously, scheme (4.41) can be implemented without explicit evaluation of $\mathbf{F}(\mathbf{q}_L, \mathbf{q}_R)$. It suffices to calculate the *fluctuations*

$$\hat{\mathbf{A}}^-(\mathbf{q}_L, \mathbf{q}_R)\Delta\mathbf{q} = \sum_{\hat{\lambda}_m<0} a_m \hat{\lambda}_m \hat{\mathbf{r}}_m \ , \quad \hat{\mathbf{A}}^+(\mathbf{q}_L, \mathbf{q}_R)\Delta\mathbf{q} = \sum_{\hat{\lambda}_m\geq 0} a_m \hat{\lambda}_m \hat{\mathbf{r}}_m \ . \tag{4.43}$$

With the notations $\mathcal{A}^\pm\Delta := \hat{\mathbf{A}}^\pm(\mathbf{q}_L, \mathbf{q}_R)\Delta\mathbf{q}$ and by utilizing the *waves* $\mathcal{W}_m := a_m\hat{\mathbf{r}}_m$ the fluctuations (4.43) can be written as

$$\mathcal{A}^-\Delta = \sum_{\hat{\lambda}_m<0} \hat{\lambda}_m \, \mathcal{W}_m \ , \quad \mathcal{A}^+\Delta = \sum_{\hat{\lambda}_m\geq 0} \hat{\lambda}_m \, \mathcal{W}_m \ . \tag{4.44}$$

The wave formulation (4.44) is the basis of the Wave Propagation Method introduced in Sec. 4.3.2.

4.3 Methods of Higher Order

Two contradictory requirements on numerical methods for nonlinear hyperbolic conservation laws are a higher order of accuracy in smooth solution regions and the absence of spurious (unphysical) oscillations near large gradients or discontinuities that are visible in simple second order schemes, like Lax-Wendroff or Beam-Warming.[5] One possibility to avoid spurious oscillations is to use a *monotone* scheme.

Definition 14 (Monotonicity). *A finite volume scheme* $\mathbf{Q}_j^{l+1} = \mathcal{H}^{(\Delta t)}(\mathbf{Q}_{j-s}^l, \ldots, \mathbf{Q}_{j+s}^l)$ *is said to be monotone, if the updates after one step* $\mathbf{V}_j^{l+1} = \mathcal{H}^{(\Delta t)}(\mathbf{V}^l; j)$, $\mathbf{W}_i^{l+1} = \mathcal{H}^{(\Delta t)}(\mathbf{W}^l; j)$ *of two given discrete sequences* $\mathbf{V}^l = (\mathbf{V}_j^l), \mathbf{W}^l = (\mathbf{W}_j^l)$ *that satisfy* $\mathbf{V}_j^l \geq \mathbf{W}_j^l$ *for all* $j \in \mathbb{Z}$, *always satisfy* $\mathbf{V}_j^{l+1} \geq \mathbf{W}_j^{l+1}$ *for all* $j \in \mathbb{Z}$.

Consistent monotone methods can be proven to converge toward the entropy solution [90, 46]. But unfortunately, the monotonicity requirement is too severe to construct numerical schemes of higher order.

Theorem 4. *A monotone method is at most first order accurate.*

The proof of Theorem 4 can be found in [90]. Less restrictive than the monotonicity property is the concept of *total variation diminishing* (TVD) schemes.

Definition 15 (TVD property). *A scheme* $\mathbf{Q}_j^{l+1} = \mathcal{H}^{(\Delta t)}(\mathbf{Q}^l; j)$ *is called total variation diminishing (TVD), if the property*

$$TV(\mathbf{Q}^{l+1}) \leq TV(\mathbf{Q}^l)$$

is satisfied for all discrete sequences $\mathbf{Q}^l$. *Herein,* $TV(\mathbf{Q})$ *denotes the discrete total variation, which is defined by*

$$TV(\mathbf{Q}^l) := \sum_{j\in\mathbb{Z}} |\mathbf{Q}_{j+1}^l - \mathbf{Q}_j^l| \ .$$

[5] Typical examples for this behavior can be found for instance in [117] or [94].

TVD schemes maintain the property that no new extrema in x can be created. Local minima are non-decreasing, while local maxima are non-increasing (see [87] for the proof). This property is called *monotonicity-preserving*.

Theorem 5 *A monotonicity-preserving three-point scheme* $\mathbf{Q}_j^{l+1} = \mathcal{H}^{(\Delta t)}(\mathbf{Q}_{j-1}^l, \mathbf{Q}_j^l, \mathbf{Q}_{j+1}^l)$ *is at most first-order accurate.*

The proof for Theorem 5 can also be found in [87]. TVD schemes of higher order employ at least five discrete points and usually have the form

$$\mathbf{Q}_j^{l+1} = \mathcal{H}^{(\Delta t)}(\mathbf{Q}_{j-2}^l, \mathbf{Q}_{j-1}^l, \mathbf{Q}_j^l, \mathbf{Q}_{j+1}^l, \mathbf{Q}_{j+2}^l) \ .$$

Theorem 6 *A conservative consistent scheme is total variation diminishing (TVD), if it can be written in viscous form (see Def. 16).*

Godlewski and Raviart show in [81] that Theorem 6 is equivalent to the *incremental form* originally utilized by Harten in [87].

The theoretical base of TVD methods is sound for scalar problems only, but the concept can be used as a guideline for the construction of powerful numerical methods for nonlinear systems that are higher-order accurate in smooth regions of the solution and that approximate discontinuities sharply without artificial overshoots. Such schemes are called *high resolution* schemes. It has to be underlined, that monotonicity-preserving TVD schemes do not necessarily converge toward the entropy solution. The Roe scheme without entropy correction (see Sec. 4.6.2) is an example for a first-order accurate scheme, which is TVD in most situations (compare Sec. 4.8.2), but can violate the entropy condition.

The TVD concept only makes sense for homogeneous conservation laws with $\mathbf{s} \equiv \mathbf{0}$. It is no appropriate guideline for the construction of numerical methods that solve the inhomogeneous equation (2.1) directly, because the source term $\mathbf{s}(\mathbf{q})$ may increase the total variation of the exact solution and it would be inadequate to try to construct numerical schemes that attempt to suppress this behavior [187]. As we employ the method of fractional steps and solve the homogeneous equation (4.17) and the ODE (4.18) separately (see Sec. 4.1.3) we are justified to employ a TVD scheme for the solution of (4.17).

4.3.1 MUSCL-Hancock Method

A method for the practical construction of second-order five-point TVD schemes, especially on the basis of Godunov-type upwind schemes, has been developed by Van Leer in a series of papers [191, 192, 193, 194, 195]. Profound descriptions of this technique, which is also called the *variable extrapolation approach* or *slope limiting* can be found in the books of Toro [187] and Hirsch [94]. To simplify the notations we restrict the description to scalar problems and note that satisfactory, oscillation free results are obtained, if the technique is simply applied component-wise in the case of nonlinear systems.

In the MUSCL (Monotone Upwind Schemes for Conservation Laws) variable extrapolation method the cell-wise constant approximation Q_j^l is replaced by a linear ($\omega = 0$) or quadratic interpolation ($\omega \neq 0$) $\tilde{Q}_j(x)$, $x \in [x_{j-1/2}, x_{j+1/2}]$ between the three values Q_{j-1}^l, Q_j^l and Q_{j+1}^l. This interpolation is second-order accurate for $\omega = 1/3$ and first-order accurate for all other values [94]. Special factors $\Phi_{j\mp1/2}^{\pm}$, called *slope limiters* are utilized to restrict the gradients used for this interpolation to ensure the TVD property. In smooth solution regions $\Phi_{j\mp1/2}^{\pm} \approx 1$ should be satisfied, while near discontinuities $\Phi_{j\mp1/2}^{\pm}$ must vanish appropriately to avoid overshoots that violate the TVD condition. At the boundaries of cell j the one-sided extrapolated and limited values read

$$\tilde{Q}_{j+\frac{1}{2}}^L = Q_j^l + \frac{1}{4}\left[(1-\omega)\,\Phi_{j-\frac{1}{2}}^{+}\Delta_{j-\frac{1}{2}} + (1+\omega)\,\Phi_{j+\frac{1}{2}}^{-}\Delta_{j+\frac{1}{2}}\right] , \tag{4.45}$$

$$\tilde{Q}_{j-\frac{1}{2}}^R = Q_j^l - \frac{1}{4}\left[(1-\omega)\,\Phi_{j+\frac{1}{2}}^{-}\Delta_{j+\frac{1}{2}} + (1+\omega)\,\Phi_{j-\frac{1}{2}}^{+}\Delta_{j-\frac{1}{2}}\right] \tag{4.46}$$

with $\Delta_{j-1/2} = Q_j^l - Q_{j-1}^l$, $\Delta_{j+1/2} = Q_{j+1}^l - Q_j^l$. Note, that only for $\omega = 0$ the following conservation property is satisfied:

$$Q_j^l = \frac{1}{\Delta x}\int_{x_{j-1/2}}^{x_{j+1/2}} \tilde{Q}(\xi)\, d\xi$$

Time Integration

It is possible to use the extrapolated values $\tilde{Q}^L$ and $\tilde{Q}^R$ for the flux approximation with any of the first-order upwind methods of the preceding sections. In this case $F(\tilde{Q}_{j+1/2}^L, \tilde{Q}_{j+1/2}^R)$ would be used for instance at $x_{j+1/2}$ instead of $F(Q_j^l, Q_{j+1}^l)$. The result would be a scheme, which is higher-order in space, but only first-order in time [94]. A scheme that gives second-order accuracy in space (for $\omega \neq 1/3$) *and* in time can be constructed by applying the Mid-Point Rule approximation in time. Following an idea of Hancock, Van Leer suggested to construct extrapolated values first and to evolve these values by $\Delta t/2$ before they are utilized for the flux approximation [196]. For instance $F(\bar{Q}_{j+1/2}^L, \bar{Q}_{j+1/2}^R)$ is now used at $x_{j+1/2}$. The *evolved* extrapolated values are constructed by a standard time-explicit first-order FV discretization by

$$\bar{Q}_{j+\frac{1}{2}}^L = \tilde{Q}_{j+\frac{1}{2}}^L - \frac{1}{2}\frac{\Delta t}{\Delta x}\left(f(\tilde{Q}_{j+\frac{1}{2}}^L) - f(\tilde{Q}_{j-\frac{1}{2}}^R)\right) ,$$

$$\bar{Q}_{j-\frac{1}{2}}^R = \tilde{Q}_{j-\frac{1}{2}}^R - \frac{1}{2}\frac{\Delta t}{\Delta x}\left(f(\tilde{Q}_{j+\frac{1}{2}}^L) - f(\tilde{Q}_{j-\frac{1}{2}}^R)\right) .$$

A slightly different second-order method can be constructed by evolving the values of the old time level by $\Delta t/2$ first, i.e.

$$Q_j^\star = Q_j^l - \frac{1}{2}\frac{\Delta t}{\Delta x}\left(F(Q_{j+1}^l, Q_j^l) - F(Q_j^l, Q_{j-1}^l)\right)$$

and by constructing extrapolated values $\tilde{Q}^L$, $\tilde{Q}^R$ from $Q^\star$ for the flux approximation in the second step. The advantage of the MUSCL-Hancock Method is that it avoids the expensive evaluation of F in the first step and uses a reasonable inter-cell flux approximation on the basis of f.

Slope Limiters

The crucial task in both approaches is of course the choice of the slope limiter function Φ that is used to define $\Phi^{\pm}_{j\mp 1/2}$ by

$$\Phi^{+}_{j-\frac{1}{2}} := \Phi\left(r^{+}_{j-\frac{1}{2}}\right) , \quad \Phi^{-}_{j+\frac{1}{2}} := \Phi\left(r^{-}_{j+\frac{1}{2}}\right) \quad \text{with} \quad r^{+}_{j-\frac{1}{2}} := \frac{\Delta_{j+\frac{1}{2}}}{\Delta_{j-\frac{1}{2}}} , \quad r^{-}_{j+\frac{1}{2}} := \frac{\Delta_{j-\frac{1}{2}}}{\Delta_{j+\frac{1}{2}}}$$

such that the entire scheme is TVD and therefore monotonicity-preserving. Using the identity $r^{-}_{j+\frac{1}{2}} = 1/r^{+}_{j-\frac{1}{2}}$ the Eqs. (4.45), (4.46) can be written in the form

$$\tilde{Q}^{L}_{j+\frac{1}{2}} = Q_j + \tfrac{1}{2}\Psi\left(r^{+}_{j-\frac{1}{2}}\right)\Delta_{j-\frac{1}{2}} , \quad \tilde{Q}^{R}_{i-\frac{1}{2}} = Q_j - \tfrac{1}{2}\Psi\left(r^{+}_{j+\frac{1}{2}}\right)\Delta_{j+\frac{1}{2}}$$

with

$$\Psi(r) = \frac{1}{2}\left[(1-\omega)\Phi(r) + (1+\omega)\, r\, \Phi\left(\frac{1}{r}\right)\right] . \tag{4.47}$$

The condition for both methods to be TVD for any Courant number $0 \le C_{CFL} \le 1$ is the well-known inequality

$$\Psi(r) < \min(2, 2r) . \tag{4.48}$$

The rigorous proof of the validity of the last relation for the MUSCL-Hancock Method can be found for instance in the book of Toro [187]. Hirsch presents a similar proof for the second, less efficient scheme [94]. Frequently used slope limiter functions Φ constructed under condition (4.48) are (in ascending order of sharp reproduction of discontinuities, compare left picture of Fig. 4.10) the *Minmod*-type limiter

$$\Phi(r) = \max(0, \min(r, 1)) , \tag{4.49}$$

the *Van Albada*-type limiter [190]

$$\Phi(r) = \max\left(0, \frac{r^2 + r}{1 + r^2}\right) , \tag{4.50}$$

the *Van Leer*-type limiter [192]

$$\Phi(r) = \frac{r + |r|}{1 + |r|} , \tag{4.51}$$

and the *Superbee*-type limiter [157]

$$\Phi(r) = \max(0, \min(2r, 1), \min(r, 2)) . \tag{4.52}$$

All these functions satisfy $\Phi(1) = 1, \Phi(0) = 0$ and the symmetry property

$$\Phi(r) = r\, \Phi\left(\frac{1}{r}\right) \tag{4.53}$$

under which Eq. (4.47) reduces to $\Psi(r) = \Phi(r)$. The functions (4.49) and (4.50) satisfy $\Phi(\infty) = 1$, while (4.51) and (4.52) satisfy $\Phi(\infty) = 2$. Comparisons of the functions (4.49) to (4.52) used as slope limiters for MUSCL are presented by Hirsch [94] and Toro [187].

4.3.2 Wave Propagation Method

The Wave Propagation Method of LeVeque is a second-order accurate extension for FDS schemes that utilize the fluctuations (4.43) instead of the numerical fluxes, see [119, 118, 107, 120]. The method is very attractive, because the wave propagation formulation allows a second-order accurate multi-dimensional scheme without any dimensional splitting (compare Sec. 4.1.3).

One Space Dimension

Utilizing the wave formulation (4.44) the one-dimensional Wave Propagation Method reads

$$\mathbf{Q}^{l+1} = \mathbf{Q}_j^l - \frac{\Delta t}{\Delta x}\left(\mathcal{A}^-\Delta_{j+\frac{1}{2}} + \mathcal{A}^+\Delta_{j-\frac{1}{2}}\right) - \frac{\Delta t}{\Delta x}\left(\tilde{\mathbf{F}}_{j+\frac{1}{2}} - \tilde{\mathbf{F}}_{j-\frac{1}{2}}\right) . \tag{4.54}$$

Herein, $\tilde{\mathbf{F}}_{j\pm 1/2}$ denote additional terms that are necessary to achieve second-order accuracy in smooth regions of the solution. The basic second-order scheme of the Wave Propagation Method is the Lax-Wendroff scheme. At each cell interface $\tilde{\mathbf{F}}_{j+1/2}$ is uniquely defined as the difference between the second-order Lax-Wendroff flux and the first-order upwind flux (4.2.1). This difference reads

$$\begin{aligned}\tilde{\mathbf{F}}_{j+\frac{1}{2}} &= \frac{1}{2}\,|\mathcal{A}|\left(1 - \frac{\Delta t}{\Delta x}\,|\mathcal{A}|\right)\Delta_{j+\frac{1}{2}} \\ &= \frac{1}{2}\sum_{m=1}^{M}|\hat{\lambda}^m_{j+\frac{1}{2}}|\left(1 - \frac{\Delta t}{\Delta x}\right)|\hat{\lambda}^m_{j+\frac{1}{2}}|\,\tilde{\mathcal{W}}^m_{j+\frac{1}{2}} .\end{aligned} \tag{4.55}$$

In order to achieve a total variation diminishing scheme, limited waves $\tilde{\mathcal{W}}^m_{j+1/2}$ are used instead of the original waves $\mathcal{W}^m_{j+1/2} := a^m_{j+1/2}\hat{\mathbf{r}}^m_{j+1/2}$. The wave limiting is calculated by

$$\tilde{\mathcal{W}}^m_{j+\frac{1}{2}} = \Phi(\Theta^m_{j+\frac{1}{2}})\,\mathcal{W}^m_{j+\frac{1}{2}} \tag{4.56}$$

with

$$\Theta^m_{j+\frac{1}{2}} = \begin{cases} a^m_{j-\frac{1}{2}}/a^m_{j+\frac{1}{2}} , & \hat{\lambda}^m_{j+\frac{1}{2}} \geq 0 , \\ a^m_{j+\frac{3}{2}}/a^m_{j+\frac{1}{2}} , & \hat{\lambda}^m_{j+\frac{1}{2}} < 0 . \end{cases}$$

All limiter functions (4.49) to (4.52) can be applied as wave limiters in (4.56). A detailed presentation of the construction of the second-order correction term (4.55) and the wave limiting (4.56) can be found in [118]. Setting $\tilde{\mathcal{A}}^+\Delta_{j+1/2} := \mathcal{A}^+\Delta_{j+1/2} + \tilde{\mathbf{F}}_{j+1/2}$ and $\tilde{\mathcal{A}}^-\Delta_{j-1/2} := \mathcal{A}^-\Delta_{j-1/2} - \tilde{\mathbf{F}}_{j-1/2}$ we can write Eq. (4.54) in short as

$$\mathbf{Q}_j^{l+1} = \mathbf{Q}_j^l - \frac{\Delta t}{\Delta x}\left(\tilde{\mathcal{A}}^-\Delta_{j+\frac{1}{2}} + \tilde{\mathcal{A}}^+\Delta_{j-\frac{1}{2}}\right) .$$

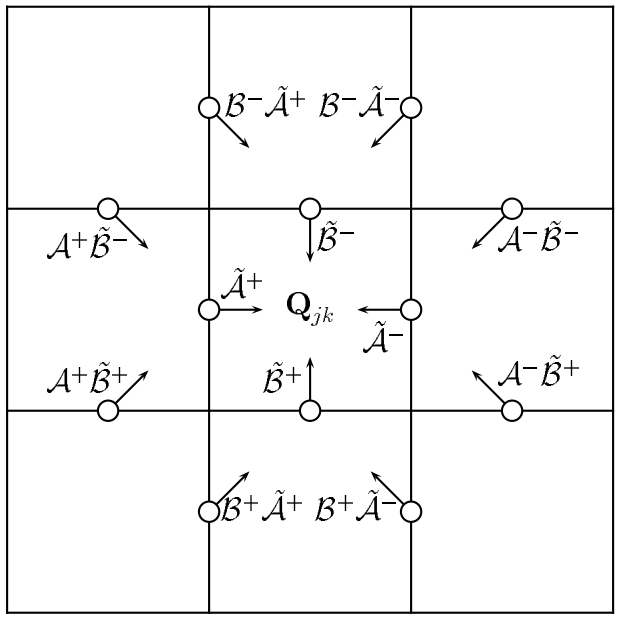

Figure 4.2: Waves included in the two-dimensional Wave Propagation scheme (4.58).

Two Space Dimensions

We only describe the Wave Propagation Method in two space dimensions. The three-dimensional extension is analogously to the two-dimensional case, but is technically more tedious. A complete description for all space dimensions can be found in [107]. For clarity, we write $\mathbf{B}$ instead of $\mathbf{A}_2$ and y for x_2 in the following.

The two-dimensional scheme is based on a second-order accurate Taylor expansion of the solution $\mathbf{q}(x, y, t)$ of the linear advection equation

$$\mathbf{q}_t + \mathbf{A}\mathbf{q}_x + \mathbf{B}\mathbf{q}_y = \mathbf{0} \tag{4.57}$$

at $t + \Delta t$ [107]:

$$\mathbf{q}(t+\Delta t) = \mathbf{q} - \Delta t(\mathbf{A}\mathbf{q}_x + \mathbf{B}\mathbf{q}_y) + \frac{1}{2}\Delta t^2 \left(\mathbf{A}^2\mathbf{q}_{xx} + \mathbf{B}\mathbf{A}\mathbf{q}_{xy} + \mathbf{A}\mathbf{B}\mathbf{q}_{yx} + \mathbf{B}^2\mathbf{q}_{yy}\right) + O(\Delta t^3)$$

Neglecting third-order terms and rearranging gives

$$\begin{aligned}\mathbf{q}(t+\Delta t) = \mathbf{q} &- \Delta t\left(\mathbf{A}\mathbf{q}_x - \frac{1}{2}\Delta t\mathbf{A}^2\mathbf{q}_{xx} - \frac{1}{2}\Delta t\mathbf{A}\mathbf{B}\mathbf{q}_{yx}\right)\\ &- \Delta t\left(\mathbf{B}\mathbf{q}_y - \frac{1}{2}\Delta t\mathbf{B}^2\mathbf{q}_{yy} - \frac{1}{2}\Delta t\mathbf{B}\mathbf{A}\mathbf{q}_{xy}\right) .\end{aligned}$$

While the terms $\mathbf{A}\mathbf{q}_x - \frac{1}{2}\Delta t\mathbf{A}^2\mathbf{q}_{xx}$, $\mathbf{B}\mathbf{q}_y - \frac{1}{2}\Delta t\mathbf{B}^2\mathbf{q}_{yy}$ are approximated appropriately by the second-order accurate fluctuation terms $\tilde{\mathcal{A}}^{\pm}\Delta$ and $\tilde{\mathcal{B}}^{\pm}\Delta$, the two cross

derivatives need further consideration. In the Wave Propagation Method they are approximated by applying a FDS scheme in the transverse direction on $\tilde{\mathcal{A}}^{\pm}\Delta$ and $\tilde{\mathcal{B}}^{\pm}\Delta$. The update formula for the two-dimensional second-order accurate method is

$$\begin{aligned}\mathbf{Q}_{jk}^{l+1} = \mathbf{Q}_{jk}^{l} - \frac{\Delta t}{\Delta x}\Bigg(&\tilde{\mathcal{A}}^{-}\Delta_{j+\frac{1}{2},k} - \frac{1}{2}\frac{\Delta t}{\Delta y}\left[\mathcal{A}^{-}\tilde{\mathcal{B}}^{-}\Delta_{j+1,k+\frac{1}{2}} + \mathcal{A}^{-}\tilde{\mathcal{B}}^{+}\Delta_{j+1,k-\frac{1}{2}}\right] + \\ &\tilde{\mathcal{A}}^{+}\Delta_{j-\frac{1}{2},k} - \frac{1}{2}\frac{\Delta t}{\Delta y}\left[\mathcal{A}^{+}\tilde{\mathcal{B}}^{-}\Delta_{j-1,k+\frac{1}{2}} + \mathcal{A}^{+}\tilde{\mathcal{B}}^{+}\Delta_{j-1,k-\frac{1}{2}}\right]\Bigg) \\ -\frac{\Delta t}{\Delta y}\Bigg(&\tilde{\mathcal{B}}^{-}\Delta_{j,k+\frac{1}{2}} - \frac{1}{2}\frac{\Delta t}{\Delta x}\left[\mathcal{B}^{-}\tilde{\mathcal{A}}^{-}\Delta_{j+\frac{1}{2},k+1} + \mathcal{B}^{-}\tilde{\mathcal{A}}^{+}\Delta_{j-\frac{1}{2},k+1}\right] + \\ &\tilde{\mathcal{B}}^{+}\Delta_{j,k-\frac{1}{2}} - \frac{1}{2}\frac{\Delta t}{\Delta x}\left[\mathcal{B}^{+}\tilde{\mathcal{A}}^{-}\Delta_{j+\frac{1}{2},k-1} + \mathcal{B}^{+}\tilde{\mathcal{A}}^{+}\Delta_{j-\frac{1}{2},k-1}\right]\Bigg)\,.\end{aligned} \tag{4.58}$$

The origins of the wave contributions in Eq. (4.58) are visualized in Fig. 4.2. If the cross derivative fluctuations are added to the fluctuations in the normal direction, Eq. (4.58) takes the simple form

$$\mathbf{Q}_{jk}^{l+1} = \mathbf{Q}_{jk}^{l} - \frac{\Delta t}{\Delta x}\left(\hat{\mathcal{A}}^{-}\Delta_{j+\frac{1}{2},k} + \hat{\mathcal{A}}^{+}\Delta_{j-\frac{1}{2},k}\right) - \frac{\Delta t}{\Delta y}\left(\hat{\mathcal{B}}^{-}\Delta_{j,k+\frac{1}{2}} + \hat{\mathcal{B}}^{+}\Delta_{j,k-\frac{1}{2}}\right)\,. \tag{4.59}$$

The proof of second-order accuracy in smooth solution regions for scheme (4.58) can be found in [119]. The exact proof is only valid for the linear equation (4.57), but the usage of *linearized* Riemann solvers analogously to Sec. 4.2.4 allows the application of formula (4.58) also in the nonlinear case. In combination with an appropriate limiting strategy, that constructs total variation diminishing second-order accurate fluctuations $\tilde{\mathcal{A}}^{\pm}$, $\tilde{\mathcal{B}}^{\pm}$, formula (4.58) defines a powerful multi-dimensional high resolution scheme.

The main disadvantage of the Wave Propagation Method is its expense. While the Strang splitting (4.23) involves the solution of three RPs, Eq. (4.58) requires the solution of two RPs in the normal and four in the transverse direction. A Strang splitting in three space dimensions needs five RPs, but the corresponding extension of the Wave Propagation Method uses three RPs in the normal direction and a minimum of 36 transverse RPs (see the three-dimensional algorithm in [107]).

4.4 Multi-Component Euler Equations

In the Secs. 4.5 to 4.7 we develop conservative high resolution finite volume methods for the homogeneous multi-component Euler equations for thermally perfect gases. In this section we supply generalities independent of a particular scheme. We formulate appropriate discrete boundary conditions and discuss the practical solution of the implicit temperature equation. Further on, a standard test case is specified.

4.4.1 Discrete Boundary Conditions

The application of a one-dimensional FV scheme (4.27) on a domain $[0, b]$ discretized with N finite volumes requires a boundary flux approximation $\mathbf{F}^l_{1/2}$ at $x = 0$ and an approximation $\mathbf{F}^l_{N+1/2}$ at $x = b$. In Sec. 2.3.1 we introduced three different types of boundaries for the multi-component Euler equations: Reflective, inflow and transmissive boundaries. Those can be implemented by prescribing the discrete fluxes at the boundaries directly or by employing fictitious values $\mathbf{Q}^l_0(\mathbf{Q}^l_1)$ and $\mathbf{Q}^l_{N+1}(\mathbf{Q}^l_N)$ leading to the computation of the required boundary fluxes in the flux approximations $\mathbf{F}(\mathbf{Q}^l_0, \mathbf{Q}^l_1)$ and $\mathbf{F}(\mathbf{Q}^l_N, \mathbf{Q}^l_{N+1})$. The usage of such *ghost cells* can be recommended especially for implementations that should be used within parallel or adaptive algorithms (compare Sec. 5.2).

If we prescribe for instance the discrete flux at a reflective boundary at $x = b$ directly, we evaluate condition (2.35) for $\mathbf{Q}^l_N$ and use

$$\mathbf{F}^l_{N+1/2} = (0, \ldots, 0, p(\mathbf{Q}^l_N), 0) \ . \tag{4.60}$$

A corresponding ghost cell value is in primitive variables

$$\rho_{i,N+1} = \rho^l_{i,N} \ , \quad u^l_{1,N+1} = -u^l_{1,N} \ , \quad p^l_{N+1} = p_N$$

or

$$\mathbf{Q}^l_{m,N+1} = \begin{cases} - \quad \mathbf{Q}^l_{m,N} \ , & \text{for } m = K+1, \\ \quad\ \ \mathbf{Q}^l_{m,N} \ , & \text{for } m = 1, ..., K, K+2 \end{cases} \tag{4.61}$$

in conservative quantities [187]. If this ghost cell value is used in the numerical flux approximation $\mathbf{F}(\mathbf{Q}^l_N, \mathbf{Q}^l_{N+1})$, every reasonable scheme for Euler equations should be identical to (4.60). If the numerical stencil requires $s > 1$ ghost cells (compare Def. 4.3), we apply condition (4.61) symmetrically, i.e. we set $\mathbf{Q}^l_{N+1+\kappa}(\mathbf{Q}^l_{N-\kappa})$ for all $\kappa = 0, \ldots, s-1$. At an inflow boundary with the time-dependent Dirichlet boundary value $\mathbf{q}_i(t)$ we simply use

$$\mathbf{F}^l_{N+1/2} = \mathbf{f}(\mathbf{q}_i(t_l)) \tag{4.62}$$

as prescribed flux and

$$\mathbf{Q}^l_{N+1} = \mathbf{q}_i(t_l)$$

as ghost cell value. At a reasonably chosen inlet the value $\mathbf{q}_i(t_l)$ is identically preserved at least in $\mathbf{Q}^l_N$ and a consistent numerical flux approximation (see Def. 13) returns (4.62). The difficult von Neumann boundary condition (2.36) at an outlet can be implemented approximately by setting

$$\mathbf{F}^l_{N+1/2} = \mathbf{f}(\mathbf{Q}^l_N) \ .$$

The same boundary flux is returned by every consistent numerical flux approximation, if

$$\mathbf{Q}^l_{N+1} = \mathbf{Q}^l_N$$

is used in the ghost cells.

4.4.2 Evaluation of the Temperature

Thermally perfect gases require the computation of the temperature T from the conserved quantities $\mathbf{Q}$ by solving the implicit equation (2.56). As the unique solvability of Eq. (2.56) has been proved in Prop. 1, the practical solution of Eq. (2.56) is a straight-forward task (see also [71]). We start the solution procedure in each computational cell by applying a standard Newton method to Eq. (2.56), i.e.

$$T_{\iota+1} = T_\iota - \frac{\varphi(\mathbf{Q}_j, T_\iota)}{\varphi'(\mathbf{Q}_j, T_\iota)} \ .$$

Herein, $\varphi'(\cdot, T)$ is the derivative of $\varphi(\cdot, T)$ with respect to T, which has already been evaluated in Eq. (2.58). We use the temperature value of the preceding time step $t - \Delta t$ as initial value $T_{\iota=0}$ to start the Newton iteration. If the Newton method does not converge in a reasonable number of iterations, we apply a standard bisection technique. The bisection method is always guaranteed to converge, because $\varphi(\cdot, T)$ is a strict monotone function (see proof of Prop. 1). Lower and upper limit of the possible temperature-range of the approximating polynomials for $c_{pi}(T)$ are the appropriate initial bounds for the bisection iteration.

In order to speed up the evaluation of $c_{pi}(T)$ and $h_i(T)$ we construct two constant tables for each species during the startup of the computational code (compare [71]). They store the values $c_{pi}(T_\nu)$ and $h_i(T_\nu)$ of all integer values T_ν in the valid temperature range. Values for intermediate temperatures $T_\nu < T < T_{\nu+1}$ are constructed by linear interpolation between T_ν and $T_{\nu+1}$. The tables are initialized by utilizing the functions of the Chemkin-II-library [102]. Throughout this thesis only the thermodynamic constants for (2.45) and (2.46) from the standard Chemkin-II thermodynamical data base [103] have been applied.

4.4.3 Shocktube Example

We use the RP of Tab. 4.1 as a first non-reactive test to evaluate the upwind schemes of the following sections. The computational domain has a length of 10 cm and has outflow boundary conditions on both sides. The gas is thermally perfect O_2. The computations are stopped after 80 μs, when the three different simple waves that occur in this RP are clearly separated. Fig. 4.3 displays a highly resolved reference computation on a grid of 4000 cells utilizing the Roe scheme of Sec. 4.6.1 with entropy correction and second-order MUSCL variable extrapolation. Fig. 4.3 shows that the solution consists of a shock at the right, a moving contact discontinuity in the middle and a transonic rarefaction wave. All numerical tests were run on a grid of 200 cells ($\Delta x = 0.05$ cm). With automatic adjustment of Δt in order to achieve a maximal Courant number of $C_{CFL} \approx 0.8$ in every step the computations require approximately 170 discrete time steps.

x [cm]	$x < 3$	$x > 3$
ρ [kg m^{-3}]	1.1	0.25
u_1 [m s^{-1}]	270	170
p [kPa]	110	25

Table 4.1: Riemann initial data for Test 1.

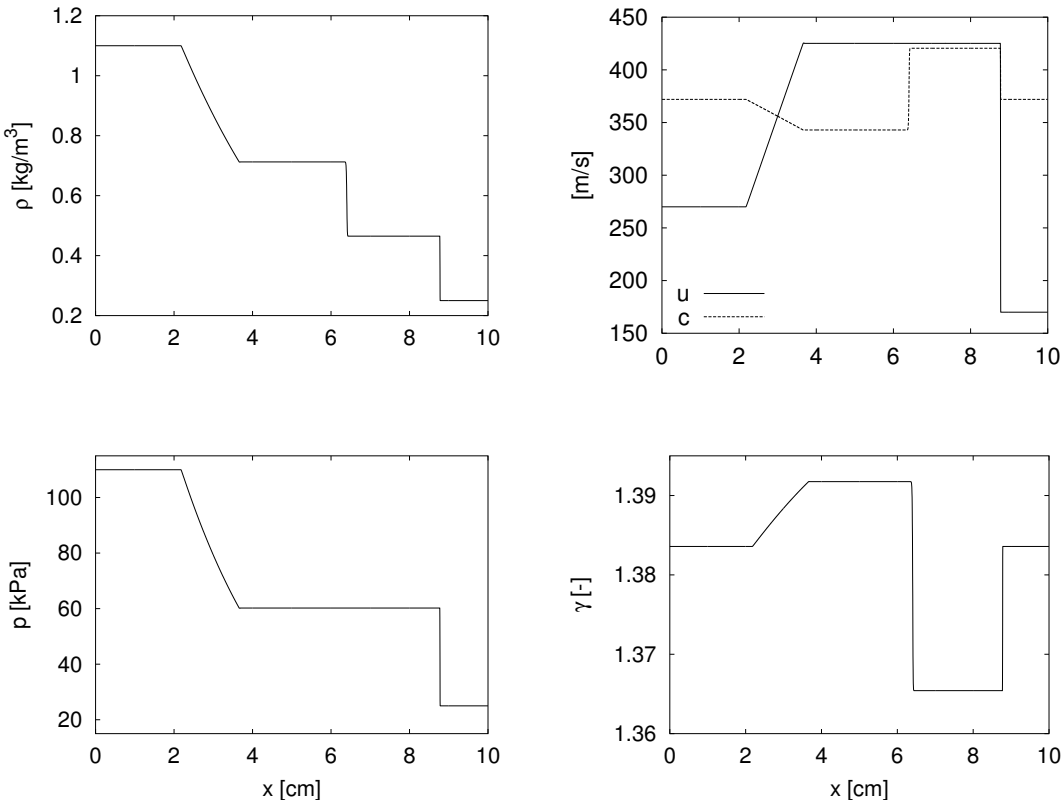

Figure 4.3: Reference solution of Test 1. Gas: O_2, thermally perfect.

4.5 Flux-Vector Splitting

In this section we apply the FVS approach introduced in Sec. 4.2.3 to the multi-component Euler equations for thermally perfect gases. Although we have assumed a one-dimensional FV scheme to simplify the notations, all numerical flux approximations are formulated for the general d-dimensional case. In a dimensional splitting method (compare Sec. 4.1.3) the given formulae correspond to to the approximation of $\mathbf{f}_1$. The flux approximations in the other directions follow directly by interchanging the velocities $u_1, \ldots, u_d$ canonically.

All presented methods have been derived around 1990 for two thermally perfect gases in one space dimension. The simple Steger-Warming FVS was published by Larrouturou and Fezoui [109], Liu and Vinokur [127] and Grossman and Cinella [84]. Extensions of the Van Leer FVS can be found in multiple works [169, 127, 109, 84], although only Shuen, Liou and Van Leer [169] and Vinokur and Montagné [198] presented the essential derivation for a single thermally perfect gas in detail. In the following, we briefly review and extend this extensive literature for our purpose.

4.5.1 Steger-Warming Splitting

If the flux function $\mathbf{f}(\mathbf{q})$ satisfies the homogeneity property, i.e. $\mathbf{f}(\mathbf{q}) = \mathbf{A}(\mathbf{q})\,\mathbf{q}$, a FVS can easily be derived by starting with an appropriate splitting of the diagonal matrix of eigenvalues $\mathbf{\Lambda}$. According to Sec. 4.2.1 we define $\mathbf{\Lambda}^+$, $\mathbf{\Lambda}^-$ by

$$\begin{aligned} \mathbf{\Lambda}^+(\mathbf{q}) &:= \mathrm{diag}(\lambda_1^+, \ldots, \lambda_M^+)\,, \qquad \lambda_m^+ = \tfrac{1}{2}(\lambda_m + |\lambda_m|) \quad \text{for all } m = 1, \ldots, M\,, \\ \mathbf{\Lambda}^-(\mathbf{q}) &:= \mathrm{diag}(\lambda_1^-, \ldots, \lambda_M^-)\,, \qquad \lambda_m^- = \tfrac{1}{2}(\lambda_m - |\lambda_m|) \quad \text{for all } m = 1, \ldots, M \end{aligned} \tag{4.63}$$

and

$$\mathbf{A}^+(\mathbf{q}) := \mathbf{R}(\mathbf{q})\,\mathbf{\Lambda}^+(\mathbf{q})\,\mathbf{R}^{-1}(\mathbf{q})\,, \qquad \mathbf{A}^-(\mathbf{q}) := \mathbf{R}(\mathbf{q})\,\mathbf{\Lambda}^-(\mathbf{q})\,\mathbf{R}^{-1}(\mathbf{q})\,. \tag{4.64}$$

The FVS then reads

$$\mathbf{f}(\mathbf{q}) = \mathbf{A}^+(\mathbf{q})\,\mathbf{q} + \mathbf{A}^-(\mathbf{q})\,\mathbf{q}$$

and the unknown intermediate flux is approximated by

$$\mathbf{F}(\mathbf{q}_L, \mathbf{q}_R) = \mathbf{A}^+(\mathbf{q}_L)\,\mathbf{q}_L + \mathbf{A}^-(\mathbf{q}_R)\,\mathbf{q}_R\,. \tag{4.65}$$

Note, that the Jacobians of the split fluxes of the Steger-Warming FVS

$$\frac{\partial \mathbf{f}^\pm(\mathbf{q})}{\partial \mathbf{q}} = \frac{\partial\left(\mathbf{A}^\pm(\mathbf{q})\,\mathbf{q}\right)}{\partial \mathbf{q}} = \mathbf{A}^\pm(\mathbf{q}) + \frac{\partial \mathbf{A}^\pm(\mathbf{q})}{\partial \mathbf{q}}\,\mathbf{q}$$

are identical to $\mathbf{A}^\pm(\mathbf{q})$ only in the linear case.

Prop. 8 states the homogeneity property for the multi-component Euler equations of Sec. 2.3. Utilizing this result, the Steger-Warming FVS is calculated directly by inserting the matrices $\mathbf{\Lambda}(\mathbf{q})$, $\mathbf{R}(\mathbf{q})$ and $\mathbf{R}^{-1}(\mathbf{q})$ derived in the Props. 9 and 10 into Eq. (4.64). With $\lambda_1 = u_1 - c$, $\lambda_2 = \cdots = \lambda_{K+d} = u_1$ and $\lambda_{K+d+1} = u_1 + c$ and $\lambda_m^\pm, m \in \{1, \ldots, K+d+1\}$ defined in (4.63) the result reads

$$\mathbf{f}^\pm(\mathbf{q}) = \mathbf{A}^\pm(\mathbf{q})\,\mathbf{q} = \frac{\rho}{2\gamma}\begin{pmatrix} Y_1\tau^\pm \\ \vdots \\ Y_K\tau^\pm \\ u_1\tau^\pm - c\,\xi^\pm \\ u_2\tau^\pm \\ \vdots \\ u_d\tau^\pm \\ H\tau^\pm - u_1 c\,\xi^\pm - 2\,\delta^\pm c^2 \end{pmatrix} \quad \text{with} \quad \begin{aligned} \delta^\pm &= \lambda_2^\pm = \cdots = \lambda_{K+d}^\pm\,, \\ \tau^\pm &= \lambda_1^\pm + 2\,\delta^\pm(\gamma - 1) \\ &\quad + \lambda_{K+d+1}^\pm\,, \\ \xi^\pm &= \lambda_1^\pm - \lambda_{K+d+1}^\pm\,. \end{aligned} \tag{4.66}$$

The same splitting is obtained in [84, 109, 127]. The corresponding stability condition is

$$C_{CFL}^{SW} := \max_{j\in\mathbb{Z}}(|u_{1,j}| + c_j) \leq 1\,. \tag{4.67}$$

At this point the validity of the Steger-Warming flux decomposition given by (4.66) has to be discussed, i.e. it would have to be proven that the eigenvalues of the

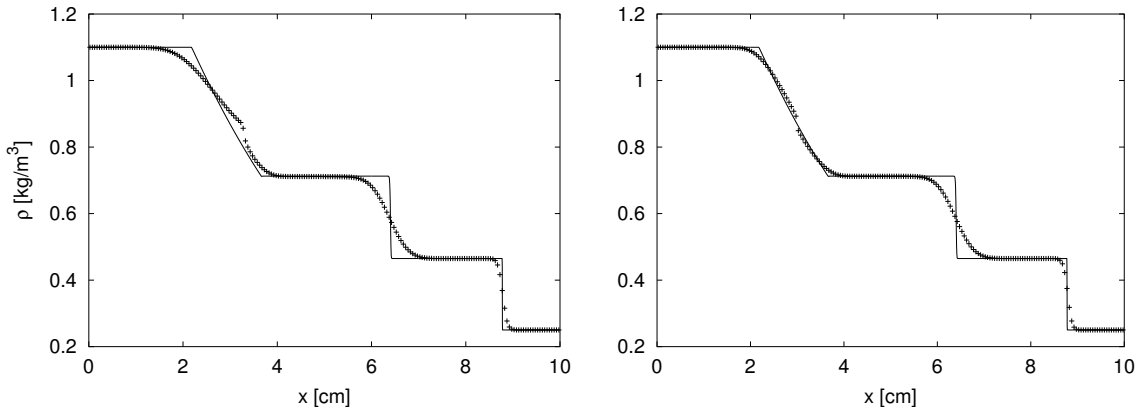

Figure 4.4: First-order results of Test 1. Density distribution computed with different FVS schemes compared to the reference solution of Fig. 4.3. Left: Steger-Warming FVS, right: Van Leer FVS.

Jacobians $\hat{\mathbf{A}}^{\pm}(\mathbf{q})$, derived from the split functions $\mathbf{f}^{+}(\mathbf{q})$, $\mathbf{f}^{-}(\mathbf{q})$, *really* satisfy the necessary conditions $\hat{\lambda}_m^{+} \geq 0$ and $\hat{\lambda}_m^{-} \leq 0$ for all admissible states. This rather lengthy and technical proof is omitted here and we refer to [109], where for the simplified case of calorically perfect species the additional necessary condition

$$\gamma_i < \frac{5}{3} \quad \text{for all } i = 1, \ldots, K \tag{4.68}$$

is found. In [198] the same condition is derived for a single thermally perfect gas. It is reasonable to assume that this condition carries over to the general case of mixtures of thermally perfect species, but [109] and [127] underline that no rigorous analysis for the validity of the FVS (4.66) seems to be possible without additional assumptions.

The Steger-Warming FVS (4.66) has the drawback that the split fluxes are not continuously differentiable, if one of the eigenvalues changes sign. In stagnation points, i.e. $u_1 = 0$, the eigenvalues calculated from the Jacobians $\hat{\mathbf{A}}^{\pm}(\mathbf{q})$ are not identical. In sonic points, i.e. $u_1 = \mp c$, the eigenvalues of one split-Jacobian $\hat{\mathbf{A}}^{\pm}(\mathbf{q})$ do not vanish and the switching to the other split flux with $\mathbf{f}^{\mp}(\mathbf{q}) = \mathbf{f}(\mathbf{q})$ is not smooth. Consequently, the Steger-Warming FVS gives comparably poor results for nearly stationary and transonic flow phenomena. The large glitch in the approximation of the sonic rarefaction wave in the left picture of Fig. 4.4 clearly illustrates this defect.

4.5.2 Van Leer Splitting

In order to obtain a FVS with less numerical diffusion, Van Leer introduced split fluxes $\mathbf{f}^{\pm}(\mathbf{q})$ for the Euler equations of a single polytropic gas that are continuously differentiable within the subsonic range $-c \leq u_1 \leq c$ and have vanishing slope for $u_1 \longrightarrow \mp c$.

The Van Leer FVS does not utilize the homogeneity property, instead it uses carefully constructed polynomials of minimal order for $\mathbf{f}^{\pm}(\mathbf{q})$ that are valid only within $-c \leq u_1 \leq c$. The ansatz of the Van Leer FVS is to express all components of the flux function $\mathbf{f}(\mathbf{q})$ by cubic polynomials of the velocity u_1

$$\mathbf{f}_m(u_1) = a_{m,0} + a_{m,1}u_1 + a_{m,2}u_1^2 + a_{m,3}u_1^3$$

where the coefficients $a_{m,0}, \ldots, a_{m,3}$ depend on $\mathbf{q}$. The splitting is then constructed component-wise by utilizing one of the relations

$$\mathbf{f}_m^+(u_1) = \mathbf{f}_m^-(u_1) \text{ , if } \mathbf{f}_m(u_1) = \mathbf{f}_m(-u_1) \text{ or}$$

$$\mathbf{f}_m^+(u_1) = -\mathbf{f}_m^-(u_1) \text{ , if } \mathbf{f}_m(u_1) = -\mathbf{f}_m(-u_1)$$

that follow from (4.30) and from the fact that the eigenvalues of the Euler equations have to be reproduced, i.e. $\lambda_1(u_1) = -\lambda_{K+d+1}(-u_1)$. Further on, the requirement of continuous differentiability at $u_1 = \mp c$ necessitates the factor $(u_1 \pm c)^2$ in all components of the constructed split fluxes.

Extensions of the Van Leer FVS to a single real gas can be found in [126] and in [198]. It is not surprising, that the polynomials of the split fluxes are not uniquely defined in the general case (see [126] for a detailed discussion). For mixtures of thermally perfect gases we therefore utilize the splitting of Van Leer-type, which is most frequently used [169, 127, 109, 84]. It reads

$$\mathbf{f}^{\pm}(\mathbf{q}) = \pm\frac{\rho}{4c}(u_1 \pm c)^2 \begin{bmatrix} Y_1 \\ \vdots \\ Y_K \\ u_1 - (u_1 \mp 2c)/\gamma \\ u_2 \\ \vdots \\ u_d \\ H - \zeta(u_1 \mp c)^2 \end{bmatrix} \quad \text{with} \quad \begin{aligned} H &= h + \frac{\mathbf{u^2}}{2} \ , \\ \zeta &= \frac{h/c^2}{1 + 2h/c^2} \ . \end{aligned} \tag{4.69}$$

The splitting (4.69) is explicitly constructed for $-c \leq u_1 \leq c$. For $|u_1| > c$ the relations (4.31) have to be applied. Note, that the necessary stability condition for the Van Leer FVS is not relation (4.67), but the more complex inequality[6]

$$C_{CFL}^{VL} := \max_{j\in\mathbb{Z}} \left[(|u_{1,j}| + c_j)\, \Pi_j \right] \frac{\Delta t}{\Delta x} \leq 1 \tag{4.70}$$

$$\text{with} \quad \Pi_j = \begin{cases} \dfrac{\gamma_j + 3}{2\gamma_j + u_{1,j}(3 - \gamma_j)/c_j} & \text{if } |u_{1,j}| < c_j \ , \\ 1 & \text{otherwise} \ . \end{cases}$$

[6]For the Van Leer FVS we implement automatic time step adjustment on the basis of relation (4.70). When we say for instance $C_{CFL} \approx 0.95$, we mean $C_{CFL}^{VL} \approx 0.95$. For the Van Leer scheme C_{CFL}^{VL} is not an approximation to the maximal signal speed, but only an upper bound for stability.

Like for the Steger-Warming FVS it would have to be shown that the Jacobians of the split fluxes (4.69) satisfy the necessary conditions $\hat{\lambda}_m^+ \geq 0$ and $\hat{\lambda}_m^- \leq 0$ for all admissible states. This property can be proven for a single polytropic gas, but numerical tests indicate that it is lost in the general real gas case [109]. Nevertheless, the necessary (but not sufficient) condition

$$\gamma_i \leq 3 \quad \text{for all } i = 1, \ldots, K$$

can be obtained [198]. The original Van Leer FVS for a single polytropic gas was constructed under the requirement that in case of subsonic flow with $|u_1| \leq c$ the smallest eigenvalue of $\hat{\mathbf{A}}^{\pm}(\mathbf{q})$ is forced to vanish. Unfortunately, this property which minimizes numerical diffusion does not carry over to the general case [126, 198]. Nevertheless, the Van Leer FVS gives significantly better numerical results than the Steger-Warming FVS (compare Fig. 4.4 and especially Fig. 4.9).

4.6 Godunov-type Methods

In this section we apply the FDS approach of Sec. 4.2.4 to the multi-component Euler equations for thermally perfect gases. In particular, we derive a consistent Roe scheme and extend it to a robust and reliable method. Following the work of Abgrall on multi-component mixtures of calorically perfect gases [1], we give a simplified derivation of the specific Roe linearization for the general thermally perfect case by Grossman and Cinella [84]. Like in the preceding section the flux approximation of $\mathbf{f}_1$ is formulated for the general d-dimensional case.

4.6.1 Roe Scheme

The difficult task in the FDS approach is the derivation of a constant matrix $\hat{\mathbf{A}}(\mathbf{q}_L, \mathbf{q}_R)$ for each RP that approximates the original Jacobian appropriately. Roe suggested the following three properties for such a matrix [156]:

(i) $\hat{\mathbf{A}}(\mathbf{q}_L, \mathbf{q}_R)$ is diagonalizable with real eigenvalues.

(ii) $\hat{\mathbf{A}}(\mathbf{q}_L, \mathbf{q}_R) \to \dfrac{\partial \mathbf{f}(\mathbf{q})}{\partial \mathbf{q}}$ smoothly as $\mathbf{q}_L, \mathbf{q}_R \to \mathbf{q}$.

(iii) $\hat{\mathbf{A}}(\mathbf{q}_L, \mathbf{q}_R)\Delta\mathbf{q} = \mathbf{f}(\mathbf{q}_R) - \mathbf{f}(\mathbf{q}_L)$

The third property ensures the conservation of the resulting scheme and is just another form of Eq. (4.39). In order to find a Roe matrix $\hat{\mathbf{A}}(\mathbf{q}_L, \mathbf{q}_R)$ for the multi-component Euler equations of Sec. 2.3 we follow Roe's original approach and look for some smooth function $\hat{\mathbf{q}} = \hat{\mathbf{q}}(\mathbf{v}, \mathbf{w})$ satisfying $\hat{\mathbf{q}}(\mathbf{v}, \mathbf{w}) = \hat{\mathbf{q}}(\mathbf{w}, \mathbf{v})$, $\hat{\mathbf{q}}(\mathbf{v}, \mathbf{v}) = \mathbf{v}$ that is inserted into the Jacobian of the original equations, i.e. $\hat{\mathbf{A}}(\mathbf{q}_L, \mathbf{q}_R) = \mathbf{A}(\hat{\mathbf{q}}(\mathbf{q}_L, \mathbf{q}_R))$. Obviously, this approach satisfies the properties (i) and (ii). To further satisfy property (iii) we use a direct method that is the essential idea of the Roe-Pike approach [158].

From Prop. 10 we know that $\mathbf{A}(\hat{\mathbf{q}})$ is diagonalizable with $\mathbf{A}(\hat{\mathbf{q}}) = \mathbf{R}(\hat{\mathbf{q}})\mathbf{\Lambda}(\hat{\mathbf{q}})\mathbf{R}^{-1}(\hat{\mathbf{q}})$ for all admissible states. Therefore, property (iii) is equivalent to

$$\Delta\mathbf{f} := \mathbf{f}(\mathbf{q}_R) - \mathbf{f}(\mathbf{q}_L) = \sum_{m=1}^{M} a_m \lambda_m(\hat{\mathbf{q}})\mathbf{r}_m(\hat{\mathbf{q}}) \quad \text{with} \quad \Delta\mathbf{q} := \mathbf{q}_R - \mathbf{q}_L = \sum_{m=1}^{M} a_m \mathbf{r}_m(\hat{\mathbf{q}}) \ . \tag{4.71}$$

The wave strengths a_m are easily found by evaluating $\mathbf{R}^{-1}(\hat{\mathbf{q}})\Delta\mathbf{q}$:

$$a_1, a_{K+d+1} = \frac{\alpha}{2} \pm \frac{\Delta\rho\hat{u}_1 - \Delta m_1}{2\hat{c}} \ , \quad a_{1+i} = \Delta\rho_i - \hat{Y}_i\alpha \quad \text{for } i = 1, \ldots, K \ , \tag{4.72}$$

$$a_{K+n} = \Delta m_n - \Delta\rho\hat{u}_n \quad \text{for } n = 2, \ldots, d$$

with

$$\alpha = \frac{\hat{\gamma} - 1}{\hat{c}^2}\left[\sum_{i=1}^{K} \Delta\rho_i \frac{\hat{\phi}_i}{\hat{\gamma} - 1} - \sum_{n=1}^{d} \hat{u}_n \Delta m_n + \Delta\bar{E}\right] \quad \text{and} \quad \Delta\rho = \sum_{i=1}^{K} \Delta\rho_i \ .$$

We expect that the sought average $\hat{\mathbf{q}}$ is a generalization of the averages

$$\hat{\rho} = \frac{\sqrt{\rho_L}\rho_R + \sqrt{\rho_R}\rho_L}{\sqrt{\rho_L} + \sqrt{\rho_R}} = \sqrt{\rho_L\rho_R} \quad \text{and} \quad \hat{v} = \frac{\sqrt{\rho_L}v_L + \sqrt{\rho_R}v_R}{\sqrt{\rho_L} + \sqrt{\rho_R}} \quad \text{for } v = u_1, u_2, u_3, H$$

that have been found by Roe for a single polytropic gas [156]. We therefore make use of a calculus tailored for these averages that has been introduced by Abgrall [1]. Its rules, which can be verified by straight-forward computations, are:

$$\Delta v = v_R - v_L \ , \quad \delta = \left(\frac{\rho_R}{\rho_L}\right)^{1/2} \ , \quad \underline{v} = \frac{v_R + \delta v_L}{1 + \delta} \ , \quad \overline{v} = \frac{v_L + \delta v_R}{1 + \delta}$$

$$\underline{\rho} = \hat{\rho} \ , \quad \overline{v} = \hat{v} \ \text{ for } v \neq \rho \ , \quad \underline{\rho v} = \underline{\rho}\,\overline{v} = \hat{\rho}\hat{v} \ , \quad \Delta(vw) = \underline{v}\,\Delta w + \overline{w}\Delta v$$

With this calculus various useful relations can be derived. For instance, we find immediately

$$\Delta m_n = \Delta(\rho u_n) = \hat{\rho}\Delta u_n + \hat{u}_n\Delta\rho \ , \quad \Delta(\rho u_n^2) = 2\hat{\rho}\hat{u}_n\Delta u_n + \hat{u}_n^2\Delta\rho \ ,$$

$$\Delta(\rho u_1 v) = \hat{\rho}\hat{v}\Delta u_1 + \hat{\rho}\hat{u}_1\Delta v + \hat{u}_1\hat{v}\Delta\rho \ \text{ for } v = H, Y_i, u_2, u_3 \ .$$

A further important relation, which can easily be shown to be true, is $\sum \hat{Y}_i = 1$.

We check the required property $\Delta\mathbf{f} = \sum a_m\lambda_m(\hat{\mathbf{q}})\mathbf{r}_m(\hat{\mathbf{q}})$ and find that the K species equations are already satisfied for the expected averages $\hat{Y}_i$ and $\hat{u}_1$. The momentum equations for $m_2, \ldots, m_n$ yield the averages $\hat{u}_2, \ldots, \hat{u}_d$. The momentum equation for m_1 gives the relation

$$\frac{\alpha\hat{c} - \hat{\rho}\Delta u_1}{2\hat{c}}(\hat{u}_1 - \hat{c})^2 + \sum_{i=1}^{K} \hat{u}_1^2\left(\Delta\rho_i - \hat{Y}_i\alpha\right) + \frac{\alpha\hat{c} + \hat{\rho}\Delta u_1}{2\hat{c}}(\hat{u}_1 + \hat{c})^2 = \Delta(\rho u_1^2 + p) \ ,$$

which can only be satisfied under the necessary condition $\Delta p = \hat{c}^2\alpha$. The same condition is obtained from the last relation by employing the averages $\hat{E}$ and $\hat{H}$:

$$\frac{\alpha\hat{c} - \hat{\rho}\Delta u_1}{2\hat{c}}(\hat{u}_1 - \hat{c})(\hat{H} - \hat{u}_1\hat{c}) + \sum_{i=1}^{K}\hat{u}_1\left(\hat{\mathbf{u}}^2 - \frac{\hat{\phi}_i}{\hat{\gamma}-1}\right)\left(\Delta\rho_i - \hat{Y}_i\alpha\right) + \sum_{n=2}^{d}\hat{u}_1\hat{u}_n\hat{\rho}\Delta u_n$$
$$+\frac{\alpha\hat{c} + \hat{\rho}\Delta u_1}{2\hat{c}}(\hat{u}_1 + \hat{c})(\hat{H} + \hat{u}_1\hat{c}) = \hat{u}_1\Delta(\rho E) + \hat{u}_1\hat{c}^2\alpha + \hat{H}\hat{\rho}\Delta u_1 = \Delta(u_1\rho H)\ ,$$

where the expression

$$\Delta(\rho E) = \hat{H}\alpha + \hat{\rho}\sum_{n=1}^{d}\hat{u}_n\Delta u_n + \hat{\mathbf{u}}^2(\Delta\rho - \alpha) - (\Delta\rho_i - \hat{Y}_i\alpha)\sum_{i=1}^{K}\frac{\hat{\phi}_i}{\hat{\gamma}-1} \tag{4.73}$$

that follows from $\Delta\mathbf{q} = \sum a_m\mathbf{r}_m(\hat{\mathbf{q}})$ is used to simplify the result. In order to find appropriate averages for the remaining terms $\hat{\phi}_i, \hat{\gamma}$ we insert

$$\Delta(\rho E) = \Delta(\rho e) + \hat{\rho}\sum_{n=1}^{d}\hat{u}_n\Delta u_n + \frac{\hat{\mathbf{u}}^2}{2}\Delta\rho$$

and $\alpha = \Delta p/\hat{c}^2$ into Eq. (4.73). We obtain

$$\Delta(\rho e) = \frac{\hat{\mathbf{u}}^2}{2}\Delta\rho + \frac{\Delta p}{\hat{c}^2}\left(\hat{H} - \hat{\mathbf{u}}^2 + \sum_{i=1}^{K}\hat{Y}_i\frac{\hat{\phi}_i}{\hat{\gamma}-1}\right) - \sum_{i=1}^{K}\Delta\rho_i\frac{\hat{\phi}_i}{\hat{\gamma}-1}\ . \tag{4.74}$$

We assume that the averaged frozen speed of sound $\hat{c}$ can be calculated according to Eq. (2.69) by

$$\hat{c}^2 = \sum_{i=1}^{K}\hat{Y}_i\,\hat{\phi}_i - (\hat{\gamma}-1)\hat{\mathbf{u}}^2 + (\hat{\gamma}-1)\hat{H} \tag{4.75}$$

and therefore replace $\hat{c}^2$ in (4.74) by the last expression. The result reads

$$\Delta(\rho e) = \frac{\Delta p}{\hat{\gamma}-1} - \sum\Delta\rho_i\left(\frac{\hat{\phi}_i}{\hat{\gamma}-1} - \frac{\hat{\mathbf{u}}^2}{2}\right)\ . \tag{4.76}$$

We assume that $\hat{\phi}_i$ can be evaluated according to Eq. (2.60) with the standard Roe-averaged quantities $\hat{e}_i$, $\hat{h}_i$ and $\hat{T}$ by

$$\hat{\phi}_i = (\hat{\gamma}-1)\left(\frac{\hat{\mathbf{u}}^2}{2} - \hat{h}_i\right) + \hat{\gamma}\,R_i\,\hat{T} = (\hat{\gamma}-1)\left(\frac{\hat{\mathbf{u}}^2}{2} - \hat{e}_i\right) + R_i\,\hat{T}\ . \tag{4.77}$$

If we insert this expression for $\hat{\phi}_i$ in Eq. (4.76), we obtain

$$\Delta(\rho e) = \frac{\Delta p}{\hat{\gamma}-1} + \sum\Delta\rho_i\left(\hat{e}_i - R_i\frac{\hat{T}}{\hat{\gamma}-1}\right)\ . \tag{4.78}$$

We introduce the average $\hat{\rho}_i$ by $\hat{\rho}_i = \underline{\rho}_i$. It can easily be verified that $\hat{\rho}_i$ satisfies the useful relations $\hat{\rho}_i = \hat{Y}_i\hat{\rho}$ and $\hat{\rho} = \sum \hat{\rho}_i$. Further on, we introduce the standard Roe-average $\hat{R}$, for which $\hat{R} = \sum \hat{Y}_i R_i$ holds true. From $\hat{R} = \mathcal{R}/\hat{W}$ the additional relations

$$\hat{W} = \left(\frac{\sqrt{\rho_L}\frac{1}{W_L} + \sqrt{\rho_R}\frac{1}{W_R}}{\sqrt{\rho_L} + \sqrt{\rho_R}} \right)^{-1} = \left(\sum \frac{\hat{Y}_i}{W_i} \right)^{-1} \tag{4.79}$$

can be derived. Utilizing the expressions for $\hat{\rho}_i$ and for $\hat{R}$, we find from $\Delta p = \Delta(\sum \rho_i R_i T) = \sum \hat{\rho}_i R_i \Delta T + \sum \hat{T} R_i \Delta\rho_i$ that the averages for the mixture satisfy the equation $\Delta p = \hat{\rho}\hat{R}\Delta T + \hat{T}\hat{R}\Delta\rho$. Finally, we introduce arbitrarily averaged specific heats $\hat{c}_{pi}, \hat{c}_{vi}$, for which we assume that they satisfy the condition $R_i = \hat{c}_{pi} - \hat{c}_{vi}$. We define averaged mixture properties by

$$\hat{c}_p := \sum \hat{Y}_i \hat{c}_{pi} \quad \text{and} \quad \hat{c}_v := \sum \hat{Y}_i \hat{c}_{vi} \quad \text{with} \quad \hat{R} = \hat{c}_p - \hat{c}_v \tag{4.80}$$

and define further $\hat{\gamma}$ as usual by $\hat{\gamma} := \hat{c}_p/\hat{c}_v$. With these new averages Eq. (4.78) can be simplified to

$$\Delta(\rho e) - \sum \hat{e}_i \Delta\rho_i = \sum \hat{\rho}_i R_i \frac{\Delta T}{\hat{\gamma} - 1} = \frac{\hat{\rho}\hat{R}\Delta T}{\hat{\gamma} - 1} = \hat{\rho}\hat{c}_v \Delta T = \sum \hat{\rho}_i \hat{c}_{vi} \Delta T \ ,$$

and by applying $\Delta(\rho e) = \Delta(\sum \rho_i e_i) = \sum \hat{\rho}_i \Delta e_i + \sum \hat{e}_i \Delta\rho_i$ we find that the only remaining necessary condition for an average state satisfying Eq. (4.71) is

$$\Delta e_i = \hat{c}_{vi} \Delta T \ . \tag{4.81}$$

Equivalent to Eq. (4.81) is the condition $\Delta h_i = \hat{c}_{pi}\Delta T$ that could be derived by an analogous computation. We insert the definitions from (2.45) for $\Delta e_i = e_i(T_R) - e_i(T_L)$ and $\Delta h_i = h_i(T_R) - h_i(T_L)$ and derive for the averaged specific heats for each species for $\Delta T > 0$

$$\hat{c}_{vi} = \frac{1}{\Delta T} \int_{T_L}^{T_R} c_{vi}(s) ds \quad \text{and} \quad \hat{c}_{pi} = \frac{1}{\Delta T} \int_{T_L}^{T_R} c_{pi}(s) ds \tag{4.82}$$

and $\hat{c}_{vi} = c_{vi}(T_L = T_R)$, $\hat{c}_{pi} = c_{pi}(T_L = T_R)$ for $\Delta T = 0$. Note, that for calorically perfect species with $c_{vi} = \hat{c}_{vi} = const.$ and $c_{pi} = \hat{c}_{pi} = const.$ the caloric equations $\hat{e}_i = h_i^0 + c_{vi}\hat{T}$ and $\hat{h}_i = h_i^0 + c_{pi}\hat{T}$ carry over to the averaged values. But, already simple examples are sufficient to prove that this property is usually lost in the general case of thermally perfect species.

Having now found a consistent average state $\hat{\mathbf{q}}$ that satisfies (4.71) and the condition $\Delta p = \hat{c}^2\alpha$ we can simplify the expressions for the wave strengths a_m by eliminating α. Equivalent to (4.72) are the more convenient expressions

$$a_1, a_{K+d+1} = \frac{\Delta p \mp \hat{\rho}\hat{c}\Delta u_1}{2\hat{c}^2} \ , \quad a_{1+i} = \Delta\rho_i - \hat{Y}_i \frac{\Delta p}{\hat{c}^2} \ , \quad a_{K+n} = \hat{\rho}\Delta u_n \ . \tag{4.83}$$

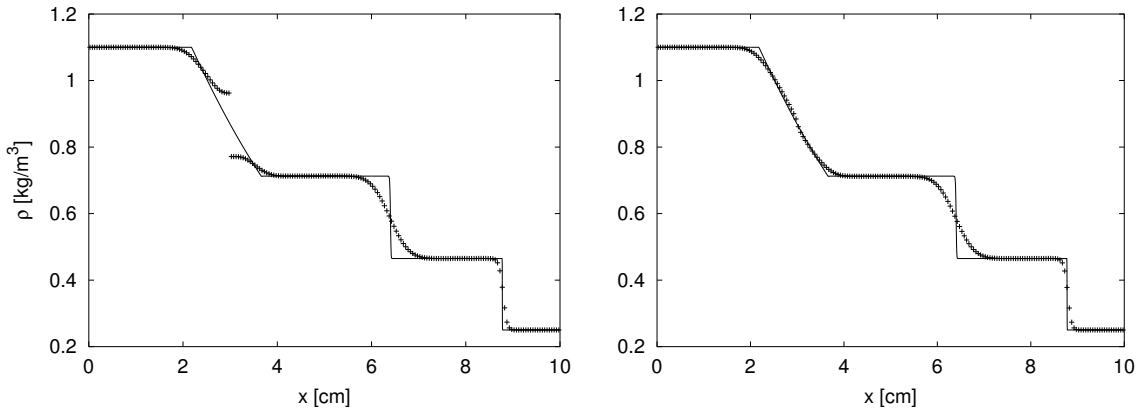

Figure 4.5: First-order results of Test 1. Density distribution computed with the Roe scheme. Left: no entropy correction, right: entropy enforcement with EF 3.

According to (4.42) the necessary stability condition of the Roe scheme for mixtures of thermally perfect species reads

$$C_{CFL}^{Roe} := \max_{j\in\mathbb{Z}}(|\hat{u}_{1,j+\frac{1}{2}}| + \hat{c}_{j+\frac{1}{2}})\frac{\Delta t}{\Delta x} \leq 1 \ . \tag{4.84}$$

The same scheme is derived by Grossman and Cinella in [84]. Their derivation follows exactly the procedure outlined by Glaister for a single real gas with arbitrary equation of state [80]. Glaister and Grossman-Cinella utilize the original Roe-Pike method that involves a further (unnecessary) linearization in the derivation, but leads to the identical result at the end. A good explanation of the original Roe-Pike method [158] can be found in the book Toro [187].

In case of the multi-component Euler equations the Roe solver approximates the solution of the RP by

$$\mathbf{q}^{Roe}(\mathbf{x},t) = \begin{cases} \mathbf{q}_L \ , & x < \hat{\lambda}_1\, t \\ \mathbf{q}_L^\star \ , & \hat{\lambda}_1\, t \leq x < \hat{\lambda}_2\, t \\ \mathbf{q}_R^\star \ , & \hat{\lambda}_2\, t \leq x \leq \hat{\lambda}_{K+d+1}\, t \\ \mathbf{q}_R \ , & x > \hat{\lambda}_{K+d+1}\, t \end{cases} \tag{4.85}$$

with $\hat{\lambda}_1 = \hat{u}_1 - \hat{c}$, $\hat{\lambda}_2 = \cdots = \hat{\lambda}_{K+d} = \hat{u}_1$, $\hat{\lambda}_{K+d+1} = \hat{u}_1 + \hat{c}$ and $\mathbf{q}_L^\star - \mathbf{q}_L = a_1\hat{\mathbf{r}}_1$, $\mathbf{q}_R - \mathbf{q}_R^\star = a_{K+d+1}\hat{\mathbf{r}}_{K+d+1}$. The linearized solution consists of discontinuous jumps only (compare Fig. 4.6 to the exact solution of the RP in Fig. 2.2). Rarefaction waves in the first and last characteristic field, which are genuinely nonlinear (see Prop. 5), are approximated by shock waves that violate the entropy condition (2.27). In most situations

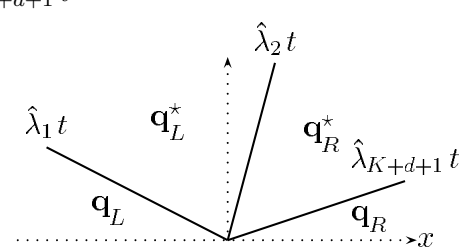

Figure 4.6: Approximation of the RP for Euler equations by the Roe scheme.

the intermediate flux approximation $\mathbf{F}(\mathbf{q}_L, \mathbf{q}_R)$ is unaffected by this simplification, but if a transonic rarefaction occurs, the intermediate flux can be heavily incorrect and the computed solution might not be an entropy solution anymore. Various techniques, so called *entropy corrections* or *entropy fixes*, have been suggested to overcome this problem.

4.6.2 Entropy Corrections

The easiest way of ensuring physically reasonable approximations is to apply finite volume methods that are based on an extended viscous equation like (2.5). Even numerical schemes that have been derived explicitly for Eq. (2.1) usually have this property. In this case, ε is not an arbitrary free parameter, but depends on the actual numerical scheme and its inherent *numerical viscosity* or *dissipation*. The numerical viscosity of a FV scheme can be quantified by writing it in viscous form.

Definition 16 (Viscous form). *We say that a finite volume scheme* $\mathbf{Q}_j^{l+1} = \mathcal{H}^{\Delta t}(\mathbf{Q}_{j-s}^l, ..., \mathbf{Q}_{j+s}^l)$ *can be put in viscous form, if there exists a positive semi-definite matrix-function* $\mathbf{D}_{j+1/2}^l = \mathbf{D}(\mathbf{Q}_{j-s+1}^l, \ldots, \mathbf{Q}_{j+s}^l)$ *called the viscosity matrix such that the scheme can be written in the form*

$$\mathbf{Q}_j^{l+1} = \mathbf{Q}_j^l - \frac{\Delta t}{2\Delta x}\left(\mathbf{f}(\mathbf{Q}_{j+1}^l) - \mathbf{f}(\mathbf{Q}_{j-1}^l)\right) + \frac{1}{2}\left(\mathbf{D}_{j+1/2}^l \Delta\mathbf{Q}_{j+1/2}^l - \mathbf{D}_{j-1/2}^l \Delta\mathbf{Q}_{j-1/2}^l\right) . \tag{4.86}$$

The numerical flux of a scheme in viscous form is

$$\mathbf{F}_{j+1/2}^V = \frac{1}{2}\left(\mathbf{f}(\mathbf{Q}_{j+1}^l) + \mathbf{f}(\mathbf{Q}_j^l) - \frac{\Delta x}{\Delta t}\mathbf{D}_{j+1/2}^l \Delta\mathbf{Q}_{j+1/2}^l\right) . \tag{4.87}$$

Comparing (4.40) with (4.87) we see that the viscosity matrix of the Roe scheme only depends on the two neighboring values $\mathbf{q}_L$, $\mathbf{q}_R$ and that the viscous term of the method reads

$$\mathbf{D}(\mathbf{q}_L, \mathbf{q}_R)\Delta\mathbf{q} = \frac{\Delta t}{\Delta x}|\mathbf{A}(\hat{\mathbf{q}})|\Delta\mathbf{q} = \frac{\Delta t}{\Delta x}\sum_{m=1}^{M} a_m|\hat{\lambda}_m|\hat{\mathbf{r}}_m . \tag{4.88}$$

Obviously, a characteristic field with $\hat{\lambda}_m = \lambda(\hat{\mathbf{q}}) = 0$ has no influence on the numerical viscosity of the Roe scheme (4.88) and we might think that the method simply is not viscous enough in transonic regimes with $\lambda_{1,K+d+1}(\hat{\mathbf{q}}) \approx 0$ to avoid violation of the entropy condition. In order to increase the entropy enforcement near sonic points Harten proposed to replace $|\lambda_m(\hat{\mathbf{q}})|$ with a suitable chosen $|\bar{\lambda}_m|$. Possible choices for $|\bar{\lambda}_m|$ are

$$\text{EF 1} : |\bar{\lambda}_m| = |\lambda_m(\hat{\mathbf{q}})| + \eta , \tag{4.89}$$

$$\text{EF 2} : |\bar{\lambda}_m| = \max(|\lambda_m(\hat{\mathbf{q}})|, \eta) , \tag{4.90}$$

$$\text{EF 3} : |\bar{\lambda}_m| = \begin{cases} |\lambda_m(\hat{\mathbf{q}})| , & \text{if} |\lambda_m(\hat{\mathbf{q}})| \geq 2\eta , \\ |\lambda_m(\hat{\mathbf{q}})^2|/4\eta + \eta , & \text{otherwise} , \end{cases} \tag{4.91}$$

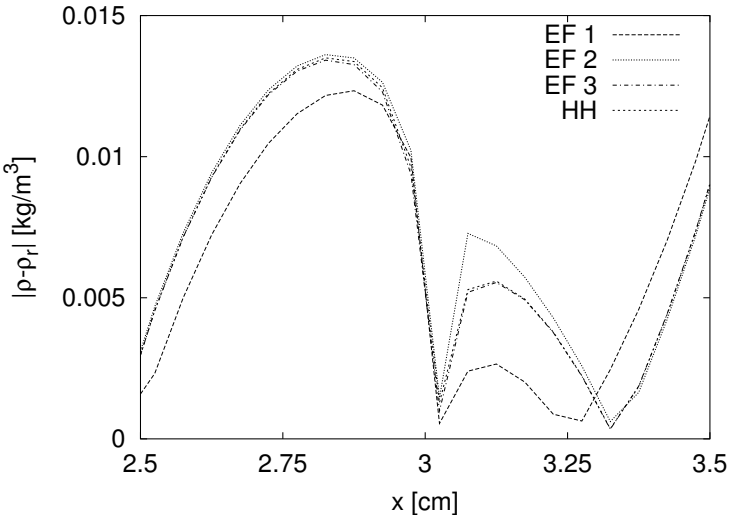

Figure 4.7: First-order results of Test 1. Difference between the density distribution computed with the Roe scheme and different entropy fixes against the reference solution in the transsonic rarefaction region.

where $\eta = \eta(\mathbf{q}_L, \mathbf{q}_R) \geq 0$ [87]. Unfortunately, the actual tuning of η is empirical and depends on the problem. For the Euler equations Sanders et al [160] proposed the natural choice

$$\eta(\mathbf{q}_L, \mathbf{q}_R) = \frac{1}{2} \max_m \left(|\lambda_m(\mathbf{q}_R) - \lambda_m(\mathbf{q}_L)| \right) = \frac{1}{2}(|u_{1,R} - u_{1,L}| + |c_R - c_L|) \ . \quad (4.92)$$

Note, that the Euler equations require an entropy correction only in the first and the last characteristic field. In order to avoid an unnecessary smearing of contact discontinuities we use $|\bar{\lambda}_m| \equiv |\lambda_m(\hat{\mathbf{q}})|$ in all other characteristic fields. Fig. 4.7 shows a comparison of the three entropy fixes EF 1 to 3 utilizing (4.92) and the Harten-Hyman (HH) method of the next section. As the differences are relatively small, Fig. 4.7 displays the local difference of the total density against the reference solution, i.e. $|\rho(x) - \rho_r(x)|$ (see also Fig. 4.9). EF 1 adds numerical viscosity to all shock waves and consequently has the largest error in the shock approximation (not shown). All other entropy corrections give a similar result on the shock, but the resolution of the transonic rarefaction is worst with EF 2 (compare Fig. 4.7). EF 3 and the Harten-Hyman method are nearly identical and give the best result.

Harten-Hyman Method

A further entropy correction that avoids adding numerical viscosity in an empirical manner has been presented by Harten and Hyman [89]. Their method is most frequently used today, because it gives sharply resolved results without an empirical parameter η (compare Fig. 4.7).

The basic idea of the method is to replace the simple wave solution of an entropy-violating shock by the simple wave of a rarefaction (2.23) with $\mathbf{v}(x/t) = \mathbf{q}^\star = const.$ The correction is applied only to transonic phenomena, because only those affect the inter-cell flux approximation. An entropy-violating transonic shock can easily be detected with Liu's entropy condition 2.27 by checking the inequality

$$\lambda_\nu(\mathbf{q}_\nu^l) < 0 < \lambda_\nu(\mathbf{q}_\nu^r) \ .$$

In case of the multi-component Euler equations, we have $\nu = 1, K+d+1$ with $\mathbf{q}_1^l = \mathbf{q}_L$, $\mathbf{q}_1^r = \mathbf{q}_L^\star$ and $\mathbf{q}_{K+d+1}^l = \mathbf{q}_R^\star$, $\mathbf{q}_{K+d+1}^r = \mathbf{q}_R$.

The new intermediate state $\mathbf{q}_\nu^\star$ is found by evaluating the integral form (2.4) for the simple wave solutions of the unphysical shock and the simplified rarefaction wave over $[\lambda_\nu^l \Delta t, \lambda_\nu^r \Delta t] \times [0, \Delta t]$ and by canceling all unnecessary terms. With the notations $\lambda_\nu^l := \lambda_\nu(\mathbf{q}_\nu^l)$, $\lambda_\nu^r := \lambda_\nu(\mathbf{q}_\nu^r)$ the results reads

$$(\lambda_\nu^r - \hat{\lambda}_\nu)\, \mathbf{q}_\nu^r + (\hat{\lambda_\nu} - \lambda_\nu^l)\, \mathbf{q}_\nu^l = (\lambda_\nu^r - \lambda_\nu^l)\, \mathbf{q}_\nu^\star$$

from which we immediately find

$$\mathbf{q}_\nu^\star = \frac{\mathbf{q}_\nu^l(\lambda_\nu^l - \hat{\lambda}_\nu) + \mathbf{q}_\nu^r(\hat{\lambda}_\nu - \lambda_\nu^r)}{\lambda_\nu^l - \lambda_\nu^r} \ . \tag{4.93}$$

Utilizing (4.93) we can express the new jumps $\mathbf{q}_\nu^\star - \mathbf{q}_\nu^l$ and $\mathbf{q}_\nu^r - \mathbf{q}_\nu^\star$ in terms of the wave $\mathbf{q}_\nu^r - \mathbf{q}_\nu^l = a_\nu \hat{\mathbf{r}}_\nu$ by

$$\mathbf{q}_\nu^\star - \mathbf{q}_\nu^l = \frac{\hat{\lambda}_\nu - \lambda_\nu^r}{\lambda_\nu^l - \lambda_\nu^r}\, a_\nu \hat{\mathbf{r}}_\nu \ , \qquad \mathbf{q}_\nu^r - \mathbf{q}_\nu^\star = \frac{\lambda_\nu^l - \hat{\lambda}_\nu}{\lambda_\nu^l - \lambda_\nu^r}\, a_\nu \hat{\mathbf{r}}_\nu \ .$$

The jumps in the flux approximation over λ_ν^l and λ_ν^r are therefore

$$\Delta_\nu^l \mathbf{F} = \lambda_\nu^l \frac{\hat{\lambda}_\nu - \lambda_\nu^r}{\lambda_\nu^l - \lambda_\nu^r}\, a_\nu \hat{\mathbf{r}}_\nu =: \bar{\lambda}_\nu^l\, a_\nu \hat{\mathbf{r}}_\nu \ , \quad \Delta_\nu^r \mathbf{F} = \lambda_\nu^r \frac{\lambda_\nu^l - \hat{\lambda}_\nu}{\lambda_\nu^l - \lambda_\nu^r}\, a_\nu \hat{\mathbf{r}}_\nu =: \bar{\lambda}_\nu^r\, a_\nu \hat{\mathbf{r}}_\nu \ .$$

Instead of (4.38) the numerical flux then reads

$$\mathbf{F}(\mathbf{q}_L, \mathbf{q}_R) = \mathbf{f}(\mathbf{q}_L) + \sum_{\substack{\hat{\lambda}_m < 0 \\ m \neq \nu}} a_m \hat{\lambda}_m \hat{\mathbf{r}}_m + \bar{\lambda}_\nu^l\, a_\nu \hat{\mathbf{r}}_\nu = \mathbf{f}(\mathbf{q}_R) - \sum_{\substack{\hat{\lambda}_m \geq 0 \\ m \neq \nu}} a_m \hat{\lambda}_m \hat{\mathbf{r}}_m - \bar{\lambda}_\nu^r\, a_\nu \hat{\mathbf{r}}_\nu \ . \tag{4.94}$$

Detailed derivations of the Harten-Hyman entropy fix can also be found in the books of LeVeque [117] and Toro [187]. For the Euler equations the flux approximation (4.38) simplifies to $\mathbf{F}(\mathbf{q}_L, \mathbf{q}_R) = \mathbf{f}(\mathbf{q}_L) + \bar{\lambda}_1^l\, a_1 \hat{\mathbf{r}}_1$ for a sonic rarefaction in the first and to $\mathbf{F}(\mathbf{q}_L, \mathbf{q}_R) = \mathbf{f}(\mathbf{q}_R) - \bar{\lambda}_{K+d+1}^r\, a_{K+d+1} \hat{\mathbf{r}}_{K+d+1}$ for a sonic rarefaction in the last characteristic field.

4.6.3 A Robust Roe-type Method

In order to complete our explanations on the Roe scheme for multi-component gas-mixtures we formulate an algorithm that implements the Roe method and incorporates all corrections that will be derived in the following sections to make the scheme robust and reliable.

(S1) Calculate the standard Roe-averages $\hat{\rho}$, $\hat{u}_n$, $\hat{H}$, $\hat{Y}_i$, $\hat{T}$.

(S2) Compute $\hat{\gamma}$ by evaluating both $\hat{c}_v$ and $\hat{c}_p$ from (4.82) and (4.80) or evaluate only one and utilize the standard Roe-average $\hat{R}$ or calculate $\hat{W}$ from (4.79).

(S3) Calculate $\hat{\phi}_i$ from (4.77) with the standard Roe-averages $\hat{e}_i$ or $\hat{h}_i$.

(S4) Use (4.75) to evaluate $\hat{c}$.

(S5) Use $\Delta\mathbf{q} = \mathbf{q}_R - \mathbf{q}_L$ and Δp to compute the wave strength a_m from (4.83).

(S6) Calculate $\mathbf{W}_1 = a_1\hat{\mathbf{r}}_1$, $\mathbf{W}_2 = \sum_{m=2}^{K+d} a_m\hat{\mathbf{r}}_m$, $\mathbf{W}_3 = a_{K+d+1}\hat{\mathbf{r}}_{K+d+1}$ from Prop. 10.

(S7) Evaluate $s_1 = \hat{u}_1 - \hat{c}$, $s_2 = \hat{u}_1$, $s_3 = \hat{u}_1 + \hat{c}$.

(S8) Evaluate $\rho^\star_{L/R}$, $u^\star_{1,L/R}$, $e^\star_{L/R}$, $c^\star_{1,L/R}$ from $\mathbf{q}^\star_L = \mathbf{q}_L + \mathbf{W}_1$, $\mathbf{q}^\star_R = \mathbf{q}_R - \mathbf{W}_3$.

(S9) If $\rho^\star_{L/R} \leq 0$ or $e^\star_{L/R} \leq 0$ use $\mathbf{F}_{HLL}(\mathbf{q}_L, \mathbf{q}_R)$ from Eq. (4.96) and skip (S10) and (S11).

(S10) Entropy correction:

(a) Numerical viscosity methods EF 1/2/3:

i. Calculate $|\bar{s}_{1/3}|$ from $|s_{1/3}|$ according to (4.89)/(4.90)/(4.91). $|\bar{s}_2| \equiv |s_2|$.

ii. $$\mathbf{F}_{Roe}(\mathbf{q}_L, \mathbf{q}_R) = \frac{1}{2}\left(\mathbf{f}(\mathbf{q}_L) + \mathbf{f}(\mathbf{q}_R) - \sum_{\iota=1}^{3} |\bar{s}_\iota|\mathbf{W}_\iota\right)$$

(b) Harten-Hyman method (HH):

i. If $u_{1,L} - c_L < 0 < u^\star_{1,L} - c^\star_L$ set
$$s_1 := \frac{(\hat{u}_1 - \hat{c}) - (u^\star_{1,L} - c^\star_L)}{(u_{1,L} - c_L) - (u^\star_{1,L} - c^\star_L)}(u_{1,L} - c_L).$$

ii. If $u^\star_{1,R} + c^\star_R < 0 < u_{1,R} + c_R$ set
$$s_3 := \frac{(\hat{u}_1 + \hat{c}) - (u_{1,R} + c_R)}{(u^\star_{1,R} + c^\star_R) - (u_{1,R} + c_R)}(u^\star_{1,R} + c^\star_R).$$

iii. $$\mathbf{F}_{Roe}(\mathbf{q}_L, \mathbf{q}_R) = \mathbf{f}(\mathbf{q}_L) + \sum_{\substack{s_\iota<0 \\ \iota=1,\ldots,3}} s_\iota\mathbf{W}_\iota.$$

(S11) Positivity correction: Replace $\mathbf{F}_{i,Roe}$ by $\mathbf{F}^\star_{i,Roe}$ according to Eq. (4.107).

Algorithm 1: Hybrid Roe-HLL scheme with mass fraction positivity correction. Step (S10a) is used with one of the entropy enforcement (EF) formulas (4.89) to (4.91). Step (S10b) is applied for the Harten-Hymann (HH) entropy correction.

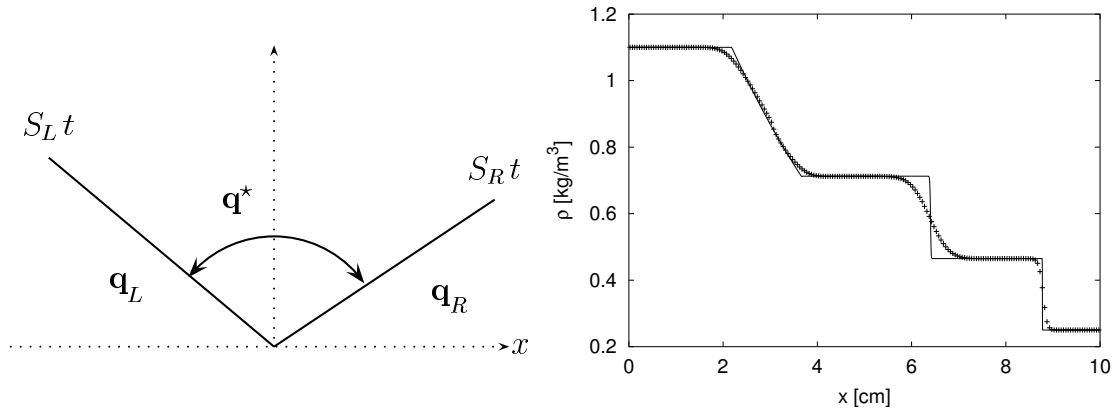

Figure 4.8: Left: simplified approximation of the RP by the HLL scheme, right: first-order results of Test 1 computed with HLL.

4.6.4 Harten-Lax-Van Leer Scheme

The Harten, Lax and Van Leer (HLL) scheme is a Godunov-type method that uses a very simple approximative Riemann solver [91].[7] It approximates the solution of the RP simply by two discontinuous waves. The intermediate state $\mathbf{q}^\star$ is assumed to be constant (compare Fig. 4.8). The approximative solution is

$$\bar{\mathbf{q}}(\mathbf{x},t) = \begin{cases} \mathbf{q}_L\,, & x < S_L\,t\,, \\ \mathbf{q}^\star\,, & S_L\,t \le x \le S_R\,t\,, \\ \mathbf{q}_R\,, & x > S_R\,t\,, \end{cases} \tag{4.95}$$

where S_L and S_R denote suitable approximations to the smallest and largest signal speed involved in the RP. From (4.95) the flux approximation

$$\mathbf{F}(\mathbf{q}_L,\mathbf{q}_R) = \begin{cases} \mathbf{f}(\mathbf{q}_L)\,, & 0 < S_L\,, \\ \dfrac{S_R\mathbf{f}(\mathbf{q}_L) - S_L\mathbf{f}(\mathbf{q}_R) + S_L S_R(\mathbf{q}_R - \mathbf{q}_L)}{S_R - S_L}\,, & S_L \le 0 \le S_R\,, \\ \mathbf{f}(\mathbf{q}_R)\,, & 0 > S_R\,, \end{cases} \tag{4.96}$$

can be derived. The only non-trivial case is $S_L \le 0 \le S_R$. Like in Sec. 4.2.4 the obvious choice $\mathbf{F}(\mathbf{q}_L,\mathbf{q}_R) = \mathbf{f}(\mathbf{q}^\star)$ would lead to a scheme that would be inconsistent with the original conservation law; and analogously to Sec. 4.2.4 the correct flux approximation is found by evaluating the integral form (2.4) over the domains $[0, S_R\Delta t]\times[0,\Delta t]$ and $[S_L\Delta t, 0]\times[0,\Delta t]$. After canceling Δt we obtain the equations

$$\mathbf{F}(\mathbf{q}_L,\mathbf{q}_R) = \mathbf{f}(\mathbf{q}_L) + S_L(\mathbf{q}^\star - \mathbf{q}_L) \quad \text{and} \quad \mathbf{F}(\mathbf{q}_L,\mathbf{q}_R) = \mathbf{f}(\mathbf{q}_R) + S_R(\mathbf{q}^\star - \mathbf{q}_R)$$

that allow the elimination of the unknown intermediate state $\mathbf{q}^\star$ and lead directly to the proposed result.

[7] The name HLLE after Einfeldt [62] is also used.

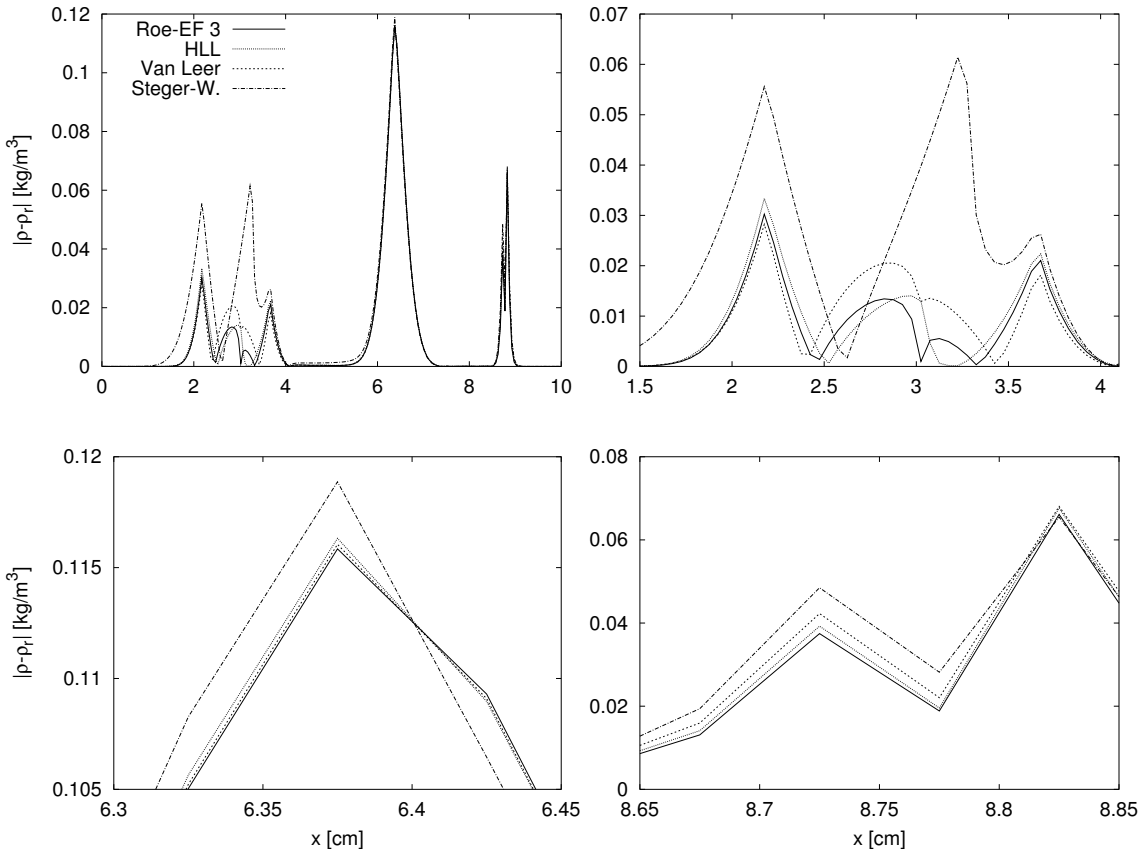

Figure 4.9: First-order results for Test 1. Difference of the total density against the reference solution for Roe-EF 3, HLL and the FVS of Van Leer and Steger-Warming. Top, left: whole computational domain. Top, right: transonic rarefaction. Bottom, left: contact discontinuity. Bottom, right: shock.

The HLL scheme requires estimates of the signal speeds S_L and S_R. Possible choices in our case of multi-component Euler equations are the Roe-averaged eigenvalues

$$S_L = \hat{u}_1 - \hat{c} \ , \quad S_R = \hat{u}_1 + \hat{c}$$

or the simpler estimates

$$S_L = \min(u_{1,L} - c_L, u_{1,R} - c_R) \ , \quad S_R = \max(u_{1,L} + c_L, u_{1,R} + c_R) \tag{4.97}$$

that have been suggested by Davis [48]. Throughout this thesis only the last estimate has been utilized. The necessary stability condition for Davis' estimate is

$$C_{CFL}^{HLL} := \max_{j \in \mathbb{Z}} (|u_{1,j}| + c_j) \frac{\Delta t}{\Delta x} \leq 1 \ . \tag{4.98}$$

In order to compare all upwind schemes, Fig. 4.9 displays the local difference of the total density against the reference solution, i.e. $|\rho(x) - \rho_r(x)|$, for all three simple wave phenomena involved in Test 1. The best results are obtained with the Roe scheme and entropy correction, while the Steger-Warming scheme gives the largest errors. HLL and the Van Leer FVS do not differ significantly for this example.

4.7 Application of Higher-Order Methods

In this section we incorporate the previously derived first-order upwind schemes for multi-component Euler equations into the high resolution methods of Sec. 4.3. Although the MUSCL extrapolation technique is tailored for Godunov-type methods, it can be used with all previously derived schemes.[8] The Wave Propagation Method requires a FDS scheme to calculate transverse fluctuations and consequently is intended to be utilized with the Roe method of Sec. 4.6.1, respectively with the robust extension of Sec. 4.6.3.

4.7.1 MUSCL Extrapolation

The MUSCL variable extrapolation technique can be implemented in conservative and in primitive variables. An extrapolation of the primitive variables usually gives sharper refined discontinuities [94], but has the significant disadvantage that the conservative quantities calculated from these primitive variable values do not necessarily satisfy the TVD constrain. For usual FV schemes formulated in conserved variables the MUSCL extrapolation therefore should reconstruct conservative quantities whenever possible to lead to a robust and reliable high resolution method.

In case of the multi-component Euler equations of Sec. 2.3 a direct extrapolation of the total energy density $\bar{E}$ is only possible, if all species are calorically perfect. In the general case of thermally perfect gases this reconstruction has to be replaced by an extrapolation of one of the primitive quantities T or p, because it otherwise could not be guaranteed that the reconstructed vector of state $\tilde{\mathbf{q}}$ remains in the space of admissible states S. In particular, for arbitrary enthalpy functions h_i the implicit temperature equation (2.56) does not need to have a solution $\tilde{T}$ corresponding to $\tilde{\mathbf{q}}$, if $\tilde{\bar{E}}$ is reconstructed directly. Further on, we *enforce* that all species are treated equally.

We recommend to extrapolate the primitive quantities $\tilde{\rho}$, $\tilde{p}$ and $\tilde{Y}_1, \ldots, \tilde{Y}_K$ and the conserved quantities $\tilde{m}_1, \ldots, \tilde{m}_d$. The remaining entries of $\tilde{\mathbf{q}}$ are then calculated from these values by

$$\tilde{\rho}_i = \tilde{Y}_i \tilde{\rho} \,, \quad \tilde{\bar{E}} = \tilde{\rho} \sum_{i=1}^{K} \tilde{Y}_i h_i(\tilde{T}) - \tilde{p} + \frac{\tilde{\mathbf{m}}^2}{2\tilde{\rho}} \quad \text{with} \quad \tilde{T} = \frac{\tilde{p}}{\mathcal{R}} \left(\sum_{i=1}^{K} \frac{\tilde{\rho}_i}{W_i} \right)^{-1} .$$

In order to ensure that both $\tilde{\rho}$ and all $\tilde{\rho}_i$ are TVD and to avoid an inconsistency between $\sum \tilde{\rho}_i$ and $\tilde{\rho}$, it has to be enforced that the reconstructed mass fractions $\tilde{Y}_i$ satisfy the condition $\sum \tilde{Y}_i = 1$. From Eqs. (4.45), (4.46) we get for $\tilde{Y}_i^L$, $\tilde{Y}_i^R$ with Y_i denoting the ith mass fraction in the middle cell and Y_i^{-1}, Y_i^1 the values in the left

[8] Hirsch gives a detailed comparison between the MUSCL variable extrapolation with slope limiting and the flux extrapolation with flux limiting for both Steger-Warming and Van Leer FVS for standard Euler equations that clearly shows the superiority of the MUSCL technique over the flux limiting also for FVS methods [94].

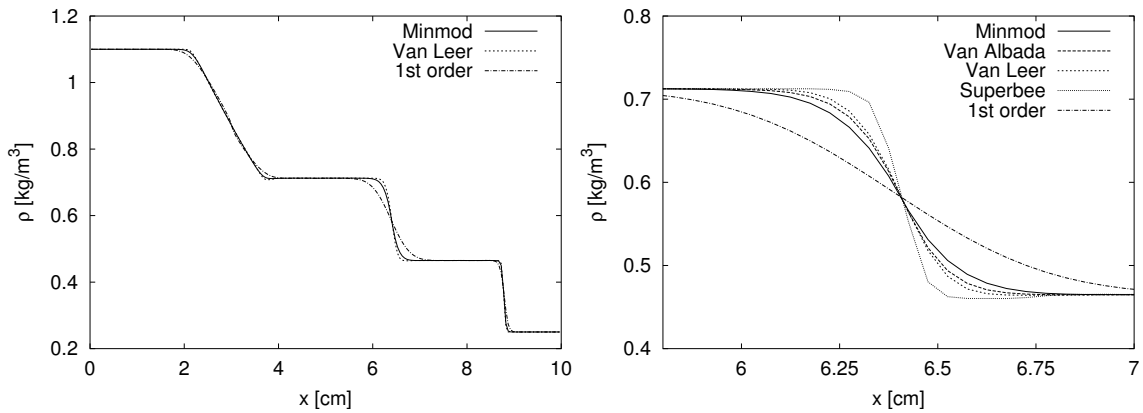

Figure 4.10: Second-order results of Test 1 with MUSCL-Hancock Method utilizing the Roe scheme with EF 3 and different slope limiters. Left: solution with Minmod- (4.49) and Van Leer-limiter (4.51). Right: comparison of the result at the contact discontinuity with the limiter-functions (4.49) to (4.52).

and the right neighbor, respectively

$$\tilde{Y}_i^L = Y_i + \frac{1}{4}\left[(1-\omega)\,\Phi_i^+\,(Y_i - Y_i^{-1}) + (1+\omega)\,\Phi_i^-\,(Y_i^1 - Y_i)\right] \;, \tag{4.99}$$

$$\tilde{Y}_i^R = Y_i - \frac{1}{4}\left[(1-\omega)\,\Phi_i^-\,(Y_i^1 - Y_i) + (1+\omega)\,\Phi_i^+\,(Y_i - Y_i^{-1})\right] \;. \tag{4.100}$$

Herein

$$\Phi_i^+ := \Phi\left(\frac{Y_i^1 - Y_i}{Y_i - Y_i^{-1}}\right) \;, \qquad \Phi_i^- := \Phi\left(\frac{Y_i - Y_i^{-1}}{Y_i^1 - Y_i}\right)$$

are the limiter values of ith mass fraction. Summing up all K reconstructed values $\tilde{Y}_i^L$, $\tilde{Y}_i^R$ we derive with $\sum \tilde{Y}_i^R = \sum \tilde{Y}_i^L = \sum Y_i = 1$ from (4.99), (4.100)

$$-\sum(1-\omega)\Phi_i^+ Y_i^{-1} + \sum\left[(1-\omega)\Phi_i^+ - (1+\omega)\Phi_i^-\right] Y_i + \sum(1+\omega)\Phi_i^- Y_i^1 = 0 \;,$$

$$-\sum(1+\omega)\Phi_i^+ Y_i^{-1} + \sum\left[(1+\omega)\Phi_i^+ + (1-\omega)\Phi_i^-\right] Y_i - \sum(1-\omega)\Phi_i^- Y_i^1 = 0 \;.$$

Summation of these two equations gives the condition

$$\sum_{i=1}^{K} \Phi_i^+\,(Y_i - Y_i^{-1}) + \omega \sum_{i=1}^{K} \Phi_i^-\,(Y_i^1 - Y_i) = 0$$

that can only be satisfied, iff $\Phi_1^+ = \cdots = \Phi_K^+$ and $\Phi_1^- = \cdots = \Phi_K^-$. This equality can easily be enforced by applying the same limiter values Φ^+, Φ^- to all mass fractions. A possible choice for symmetric slope limiters satisfying Eq. (4.53) that guaranties the TVD property in all components is

$$\Phi^+ = \Phi^- = \min(\Phi_1^+, \ldots, \Phi_K^+, \Phi_1^-, \ldots, \Phi_K^-) \;. \tag{4.101}$$

A numerical example utilizing the proposed reconstruction strategy is shown in Fig. 4.10. The improvement in employing a thoroughly constructed second-order method, especially in the approximation of the contact discontinuity is obvious.

4.7.2 Multi-Dimensional Wave Propagation

Analogously to the previous section, the wave limiting (4.56) is only reliable for multi-component Euler equations, if all species are calorically perfect gases. In the thermally perfect case, the separate construction of a limited wave $\tilde{\mathcal{W}}^m$ in each characteristic field can create fluctuations $\mathcal{A}^{\pm}\Delta = \sum \hat{\lambda}_m^{\pm} \tilde{\mathcal{W}}_m$ leading to values $\mathbf{Q}$ outside of the space of admissible states S. Consequently, the one-dimensional variant of the Wave Propagation Method (4.54) is no appropriate higher-order scheme for thermally perfect Euler equations. But the two-dimensional scheme (4.58) is still applicable. Formula (4.58) is a second-order multi-dimensional scheme that only requires arbitrarily constructed second-order accurate fluctuations in the normal direction. For Euler equations of thermally perfect gases we calculate these fluctuations from the second-order fluxes of the previously described reliable MUSCL-Hancock method and by applying Eq. (4.39). For instance, the fluctuations $\tilde{\mathcal{A}}^{\pm}\Delta$ are therefore defined by

$$\tilde{\mathcal{A}}^{-}\Delta_{j+\frac{1}{2},k} := \mathbf{F}_1(\bar{\mathbf{Q}}^L_{j+\frac{1}{2},k}, \bar{\mathbf{Q}}^R_{j+\frac{1}{2},k}) - \mathbf{f}_1(\mathbf{Q}^l_{jk}) \ , \tag{4.102}$$

$$\tilde{\mathcal{A}}^{+}\Delta_{j+\frac{1}{2},k} := \mathbf{f}_1(\mathbf{Q}^l_{j+1,k}) - \mathbf{F}_1(\bar{\mathbf{Q}}^L_{j+\frac{1}{2},k}, \bar{\mathbf{Q}}^R_{j+\frac{1}{2},k}) \ . \tag{4.103}$$

This simple trick, which allows the computation of fluctuations from standard numerical fluxes, is also mentioned in [107] as an opportunity to incorporate for instance an exact Riemann solver for Euler equations into the Wave Propagation scheme. In our particular case, it allows the direct application of the robust Roe-type scheme formulated in Algorithm 1 in Sec. 4.6.3 on the one hand and the usage of the appropriate higher-order reconstruction technique on the other hand.

The Riemann solver in the normal direction implements the MUSCL-Hancock method and calculates the temporary values $\bar{\mathbf{Q}}^L$, $\bar{\mathbf{Q}}^R$. All steps (S1) to (S11) of Algorithm 1 are then employed to compute numerical fluxes on the basis of $\bar{\mathbf{Q}}^L$ and $\bar{\mathbf{Q}}^R$. At the end of the solution routine these fluxes are transformed with $\mathbf{f}_{1/2}(\mathbf{Q})$ according to Eq. (4.39) into fluctuations (see Eqs. (4.102), (4.103) for the x_1-direction). In the transverse solution routine we execute just the steps (S1) to (S7) and use (4.44) to evaluate the transverse flux splitting of the previously derived second-order fluctuations.

It has to be underlined, that the multi-dimensional update formula (4.58) does not satisfy a maximum principle for the mass fractions Y_i in the multi-component case (compare Sec. 4.9.1). Consequently, scheme (4.58) can create negative mass fraction values. Although the appropriate correction (4.107) is considered in the computation of $\tilde{\mathcal{A}}^{\pm}\Delta$, $\tilde{\mathcal{B}}^{\pm}\Delta$, the summation of cross-derivate terms can produce multi-dimensional fluctuations $\hat{\mathcal{A}}^{\pm}\Delta$, $\hat{\mathcal{B}}^{\pm}\Delta$ that lead to violations of the maximum principle. We enforce the validity of the maximum principle for the entire Wave

x [cm]	$x < 5$	$x > 5$
ρ [kg m^{-3}]	0.25	0.25
u_1 [m s^{-1}]	-5000	5000
p [kPa]	25	25

Table 4.2: Riemann initial data for Test 2. Domain: 10 cm, outflow boundaries.

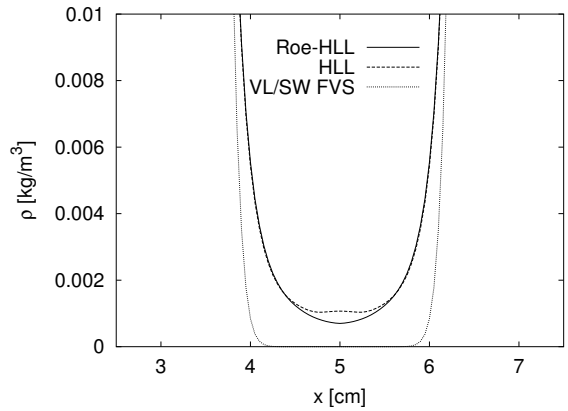

Figure 4.11: First-order results of Test 2 at $t = 3\,\mu$s after ca. 40 time steps with $C_{CFL} \approx 0.8$, $\Delta x = 0.05$ cm. Gas: O_2.

Propagation Method by transforming $\hat{\mathcal{A}}^{\pm}\Delta$, $\hat{\mathcal{B}}^{\pm}\Delta$ with (4.39) back into numerical fluxes $\hat{\mathbf{F}}^1$, $\hat{\mathbf{F}}^2$ and by applying the usual positivity correction (4.107) on $\hat{\mathbf{F}}^1$, $\hat{\mathbf{F}}^2$. Instead of Eq. (4.59) we finally use the standard formula (4.4) to calculate the numerical update.

4.8 Problems and Failures of Upwind Schemes

Shock-capturing upwind schemes give physically reasonable and satisfactory approximations for many practical problems. But specific situations exist, where different schemes show a very different behavior. In particular the Roe scheme, which gives the best result in Test 1 suffers from various approximation problems and failures. As our goal is the derivation of a reliable high resolution shock-capturing method for detonation flow we recall these problems as they are known today, because most of them have to be circumvented in a reliable transport scheme for this problem class.

4.8.1 Unphysical Values

It is possible that the Roe scheme of Sec. 4.6.1 produces unphysical approximations to the total density or the internal energy, i.e. $\rho \leq 0$ or $e \leq 0$. The FVS schemes and the HLL method do not show this behavior and are much more robust. The problem can occur near the vacuum state, but also in the approximation of very strong shock waves with small density or internal energy values at one side. Riemann initial data for a typical test problem near vacuum for thermally perfect oxygen are given in Tab. 4.2. Without entropy fix the Roe scheme breaks down right in the first step; with entropy correction EF 3 a negative total density occurs after approximately 30 time steps with intended Courant number $C_{CFL} \approx 0.8$.

A detailed analysis of the origin of unphysical approximations for flows near vacuum state can be found in a paper by Einfeldt et al. [62]. For the standard case of a single calorically perfect gas it is shown, that the production of unphysical flow values is an intrinsic deficiency of all Godunov-type methods based on linearized

x	$x < 5$	$x > 5$
ρ	9.6172813	1.0
u_1	-0.6499430	-8.8358689
p	75.785546	1.0
c	2.919	1.095

Table 4.3: Initial data for Test 3.

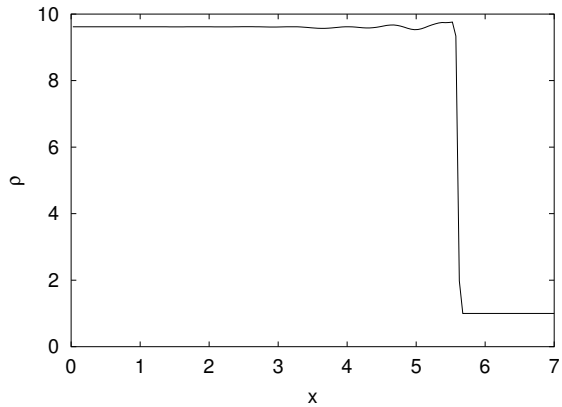

Figure 4.12: Oscillating numerical solution of Godunov's Method at $t = 2$.

Riemann solvers and does not occur when using the HLL approximate Riemann solver instead.

For the standard Euler equations Einfeldt et al. proved rigorously that the HLL scheme is positivity preserving in ρ and e supposed the numerical signal velocities are suitable bounds for the physical signal velocities [62]. Similar proofs for the FVS schemes of Steger-Warming and Van Leer have been presented recently by Gressier, Villedieu and Moschetta in [83].

A simple possibility to avoid the erroneous behavior of the Roe method is to replace its flux approximation where necessary by the flux of a robust method, for instance by the HLL flux. A reliable switching-criterion can be constructed easily by evaluating the approximative intermediate states $\mathbf{q}_L^\star$ and $\mathbf{q}_R^\star$ in (4.85) by

$$\mathbf{q}_L^\star = \mathbf{q}_L + a_1 \hat{\mathbf{r}}_1 \ , \quad \mathbf{q}_R^\star = \mathbf{q}_R - a_{K+d+1} \hat{\mathbf{r}}_{K+d+1} \tag{4.104}$$

(compare Sec. 2.2.1) and by checking $\rho_{L/R}^\star > 0$ and $e_{L/R}^\star > 0$. Numerical results for such a hybrid method that utilizes Roe and HLL approximation together are compared to the FVS schemes, which give an identical result for this problem, and to HLL alone in Fig. 4.11. In this example, the hybrid method switches to HLL only in the two cells near the initial discontinuity in the first five time steps.

4.8.2 Slowly Moving Strong Shocks

Some accurate shock-capturing Godunov-type schemes for Euler equations, like Godunov's Method and the Roe scheme are known to produce oscillations at isolated slowly moving shock waves. "Slowly moving" in this context means that the ratio of the shock velocity σ and the maximum wave speed in the characteristic field of the shock ($\nu = 1, K + d + 1$) in the domain is small, i.e.

$$\frac{|\sigma|}{\max\limits_{j \in \mathbb{Z}}(|\lambda_{\nu,j}|)} \ll 1 \ .$$

Usually the influence of these disturbances is negligible. However, if the shock is sufficiently strong, the weakness is clearly present. This problem was first reported

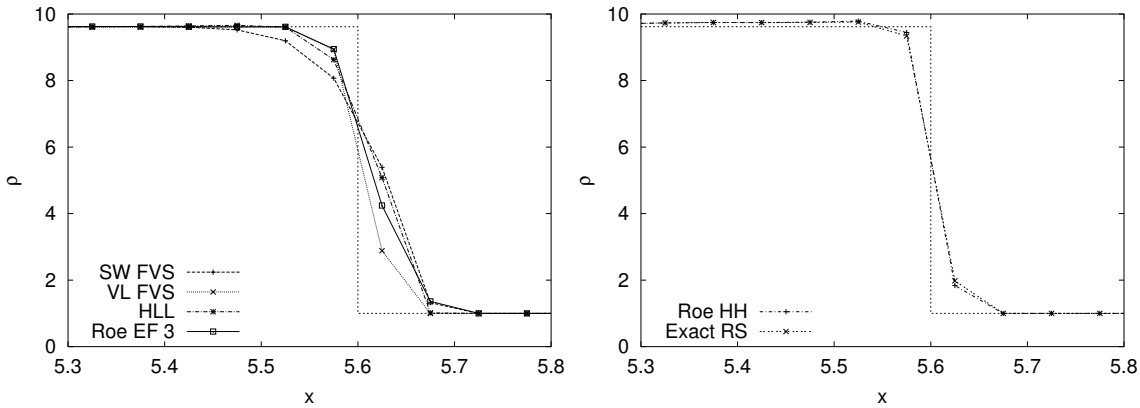

Figure 4.13: Density distributions for Test 3 with different first-order accurate upwind schemes plotted onto the exact solution (graphs without dots). $t_{end} = 2$.

by Colella and Woodward [44], but is also mentioned by Quirk [150, 151]. A first analysis of the origin of the error was given by Roberts [154]. A recent paper of Arora and Roe extends Roberts' work [9].

We choose a very special example for the standard Euler equations of a polytropic gas to demonstrate the defect. Our example is an isolated shock wave associated to $\lambda_3 = u_1 + c$ which is the simple wave solution of the RP in Tab. 4.3. This RP is identical to the flow situation at the head of an steady ZND detonation with simplified chemistry for the parameters[9] $\gamma = 1.2$, $Q_0 = 50$, $f = 1.8$ and therefore corresponds to the RP at the detonation front in the limit of spatial refinement, if the Godunov-splitting (4.19) is applied to simulate the inhomogeneous ZND equations (see Sec. 3.1.1). We shift both velocities by +0.3 to achieve an isolated, but slowly moving shock wave. During the simulation, the shock travels from its initial position at $x = 5$ to $x = 5.6$ at $t_{end} = 2$. For this test we utilize the domain $[0, 10]$ which is discretized with 200 cells ($\Delta x = 0.05$). Automatic time step adjustment for an intended Courant number of $C_{CFL} \approx 0.8$ is used.

First-Order Results

We test the upwind schemes of the preceding sections without higher-order reconstruction first. The front pressure histories of these first-order computations are displayed in the two pictures at the top of Fig. 4.14. It is apparent, that none of our shock-capturing schemes is monotone for this example. All schemes produce oscillations in all flow variables. In particular, none of the tested schemes approximates

[9]The flow values in the von Neumann point of a ZND detonation with simplified Arrhenius law are calculated from the Eqs. (3.22), (3.27) and (3.28) for $Z = 0$ and do not depend on $E_A^\star$. Equivalently to the equation of state $p = (\gamma - 1)(\rho e - \rho q_0)$ the standard equation $p = (\gamma - 1)\rho e^\star$ can be used. All flow variables are identical, only the specific internal and total energy differ by the constant q_0, i.e. $e^\star = e - q_0$ and $E^\star = E - q_0$.

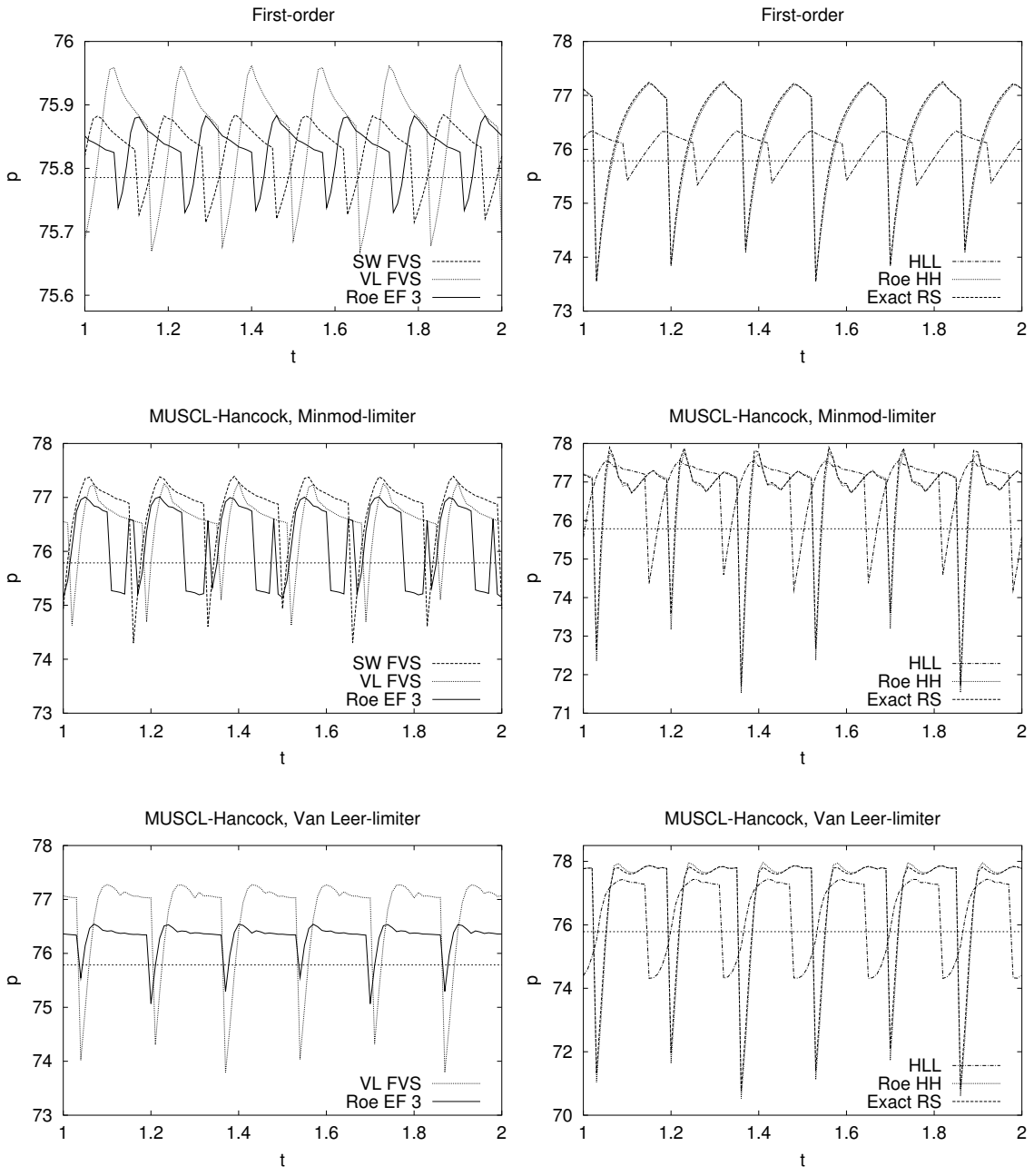

Figure 4.14: Front pressure histories of Test 3 for different first- and second -order accurate FV upwind schemes. The dotted horizontal lines display the exact front pressure. $C_{CFL} \approx 0.8$.

the first intercell flux at the head of the shock wave exactly with an isolated simple wave solution. This behavior is not surprising for the FVS schemes and the HLL approximate Riemann solver, but it is astonishing for the Roe scheme and especially for Godunov's Method.[10]

The movement of a discontinuous jump between the two state values $\mathbf{q}_L$ and $\mathbf{q}_R$ through a fixed mesh involves an intermediate state $\mathbf{q}^\star$ in the cell, where the discontinuity is actually located. In our case of a 3-shock wave with positive signal speed a Godunov-type method would propagate the discontinuity by solving the RP between $\mathbf{q}^\star$, $\mathbf{q}_R$ in the next time-step. Roberts points out that this RP only corresponds to the sought 3-shock wave solution, if the value $\mathbf{q}^\star$ lies exactly on the Hugoniot curve in phase space[11] connecting $\mathbf{q}_L$ and $\mathbf{q}_R$ by a 3-shock. In [154] he demonstrates that the Roe scheme, but also Godunov's Method fail in approximating such a value $\mathbf{q}^\star$ to high accuracy in case of nonlinear systems and produce significant errors in the other characteristic fields. As the Roe scheme with Harten-Hyman entropy correction (Roe HH) and Godunov's Method (Exact RS) do not introduce any numerical viscosity over a shock wave these errors are not damped. The right picture of Fig. 4.13 illustrates that these methods capture the shock very sharply within two cells, but generate unphyscial overshoots. Especially the temporal development of the front pressure displayed in the upper row of Fig. 4.14 uncovers the huge oscillation amplitude of these schemes.

If the Harten-Hyman entropy correction is replaced by an entropy enforcement technique, for instance by EF 3, the results of the Roe scheme are improved (Roe EF 3). Roe EF 3 needs three cells to capture the shock (see left picture of Fig. 4.13), but creates the smallest oscillations of all tested methods (see Fig. 4.14). Although the shock wave is admissible and does not require any entropy correction the entropy enforcement formulas EF 1 to EF 3 add numerical viscosity in the shock capturing region. The shock involves such a large jump in u_1 (compare Tab. 4.3) that the parameter η computed by (4.92) usually exceeds the Roe-averaged eigenvalue $\hat{u}_1 + \hat{c}$ at least at one cell interface.

For fast moving shock waves all considered upwind schemes give an identical approximation without any oscillations. Fig. 4.15 displays the result of Godunov's Method, if all velocities in Test 3 are increased by 8.8358689. Six cells are now necessary to capture the shock. The results only depend on the discretization and the numerical viscosity is so large that no differences between the different schemes are visible.

[10] From property (iii) on page 77 follows the condition $\hat{s}(\mathbf{q}_L, \mathbf{q}_R)\Delta\mathbf{q} = \mathbf{f}(\mathbf{q}_R) - \mathbf{f}(\mathbf{q}_L)$ for the approximation of isolated discontinuities by the Roe scheme. Together with property (i) on page 77 this condition should ensure that an isolated shock or contact discontinuity is approximated with a single simple wave solution [117].

[11] A detailed explanations of these notions in the case of nonlinear systems can be found in the book of LeVeque [117].

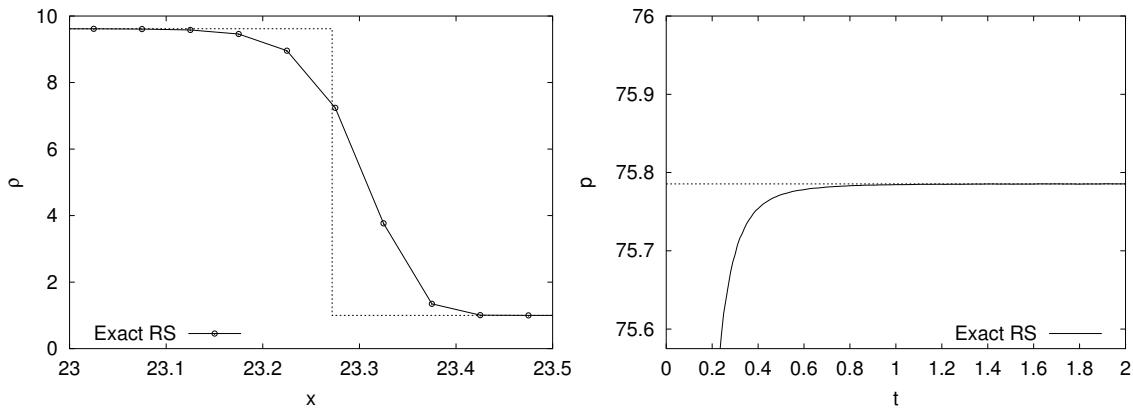

Figure 4.15: Result of Godunov's Method for a fast moving shock wave plotted onto the exact solution (graphs without dots). Left: density distribution at $t_{end} = 2$, right: front pressure history.

Higher-Order Results

We test the MUSCL-Hancock method of Sec. 4.3 with a variable extrapolation in conservative variables with all previously introduced upwind schemes. The front pressure histories for Test 3 with Minmod- and Van-Leer-limiter are shown in Fig. 4.14. The oscillations observed in the first-order computations are amplified. For this specific example, the higher-order reconstruction is obviously not total variation diminishing, because the basic assumption in the derivation of the method in Sec. 4.3, a monotone upwind scheme, is not satisfied.

With the diffusive Minmod-limiter (4.49) the FVS schemes, HLL and Roe EF 3 give similar results. With the Van-Leer-limiter (4.51), which resolves discontinuities sharper, quite different results are obtained. While the oscillations of Roe EF 3 decrease slightly, Van Leer FVS and HLL show worse results. The simple Steger-Warming FVS even breaks down with this limiter.

4.8.3 Multi-Dimensional Strong Shocks

The so-called carbuncle phenomenon is a multi-dimensional numerical crossflow instability that occurs at strong grid-aligned shock waves, if sophisticated shock-capturing schemes are applied. It was first discovered by Perry and Imlay in blunt body computations utilizing the Roe scheme for standard Euler equations [148]. They observed a spurious, but fully converged, steady-state solution for flows at supersonic speed. It was studied in more detail from a numerical point of view by Quirk, who introduced a simplified instationary test case on a rectangular grid with a slightly perturbed mesh to trigger the unwanted instability [150]. In this test, initially very weak transverse disturbances directly downstream of the shock are amplified disastrously and lead to the total degeneration of the planar shock struc-

ture. Like in the preceding sections the defect is caused by the capturing of a very strong shock wave on a fixed mesh, but unlike the unphysical oscillations observed at slowly moving shock waves, the carbuncle phenomenon is also present for standing and rapidly propagating shocks. A drastic increase of the numerical viscosity in the characteristic field of the shock can moderate the size of the carbuncle prones, but it does not avoid them completely. All problems are reported to vanish entirely, if the shock is resolved accurately, for instance with a front-tracking technique [142, 143]. Up to now, no profound explanation has been found to explain the instability satisfactory, but recently Robinet, Gressier, Casalis and Moschetta presented a linear stability analysis for the two-dimensional standard Euler equations that uncovered an unstable mode in the equations downstream of shocks at higher Mach numbers [155].

Recent numerical investigations [143, 58] have shown that the carbuncle phenomenon is produced by all upwind schemes which conserve steady contact discontinuities exactly. Some of these schemes are Godunov's Method, the Roe scheme (Sec. 4.6.1), Osher's Riemann solver [63, 141, 140] and the HLL approximate Riemann solver with restored contact-wave (these improved variants are HLLEM [62] and HLLC [188, 187]). A FVS-type scheme that also preserves steady contact discontinuities and consequently creates carbuncles is AUSMDV [201], a recent variant of the Advection Upstream Splitting Method (AUSM) by Liou and Steffen [125, 124]. On the other hand, schemes introducing numerical viscosity at steady contact discontinuities, like Steger-Warming (Sec. 4.5.1), Van Leer (Sec. 4.5.2), AUSM FVS or for instance the simple HLL scheme (Sec. 4.6.4), do not suffer from the carbuncle phenomenon. It is interesting to note, that physical viscosity introduced by the diffusive terms of the Navier-Stokes equations is usually not sufficient to suppress the unphysical behavior [143].

Detonation simulations can suffer significantly from unphysical crossflow instabilities, because the shock at the detonation front is usually extraordinarily strong. The total failure of simulations of strong grid-aligned detonation waves due to such instabilities is reported by Quirk [151] and Bale, Helzel [14, 92]. All detonation configurations (with simplified or with detailed chemical reaction) considered throughout this thesis involve strong enough shock waves to create the carbuncle phenomenon. As multi-dimensional detonation waves in general do not remain planar (compare Sec. 3.2) they intrinsically produce weak disturbances perpendicular to the detonation front that initiate typical carbuncles in multi-dimensional grid-aligned computations rapidly.

Test with a Strong Shock Wave

We study the appearance of unwanted crossflow instabilities at strong grid-aligned shock waves by a simple non-reactive two-dimensional test problem. This test is easier to implement than Quirk's original test case [150], since it does not require a non-Cartesian mesh. Furthermore, it illustrates that the shocks ahead of detonation waves are usually strong enough to trigger a continuous carbuncle growth without

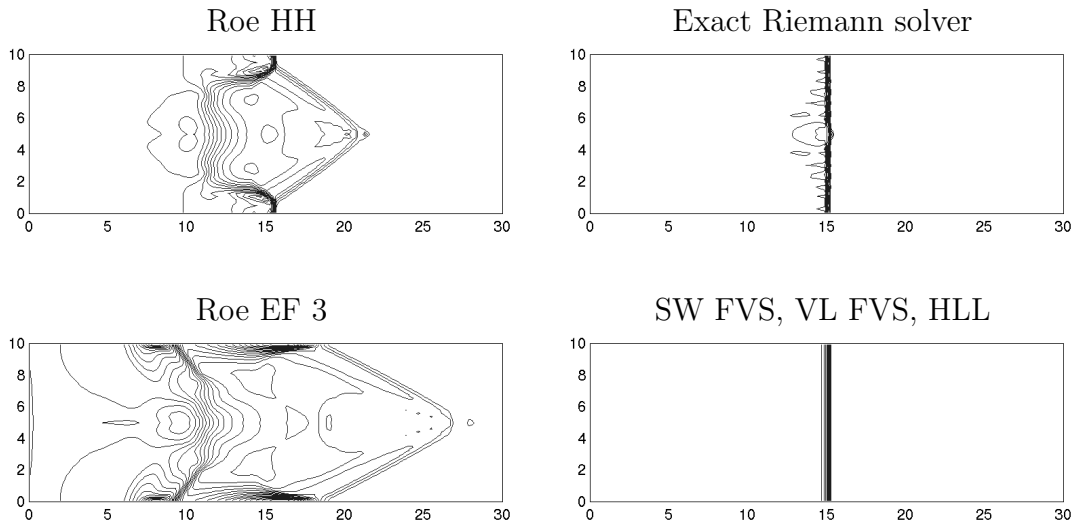

Figure 4.16: Results of the carbuncle test with different upwind schemes. Isolines of the density distribution at $t = 10$. $C_{CFL} \approx 0.5$.

any continuous artificial perturbation.

The RP of Tab. 4.3 is extended to two space dimensions with $u_2 = 0$ and placed on a rectangular domain of the size 30×10 at $x_1 = 20$. In order to obtain large carbuncle prones in minimal computational time, we reduce all velocities u_1 by 0.8 giving a shock propagation velocity of -0.5. We employ a Cartesian grid of 150×51 cells. Initially, the pressure value in the middle cell right of the discontinuity ($j = 100$, $k = 26$) is increased by $+1\%$ to initiate the two-dimensional instability. Outflow boundary conditions are applied at the left and right side; reflective boundary conditions are used in the x_2-direction.

We carry out first-order accurate computations with automatic time step adjustment for an intended Courant number of $C_{CFL} \approx 0.5$ to $t_{end} = 10$. At t_{end} the shock wave should be located exactly at $x_1 = 15$. The Godunov splitting $\mathbf{Q}^{l+1} = \mathcal{X}_2^{(\Delta t)} \mathcal{X}_1^{(\Delta t)}(\mathbf{Q}^l)$ is used for the dimensional extension of all previously introduced upwind schemes. The results are displayed in Fig. 4.16. All expected upwind schemes have produced characteristic carbuncle prones. In particular, the instability is most clearly present with Roe EF 3, which underlines that the error can not be overcome simply by increasing the numerical viscosity at the shock in x_1-direction. Note, that the carbuncle phenomenon also occurs, if the two-dimensional Wave Propagation scheme (4.58) is used (see upper row of Fig. 4.17) and does not have its origin in the dimensional splitting.

The initial perturbation downstream of the shock front initiates weak disturbances in the x_2-direction in all four characteristic fields. But the carbuncle phenomenon is triggered by the noise in the linearly degenerate fields corresponding to the double eigenvalue $u_2 \approx 0$. While upwind schemes, which do not resolve the contact discontinuity exactly, smooth out this noise rapidly, it is not damped in

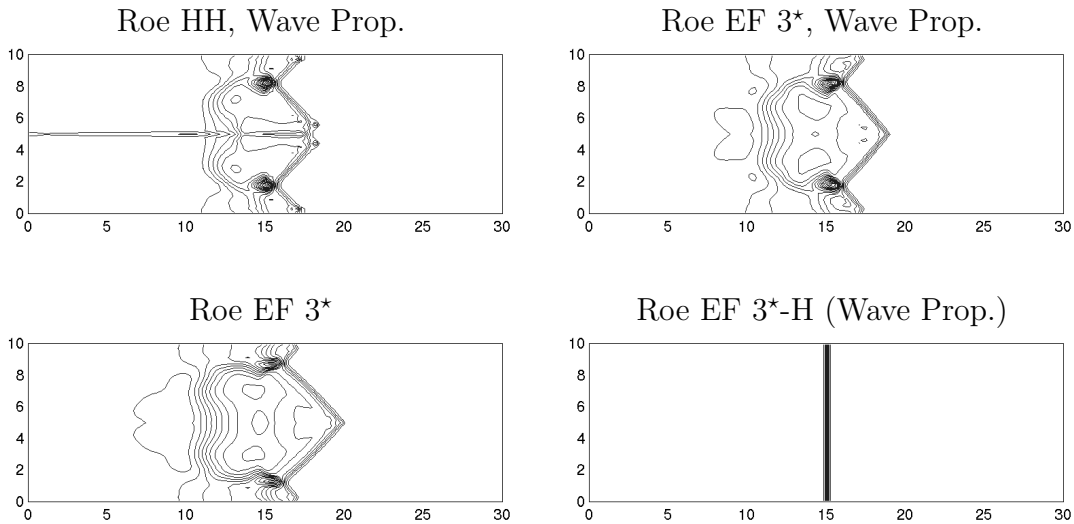

Figure 4.17: Results of the carbuncle test with different upwind schemes. Isolines of the density distribution at $t = 10$. $C_{CFL} \approx 0.5$. Right, bottom: The H-correction (4.105) avoids the carbuncle phenomenon.

Godunov's Method or when using the Roe scheme. Sanders, Morano and Druguet note that the viscosity matrices (see Sec. 4.6.2) in the x_2-direction of these accurate schemes becomes nearly singular for $u_2 \approx 0$ and consequently do not damp the unwanted transverse noise, but amplify it [160]. If the entropy enforcement formulas EF 1 to EF 3 in the Roe scheme are also applied to the contact wave in the x_2-direction the carbuncle growth is therefore moderated. The left picture of Fig. 4.17 shows the improved result of this variant of EF 3, which we denote by Roe EF 3⋆. But in the x_2-direction the variations of the eigenvalues $\hat{u}_2 \pm \hat{c}$ in neighboring cells are extremely small and the correction term $\eta_{j,k+\frac{1}{2}} := \eta(\mathbf{Q}_{j,k}, \mathbf{Q}_{j,k+1})$ calculated from (4.92) does not add sufficient viscosity to avoid the instability completely. Sanders, Morano and Druguet propose a multi-dimensional evaluation of the correction term in order to consider the strength of the shock in the x_1-direction also in the numerical viscosity added in the x_2-direction. Instead of $\eta_{j,k+\frac{1}{2}}$ they suggest to use

$$\tilde{\eta}_{j,k+\frac{1}{2}} = \max\left\{\eta_{j+\frac{1}{2},k}, \eta_{j-\frac{1}{2},k}, \eta_{j,k+\frac{1}{2}}, \eta_{j-\frac{1}{2},k+1}, \eta_{j+\frac{1}{2},k+1}\right\}, \tag{4.105}$$

where η is still calculated by Eq. (4.92). They call Eq. (4.105) "H-correction" (see Fig. 4.18). If the correction term of the H-correction $\tilde{\eta}$ is only applied to the contact wave in the x_2-direction, the instability is already completely avoided. But in a reliable multi-purpose code the H-correction should be implemented in both directions and $\tilde{\eta}$ will usually be used also as the correction term for the first

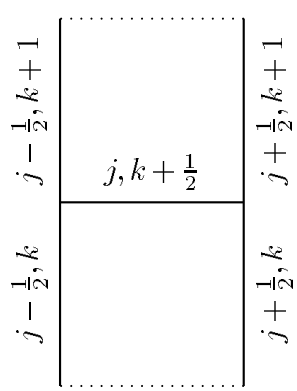

Figure 4.18: H-correction between the cells (j,k) and $(j,k+1)$.

and last characteristic field. In the following we denote the Roe scheme that uses EF 3 for all waves in combination with the H-correction by Roe EF 3*-H (see right column of Fig. 4.17). The H-correction avoids the occurrence of carbuncle prones in any dimensional splitting and within the multi-dimensional Wave Propagation scheme of Sec. 4.3.2.

Other cures for the carbuncle phenomenon usually detect strong shock waves by a heuristic criterion (for instance by evaluating pressure jumps) and switch to a diffusive scheme, like HLL [150] or AUSM FVS [201] in the transverse direction. The H-correction has the advantage that it does not involve an additional scheme.

4.9 Multi-Component Specific Problems

While the problems mentioned in the preceding section are already present in the single-component case, upwind methods for multiple components face additional difficulties. In particular, the Roe scheme can produce negative mass fractions, which can lead to significant problems in evaluating detailed chemical reaction terms correctly.

4.9.1 Mass Fraction Positivity

In contrast to Steger-Warming FVS, Van Leer FVS and the HLL method, the Roe scheme of Sec. 4.6.1 has the weakness that it can produce negative partial densities ρ_i. If this happens, some mass fraction values violate the condition

$$0 \leq Y_i \leq 1 \ , \quad i = 1, \ldots, K \ . \tag{4.106}$$

A typical RP illustrating the unphysical behavior of the Roe scheme independent of the internally employed entropy correction is given in Tab. 4.5. The result after one time step is shown in Fig. 4.19. Especially multi-component simulations of thermally perfect gases can suffer significantly from this deficiency, but it is important to note that the defect also occurs in flows of calorically perfect gases with constant γ. In Tab. 4.4 Riemann initial data demonstrating the problem for the simplified model of Sec. 3.1.1 without reaction term are supplied. As the solution involves rarefaction waves, it depends on the entropy correction in use, whether the error occurs already in the first or in the second time step.

	Left	Right
$\bar{\rho}$	1.0	1.0
U_1	0.0	0.0
P	1.0	50.0
Z	1.0	0.0

Table 4.4: Riemann initial data for simplified chemistry. $Q_0 = 0.0$, $\gamma = 1.4$.

In the Roe scheme the numerical fluxes of the partial densities $\mathbf{F}_i(\mathbf{q}_L, \mathbf{q}_R)$ are computed with Eq. (4.38) utilizing the specific Roe matrix of Sec. 4.6.1. In [108] Larrouturou suggests to enforce condition (4.106) by replacing $\mathbf{F}_i(\mathbf{q}_L, \mathbf{q}_R)$ by a modified approximation $\mathbf{F}_i^\star(\mathbf{q}_L, \mathbf{q}_R)$ that is derived from a discrete analogue

of relation (2.77) by

$$\mathbf{F}_i^\star(\mathbf{q}_L, \mathbf{q}_R) = \mathbf{F}_\rho(\mathbf{q}_L, \mathbf{q}_R) \cdot \begin{cases} Y_{i,L}\ , & \mathbf{F}_\rho(\mathbf{q}_L, \mathbf{q}_R) > 0\ , \\ Y_{i,R}\ , & \mathbf{F}_\rho(\mathbf{q}_L, \mathbf{q}_R) < 0\ . \end{cases} \tag{4.107}$$

Herein, $\mathbf{F}_\rho(\mathbf{q}_L, \mathbf{q}_R) = \sum \mathbf{F}_i(\mathbf{q}_L, \mathbf{q}_R)$ denotes the total mass flux of the Roe scheme. Larrouturou proves that a Godunov-type scheme defined on a usual FV grid indexed by j in space and by l in time, which utilizes (4.107), preserves the maximum principle

$$\min_{k\in\mathbb{Z}} Y_{i,k}^0 \le Y_{i,j}^l \le \max_{k\in\mathbb{Z}} Y_{i,k}^0 \tag{4.108}$$

for all $j \in \mathbb{Z}$, $l \in \mathbb{N}_0$ and $i = 1, \ldots, K$ under the CFL-like condition

$$\frac{\Delta t}{\Delta x}\left[\frac{\max(\mathbf{F}_\rho^l(\mathbf{Q}_{j+1}, \mathbf{Q}_j), 0)}{\rho_j^l} - \frac{\min(\mathbf{F}_\rho^l(\mathbf{Q}_j, \mathbf{Q}_{j-1}), 0)}{\rho_j^l}\right] \le 1 \quad \text{for all } j \in \mathbb{Z},\ l \in \mathbb{N}_0\ .$$

Condition (4.106) then follows directly from (4.108) for all admissible initial data. Instead of repeating the proof in [108], we apply a similar technique to verify that the FVS schemes of Secs. 4.5.1 and 4.5.2 and the HLL scheme of Sec. 4.6.4 already preserve the maximum principle (4.108) and do not require any modification.

Proposition 7 (Maximum principle for the mass fractions.) *A FV scheme that has a numerical flux for the partial densities $\mathbf{F}_i(\mathbf{q}_L, \mathbf{q}_R)$, which can be written in the form*

$$\mathbf{F}_i(\mathbf{q}_L, \mathbf{q}_R) = Y_{i,L}\, \phi^+(\mathbf{q}_L) + Y_{i,R}\, \phi^-(\mathbf{q}_R) \quad \textit{for all} \quad i = 1, \ldots, K \tag{4.109}$$

with two scalar functions $\phi^+(\mathbf{q})$, $\phi^-(\mathbf{q})$ that satisfy $\phi^+(\mathbf{q}) \ge 0$, $\phi^-(\mathbf{q}) \le 0$ for all admissible states $\mathbf{q} \in S$, preserves the maximum principle (4.108) under the CFL-like condition

$$\frac{\Delta t}{\Delta x}\left[\frac{\phi^+(\mathbf{Q}_j^l) - \phi^-(\mathbf{Q}_j^l)}{\rho_j^l}\right] \le 1 \quad \textit{for all } j \in \mathbb{Z},\ l \in \mathbb{N}_0\ . \tag{4.110}$$

Proof. We insert (4.109) into Eq. (4.12) and set $\Lambda := \Delta t/\Delta x$ and $\phi_j^\pm := \phi^\pm(\mathbf{Q}_j^l)$ to simplify the notations. With $\mathbf{F}_\rho = \sum \mathbf{F}_i$ and $\sum Y_{i,L} = \sum Y_{i,R} = 1$ we obtain

$$\rho_j^{l+1} = \rho_j^l - \Lambda\left[\phi_j^+ + \phi_{j+1}^- - \left(\phi_{j-1}^+ + \phi_j^-\right)\right]\ , \tag{4.111}$$

$$\rho_j^{l+1}\, Y_{i,j}^{l+1} = \rho_j^l\, Y_{i,j}^l - \Lambda\left[Y_{i,j}^l\, \phi_j^+ + Y_{i,j+1}^l\, \phi_{j+1}^- - \left(Y_{i,j-1}^l\, \phi_{j-1}^+ + Y_{i,j}^l\, \phi_j^-\right)\right]\ . \tag{4.112}$$

We divide (4.112) by (4.111) and get

$$Y_{i,j}^{l+1} = \frac{Y_{i,j-1}^l \Lambda\phi_{j-1}^+ + Y_{i,j}^l\left(\rho_j^l - \Lambda(\phi_j^+ - \phi_j^-)\right) - Y_{i,j+1}^l \Lambda\phi_{j+1}^-}{\Lambda\phi_{j-1}^+ + \left(\rho_j^l - \Lambda(\phi_j^+ - \phi_j^-)\right) - \Lambda\phi_{j+1}^-}\ . \tag{4.113}$$

ϕ_{j-1}^+ and ϕ_{j+1}^- satisfy $\phi_{j-1}^+ \ge 0$, $\phi_{j+1}^- \le 0$ by definition. If furthermore

$$\rho_j^l - \Lambda(\phi_j^+ - \phi_j^-) \ge 0 \tag{4.114}$$

is satisfied, Eq. (4.113) is just a convex combination of $Y_{i,j-1}^l, Y_{i,j}^l, Y_{i,j+1}^l$ and by extending condition (4.114) appropriately, we obtain (4.110) and the maximum principle (4.108). ■

x [cm]	$x < 3$	$x > 3$
ρ [kg m^{-3}]	1.1	0.15
u_1 [m s^{-1}]	270	170
p [kPa]	110	25
Y_{O_2}	1.0	0.0
Y_{H_2O}	0.0	1.0

Table 4.5: Riemann initial data for Test 4. Domain: 10 cm, outflow on both sides.

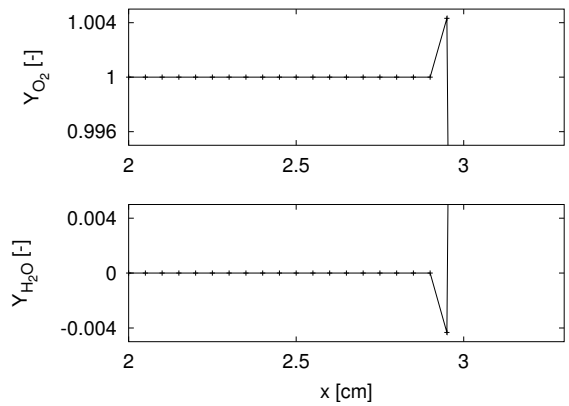

Figure 4.19: (Right) First-order results of Test 4 for the Roe scheme after 1 time step with $C_{CFL} = 0.643$, $\Delta x = 0.05$ cm.

Maximum principle for the Flux-Vector Splittings

The FVS schemes (4.66), (4.69) can easily be written in the form (4.109) by using $\phi^+(\mathbf{q}_L) := \mathbf{f}_\rho^+(\mathbf{q}_L)$ and $\phi^-(\mathbf{q}_R) := \mathbf{f}_\rho^-(\mathbf{q}_R)$ with $\mathbf{f}^+(\mathbf{q}_L) = \sum \mathbf{f}_i^+(\mathbf{q}_L)$, $\mathbf{f}^-(\mathbf{q}_R) = \sum \mathbf{f}_i^-(\mathbf{q}_R)$. The functions $\mathbf{f}_\rho^\pm(\mathbf{q})$ satisfy $\mathbf{f}_\rho^-(\mathbf{q}) \geq 0$ and $\mathbf{f}_\rho^+(\mathbf{q}) \leq 0$ by definition. From (4.66) we find $\mathbf{f}_\rho^\pm(\mathbf{q}) = \rho\tau^\pm/(2\gamma)$ for the Steger-Warming FVS and from (4.69) $\mathbf{f}_\rho^\pm(\mathbf{q}) = \pm\rho(u_1 \pm c)^2/(4c)$ for the Van Leer FVS. For both schemes condition (4.110) does not impose a further restriction. As an example we discuss the case of the Steger-Warming scheme. In each time step we have to satisfy $\Lambda(\tau^+ - \tau^-)/(2\gamma) \leq 1$ in every cell. By inserting $\tau^\pm = \lambda_1^\pm + 2\,\delta^\pm(\gamma - 1) + \lambda_{K+d+1}^\pm$ into this relation we easily find a suitable upper bound

$$\frac{\Lambda}{2\gamma}(|u_1 - c| + 2\,|u_1|(\gamma - 1) + |u_1 + c|) \leq \frac{\Lambda}{2\gamma}(2\,|u_1| + 2c + 2\,|u_1|(\gamma - 1)) = \Lambda\left(|u_1| + \frac{c}{\gamma}\right)$$

that itself is bounded by the standard CFL condition (4.84) by

$$\Lambda\left(|u_1| + \frac{c}{\gamma}\right) \leq \Lambda(|u_1| + c) \leq 1\ ,$$

which proves that (4.110) is automatically satisfied for the Steger-Warming FVS under the standard CFL condition (4.84).

Maximum Principle for the HLL Scheme

Only the non-trivial case with $S_L \leq 0 \leq S_R$ needs special attention. A straightforward calculation shows that the HLL method (4.96) can be expressed in terms of (4.109) by setting

$$\phi^+(\mathbf{q}_L) := \frac{S_R\,\rho_L\,u_{1,L} - S_L S_R\,\rho_L}{S_R - S_L}\ , \quad \phi^-(\mathbf{q}_R) := \frac{S_L S_R\,\rho_R - S_L\,\rho_R\,u_{1,R}}{S_R - S_L}\ .$$

It is easy to check that the necessary conditions $\phi^+(\mathbf{q}_L) \geq 0$, $\phi^-(\mathbf{q}_R) \leq 0$ are always satisfied under the relations $S_L \leq 0 \leq S_R$ and $S_L < u_{1,L}$, $u_{1,R} < S_R$. The last two conditions are trivial for the estimate of Davis (4.97). Utilizing (4.97) it can also be shown that the HLL method satisfies condition (4.110) automatically, if the standard CFL condition (4.84) is satisfied in every computational cell. The computation is simple, but lengthy, because $\phi^+(\mathbf{Q}_j)$ requires the signal speed estimates $S_{L,j+1/2}$ and $S_{R,j+1/2}$ at the right side of cell j, while $\phi^-(\mathbf{Q}_j)$ uses the estimates at the left side $S_{L,j-1/2}$ and $S_{R,j-1/2}$.

4.9.2 Contact Discontinuities

The FVS schemes of Steger-Warming and Van Leer do not reproduce isolated contact discontinuities correctly. Even in the standard case of a single calorically perfect gas the Riemann invariants p and u_1 (see Prop. 6) are not constant over a contact discontinuity. After the first time step the approximations of pressure and velocity show small, but unphysical oscillations in the cells near the initial discontinuity. Usually, the influence of these oscillations on the entire simulation is negligible, but special situations exist, where the deficiency affects the result significantly.

In case of a single calorically perfect gas the error at contact discontinuities can perfectly be avoided by employing one of the approximative Riemann solvers of Sec. 4.6.1 and Sec. 4.6.4. If γ is constant over the contact discontinuity, HLL and the Roe scheme reproduce a constant pressure and velocity. In case of a single thermally perfect gas (two different values of γ on both sides of the contact due to the temperature difference) the HLL scheme produces a kink in the pressure independent of u_1 in the first step. The approximation of the velocity is correct after the first time step, but becomes corrupted after the second step due to the pressure oscillations. The Roe scheme shows the same behavior for moving contact discontinuities with $u_1 \neq 0$. In the special case of $u_1 = 0$ the Roe method approximates contact discontinuities with $\gamma_L \neq \gamma_R$ correctly without any artificial oscillations.

A typical example of a moving contact discontinuity for thermally perfect oxygen is given in Tab. 4.6. A comparison of first-order results of all schemes is shown in Fig. 4.20. It is obvious, that the Roe scheme produces the best approximation. HLL and Van Leer's FVS give a similar error in the pressure p, but HLL approximates the velocity u_1 correctly. The FVS of Steger-Warming gives the worst result.

The correct approximation of contact discontinuities with $\gamma_L \neq \gamma_R$ is important for the correct simulation of non-mixing fluids with clearly defined interfaces. Various correction techniques have been proposed in recent years for the Roe scheme for the simplified case of mixtures of calorically perfect species. An obvious idea is to avoid any inadequate averaging of γ over the interface [186] by using

x [cm]	$x < 5$	$x > 5$
ρ [kg m^{-3}]	0.385	1.283
u_1 [m s^{-1}]	100	100
p [kPa]	100	100
γ [−]	1.31296	1.39455

Table 4.6: Riemann initial data for Test 5. Domain: 10 cm, outflow on both sides.

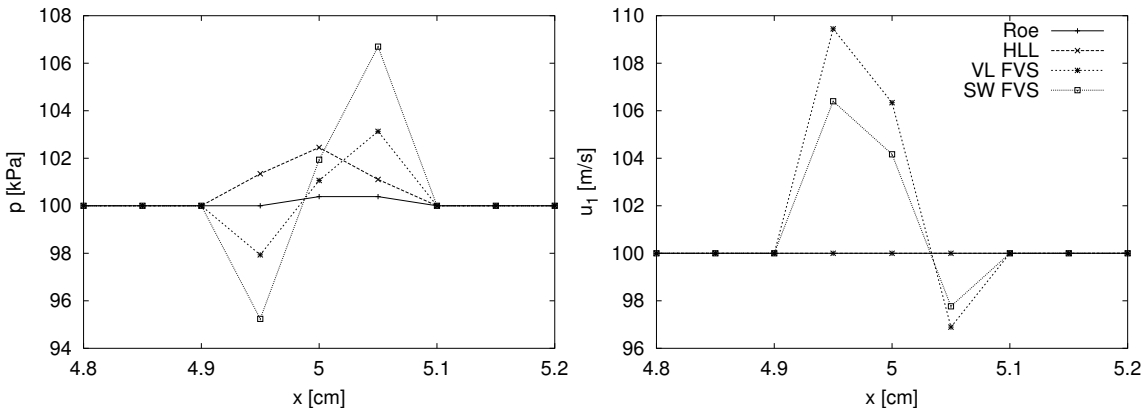

Figure 4.20: 1st-order results of Test 5 with thermally perfect O_2 after 1 time step at $t = 0.4\,\mu$s with $\Delta x = 0.05\,$cm.

two standard Roe schemes in both fluids separately. Suitable internal boundary conditions are constructed in additional internal ghost cells by employing a level-set function [132], which tracks the position of the interface [101, 152, 69]. The extension of this technique to chemically reactive flows is problematic, because in general new contact surfaces could be created by chemical reaction. But the application of the level-set technique is straight-forward, if only reaction fronts need to be tracked that are initially present. A successful combination of the level-set technique with the conservative ghost fluid method has been applied to detonation, but especially to deflagration waves by Fedkiw and his collaborators [72, 70].

A different correction technique for the Roe scheme is based on the quasi-linear transport equation

$$\frac{\partial}{\partial_t}\left(\frac{1}{\gamma-1}\right) + \sum_{n=1}^{d} u_n \frac{\partial}{\partial_{x_n}}\left(\frac{1}{\gamma-1}\right) = 0\,. \tag{4.115}$$

In [2] Abgrall noticed that a FV scheme satisfying Eq. (4.115) in the discrete sense preserves constant pressure and constant velocity over a contact discontinuity. Various ideas have been developed, how Eq. (4.115) might be incorporated into Roe-type discretizations [2, 97, 170, 49, 161, 11]. A good review of these methods, that have in common that they require a non-conservative discretization, can be found in a recent paper by Abgrall and Karni [3]. Note, that Eq. (4.115) can only be derived for simplified equations of state like Eq. (2.59) that use a non-temperature dependent adiabatic coefficient γ. For the general case of temperature-dependent γ, in particular for thermally perfect species, which are of major interest for combustion simulation, no similar condition has been found yet.

Fortunately, contact discontinuities with significantly different γ-values do not play an important role in shock wave induced combustion in premixed gases. But they are present even in premixed regimes, if the reaction is thermally induced, e.g.

in deflagration waves. Throughout this thesis only shock wave induced combustion phenomena, especially self-sustaining detonations waves are considered and the described problem therefore does not corrupt the numerical results.

4.10 Source Term Integration

The numerical incorporation of chemical reaction terms into a FV method with the operator splitting method of Sec. 4.1.3 requires the numerical integration of an stiff ordinary differential equation. Various reliable numerical methods are available for this standard task today and we report briefly on our particular choice and its application in practice.

4.10.1 Integration of the Rate Equation

The integration of reactive source terms according to Sec. 2.3.7 in a fractional step method requires the solution of the ODE

$$\frac{\partial \rho_i}{\partial t} = W_i \dot{\omega}_i \left(\rho_1, \ldots, \rho_K, T\right) \ , \quad i = 1, \ldots, K \tag{4.116}$$

with initial condition $\rho_i(0) = \rho Y_i^0$, $i = 1, \ldots, K$ in every FV cell. The total density ρ in this cell, the specific energies E, e and the velocities u_n remain unchanged during the integration. This corresponds to a chemical reaction in an adiabatic constant volume environment.

Mixtures of thermally perfect gases require the calculation of the time-dependent temperature T from the implicit Eq. (2.56) in every evaluation of the right side of (4.116) by applying the robust root-finding method derived in Sec. 4.4.2. The temperature in mixtures of calorically perfect gases can be calculated directly from (2.59).

In numerical simulations with detailed non-equilibrium chemistry the stiffness of the ODE (4.116) necessarily has to be considered. At least for some admissible states Eq. (4.116) usually satisfies the following definition of Lambert [106]:

Definition 17 (Stiff ODEs). *An ordinary differential equation* $\mathbf{y}' = \mathbf{g}(\mathbf{y})$ *is said to be stiff, if the complex-valued eigenvalues* ξ_m *of the Jacobian* $\mathbf{G} = \partial \mathbf{g}(\mathbf{y}) / \partial \mathbf{y}$ *satisfy the properties*

- $Re(\xi_m) < 0, m = 1, \ldots, \tilde{M}$ *and*
- $\max\limits_m |Re(\xi_m)| \gg \min\limits_m |Re(\xi_m)|$.

Detailed chemical kinetics are a typical source of stiff ODEs and the usage of an appropriate implicit or semi-implicit ODE solver is essential for detonation simulation.

Throughout this thesis only the semi-implicit (or linearly implicit) Runge-Kutta method GRK4A of Kaps and Rentrop [100] has been employed to integrate stiff

reaction terms with the local sub-cycling explained in Sec. 4.1.3. GRK4A is a robust fourth-order "black-box" ODE integrator with automatic step size adjustment. Although a second-order ODE scheme in principle would be sufficient within a second-order accurate operator splitting (compare Sec. 4.1.3), we decided to employ the very accurate, but computationally more expensive GRK4A method. With a sufficiently high accuracy (see Sec. 4.10.2) this decision should lead to numerical results that are mostly independent of our specific ODE scheme and should be better reproducible by other researchers.[12]

The scalar source term arising from simplified chemistry in Chap. 6 is always integrated with a classical explicit fourth-order accurate Runge-Kutta method with automatic time size adjustment [56, 106] nearly to machine accuracy.

Semi-Implicit ODE Methods

The basic idea of the semi-implicit approach is to avoid the expensive solution of a system of nonlinear algebraic equations by replacing $\mathbf{g}(\mathbf{Y}^{\iota+1})$ on the right-hand side of an implicit update formula by the linear approximation

$$\mathbf{g}(\mathbf{Y}^{\iota+1}) \approx \mathbf{g}(\mathbf{Y}^{\iota}) + \left.\frac{\partial \mathbf{g}}{\partial \mathbf{y}}\right|_{\mathbf{Y}^{\iota}} \cdot \left(\mathbf{Y}^{\iota+1} - \mathbf{Y}^{\iota}\right) \ .$$

If we insert this approximation for instance into the Trapezoidal Rule (compare Eq. (4.15)), we get

$$\mathbf{Y}^{\iota+1} = \mathbf{Y}^{\iota} + \Delta h \left(\mathbf{g}(\mathbf{Y}^{\iota}) + \frac{1}{2} \left.\frac{\partial \mathbf{g}}{\partial \mathbf{y}}\right|_{\mathbf{Y}^{\iota}} \cdot \left(\mathbf{Y}^{\iota+1} - \mathbf{Y}^{\iota}\right) \right)$$

from which we derive the linearly implicit update formula

$$\left(\mathbf{I} - \frac{\Delta h}{2} \left.\frac{\partial \mathbf{g}}{\partial \mathbf{y}}\right|_{\mathbf{Y}^{\iota}} \right) \cdot \mathbf{Y}^{\iota+1} = \left(\mathbf{I} - \frac{\Delta h}{2} \left.\frac{\partial \mathbf{g}}{\partial \mathbf{y}}\right|_{\mathbf{Y}^{\iota}} \right) \cdot \mathbf{Y}^{\iota} + \Delta h \, \mathbf{g}(\mathbf{Y}^{\iota}) \ ,$$

which defines a linear system of equations for the unknown $\mathbf{Y}^{\iota+1}$ with coefficient matrix $\mathbf{I} - \frac{1}{2} \left.\frac{\partial \mathbf{g}}{\partial \mathbf{y}}\right|_{\mathbf{Y}^{\iota}}$.

The construction of higher-order linearly implicit methods, especially with efficient automatic step size adjustment, is quite complicated and we omit a description here, because the details of the approach are not essential for our purpose. A profound presentation of the numerous design rules to derive the Runge-Kutta coefficients in the semi-implicit case, which is also said to be of Rosenbrock-Wanner-type, can be found in the second book of Hairer and Wanner [85] and in the review article of Cash on this subject in [6].

[12] A comparison of various black-box ODE solvers applied to stiff reaction terms has been done by Geßner [78]. He analyzed the computational times of typical induction time calculations with the hydrogen-oxygen mechanism of Oran et al. in [136, 139, 138]. The most efficient methods he found are SAIM, a second-order hybrid method of Young and Boris tailored for chemical kinetics [208] and GRK4A. In his tests SAIM is about three times faster than GRK4A.

A further second-order accurate black-box ODE solver that can also be recommended for stiff reaction terms is METAN by Bader and Deuflhard [12].

4.10.2 Accuracy Considerations

The automatic step size adjustment of ODE solvers is in general based on the estimation of the local truncation error of the current step. Usually the actual step is rejected (and repeated with decreased step size), if the relation

$$\frac{|\tau_m^{ODE}(\mathbf{Y}^{\iota+1})|}{\max(|\mathbf{Y}_m^{\iota+1}|, S_m^{ODE})} > \eta_{ODE} \tag{4.117}$$

is satisfied for any of the components of the discrete solution vector $\mathbf{Y}$. Herein, $\tau_m^{ODE}(\mathbf{Y}^{\iota+1})$ denotes a suitable estimation of the local error in the mth component in the next step. Relation (4.117) uses the relative local error above the positive threshold S_m^{ODE} and the absolute local error below.

The parameters η_{ODE}, S_m^{ODE} have to be adjusted with special care, if the operator splitting approach is used within a dynamically adaptive method (compare Sec. 5.7) that applies an error estimation criterion to the result of the entire splitting method. For instance, the heuristic error estimation by Richardson extrapolation in Sec. 5.4.2 depends on the accuracy of the hydrodynamic transport scheme, but also on the accuracy of the ODE solver. If the ODE integration is significantly less accurate, the error of the entire method can be corrupted and if relatively small refinement tolerances are used, an unnecessary grid adaptation will be the result.

Throughout this thesis, relation (5.26) is applied as a refinement criterion on the mass fractions Y_i, when detailed reaction mechanisms are considered. The discussed problem is avoided completely by choosing a tolerance for the ODE solver under the constrain

$$\eta_{ODE} \gg \min_i(\eta_{Y_i}^r)$$

and scaling factors that satisfy[13]

$$\max_i(\eta_{ODE} \cdot S_{Y_i}^{ODE}) \leq \min_i(\eta_{Y_i}^r \cdot S_{Y_i}) \ . \tag{4.118}$$

For instance, for the refinement criteria of Tab. 7.3 we simply select $\eta_{ODE} = 10^{-5}$ and $S_{Y_1}^{ODE} = \cdots = S_{Y_K}^{ODE} = 10^{-3}$.

4.10.3 Evaluation of Reaction Rates

We always evaluate detailed chemical reaction rates on basis of the Chemkin-II-library [102]. The thermodynamic constants for (2.45) and (2.46) are always taken from the standard Chemkin-II thermodynamical data base [103]. The Jacobian of the vector-valued rate function $\dot{\omega}(\rho_1, \ldots, \rho_K, T)$, which is required by any semi-implicit ODE solver, is always approximated by standard difference quotients. Its

[13] In Eq. (4.118) the scaling factors $S_{Y_i}^{ODE}$ are derived for the mass fractions Y_i, but they can be transformed directly into scaling factors for partial densities by multiplying with the constant total density, i.e. $S_{\rho_i}^{ODE} := \rho S_{Y_i}^{ODE}$.

computation needs K evaluations of $\dot{\omega}(\cdot)$ in every time step. Further on, the four-stage Runge-Kutta scheme in GRK4A needs three evaluations of $\dot{\omega}(\cdot)$ in every step. Therefore, the computer code implementing $\dot{\omega}(\cdot)$ with respect to a particular mechanism is the first candidate for technical optimizations to decrease the computational time.

With the original Chemkin-II-library[14] approximately 10^5 time steps of GRK4A with Mechanism 1 require about 68 s on a single Pentium-850 MHz processor. As the Chemkin-library is of course independent of a specific mechanism the parameters $\nu_{ji}^{f/r}$, $A_j^{f/r}$, $-E_j^{f/r}$ in the formulae of Sec. 2.3.7 are stored in fields that are accessed via numerous loops. The evaluation of $\dot{\omega}(\cdot)$ involves a permanent reload of these data fields into the highest level cache. If the general-purpose Chemkin-function is replaced by a numerically identical function, implemented only for a single mechanism with loop-unrolling and without any unnecessary field accesses, the computational time for $\approx 10^5$ GRK4A time steps reduces to less than 18 s.[15] We have applied a specified function of this type for Mechanisms 1 in all computations in Chap. 7.

[14]Compiled with standard Fortran-77 optimizations.

[15]We have implemented a simple Fortran-77 code generator on top of the Chemkin-routines that creates the necessary mechanism-specific function automatically. It has to be executed once for every new mechanism. Its output is standard Fortran-77 code that can be compiled and linked as usual. The code generator implements the formulas of Sec. 2.3.7 without any loops and inserts the parameter values $\nu_{ji}^{f/r}$, $A_j^{f/r}$, $-E_j^{f/r}$ as constants directly into the code. See the Chemkin manual [102] for details on the implementation of the third body reactions in Mechanisms 1.

Chapter 5

Adaptive Mesh Refinement

In this chapter we develop the blockstructured dynamically adaptive mesh refinement (AMR) strategy after Berger and Collela [21] which has been employed for the large-scale computations throughout this thesis. The presented AMR algorithm is especially tailored for time-explicit finite volume schemes for hyperbolic conservation laws and its application is essential for the efficiency of the sufficiently resolved detonation simulations in the Chaps. 6 and 7.

Unlike other refinement strategies mentioned in Sec. 5.1 the hierarchical AMR approach allows an effective refinement in space and in time. The single-processor version of the AMR algorithm is developed in Sec. 5.2. In Sec. 5.3 a parallelization strategy for parallel machines with distributed memory is presented. A rigorous domain decomposition is applied that separates the entire AMR hierarchy from the base level on. This strategy reduces the communication overhead and simplifies the implementation [145]. In contrast to other presentations [21, 20, 133] a topological notation is employed throughout the Secs. 5.2 and 5.3. The exactness of the formulation ensures that the AMR sub-routines in pseudo-code could be used as guide-lines for practical implementations. Important components, like load-balancing [145], the creation of refinement grids from flagged cells [19] or the numerical treatment of refinement boundaries inside the computational domain are described. Sec. 5.4 summarizes standard refinement criteria. In Sec. 5.5 we explain the object-oriented design of our own AMR code AMROC [53]. The last section presents two highly adaptive non-reactive standard tests: a Mach reflection and a shock wave diffraction. The examples demonstrate the efficiency of the parallel implementation and provide the basic hydrodynamic flow patterns for the interpretation of the detonation simulations in the last section of Chap. 7.

5.1 Adaptive Mesh Refinement Strategies

Detonation simulations, but also non-reactive inviscid fluid flow computations usually involve a wide range of different scales. In order to achieve a high resolution of the physical relevant phenomena only efficient implementations of the FV shock-

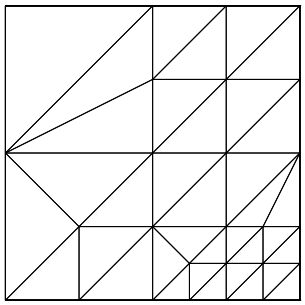

Figure 5.1: Unstructured refinement strategy. Hanging nodes can be avoided.

capturing schemes of the previous chapter have to utilize non-uniform grids. Various adaptation techniques to adapt the discretization dynamically to the solution have been developed during the last two decades.

5.1.1 Unstructured Approach

Unstructured triangulations offer superior geometrical flexibility. The coordinates of all vertices have to be stored explicitly and the basic discretization is intrinsically non-uniform (compare Fig. 5.1). Consequently, existing implementations can relatively easily be supplemented with dynamical adaptation. Cells that have been flagged for refinement are simply replaced by finer ones and the numerical solution is advanced on the entire grid simultaneously. A coarsening step is necessary to recombine fine cells. For time-explicit FV schemes this simple strategy can be inefficient, because it requires a global time step that satisfies the CFL condition for the smallest cell. Further on, unstructured triangulations are usually implemented with cell-based data structures that store all neighborhood relationships explicitly. The memory access during computation is strongly irregular and the performance on vector or super-scalar computers therefore is poor. The capabilities of modern computers with large high-level caches are difficult to exploit. Implementations on parallel computers with distributed memory have to solve complex load-balancing problems on the fly. In particular, appropriate synchronization regions (overlaps) with respect to the numerical stencil are difficult to compute. A freely available generic C++-library that supports unstructured meshes on distributed memory machines is GrAL (Grid Algorithms Library) by Berti [29, 27, 28].

5.1.2 Structured Approach

If geometric flexibility is only of secondary interest, the numerical scheme can be formulated on a logically rectangular (not necessarily Cartesian) mesh. Rectangular meshes allow optimizations that moderate some of the technical disadvantages of unstructured refinement techniques. A structured refinement strategy replaces or overlays a single coarse cell by a regular refinement block of r^d cells. For simplicity,

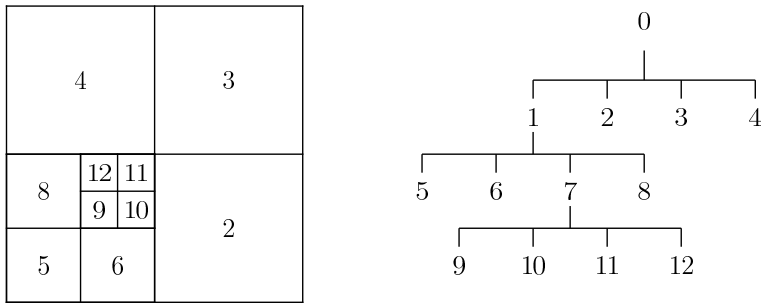

Figure 5.2: Mesh and corresponding local quadtree-tree of a structured mesh refinement strategy. $r = 2$, $d = 2$.

the refinement factor r is often fixed and all successively generated refinement blocks can be accessed efficiently by utilizing a regular data tree (see Fig. 5.2). The data tree avoids explicit storage of parent- or child-relations and the use of a global integer coordinate system (compare Sec. 5.5.2) allows an easy evaluation of neighborhood relationships.

In the case of time-explicit FV schemes the construction of time-space interpolated internal boundary conditions can be implemented with moderate expense allowing a successive time step refinement with factor r. A disadvantage of structured refinement is that hanging nodes along the coarse-fine interfaces are unavoidable (compare left picture of Fig. 5.2).[1] A recent freely available FV program for distributed memory machines that allows arbitrary refinement factors is the NASA-code PARAMESH by MacNeice and his collaborators [129].

Although the structured approach uses the available computer memory better than the unstructured technique, consecutive memory blocks of r^d cells are usually not large enough to fill the vector pipelines of modern super-computers satisfactory. Furthermore, a large number of small refinement blocks requires an enormous overhead for synchronization and boundary setting. If the numerical scheme is implemented with ghost cells, the waste due to overlapping neighboring ghost cells may be non-negligible (see [133] for a detailed discussion). In particular, high resolution schemes require a boundary size of at least two ghost cells and the memory demand for the boundaries only can exceed that of the mere refinement regions drastically.

Unnecessary overlapping refinement boundaries can be eliminated completely, if refinement blocks of arbitrary size are considered. This highly efficient strategy, which involves a significantly higher algorithmic complexity and requires an elaborated software infra-structure, is used within the *blockstructured* approach.

[1] A conforming closure is possible, if unstructured cells are employed. Such a hybrid refinement strategy is used in the UG multigrid package of Bastian and Wittum [18]. But hybrid techniques require implementations of the numerical scheme on unstructured and logically rectangular meshes and are usually more complex that an accurate modification of the numerical stencil at hanging nodes.

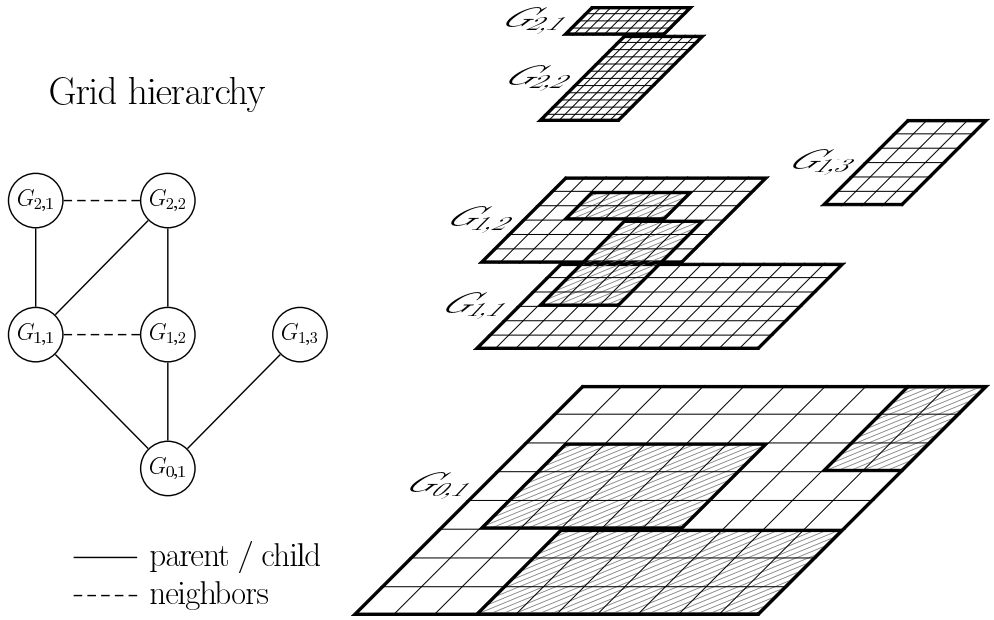

Figure 5.3: The blockstructured refinement grids of the AMR method creates a hierarchy of rectangular subgrids.

5.1.3 Blockstructured Adaptive Mesh Refinement

The blockstructured adaptive mesh refinement technique (AMR or SAMR) for hyperbolic partial differential equations has been pioneered by Berger and Oliger in [20] and [23]. While the first approach utilized rotated refinement grids that required complicated conservative interpolation operations, AMR denotes today especially the simplified variant of Berger and Collela [21] that only allows refinement patches aligned to the coarse grid mesh. The striking efficiency of this simplified variant, in particular on vector and super-scalar computers, was demonstrated by Berger and her collaborators in [19].

Instead of replacing single cells by finer ones the AMR method follows a patchwise refinement strategy. Cells being flagged by various error indicators are clustered with a special algorithm (see [19] for details) into rectangular boxes of appropriate size. They describe refinement regions geometrically and subgrids with the same refinement factor in all space-directions and also in time are generated according to them. Refined grids are derived recursively from coarser ones and an entire hierarchy of successively embedded grid patches is thereby constructed, cf. Fig. 5.3. On each level i of the hierarchy a separate refinement factor r_i can be used. Like in the structured approach, only the implementation of the numerical scheme on a single rectangular grid is required. The adaptive algorithm calls this application-dependent routine automatically. Further on, it uses conservative interpolation functions to transfer cell values between refined subgrids and their coarser parents appropriately.

It is important to note, that refined grids overlay the coarser subgrids from which

they have been created. The numerical solution on a particular level is first of all advanced independently. Values of cells covered by refined subgrids are overwritten by averaged fine grid values subsequently. The superfluous work on the coarse grid is usually negligible compared to the computational costs for integrating the superimposed fine grids. Unlike the refinement technique of Sec. 5.1.2 that only allows for one parent cell, the AMR method requires a general data tree, because arbitrary parent- and child-relations need to be considered. In Fig. 5.3 this generality is expressed by grid $G_{2,2}$, which overlays two parents.

Replacing coarse cell values by averaged fine grid values modifies the numerical stencil on the coarse grid. In general the important property of conservation is lost. A flux correction replacing the coarse grid flux at the affected side of a neighboring cell by accumulated fine grid fluxes is necessary to ensure conservation. In the AMR method this *conservative fixup* is usually implemented as a correction pass. Like in the structured approach described in the previous subsection hanging nodes additionally have to be considered in two and three space dimensions. The correction procedure is explained in detail in Sec. 5.2.3.

Up to now, various reliable implementations of the AMR method for single processor computers have been developed [22, 47, 76, 133]. Even implementations for parallel computers with shared memory architecture have reached a stable state [19]. Parallelism is an inherent feature of the AMR algorithm and in a shared memory environment simply the numerical solution on the whole sequence of grids has to be advanced in parallel to achieve a sufficient load-balancing.

The question for an efficient parallelization strategy becomes more delicate for distributed memory machines, because the costs of communication can not be neglected anymore. Due to the technical difficulties in implementing dynamical adaptive methods in a distributed memory environment only few parallelization strategies have been considered in practice yet, cf. [50, 10, 153, 146, 104, 116].

Recent freely available implementations of the AMR algorithm for distributed memory computers are for instance Berkeley-Lab-AMR [153] and our own implementation AMROC [53]. The basic object-oriented abstractions in both approaches in principle are similar, but they differ significantly in the parallel data distribution strategy. While AMROC uses a domain decomposition technique that minimizes interprocessor communication (compare Sec. 5.3), the communication costs have not been considered in the development of Berkeley-Lab-AMR [153]. In Berkeley-Lab-AMR each level is distributed separately in a load-balancing manner and parallelized level-transfer operations are consequently required.

5.2 Serial Algorithm

In the following, we define the AMR method exactly. Like in Sec. 4.1.1 we concentrate (without loss of generality) on the two-dimensional case. We assume that the numerical scheme is a conservative time-explicit FV method in two space dimensions (see Def. 12) that is formulated on a rectangular Cartesian grid G. Further on, we

assume that the implementation requires $s \geq 1$ auxiliary cells (ghost cells) around G to define discrete boundary conditions.[2]

5.2.1 The Grid Hierarchy

Let the AMR hierarchy consist of a sequence of levels $i = 0, \ldots, i_{\max}$. Analogously to Sec. 4.1.1 we define a discretization of the computational domain on each level i with successively finer mesh widths $\Delta x_{n,i}$, $n = 1, \ldots, d$ with $d = 2$ and a refined time step Δt_i. All mesh widths of Level $i > 0$ are set to be r_i-times smaller than those of level $i - 1$. With $r_i \in \mathbb{N}, r_i \geq 2$ for $i > 0$ and $r_0 = 1$ we define $\Delta t_i := \Delta t_{i-1}/r_i$ and $\Delta x_{n,i} := \Delta x_{n,i-1}/r_i$ for all $n = 1, \ldots, d$. Therefore, the ratios

$$\frac{\Delta t_i}{\Delta x_{n,i}} = \frac{\Delta t_{i-1}}{\Delta x_{n,i-1}} = \cdots = \frac{\Delta t_0}{\Delta x_{n,0}} \quad \text{for all } n = 1, \ldots, d$$

remain constant on all levels and a time-explicit FV scheme can be expected to be stable under a CFL condition on all grids of the hierarchy [21]. The application of successively refined time steps avoids the unnecessary update of coarse grid cells at intermediate fine time steps and is one reason for the striking efficiency of blockstructured AMR methods for hyperbolic equations.

Topology

With the notations of expression (4.2) we define the domain of the mth grid on level i by

$$G_{i,m} \ :=]x_{1,i}^{j-1/2}, x_{1,i}^{j+\mu_1-1/2}[\times]x_{2,i}^{k-1/2}, x_{2,i}^{k+\mu_2-1/2}[\ . \tag{5.1}$$

It has $\mu_1 \cdot \mu_2$ FV cells and corresponds to the interior grid of Fig. 5.4. The boundary of $G_{i,m}$ is $\partial G_{i,m}$ and $\bar{G}_{i,m} = G_{i,m} \cup \partial G_{i,m}$ is its hull. With a total number of M_i grids on level i the domain of the entire level is

$$G_i := \bigcup_{m=1}^{M_i} G_{i,m} \quad \text{with} \quad G_{i,m} \cap G_{i,n} = \emptyset \ \text{ for } m \neq n \ , \tag{5.2}$$

where we have assumed that the grids $G_{i,m}$ do not overlap. The problem domain $G_0 = \bigcup_m G_{0,m}$ does not need to be a single grid. In order to specify the setting of ghost cell values exactly and to derive geometric relations between the grids of different levels we introduce enlarged grid domains $G_{i,m}^{\sigma}$ that extend $G_{i,m}$ at all sides by $\sigma > 0$ additional cells, i.e.

$$G_{i,m}^{\sigma} \ :=]x_{1,i}^{j-\sigma-1/2}, x_{1,i}^{j+\mu_1+\sigma-1/2}[\times]x_{2,i}^{k-\sigma-1/2}, x_{2,i}^{k+\mu_2+\sigma-1/2}[\ . \tag{5.3}$$

Analogously to G_i we denote the enlarged level domain $\bigcup_m G_{i,m}^{\sigma}$ by G_i^{σ}. For $\sigma = s$ expression (5.3) yields the domain required for the numerical update on grid $G_{i,m}$.

[2]The parameter denotes s the radius of the numerical stencil (compare Def. 12). For a first-order FV method we have $s = 1$, while a second-order method requires at least $s = 2$ (compare Sec. 4.3).

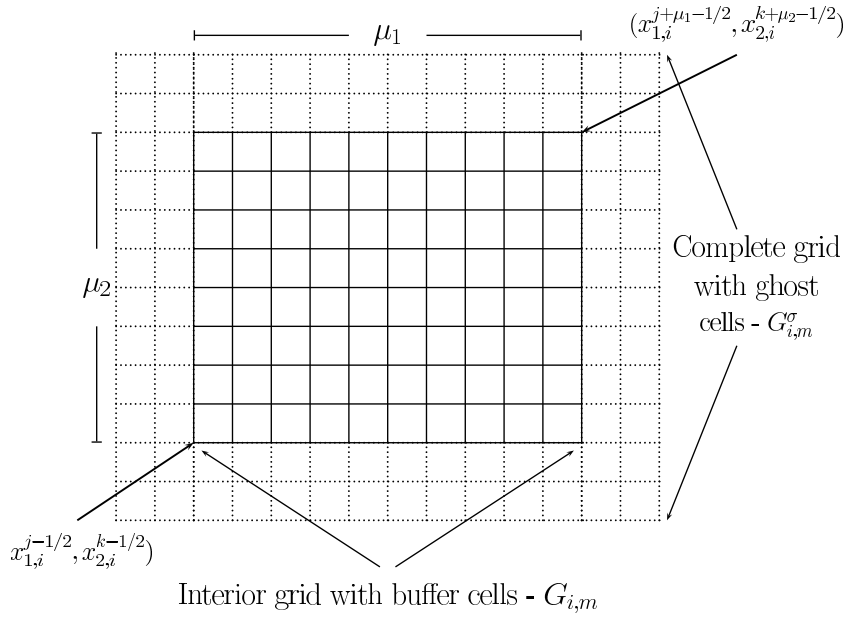

Figure 5.4: Parts of a refinement grid $G_{i,m}$.

We denote the additional necessary ghost cell region $G_{i,m}^s \backslash \bar{G}_{i,m}$ by $\tilde{G}_{i,m}^s$. But values $\sigma \neq s$ are also used in the following description to express geometric inter-level relations. An example is condition (5.4).

We only allow *properly nested* refinements that satisfy the equation

$$G_i^{r_i} \cap G_{i-1} = G_i^{r_i} \cap G_0 \tag{5.4}$$

for all $i > 0$ (compare Fig. 5.3). Condition (5.4) assures that internal cells of level i only can abut internal cells of the levels $i-1$ and $i+1$.

Grid-based Data

The notation $\mathbf{Q}(G_{i,m}^s, x_{1,i}^j, x_{2,i}^k)$ denotes the finite set of discrete approximations to the vector of state which are defined on all discrete points $(x_{1,i}^j, x_{2,i}^k)$, $j, k \in \mathbb{Z}$ that satisfy $(x_{1,i}^j, x_{2,i}^k) \in G_{i,m}^s$. In general, some points $(x_{1,i}^j, x_{2,i}^k)$ will be contained in multiple extended grids $G_{i,m}^s$. We assume that the data values associated to such points are equal in all sets $\mathbf{Q}(G_{i,m}^s, \cdot, \cdot)$. Under this assumption, we define the vector of state on level i as the union of all grid-based data sets $\mathbf{Q}(\cdot, x_{1,i}^j, x_{2,i}^k)$ by

$$\mathbf{Q}^i := \bigcup_{m=1}^{M_i} \mathbf{Q}(G_{i,m}^s, x_{1,i}^j, x_{2,i}^k) \ . \tag{5.5}$$

The notations $\mathbf{F}^n(\bar{G}_{i,m}, \cdot, \cdot)$, $n = 1, \ldots, d$ denote the numerical fluxes on the edges of $\bar{G}_{i,m}$. While $\mathbf{F}^1(\bar{G}_{i,m}, x_{1,i}^{j+1/2}, x_{2,i}^k)$ is used for the discrete fluxes in the x_1-direction,

$\mathbf{F}^2(\bar{G}_{i,m}, x^j_{1,i},\ x^{k+1/2}_{2,i})$ denotes the flux approximations in the x_2-direction. Analogously to $\mathbf{Q}^i$ the numerical fluxes on level i are defined by

$$\mathbf{F}^{n,i} := \bigcup_{m=1}^{M_i} \mathbf{F}^n(\bar{G}_{i,m}, \cdot, \cdot)\ . \tag{5.6}$$

The notations $\delta\mathbf{F}^n(\partial G_{i,m}, \cdot, \cdot)$, $n = 1, \ldots, d$ are only used on levels with $i > 0$. They denote correction terms associated to the numerical fluxes of level $i-1$ that are defined on the boundary of $G_{i,m}$. The set of correction terms for $\mathbf{F}^{1,i-1}$ is $\delta\mathbf{F}^1(\partial G_{i,m}, x^{j+1/2}_{1,i-1}, x^k_{2,i-1})$ and the corrections for $\mathbf{F}^{2,i-1}$ are stored in $\delta\mathbf{F}^2(\partial G_{i,m}, x^j_{1,i-1}, x^{k+1/2}_{2,i-1})$. The correction terms on level i are

$$\delta\mathbf{F}^{n,i} := \bigcup_{m=1}^{M_i} \delta\mathbf{F}^n(\partial G_{i,m}, \cdot, \cdot)\ . \tag{5.7}$$

The values of correction terms are only required on lower-dimensional domains $\partial G_i \backslash \partial G_0$ where a fine level $i > 0$ abuts the next coarser level. As the geometric location of the data values in the different sets is now clear, we neglect the point information in the following.

5.2.2 Numerical Update

Suppose all cell values $\mathbf{Q}^i$ are set appropriately, a whole level i is updated by applying the solution operator $\mathcal{H}^{(\cdot)}$ implemented in formula (4.4) to all grids on level i in a simple loop:

```
For all m = 1 To M_i Do
```
$$\mathbf{Q}(G^s_{i,m}, t)\ , \mathbf{F}^n(\bar{G}_{i,m}, t) \xrightarrow{\mathcal{H}^{(\Delta t_i)}} \mathbf{Q}(G_{i,m}, t + \Delta t_i)$$

The loop involves the grid-wise update of the flux approximations $\mathbf{F}^{n,i}$.

Conservative Averaging

When two levels i and $i+1$ reach the same discrete time, the finer level values are projected onto the coarser level, because the finer level approximation is expected to be more accurate. Each interior cell value of level i in $G_i \cap G_{i+1}$ is replaced by the conservative average of the r^2_{i+1} internal cells of level $i+1$ that overlay it. We simply overwrite the value $\mathbf{Q}^i_{jk}$ of cell (j,k) with

$$\hat{\mathbf{Q}}^i_{jk} := \frac{1}{(r_{i+1})^2} \sum_{\kappa=0}^{r_{i+1}-1} \sum_{\iota=0}^{r_{i+1}-1} \mathbf{Q}^{i+1}_{v+\kappa,w+\iota}\ . \tag{5.8}$$

Although new fine-level cells are initialized from the coarser level by a conservative interpolation formula like (5.15), the application of the projection formula (5.8)

usually leads to a violation of the important property of discrete conservation on the coarse level. In particular, numerical fluxes between the fine and the coarse level domain are neglected. A special flux correction is necessary to consider numerical fluxes at coarse-fine boundaries appropriately and to ensure the discrete conservation across the entire hierarchy. The correction has to be applied in all coarse level cells abutting a higher-level refinement region.

5.2.3 Conservative Flux Correction

In the update formula (4.4) of all cells of level i in $(G_{i+1}^{r_{i+1}} \backslash G_{i+1}) \cap G_i$, we have to replace the coarse flux approximation with all modified neighboring cells by the sum of all overlying fine level fluxes [21]. Note, that condition (5.4) ensures that only cells of level i need to be corrected. Fig. 5.5 shows these cells for a particular refinement. As an example we consider the cell (j, k). The correct update for $\mathbf{Q}_{jk}^i$ would be

$$\begin{aligned}\check{\mathbf{Q}}_{jk}^i(t+\Delta t_i) = \mathbf{Q}_{jk}^i(t) &- \frac{\Delta t_i}{\Delta x_{1,i}} \left(\mathbf{F}_{j+\frac{1}{2},k}^{1,i} - \frac{1}{r_{i+1}^2} \sum_{\kappa=0}^{r_{i+1}-1} \sum_{\iota=0}^{r_{i+1}-1} \mathbf{F}_{v+\frac{1}{2},w+\iota}^{1,i+1}(t+\kappa\Delta t_{i+1}) \right) \\ &- \frac{\Delta t_i}{\Delta x_{2,i}} \left(\mathbf{F}_{j,k+\frac{1}{2}}^{2,i} - \mathbf{F}_{j,k-\frac{1}{2}}^{2,i} \right)\end{aligned}$$

In order to replace $\mathbf{Q}_{jk}^i(t+\Delta t_i)$ calculated from (4.4) by $\check{\mathbf{Q}}_{jk}^i(t+\Delta t_i)$ we use the correction procedure proposed in [21] that avoids the modification of the numerical scheme and is most convenient for practical purposes. After the update on level i we initialize the correction term $\delta\mathbf{F}_{j-\frac{1}{2},k}^{1,i+1}$ which belongs to the fine level boundary, but is associated to the point $(x_{1,i}^{j-1/2}, x_{2,i}^k)$ by

$$\delta\mathbf{F}_{j-\frac{1}{2},k}^{1,i+1} := -\mathbf{F}_{j-\frac{1}{2},k}^{1,i} \ . \tag{5.9}$$

During the r_{i+1} update steps of level $i+1$ we accumulate all necessary fine level fluxes, i.e.

$$\delta\mathbf{F}_{j-\frac{1}{2},k}^{1,i+1} := \delta\mathbf{F}_{j-\frac{1}{2},k}^{1,i+1} + \frac{1}{r_{i+1}^2} \sum_{\iota=0}^{r_{i+1}-1} \mathbf{F}_{v+\frac{1}{2},w+\iota}^{1,i+1}(t+\kappa\Delta t_{i+1}) \ . \tag{5.10}$$

When the integration of the fine level is complete, the correction is applied by modifying $\mathbf{Q}_{jk}^i(t+\Delta t_i)$ by

$$\check{\mathbf{Q}}_{jk}^i(t+\Delta t_i) := \mathbf{Q}_{jk}^i(t+\Delta t_i) + \frac{\Delta t_i}{\Delta x_{1,i}} \delta\mathbf{F}_{j-\frac{1}{2},k}^{1,i+1} \ . \tag{5.11}$$

To avoid the usage of the numerical fluxes of the entire level, we combine the numerical update and the computation of the correction terms in a single loop:

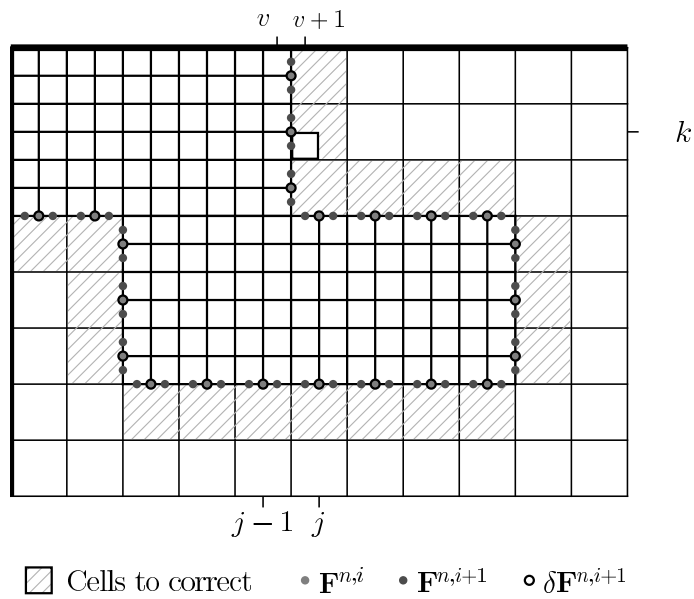

Figure 5.5: Usage of fine instead of coarse grid fluxes to integrate cells abutting a fine grid. Cells needing correction are shaded. The circles mark the locations of the relevant fluxes $\mathbf{F}^{n,i}$, $\mathbf{F}^{n,i+1}$ and of the correction terms $\delta\mathbf{F}^{n,i+1}$.

```
UpdateLevel(i)
  For all m = 1 To M_i Do
      Q(G^s_{i,m}, t) , F^n(Ḡ_{i,m}, t) --H^(Δt_i)--> Q(G_{i,m}, t + Δt_i)
      If level i > 0
          Add F^n(∂G_{i,m}, t) to δF^{n,i}
      If level i + 1 exists
          Init δF^{n,i+1} with F^n(Ḡ_{i,m} ∩ ∂G_{i+1}, t)
```

Algorithm 2: Numerical update of $\mathbf{Q}$ and calculation of correction terms on level i.

5.2.4 Boundary Conditions

Three different types of boundary conditions have to be considered in the AMR method to set the values of $\mathbf{Q}(\tilde{G}^s_{i,m})$ in the ghost cell region $\tilde{G}^s_{i,m} := G^s_{i,m} \backslash \bar{G}_{i,m}$. Cells in

$$\tilde{P}^s_{i,m} = \tilde{G}^s_{i,m} \backslash G_0 \tag{5.12}$$

are auxiliary cells outside of the physical domain. Their values are used to implement *physical* boundary conditions. Cells in

$$\tilde{S}^s_{i,m} = \tilde{G}^s_{i,m} \cap G_i \tag{5.13}$$

have a unique interior cell analogue and are set by copying the data value from the data set of the grid, where the interior cell is contained. We call the overwriting of

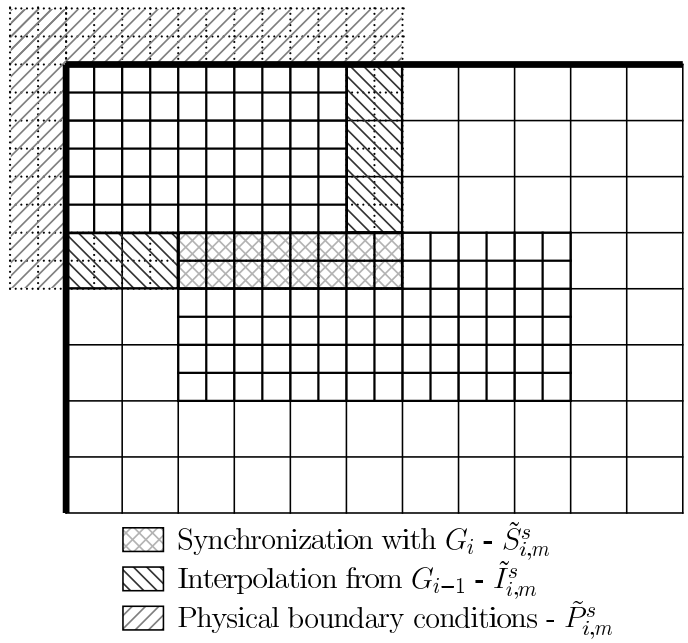

Figure 5.6: Ghost cell regions of a refinement grid $G_{i,m}$.

ghost cell values with internal cell values *synchronization*. It assures the validity of the equal data assumption necessary for the definitions (5.5) to (5.7).

On the root level no further boundary conditions need to be considered. But for $i > 0$ also *internal* boundaries can occur. In the AMR method ghost cells in the domain

$$\tilde{I}^s_{i,m} = \tilde{G}^s_{i,m} \backslash (\tilde{S}^s_{i,m} \cup \tilde{P}^s_{i,m}) \tag{5.14}$$

are used to set internal Dirichlet boundary condition by time-space interpolation where $G_{i,m}$ abuts G_{i-1}. The AMR method is usually implemented with simple linear interpolation operations [21]. For instance for the ghost cell $(v+1, w)$ of the fine grid in Fig. 5.5 a frequently used bilinear space-interpolation reads

$$\begin{aligned} \check{\mathbf{Q}}^i_{v+1,w} := (1-f_1)(1-f_2)\,\mathbf{Q}^{i-1}_{j-1,k-1} + f_1(1-f_2)\,\mathbf{Q}^{i-1}_{j,k-1} + \\ (1-f_1)f_2\,\mathbf{Q}^{i-1}_{j-1,k} + f_1 f_2\,\mathbf{Q}^{i-1}_{jk} \end{aligned} \tag{5.15}$$

with factors

$$f_1 := \frac{x^{v+1}_{1,i} - x^{j-1}_{1,i-1}}{\Delta x_{1,i-1}}\,, \quad f_2 := \frac{x^{w}_{2,i} - x^{k-1}_{2,i-1}}{\Delta x_{2,i-1}}\,.$$

The interpolation (5.15) is followed by a linear time-interpolation to supply suitable internal boundary conditions at discrete time steps that do not exist on level $i-1$, i.e.

$$\tilde{\mathbf{Q}}^i(t+\kappa\Delta t_i) := \left(1 - \frac{\kappa}{r_i}\right)\check{\mathbf{Q}}^i(t) + \frac{\kappa}{r_i}\check{\mathbf{Q}}^i(t+\Delta t_{i-1}) \quad \text{for } \kappa = 0, \ldots r_i - 1\,. \tag{5.16}$$

Fig. 5.6 displays all types of boundary conditions for levels with $i > 0$. The setting of all ghost cell values on level i requires just a loop over all subgrids and the

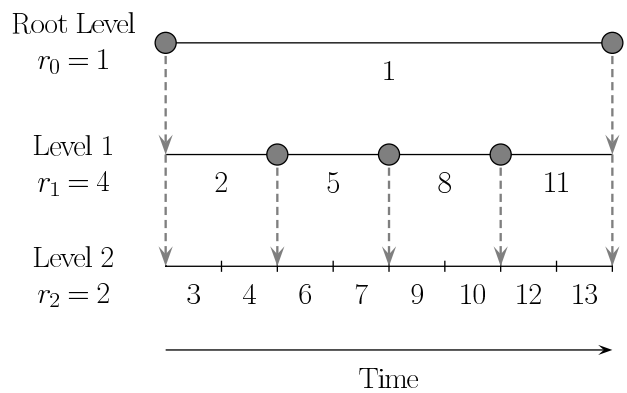

Figure 5.7: Recursive integration order of AMR. The arrows denote regridding of finer levels. The level at which the regridding procudure is initiated (marked by the circles) stays fixed.

application of the three types of boundary conditions. As the domains $\tilde{P}^s_{i,m}$, $\tilde{S}^s_{i,m}$, $\tilde{I}^s_{i,m}$ do not overlap the order is arbitrary.

The interpolation formulae (5.15), (5.16) are also employed to initialize $\mathbf{Q}^i$ in new refinement regions during the regridding procedure. The maximal domain of the space-interpolation (5.15) is G^ν_i with $\nu = (\lfloor s/r_i \rfloor + 1)\, r_i$.[3] As the condition $\lfloor s/r_i \rfloor + 1 \leq s$ is satisfied for all $r_i \geq 2$, $s \geq 1$ the interpolation domain G^ν_i is always fully contained in G^s_{i-1}, but in general it exceeds the interior grid domain G_{i-1}. Consequently, time-space interpolation on level i requires the previous ghost cell setting for $\mathbf{Q}^{i-1}$ on the entire domain at both time steps t and $t + \Delta t_{i-1}$.

5.2.5 The Recursive Algorithm

The time-space interpolation formulae (5.15), (5.16) need the coarse level values $\mathbf{Q}^{i-1}(t)$ and $\mathbf{Q}^{i-1}(t + \Delta t_{i-1})$ to interpolate boundary conditions during the r_i time steps on level i. Therefore, the numerical update must be calculated first on level $i-1$. Further on, the ghost cell values of $\mathbf{Q}^{i-1}(t+\Delta t_{i-1})$ must be set before advancing level i. On the other hand, we want to replace coarse level values successively with the highest level approximation available at equal discrete times. A recursive algorithm is most appropriate to achieve these purposes. The basic AMR algorithm is formulated in Algorithm 3. Except the function `Regrid(`i`)`, that modifies the grid hierarchy, all elements of Algorithm 3 have already been explained. Note, that the setting of the boundary values of $\mathbf{Q}^i(t)$ at the beginning of `AdvanceLevel(`i`)` is mandatory. Although boundary values of coarser levels have already been set before advancing the next finer level, a further application of the boundary conditions is necessary to take changes due to projection and flux correction into account. An example for the temporal integration order of the numerical solution on a three level hierarchy is shown in Fig. 5.7. The recursive integration of Algorithm 3 can be started by calling `AdvanceLevel(0)` on the root level.

[3] $\lfloor . \rfloor$ denotes the Gauss-function which rounds off to the next integer.

```
AdvanceLevel(i)
  Repeat r_i times
     Set ghost cells of Q^i(t)
     If time to regrid
        Regrid(i)
     UpdateLevel(i)
     If level i+1 exists
        Set ghost cells of Q^i(t + Δt_i)
        AdvanceLevel(i + 1)
        Average Q^{i+1}(t + Δt_i) onto Q^i(t + Δt_i)
        Correct Q^i(t + Δt_i) with δF^{n,i+1}
     t := t + Δt_i
```

Algorithm 3: The basic recursive AMR algorithm.

5.2.6 Grid Generation

A level i initiates the creation of new refinement grids based upon the data of all levels ι that satisfy $\iota \geq i$. Level i by itself is not modified. To consider the nesting condition (5.4) already in the grid generation, the regridding procedure starts at the highest level available which allows further refinement. We denote its level number by i_c. It satisfies the condition $0 \leq i_c < i_{\max}$.

Appropriate refinement criteria (see Sec. 5.4) are used to flag cells which have to be refined. Grid-based integer data sets $N^\iota := \bigcup_m N(G_{\iota,m}, x^j_{1,\iota}, x^k_{2,\iota})$ are useful to store the flags. Additional buffer cells are marked around each flagged cell. In order to ensure that a flow phenomenon which has caused the flagging remains within the refinement region until the next regridding, the size of the buffer zone b must satisfy the relation $b \geq \kappa_r$. Herein, κ_r denotes the number of time steps between two regridding operations. To minimize the influence of internal boundary conditions on the solution $b > \kappa_r$ should be used. A buffer zone of two cells is typical for the standard strategy of regridding in every time step (compare Fig. 5.7).

A clustering algorithm (see detailed explanation below) is necessary to create new refinement grids $\breve{G}_{\iota+1,m} \subset G_0$ on the basis of N^ι. This algorithm generates successively smaller grids until the ratio between flagged and all cells in every new grid $\breve{G}_{\iota+1,m}$ is above a prescribed threshold $0 < \eta_{tol} < 1$. As usual we define $\breve{G}_\iota := \bigcup_m \breve{G}_{\iota,m}$. In order to ensure that the previously generated new refinement grids of the next finer level are fully contained in $\breve{G}_{\iota+1}$ all cells in N^ι below $\breve{G}_{\iota+2}$ are also flagged before creating the buffer zone.

Before the new grids $\breve{G}_{\iota+1}$ can be used to replace $G_{\iota+1}$, the validity of the nesting condition (5.4) has to be enforced over the modified hierarchy. In Algorithm 4 we evaluate the invalid region for level $\iota + 1$ by calculating the complement $C\breve{G}_\iota := G_0 \backslash \breve{G}_\iota$ of the next coarser level domain $\breve{G}_\iota$ in G_0 and by enlarging $C\breve{G}_\iota$ by one additional cell, i.e. $C\breve{G}^1_\iota$. The operation $\breve{G}_{\iota+1} := \breve{G}_{\iota+1} \backslash C\breve{G}^1_\iota$ then eliminates all regions violating (5.4) from the new level domain $\breve{G}_{\iota+1}$.

Note, that Algorithm 4 can create only one new level above i_c, but all levels above i could be removed.

```
Regrid(i) - Regrid all levels ι > i
  For ι = i_c Downto i Do
      Flag N^ι according to Q^ι(t)
      If level ι + 1 exists?
          Flag N^ι below Ğ_{ι+2}
      Flag buffer zone on N^ι
      Generate Ğ_{ι+1} from N^ι
  Ğ_i := G_i
  For ι = i To i_c Do
      CĞ_ι := G_0\Ğ_ι , Ğ_{ι+1} := Ğ_{ι+1}\CĞ_ι^1
  Recompose(i)
```

Algorithm 4: The regridding procedure.

The reinitialization of the hierarchy is done in `Recompose(i)`. In particular, grid-based auxiliary data $\breve{\mathbf{Q}}(\breve{G}_\iota, t)$ is necessary to reorganize the grid-based data of the vector of state. Cells in newly refined regions $\breve{G}_\iota \backslash G_\iota$ are initialized by interpolation, values of cells in $\breve{G}_\iota \cap G_\iota$ are copied. As interpolation requires the previous reorganization of $\mathbf{Q}^{\iota-1}(t)$ (including an update of ghost cell values) recomposition begins on level $i+1$.

```
Recompose(i) - Reorganize all levels ι > i
  For ι = i + 1 To i_c + 1 Do
      Interpolate Q^{ι-1}(t) onto Q̆^ι(t)
      Copy Q^ι(t) onto Q̆^ι(t)
      Set ghost cells of Q̆^ι(t)
      Q^ι(t) := Q̆^ι(t) , G_ι := Ğ_ι
```

Algorithm 5: Serial recomposition.

Clustering by Signatures

We use the algorithm proposed in [19] to cluster flagged cells into new Grids $\breve{G}_{\iota+1,m}$. It counts the number of flagged cells in each row and column on the entire domain of N^ι. These sums Υ are called *signatures*. First, cuts into new boxes are placed on all edges, where Υ vanishes at one side (first picture of Fig. 5.8). In the second

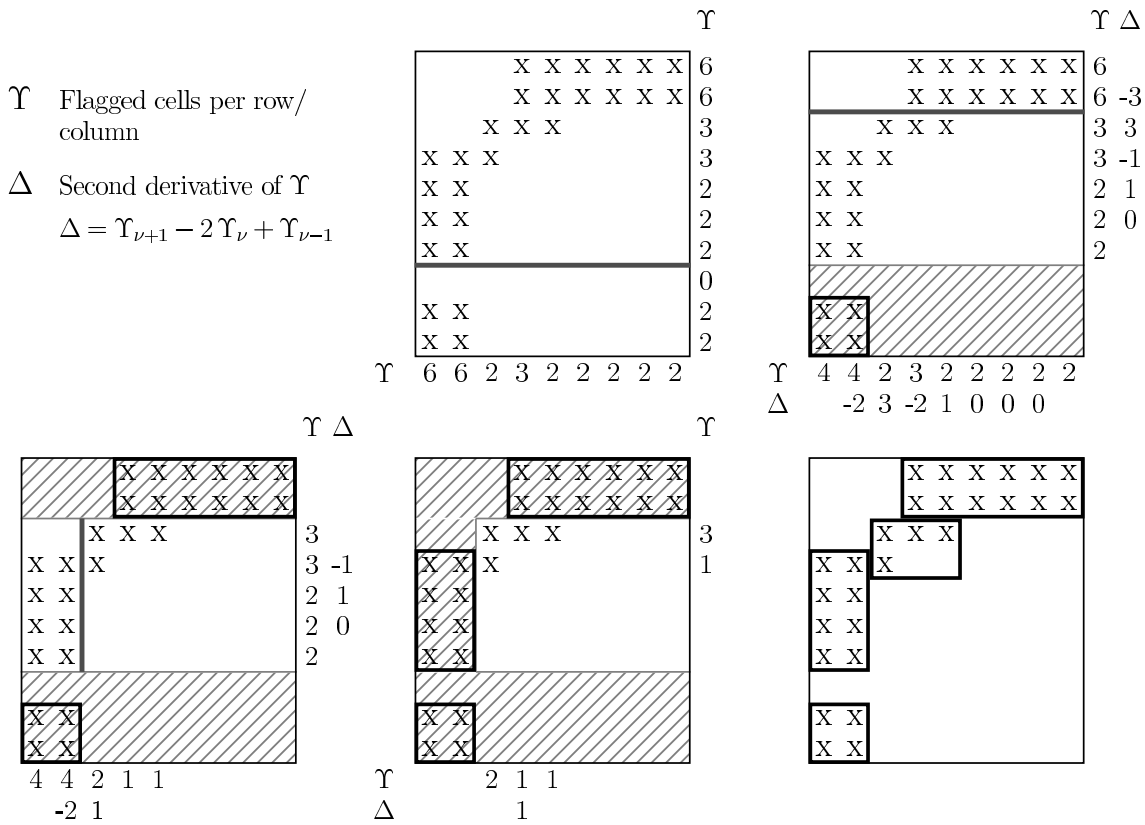

Figure 5.8: Grid generation by signatures [19].

step, cuts are placed at zero crossings of the discrete second derivative Δ. The algorithm starts with the steepest zero crossing and uses successively weaker cuts, until the ratio between flagged and all cells in every new grid is above the prescribed threshold value η_{tol} (second and third picture of Fig. 5.8). Throughout this thesis threshold values between 0.7 and 0.9 have been applied.

5.3 Parallel Algorithm

The computationally most expensive operation of Algorithm 3 is the numerical update in `UpdateLevel(`i`)`. The update loop over all subgrids $G^s_{i,m}$ can be parallelized in a natural way by computing the update of different grids on different computing nodes. A time-explicit scheme only requires the synchronization of $\mathbf{Q}^i(t)$ before the grid-based data is distributed and this operation is already part of the boundary update in the basic algorithm. Consequently, the efficient usage of parallel computers with shared memory is straight-forward. Only an estimation of the necessary work on each subgrid is necessary to split up the loop in `UpdateLevel(`i`)` in a load-balancing manner.

This simple strategy is not practicable on parallel computers with distributed

memory. The computing nodes of distributed memory architectures usually do not have enough memory to store the complete data of large-scale problems. Therefore, the hierarchical data must be split between the available nodes. As communication times usually can not be neglected in these environments, this splitting should be done in a way that minimizes communication on the one hand and balances the work on the other hand. In the following, we describe a parallelization strategy for blockstructured AMR that takes both goals into account. Its main idea has been proposed by Parashar and Browne in [145, 146].

5.3.1 Decomposition of the Hierarchy

We assume a parallel machine with P identical nodes. We follow a rigorous domain decomposition approach and partition the computational domain. The root domain G_0 is split into P non-overlapping portions G_0^p, $p = 1, \ldots, P$ by

$$G_0 = \bigcup_{p=1}^{P} G_0^p \quad \text{with} \quad G_0^p \cap G_0^q = \emptyset \;\; \text{for } p \neq q \;,$$

which are defined as usual as the union of new non-overlapping grids $G_{i,m}^p$ by

$$G_0^p := \bigcup_{m=1}^{M_0^p} G_{0,m}^p \;.$$

The key idea now is that all higher level domains G_i are required to follow the decomposition of the root level:

$$G_i^p := G_i \cap G_0^p \tag{5.17}$$

Condition (5.17) can cause the splitting of a subgrid $G_{i,m}$ into multiple subgrids $G_{i,\kappa}^p$ on different processors. Although the merging of subgrids $G_{i,\kappa}^p$ on processor p is allowed, the total number of grids in $\bigcup_p G_i^p$ usually exceeds the number of grids in G_i, i.e. $\sum_p M_i^p > M_i$.[4] Under requirement (5.17) we estimate the work on an arbitrary rectangular subdomain $\Omega \subset G_0$ by

$$\mathcal{W}(\Omega) = \sum_{i=0}^{i_{\max}} \left[\mathcal{N}_i(G_i \cap \Omega) \prod_{\kappa=0}^{i} r_\kappa \right] \;. \tag{5.18}$$

Herein, $\mathcal{N}_i(G)$ is the total number of FV cells of level i that are completely contained in $\bar{G}$. The product in (5.18) is used to consider the time step refinement. A nearly equal distribution of the work necessitates

$$\mathcal{L}^p := \frac{P \cdot \mathcal{W}(G_0^p)}{\mathcal{W}(G_0)} \approx 1 \quad \text{for all } p = 1, \ldots, P \;. \tag{5.19}$$

The creation of a load-balanced decomposition G_0^p requires an appropriate partitioning algorithm.

[4] For the example of Fig. 5.9 we have $M_1^p = 2$, $M_1^q = 1$ and $M_1 = 2$.

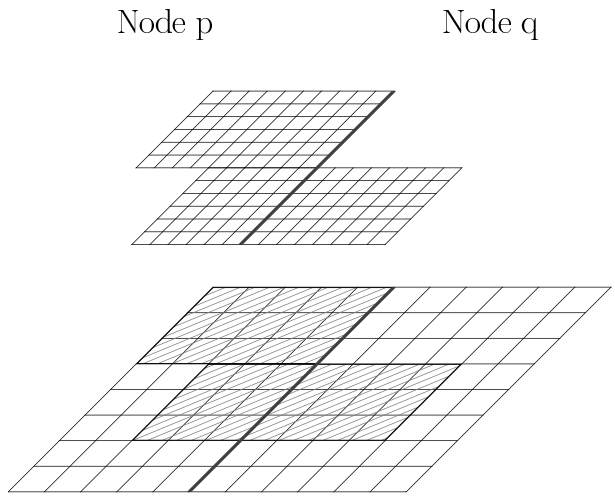

Figure 5.9: Splitting of refinement grids due to distribution based on the root level.

5.3.2 The Parallel Recursive Algorithm

The second goal in designing an efficient parallelization strategy, the reduction of the communication overhead, is already considered in condition (5.17) in a natural way. Together with the use of synchronized ghost cells this condition allows a strictly local execution of most AMR operations. In particular, no major modification of Algorithm 3 is necessary. We start our explanation of this fact, which simplifies the practical implementation enormously, with the setting of the ghost cell values in parallel.

Boundary Conditions

The domain decomposition technique increases the complexity of the ghost cell synchronization. In the parallel algorithm, the synchronization domain of a decomposed grid $G_{i,m}^{s,p}$ on node p is divided into the local domain

$$\tilde{S}_{i,m}^{s,p} = \tilde{G}_{i,m}^{s,p} \cap G_i^p \ ,$$

and the parallel domains

$$\tilde{S}_{i,m}^{s,q} = \tilde{G}_{i,m}^{s,p} \cap G_i^q \ , \quad q = 1, \ldots, P \ , \quad q \neq p \ .$$

While the cell values in $\tilde{S}_{i,m}^{s,p}$ can be copied from interior cells, which are locally available on p, the setting of cells in $\tilde{S}_{i,m}^{s,q}$ requires communication with node q on which the interior cells originally reside.

The setting of physical and internal boundaries remains strictly local. Analogously to Sec. 5.2.4 the domain for the space-interpolation $G_i^{\nu,p}$ is fully contained in $G_{i-1}^{s,p}$, the local domain of the next coarser level. The parallel synchronization of $\mathbf{Q}^{i-1}(t)$, $\mathbf{Q}^{i-1}(t + \Delta t_{i-1})$ is guaranteed by the AMR algorithm itself and therefore the parallel synchronization of level i is the only communication operation necessary to set the ghost cells on level i.

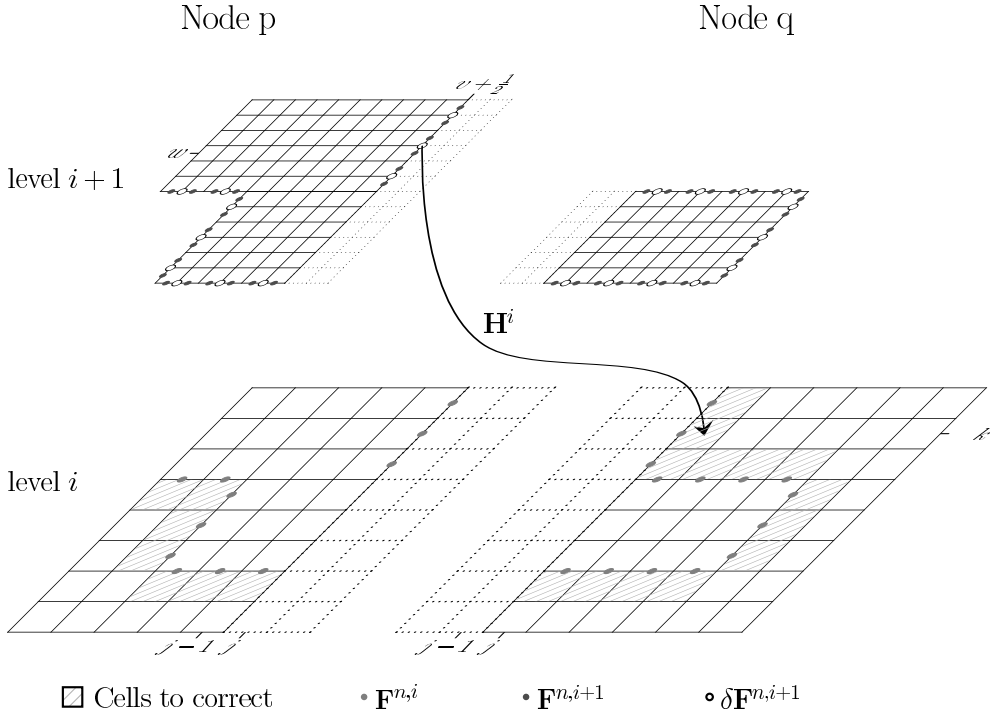

Figure 5.10: Conservative flux correction in parallel. Cells needing correction are shaded. The circles mark the locations of the relevant fluxes $\mathbf{F}^{n,i}$, $\mathbf{F}^{n,i+1}$ and of the correction terms $\delta\mathbf{F}^{n,i+1}$.

Numerical Update and Flux Correction

The function `UpdateLevel(`i`)` does not involve any parallel overhead. Apparently, the new vector of state $\mathbf{Q}(G^p_{i,m}, t+\Delta t_i)$ on each grid $G^p_{i,m}$ and the fluxes $\mathbf{F}^n(\bar{G}^p_{i,m}, t)$ can be computed strictly local on the basis of $\mathbf{Q}(G^{s,p}_{i,m})$, but also the computation of the correction terms does not require communication.

To illustrate this, we assume a parallel border in Fig. 5.5 at $j-\frac{1}{2}$. Let cell (j,k) be contained in G^q_i and let cell (v,w) be contained in G^p_{i+1}. Then the necessary correction term $\delta\mathbf{F}^{1,i+1}_{j-1/2,k}$ resides on node p, because it is assigned to the fine level. The initialization of this term in (5.9) requires the coarse grid flux $\mathbf{F}^{1,i}_{j-1/2,k}$. This flux is available on node p, because the basic AMR strategy ensures that below (v,w) an interior coarse cell $(j-1,k)$ exists on p having $\mathbf{F}^{1,i}_{j-1/2,k}$ as flux into a ghost cell (j,k). On the other hand, $\mathbf{F}^{1,i}_{j-1/2,k}$ is also computed on q, where (j,k) is interior and $(j-1,k)$ is a ghost cell. As the ghost cells have been synchronized before the numerical update, the same boundary flux is calculated on both nodes (compare level i in Fig. 5.10). The fine grid fluxes $\mathbf{F}^{1,i+1}_{v+1/2,w+\iota}$ are only available on p, because no abutting interior fine grid cell exists on q. As the correction term $\delta\mathbf{F}^{1,i+1}_{j-1/2,k}$ is also stored on p the summation in (5.10) remains local (compare level $i+1$ of node p in Fig. 5.10).

The only operation of the flux correction that necessarily requires communica-

tion is the application of correction terms like in (5.11). In our example, the term $\delta\mathbf{F}^{1,i+1}_{j-1/2,k}$ of node p has to be applied onto the value of the interior cell (j,k), which is stored on node q. Our practical implementation only allows the setting of ghost cell values from interior cells. We achieve the parallel exchange by employing auxiliary grid-based *cell-centered* data $\mathbf{H}(G^{1,p}_{i,m}, x^{j^*}_{1,i}, x^{k^*}_{2,i})$ that has an overlap of one cell. $\mathbf{H}^i$ is initialized with zero everywhere. On node p the value $\delta\mathbf{F}^{1,i+1}_{j-1/2,k}$ is copied into the interior cell $(j-1,k)$. Then $\mathbf{H}^i$ is synchronized and all values are shifted by one cell to the right. On node q this technique transfers $\delta\mathbf{F}^{1,i+1}_{j-1/2,k}$ from the ghost cell $(j-1,k)$ to the interior cell (j,k), where it can be applied. The simultaneous application of this trick to all correction terms $\delta\mathbf{F}^{n,i+1}$ reduces the parallel overhead for the entire procedure to two synchronization operations per space-direction. The transfer and application of $\delta\mathbf{F}^{1,i+1}_{j-1/2,k}$ via $\mathbf{H}^i$ to the interior cell (j,k) is expressed by the black arrow in Fig. 5.10.

Finally, we remark that strict locality of the inter-level averaging (5.8) follows directly from condition (5.17). This property avoids the expensive parallel communication of volume data during the averaging operation.

5.3.3 Parallel Grid Generation

Analogously to Algorithm 3 the regridding procedure formulated in Algorithm 4 is hardly affected by the parallelization. The flagging of cells on each level can be done locally. If an error estimation criterion like the one explained in 5.4 is used, the computation of auxiliary time steps involves parallel boundary synchronization, but this does not modify Algorithm 4. The only difficult task in the creation of $\breve{G}_{\iota+1}$ from N^ι in Algorithm 4 is the clustering.

Two possibilities exist for running the clustering algorithm in parallel. The clustering algorithm could be executed strictly locally on $N(G^p_\iota)$ or it could be executed on the data of the entire level $N(G_\iota)$. Note, that both options can be guaranteed to give an identical result only for a clustering threshold of $\eta_{tol} = 1$. For $\eta_{tol} < 1$ the algorithm has some freedom in combining flagged and non-flagged cells leading to slightly different results for both approaches. The second option would require a global concatenation of all data sets $N(G^p_\iota)$ to $N(G_\iota)$. This parallel operation is extremely expensive and we therefore execute the clustering algorithm strictly locally and communicate only the result $\breve{G}^p_{\iota+1}$ globally to obtain the global list $\breve{G}_{\iota+1} = \bigcup_p \breve{G}^p_{\iota+1}$. The global list $\breve{G}_{\iota+1}$ is mandatory to ensure the correct proper nesting of the new hierarchy. To consider the buffer zone before local clustering, we use extended grid-based data $\tilde{N}^\iota := \bigcup_m N(G^b_{\iota,m}, x^j_{1,\iota}, x^k_{2,\iota})$ instead of N^ι. Herein, b is the size of the buffer region (see Sec. 5.2.6). By synchronizing $\tilde{N}^\iota$ before creating the buffer zone we ensure that all interior cells are flagged correctly.

The main changes in the regridding procedure are in `Recompose(`i`)`. Instead of Algorithm 5 we apply Algorithm 6. Due to our distribution strategy we now have to consider a complete reorganization of the entire hierarchy even for a regridding at a higher level. In Fig. 5.7 this corresponds to the three regridding operations

initiated by level 1. In particular, the whole relevant data of levels with $\iota \leq i$ has to be copied. Like the synchronization operation, these copy operations are partially local and parallel. For levels with $\iota < i$ the relevant data is $\mathbf{Q}^\iota(t)$, $\mathbf{Q}^\iota(t + \Delta t_\iota)$ and $\delta\mathbf{F}^{n,\iota}$, for level i we have to copy $\mathbf{Q}^i(t)$ and $\delta\mathbf{F}^{n,i}$. The initialization of a level with $\iota > i$ is in principle identical to Algorithm 5. As explained in the previous section the interpolation is a strictly local operation, supposed the next coarser level has already been reorganized. The copy operation is a combination of local and parallel copy.

```
Recompose(i) - Reorganize all levels
  Generate G_0^p from {G_0, ..., G_i, Ğ_{i+1}, ..., Ğ_{i_c+1}}
  For ι = 0 To i_c + 1 Do
      If ι > i
          Ğ_ι^p := Ğ_ι ∩ G_0^p
          Interpolate Q^{ι-1}(t) onto Q̆^ι(t)
      else
          Ğ_ι^p := G_ι ∩ G_0^p
          If ι > 0
              Copy δF^{n,ι} onto δF̆^{n,ι}
              δF^{n,ι} := δF̆^{n,ι}
      If ι ≥ i then κ_ι = 0 else κ_ι = 1
      For κ = 0 To κ_ι Do
          Copy Q^ι(t + κΔt_ι) onto Q̆^ι(t + κΔt_ι)
          Set ghost cells of Q̆^ι(t + κΔt_ι)
          Q^ι(t + κΔt_ι) := Q̆^ι(t + κΔt_ι)
      G_ι^p := Ğ_ι^p, G_ι := ⋃_p G_ι^p
```

Algorithm 6: Parallel recomposition. Executed on each node $p = 1, \ldots, P$.

5.3.4 Partitioning

It is evident, that the overall efficiency of the chosen parallelization strategy depends especially on the first step of `Recompose(i)`, the partitioning algorithm. This algorithm has to create a load-balanced domain decomposition for the new hierarchy, which consists for $\iota \leq i$ of unchanged level domains G_ι and for $\iota > i$ of new domains $\breve{G}_\iota$. The topology of the entire hierarchy is globally available and the partitioning algorithm therefore can be called locally with an identical result everywhere.

The algorithm has to meet several requirements. It must balance the estimated workload, while the amount of data that has to be synchronized during the numerical solution procedure should be as small as possible. A slight change of the grid

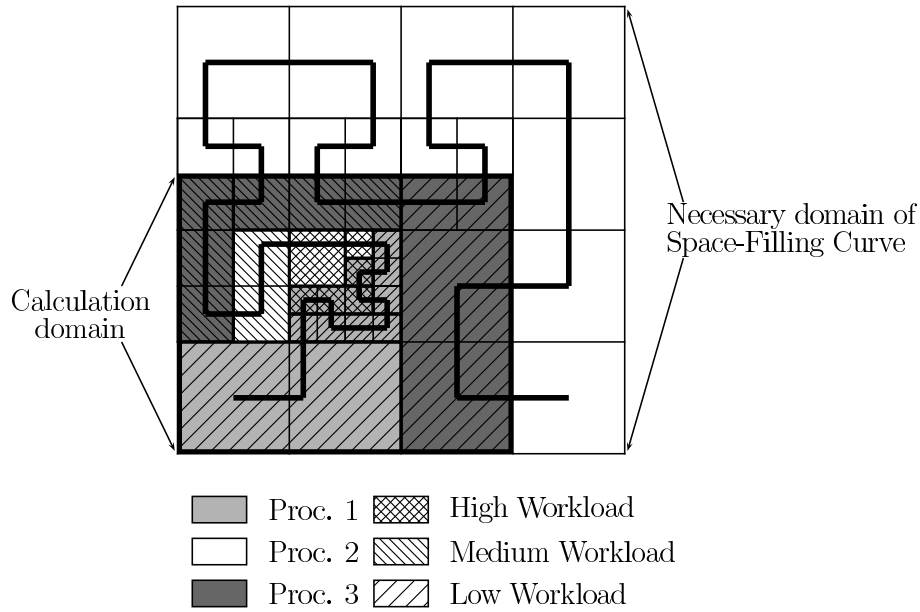

Figure 5.11: A generalization of Hilbert's space-filling curve is used to distribute grid blocks. The domain of the space-filling exceeds the calculation domain, because the number of cells in x_1- and x_2-direction are not of the same power of 2.

hierarchy should involve a moderate data redistribution. The paritioning algorithm must be fast, because it is carried out on-the-fly.

Distribution strategies based on space-filling curves give a good compromise between these partially competing requirements. A space-filling curve defines a continuous mapping from $[0,1]$ onto $[0,1]^d$, $d \geq 2$, cf. [159]. As such curves can be constructed recursively, they are locality preserving and therefore avoid an excessive redistribution overhead. Further on, the surface is small, which reduces the synchronization costs.

By applying the mapping of a space-filling curve to the discrete index space of the root level, the root level cells become ordered. This sequence can easily be split into portions of equal size yielding load-balanced new distributions G_0^p. The computational time necessary for distribution can be decreased, if neighboring cells with the same workload are concatenated. In this case, generalized space-filling must be employed [145, 146].

It has to be noted that for instance Hilbert's space-filling curve can only be defined on index domains satisfying $(2^\nu)^d$ with $\nu \in \mathbb{N}$. Consequently, the domain for the space-filling curve exceeds the computational domain in most cases (see Fig. 5.11). This is the reason why space-filling curves sometimes fails in producing perfectly connected subdomains.

5.4 Refinement Criteria

Throughout this thesis only the refinement criteria presented in this section are utilized. The criteria are always applied to selected scalar quantities, e.g. to some components of the vector of state and/or additionally evaluated derived quantities like the hydrodynamic pressure p.

5.4.1 Scaled Gradients

An adaptation along discontinuities can easily be achieved by evaluating gradients multiplied by the step size (scaled gradients) in all directions. Cell (j,k) is flagged for refinement, if any of the relations

$$|w(\mathbf{Q}_{j+1,k})-w(\mathbf{Q}_{jk})| > \epsilon_w \,,\ |w(\mathbf{Q}_{j,k+1})-w(\mathbf{Q}_{jk})| > \epsilon_w \,,\ |w(\mathbf{Q}_{j+1,k+1})-w(\mathbf{Q}_{jk})| > \epsilon_w \tag{5.20}$$

is satisfied for an arbitrary scalar quantity w, which is derived from the vector of state $\mathbf{Q}^i(t)$. The constant ϵ_w denotes a prescribed refinement limit. In case of Euler equations, the scalar quantities ρ and p are often sufficient to achieve a reasonable refinement.

5.4.2 Heuristic Error Estimation

A simple adaptation criterion for regions of smooth solutions is the heuristic estimation of the local truncation error by Richardson extrapolation [21, 23, 20]. The local truncation error of a difference scheme of order o (compare Def. 11) satisfies

$$\mathbf{q}(\mathbf{x}, t+\Delta t) - \mathcal{H}^{(\Delta t)}(\mathbf{q}(\cdot, t)) = \mathbf{C}\Delta t^{o+1} + O(\Delta t^{o+2}) \,.$$

If $\mathbf{q}$ is sufficiently smooth, we have for the local error at $t+\Delta t$ after two time steps with Δt

$$\mathbf{q}(\mathbf{x}, t+\Delta t) - \mathcal{H}_2^{(\Delta t)}(\mathbf{q}(\cdot, t-\Delta t)) = 2\,\mathbf{C}\Delta t^{o+1} + O(\Delta t^{o+2}) \tag{5.21}$$

and for the local error at $t+\Delta t$ after one time step with $2\Delta t$

$$\mathbf{q}(\mathbf{x}, t+\Delta t) - \mathcal{H}^{(2\Delta t)}(\mathbf{q}(\cdot, t-\Delta t)) = 2^{o+1}\mathbf{C}\Delta t^{o+1} + O(\Delta t^{o+2}) \,. \tag{5.22}$$

Subtracting (5.21) from (5.22) we obtain the relation

$$\mathcal{H}_2^{(\Delta t)}(\mathbf{q}(\cdot, t-\Delta t)) - \mathcal{H}^{(2\Delta t)}(\mathbf{q}(\cdot, t-\Delta t)) = (2^{o+1}-2)\mathbf{C}\Delta t^{o+1} + O(\Delta t^{o+2}) \,, \tag{5.23}$$

which can be employed to approximate the leading-order term $\mathbf{C}\Delta t^{o+1}$ of the local error at $t+\Delta t$. The implementation of a criterion based on (5.23) requires a discrete solution $\mathcal{Q}^i$ defined on a mesh two times coarser than the mesh of level i. With $y_{1,i}^j = (2j+1)\Delta x_{1,i}$ and $y_{1,i}^k = (2k+1)\Delta x_{2,i}$, $j,k \in \mathbb{Z}$ we therefore introduce

$$\mathcal{Q}^i := \bigcup_m \mathcal{Q}(G_{i,m}^s, y_{1,i}^j, y_{2,i}^k) \,.$$

The coarser approximation $\mathcal{Q}^i(t-\Delta t)$ is initialized by averaging the previous solution $\mathbf{Q}^i(t-\Delta t)$ onto it and by setting the ghost cell values $\tilde{\mathcal{Q}}^i(t-\Delta t)$ appropriately. Then $\mathbf{Q}^i(t)$ and $\mathcal{Q}^i(t-\Delta t)$ are updated as usual:

$$\mathbf{Q}^i(t) \overset{\mathcal{H}^{(\Delta t_i)}}{\longrightarrow} \mathbf{Q}^i(t+\Delta t) \quad \text{and} \quad \mathcal{Q}^i(t-\Delta t) \overset{\mathcal{H}^{(2\Delta t_i)}}{\longrightarrow} \mathcal{Q}^i(t+\Delta t)$$

Finally, $\mathbf{Q}^i(t+\Delta t)$ is averaged onto a second coarsened solution $\bar{\mathcal{Q}}^i$ to compare it to $\mathcal{Q}^i$. The difference

$$\tau_{jk} := \frac{|\bar{\mathcal{Q}}^i_{jk}(t+\Delta t) - \mathcal{Q}^i_{jk}(t+\Delta t)|}{2^{o+1}-2}$$

is an approximation to the leading-order term of the local error. But from the local approximation τ_{jk} no approximation to the global error can be derived. The practical usage of τ_{jk} therefore remains empirical. Analogously to (5.20) we define

$$\tau^w_{jk} := \frac{|w(\bar{\mathcal{Q}}^i_{jk}(t+\Delta t)) - w(\mathcal{Q}^i_{jk}(t+\Delta t))|}{2^{o+1}-2} \ . \tag{5.24}$$

If the relation

$$\tau^w_{jk} > \eta_w \tag{5.25}$$

is satisfied, all four cells below the coarsened cell (j,k) are flagged for refinement. While the criterion (5.25) uses an approximation to the absolute local error, better results are often obtained with the criterion

$$\frac{\tau^w_{jk}}{\max(|w(\mathcal{Q}^i_{jk}(t+\Delta t))|, S_w)} > \eta^r_w \tag{5.26}$$

that is formulated analogously to relation (4.117) and combines relative and absolute error.

5.5 Object-oriented Implementation

The profound explanation of the AMR method in the Secs. 5.2 and 5.3 forms the basis of our object-oriented framework AMROC (Adaptive Mesh Refinement in Object-oriented C++). In the following this framework and its implementation will be sketched.

5.5.1 Three-level Design

In principle, three main abstraction levels can be identified in AMR. At the top level, the specific application is formulated. Only single-grid routines operating on $\mathbf{Q}(G^s_{i,m})$ are necessary. Mandatory are the numerical scheme and functions to set the initial and physical boundary conditions. In our implementation these functions are in Fortran-77 and mimic the syntax of the popular non-adaptive code Clawpack

[121, 120]. No knowledge about adaptivity is required to specify them. Interface-objects in C++ supply a generic access to these functions to the AMR level below.

The parallel AMR algorithm and its components for error estimation, grid generation and flux correction make up the middle level which is completely in C++. The Algorithms 2 and 3 are implemented in the central class AMR-Solver. An object of this type coordinates the whole computation and calls methods of the component-classes Flagging, Clustering and Fixup according to the Algorithms 2 and 3. We denote this level, which is formulated exactly along the lines of Secs. 5.2 and 5.3 the mere AMROC level. It is written independent of the spatial dimension and of the specific numerical scheme at the application level. The Flagging-object is exchangeable and the adaptive algorithm is therefore not restricted to the refinement indicators presented in Sec. 5.4.

The middle level operates mainly on grid-based hierarchical data structures that are supplied by the base level. The definitions in the Secs. 5.2 and 5.3 are the basis for its design.

5.5.2 The Hierarchical Data Structures

The base level stores the topology of the hierarchy and allocates all kind of grid-based data. Additionally, it provides standard operations that require topological information, like ghost cell synchronization, interpolation or averaging to the middle level. Furthermore, elementary topological operations on grids $G_{i,m}$ and on grid sets are supplied. Some of these operations are $\cap$, $\cup$, $\setminus$ and the enlargement operation $G^{\sigma}_{i,m}$. The implementation of these operations can be simplified significantly, if a global integer coordinate system is employed. All coordinates in the description in Sec. 5.2 can be mapped uniquely into this integer coordinate system by replacing the mesh widths $\Delta x_{n,i}$, $i = 0, \ldots, i_{\max}$ by increasing integers, i.e.

$$\Delta x_{n,i} \cong \prod_{\kappa=i+1}^{i_{\max}} r_{\kappa} \quad \text{for all } n = 1, \ldots, d \; .$$

Further on, we use a similar mapping to denote the discrete time steps by a unique positive integer. The use of integer coordinates eliminates round-off errors completely [19] and speeds up the execution.

The most important elementary class of the base level is the GridBox-class. It defines a rectangle $G_{i,m}$ in the global integer index space. A list of GridBoxes is stored inside the GridBoxList-class. Methods for topological operations on GridBoxes and GridBoxLists are provided. GridBoxLists are employed by the GridHierarchy-class to store the topology of the hierarchy. GridHierarchy holds the global GridBoxLists G_i and the local GridBoxLists G^p_i that store each processor's local contribution.

Grid-based data are allocated locally with respect to G^p_i inside the GridFunction-class. For each grid $G^p_{i,m}$ GridFunction allocates a GridDataBlock-object, which adds consecutive data storage in Fortran-format to the GridBox-object. The type of data used by GridDataBlock is a template parameter for GridFunction. GridFunction is

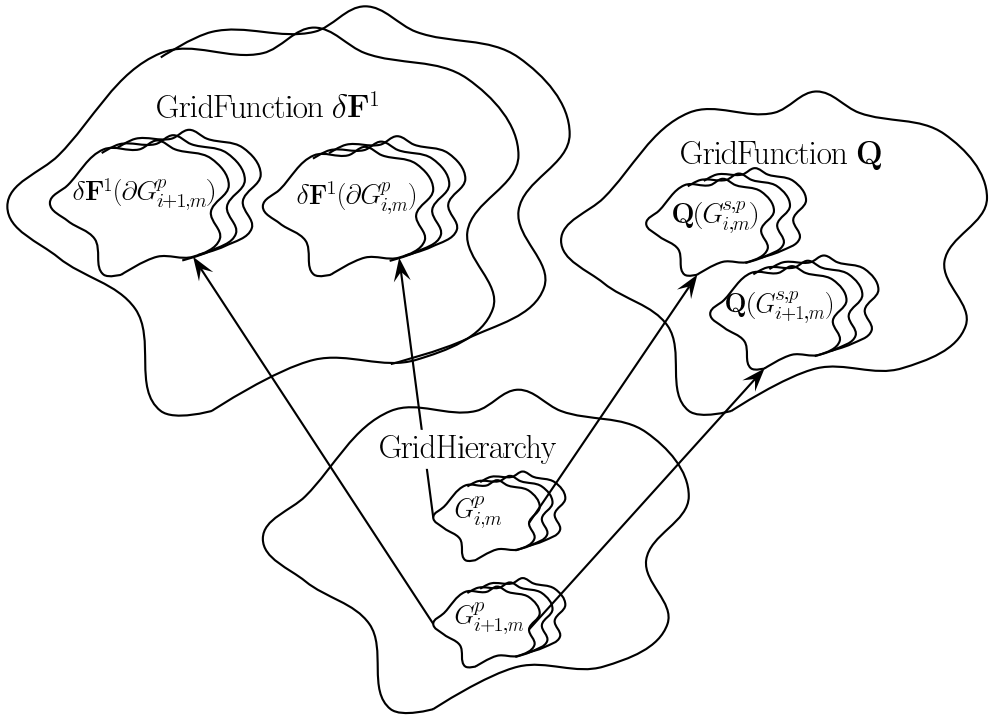

Figure 5.12: All GridFunctions for the AMR method allocate grid-based data with respect to a single GridHierarchy-object which stores the grid lists for each level.

very flexible and allows beside different staggerings also the reduction of grids to lower-dimensional slices and the extension with differently sized ghost cell regions. Hence, the grid-based data $\mathbf{Q}^i$, $\delta\mathbf{F}^{n,i+1}$, N^i are stored in different GridFunction-objects. The usage of a single base class for all kind of hierarchical grid-based data exploits the commonality in organizing rectangular data blocks independent of their storage type and reduces the implementation work significantly. By employing template data types and compile-time parameters carefully we were able to derive all necessary GridFunction-objects from the base class without a loss of computational performance.

All GridFunction-objects are equally distributed with respect to a single GridHierarchy-object (see Fig. 5.12). When the AMR-Solver-object calls the GridHierarchy method `Recompose()` with new lists $\breve{G}_i$, the partitioner is called and new GridBoxLists G_i and G_i^p are created. Initiated by `Recompose()` the GridFunction-objects then redistribute their data automatically. This corresponds to the partially local and parallel copy-operations in Algorithm 6. Further on, GridFunction implements the setting of boundary conditions for $\mathbf{Q}^i$. In this case, each GridDataBlock allocates extended data $\mathbf{Q}(G^{s,p}_{i,m})$ and stores detailed topological information on $P^s_{i,m}$, $I^s_{i,m}$, $S^{s,p}_{i,m}$ and $S^{s,q}_{i,m}$. GridFunction sets ghost cells in $P^s_{i,m}$ by a call to the user-defined physical boundary function. Cells in $I^s_{i,m}$ are set by applying the interpolation function to $\mathbf{Q}^{i-1}$.

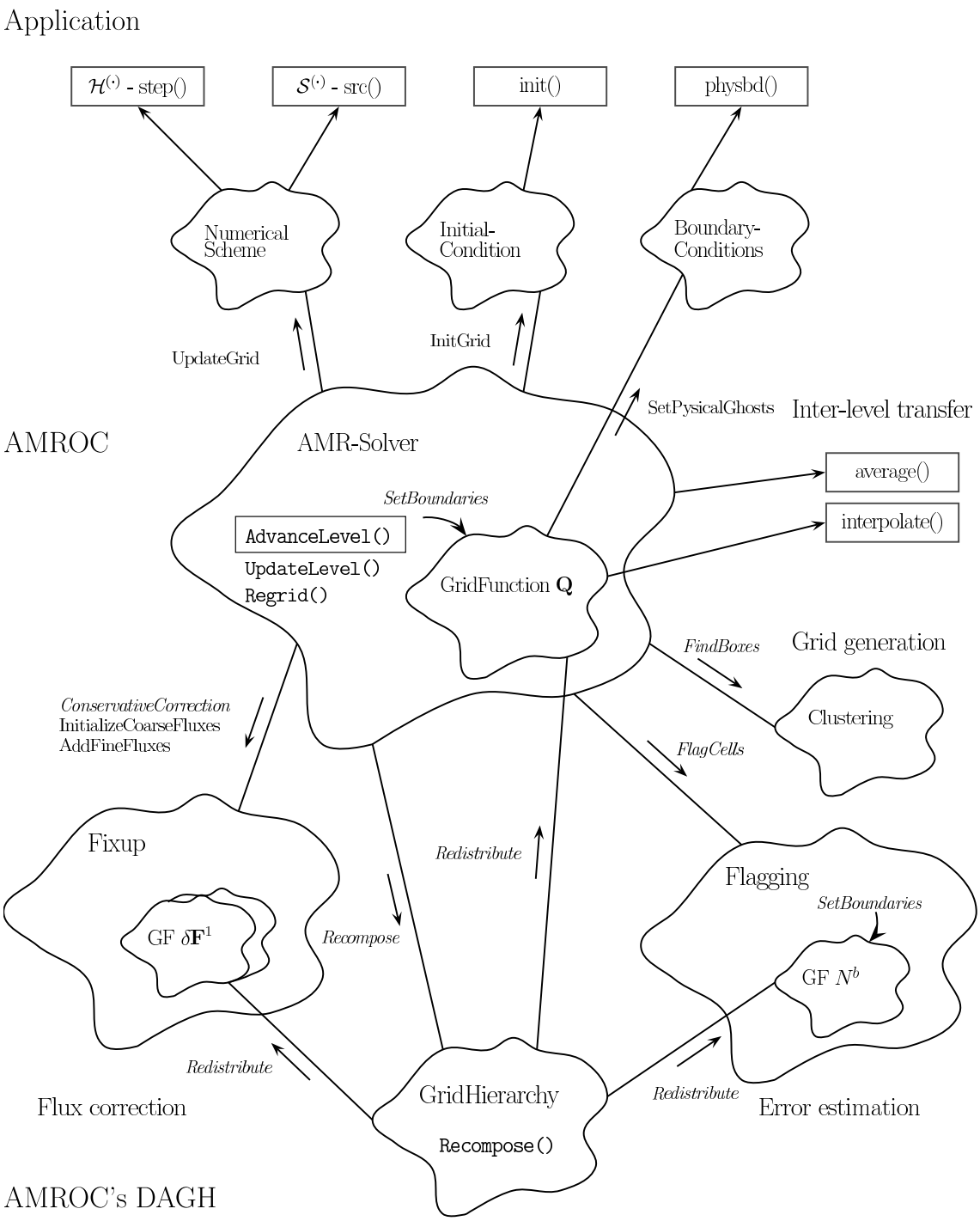

Figure 5.13: Object-oriented design of the AMROC framework. GF means Grid-Function.

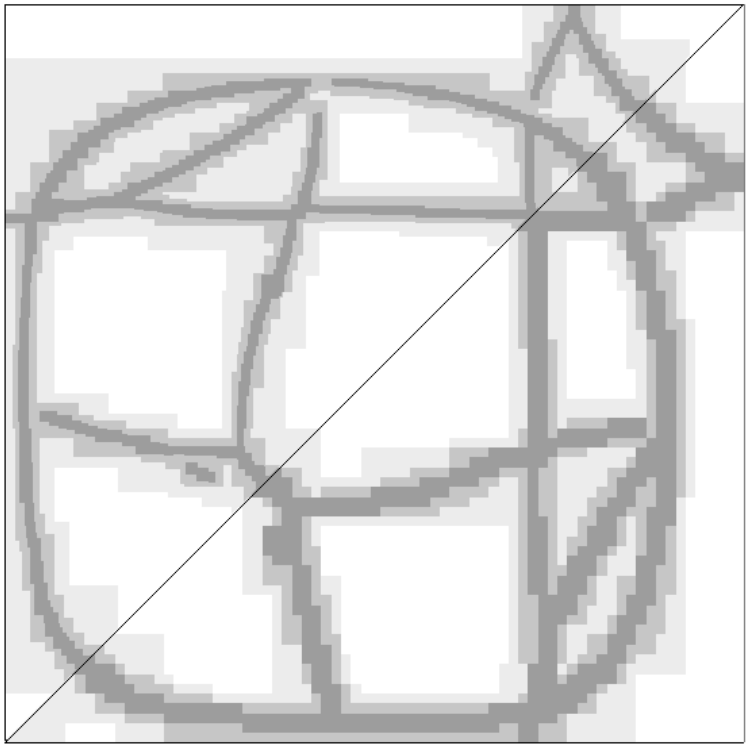

Figure 5.14: Comparison of the refinement grids of a four-level solution with AMROC's DAGH (top left) and the original DAGH (bottom right).

An object diagram of the entire design with focus on the middle level is displayed in Fig. 5.13. It is in Booch's notation [30]. An arrow denotes a simple message to the object to which it points.

AMROC's DAGH Package

In our implementation the base level is an extension of the DAGH (Distributive Adaptive Grid Hierarchies) package by Parashar and Browne [145, 146] and is completely in C++. We call this level AMROC's DAGH. A complete redesign of parts of the DAGH package was necessary to allow the AMR algorithm like it was described in Secs. 5.2 and 5.3. AMROC's version of DAGH implements GridFunction- and GridHierarchy-classes that are much more general and allow a more efficient adaptation than those of the original DAGH package. The GridFunction-class of the original DAGH package is restricted to grids that are aligned to the base mesh coarsened by a factor of 2, i.e.

$$G^\star_{i,m} :=](2j-1)\Delta x_{1,0}, (2j+\mu^\star_1-1)\Delta x_{1,0}[\times](2k-1)\Delta x_{2,0}, (2k+\mu^\star_2-1)\Delta x_{2,0}[\ . \tag{5.27}$$

In general we have $G_i \subseteq G^\star_i$, but for $i > 0$ usually $G_i \subset G^\star_i$ is satisfied. Therefore, the original DAGH usually refines more cells than required. The restriction in DAGH

	$i_{\max}$	Level 0	Level 1	Level 2	Level 3	Level 4
AMROC's DAGH grids/cells	1	43/22500	145/38696			
	2	42/22500	110/48708	283/83688		
	3	36/22500	78/54796	245/109476	582/165784	
	4	41/22500	88/56404	233/123756	476/220540	1017/294828
Original DAGH grids/cells	1	238/22500	125/41312			
	2	494/22500	435/48832	190/105216		
	3	695/22500	650/55088	462/133696	185/297984	
	4	875/22500	822/57296	677/149952	428/349184	196/897024

Table 5.1: Refinement after the last time step of a typical test problem for four computations with an increasing number of refinement levels with AMROC's DAGH (lines 2 to 5) and the original DAGH (lines 6 to 9). $r_{1,2,3,4} = 2$.

follows from the simplifying assumption that two grids on neighboring levels only can be connected by an $1:1$ relation. A coarse grid may only have one child and a fine grid has exactly one parent. If this assumption is violated, the coarser level grids are split. Consequently, the maximal number of grids on all levels is equal. This reduces the recomposition overhead on higher levels, but leads to an increasing waste in advancing the numerical solution. As the entire computational time is usually dominated by the numerical update (especially in three space dimensions or with a detailed chemical reaction term) AMROC's DAGH is a significant improvement over the original package.

Fig. 5.14 displays the grids on a four-level solution of a typical non-reactive shock wave test problem used by AMROC's DAGH and the original DAGH. Tab. 5.1 shows the number of grids and cells for a uniform refinement factor of 2. All solutions have been computed with Hilbert's space-filling curve on 7 computing nodes. The simplification in DAGH does not fall into account, if only one or two refinement levels are used. But if a higher number of levels is necessary, the drastic improvement by allowing arbitrary AMR grids is apparent.

Additional new useful features in AMROC's DAGH are level-dependent refinement factors, multiple periodic boundary conditions, a restart option from memory for automatic time step algorithms and a restart feature for a variable number of computing nodes.

5.5.3 Comparison with Other Implementations

One of the few available parallel implementations of the AMR algorithm for distributed memory computers beside AMROC is Berkeley-Lab-AMR [153]. Both packages are implemented basically in C++, while computational expensive grid-dependent operations are written in Fortran. Berkeley-Lab-AMR involves approximately 50,000 lines of code (loc) [153], while AMROC currently consists of approximately $46,000$ loc plus approximately $6,000$ loc for visualization and data conver-

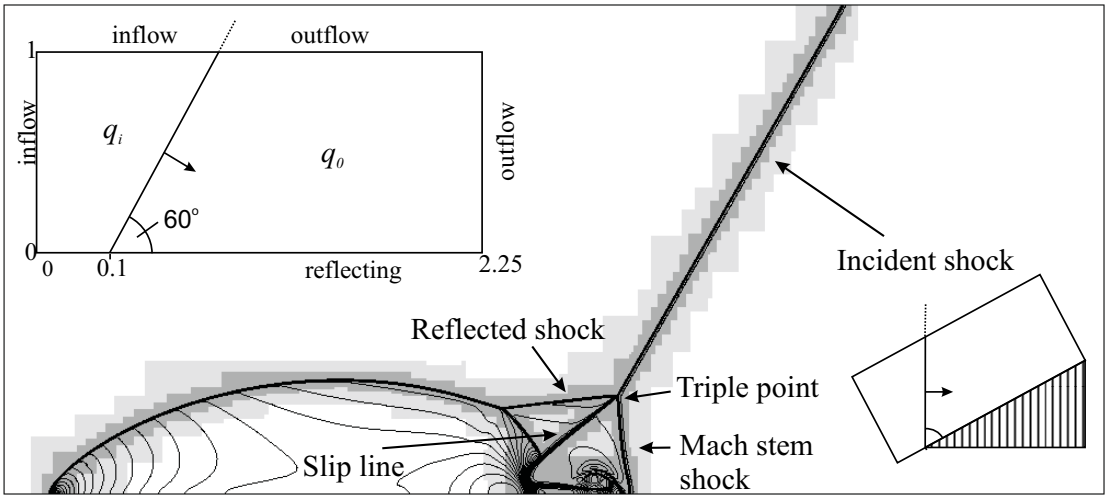

Figure 5.15: Mach reflection at a wedge. Adaptive solution with two levels of refinement with the Wave Propagation Method and MUSCL reconstruction. Isolines of ρ on refinement grids at $t = 0.09$. Left: grid extensions and boundary conditions.

sion.[5] Although both packages are written independently of the spatial dimension whenever possible, the drastic increase in complexity compared to the serial two-dimensional Fortran-77 code AMRClaw [22] with approximately $8,500$ loc due to the support of distributed memory machines is apparent.

5.6 Non-reactive Examples

We use two standard test problems in two space dimensions for non-reactive polytropic Euler equations to validate the AMR method and to measure the efficiency of the implementation. Both examples use the constant adiabatic coefficient $\gamma = 1.4$ which corresponds to air at room temperature and atmospheric pressure. Both calculations are done in dimension-less variables.

5.6.1 Mach Reflection at a Wedge

The first test (AMR Test 1) is the Mach reflection of a Mach-10 shock wave at a 30 degree wedge (compare lower left corner of Fig. 5.15). This well-known example was utilized in [205] to evaluate upwind schemes for standard Euler equations and was used by Berger and Collela to demonstrate the advantages of the AMR algorithm in [21]. We have selected it to allow a direct comparison on the one hand, but especially

[5] Approximately $21,000$ loc of the packages that the author of this thesis has combined to AMROC, in particular the $\approx 7,000$ loc that implement the parallel AMR method and also the $\approx 6,000$ loc for post-processing have been coded by himself and only just made the high quality results in this thesis possible.

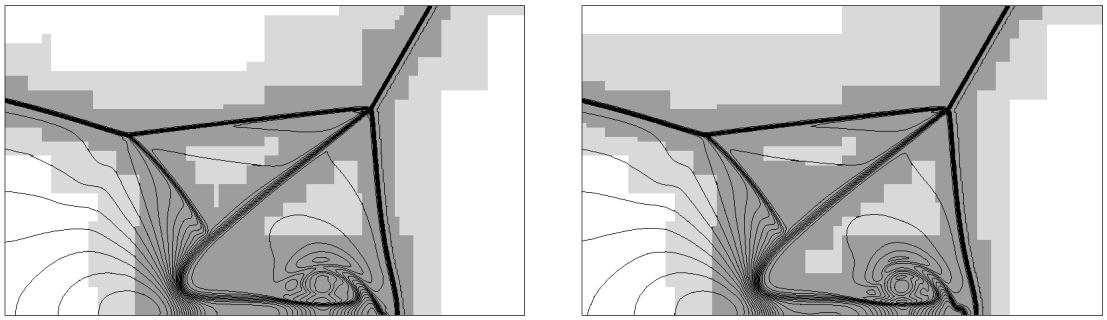

Figure 5.16: Comparison of the Wave Propagation Method with MUSCL extrapolation (left) and standard wave limiting (right).

to introduce the Mach reflection in the non-reactive case which will provide a sound base for Sec. 7.4.1, where the Mach reflection of a hydrogen-oxygen detonation will be studied.

The angle of 30° is too large to allow a regular reflection exactly in the point, where the incident shock hits the wall. Instead a Mach reflection occurs (see for instance [45] for details). The origin of the reflected shock lifts up from the surface and a third shock, the Mach stem, appears. Incident and reflected shock hit the Mach stem in a triple point. A contact discontinuity, the slip line, originates in the triple point and separates material passing through the Mach stem from that passing through incident and reflected shock (compare Fig. 5.15). The pressure behind the Mach stem is significantly higher than that of the incident shock.

Computational Setup and Initialization

In order to simulate a 30 degree wedge with a Cartesian code that does not allow the embedding of non-Cartesian internal walls we exploit the rotational invariance property of the two-dimensional Euler equations (compare Prop. 3) and rotate the surface of the wedge and the velocity vector of the incident shock by -30°. The values $\mathbf{q}_i$ of the incident shock are therefore $\rho_i = 1.0$, $p_i = 116.5$, $u_{1,i} = 8.25\cos(30^o)$, $u_{2,i} = -8.25\sin(30^o)$. It propagates with $M_s = 10.0$ into the region $\mathbf{q}_0$ with $\rho_0 = 1.4$, $p_0 = 1.0$, $u_{1,0} = 0.0$, $u_{2,0} = 0.0$.

The computational domain and the initial and boundary conditions are displayed in the upper left corner of Fig. 5.15. At $t = 0$ the incident shock crosses the lower boundary at $x_{1,l} = 0.1$ and the upper boundary at $x_{1,u} = 0.1 + \tan(30^o)$. The propagation speed in the x_1-direction is $M_s \cos(30^o)$. To avoid disturbances at the upper boundary a time-dependent boundary condition is applied here. All ghost cells left of the shock front are set to the inflow value $\mathbf{q}_i$; all ghost cells right of it are

	Level 0	Level 1	Level 2
Grids	26	42	96
Cells	27500	15572	109376

Table 5.2: Number of grids and cells of the adaptive solution in Fig. 5.15.

Task	P=1		P=2		P=4	
	s	%	s	%	s	%
Integration	3406	81.9	1607	68.2	803	56.6
Flux correction	176	4.2	107	4.5	106	7.5
Boundary setting	139	3.3	364	15.5	291	20.5
Recomposition	227	5.5	197	8.4	161	11.4
Clustering	116	2.8	31	1.3	16	1.1
Misc.	87	2.3	41	2.1	31	2.9
Total / Parallel Efficiency	**4150**	**100.0**	**2348**	**88.4**	**1409**	**73.7**

Table 5.3: Mach reflection at a wedge. Computational times on a PC-Cluster of Pentium III-850 MHz-PC's connected with Fast Ethernet. All timings have been calculated with the Wave Propagation Method utilizing the standard wave limiting (4.56) and the conservative fluctuation correction proposed in [22].

set by using transparent outflow boundary conditions.

We utilize a base grid of 250×110 cells and calculate 262 time steps with intended Courant number $CFL_{CFL}^{Roe} \approx 0.8$ to $t_{end} = 0.09$. A two-level refinement with the factors $r_1 = 2$ and $r_2 = 4$ is employed which corresponds to a uniform grid of 2000×880 cells (1.76 M). The refinement criteria are only applied to the total density ρ. For (5.20) we apply $\epsilon_\rho = 0.4$ and for (5.25) we use $\eta_\rho = 0.1$.

For this example, we employ the two-dimensional Wave Propagation Method (4.58) and the Roe scheme of Sec. 4.6.1 with Harten-Hyman entropy fix for a single polytropic gas. As the fluctuation formulation of the Wave Propagation Method is not directly compatible to the conservative flux correction of Sec. 5.2.3, we recommend to utilize Eq. (4.39) to transform the final fluctuations into numerical fluxes and to calculate the correction terms as usual (compare last paragraph of Sec. 4.7.2). Note, that Eq. (4.39) is only applicable to hyperbolic equations in conservation-law form (2.1). A formulation of the conservative correction in terms of the fluctuations that is applicable also to quasi-linear hyperbolic equations has been proposed by Berger and LeVeque in [22], but it requires the solution of additional RPs and introduces unneccesary overhead for systems in conservation-law form, like the Euler equations.

Benchmark Computations

To allow a direct comparison to the popular AMRClaw code we use the special fluctuation correction in [22] and the standard wave-by-wave limiting (see Sec. 4.3.2) for the benchmark computations of Tab. 5.3. But the results with MUSCL-Hancock extrapolation in conservative variables as proposed in Sec. 4.7.2 are nearly identical. Fig. 5.16 displays a comparison between the adaptive solutions with both techniques and Minmod-limiter. It seems that the MUSCL approach gives even slightly better results than the standard wave-by-wave limiting technique (compare isolines near the lower boundary). With both variants the differences between adaptive and

corresponding uniform solution are negligible. The Figs. 5.15 and 5.16 illustrate that all relevant discontinuities are perfectly refined and that no artificial kinks appear at the level boundaries.[6]

A standard PC-Cluster of Pentium-III-850 MHz CPUs connected with 100 MHz-Fast Ethernet has been used for the benchmark calculations. Like in all computations throughout this thesis the executables were generated with the highest optimization level possible. While the run with a uniform mesh would require ≈ 29 h on one node, the AMROC computation achieves a solution of similar quality in about 69 min. With four symmetric parallel nodes the computational time decreases to less than 23.5 min. The two-dimensional single-processor code AMRClaw of Berger and LeVeque [22], which is written completely in Fortran-77, solves the problem with the same implementation of the numerical scheme and a nearly identical refinement in about 58 min. The speed-up is only moderate, which underlines the high quality of the C++ implementation of the parallel and multi-dimensional AMROC code.

Tab. 5.3 shows a breakdown of the computational time for the most important AMR operations in AMROC. For one node the fractions spent in different parts of the code are in good agreements with the results in [21]. For two-dimensional standard Euler equations 70% to 80% of the computational time are used for numerical integration. Typical for AMR computations is that this portion scales up perfectly in parallel, while the overhead for the ghost cell setting, especially on the highest level, increases continuously. On one node only the interpolation at the fine boundaries is expensive, but in parallel the synchronization overhead becomes dominant. It takes more than 90 % of the time for the boundary setting.

5.6.2 Shock Wave Diffraction

The second test (AMR Test 2) is the diffraction of a Mach-1.5 shock wave over a 90 degree sharp corner in three space dimensions. It has been inspired by a planar standard test case, which has been studied extensively in the past [184]. The example introduces the basic hydrodynamic structure of diffracting shock waves (see also Sec. 7.4.2, where diffracting detonation waves are studied) and demonstrates the parallel domain decomposition strategy developed in Sec. 5.3.1 in combination with a generalization of Hilbert's space filling curve as a partitioner (see Sec. 5.3.4).

An incident shock wave propagating out of confinement into an unconfined region is diffracted due to the area increase. The diffraction emanates from the boundary and weakens the incident shock continuously. The right picture of Fig. 5.17 displays a snapshot, where the diffraction has not affected the whole incident shock wave yet. The shock is separated into an incident shock wave with still unmodified flow values and the diffracted shock with continuously decreasing pressure and density values toward the left boundary. An expanding rarefaction wave occurs behind the

[6]This would not be the case, if a relevant discontinuity would leave the highest level during the simulation. The interpolation at level borders can cause an excessive smearing of strong discontinuities that can corrupt the results drastically. This problem is discussed in detail in [21]. Strong discontinuities always have to remain in the highest level of refinement.

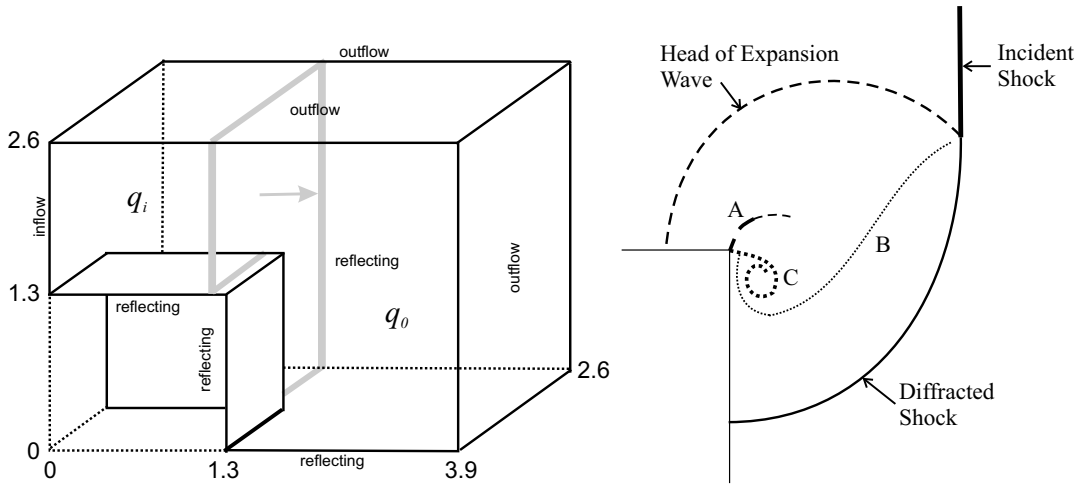

Figure 5.17: Shock wave diffraction over a 90 degree corner in three space dimensions. Left: grid extensions and boundary conditions, right: main flow features.

diffracted shock wave. It propagates backward into the post-shock region. In Fig. 5.17 the actual upstream boundary of this expansion wave is plotted. The isolines of the expansion wave merge along the line A exactly in the corner. The parts of the flow field processed by diffracting and incident shock wave are separated by the weak contact discontinuity B. A stronger contact discontinuity C with a characteristic vortex originates in the corner.

A more detailed description of the entire phenomenon that also includes minor flow features has been given by Hillier [93].

Basic Setup and Initialization

The computational domain and the boundary conditions are displayed in the left picture of Fig. 5.17. We normalize all flow values with respect to $\mathbf{q}_0$. The values $\mathbf{q}_i$ of the incident shock are $\rho_i = 1.862$, $p_i = 2.4583$, $u_{1,i} = 0.8216$, $u_{2,i} = 0.0$, $u_{3,i} = 0.0$. The normalized values ahead of the shock are $\rho_0 = 1.0$, $p_0 = 1.0$, $u_{1,0} = 0.0$, $u_{2,0} = 0.0$, $u_{3,0} = 0.0$. Initially, the incident shock is placed at $x_1 = 1.25$.

We employ the Roe scheme of Sec. 4.6.1 for a single polytropic gas in combination with the MUSCL-Hancock method of Sec. 4.3.1 with a reconstruction in conservative quantities and Van Albada-limiter. The Godunov dimensional splitting $\mathbf{Q}^{l+1} = \mathcal{X}_3^{(\Delta t)}\mathcal{X}_2^{(\Delta t)}\mathcal{X}_1^{(\Delta t)}(\mathbf{Q}^l)$ is applied. Note, that the usage of dimensional splitting within a domain decomposition strategy requires the synchronization of the ghost cells after *each* dimensional step $\mathcal{X}_n^{(\Delta t)}$. Note further, that near the internal corner $(1.3, 1.3, 1.3)$ ambiguous ghost cells have to be considered. The correct application of fixed wall boundary conditions requires a re-setting of the values of these ghost cells with respect to the next dimensional step.

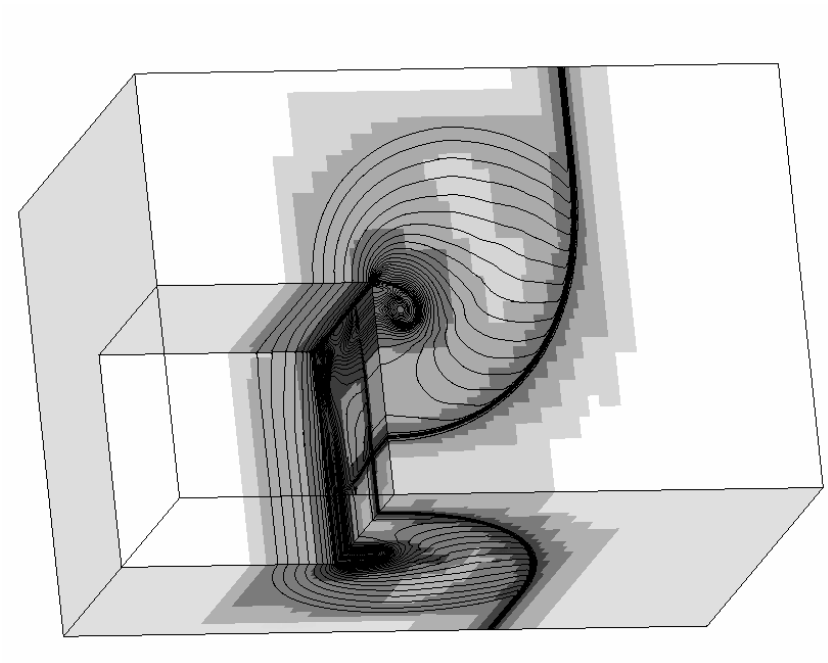

Figure 5.18: Isolines of the density at $\Delta\rho = 0.04\,\rho_0$ on refinement grids at $t_{end} = 0.75$.

Parallel Adaptive Computation

We utilize a base grid of $60 \times 40 \times 40$ cells and calculate 36 time steps with intended Courant number $C_{CFL}^{Roe} \approx 0.95$ to $t_{end} = 0.75$. A three-level adaptation with constant refinement factors $r_{1,2,3} = 2$ is used, which corresponds to a uniform grid of 49.15 M cells. The refinement criteria for (5.20) are $\epsilon_\rho = 0.2$ and $\epsilon_{\bar{E}} = 0.15$. This setting achieves a complete adaptation of the expanding shock wave and the strong discontinuity C, but avoids the refinement of the entire expansion wave. Only line A is contained in level 3 and the weak discontinuity B is not considered. The adaptation displayed in Fig. 5.18 is in principle in good agreement with the two-dimensional adapted grids considered in [184].

During the adaptive simulation the total number of cells increases continuously from 1.55 M at $t = 0$ to 6.14 M at t_{end}. The computation required ≈ 4.1 h on a PC-Cluster of eight Pentium-III-850 MHz double-processor machines connected with 1 GHz Myrinet. The successive improvement of the numerical solution by adaptation and the distribution to the 16 processors involved is visualized in Fig. A.30. The right column of Fig. A.30 demonstrates our parallel domain decomposition technique in practice. The affiliation of subgrids to the processors is indicated by color. It is obvious, that the distribution of grids on levels $i > 0$ is determined by the grids on level 0. Further on, Fig. A.30 shows that the domains G_0^p generated by a generalized space filling curve are mostly connected and have a relatively small surface. Although they vary remarkably in geometric size, the overall computational

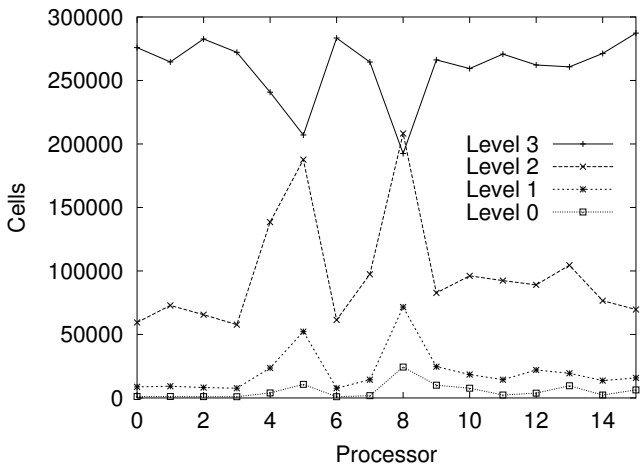

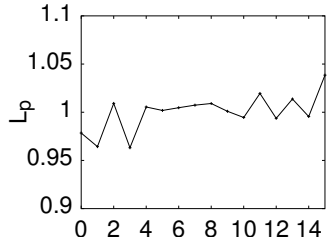

i	Grids	Cells
0	96	88000
1	117	331480
2	316	1559824
3	649	4161432

Figure 5.19: Decomposition of the AMR hierarchy at $t_{end} = 0.75$ to 16 computing nodes. Left: cells on each level. Right, top: workload according to Eq. (5.19) on each node. Right, bottom: total number of grids and cells.

work is nearly equally distributed among the different nodes. The left graphic of Fig. 5.19 displays the number of cells per processor on each level and the large variation, especially on level 2, is apparent. Nevertheless, the current workload estimations according to Eq. (5.19) in the right plot of Fig. 5.19 vary only in a range of less than 4%, which guarantees that the work in advancing the numerical solution will be nearly equally distributed in the next time step Δt_0.

5.7 Reactive flows

We use the method of fractional steps (compare Sec. 4.1.3) to incorporate source terms into the parallel AMR algorithm. In case of multi-component Euler equations with reaction term (2.78), the conservative flux correction of Sec. 5.2.3 then ensures the conservation of total density ρ, momentum densities m_n and total energy density $\bar{E}$.

As the numerical integration of the source term is only a cell-wise operation, the extension to inhomogeneous equations is a straight-forward task. Only the grid-based implementation of the numerical scheme has to be extended. For the Godunov splitting (4.19) the grid-based update in `UpdateLevel(`i`)` simply reads

$$\mathbf{Q}(G^s_{i,m}, t)\ , \mathbf{F}^n(\bar{G}_{i,m}, t) \stackrel{\mathcal{H}^{(\Delta t_i)}}{\longrightarrow} \tilde{\mathbf{Q}}(G_{i,m}, t + \Delta t_i)$$
$$\tilde{\mathbf{Q}}(G_{i,m}, t + \Delta t_i) \stackrel{\mathcal{S}^{(\Delta t_i)}}{\longrightarrow} \mathbf{Q}(G_{i,m}, t + \Delta t_i) \quad ,$$

while the Strang splitting (4.20) requires the integration of the source term over the

extended domain $G^s_{i,m}$ in the first step to avoid an additional ghost cell synchronization before the transport step, i.e.

$$\begin{aligned}
&\mathbf{Q}(G^s_{i,m},t) \overset{\mathcal{S}^{(\frac{1}{2}\Delta t_i)}}{\longrightarrow} \tilde{\mathbf{Q}}(G^s_{i,m},t) \\
&\tilde{\mathbf{Q}}(G^s_{i,m},t)\ ,\mathbf{F}^n(\bar{G}_{i,m},t) \overset{\mathcal{H}^{(\Delta t_i)}}{\longrightarrow} \tilde{\mathbf{Q}}(G_{i,m},t+\Delta t_i) \\
&\tilde{\mathbf{Q}}(G_{i,m},t+\Delta t_i) \overset{\mathcal{S}^{(\frac{1}{2}\Delta t_i)}}{\longrightarrow} \mathbf{Q}(G_{i,m},t+\Delta t_i) \quad .
\end{aligned}$$

In a flexible framework the operators $\mathcal{H}^{(\cdot)}$ and $\mathcal{S}^{(\cdot)}$ should be implemented in separate functions (compare `step()` and `src()` in Fig. 5.13).

Finally, a minor extension of the averaging and interpolation operators can be necessary in combination with the temperature computation strategy described in Sec. 4.4.2. As the dependence of T on $\mathbf{Q}$ is usually nonlinear, the actual temperature value has to re-computed in all cells modified by the level-transfer operators.

Chapter 6

Validation with Simplified Chemistry

In this chapter we validate the numerical methods that have been derived in the Chaps. 4 and 5 by detonation simulations with the simplified Arrhenius kinetics introduced in Sec. 3.1.1. A suitable numerical method for detonation simulation should capture detonation waves correctly at smallest resolutions (compare Chap. 1). Although dynamic adaptive mesh refinement can moderate the expense of detonation calculations significantly, the application of a suitable high resolution scheme is essential for the efficiency of a computation. All calculations in this chapter are carried out in normalized quantities according to (3.18) and under the length normalization (3.20).

In Sec. 6.1 a stable and an unstable overdriven one-dimensional detonation close to the limit of absolute stability are considered. It is demonstrated that the solution can be corrupted significantly due to artificial oscillations similar to those observed at slowly moving strong shock waves in Sec. 4.8.2. We demonstrate that the problem can be cured within the Roe scheme by adding numerical viscosity via the entropy fix. Further on, we show the enormous resolution improvements by second-order reconstruction and by utilizing quasi-stationary detonation configurations, whenever possible.

In Sec. 6.2 two-dimensional cellular structures of overdriven detonations are simulated. The results underline the superiority of the hybrid Roe-type method of Sec. 4.6.3 over all tested scheme especially in the multi-dimensional case. The last section of this chapter presents large-scale adaptive computations of the cellular structure for one of the overdriven configurations of Sec. 6.2. The results verify the correctness and high efficiency of the parallel AMR algorithm developed throughout the previous chapter.

6.1 Planar Detonation Structure

For the one-dimensional calculations with the simplified ZND model we always utilize the parameters $\gamma = 1.2$, $E_0^\star = 50$, $Q_0 = 50$ that are typical for a wide range of

real gaseous systems. The overdrive factor f is varied. The computational domain always has the length 400. The exact ZND solution of Sec. 3.1.1 is used as initial condition, but all velocities are shifted by $-D$. Therefore the velocity ahead of the detonation is $-D$, while downstream of the detonation front it is $-\grave{U}$. Due to this transformation the detonation front remains quasi-stationary at its initial position, which we set to 395. Constant in- and outflow boundary conditions are applied at the right and the left side. A relatively large domain is necessary to avoid that disturbances generated at the outflow boundary reach the detonation front before the simulation is stopped.[1]

The basic numerical method of the one- and two-dimensional computations in this chapter is the second-order accurate fractional step method of Strang (4.20). The ODE of the mass fraction of product B due to chemical reaction

$$\frac{dZ}{dt} = L_{1/2}(1-Z)\exp\left(\frac{-E_0^\star}{PV}\right) = L_{1/2}(1-Z)\exp\left(\frac{-E_0^\star}{T}\right) \tag{6.1}$$

is integrated with an explicit standard fourth-order accurate Runge-Kutta method nearly to machine accuracy (compare Sec. 4.10.1). Some authors [35, 122] solved Eq. (6.1) exactly under the assumption of constant T, i.e.

$$Z(t) = 1 - (1 - Z(t_0))\exp\left(-L_{1/2}\exp(-E_0^\star/T)t\right) \ ,$$

but this simplification is not possible, if detailed reactive source terms with stiff non-equilibrium chemistry have to be considered. As we are interested especially in numerical methods suitable for this general case, we do not use this simplification, which would lead to slightly, but not essentially, different numerical results.

Following [35, 122, 95, 144] we plot the temporal development of the von Neumann pressure, the pressure directly at the head of the detonation front. Note, that the front pressure is identical to the maximal pressure over the entire domain only for stable and moderately unstable detonation waves. If the oscillations are large, the von Neumann pressure can drop below the global maximum. Fig. 6.1 illustrates this effect, which is called *clipping* [95].

6.1.1 Validation of Upwind Schemes

In order to test different FV upwind schemes within the fractional step method, we employ the two one-dimensional detonation test problems for $\gamma = 1.2$, $E_0^\star = 50$, $Q_0 = 50$ proposed by Fickett and Wood [74] that also have been utilized frequently to evaluate numerical schemes [35, 151, 122, 95, 144].

The two test cases are $f = 1.8$ (ZND Test 1) and $f = 1.6$ (ZND Test 2). It was noted in Sec. 3.2 that the ZND detonation is stable for $f = 1.8$ and has one

[1] An approximation to the upstream signal speed of these disturbances is $-\grave{U}(Z = 1) + C(Z = 1)$. A detailed discussion of the minimal computational domain size necessary to suppress any interactions with the left boundary completely in case of a detonation traveling with velocity D can be found in [95].

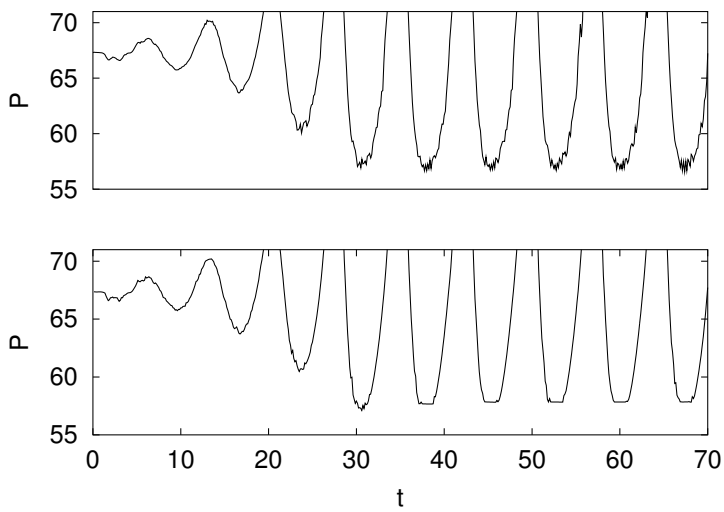

Figure 6.1: Difference between von Neumann pressure (top) and global pressure maximum (bottom) for $\gamma = 1.2$, $E_0^\star = 50$, $Q_0 = 50$, $f = 1.6$.

unstable mode for $f = 1.6$. Both test cases are sufficiently far away from the limit of absolute stability $f_0^\star = 1.73$ so we can expect that suitable schemes should reproduce the qualitative correct behavior of the detonation wave at moderate resolutions. The test resolutions are 5, 10 and 20 finite volumes (Pts) per half reaction length $L_{1/2}$. The FV upwind schemes are varied. The schemes to be tested are the Flux-Vector Splittings of Steger-Warming (Sec. 4.5.1) and Van Leer (Sec. 4.5.2) and the Godunov-type methods with the approximate Riemann solvers of Harten-Lax-Van Leer (HLL) (Sec. 4.6.4) and Roe (Sec. 4.6.1). The Roe scheme is implemented with enforced mass fraction positivity and entropy enforcement EF 3 (Roe EF 3: steps (S1) to (S7), (S10a), (S11) of Algorithm 1) or with Harten-Hymann entropy correction (Roe HH: steps (S1) to (S7), (S10b), (S11) of Algorithm 1). Further on, Godunov's Method with exact Riemann solver is used for comparisons [187].[2]

6.1.2 Stable ZND Detonation

The ZND detonation with parameters $\gamma = 1.2$, $E_0^\star = 50$, $Q_0 = 50$, $f = 1.8$ is stable. A stationary flow approximation depending on the resolution of the grid should be produced by any suitable scheme. First, we test the applicability of the different upwind schemes to detonation waves in general and do not employ the

[2]All upwind schemes that have been developed originally for the standard case of a single polytropic gas can easily be extended to the simplified ZND model, because in this model γ is assumed to be constant. In particular, derivations of exact Riemann solvers carry over immediately, only the slightly different equation of state (3.1) and a further advection equation for Z have to be considered. See [187] for the exact Riemann solver that has been employed here for comparisons. A complete derivation of an exact Riemann solver for the simplified detonation model can be found in the thesis of Helzel [92].

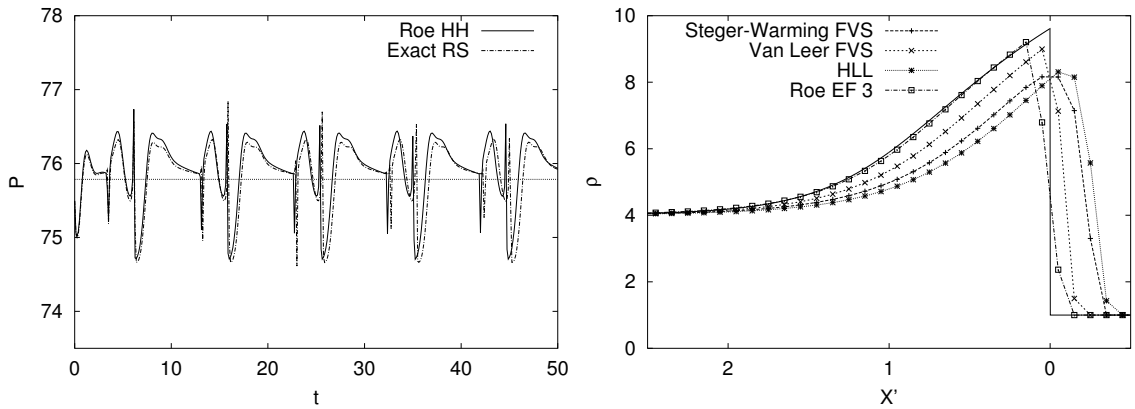

Figure 6.2: First-order results of ZND Test 1. Left: unphysical oscillation of the front pressure with Roe HH and the Godunonv's Method. Right: density distributions of stable approximations to the detonation front at $t_{end} = 50$. $10\,\mathrm{Pts}/L_{1/2}$.

MUSCL-Hancock method. All computations end at $t_{end} = 50$. Automatic time-step adjustment based on an intended Courant number of $C_{CFL} \approx 0.9$ is used.

Comparison of the Results with Different Upwind Schemes

The results of the considered upwind methods differ remarkably. No stable approximation is obtained with the upwind schemes with the smallest numerical viscosity, the Roe scheme with Harten-Hyman entropy correction (Roe HH) and Godunov's Method (Exact RS) (see left picture in Fig. 6.2). The other tested upwind schemes reproduce the stable solution, but as the grid is refined (and the numerical viscosity decreases) the time necessary to obtain a constant solution enlarges (compare Fig. A.1). The right picture of Fig. 6.2 compares the stationary approximations at $t_{end} = 50$ to the exact solution of Fig. 3.3, which is plotted into Fig. 6.2 with the full line without any dots. It is obvious, that the HLL scheme gives the worst result. The detonation front is smeared over three computational cells and the pressure maximum of the approximation is clearly ahead of the exact solution. For $20\,\mathrm{Pts}/L_{1/2}$ the HLL scheme still gives an oscillating solution at t_{end} (see Fig. A.1). The Steger-Warming FVS gives the second worst approximation. The front is smeared over three cells, but the pressure maximum is much closer to the exact maximum than with HLL and the remaining oscillation at t_{end} for $20\,\mathrm{Pts}/L_{1/2}$ is smaller. Van Leer FVS gives a significantly better approximation. A stationary result is obtained for all three test resolutions. The detonation front is sharply represented within two computational cells and the pressure maximum is near to the maximum of the exact solution. But the approximation of the smooth reaction region is still poor. The Roe scheme with entropy enforcement 3 gives a better result here. Roe EF 3 approximates the reaction region well, needs only two cells to capture the detonation front and reproduces the pressure maximum one cell behind the exact solution. In order

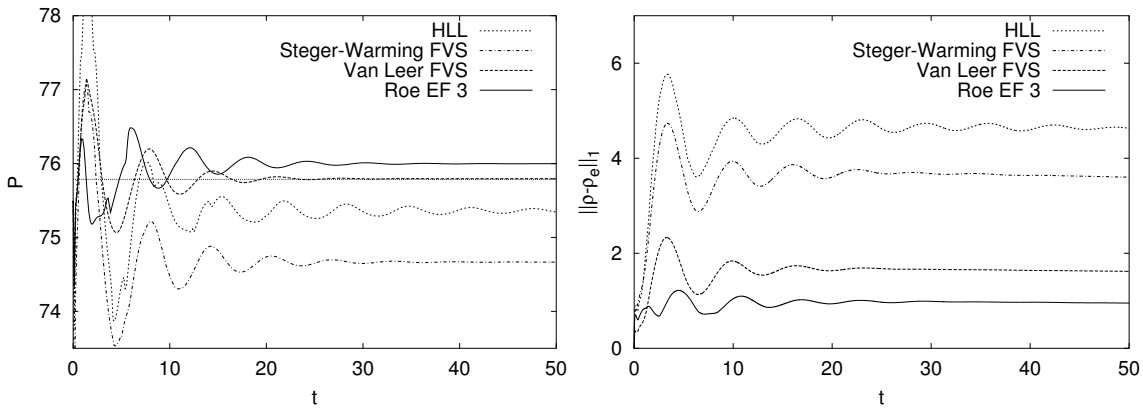

Figure 6.3: First-order results of ZND Test 1. Left: front pressure histories. The dotted line at $P \approx 75.79$ corresponds to the exact ZND value. Right: L^1-norm of the density. $10\,\mathrm{Pts}/L_{1/2}$.

to quantify exactly the quality of the different upwind schemes Fig. 6.3 displays the temporal development of the front pressure (left picture) and the error in the density computed in the L^1-norm (4.6) against the exact solution (right picture). The smallest error is achieved by Roe EF 3. The error norm with Van Leer FVS is larger, but this scheme gives the best approximation to the stationary front pressure and achieves a stationary solution at all test resolutions in the shortest time.

The Roe HH scheme and Godunov's Method show a complex, but regular pattern of non-decreasing oscillations in the von Neumann pressure (see left picture in Fig. 6.2). The error in the L^1-norm increases continuously as these unphysical oscillations are transported downstream and affect the solution on the entire domain (not displayed). Apparently, these two upwind schemes introduce a numerical instability into the fractional step method and it fails to compute a stable solution profile at all test resolutions (compare Fig. A.1). In particular, even the choice of smaller intended Courant numbers (and therefore smaller time-steps) hardly affects the result (see left picture of Fig. 6.4 for an exemplary time resolution study for Godunov's Method).

Explanation for the Failure of Accurate Riemann Solvers

In Sec. 4.8.2 we studied the applicability of the different upwind schemes to slowly moving strong shocks. Roe HH and Godunov's Method were found to produce large oscillations, while all other schemes gave significant better results. The smallest oscillations were generated by Roe EF 3. This qualitative behavior is reproduced exactly in our quasi-stationary detonation simulations, because the occurrence of a slowly moving strong shock wave will usually be unavoidable.

In a fractional step method the inhomogeneous equations are decomposed in a homogeneous transport step and a reaction step. As illustrated in Sec. 4.8.2 the

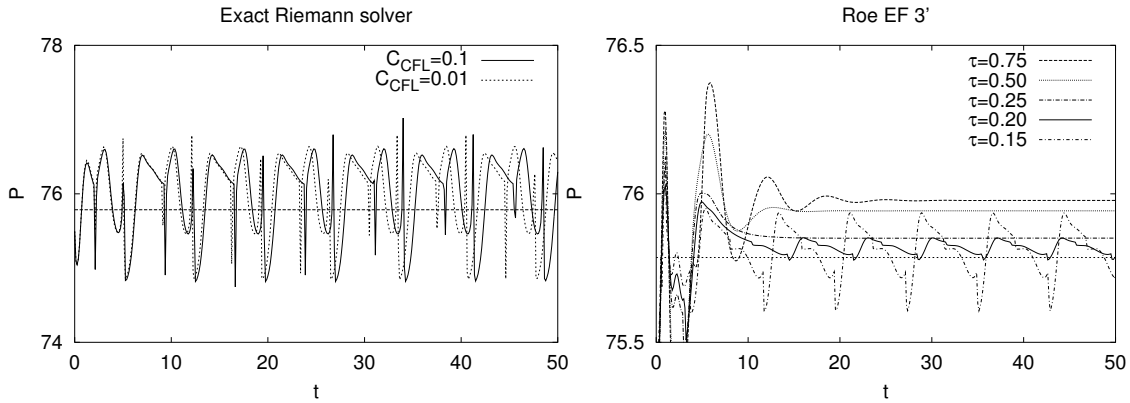

Figure 6.4: Numerical tests for ZND Test 1. Left: variation of C_{CFL} for Godunov's Method. Right: Roe EF 3' with variation of τ in (6.2). $10\,\mathrm{Pts}/L_{1/2}$

solution of the homogeneous RP at the head of a stationary ZND detonation should be an isolated shock wave solution with zero propagation velocity. Such a simple wave solution would be reproduced exactly by the accurate Riemann solvers and they consequently would require initial values for a homogeneous RP that has the sought stationary shock as exact solution. Analogously to the explanation given in Sec. 4.8.2 the approximated value at the detonation front $\mathbf{q}^\star$ and the value in the unburned region $\mathbf{q}_R$ that make up this RP have to reside on the Hugoniot curve of a single shock wave with zero velocity. This strong requirement will usually not be fulfilled after an integration step with a nonlinear source term. Hence, the homogeneous RP does not have the required simple wave solution, but involves a strong shock wave with usually not vanishing propagation velocity. As explained in Sec. 4.8.2 the approximation of this slowly moving strong shock introduces minor oscillations that are not damped by the Riemann solvers with minimal numerical viscosity. Consequently, they fail in approximating a qualitatively correct solution near the limit of absolute stability. For overdrive factors far away from $f_0^\star$ the source term dominates the computations and the oscillations introduced by these Riemann solvers also become negligible.

The Influence of Numerical Viscosity on the Solution of the Roe Scheme

In order to demonstrate the dependence of the approximation on the numerical viscosity of the upwind schemes we utilize a linear convex-combination of Eq. (4.91) and $|\bar{\lambda}_m(\hat{\mathbf{q}})|$ instead of Eq. (4.91) in Roe EF 3, i.e.

$$\text{EF 3'} : |\bar{\lambda}_m| = \begin{cases} |\lambda_m(\hat{\mathbf{q}})| \,, & \text{if} |\lambda_m(\hat{\mathbf{q}})| \geq 2\eta \,, \\ \tau(|\lambda_m(\hat{\mathbf{q}})^2|/4\eta + \eta) + (1-\tau)|\lambda_m(\hat{\mathbf{q}})| \,, & \text{otherwise} \,, \end{cases} \tag{6.2}$$

which is identical to EF 3 for $\tau = 1$ and does not add any numerical viscosity to shocks for $\tau = 0$, like the Harten-Hyman entropy fix (Roe HH). The results of

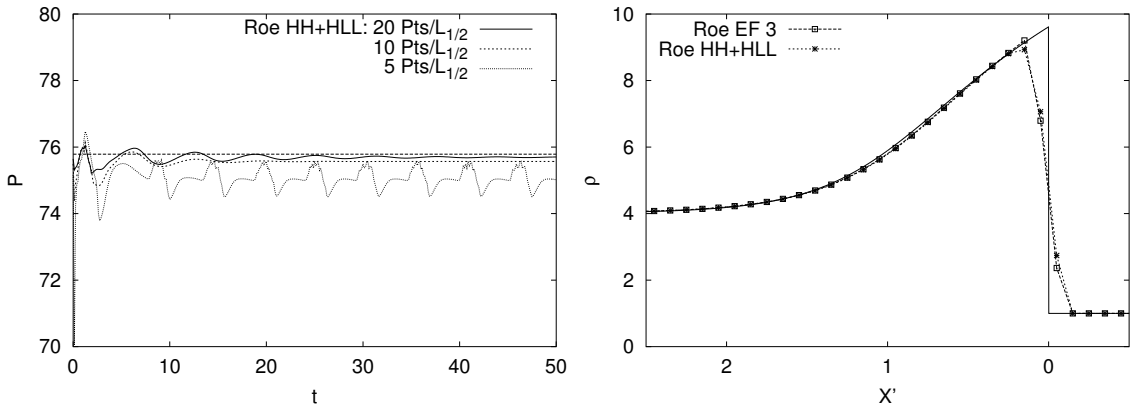

Figure 6.5: Numerical test for ZND Test 1 with the Roe HH-HLL hybrid scheme. Left: front pressure histories for Roe HH-HLL. Right: density distribution at $t_{end} = 50$ for compared to Roe EF 3. $10\,\mathrm{Pts}/L_{1/2}$, the full line is the exact solution of Fig. 3.3.

this study are displayed in the right picture of Fig. 6.4. It is obvious, that EF 3 adds more numerical viscosity than it is required to stabilize the solution, while the numerical instability becomes more and more dominant as τ approaches 0. For the particular configuration studied an optimal choice seems to be $\tau \approx 0.25$.

Another empirical method to add numerical viscosity directly at the detonation front would be to switch only here from Roe HH or the exact Riemann solver to a more viscous scheme like HLL. When using the Roe scheme this switching can easily be accomplished by monitoring the wave strength of the last genuinely nonlinear field. In Fig. 6.5 numerical results for such a hybrid variant of Roe HH are displayed. The heuristic switching criterion is $|a_{K+d+1}| > 1$. In every time-step, this criterion enforces the usage of the HLL flux at the three cell-interfaces near the leading shock wave. Stable results are obtained with this technique, but the approximation is worse than with Roe EF 3 (compare left picture of Fig. 6.4). This is not surprising, because HLL is more viscous than Roe EF 3 and we already have seen in the preceding numerical analysis that even Roe EF 3 adds more numerical viscosity than necessary.

6.1.3 Unstable ZND Detonation

The overdrive factor $f = 1.6$ is below the limit of absolute stability and the ZND detonation has one unstable mode. After an initial period, the flow pattern of the numerical results should change regularly and clearly defined oscillations should travel downstream. A reference solution at high resolution is displayed in Fig. 6.6. The left graph shows the regular oscillating front pressure over time, while the right one displays the pressure distribution in the whole computational domain at $t = 70$. For $t > 40$ the oscillation is very regular.

Like in the preceding section, we test the six different upwind schemes by first-

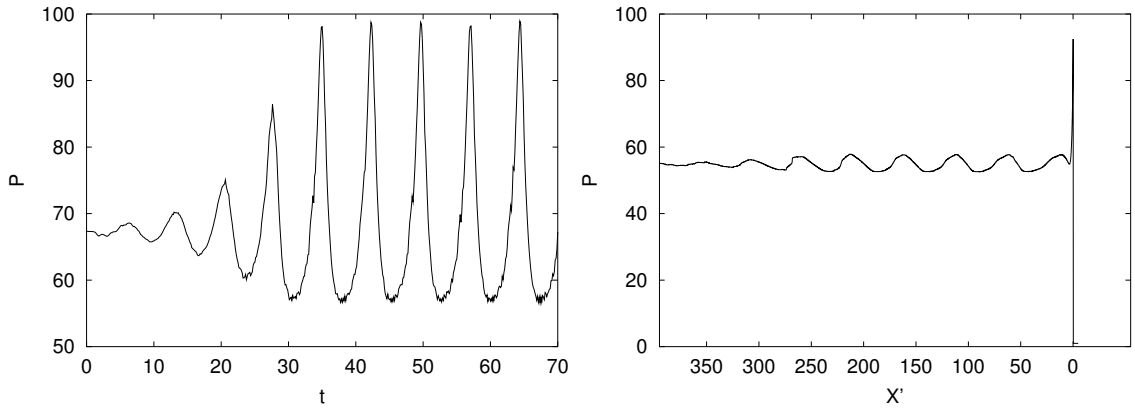

Figure 6.6: Reference solution for ZND test 2. Left: temporal development of front pressure. Right: pressure distribution at $t = 70$. The instability at the front creates regular pressure waves in the downstream direction.

order computations. All simulations end at $t_{end} = 50$, when the instability should be clearly established. Automatic time step adjustment based on a Courant number $C_{CFL} \approx 0.9$ is used. The front pressure histories for all upwind schemes applied to this test (ZND Test 2) are displayed in Fig. A.2. All upwind schemes show a behavior similar to ZND Test 1. Roe HH and Godunov's Method fail in approximating a qualitatively correct instability. Once again, the physically correct behavior is suppressed at all test resolutions by the numerical instability that has already been observed in ZND Test 1. Like in the preceding test, the best results are obtained with Van Leer FVS and Roe EF 3. Both schemes reproduce the unstable behavior with $10\,\mathrm{Pts}/L_{1/2}$, but like in ZND Test 1 Van Leer FVS gives a better approximation to the peak pressure. The worst physically reasonable results are obtained with Steger-Warming FVS and HLL, which reproduce the instability only at the highest test resolution.

6.1.4 Second-order Accuracy

In order to increase the accuracy of the results the second-order accurate MUSCL-Hancock method of Sec. 4.3 is applied. Following Sec. 4.7.1 the total density, the momentum density, the energy density and the mass fractions Z, $1 - Z$ are extrapolated, where the limiter value for the mass fractions is computed by Eq. (4.101). We repeat ZND Test 1 and apply the Minmod-limiter (4.49) in all computations. A sharper representation of the detonation front is obtained with all upwind schemes (compare the left picture of Fig. 6.7 to the right picture of Fig. 6.2), but the front is captured now one cell to the left. In perfect agreement with the second-order results of Sec. 4.8.2 all schemes show larger oscillations in the front pressure than in Sec. 6.1.2 (compare Fig. A.3). As it can be expected from of Sec. 4.8.2, the numerical instability observed for Roe HH and Godunov's Method in the first-order

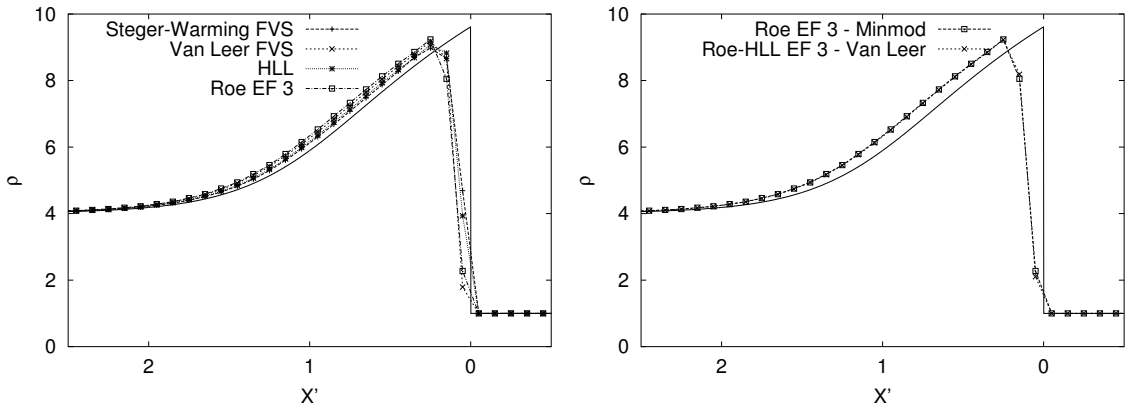

Figure 6.7: Density distributions of second-order results of ZND Test 1 at $t_{end} = 50$, $10\,\mathrm{Pts}/L_{1/2}$, the full line is the exact solution of Fig. 3.3. Left: Minmod-limiter. Right: comparison of the robust Roe-HLL EF 3 with Van Leer-limiter and Roe EF 3 with Minmod-limiter.

test is amplified. Also Van Leer FVS shows a small oscillation for $10\,\mathrm{Pts}/L_{1/2}$ that indicates that the scheme does not harmonize perfectly with the MUSCL approach for these kind of problems. Like in Sec. 4.8.2 the Roe EF 3 scheme seems to be superior in combination with MUSCL. Fig. A.3 shows that Roe EF 3 achieves the smallest front pressure variations at t_{end} at all resolutions.

For both ZND tests the Roe schemes and Steger-Warming FVS only work with Minmod. For other limiters with a sharper discontinuity reconstruction (see Sec. 4.3.1) unphysical cell values occur that terminate the calculations after a few time-steps (compare Sec. 4.8.1). In case of the Roe scheme, the reason for this behavior is that the Roe linearization becomes unphysical for the first extrapolated RP directly at the head of the detonation front. We therefore recommend to include the steps (S8), (S9) of Algorithm 1 into Roe EF 3. We denote this robust variant, which consists of the steps (S1) to (S9), (S10a), (S11) of Algorithm 1, by Roe-HLL EF 3. Roe-HLL EF 3 gives a reliable result with every slope limiter. The right picture of Fig. 6.7 shows that the resolution of the detonation front can be improved further, if Roe-HLL EF 3 is used together for instance with the Van Leer-limiter (4.51). For this limiter, Roe-HLL EF 3 switches to HLL nearly in every time-step, but the application of HLL is restricted to the single cell interface abutting the unburned gas region. Hardly any switching to HLL occurs with Minmod. No usage of HLL has been observed in all first-order computations.

A drastic improvement of the first-order results for Steger-Warming and Van Leer FVS, HLL and Roe-HLL EF 3 can be achieved, if the MUSCL-Hancock method is applied to ZND Test 2 (compare Fig. A.4). The schemes that allow the Van Leer-limiter now reproduce the instability at all test resolutions. For resolutions $\geq 10\,\mathrm{Pts}/L_{1/2}$ a very regular oscillation is visible for $t > 40$. To quantify the approximation quality exactly we follow Quirk [151] and Hwang, Fedkiw et al. [95]

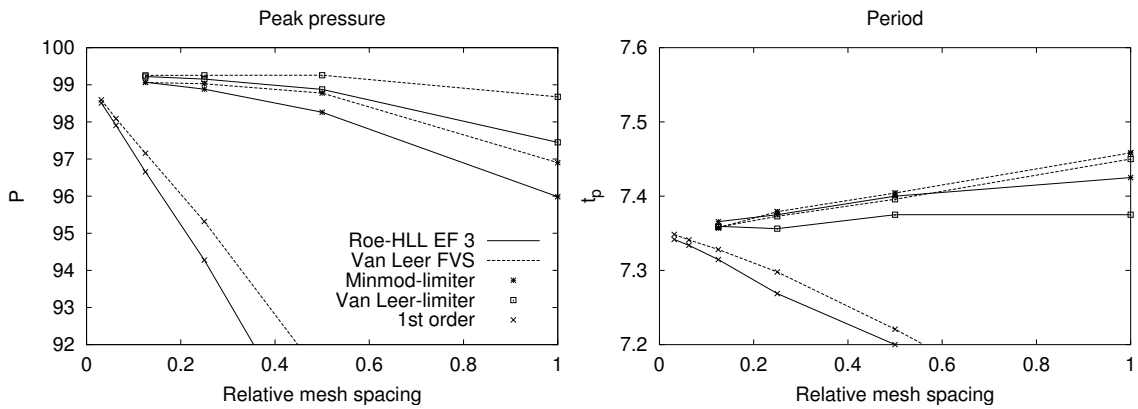

Figure 6.8: First and second-order results for Roe-HLL EF 3 and Van Leer FVS for ZND Test 2. Left: peak pressure. Right: period of time between successive pressure peaks. Averaged values over the time interval $[70, 100]$ are displayed.

and plot the peak front pressure and the time period between two successive pressure peaks against the relative mesh spacing ($10 : [\mathrm{Pts}/L_{1/2}] \Rightarrow 10\,\mathrm{Pts}/L_{1/2} \cong 1$). The averages of the four peak values within the time interval $[70, 100]$ are used. The results for Roe-HLL EF 3 and Van Leer FVS with Minmod- and Van Leer-limiter are displayed in Fig. 6.8. A comparison with first-order reference results uncovers that the MUSCL-Hancock method reduces the necessary resolution at least by a factor of 4, but especially for the Roe scheme even factors around 8 to 10 can be achieved. The peak pressure values converge toward ≈ 99.06 with Minmod and toward ≈ 99.23 with Van Leer-limiter. The time period limit is ≈ 7.360. These values do not fully agree to theoretical estimates that have been published earlier, but they are in good agreement with other numerical results and are probably more correct.[3] The best scheme of this test is Roe-HLL EF 3 with Van Leer-limiter. It converges quickly against the peak pressure limit and achieves an extraordinarily good approximation to the time period limit even at coarser resolutions.

6.1.5 Comparison with Other Numerical Results

In most numerical studies [35, 151, 122, 95, 144] ZND detonations were simulated with zero inflow velocity, i.e. in these studies the detonations move with velocity D through the computational domain. But the movement of the detonation through the fixed grid introduces a significant discretization error. The temporal develop-

[3]Fickett and Wood [74] estimated a peak pressure of 98.6. Erpenbeck [66] estimated a period of 7.41 to 7.49, depending on the perturbation method he used. Hwang, Fedkiw et al. observed a convergence of their third-order ENO methods to a peak pressure of ≈ 99 and to a time period of 7.33 to 7.37 [95]. LeVeque and Shyue approximated a peak pressure of 99.83 ± 0.2 and a time period of 7.38 ± 0.11 utilizing a MUSCL-type reconstruction with the Roe scheme and front-tracking algorithm [122] (see also Sec. 6.1.5).

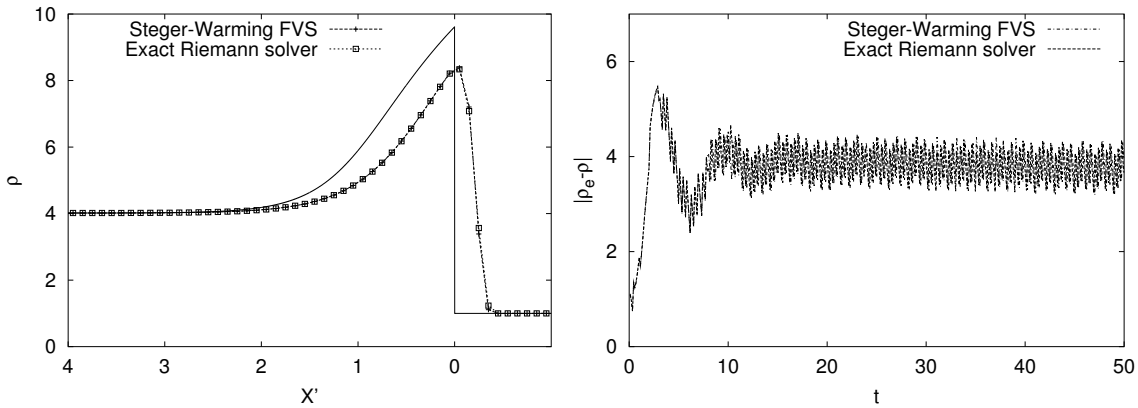

Figure 6.9: Exemplary first-order results for ZND Test 1 with a moving detonation. Left: density distributions at $t_{end} = 50$, the full line is the exact solution of Fig. 3.3. Right: L^1-norm of the density. $10\,\mathrm{Pts}/L_{1/2}$.

ment of the L^1-error (right picture of Fig. 6.9) visualizes the oscillations generated by this effect. The enlarged discretization error increases the numerical viscosity drastically and all previously studied upwind schemes now give the same poor approximation. In particular, the larger amount of numerical viscosity stabilizes also Godunov's Method and Roe HH. Consequently, all upwind schemes can now be used within MUSCL with all limiters without any problems. Exemplary data of a first-order computation of ZND Test 1 are displayed in Fig. 6.9. The graphs clearly illustrate that the results for instance of Godunov's Method and of Steger-Warming FVS are now nearly identical.

Second-order results of ZND Test 2 are shown in Fig. 6.10. Like in the preceding section, we plot the peak front pressure and the time period between two peaks. It is apparent, that for resolutions $\geq 20\,\mathrm{Pts}/L_{1/2}$ the data hardly depend on the particular upwind scheme, but mostly on the limiter. Consequently, the graphs of Fig. 6.10 reflect mainly the ability of the MUSCL approach to handle fast moving detonations, but not the possible approximation quality of a particular upwind scheme for detonation waves. For fast traveling detonations our results are in good agreement with the observations of Quirk [151], who also used the MUSCL approach, but only in combination with the Roe scheme. If peak pressure and time period approximation are considered together, MUSCL seems to give better results than a second-order ENO reconstruction and slightly worse results than third-order ENO schemes, depending on the limiter (see [95] for results of ENO methods for ZND Test 2 with a moving detonation).

In order to decrease the large discretization error of a moving detonation, Bourlioux, Majda and Roytburd [35] and also LeVeque and Shyue [122] combined their numerical methods with front-tracking algorithms. Bourlioux et al. use a standard technique [42] that treats the leading shock wave as an explicitly stored moving boundary and calculates the front velocity from the Rankine-Hugoniot rela-

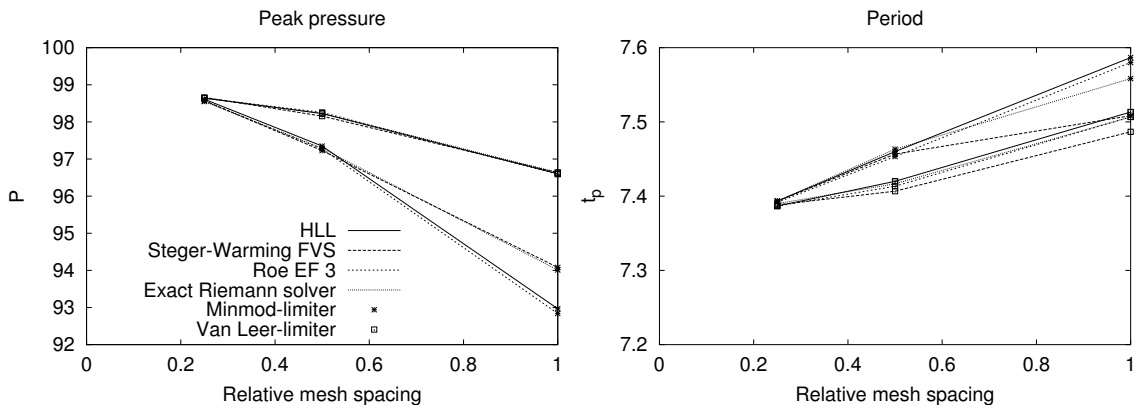

Figure 6.10: Exemplary second-order results for ZND Test 2 with a moving detonation. Left: peak pressure. Right: period of time between successive pressure peaks. Averaged values over the time interval $[70, 100]$ are displayed.

tion (2.10). For their best scheme, the piecewise parabolic method [44] with front-tracking, Bourlioux et al. report a peak pressure of 104 ± 0.4 for $10\,\mathrm{Pts}/L_{1/2}$ and 101 ± 0.3 for $20\,\mathrm{Pts}/L_{1/2}$, which is comparable to MUSCL with Minmod without front-tracking. LeVeque and Shyue adapt the space-discretization and ensure that the detonation front is always aligned to a cell interface. They estimate the front velocity by applying (2.10) to the Roe linearization (see [122] for details). The Roe scheme is used within a MUSCL approach that allows one-sided reconstructions near the tracked detonation front. For $16\,\mathrm{Pts}/L_{1/2}$ they approximated a peak pressure of 99.83 ± 0.2 and time period of 7.38 ± 0.11. For a moving detonation our standard MUSCL technique requires about the double resolution to reproduce this good result (see Fig. 6.10), but for a quasi-stationary detonation we obtain similar results at the same resolution with Roe-HH EF 3 or Van Leer FVS (compare Fig. 6.8).

Another interesting approach to improve the capturing of the leading shock front is the level-set method, which is applied by Fedkiw and his collaborators in combination with the conservative ghost fluid method to detonation waves [70, 134]. The idea of this technique is to use a level-set function [132] to track the location of the shock front. From the level-set function an internal boundary is reconstructed at the shock location. On both sides of this boundary auxiliary ghost cells are utilized allowing a decoupled solution with a standard shock-capturing scheme, e.g. with an approximate Riemann solver. The shock velocity necessary to update the level-set function is calculated by applying the Rankine-Hugoniot relation (2.10) to the internally reconstructed values. The technique avoids the explicit storage of internal boundary locations by utilizing a globally defined level-set function (which can be treated as an additional component of the vector of state in a computer program) and ensures that the shock-capturing scheme is applied exactly at the detonation front. Unfortunately, Fedkiw and his collaborators do not provide any exact measurements for ZND Test 2 with this method.

A further test is the reproduction of the limit of absolute stability $f_0^\star = 1.73$. For a resolution of $16\,\mathrm{Pts}/L_{1/2}$ LeVeque and Shyue report an amplification of the peak pressure for $f = 1.72$ and a decline for $f = 1.74$. Bourlioux et al. obtained comparable results for resolutions $\geq 20\,\mathrm{Pts}/L_{1/2}$. The overdrive parameter variations in Fig. A.5 and A.6 that have been calculated with our best scheme, the Roe-HLL EF 3 scheme with MUSCL variable extrapolation and Van Leer-limiter, illustrate that for quasi-stationary detonations our method easily reproduces the limit of stability for resolutions $\geq 20\,\mathrm{Pts}/L_{1/2}$ without any front-tracking.

The other computations shown in Fig. A.5 and A.6 are intended as a reference. For $f = 1.36, 1.38, 1.40, 1.50, 1.54, 1.58$ these computations are qualitatively identical to the results in [35] obtained at the same resolution. The two highly unstable cases $f = 1.1$ and $f = 1.3$ are comparable to the calculations of Papalexandris et al. in [144] at similar resolutions. But note, that a simulation time of 100 time units is too short to allow the development of a regular oscillation as f approaches 1.0. At least for $f = 1.1$ and $f = 1.2$ it can not be concluded reliably from Fig. A.5, whether the approximation has already converged toward a regular oscillation or not. A study of the necessary grid resolutions and the simulation times that can be required in extreme cases has been presented by Sharpe and Falle [164].

6.2 Two-dimensional Cellular Structure

In this section we simulate typical unstable two-dimensional ZND detonations with the previously derived upwind schemes. In particular, we compare the Godunov dimensional splitting (4.22) with the two-dimensional Wave Propagation Method (4.58). To suppress the carbuncle phenomenon that would destroy every simulation with the Roe scheme, we extend the entropy enforcement formula EF 3 by the multi-dimensional H-correction in all three waves that has been introduced in Sec. 4.8.3. Following the notation of Sec. 4.8.3 we denote this variant by Roe-HLL EF 3*-H.

6.2.1 Validation of Dimensional Splitting

We start our considerations with a test of the applicability of the Godunov dimensional splitting (4.22) for the approximation of multi-dimensional detonation waves in general. Further on, the basic computational setup to record triple point tracks is introduced. To provide results that are easily reproducible, intentionally a configuration has been chosen that develops typical detonation cells already at coarsest resolutions.

Initialization

The unstable ZND detonation with $\gamma = 1.2$, $E_0^\star = 50$, $Q_0 = 50$, $f = 1.6$ of Sec. 6.1.3 is extended to two space dimensions with $U_2 = 0$ and placed on a rectangular domain of the size $[0, 20] \times [0, 5]$ (ZND Test 3). Like in the previous section all velocities in the x_1-direction are shifted by $-D$. Initially, the von Neumann point

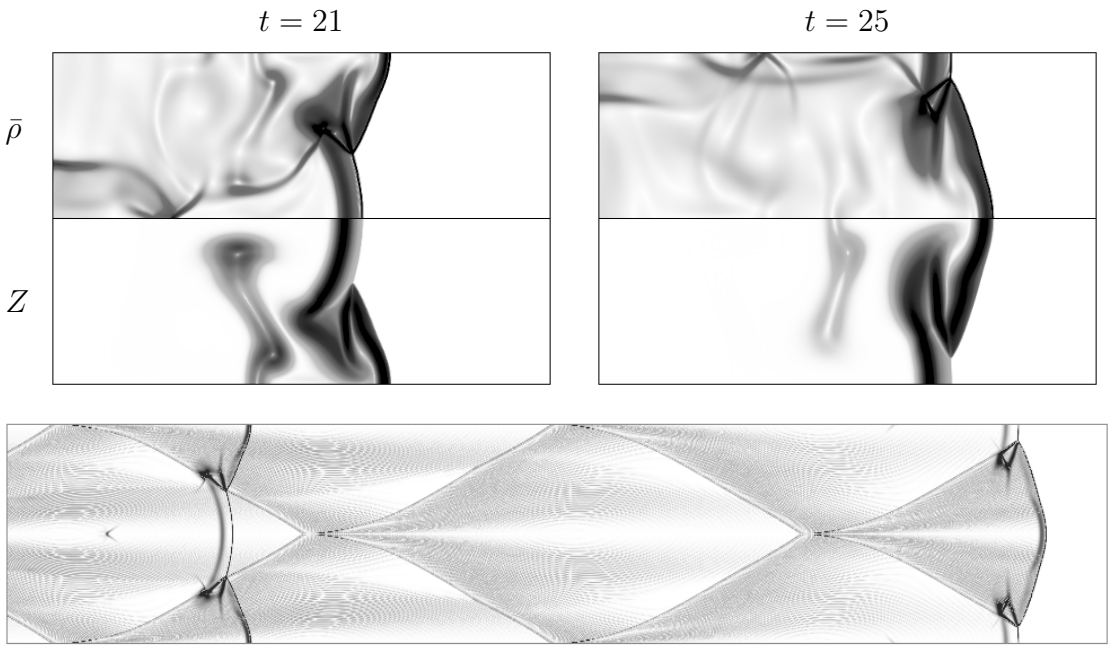

Figure 6.11: Flow field at $t = 21$ and $t = 25$ for ZND Test 3. Top: schlieren plots of $\bar{\rho}$ and Z (mirrored) on $[0, 15] \times [0, 5]$, bottom: detonation fronts plotted on distribution of Σ (domain doubled).

is at $X_1 = 6$. In- and outflow boundary conditions are applied at the right and left side, reflective boundary conditions are used in the x_2-direction. Following Geßner, who also studied this particular example in his thesis [78], we initiate a transverse perturbation of the planar detonation by increasing the pressure by +15% inside the pocket $[5.45, 5.94] \times [0.0, 0.25]$.

Reference Computation

To test the Godunov splitting (4.22) in general, we carry out a reference computation with Van Leer FVS without MUSCL reconstruction on a uniform grid of 800×200 cells, i.e. $40\,\mathrm{Pts}/L_{1/2}$. The computation ends at $t_{end} = 25$. Automatic time step adjustment based on $C_{CFL}^{VL} \approx 0.95$ is applied (see Eq. (4.70).

The numerical simulation clearly represents the unstable behavior of a multi-dimensional detonation wave. While a regular longitudinal pulsation is visible in the one-dimensional results (compare Sec. 6.1.3), the two-dimensional computation uncovers an instability in the transverse direction. As it can be expected (compare Sec. 3.3), the transverse instability is much stronger than the pulsation in the normal direction and suppresses it completely. After approximately 10 time units the transverse oscillation is fully established and dominates the computation. An instationary transverse pressure wave travels regularly up- and downward. A triple point with the typical sub-structure explained in Sec. 3.3 is formed where the transverse wave hits the detonation front.

The distributions of $\bar{\rho}$ and Z at $t = 21$ and $t_{end} = 25$ in Fig. 6.11 display the

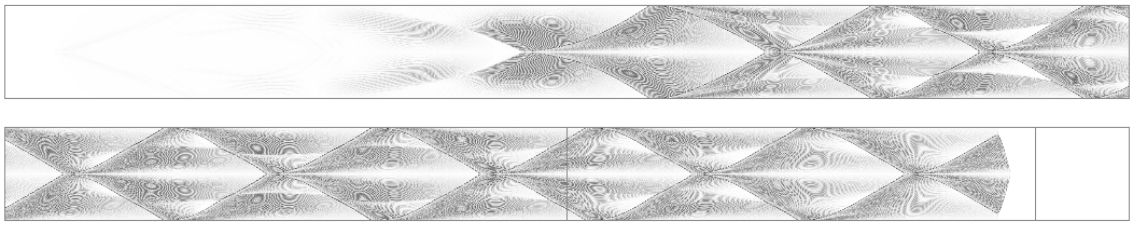

Figure 6.12: Maximal amount of vorticity at every point in space overrun by the detonation of ZND Test 3. The auxiliary grid is mirrored at $X_2 = 0$ for visualization. Top: $[0, 120] \times [-5, 5]$, bottom: $[120, 240] \times [-5, 5]$. First-order accurate computations with Van Leer FVS, $40\,\mathrm{Pts}/L_{1/2}$, $C_{CFL}^{VL} \approx 0.95$.

temporal development of the flow field while the triple point is moving. The graphic at $t = 21$ is a snapshot of the flow situation in the second half of a detonation cell, while the other graphic at $t = 25$ displays the first half. At $t = 21$ the shock at the symmetry axis is the incident shock. It is strong enough to achieve a complete rapid reaction directly behind it. No further reaction is possible behind this combustion region and the transverse wave is therefore not visible in the schlieren plot of the mass fraction. It is interesting to note, that the flame front in this example becomes so wrinkled at the end of a detonation cell that an unreacted pocket is formed on each side of the symmetry axis. The mass fraction distribution at $t = 21$ uncovers two of these pockets.

At $t = 25$ the shock at $X_2 = 0$ is a Mach stem. It is much stronger than the incident shock and the distance between detonation front and the beginning of the reaction region is drastically decreased. The vorticity track (see explanation below) in Fig. 6.11 reflects this decrease of reaction velocity behind the shock inside the detonation cell by a continuous decrease of Σ (see explanation below).

Obtaining Triple Point Tracks

As the velocities have their maximal changes in the triple point region, the vorticity

$$\omega = \frac{\partial U_2}{\partial X_1} - \frac{\partial U_1}{\partial X_2} \tag{6.3}$$

is an appropriate quantity to detect the triple point and a local maximum in $|\omega|$ exactly at the triple point can be expected. Eq. (6.3) is approximated by standard difference quotients. We utilize an auxiliary grid for a scalar quantity Σ to record the maximum of $|\omega|$ over time at every point in space overrun by the detonation in the quasi-stationary simulation. In the reference computation the auxiliary grid has the size $[0, 240] \times [0, 5]$ and 9600×200 uniform cells. It is initialized with $\Sigma \equiv 0$. During the simulation the auxiliary cell values $\Sigma_{j^\star,k^\star}$ are updated by

$$\Sigma_{j^\star,k^\star} := \max(\Sigma_{j^\star,k^\star}, |\omega_{j,k}|)$$

$$\text{with} \quad j^\star = \left[\frac{t\,D}{\Delta X_1}\right] + j\ , \quad k^\star = k \quad \text{for all } j = 1, \ldots, 800\,,\ k = 1, \ldots, 200\ ,$$

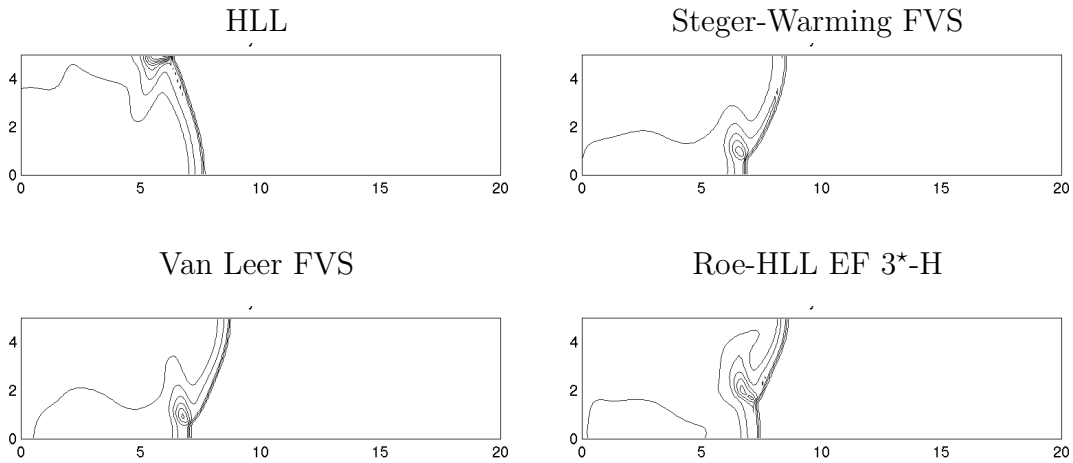

Figure 6.13: Density distribution for ZND Test 3 with different first-order upwind schemes at $t = 25$, $10\,\mathrm{Pts}/L_{1/2}$.

which corresponds to a constant movement with velocity $-D$ of the auxiliary grid through the domain. Fig. 6.12 displays the distribution of Σ at the end of the computation. The grid is mirrored at $X_2 = 0$ to visualize the regular cellular structure written by the triple points tracks. Each detonation cell has a length of $L \approx 22.6\,L_{1/2}$. With $D \approx 8.6134$ this corresponds to a time period of $t_p \approx 2.62$.

6.2.2 Validation of Upwind Schemes

We repeat ZND Test 3 on a coarse grid of 200×50 cells ($10\,\mathrm{Pts}/L_{1/2}$) with the first-order FVS schemes of Steger-Warming, Van Leer and with the first-order approximate Riemann solvers HLL and Roe-HLL EF 3*-H. Like in the preceding section the first-order Godunov splitting (4.22) is utilized for the dimensional extension.

All schemes reproduce the cellular structure qualitatively correctly. The results of the FVS schemes are nearly identical, but Van Leer FVS gives sharper resolved results than Steger-Warming FVS (compare Fig. 6.13), as we expect it from our one-dimensional results. The periodic movement of the triple point in the FVS approximation is slightly ahead of the approximation with the Roe-HLL EF 3*-H scheme. Roe-HLL EF 3*-H shows a resolution of the detonation front similar to Van Leer FVS, but as in Sec. 6.1.2 the Roe solver seems to approximate the reaction region better and more details show up here. The HLL scheme approximates a triple point that is drastically delayed compared to the results of all other upwind methods and as in Sec. 6.1 this simple Riemann solver gives the worst result.

6.2.3 Validation of the MUSCL-Hancock Method

In order to get a rough estimate on the accuracy improvement by applying the MUSCL-Hancock reconstruction technique in the multi-dimensional case, we com-

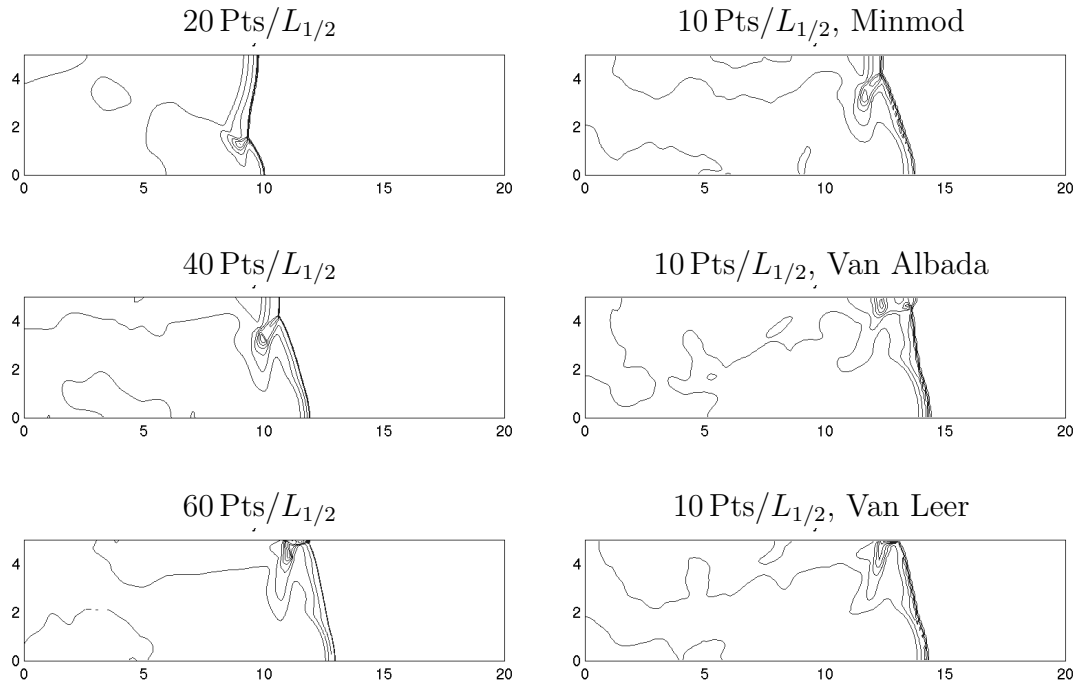

Figure 6.14: Improvement of the solution by MUSCL reconstruction. Left column: without MUSCL, right column: MUSCL-Hancock method with different slope limiters. Density distributions for ZND Test 3 at $t = 25$.

pare coarse-grid solutions of ZND Test 3 computed with MUSCL to higher resolved results obtained with a first-order upwind scheme alone. All computations used the first-order dimensional splitting (4.22).

In the multi-dimensional case the one-dimensional MUSCL-Hancock reconstruction of Sec. 4.3.1 is applied in every dimensional sweep $\mathcal{X}_n^{(\Delta t)}$ separately. Analogously to Sec. 6.1.4 the variable extrapolation for multi-component Euler equations of Sec. 4.7.1 is used. Based on our experiences in the one-dimensional case (compare Fig. 6.8) we utilize Van Leer FVS and not Roe-HLL EF 3*-H for this comparison to obtain an estimation for the minimal resolution reduction factor that can be expected.

The results at $t = 25$ are displayed in Fig. 6.14. The reference calculations with the upwind scheme alone (left column) show that the triple point approaches the upper boundary with increasing resolution. This behavior is reproduced in the coarser MUSCL results, if a slope limiter with sharp discontinuity reconstruction is employed (compare Fig. 6.7). The factors of grid refinement of corresponding reference solutions are in good agreement with the values found in the one-dimensional case in Sec. 6.1.4. With the diffusive Minmod-limiter the MUSCL computation corresponds to a solution that is about four times finer, with the sharper Van Leer-limiter the MUSCL result is similar to a six times finer result. As it is reasonable, the Van Albada-limiter produces an approximation that lies between both other results.

Test	$E_0^\star$	Q_0	f	D	t_{end}
4	50.0	50.0	3.0	11.794	50.0
5	10.0	50.0	1.2	7.459	70.0

Table 6.1: Parameters of the ZND Tests 4 and 5, $\gamma = 1.2$.

6.2.4 Dimensional Splitting versus Wave Propagation

In this section, we simulate two-dimensional unstable ZND detonations that require a significantly higher resolution than the example in Sec. 6.2.1. The two configurations studied have been proposed by Bourlioux and Majda in [34]. In particular, the parameters of ZND Test 5 correspond roughly to low pressure $H_2 : O_2$ mixtures diluted with $60\% - 80\%$ argon and the configuration is a reasonable test for the computations in the next chapter. ZND Test 4 has the same parameters as the calculations in Sec. 6.1. Its overdrive parameter $f = 3.0$ is drastically above the one-dimensional limit of absolute stability and in the planar case this detonation would remain stable (compare Sec. 3.2).

In order to determine the approximation quality of the available multi-dimensional transport schemes, we test the Van Leer FVS and the Roe-HLL EF 3*-scheme with MUSCL-Hancock reconstruction within the splitting method

$$\mathbf{Q}^{l+1} = \mathcal{S}^{(\frac{1}{2}\Delta t)}\mathcal{X}_2^{(\Delta t)}\mathcal{X}_1^{(\Delta t)}\mathcal{S}^{(\frac{1}{2}\Delta t)}(\mathbf{Q}^l) \tag{6.4}$$

and the Roe-HLL EF 3*-scheme in the splitting scheme

$$\mathbf{Q}^{l+1} = \mathcal{S}^{(\frac{1}{2}\Delta t)}\mathcal{H}_W^{(\Delta t)}\mathcal{S}^{(\frac{1}{2}\Delta t)}(\mathbf{Q}^l)\ . \tag{6.5}$$

Herein, $\mathcal{H}_W^{(\Delta t)}$ denotes the two-dimensional Wave Propagation scheme (4.58) that is implemented as described in detail in Sec. 4.7.2 with MUSCL-Hancock variable extrapolation and positivity correction. Scheme (6.4) is formally only first-order accurate, but Eq. (6.5) is a fully two-dimensional second-order accurate method that can be expected to produce even better results than a splitting method utilizing the second-order accurate dimensional splitting (4.23).

Computational Setups and Initialization

The ZND parameters for both test cases are displayed in Tab. 6.1. The basic computational setup is nearly identical to ZND Test 3. The exact quasi-stationary one-dimensional ZND solutions are placed on the same two-dimensional domain $[0, 20] \times [0, 10]$ with the von Neumann point at $X_1 = 12$ and disturbed by a 15% pressure increase in the pocket $[11.45, 11.95] \times [5.25, 4.75]$.

We employ base grids with a resolution of $10\,\mathrm{Pts}/L_{1/2}$ in both directions, i.e. with 200×100 cells and use the AMR algorithm of the preceding chapter as explained in Sec. 5.7 to achieve a moderate reduction of the computational costs. Only one refinement level is applied ($r_1 = 4$). An extensive adaptation is ensured by

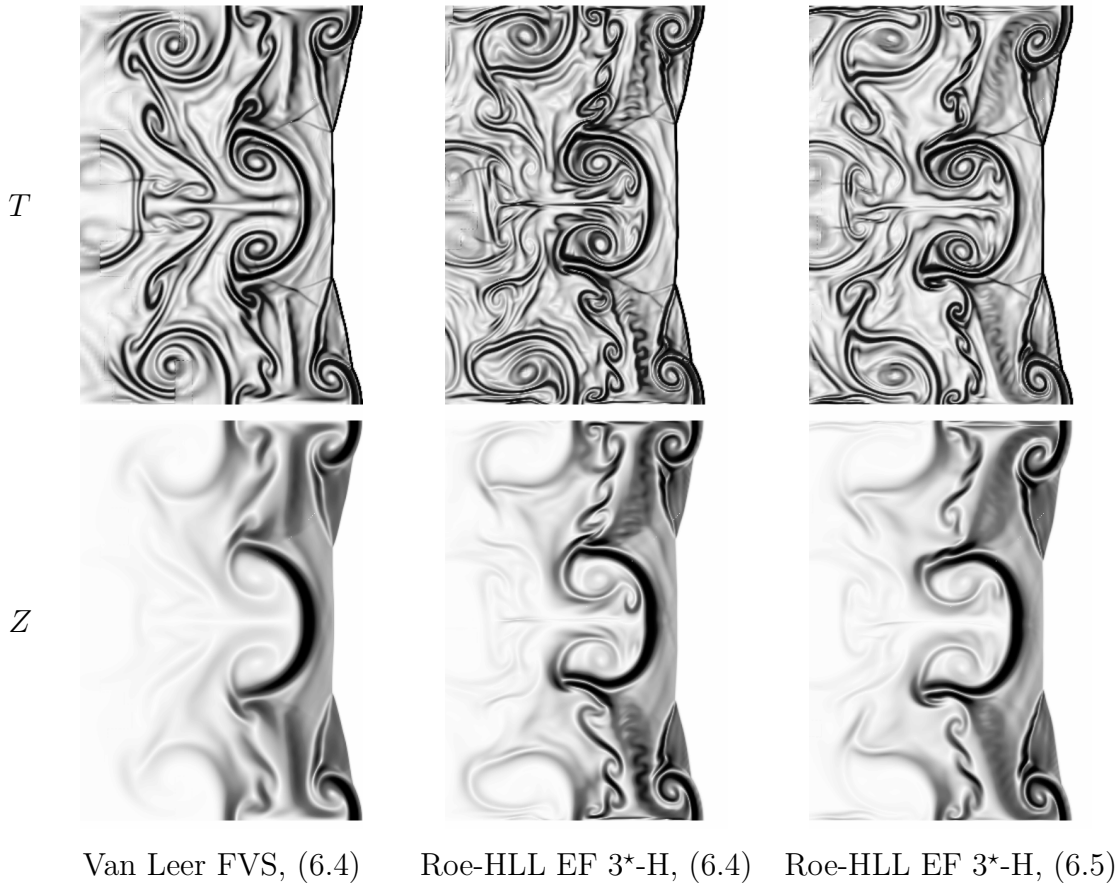

Figure 6.15: Schlieren plots of T and Z for ZND Test 4 at $t = 30.4$ for the three transport schemes, displayed: $6.0 < X_1 < 15.0$.

selecting the very sensitive adaptation criteria $\epsilon_{\bar{\rho}} = 5.0$, $\epsilon_P = 20.0$ and $\epsilon_Z = 0.005$. Consequently, the results agree mostly with uniformly refined reference data (not shown). The effective resolution of $40\,\mathrm{Pts}/L_{1/2}$ is 1.67 times finer than the highest resolution of $24\,\mathrm{Pts}/L_{1/2}$ in [34] and we therefore expect mostly converged solutions for our specific setup (compare Sec. 6.1.5).[4] Based on the results of Sec. 6.2.3 we employ the Van Albada-limiter. Like in Test 3, we use automatic step size adjustment with $C_{CFL} \approx 0.95$ (Test 4 needs ≈ 7000 time steps, Test 5 requires ≈ 6500 time steps).

[4]Analogously to their studies in the one-dimensional case [35] Bourlioux and Majda simulated fast propagating detonations with zero inflow velocity with the Piecewise Parabolic Method in combination with dimensional splitting and conservative front tracking in [34] and obtained mostly converged solutions at $24\,\mathrm{Pts}/L_{1/2}$. Based on the one-dimensional comparisons in Sec. 6.1.5 we can expect to achieve slightly improved results with the second-order accurate shock-capturing schemes for our quasi-stationary setup already at this resolution.

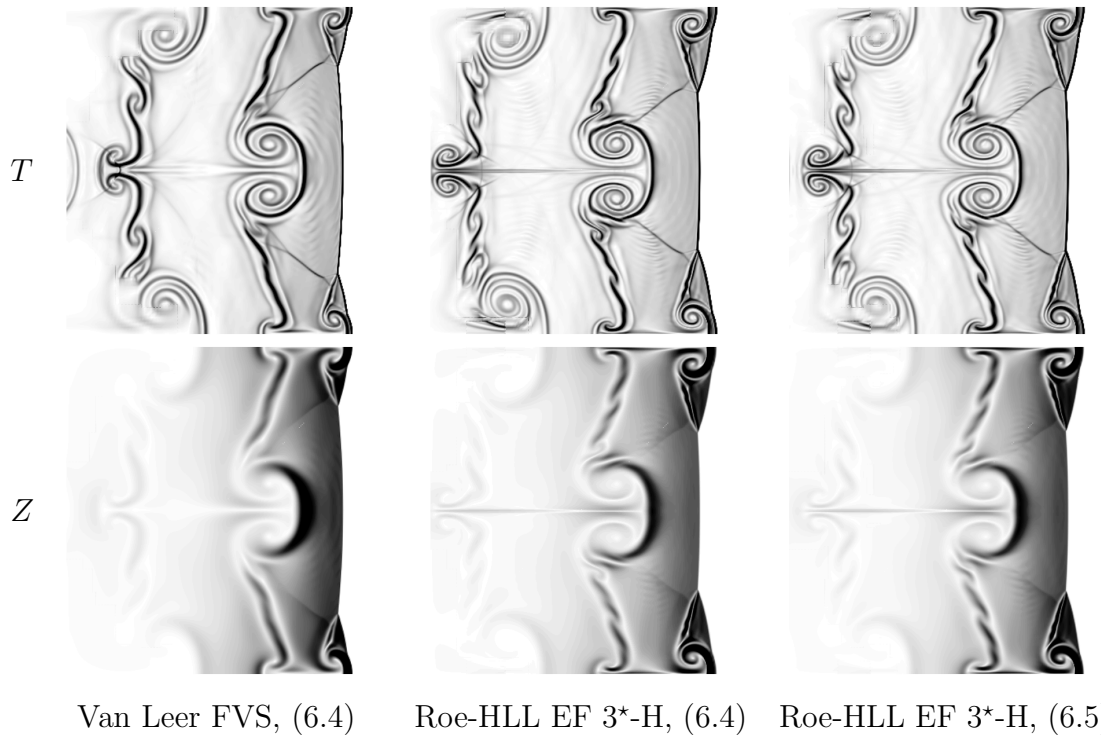

Figure 6.16: Schlieren plots of T and Z for ZND Test 5 at $t = 54.5$ for the three transport schemes, displayed: $6.0 < X_1 < 15.0$.

Computational Results and Comparison with Other Numerical Results

For all three transport schemes we obtain similar numerical approximations that are nearly converged in time and in space. As expected, all results are in perfect agreement with the solutions in [34], but have a significantly sharper resolution. Therefore, we omit an explanation for the different unstable behavior (see [34] for a detailed interpretation) and focus our attention on the differences between our three transport schemes instead.

The Figs. 6.16 and 6.15 display exemplary snapshots for both configurations. It is apparent, that all results with Roe-HLL EF 3⋆-H are remarkably sharper resolved than with Van Leer FVS. While the second-order MUSCL results of the Roe scheme were only slightly better in one space dimension (compare Sec. 6.1.4), its superiority for multi-dimensional problems is indisputable. Further on, we have to note that the differences between the results of the formally first-order method (6.4) and the fully multi-dimensional second-order scheme (6.5) are negligible. As it can be expected, scheme (6.5) approximates two-dimensional structures smoother and produces less grid-aligned results than method (6.4), but the improvements are minor. For regular detonation cell simulation in open space both methods are mostly equivalent. The Figs. A.8, A.7 display reference results and triple point tracks for Roe-HLL EF 3⋆-H within (6.5). For ZND Test 4 regular detonation cells with length $L \approx 25.2\, L_{1/2}$ and

time period $t_p \approx 2.14$ can be measured. ZND Test 5 develops regular cells with $L \approx 23.9\, L_{1/2}$ and a time period of $t_p \approx 3.20$. Although ZND Test 4 would remain stable in one space dimension, the simulation uncovers a stronger two-dimensional instability than in ZND Test 5.

It is interesting to note, that at least in a distributed memory environment the two-dimensional methods (6.4) and (6.5) require similar computational times (compare Sec. 6.3.1 for the three-dimensional case). For example, ZND Test 4 took exactly 11.6 h with both methods on four nodes of a Pentium III-850 MHz-cluster connected with Fast Ethernet (Van Leer FVS with scheme (6.4) required 8.5 h). The Wave Propagation Method is computationally more expensive (compare last paragraph of Sec. 4.3.2), but the dimensional splitting scheme requires an additional parallel synchronization step (compare Sec. 5.6.2).

6.3 Three-dimensional Cellular Structure

Although it is known experimentally that detonations exhibit an inherently three-dimensional structure (compare Sec. 3.3) most simulations so far considered only the two-dimensional case. While the computational expense of two-dimensional ZND simulations with a necessary resolution of 20 to 40 Pts/$L_{1/2}$ is moderate from today's point of view, the costs of three-dimensional computations are still enormous.

A completely documented three-dimensional test case has been presented by Williams, Bauwens and Oran [203]. To our best knowledge, their work is the only successful extension of some earlier attempts, e.g. [77], and is the only source of comparative data for the three-dimensional case up to now. In [203] Williams, Bauwens and Oran studied the configuration of ZND Test 5 in a quasi-stationary setup with a resolution of 16 Pts/$L_{1/2}$. Based upon the expectation that the cell width λ will remain unchanged in three dimensions as long as only no-slip or symmetry boundary conditions are applied, they utilized a quadratic channel with 10×10 cross-section. They exploited the symmetry of the problem and simulated just one quarter of the domain. As expected, they observed regular detonation cells with $\lambda = 10$ in x_2- and in x_3-direction. The detonation cells were formed by straight triple point lines mostly parallel to the boundaries and orthogonal to each other. They discovered a remarkable phase-shift between the waves in both direction of approximately 90 degree.

6.3.1 Validation of the AMR Method

We use the three-dimensional example proposed in [203] to verify the applicability of the parallel AMR algorithm as described in Sec. 5.7 to complex unstable detonation waves. The hydrodynamic transport is computed with our most efficient method, the Godunov dimensional splitting with Roe-HLL EF 3* Riemann solver and MUSCL-Hancock reconstruction. In Sec. 6.2.4 we compared this formally first-order scheme to the fully multi-dimensional second-order accurate Wave Propagation Method and

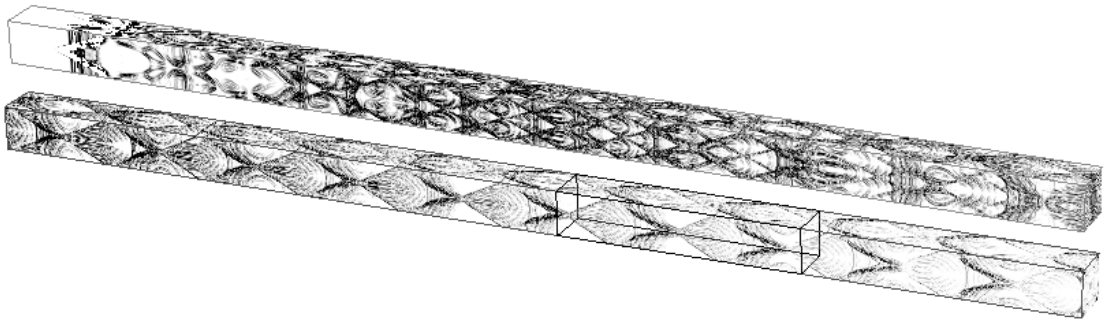

Figure 6.17: Maximum of $|\omega|$ at every point in space overrun by the detonation of ZND Test 6b. Mirrored at $X_2 = 0$, $X_3 = 0$ for visualization. Top: $[0, 250] \times [-5, 5] \times [-5, 5]$, bottom: $[250, 500] \times [-5, 5] \times [-5, 5]$.

found that both schemes approximate unstable two-dimensional detonation structures in open space with similar quality. Consequently, only negligible differences between both transport schemes could be observed in first three-dimensional test simulations at $20\,\mathrm{Pts}/L_{1/2}$. But unlike to the two-dimensional case, where both variants were found to require similar computational times in parallel (compare last paragraph of Sec. 6.2.4), these computations uncovered that the application of the three-dimensional Wave Propagation Method results nearly in a doubling of the overall computational time. We do not describe these test simulations further, but present the results of finer resolved adaptive simulations instead.

Computational Setups and Initialization

We use a computational setup that is in principle identical to the setup in the two-dimensional case. Analogously to ZND Test 5 the exact quasi-stationary ZND solution with parameters $\gamma = 1.2$, $E_0^\star = 10$, $Q_0 = 50$, $f = 1.2$ is extended to three dimensions with $U_2 = 0$, $U_3 = 0$. The von Neumann point is placed at $X_1 = 12$ on a $[0, 20] \times [0, 5] \times [0, 5]$ grid. Except the usual in- and outflow at the right and left side, reflective boundary conditions are applied. The transverse wave is initiated by a pressure increase of +15% in the pocket $[11.45, 11.95] \times [0.25, 0.0] \times [0.0, 5.0]$. In contrast to the recommendation in [203] an orthogonal perturbation is generated by an identical pocket at $[11.45, 11.95] \times [5.0, 0.0] \times [X_p, X_p + 0.5]$. The starting location X_p of this pocket is varied to verify the independence of the periodic three-dimensional cellular structure from the initial disturbance. We test the three values $X_p = 0.65$ (ZND Test 6a), $X_p = 1.45$ (ZND Test 6b), $X_p = 2.25$ (ZND Test 6c).

Based on the previously discussed test computations and Sec. 6.2.4 we apply the splitting scheme $\mathbf{Q}^{l+1} = \mathcal{S}^{(\Delta t)}\mathcal{X}_3^{(\Delta t)}\mathcal{X}_2^{(\Delta t)}\mathcal{X}_1^{(\Delta t)}(\mathbf{Q}^l)$ in combination with Roe-HLL EF 3* and MUSCL variable extrapolation as described in Sec. 6.2.3 and Van Albada-limiter. Like in all quasi-stationary computations we use an auxiliary grid for a scalar quantity Σ moving constantly with velocity $-D$ to record the maximum value of $|\omega|$, the magnitude of the vorticity vector. In the three-dimensional case

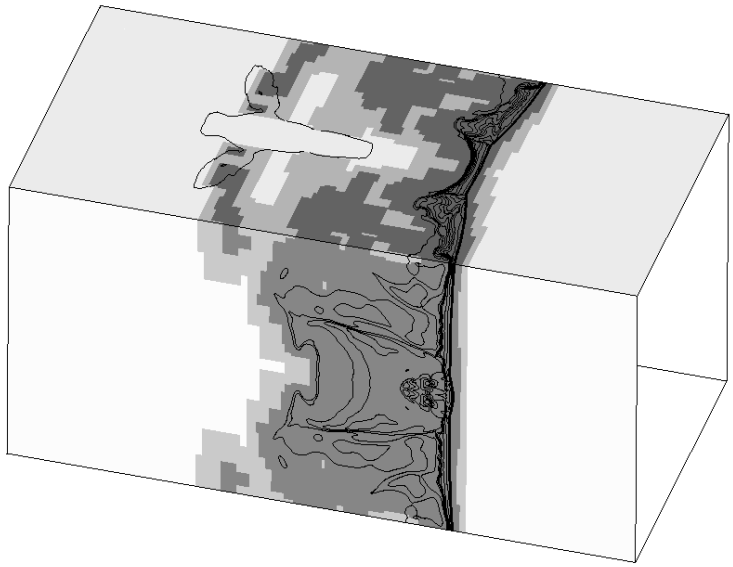

Figure 6.18: ZND Test 6b. Isolines of $\bar{\rho}$ on the two levels of refinement at $t = 53.5$, mirrored at $X_2 = 0$, $X_3 = 0$ for visualization, $[0, 20] \times [-5, 5] \times [-5, 5]$.

the vorticity vector is defined as

$$\omega = \left(\frac{\partial U_3}{\partial X_2} - \frac{\partial U_2}{\partial X_3}, \frac{\partial U_1}{\partial X_3} - \frac{\partial U_3}{\partial X_1}, \frac{\partial U_2}{\partial X_1} - \frac{\partial U_1}{\partial X_2} \right)^T . \tag{6.6}$$

In the ZND Tests 6a to 6c this auxiliary grid has the mesh widths of the adaptive base grid and consists of $3200 \times 25 \times 25$ cells. Like in ZND Test 5, it is shifted with the constant velocity -7.459 through the computational domain.

The adaptive grid has $100 \times 25 \times 25$ cells at the coarsest level and two levels of refinement with $r_1 = 2$ and $r_2 = 3$, which corresponds to an effective resolution of $30\,\mathrm{Pts}/L_{1/2}$ and is nearly twice as fine as the resolution used in [203]. The adaptation criteria are set to $\epsilon_{\bar{\rho}} = 5.0$, $\epsilon_P = 20.0$ and $\epsilon_Z = 0.05$. This setting achieves an adaptation to the stronger flow phenomena, but is not as stringent as in Sec. 6.2.4. Instead of 13.5 M cells like a uniformly refined computation the adaptive simulations use around 3.6 M cells. A typical snapshot of the dynamic refinement is shown in Fig. 6.18. All computations end at $t_{end} = 70.0$ and require approximately 3300 time steps with an automatically adjusted step size of $C_{CFL}^{Roe} \approx 0.95$.

The computations were run on the Helics (HEidelberg LInux Cluster System) at the University of Heidelberg. The Helics cluster consists of 256 Athlon-1.4 GHz double-processor boards connected with 2 Gb Myrinet high-speed network. On 32 processors each run took about 48 h real time.

Comparison of the Computational Results

Regular three-dimensional detonation cells are developed in the ZND Tests 6a and 6b. In ZND Test 6c three-dimensional detonation cells are initiated, but the strength

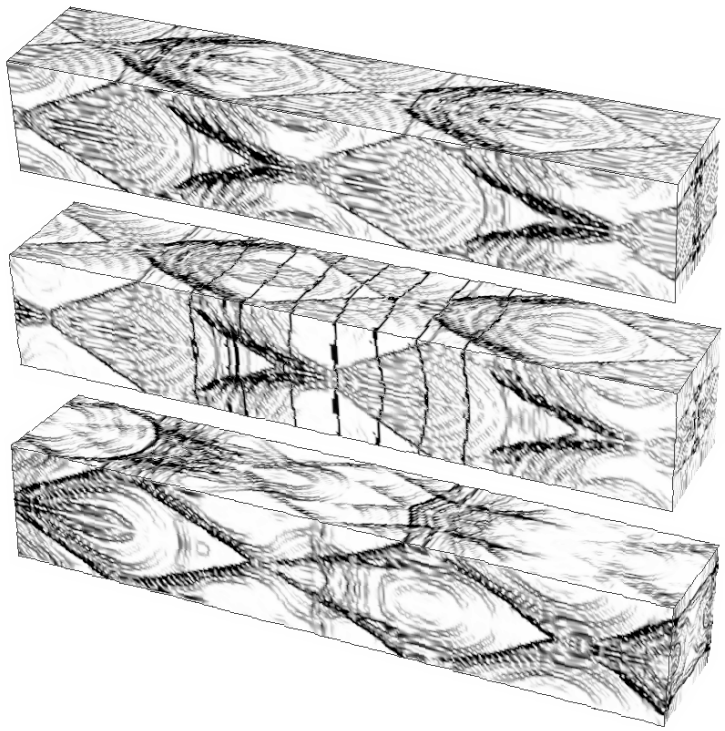

Figure 6.19: $\max(|\omega|)$ at $[385.0, 440.0] \times [-5, 5] \times [-5, 5]$ for ZND Test 6a (top), 6b (middle), 6c (bottom). The middle picture also shows the detonation front.

in both transverse directions is not equal and the waves in the x_3-direction disappear during the simulation. The different character of the calculations can be seen clearly in the maximal vorticity notated on the auxiliary meshes. Fig. 6.17 displays this mesh mirrored twice for ZND Test 6b. Analogously to ZND Test 5 (compare triple point tracks of Fig. A.8) two detonation cells with $\lambda = 5\,L_{1/2}$ can be observed during the first quarter of the simulation, but the detonation changes its mode quickly and in the second half of the computation regular detonation cells with $\lambda = 10\,L_{1/2}$ evolve.

Fig. 6.19 compares the tracks of the triple point lines within the temporal range $t \approx 49$ to $t \approx 57$ for all three computations. Obviously, Test 6a and 6b simulate the same three-dimensional periodic situation. The small temporal shift is due to the different initial conditions. The detonation cells in both transverse directions have the same length as in the two-dimensional case of ZND Test 5, i.e. $L \approx 23.9\,L_{1/2}$ and the same time period $t_p \approx 3.20$. The initiation of the detonation cell in the x_3-direction is delayed roughly by 0.80 which corresponds to a phase delay between x_2- and x_3-direction of about 90 degree. Test 6c shows only the regular oscillation in x_2-direction. Around $t \approx 50$ the waves in x_3-direction die out and only waves in x_2-direction remain. While the transverse waves seem to have equal strength in Test 6a and 6b, the waves in x_2-direction are significantly stronger in Test 6c and suppress the weaker orthogonal waves for $t > 50$.

All graphics of Fig. 6.19 reproduce the phenomenon of *slapping* waves that

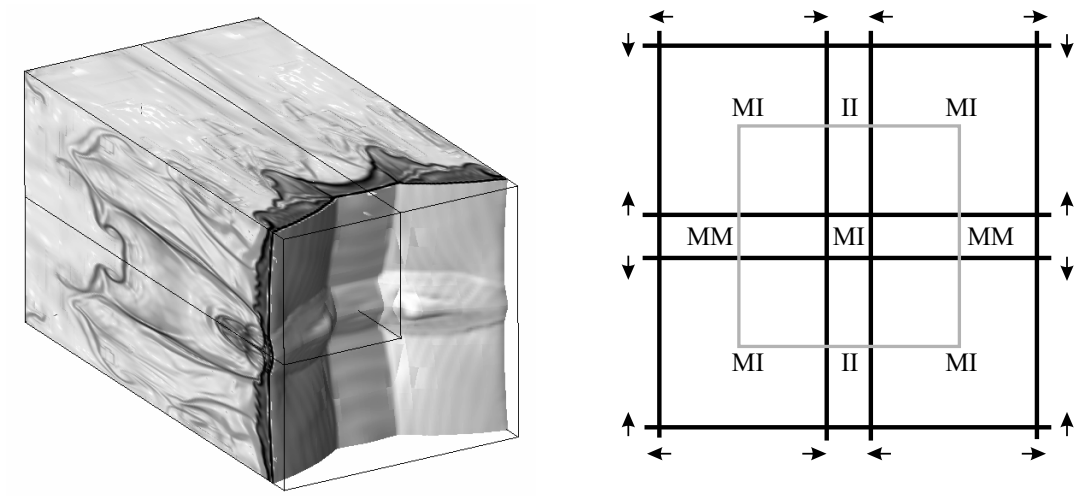

Figure 6.20: Left: three-dimensional detonation front of ZND Test 6b at $t = 53.5$, right: sketch of the periodic rectangular shock structure for $t = 53.5$. The grey square corresponds to the domain of the left picture.

frequently has been observed in experiments [203]. When a triple point line is reflected it seems to slap multiple times against the wall. The slapping is associated to the complex process of triple point reinitiation (compare Sec. 7.2.3). Especially in the top picture of Fig. 6.19 the slapping is clearly visible twice in both transverse directions.

Test 6c reproduces only the two-dimensional unstable mode already seen in ZND Test 5, but Test 6a and 6b develop a new, genuinely three-dimensional mode of oscillation. In both transverse directions the strong two-dimensional oscillations is present and forces the creation of detonation cells of equal size, but both transverse modes are now coupled in a complex three-dimensional manner. This coupling seems to be unique and in all our computations (also with different initial conditions) we only observed this complex three-dimensional mode or the purely two-dimensional mode of ZND Test 5.

The Periodic Three-dimensional Structure

The Figs. A.9 to A.11 visualize the periodic change of three-dimensional detonation structures during one detonation cell. Like in the previous plots the computational domain has been mirrored twice. The three-dimensional graphics show schlieren plots of $\bar{\rho}$ and an isosurface of the detonation front. The two-dimensional graphics are roll-ups of the four sides of the cube marked in the three-dimensional plots (see also the sketch in Fig. A.11). They display schlieren plots of $\bar{\rho}$ and P.

The isosurfaces of the detonation front clearly represent the four triple point lines formed by the transverse waves. During a complete detonation cell the four lines remain mostly parallel to the boundary and hardly disturb each other. The schlieren plots of the Figs. A.9 to A.11 show the characteristic triple point flow pattern of Fig. 3.6 in all planes perpendicular to a triple point line. Each triple point line is

driven forward by a Mach stem line into an incident shock region. A region which is a Mach stem in one direction can be either a Mach stem or an incident shock in the orthogonal direction. The same is true for the incident shock and we consequently have three different types of rectangular shock regions at the detonation front: Mach stem - Mach stem (MM), Incident - Incident (II) and mixed type regions (MI) [203]. An MM region is bounded only by Mach stems and expands in x_2- and x_3-direction. An II rectangle is formed only by incident shocks and shrinks in both directions. The MI region is of mixed type and expands in one direction, while it shrinks in the other. Fig. 6.20 displays the different rectangular shock regions for $t = 53.5$. As the computation corresponds only to a section of a periodic situation the sketch in Fig. 6.20 displays an enlarged region.

A comparison of the schlieren plots for ZND Test 6b with those of ZND Test 5 (see Fig. A.8) uncovers that the three-dimensional mode of propagation is considerably more unstable than the purely two-dimensional one. The graphics of the three-dimensional computation show remarkable minor disturbances behind the detonation front and the degree of instability seems to correspond more to the unstable ZND Test 5 than to its own two-dimensional analogue. Together with the characteristic phase shift this observation could be an indication that beside the two strong two-dimensional modes of oscillation a third, genuinely three-dimensional, mode shows up in these computations.

Comparison with Other Numerical Results

In principle our results are in perfect agreement with the uniform results in [203]. The successful application of the parallel AMR algorithm allowed simulations with an effective resolution, which was nearly twice times finer in space and time than the results in [203]. Consequently, our results are significantly better resolved. This improvement in approximation quality is probably the reason, why the periodic three-dimensional oscillation was clearly present in our computations at the same physical time as in the two-dimensional reference computation (compare Sec. 6.2.4). This is remarkably earlier than it was reported by Williams, Bauwens and Oran, and in contrast to their recommendation in [203] no modified initial perturbation technique had to be applied.

The example demonstrates that the application of a thoroughly validated high resolution transport method within the blockstructured AMR algorithm has the potential to simulate even three-dimensional unstable detonation waves with high resolution at a reasonable expense. The implemented parallelization strategy ensures that these simulations can be run on todays distributed memory machines in an acceptable computing time. In the last chapter we therefore apply our computational framework to detonations with detailed chemical reaction.

Chapter 7

Detonations with Real Chemistry

In this chapter we extend the simulation techniques validated in the previous chapter to CJ detonations with detailed non-equilibrium chemistry. We simulate multi-dimensional structures of detonation waves in low-pressure hydrogen-oxygen mixtures with high argon diluent that would occur in open space and their changes under transient conditions.

In Sec. 7.1 we carry out purely chemical kinetics computations in order to verify the employed reaction mechanism. In Sec. 7.2 we simulate the two-dimensional cellular structure of a $H_2 : O_2 : Ar$ CJ detonation with molar ratios $2 : 1 : 7$ at $T_0 = 298\,\mathrm{K}$ and $p_0 = 6.67\,\mathrm{kPa}$. We present a reference solution that is remarkably finer resolved than previously published results [138, 59, 78]. The given hydrodynamic analysis of the instationary detonation structure is the most detailed one that has been presented so far [113, 138]. The CJ detonation of Sec. 7.2 is extended to three space dimensions in Sec. 7.3. To our best knowledge, Sec. 7.3 presents the first successful simulation of three-dimensional cellular detonation structure with detailed chemistry up to now. The simulation uncovers that the reinitiation process at the beginning of a new detonation cell involves a considerably higher local overdrive factor than in the two-dimensional case. Further on, the formation of unreacted regions toward the end of a detonation cell is analyzed.

In the last section of this final chapter two complex two-dimensional problems are tackled with highly adaptive setups: the Mach reflection of a CJ detonation wave at a wall and its diffraction when propagating out of a rectangular tube into an unconfined region. The simulations demonstrate the efficiency of the AMR algorithm for detonation simulation and the solution quality that can be obtained on recent parallel computers of moderate size. The computational setups are similar to those utilized in Sec. 5.6. Except an initial pressure of $p_0 = 10.0\,\mathrm{kPa}$ the configuration in the unreacted gas is identical to the two previous sections. All simulations are sufficiently resolved to display the development of the cellular structure under transient conditions. The numerical results are in perfect qualitative agreement with experimental observations [7, 163]. In particular, the experimentally measured critical tube width of approximately 10 detonation cells in rectangular channels [112] is reproduced in the diffraction simulations in Sec. 7.4.2.

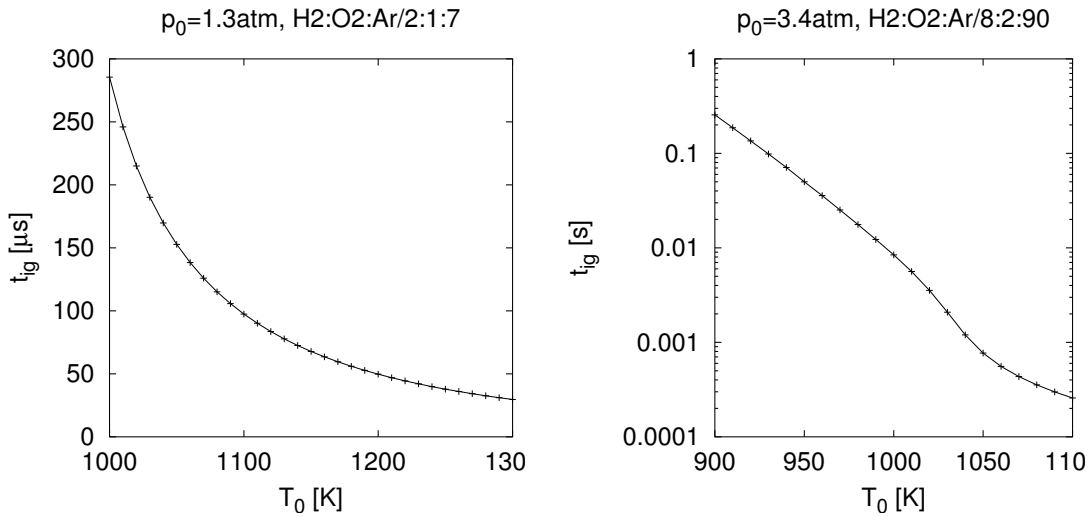

Figure 7.1: Induction times t_{ig} with respect to the initial temperature T_0 in an adiabatic constant volume environment for two configurations using Mechanism 1.

7.1 Reaction Mechanism

For all simulations we utilize the reaction mechanism of Westbrook [202] that has been derived originally for hydrocarbon oxidations in gaseous detonations. While the entire mechanism in [202] consists of 174 elementary reactions we only use the first 34 elementary reactions that are required for hydrogen-oxygen combustion. The mechanism is tabulated on page 225 (Mechanism 1). In order to validate Mechanism 1 and the integration of the chemical source terms according to Sec. 2.3.7 separately, we measure auto-ignition times with respect to the initial temperature T_0 by purely chemical kinetics computations in an adiabatic constant volume environment. This specific configuration corresponds exactly to the integration of a reaction term (2.78) in a fractional step method (see Sec. 4.10.1), where the total density ρ and the specific internal energy e are held constant when integrating the source term. The initial condition for the ODE (4.116) is uniquely specified by the initial molar ratios X_i^0 and the initial values T_0 and p_0 by

$$\rho_i(0) = \rho Y_i^0 \text{ for all } i = 1, \ldots, K \text{ with } \rho = \frac{p_0 W_0}{T_0 \mathcal{R}} \ , \ Y_i^0 = X_i^0 \frac{W_i}{W_0} \ , \ W_0 = \sum_{i=1}^{K} X_i^0 W_i \ .$$

We solve the stiff ODE (4.116) with the semi-implicit GRK4A method and the techniques described in Sec. 4.10. A computation is terminated, if the temperature satisfies the criterion $T > T_0 + 20\,\mathrm{K}$. The current time then defines the induction time $t_{ig}(T_0)$.

Two different $H_2 : O_2 : Ar$ mixtures discussed in detail in [139] are considered. The first configuration has molar ratios $2 : 1 : 7$ and an initial pressure of $p_0 = 1.3\,\mathrm{atm}$, the second one has molar ratios $8 : 2 : 90$ and a pressure of $p_0 = 3.4\,\mathrm{atm}$.

d_{CJ}[m/s]	1626.9
p_{vN}[kPa]	177.3
$\grave{u}_{vN}$[m/s]	395.5
$T_{vN}[K]$	1921.7
$t_{ig}[\mu s]$	3.55
l_{ig}[mm]	1.404

Table 7.1: Values of the $H_2 : O_2 : Ar/2 : 1 : 7$ CJ detonation at $T_0 = 298\,K$ and $p_0 = 6.67\,kPa$.

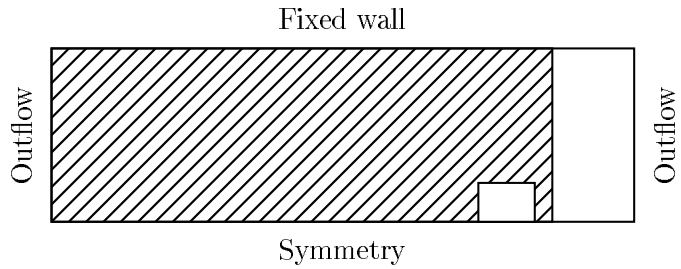

Figure 7.2: The computational domain has the size $10\,cm \times 3\,cm$. The leading shock of the CJ-detonation is placed at $x_1 = 8.6\,cm$. The center of the unreacted pocket is at $x_1 = 7.8\,cm$.

The computed induction times over a suitable initial temperature range for both configurations are visualized in Fig. 7.1.

7.2 Two-dimensional Cellular Structure

We start our considerations with simulations of the cellular structure of self-sustained CJ detonations analogously to Sec. 6.2. The $H_2 : O_2$-system diluted with a large portion of Ar is known experimentally [176] to produce very regular detonation cells (compare Fig. 3.5). Hence, it is an ideal candidate for numerical simulations and especially the early computations were done for this system. The primary goal of the first calculations [185, 99, 114, 115] was a qualitatively correct reproduction of the detonation cells in two space dimensions. Due to the strong limitations of the computational resources in these times only simplified one- or two-step reaction models were applied. The basic flow structure around a triple point (compare right picture of Fig. 3.6) was roughly reproduced.

The first successful two-dimensional detonation structure simulation with detailed non-equilibrium chemistry was presented by Oran and her collaborators in [138]. They applied uniform Cartesian meshes to investigate the CJ detonation of a $H_2 : O_2 : Ar$ mixture with molar ratios $2 : 1 : 7$ at room temperature $T_0 = 298\,K$ and pressure $p_0 = 6.67\,kPa$ for which the one-dimensional detonation structure has already been shown in Fig. 3.4.

Geßner [78] repeated the test case in [138] on unstructured adaptive grids and discovered that Mechanism 1 and the mechanism of Oran et al. [136, 139, 138] both create cellular structures with identical macroscopic parameters L and λ, but Mechanism 1 produces significantly sharper triple point tracks. As Mechanism 1 is smaller than the mechanism utilized in [136, 139, 138] we only use the faster Mechanism 1 in all our computations. Tab. 7.1 displays the flow values at the von Neumann point and the estimated induction length l_{ig} (see Sec. 3.1.2) for the test detonation and Mechanism 1.

In a recent work, Eckett [59] employed a serial version of the blockstructured AMR algorithm of Sec. 5.2 to solve the example in [138] with a reduced mechanism.

Setup	Base grid	r_1	r_2	Pts/l_{ig}
1	100×20	2	4	11.2
2	100×20	4	4	22.4
3	200×40	4	4	44.8

Table 7.2: Base grid and refinement factors of the three different setups.

Y_i	$S_{Y_i} \cdot 10^{-4}$	$\eta^r_{Y_i} \cdot 10^{-4}$
O_2	10.0	2.0
H_2O	8.5	1.0
H	0.2	5.0
O	1.0	5.0
OH	1.3	5.0
H_2	1.2	2.0

$\epsilon_T = 500\,\mathrm{K}$, $\epsilon_p = 15\,\mathrm{kPa}$, $\epsilon_\rho = 0.01\,\mathrm{kg\,m^{-3}}$

Table 7.3: Refinement criteria used in all three computations.

He successfully applied the reduction technique of Intrinsic Low-Dimensional Manifolds (ILDM) originally developed by Maas and Pope [128] for flame calculations and was able to reproduce the results of Oran et al. at a similar resolution with the ILDM reduced mechanism.

7.2.1 Computational Setups and Initialization

The computational setup in [138] is similar to Sec. 6.2. The one-dimensional CJ detonation is extended to two space dimensions with $u_2 = 0$ and transverse disturbances are initiated by placing a rectangular unreacted pocket downstream of the detonation front. Based on their experiences with simplified models [114, 99] Oran et al. proposed to use a pocket of unreacted gas of the size $10\,\mathrm{mm} \times 14\,\mathrm{mm}$ with a temperature of $2086\,\mathrm{K}$ starting $3\,\mathrm{mm}$ behind the leading shock front for this purpose. They employed a computational domain of $6\,\mathrm{cm}$ width and measured a detonation cell height λ of approximately $3\,\mathrm{cm}$.

After our good experience with quasi-stationary detonations in Sec. 6.1, we do not simulate the example from [138] with zero inflow velocity like it is usually done [138, 78, 59], but shift all velocities in the x_1-direction by $-d_{CJ}$. This allows us to use a channel of only $10\,\mathrm{cm}$ length. Analogously to Sec. 6.2.1 we use a larger auxiliary grid to record the maximum of $|\omega|$ for the visualization the triple point tracks. Furthermore, we exploit the symmetry of the problem and simulate only the upper half of the physical domain. The computational setup with boundary conditions is shown in Fig. 7.2.

Like in the preceding chapter we use the operator splitting approach to treat the chemical kinetics and the homogeneous fluid dynamic equations separately. Based on the results of the preceding chapter we apply the splitting method $\mathbf{Q}^{l+1} = \mathcal{S}^{(\Delta t)}\mathcal{X}_2^{(\Delta t)}\mathcal{X}_1^{(\Delta t)}(\mathbf{Q}^l)$ and utilize the Roe-HLL EF 3*-H scheme for the fluid dynamic integration. Like in all simulations with detailed chemistry the rate equations are integrated with the GRK4A method.

We utilize the three different adaptive setups of Tab. 7.2 with the resolutions of 11.2, 22.4 and 44.8 Pts/l_{ig} on the finest level to study the convergence of the

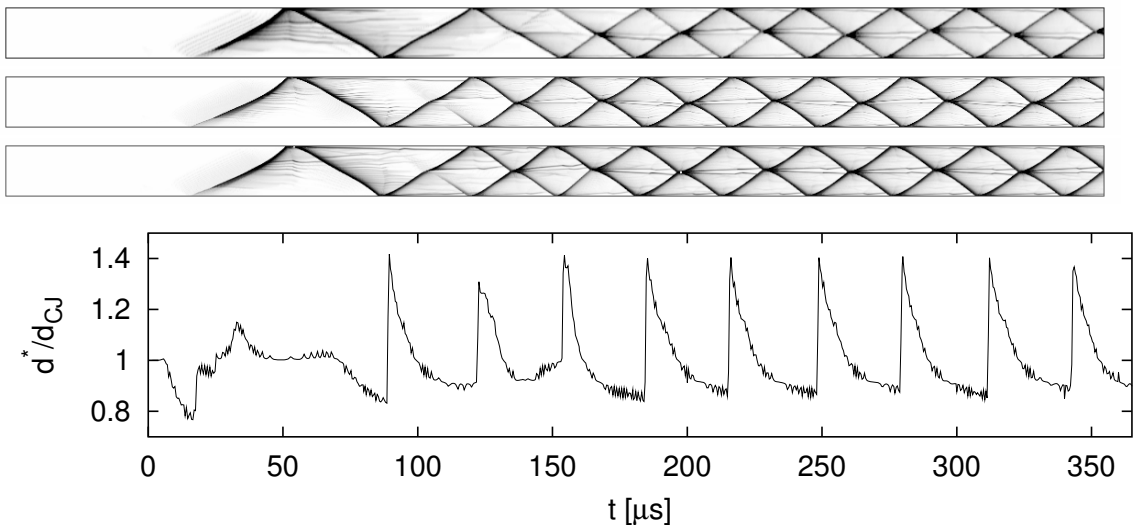

Figure 7.3: Triple point tracks for the time interval $[0\,\mu\text{s}, 400\,\mu\text{s}]$ with temporal development of the detonation velocity at $x_2 = 0.0\,\text{cm}$. Top: Setup 1, middle: Setup 3, bottom: Setup 2. After $\approx 200\,\mu\text{s}$ the detonation velocity d oscillates regularly.

solution and to obtain highly resolved reference results.[1] All computation end at $t_{end} = 800\,\mu\text{s}$, where automatic time step adjustment based on $C_{CFL}^{Roe} \approx 0.95$ (see Eq. (4.84)) was applied.

A physically motivated combination of scaled gradients and heuristically estimated relative errors is used as adaptation criteria (compare Sec. 5.4). The scaled gradients of total density ρ, total hydrodynamic pressure p and temperature T are used to achieve a reasonable adaptation to the most relevant discontinuous flow phenomena, which are the shock front of the detonation, the transverse waves and the slip lines (see Fig. 3.6). An appropriate adaptation to the chemical reaction region (see Fig. 3.6) is realized by applying the relative error criteria (5.26) to the mass fractions Y_i of the most relevant chemical species. For all six species tabulated in Tab. 7.3 the scaling limit S_{Y_i} is chosen to be 1% of the maximal value of Y_i for the undisturbed CJ detonation.

7.2.2 Comparison of the Computational Results

The adaptive setups 1 to 3 lead to basically similar numerical results. All computations reproduce the basic flow pattern discussed in Sec. 3.3 clearly and after an initial period, regular detonation cells with $\lambda = 3\,\text{cm}$ show up. Triple point tracks of the initial phase with the generation of a new triple point are shown in Fig. 7.3. Further on, Fig. 7.3 displays the detonation velocity d along the line of symmetry $x_2 = 0.0\,\text{cm}$ for Setup 2. After $\approx 200\,\mu\text{s}$ the oscillation becomes regular. The

[1] In a resolution study in [138] Oran et al showed that a minimal resolution of about $6\,\text{Pts}/l_{ig}$ is necessary to allow the correct approximation of the macroscopic parameter λ and the convergence of the numerical solution on the three setups can therefore be expected.

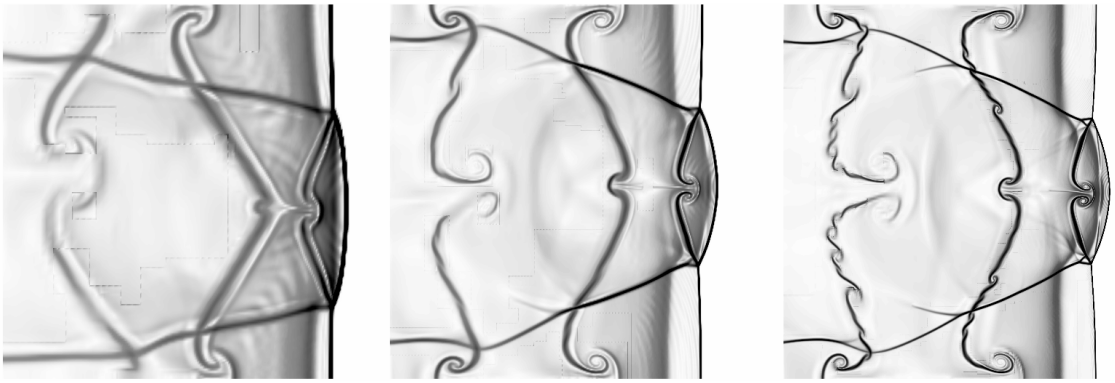

Setup 1: 11.2 Pts/l_{ig} Setup 2: 22.4 Pts/l_{ig} Setup 3: 44.8 Pts/l_{ig}

Figure 7.4: Schlieren plots of T for the three computational setups.

oscillation period t_p ranges from $\approx 31.3\,\mu$s for Setup 1 to $\approx 32.5\,\mu$s for Setup 3, which corresponds to an increase of the cell length L from ≈ 5.1 cm to ≈ 5.3 cm as the grid is refined. A direct comparison of the triple point tracks uncovers that the generation of the second triple point after the initial disturbance is delayed by one detonation cell in the coarsest computation. Further on, the triple point tracks appear to be more curved with increasing resolution.

A comparison of typical schlieren plots of relevant flow quantities for all three setups is presented in Fig. 7.4. While the results of the coarsest computation only allow the distinction of the discontinuities of the basic triple point structure visualized in Fig. 3.6, the results of Setup 2 and especially of Setup 3 show important sub-structures. In particular, a secondary triple point can clearly be distinguished along the transverse wave. The detailed flow pattern along a single transverse wave will be analyzed in Sec. 7.2.3.

The dynamic adaptation is qualitatively similar in all computations. Two typical situations in the first and the second half of a detonation cell are displayed in Fig. A.12. In case of Setup 1 the adaptive computation uses about 36.000 cells instead of 128.000 cells (uniform refinement).[2] A breakdown of the computational time spent in the computationally most expensive parts of the code analogously to the analyzes in Chap. 5 is given in Tab. 7.4. The numerical integration is split into the two main steps of the fractional step method: the homogeneous fluid dynamic update and the integration of the reactive source term. The ratio of the times for advancing the chemistry and the hydrodynamic transport is about 1.1 in all computations. This corresponds well to a ratio of about 0.8 in [138], where the usually faster ODE solver

[2]The threshold values for the scaled gradients in Tab. 7.3 have been adjusted to achieve also an adaptation to the downstream slip lines that have been torn off the detonation front in the reinitiation of previous detonation cells (compare Sec. 3.2). As the downstream slip lines do not influence the flow at the detonation front their adaptation can be omitted by increasing ϵ_ρ, ϵ_p without changing the cellular structure. For $\epsilon_\rho = 0.03\,\mathrm{kg\,m^{-3}}$, $\epsilon_p = 40\,\mathrm{kPa}$ Setup 1 uses only about 13.000 cells. The computational time for Setup 1 than reduces to 3.4 h.

Task	Setup 1		Setup 2		Setup 3	
	s	%	s	%	s	%
Fluid dynamics	10049	31.5	72216	31.0	366496	33.5
Chemical kinetics	11347	35.5	77435	33.2	403006	36.8
Boundary setting	9776	30.6	78922	33.9	293798	26.8
Recomposition	595	1.9	3685	1.6	26392	2.4
Misc.	158	0.5	719	0.3	5558	0.5
Total	**31925**	8.9 h	**232977**	2.7 d	**1095250**	12.8 d

Table 7.4: Breakdown of total computational times for the three different setups on a PC-Cluster of 7 Pentium III-850MHz-PCs connected with 1 Gb Myrinet.

SIAM was employed (compare Sec. 4.10.1). On the other hand, the good ratio of 1.1 proves that the distribution strategy presented in Sec. 5.3 achieves a reasonable load-balancing for this current problem without considering the number of expected local time steps for the source integration in the workload estimation as it has been done in [138]. The third important portion in Tab. 7.4 is the time for setting the ghost cell values, which is dominated ($\approx 90\,\%$) by the parallel synchronization overhead.

7.2.3 Flow Features of the Reference Solution

The comparisons in the previous section enlightened that the highest resolved simulation allows the deepest insight into the detailed sub-structures of the flow. Hence, the following discussion is based on the results of Setup 3, which can be regarded as a new reference for the problem in [138] with an increase of spatial resolution compared to all published results [138, 78, 59] by a factor > 4.5 in both space dimensions.

The highly resolved results of Setup 3 uncover a flow structure in the vicinity of a triple point that is remarkably more complex than the basic flow field shown in Fig. 3.6. The first refinement of the basic flow interpretation for low-pressure $H_2 : O_2$ CJ detonations was given by Lefebvre and Oran in [113] utilizing a two-step reaction model and extended (at least partially) to detailed chemistry in [138]. The results of Setup 3 allow a significant improvement of these previously published results [113, 138]. In particular, the formation of an unreacted region during the reinitiation process at the end of a regular detonation cell and the interaction of pressure waves emanating from the burning of this region with the reinitiated triple points will be described in detail.

Initialization of the Periodic Oscillation

The situation at the beginning of the simulation is visualized in Fig. A.14, where schlieren plots of the density for the region $[6\,\text{cm}, 9\,\text{cm}] \times [0\,\text{cm}, 3\,\text{cm}]$ are displayed. The burning of the unreacted region downstream of the detonation initiates shock

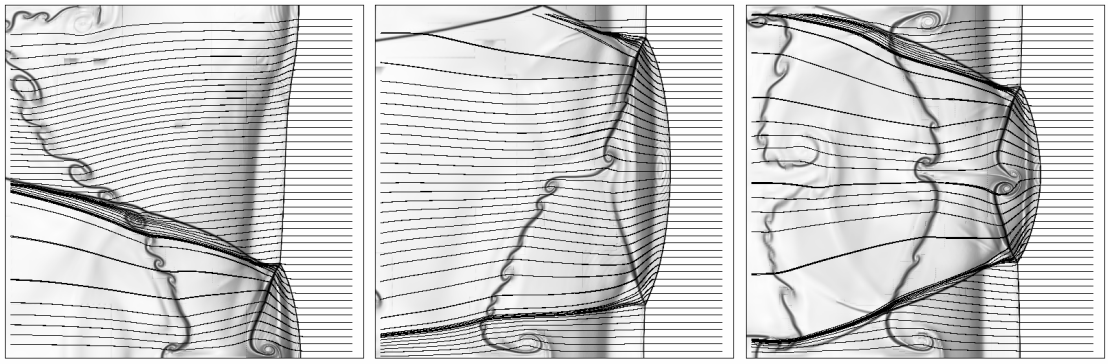

$t = 100\,\mu$s $t = 120\,\mu$s $t = 180\,\mu$s

Figure 7.5: Stream lines (black) on schlieren plots of T (gray) show the generation of the new triple point.

waves that form a triple point at the detonation front quickly (see $t = 20\,\mu$s). This triple point propagates through the channel with the flow pattern shown in Fig. 3.6 (see $t = 80\,\mu$s). Approximately at $t = 90\,\mu$s the triple point is reflected at the lower boundary, which corresponds exactly to the reinitiation phase between the two artificially generated triple points of a double-sized computation. No incident shock wave exists at the point of reflection and the old slip line is torn off (compare Sec. 3.2). When the triple point is reinitiated, a new slip line is established at the detonation front and the old one remains behind (see $t = 100\,\mu$s).

At $t = 100\,\mu$s the generation of a new triple point near the upper boundary can be observed. The long induction length between the beginning of the combustion zone and the incident shock decreases continuously around an inflection point at $x_2 \approx 2.3\,$cm. No discontinuous transverse pressure wave is present yet, but the beginning formation of the new triple point can be seen very well by observing the stream lines at $t = 100\,\mu$s in Fig. 7.5 that already point downward around the inflection. The new triple point and its discontinuous transverse wave come into existence at $t \approx 110\,\mu$s, directly after the collision of the inflection region with the old triple point. The newly created transverse wave spreads out downstream with $\grave{u}_1 - c$. A very rough estimate for this velocity is $-500\,$m/s and the new pressure wave consequently has a length of about $1.5\,$cm at $t = 140\,\mu$s. At $t = 180\,\mu$s the flow patterns around both triple points show only differences in the minor sub-structures. A few detonation cells later a perfectly symmetric flow is established.

Regularity of the Cell Structure

The two transverse waves form a perfectly regular hydrodynamic flow that is reproduced almost identically after $t_p \approx 32.5\,\mu$s. The flow during a regular detonation cell is presented in the Figs. A.15 and A.16. The symmetry line at $x_2 = 1.5\,$cm is apparent. This perfect regularity allows us to reduce the following detailed hydrody-

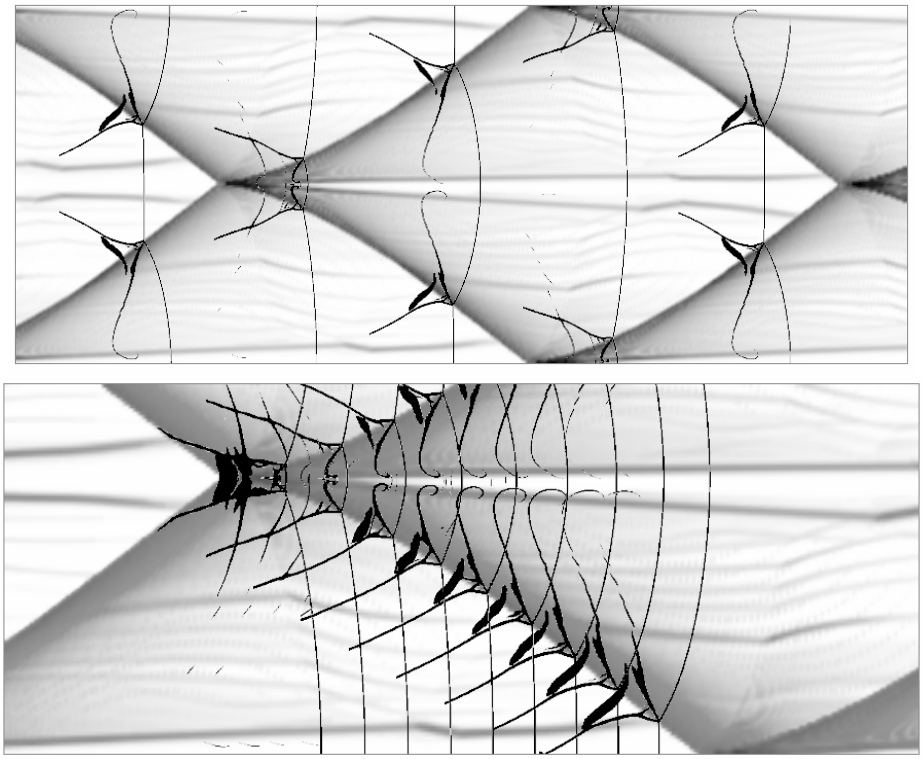

Figure 7.6: Consecutive schlieren plots (black) of the density plotted on triple point tracks (gray) display the temporal development of the triple point structure. Top: regular detonation cell, bottom: enlargement of a single triple point between two triple point collisions, 44.8 Pts/l_{ig}.

namic analysis to a single triple point between two triple point collisions. The upper graphic of Fig. 7.6 illustrates the flow symmetry after $\frac{1}{2}t_p \approx 16.25\,\mu$s. It displays the strongest discontinuities and the combustion region between transverse wave and slip line for $t = 616, 624, 632, 640, 648\,\mu$s. The lower picture shows in detail the strongest phenomena around the lower triple point from $t = 622\,\mu$s to $t = 634.8\,\mu$s where an output time step of $1.6\,\mu$s was used. The first collision considered in the lower picture of Fig. 7.6 occurs at $t = 620.4\,\mu$s, the second one, which ends our description, takes place at $t = 636.25\,\mu$s.

Triple Point Structure Before a Collision

We start our presentation of the detailed triple point flow structure with the situation that is mostly preserved from $t = 630\,\mu$s until the collision at $t = 636.25\,\mu$s. Schlieren plots allowing the separation of all flow phenomena discussed are shown in Fig. 7.7. Fig. A.13 presents various color plots to read physical values in the triple point region. The color graphics for the mass fractions additionally display the main discontinuities in ρ, the other plots are supplemented with isolines of Y_{OH}

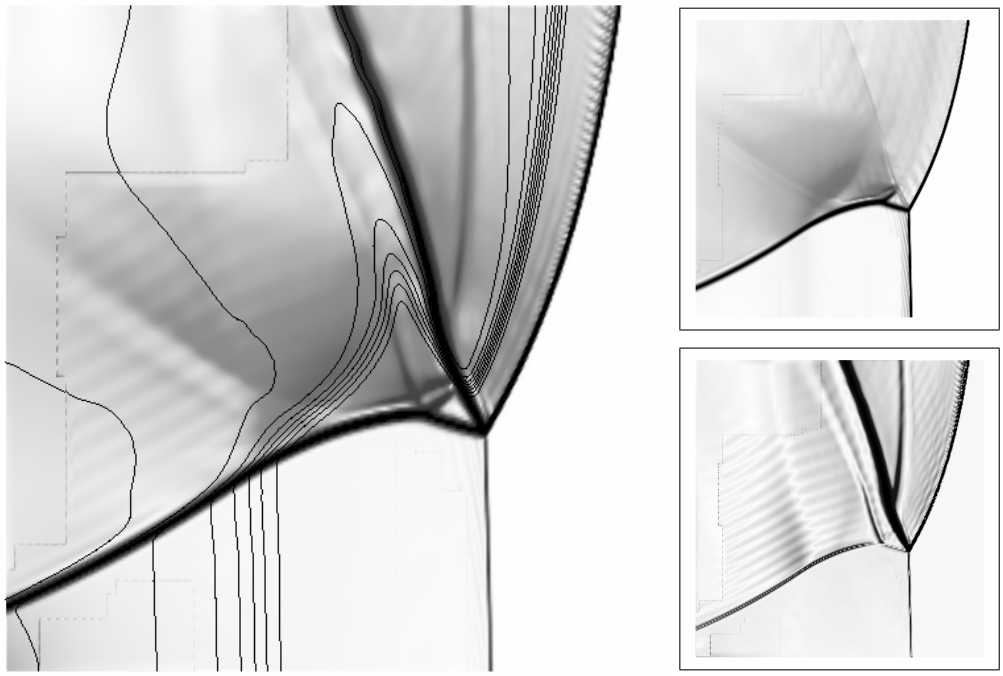

Figure 7.7: Flow structure before the next collision $t = 632\,\mu s$. Large: isolines of Y_{OH} (black) on schlieren plot of u_2 (gray). Small: schlieren plot of p (top) and $|\omega|$ (bottom).

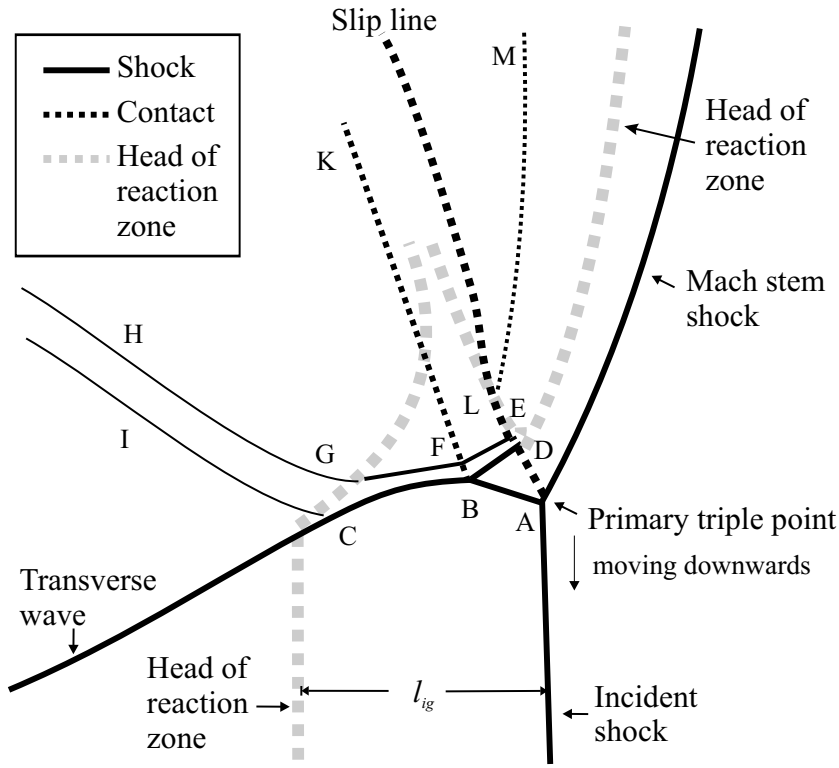

Figure 7.8: Flow structure around a single triple point before the next collision.

to visualize the induction length. In particular, an enormous increase in hydrodynamic pressure due to the transverse wave can be observed. The temperature in the incident shock region along the transverse wave is nearly as high as behind the Mach stem. Unreacted gas downstream of the incident shock passes through the transverse wave and is heated further. The particle movement relative to the triple point flow pattern can be seen in the color plot of the total velocity $|\mathbf{u}|$ where the actual stream lines at $t = 632\,\mu$s relative to the primary triple point A have been plotted.

Fig. 7.8 displays two minor triple points along the transverse wave behind the primary triple point A. While the characteristic inflection at point B is clearly visible, the triple point C is very diffused and the inflection of the transverse wave is extremely small. B is caused by the interaction of the strong shock wave BD with the transverse wave. The slip line emanating from B to K is clearly present. C seems to be caused by the reaction front (which can be interpreted as a diffused contact discontinuity) and generates the very weak shock wave CI. Downstream of BD a weaker shock wave EF shows up. It is refracted in the point F, when it hits the slip line BK. From F to G this minor shock is parallel and close to the transverse wave, which results in a higher pressure increase in the region FG than in the region EF (see Fig. A.13). Unreacted gas crossing the transverse wave between B and C therefore shows a shorter induction length than gas entering through AB (compare color plot of T in Fig. A.13). The minor shock is refracted and weakened by the reaction front at point G and forms the shock GH that is almost parallel to CI.

The downstream line of separation between particles which have passed through incident or Mach Stem shock is the slip line AD. The movement of the triple point A creates a shear flow along DEL between the reaction front behind the Mach stem and the reaction zone downstream of BD. In the actual picture the contact discontinuity LM seems to originate in this shear flow region, but in fact it is only a relict of the reinitiation phase and propagates constantly downstream. It has been caused by the interaction of a shock wave produced by the burning of an unreacted region during the reinitiation phase with the Mach stem shock (see below).

Temporal Development of the Triple Point Structure

The flow pattern described in the previous subsection develops out of the reinitiation after the triple point collision at $t = 620.4\,\mu$s in a time of about $10\,\mu$s. This complex flow process is shown in the schlieren plot of the Figs. A.17, A.18 and schematically sketched in the graphics of the Figs. 7.9 and 7.10. Color plots of the reinitiation phase are displayed in Fig. A.19. Analogously to Fig. A.13 isolines of Y_{OH} visualize the induction zone.

When the two triple points A hit at $t = 620.4\,\mu$s in one single point, the stable configurations around both triple points break down and the old slip lines are torn off immediately (compare the steps $t = 620.4\,\mu$s and $t = 620.8\,\mu$s in Fig. A.17). They start to propagate downstream and after the merging of both points D at $t \approx 620.8\,\mu$s they travel as one contact discontinuity. At the same time the new

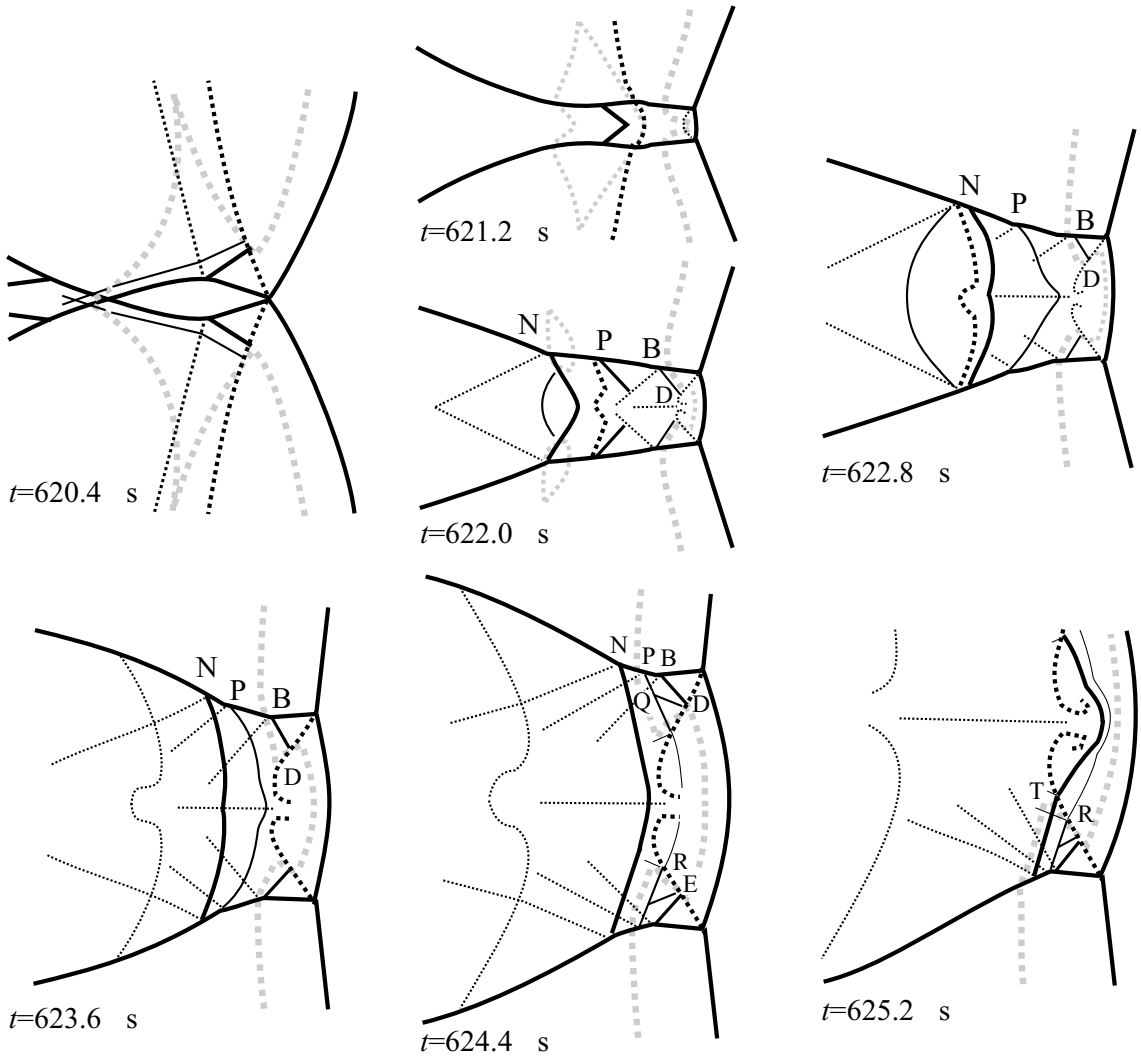

Figure 7.9: Collision of triple points and development of the double Mach structure.

Mach stem is initiated in a point-wise fashion. The temperature behind this new Mach stem is drastically higher than the temperature behind the old Mach stem before the collision. It increases rapidly from $\approx 2500\,\mathrm{K}$ at $t = 619.6\,\mu\mathrm{s}$ to more than $3500\,\mathrm{K}$ at $t = 621.6\,\mu\mathrm{s}$. The isolines of Y_{OH} in Fig. A.19 clearly represent the extraordinarily small induction length behind the Mach stem directly after the reinitiation.

The reinitiation separates the combustion zone behind the leading shock waves from the reaction regions downstream of the transverse wave. An unreacted region forms. It is bounded to the right by the old slip lines (see $t = 621.2\,\mu\mathrm{s}$ in Fig. 7.9). Its burning generates shock waves that hit the transverse waves in minor triple points N and P. At $t = 622.0\,\mu\mathrm{s}$ two shocks emanating in the upstream direction are visible. Further on, a thorough analysis of the time step $t = 622.0\,\mu\mathrm{s}$ uncovers that the secondary triple point B and its shock wave BD are already present. This is very

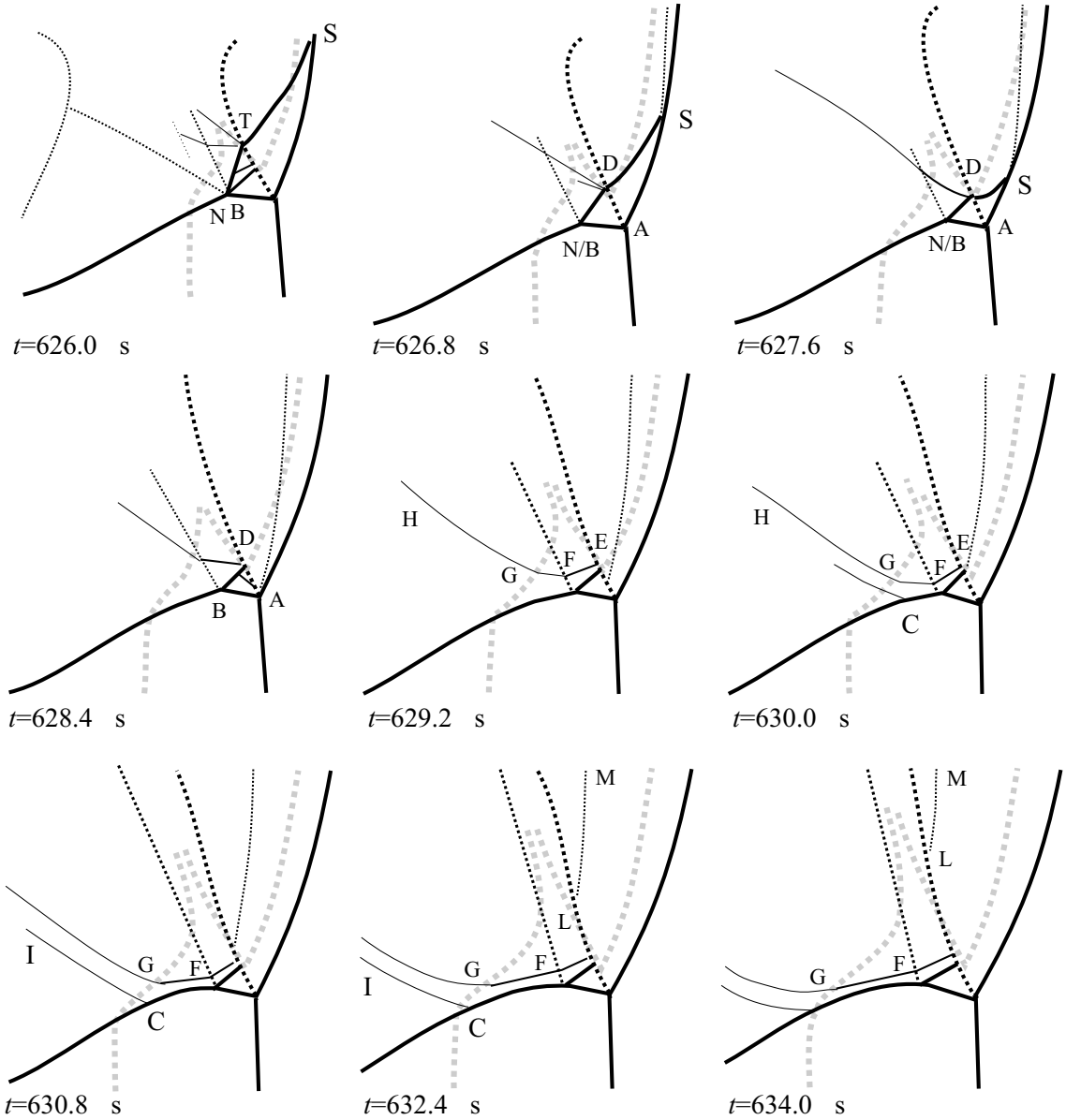

Figure 7.10: Development of the triple Mach structure out of the double Mach structure before the next collision.

much earlier than it was found in [113]. It is therefore reasonable to assume that the triple point B is inherently connected to the primary triple point A and that only the limited resolution prevents its appearance in the simulation at an earlier stage.

At $t = 624.4\,\mu$s both shock waves spreading out from the unreacted region have passed the old slip line and the first shock interacts with the new slip lines. It is refracted slightly and very weak triple points R are formed on the new slip lines. Further on, the minor shock emanating from E can be distinguished. Its refraction on the slip line of B can not be observed yet, because the shock forms a weak triple

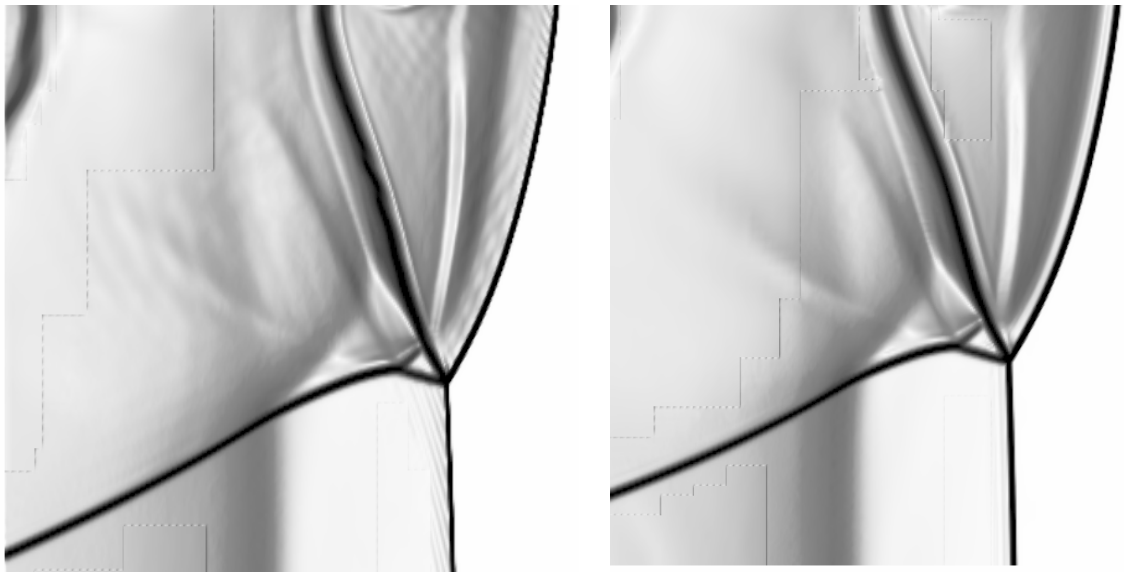

Figure 7.11: Comparison of schlieren plots of T for a quasi-stationary (left) and a fast propagating (right) detonation with $44.8\,\mathrm{Pts}/l_{ig}$.

point Q with the shock wave PR. In the next time step also the stronger second shock reaches the new slip lines and forms the triple point T. The triple points Q, R and T are so weak that no corresponding slip lines can be observed at this resolution. The upstream velocity of the stronger shock NT is higher than that of PR and at $t = 626.0\,\mu$s NT has caught up with PR and strengthens it (compare $t = 626.0\,\mu$s of Fig. 7.10). The triple point R is overrun by T. At $t = 626.8\,\mu$s NT has merged with BD and the shock wave EQ has vanished completely during the passage of NT. The shock wave NT forms a triple point S where it hits the Mach stem. The contact discontinuity emanating from S is clearly visible. In the following, the shock NTS propagates even through the area ABDS and finally reaches the primary triple point A at $t = 628.4\,\mu$s. At $t = 628.4\,\mu$s this shock has vanished completely above the slip line AD, only below AD a minor pressure wave has been preserved. Also the minor shock behind BD has reappeared at this time. From $t = 629.2\,\mu$s on the double refraction of this minor shock at F and G can be clearly observed. During the following time steps FG approaches the transverse wave and becomes tangential. The diffusive triple point C is observed first at $t = 630.0\,\mu$s. It seems to appear upstream of the reaction front at first, but merges with the beginning of the combustion region subsequently. The contact discontinuity LM, which has been created originally in the triple point S, propagates constantly downstream bounded by the primary slip line.

7.2.4 Comparison with Other Numerical Results

All previously published two-dimensional simulations of the CJ detonation of Tab. 7.1 used computational setups with zero inflow velocity. As explained in Sec. 6.1.5

the rapid propagation of a detonation wave through a fixed mesh introduces a discretization error especially at the detonation front that can mostly be avoided by employing a quasi-stationary setup. Fig. 7.11 compares a typical triple point structure obtained in Setup 3 with the result of an analogous adaptive computation in a long channel with zero inflow velocity [52]. Both simulations have the same maximal resolution of $44.8\,\mathrm{Pts}/l_{ig}$ in the x_1-direction and require similar computational times (because of the usage of dynamic mesh adaptation), but the quasi-stationary computation is obviously sharper resolved.

In [138] Oran et al. presented results for a resolution of $9.4\,\mathrm{Pts}/l_{ig}$ in the x_1-direction. They applied the method of fractional steps with local sub-cycling (compare Sec. 4.1.3). Their transport scheme was a recent version of the second-order accurate Flux-Corrected Transport (FCT) algorithm of Boris and Book [31, 33, 32] with fourth-order phase accuracy in space, which was extended by dimensional splitting to two space dimensions. With automatic time step adjustment based on an intended Courant number $C_{CFL} \approx 0.30$ their results on uniform grids are slightly better than our adaptive results and the approximation quality in [138] ranges between Setup 1 and Setup 2. The triple point tracks are clearly curved and secondary triple points can be identified at least at the end of a detonation cell (compare Fig. 7.8).

Eckett [59] used the same computational setup as Oran et al., but employed the sequentiel AMR algorithm of Sec. 5.2 and an ILDM reduced reaction mechanism to minimize the computational costs. Instead of FCT he utilized the Roe scheme of Sec. 4.6.1 with entropy enforcement in combination with switching to HLL to prevent the carbuncle phenomenon [150]. Probably a MUSCL reconstruction technique was applied. Because of the smaller intended Courant number the results in [59] at $9.4\,\mathrm{Pts}/l_{ig}$ seem to be slightly better than our results in Setup 1. Like in Setup 1 secondary triple points are not sufficiently resolved.

Geßner [78] utilized an unstructured adaptation strategy (see Sec. 5.1.1) to solve the example of [138]. He also used the method of fractional steps with local sub-cycling, but applied the Van Leer FVS of Sec. 4.5.2 without higher-order reconstruction as transport scheme. His simulations are for a maximal resolution of $7.2\,\mathrm{Pts}/l_{ig}$ in the x_1-direction and reproduce the macroscopic parameters λ and L correctly, but the approximation quality is below the results of Setup 1.

7.3 Three-dimensional Cellular Structure

In this section we simulate the regular cellular structure of the CJ detonation of Tab. 7.1 in a rectangular three-dimensional channel. The effective resolution of all computations is $16.8\,\mathrm{Pts}/l_{ig}$ in the x_1-direction. Although the dynamically adaptive method validated with similar computations in Sec. 6.3 was utilized, each run required about 3.3 d real time on 48 processors of the Helics cluster (compare page 167). To our best knowledge our results document the first successful attempt to simulate the three-dimensional regular structure of a detonation with detailed chemical reaction.

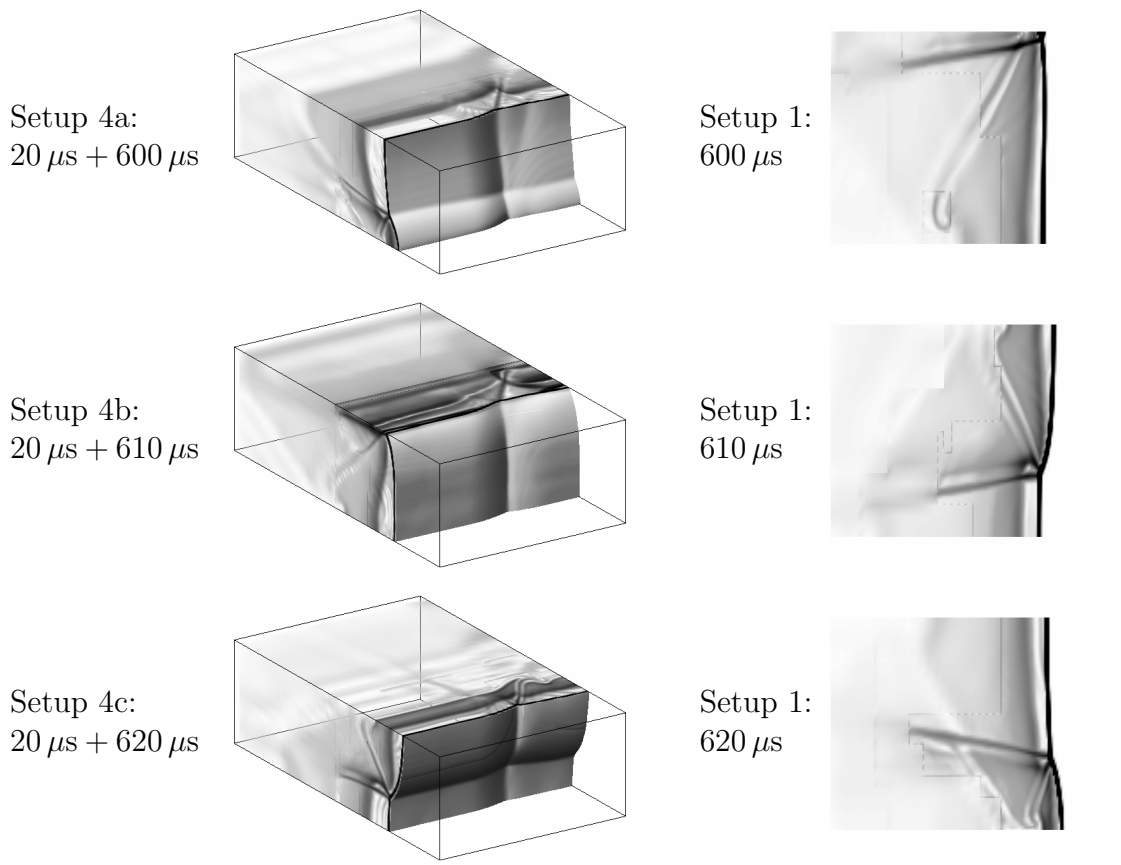

Figure 7.12: Two-dimensional initial conditions for Setup 4a to 4c and flow field after 20 μs simulation time, schlieren plots of ρ, $3\,\mathrm{cm} < x_1 < 5\,\mathrm{cm}$.

7.3.1 Computational Setups and Initialization

The computational setup is almost identical to ZND Test 6a to 6c, but unlike Sec. 6.3 we do not simulate just one quarter of a detonation cell, but one half. The computational domain has the size $[0\,\mathrm{cm}, 7\,\mathrm{cm}] \times [0\,\mathrm{cm}, 1.5\,\mathrm{cm}] \times [0\,\mathrm{cm}, 3\,\mathrm{cm}]$. In contrast to ZND Test 6a to 6c we use the regular oscillating solution of Setup 1 of Sec. 7.2 as initial condition and disturb the oscillation in the x_2-direction with an appropriate unreacted pocket in the orthogonal direction. We use the solution of Setup 1 at the three time steps 600 μs, 610 μs and 620 μs in the range $0\,\mathrm{cm} < x_2 < 1.5\,\mathrm{cm}$ and extend it to three dimensions with $u_3 = 0\,\mathrm{m/s}$. The different initial conditions are shown in the upper row of Fig. 7.12. They define the computational Setups 4a to 4c. In all setups the regular structure is shifted equally to the left, such that the nearly planar detonation front in Setup 4a is aligned to $x_1 = 4.6\,\mathrm{cm}$. In all configurations unreacted gas at 2086 K is placed in the region $[4.1\,\mathrm{cm}, 4.3\,\mathrm{cm}] \times [0\,\mathrm{cm}, 3\,\mathrm{cm}] \times [0\,\mathrm{cm}, 0.2\,\mathrm{cm}]$. While the initial triple point line orthogonal to the x_1-x_2-plane continuous to propagate regularly, the burning of the unreacted pocket initiates a triple point line perpendicular to the x_1-x_3-plane that is clearly established after 20 μs simulation time (see lower row of Fig. 7.12).

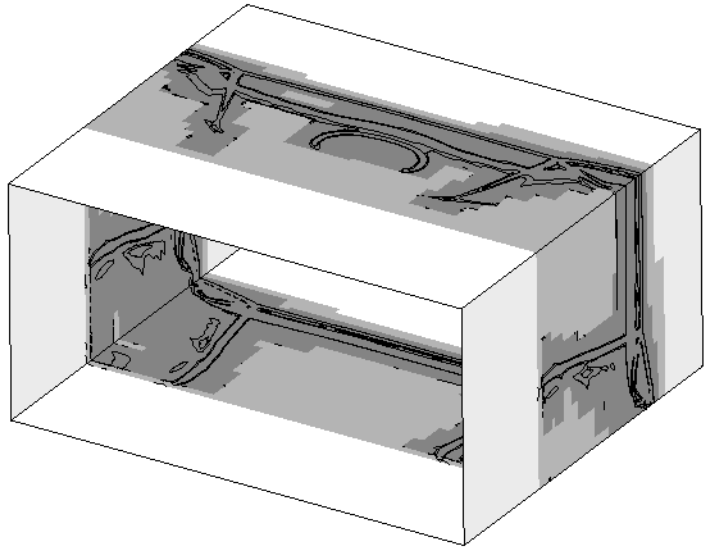

Figure 7.13: Detonation structure plotted on refinement grids. Result of Setup 4c at $t = 660\,\mu\text{s} + 620\,\mu\text{s}$, displayed: $4.5\,\text{cm} < x_1 < 7.0\,\text{cm}$.

Analogously to Sec. 7.2 the splitting method $\mathbf{Q}^{l+1} = \mathcal{S}^{(\Delta t)}\mathcal{X}_3^{(\Delta t)}\mathcal{X}_2^{(\Delta t)}\mathcal{X}_1^{(\Delta t)}(\mathbf{Q}^l)$ and the Roe-HLL EF $3^\star$-H scheme are applied. As usual, the chemical rates are integrated with GRK4A. Like in the two-dimensional case, all calculations end at $t_{end} = 800\,\mu\text{s}$ and use automatic time step adjustment based upon $C_{CFL}^{Roe} \approx 0.95$. All setups utilize a base grid of $140 \times 12 \times 24$ cells and use two levels of refinement with $r_1 = 2$ and $r_2 = 3$, which corresponds to a uniformly refined grid of 8.7 M cells.

We apply the adaptation criteria of Tab. 7.3, but set ϵ_p and ϵ_ρ to the higher values $\epsilon_p = 40\,\text{kPa}$ and $\epsilon_\rho = 0.03\,\text{kg}\,\text{m}^{-3}$. Further on, all refinement flags are overall deleted in the range $0\,\text{cm} < x_1 < 4\,\text{cm} + v_0 t$. Herein, $v_0 := 20\,\text{m/s}$ is a constant velocity that is used to extend the definitely unrefined region continuously to $0\,\text{cm} < x_1 < 5.6\,\text{cm}$ at t_{end}. As the computational domain is chosen as small as possible, the flow values have not completely reached the equilibrium state at the left boundary and a minor propagation of the quasi-stationary detonation to the right occurs. The parameter v_0 is used to extend the region without refinement with respect to this motion. With this trick the average refinement width is about 1 cm and the average total number of cells is around 1.35 M. Fig. 7.13 clearly reflects the artificial removal of refinement flags in the downstream region.

A uniform auxiliary grid of $2560 \times 12 \times 24$ cells with the mesh widths of the base grid is utilized to record the maximal magnitude of the vorticity as explained in Sec. 6.3.1.

7.3.2 Flow Features of the Periodic Solution

After approximately $250\,\mu\text{s}$ simulation time a second triple point line orthogonal to the x_1-x_3-plane has formed in all computational setups. In Setup 4a and Setup 4c the triple point lines in x_2 and x_3-direction have equal strength after about $600\,\mu\text{s}$,

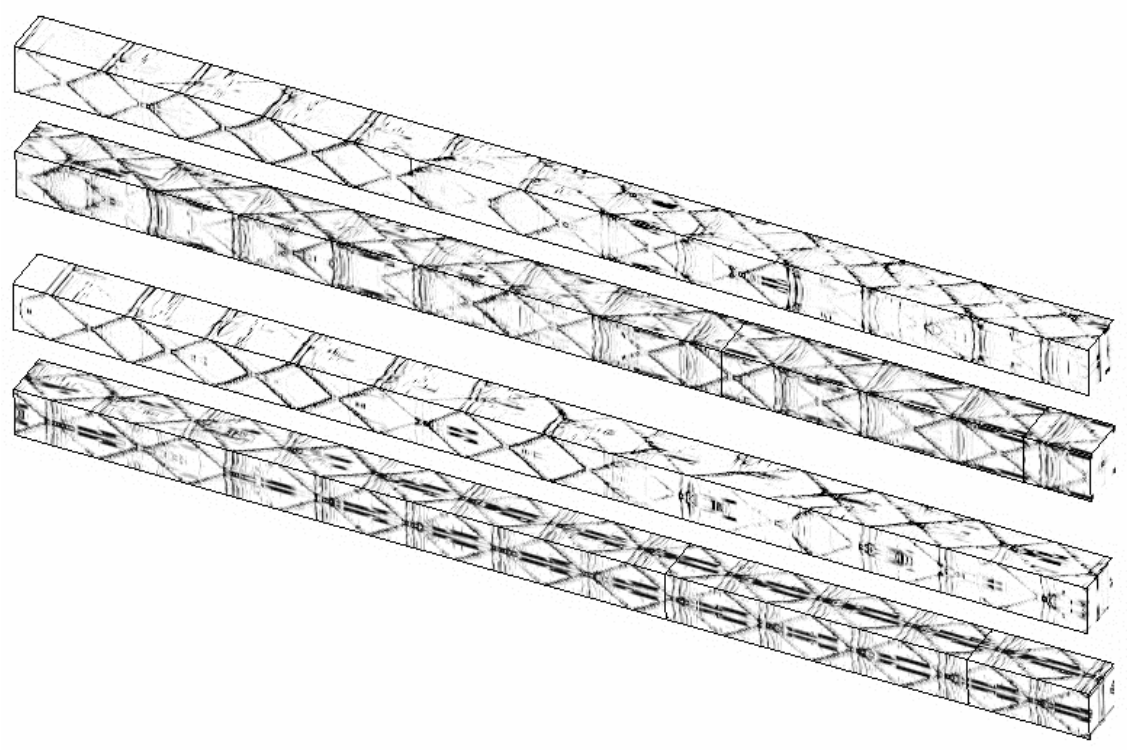

Figure 7.14: Triple point tracks of Setup 4a (upper two tracks) and 4c (lower two tracks). Mirrored at $x_2 = 0\,\text{cm}$ for visualization, the regions $[0\,\text{cm}, 64\,\text{cm}] \times [-1.5\,\text{cm}, 1.5\,\text{cm}] \times [0\,\text{cm}, 3\,\text{cm}]$ and $[64\,\text{cm}, 128\,\text{cm}] \times [-1.5\,\text{cm}, 1.5\,\text{cm}] \times [0\,\text{cm}, 3\,\text{cm}]$ are shown.

but the particular configuration of Setup 4b does not admit a three-dimensional mode of propagation and the initial triple point line propagating in the x_2-direction is suppressed by the regular oscillation in the x_3-direction after about $400\,\mu$s (not shown). The triple point tracks of Setup 4a and Setup 4c seem to be different at a first glance (compare Fig. 7.14), but a detailed analysis uncovers that both calculations simulate the same periodic flow situation, similar, but not identical, to the one studied in Sec. 6.3.

Periodicity of the Regular Structure

Like in Sec. 6.3 the typical triple point flow pattern known now in detail from Sec. 7.2.3 is preserved in three space dimensions. The similarity of the schlieren plots of Fig. 7.16 along planes perpendicular to the detonation front with those of Sec. 7.2.3 is apparent. Fig. 7.16 displays the flow field in Setup 4a at $680\,\mu$s and in Setup 4c at $660\,\mu$s simulation time, and it is obvious that both computations display the same periodic flow situation. Only the triple point lines propagating in the x_3-direction are periodically shifted by $x_3 = 1.5\,\text{cm}$. The triple point line moving in x_2-direction is at the same position and it is interesting to note, that the temporal delay of $20\,\mu$s between the initial values is exactly preserved throughout both calculations. Because of this reason we add the time value of the initial data to the simulation

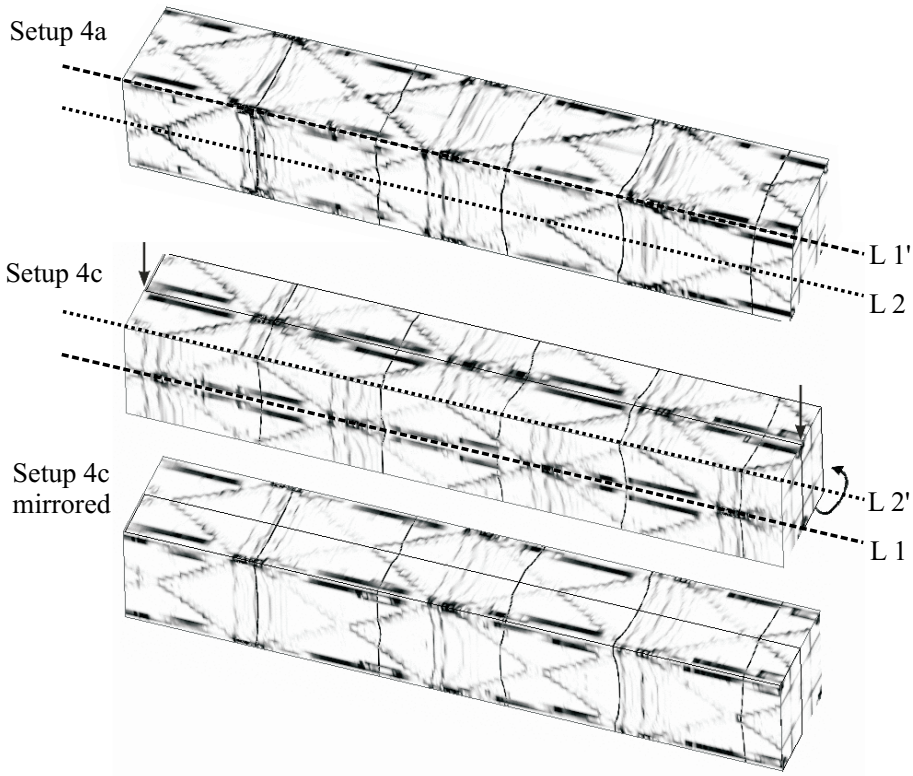

Figure 7.15: Top: regular triple point tracks of Setup 4a, middle: regular triple point tracks of Setup 4c. Bottom: Bisecting the middle vorticity record at $x_3 = 1.5\,\mathrm{cm}$ and mirroring it at $x_3 = 0\,\mathrm{cm}$ gives triple point tracks that are de facto identical to upper ones.

time in the following description. The equivalence of both computations can also be seen, if the maximal vorticity record of one calculation is bisected at $x_3 = 1.5\,\mathrm{cm}$ and mirrored at $x_3 = 0\,\mathrm{cm}$. Beside the temporal shift of $20\,\mu\mathrm{s}$ the result is de facto identical to the vorticity record of the other computation. Fig. 7.15 displays the mirroring for Setup 4c and the equivalence of the result with the vorticity record of Setup 4a.

Unlike the example in Sec. 6.3 no phase shift between x_2- and x_3-direction can be observed. Consequently, the Incident-Incident (II) and Mach stem-Mach stem (MM) regions (compare page 170) are always quadratic. The periodic triple line configuration shown in Fig. 7.16 at $t = 660\,\mu\mathrm{s} + 620\,\mu\mathrm{s} \equiv 680\,\mu\mathrm{s} + 600\,\mu\mathrm{s}$ is visualized in Fig. 7.17. The gray square corresponds to the sector visible in Setup 4a at $t = 680\,\mu\mathrm{s} + 600\,\mu\mathrm{s}$, the black dotted square displays the sector in Setup 4c at $t = 660\,\mu\mathrm{s} + 620\,\mu\mathrm{s}$. Further on, the middle row of Fig. 7.16 presents roll-ups of the cube marked in the three-dimensional graphics. They display schlieren plots of ρ and p. The lower graphic of Fig. 7.16 visualizes the location and orientation of these roll-ups with respect to the 3D graphic of Setup 4a. As the triple point lines in both transverse directions are exactly in phase, two orthogonal sides of the cube are almost perfectly symmetric, respectively. Therefore, a visualization of a single

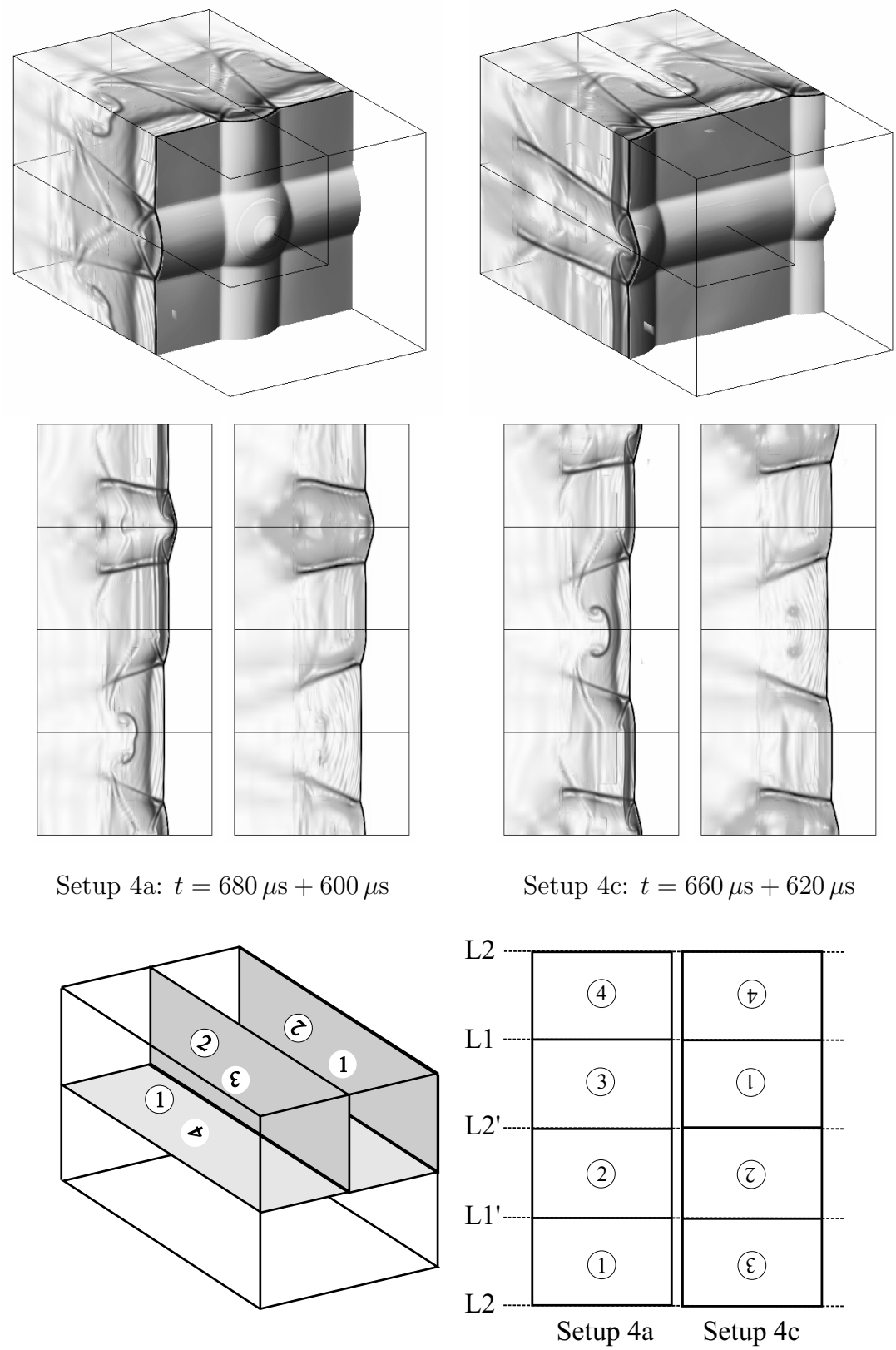

Figure 7.16: The schlieren plots of Setup 4a at $t = 680\,\mu s + 600\,\mu s$ and Setup 4c at $t = 660\,\mu s + 620\,\mu s$ display the same periodic situation. Mirrored at $x_2 = 0\,\text{cm}$ for visualization, $5.0\,\text{cm} < x_1 < 7.0\,\text{cm}$. Top: 3D graphics show ρ, middle: 2D roll-ups of ρ (left) and p (right), bottom: location and orientation of the 2D roll-ups in both setups.

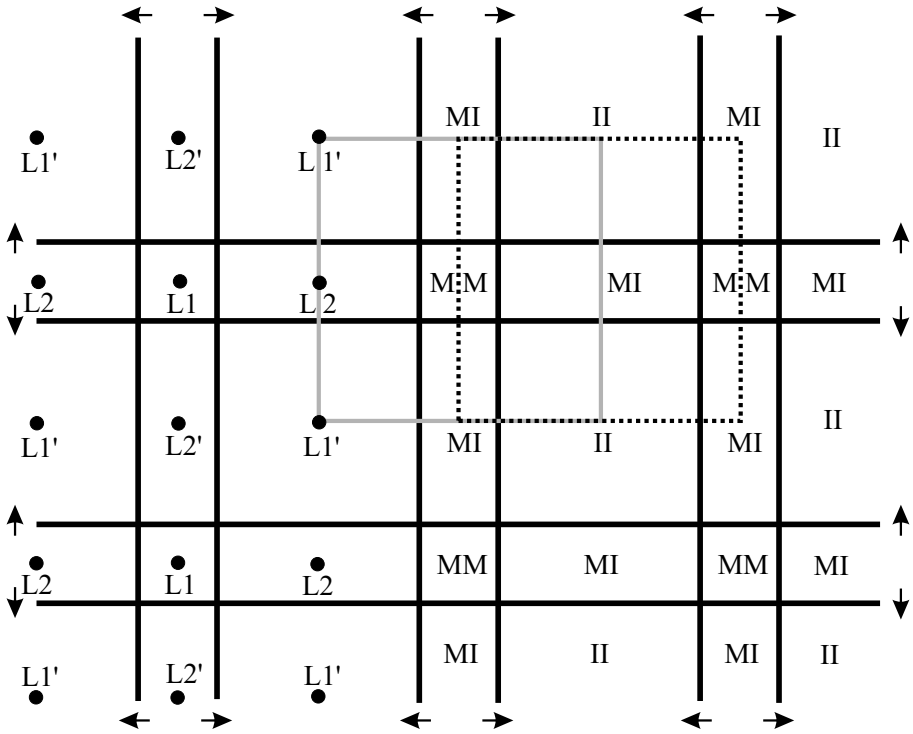

Figure 7.17: Schematic front view of the periodic triple point line structure at $t = 1280\,\mu$s. Gray square: Setup 4a at $t = 680\,\mu\text{s} + 600\,\mu$s. Black dotted square: Setup 4c at $t = 660\,\mu\text{s} + 620\,\mu$s. Compare 3D graphics of Fig. 7.16.

side from each of these pairs is sufficient to analyze the entire periodic flow field. This is done in the upper of Fig. A.20, where only color graphics of the sections 2 and 3 are displayed.

Although Setup 4a and 4c start from very different initial conditions, they both develop the same three-dimensional mode of propagation with a perfect symmetry between x_2- and x_3-direction. This mode is extremely regular and, compared to the overdriven detonation with simplified chemistry in Sec. 6.3, extraordinarily stable. While the vorticity record in Fig. 6.17 uncovers a continuous weakening of the three-dimensional oscillations toward the end of the simulation, no decrease in vorticity production is visible in Fig. 7.14. In all our computations only this particular three-dimensional mode or a purely two-dimensional mode with triple point lines just in x_2- or x_3-direction did occur. The three-dimensional mode of propagation, called "rectangular-mode-in-phase", has recently also been found in experiments with hydrogen-oxygen CJ detonations [86].

Temporal Development of the Triple Point Line Structure

Analogously to Sec. 7.2.2 we monitor the temporal development of the detonation velocity along specially selected lines perpendicular to the x_2-x_3-plane. These lines are displayed in topview in the left part of Fig. 7.17. Fig. 7.15 also displays some exemplary sideviews.

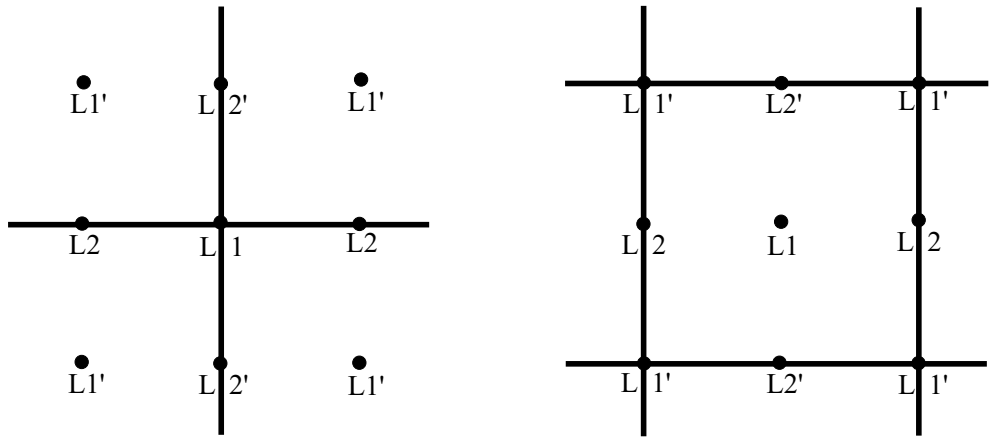

Figure 7.18: Point-wise reinitiation along L1 (left) and L1' (right). The time between both flow situations is exactly a half oscillation period.

The reinitiation of rectangular detonation cells only occurs along the lines L1 and L1'. At the beginning of a new detonation cell stands a point-wise reinitiation, when the four triple point lines bounding an II-square merge exactly in a single point. Because of the regularity of the oscillation these points lie all along lines L1 and L1'. The time between the reinitiation on all lines L1 and along all lines L1' is exactly a half oscillation period (compare Fig. 7.18). After the reinitiation the four triple point lines are diverging and the former II-sector has become an MM-square.

A line-wise reinitiation occurs when the converging two triple point lines of an MI-rectangle merge in a single line. Beside L1 and L1' a merging of triple point lines in both transverse directions occurs only along the lines L2 and L2'. The lines L2 and L2' pass through the center of the MI-rectangles. The time between the intersection of two triple point lines on L2 or L2' is a half oscillation period (compare Fig. 7.18).

Fig. 7.19 displays the temporal development of the detonation velocity relative to d_{CJ} along the lines L1 and L2 in Setup 4a (see also Figs. 7.15, 7.17 and the 2D sketch in Fig. 7.16) and both functions show the proposed periodicity. The time period between two cell reinitiations along L1 is $\approx 31.7\,\mu$s. This estimate is in good agreement with our two-dimensional measurements in Sec. 7.2.2 and corresponds exactly to the oscillation time that can be expected for our numerical method for $16.8\,\mathrm{Pts}/l_{ig}$. The result clearly underlines that the basic two-dimensional instability is exactly preserved in three dimensions, although its manifestation in the hydrodynamic flow field is different. In particular, a direct comparison of the graphs in the two- and three-dimensional case in Fig. 7.20 (compare also Fig. 7.3) uncovers that the three-dimensional detonation is significantly higher overdriven in the reinitiation points of the detonation cells than in the two-dimensional case. On the other hand, the line-wise reinitiation along L2 or L2' involves a considerably less overdriven detonation. It is interesting to note, that the minimal overdrive factor throughout a detonation cell seems to be independent of the dimension.

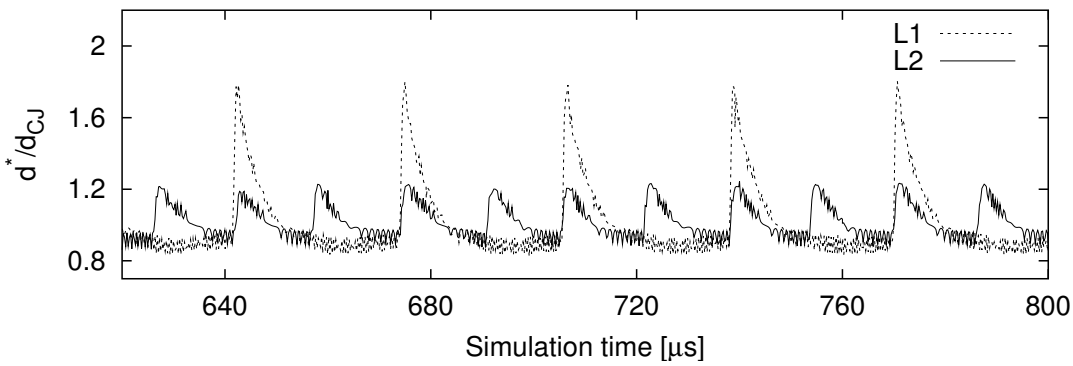

Figure 7.19: Temporal development of the detonation velocity along the lines L1 and L2 in Setup 4a.

The development of the three-dimensional flow field in the one detonation cell completely covered by Fig. 7.20 is displayed in the Figs. A.21 and A.22. While the graphics of the left column display schlieren plots of ρ analogously to Fig. 7.16, the right column shows schlieren plots of Y_{OH} overlaid by a transparent blue isosurface of the density. The distance between this isosurface and the gray isosurface of Y_{OH} behind it visualizes the induction distance l_{ig} in the three-dimensional case. The Figs. A.23 and A.24 show two-dimensional roll-ups of ρ and Y_{OH}. Together with the three-dimensional graphics in the Figs. A.21, A.22 these two-dimensional plots allow the detailed analysis of the entire flow situation. As the periodic oscillation is symmetric in both transverse directions, it suffices to display the four sides 1 to 4 during one half of a regular oscillation to visualize the flow over an entire detonation cell. In particular, the sides 1 and 2 in the Figs. A.23, A.24 show already the flow field along the sides 3 and 4 in the second half of the detonation cell, which is therefore omitted.

The detonation cell is reinitiated on L1 at $t \approx 675\,\mu\mathrm{s} + 600\,\mu\mathrm{s}$. Fig. A.21 shows the first half of the detonation cell, when L1 is in the center of the MM-square. The two-dimensional graphics clearly reflect the enormous decrease of the induction length immediately after the reinitialization due to the high overdrive factor by the merging of orthogonal triple point lines in the MM-region. The high overdrive factor also changes the appearance of the transverse waves. This can be seen for instance by observing the 2D graphics of Fig. 7.16 or Fig. A.21. Two parallel sides $1, 3$ or $2, 4$ always display perpendicular cuts through the same triple point line. While the triple point line acts as a diverging boundary of an MM-square on the one side, it is a converging boundary of an II-region on the other. The 2D graphic uncovers that the transverse waves of the same triple point line form very different angles with their corresponding incident shock region. While the angle between transverse wave and plane II-shock is approximately 24° at $t \approx 680\,\mu\mathrm{s} + 600\,\mu\mathrm{s}$, the angle between transverse wave and MI-shock is only $\approx 10^o$. Nevertheless, the propagation velocity of the triple point lines is equal everywhere. This observation is a strong indication that the transverse waves are only the result of the triple point lines. The triple

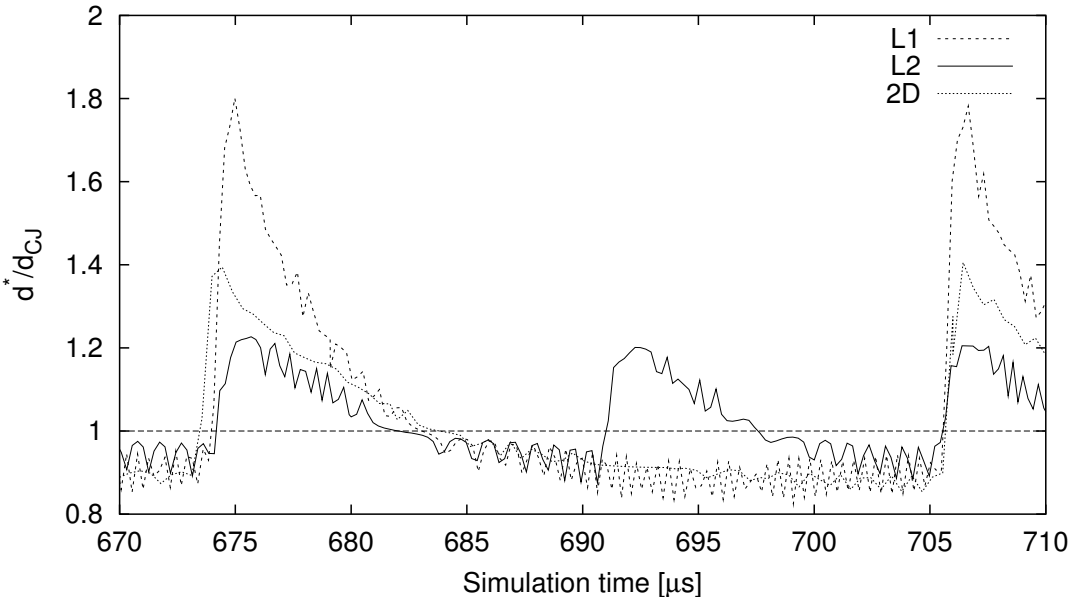

Figure 7.20: Temporal development of the detonation velocity along the lines L1 and L2 in Setup 4a compared to the result of a purely two-dimensional simulation.

point lines by themselves seem to be the fluid dynamical manifestation of a general oscillation mechanism. Their actual geometry seems to be determined just by the shape of the surrounding combustion chamber.

The development of the detonation front in the second half of a detonation cell is shown in Fig. A.22. Especially the right 3D graphic for $t = 704\,\mu\text{s} + 600\,\mu\text{s}$ clearly displays the formation of unreacted regions similar to the one analyzed in the two-dimensional case. In three space dimensions a deep unreacted region is formed by the four converging triple point lines of the II-square, shallower oblong unreacted regions are developed through the merging of two triple point lines in the MI-regions. The formation of unreacted regions at the boundary of the computational domain can be seen on the sides 1 and 2 of Fig. A.24. The schlieren plot of Y_{OH} at $t = 690.4\,\mu\text{s} + 600\,\mu\text{s}$ displays the formation of the deep unreacted region along L1' and the simultaneous closing of the oblong unreacted regions. The three-dimensional shape of these regions is visualized in the lower graphics of Fig. A.20. The sequence in Fig. A.20 displays the rapid burning of these regions leading to extraordinary high local values of Y_{OH} especially behind the new MM-squares (the uncolored regions in the graphics for $t = 691.2\,\mu\text{s} + 600\,\mu\text{s}$ and $t = 692.0\,\mu\text{s} + 600\,\mu\text{s}$ are above the previous maximum).

Analogously to the two-dimensional case, the merging of two triple point lines in a single line causes a temporary breakdown of the stable triple point configuration. In particular, the old slip lines are torn off from the detonation front and remain behind. These slip lines have the usual shape along planes perpendicular to a particular triple point line, but they appear as almost straight lines on planes orthogonal to the triple point lines' vector of motion. The time steps $t \geq 696\,\mu\text{s} + 600\,\mu\text{s}$ of Fig. A.22 display

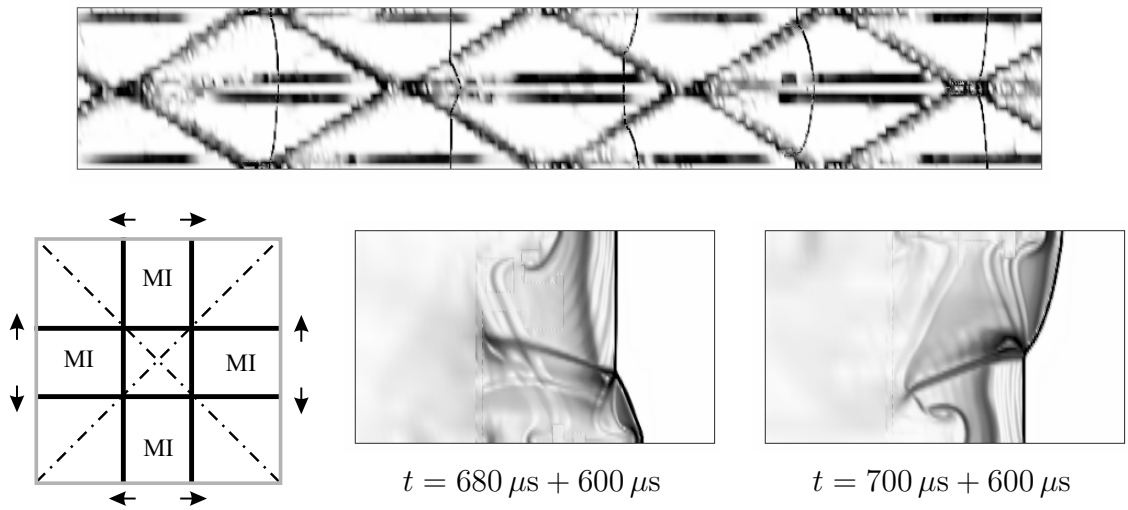

Figure 7.21: Results of Setup 4a. Top: Triple point tracks along diagonal cut, mirrored at $x_2 = 0\,\text{cm}$. Bottom, left: cutting planes shown on front view of triple point line structure at $t = 680\,\mu\text{s}+600\,\mu\text{s}$. Bottom, middle and right: schlieren plots of ρ for one half of 2nd and 3rd detonation front displayed on upper triple point track.

the downstream propagation of slip lines that have been torn off from the detonation front in the slapping of the triple point lines at the boundary at $t \approx 691\,\mu\text{s}+600\,\mu\text{s}$. The separation process along two such sides can be studied in detail in Fig. A.24 for $t \geq 691.2\,\mu\text{s} + 600\,\mu\text{s}$ for the sides $1, 2$ and in Fig. A.24 for the sides $3, 4$.

Finally, we note that regular two-dimensional detonation cells can also be found along the two diagonal cuts going through the middle axis of the computational domain. A diagonal cut through the maximal vorticity record and diagonal schlieren plots of the density for Setup 4a are displayed in Fig. 7.21. The detonation cells shown in Fig. 7.21 have the same length as for example in Fig. 7.15, but the height is $\lambda = 3\sqrt{2}\,\text{cm}$. The schlieren plots display the basic triple point pattern. It is interesting to note, that the measurable angle between transverse wave and incident shock in the four points, where II- and MM-region abut directly, is approximately 18° at $t = 680\,\mu\text{s}+600\,\mu\text{s}$ and therefore between the two previously measured angles. This indicates that the angle of the transverse waves to the detonation front depends more on the absolute strength of the Mach stem than on the differences between Mach stem and incident shock.

7.4 Cellular Structure Under Transient Conditions

In this last section of Chap. 7 we study the behavior of the previously presented regular cellular detonation structure under transient conditions. We consider two different problems in two space dimensions: the reflection of a detonation wave un-

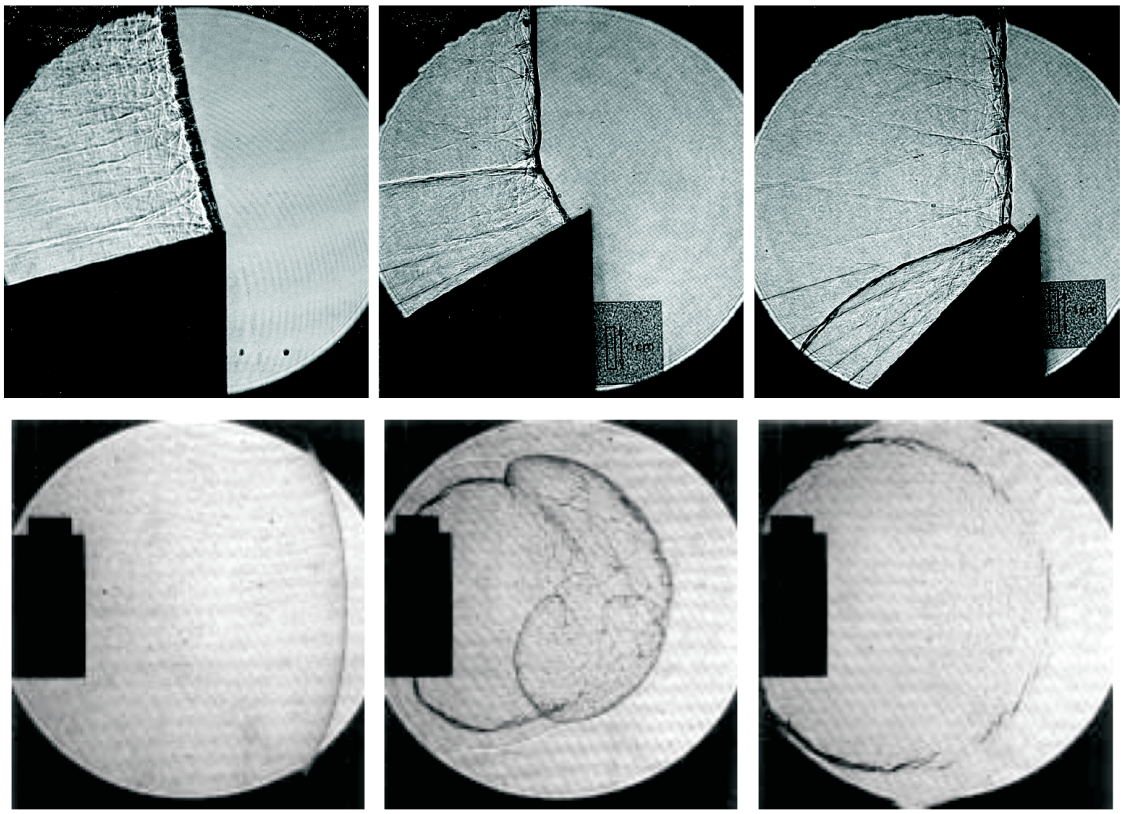

Figure 7.22: Schlieren photographs of detonation waves under transient conditions. Top: reflection, left: $\Theta = 15^o$, middle: $\Theta = 30^o$, right: $\Theta = 45^o$ [7]. Bottom: diffraction, left: super-critical, successful transmission, middle: critical, right: sub-critical, detonation failure [163].

der different angles, in particular in the case of Mach reflection (compare Sec. 5.6.1), and the detonation failure due to diffraction when a detonation wave propagates out of a duct into an unconfined region. Both studies have fundamental character and provide basic insight into the process of detonation propagation in complex geometries as they typically appear for instance in propulsion systems or in safety and hazard analysis. Hence, both cases have been investigated in numerous experiments for a large number of combustible mixtures [7, 163, 112, 61, 189].

The following subsections are intended to demonstrate the efficiency of the AMR algorithm for detonation simulation and the solution quality that can be obtained on recent parallel computers of moderate size. The physical interpretation of the combustion phenomena will be much shorter than in the preceding two sections. Detailed discussions of the computations in the subsections 7.4.1 and 7.4.2 will be presented elsewhere. All simulations utilized the same numerical methods as the calculations in Sec. 7.2.

Recently, Ohyagi et al. [135] carried out a numerical study for a two-step reaction model that investigated the devolopment of the cellular structure under Mach

d_{CJ}[m/s]	1638.5
p_{vN}[kPa]	269.5
$\grave{u}_{vN}$[m/s]	397.3
$T_{vN}[K]$	1944.6
$t_{ig}[\mu s]$	2.21
l_{ig}[mm]	0.878

Table 7.5: Values of the $H_2 : O_2 : Ar/2 : 1 : 7$ CJ detonation at $T_0 = 298\,K$ and $p_0 = 10.0\,kPa$.

Y_i	$S_{Y_i} \cdot 10^{-4}$	$\eta^r_{Y_i} \cdot 10^{-4}$
O_2	10.0	4.0
H_2O	8.5	2.0
H	0.2	10.0
O	1.0	10.0
OH	1.3	10.0
H_2	1.2	4.0

$\epsilon_T = 500\,K$, $\epsilon_p = 40\,kPa$, $\epsilon_\rho = 0.05\,kg\,m^{-3}$

Table 7.6: Refinement criteria for the computations in Sec. 7.4

reflection. They utilized the method of fractional steps in combination with the FCT scheme [31, 33, 32], but simplified the simulation by updating just cells in the vicinity of the shock at the head of the detonation. Therefore, their calculations do not provide insight into the change of the characteristic triple point pattern downstream of the leading shock front. In a different recent study Arienti and Shepherd [8] simulated the detonation diffraction process for a one-step reaction model with a parallel version of Eckett's code (compare Sec. 7.2.4).

To our best knowledge, our calculations document the first successful attempts with detailed chemical reaction in both problem classes that are suffiently resolved to study the instationary triple point structures at the detonation front in detail.

Initialization

Analogously to Sec. 7.2 we utilize a CJ detonation of a $H_2 : O_2 : Ar$ mixture with molar ratios $2 : 1 : 7$ at $T_0 = 298\,K$ in all simulations. Unlike to the previous calculations the pressure in the unreacted mixture is $p_0 = 10.0\,kPa$. Although the higher initial pressure leads to smaller detonation cells with $\lambda \approx 1.6\,cm$ and $L \approx 2.75\,cm$, the triple point pattern is similar. Characteristic flow quantities of the undisturbed CJ detonation are tabulated in Tab. 7.5.

In the following subsections we use a regular oscillating detonation propagating with velocity d_{CJ} into unreacted gas at rest as initial condition. This is a reasonable idealization for the flow situation in typical detonation tubes with rectangular cross-section directly before the experimental setup. This initial condition is effectively derived by calculating a regular oscillating solution with a width of one detonation cell in advance and by reproducing the flow field of an appropriate snapshot periodically.

7.4.1 Mach Reflection of a Detonation Wave

We simulate the reflection of a detonation wave at three different wedges ($\Theta = 15^o, 30^o, 45^o$) with the technique of Sec. 5.6.1 and rotate the surface of the wedge and the incident detonation by an angle of $-\Theta$. In particular, this transformation requires a point-wise rotation of the initial velocity vector $\mathbf{u} = (u_1, u_2)^T$ by $-\Theta$. Note,

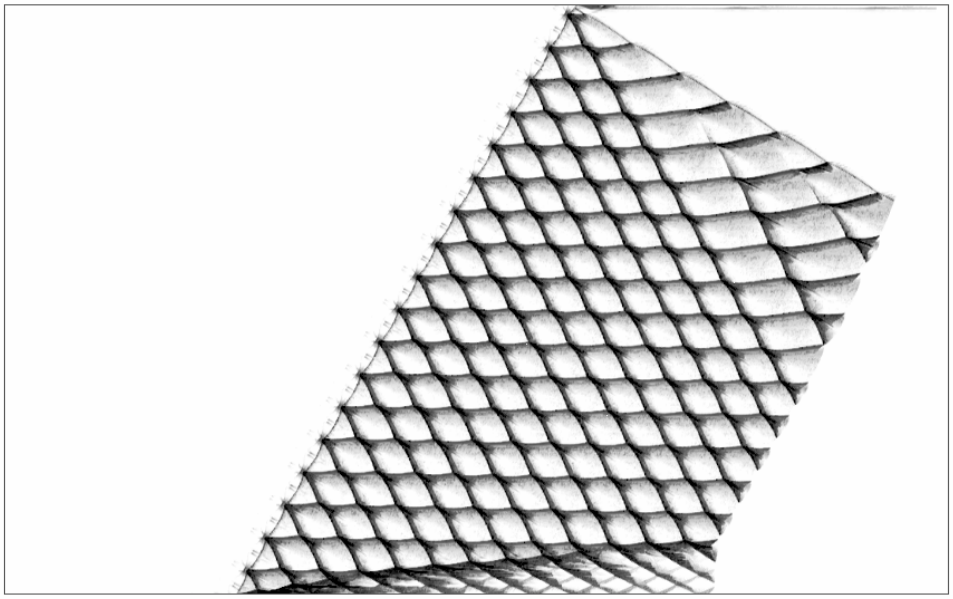

Figure 7.23: Record of triple point tracks for the entire computational domain at $t_{end} = 100\,\mu$s for Setup 5b with $\Theta = 30^o$.

that the instationary flow field calculated from these initial values it only correct below the initially highest triple point propagating downward. A strictly Cartesian code does not allow the reflection of triple points perpendicular to the detonation velocity vector. Hence, upward propagating triple points reach the uninitialized region above the detonation front some time and the height of the regular detonation structure above the lower boundary declines continuously. As we are interested just in the change of the cellular structure for a relatively small simulation time ($t_{end} = 100\,\mu s$), we ensure the correctness of the flow near the lower boundary simply by taking a sufficiently large computational domain of 40 cm × 25 cm. Fig. 7.23 illustrates the development of the triple point structure for an angle of $\Theta = 30^o$ during the simulation. The decline of the regularly oscillating region is clearly visible.

The domain is discretized with a base grid of 180 × 80 cells and five refinement levels with $r_{1,2,3,4} = 2$ and $r_5 = 4$ are applied (uniform refinement: ≈ 59.0 M cells). The effective resolution is around 20 Pts/$\mathrm{l_{ig}}$. The adaptive criteria are given in Tab. 7.6. In order to reduce the computational expense further, we allow an adaptive mesh refinement only in the declining valid flow region. With this technique the number of cells decreases continuously from 0.9 M to 400 k for $\Theta = 15^o$ and from 1.35 M to 507 k for $\Theta = 45^o$. On 16 Pentium-III-850 MHz CPUs connected with 1 GHz Myrinet the computing times range between 2.9 d ($\Theta = 15^o$) and 4.2 d ($\Theta = 45^o$), where around 50 % of the computational time are spent in the numerical solution routines.

Fig. 7.24 displays schlieren plots for all three different angles at $t = 48\,\mu$s. All flow fields are in perfect qualitative agreement with the snapshots in the upper row

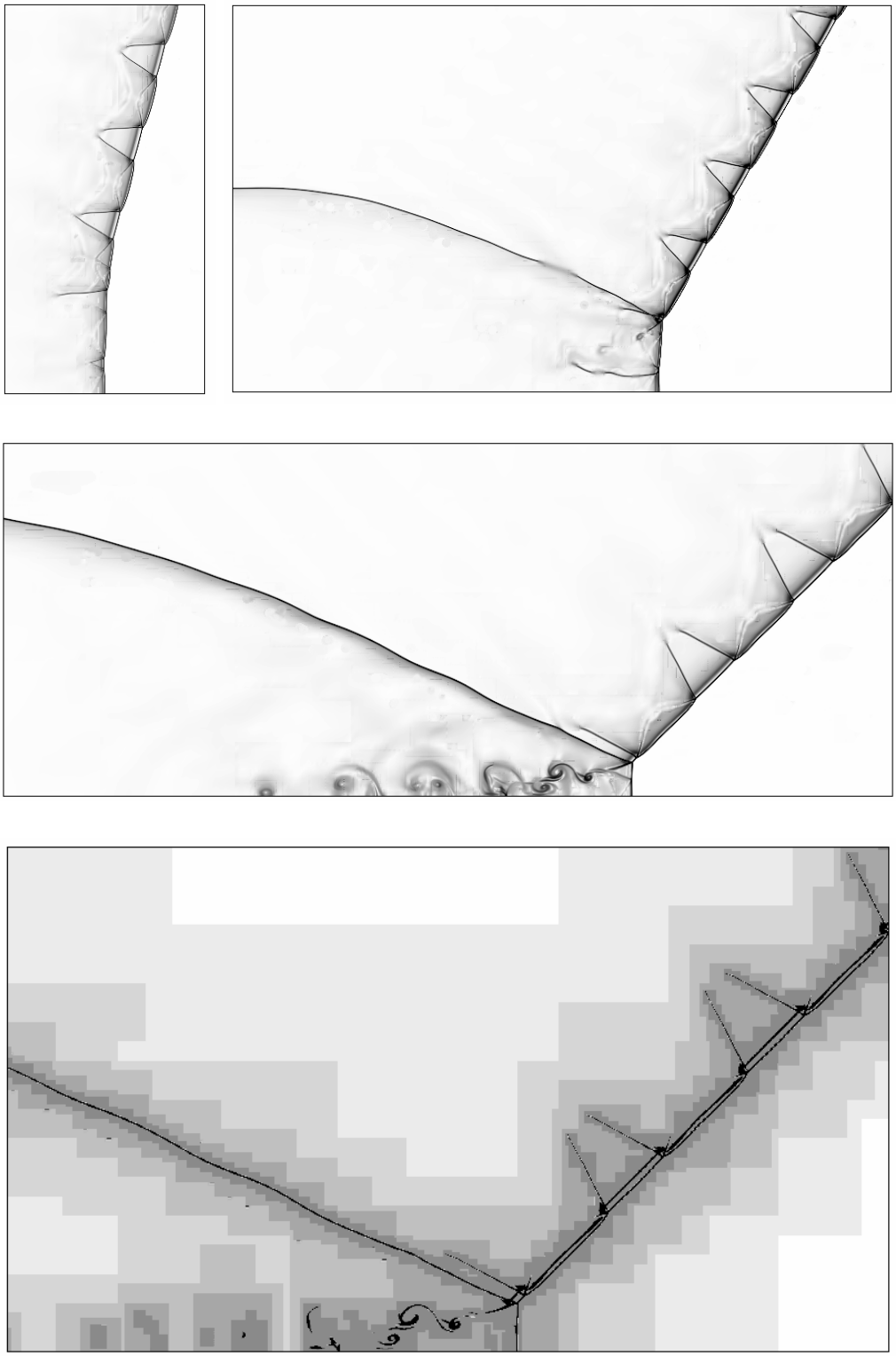

Figure 7.24: Schlieren plot of the density at $t = 48\,\mu$s for Setup 5a to 5c. Top, left: $\Theta = 15^{\circ}$, top, right: $\Theta = 30^{\circ}$, middle: $\Theta = 45^{\circ}$, bottom: schlieren plot of density on refinement levels.

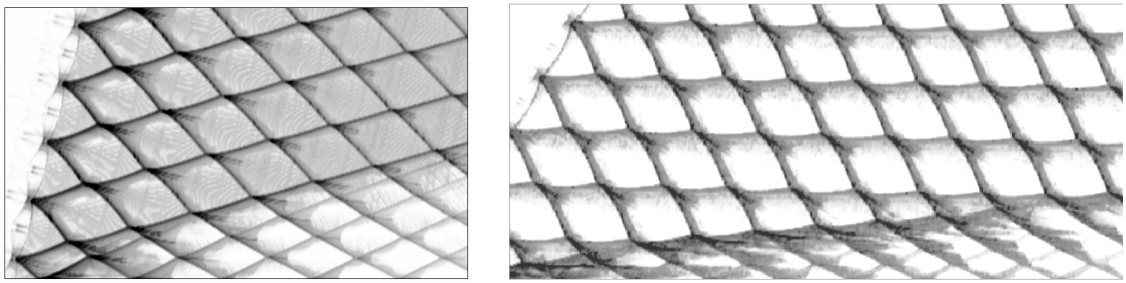

Figure 7.25: Simulated triple point tracks of Setup 5a with $\Theta = 15^o$ (left) and Setup 5b with $\Theta = 30^o$ (right).

of Fig. 7.22. The upper row of Fig. 7.22 displays schlieren photographs taken in experiments with a combustible mixture that exhibits detonation cells of similar size [7]. While the angle $\Theta = 15^o$ (Setup 5a) allows a regular reflection, the angles $\Theta = 30^o$ (Setup 5b) and $\Theta = 45^o$ (Setup 5c) cause a Mach reflection with the characteristic triple point configuration introduced in Sec. 5.6.1.[3] In the Mach stem region the detonation becomes remarkably higher overdriven than under regular reflection. While for $\Theta = 15^o$ the pressure increase due to reflection is moderate, the pressure at the detonation front under Mach reflection is almost doubled for $\Theta = 30^o$ (compare Fig. A.26). A regular reflection results in a minor decrease of the detonation cell size (see left triple point record of Fig. 7.25), but the high overdrive of a Mach reflection suppresses the instationary triple points at the detonation front quickly (see right picture of Fig. 7.25).

The height of the Mach stem in a Mach reflection is reciprocal to Θ. The Mach stem for $\Theta = 45^o$ is so small that the slip line originating in the triple point of the Mach reflection is reflected by itself directly behind the Mach stem. The reflection at the lower boundary generates unstable vortices that remain behind as the detonation wave proceeds (compare left upper picture of Fig. 7.22 and lower picture of Fig. 7.24).

7.4.2 Diffraction of a Detonation Wave

Experiments have shown that the behavior of planar CJ detonations propagating out of tubes into unconfinement is determined mainly by the width of the tube. For square tubes the critial tube width has been found to be of the order of 10 times the cell height, i.e. 10λ [112]. For widths significantly below 10λ the process of shock wave diffraction introduced in Sec. 5.6.2 causes a pressure decrease at the head of the detonation wave below the limit of detonability across the entire tube width. Hydrodynamic shock and reaction front decouple and the detonation decays to a shock-induced flame (see lower right picture of Fig. 7.22). This observation

[3]Note, that the appearance of the Mach reflected shock can not be identical in the Figs. 7.24 and 7.22, because the hydrodynamic quantities in the unreacted mixtures are not equal.

w	S_w	$\eta_w^r \cdot 10^{-3}$
ρ	$0.006\,\mathrm{kg\,m^{-3}}$	5.0
p	$3.0\,\mathrm{kPa}$	5.0
T	$30\,\mathrm{K}$	5.0

Table 7.7: Additional refinement criteria for Setup 6a, 6b beside the criteria of Tab. 7.6.

is independent of a particular mixture. While the successful transmission of the detonation is hardly disturbed for tubes widths $\gg 10\lambda$, considerable vortices are created for widths of $\approx 10\lambda$ (see lower middle picture of Fig. 7.22). The disturbances are caused by a backward-facing re-ignition wave that reinitiates the detonation in the partially decoupled region.

We are interested in the decoupling of shock and reaction and also in the re-ignition phenomenon. Therefore, we simulate the diffraction of the $H_2 : O_2 : Ar$ detonation for two different tube widths. The first tube has the half width $r_w = 5\lambda = 8.0\,\mathrm{cm}$ (Setup 6a), the second one has $r_w = 4\lambda = 5.6\,\mathrm{cm}$ (Setup 6b). Like in Sec. 5.6.2 we exploit the symmetry of the problem and simulate just one half of the tube, which laps $\approx 17.2\,\mathrm{cm}$ into the domain. The computational domain has the extensions $56\,\mathrm{cm} \times 32\,\mathrm{cm}$ and is discretized with base grids of 508×288 (Setup 6a) and 508×290 (Setup 6b) cells. We assume a wall thickness of the tube of two base grid cells. The adaptive calculation uses four levels of refinement with $r_{1,2,3} = 2$, $r_4 = 4$ and utilizes the refinement criteria of Tab. 7.7 in addition to those of Tab. 7.3 in order to achieve an almost complete adaptation to the diffracted shock. The calculations correspond to a uniform computation with $\approx 150\,\mathrm{M}$ cells and have an effective resolution of $25.5\,\mathrm{Pts/l_{ig}}$ in the x_1-direction (with respect to the initial detonation). The initial detonation is placed into the tube at $x_1 = 16.0\,\mathrm{cm}$. The simulations are stopped at $t_{end} = 240\,\mu\mathrm{s}$, when the flow situations of interest are clearly established. Each run required $\approx 4\,\mathrm{d}$ on 48 CPUs of the Helics cluster (compare page 167).

The enormous efficiency of the refinement is visualized in Fig. A.25. At t_{end} Setup 6a uses $\approx 3.0\,\mathrm{M}$ cells on all levels, where $\approx 2.4\,\mathrm{M}$ cells are inside one of the 2479 grids of the highest level (with clustering efficiency 0.8). Fig. A.27 displays the complex distribution of Setup 6a generated by a generalization of Hilbert's space-filling curve (compare Sec. 5.3.4) at t_{end} to the 48 CPUs.

Fig. 7.26 shows a comparison of the flow fields in both setups after $160\,\mu\mathrm{s}$, $200\,\mu\mathrm{s}$ and $240\,\mu\mathrm{s}$ simulation time. After $160\,\mu\mathrm{s}$ the separation of shock and reaction front is clearly visible below the outlet. The shock strength increases continously from left to right and directly downstream of the tube shock and reaction are almost coupled in both calculations. But at $t = 200\,\mu\mathrm{s}$ the extinction of the detonation in Setup 6b and the re-ignition wave in Setup 6a is already clearly developed. Color plots of both simulations at $t_{end} = 240\,\mu\mathrm{s}$ are given in the Figs. A.28, A.29. Further on, these figures show a record of the triple point tracks. The appearance of triple

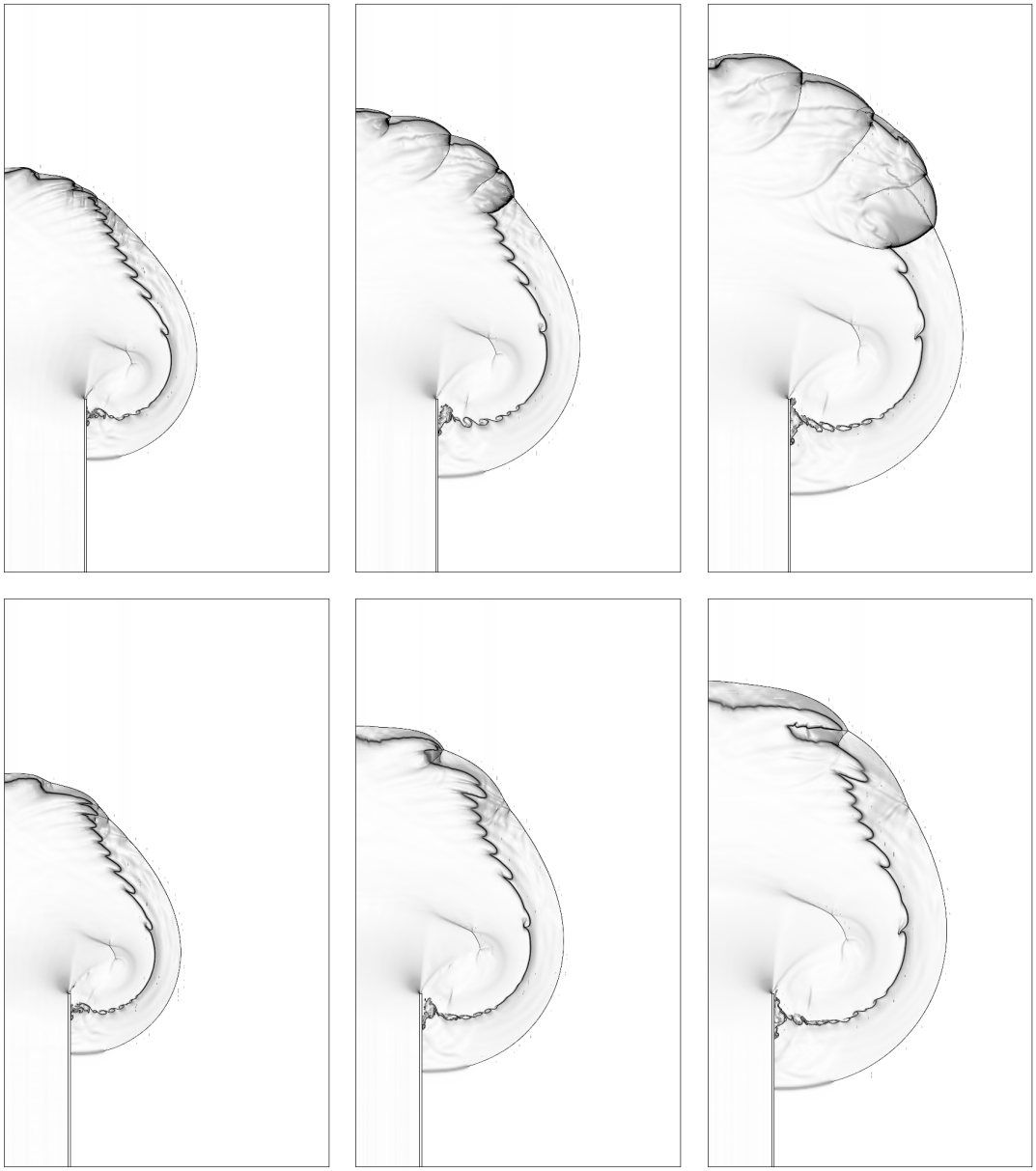

$t = 160\,\mu$s $t = 200\,\mu$s $t = 240\,\mu$s

Figure 7.26: Schlieren plot of density for Setup 6a with $r_w = 5\lambda$ (upper row) and Setup 6b with $r_w = 4\lambda$ (lower column).

points is a characteristic indicator for the preservation of a detonation throughout the diffraction. While the typical triple point pattern with transverse wave and slip line is visible multiple times in Fig. A.28, it has vanished almost completely in Fig. A.29. It is intersting to note, that the re-ignition wave in Setup 6a by itself is a detonation. The triple point track of Fig. A.28 uncovers that it has developed out of the transverse wave of an initial triple point.

Chapter 8

Conclusions and Outlook

In this thesis an efficient solution strategy for the numerical simulation of detonation waves with detailed chemical reaction has been described. All temporal and spatial scales relevant for the complex process of detonation propagation were successfully resolved. The achieved resolutions are significantly finer than in previous publications [138, 59, 78] and provide new insight into the formation and propagation of transient detonation structures. For the first time, the three-dimensional cellular structure of a detonation with detailed hydrogen-oxygen chemistry has been simulated successfully.

A time-operator splitting technique [96, 175] was applied to decouple hydrodynamic transport and chemical kinetics. It allows the separate numerical integration of the homogeneous Euler equations with fast time-explicit finite volume methods and uses an time-implicit discretization only for the stiff reaction terms. As the integration of the reaction terms is only a cell-wise operation, the mixed explicit-implicit approach avoids the expensive solution of a globally coupled system of nonlinear algebraic equations.

High-resolution shock capturing schemes were employed to reduce the number of FV cells to the minimum. In particular, a hybrid Roe-solver-based scheme has been constructed. It allows the reliable simulation of detonation waves in all space dimensions and avoids several significant problems of the unmodified Roe method [84]. Different test configurations showed that this hybrid Roe-type method is superior for detonation simulation to the Flux-Vector Splittings of Steger-Warming- and Van Leer-type [169, 127, 109, 84] and to the Harten-Lax-Van Leer scheme [91, 62].

The key to the high efficiency of the presented simulations is the blockstructured adaptive mesh refinement algorithm of Berger and Collela [21]. This algorithm is tailored especially for time-explicit FV methods and uses a hierarchy of spatially refined subgrids that are integrated recursively with reduced time steps. The AMR algorithm provides the required resolution dynamically and avoids inefficient uniform meshes. A suitable parallelization strategy for this algorithm for distributed memory machines has been developed. It is based upon a domain decomposition approach that partitions the entire hierarchy. It was implemented with modern object-oriented techniques in our code AMROC [53], which was the basis for the presented large-

scale computations. These simulations demonstrate that our approach allows the accurate simulation of detonation structures in realistic two-dimensional setups on parallel machines of moderate size. In three space dimensions basic studies are currently possible.

Outlook on Possible Future Work

The work presented in this thesis allows several reasonable extensions. The simulation of detonation waves in realistic combustion chambers necessitates a generalization of the proposed FV methods to non-Cartesian meshes. As the Euler equations satisfy the rotational invariance property (2.12), all FV schemes developed throughout this thesis can be employed directly for the flux approximation in locally rotated coordinates. Two mesh generation techniques are compatible with the blockstructured AMR algorithm: logically rectangular boundary-fitted meshes (cf. [94]) or Cartesian meshes with embedded geometries (see [24]). The classical boundary-fitted approach necessarily requires a separate mesh generating tool, but has the advantage that extremely small cells can be avoided. The Cartesian technique constructs irregular cells along complex boundaries on-the-fly, but can suffer significantly from the time step restriction due to the CFL condition, because almost arbitrary small cut-cells can occur. Several ideas have been proposed to circumvent the CFL condition for the cut-cells [25, 147, 149, 75], but up to now none of these techniques has been proven to be second-order accurate along the boundary [24].

The boundary-fitted blockstructured AMR technique is followed by the AMR++ classes of the Overture package [36] that are still under development and are not available for public use; the cut-cell approach of Pember et al. [147] is included in Berkeley-Lab-AMR [153]. Both variants are compatible with the object-oriented AMR design explained in Sec. 5.5.2. The boundary-fitted technique requires the incorporation of the geometry information almost in every object in Fig. 5.13, but the basic design and especially the parallelization strategy would remain unchanged. The cut-cell method requires a separate module for the creation of the irregular cells and needs an extended numerical method `step()`, but the AMR algorithm does not have to be modified. An accurate parallel implementation would require an appropriate generalization of the work load estimation formula (5.18).

A better approximation quality for fast propagating detonations will be achieved, if the developed FV methods would be supplemented with a technique that improves the capturing of the shock at the head of the detonation wave [35, 122, 70, 134]. Most interesting from the practical point of view are methods based upon the level-set approach [132], because essentially an additional numerical scheme is required to advance the level-set function.

For larger reaction systems, e.g. for hydrocarbon combustion, reduced reaction mechanisms will have to be utilized [59, 128]. As the evaluation of the reaction terms is just a cell-wise operation, the application of reduced mechanisms is straightforward within the proposed solution strategy.

Bibliography

[1] R. Abgrall. Généralization du schéma de Roe pour le calcul d'écoulements de mélanges de gaz a concentrations variables. *La Recherche Aérospatiale*, 6:31–43, 1988.

[2] R. Abgrall. How to prevent pressure oscillations in multicomponent flow calculations: A quasi conservative approach. *J. Comput. Phys.*, 125:150–160, 1996.

[3] R. Abgrall and S. Karni. Computations of compressible multifluids. *J. Comput. Phys.*, 169:594–523, 2001.

[4] G. Abouseif and T. Y. Toong. Theory on unstable one-dimensional detonations. *J. Combustion Flame*, 45:64–94, 1982.

[5] G. Abouseif and T. Y. Toong. Theory on unstable two-dimensional detonations: Genesis of the transverse waves. *J. Combustion Flame*, 63:191–207, 1986.

[6] R. C. Aiken, editor. *Stiff computation*. Oxford Univ. Press, New York, Oxford, 1985.

[7] R. Akbar. *Mach reflection of gaseous detonations*. PhD thesis, Rensselaer Polytechnic Institute, Troy, New York, August 1997.

[8] M. Arienti and J. E. Shepherd. Analysis of numerical simulations of detonation diffractions. In *Proc. of 17th Int. Colloquium on the Dynamics of Explosive and Reactive Systems*, Heidelberg, Jul 1999.

[9] M. Arora and P. L. Roe. On postshock oscillations due to shock capturing schemes in unsteady flows. *J. Comput. Phys.*, 130:25–40, 1997.

[10] G. Bader and R. Deiterding. A distributed memory adaptive mesh refinement package for inviscid flow simulations. In P. Jonas and V. Uruba, editors, *Proc. of Colloquium on Fluid Dynamics*, pages 9–14. Inst. of Thermodynamics, Academy of Sciences of Czech Republic, Oct 19-20 1999.

[11] G. Bader, R. Deiterding, and K. Schenk. A hybrid formulation for inviscid multicomponent flows. In *Book of abstracts 8th Int. Conf. on Hyperbolic Problems*, Magdeburg, Feb 2000.

[12] G. Bader and P. Deuflhard. A semi-implicit mid-point rule for stiff-systems of ordinary differential equations. *Numer. Math.*, 41:373–398, 1983.

[13] G. Bader, U. Nowak, and P. Deuflhard. An advanced simulation package for large chemical reaction systems. In R. C. Aiken, editor, *Stiff Computation*, pages 255–264, New York, 1985. Oxford University Press.

[14] D. S. Bale and C. Helzel. Crossflow instabilities in the approximation of detonation waves. In H. Freistühler and G. Warnecke, editors, *Proc. 8th Int. Conf. on Hyperbolic Problems: Theory, Numerics and Applications, Magdeburg, Feb/Mar 2000*, volume 140 of *ISNM*, pages 119–128, Basel, 2001. Birkhäuser Verlag.

[15] W. Bao and S. Jin. The random projection method for hyperbolic conservation laws with stiff reaction terms. *J. Comput. Phys.*, 163:216–248, 2000.

[16] H. O. Barthel. Predicted spacings in hydrogen-oxygen-argon detonations. *Phys. Fluids*, 17:1547–1553, 1974.

[17] H. O. Barthel and R. A. Strehlow. Wave propagation in one-dimensional reactive flows. *Phys. Fluids*, 9:1896–1907, 1976.

[18] P. Bastian. *Parallele adaptive Mehrgitterverfahren.* Teubner Skripten zur Numerik. B. G. Teubner, Stuttgart, 1996.

[19] J. Bell, M. Berger, J. Saltzman, and M. Welcome. Three-dimensional adaptive mesh refinement for hyperbolic conservation laws. *SIAM J. Sci. Comp.*, 15(1):127–138, 1994.

[20] M. Berger. *Adaptive Mesh Refinement for Hyperbolic Differential Equations.* PhD thesis, Stanford University. Report No. STAN-CS-82-924, Aug 1982.

[21] M. Berger and P. Colella. Local adaptive mesh refinement for shock hydrodynamics. *J. Comput. Phys.*, 82:64–84, 1988.

[22] M. Berger and R. LeVeque. Adaptive mesh refinement using wave-propagation algorithms for hyperbolic systems. *SIAM J. Numer. Anal.*, 35(6):2298–2316, 1998.

[23] M. Berger and J. Oliger. Adaptive mesh refinement for hyperbolic partial differential equations. *J. Comput. Phys.*, 53:484–512, 1984.

[24] M. J. Berger and C. Helzel. Grid aligned h-box methods for conservation laws in complex geometries. In *Proc. 3rd Intl. Symp. Finite Volumes for Complex Applications*, Porquerolles, June 2002.

[25] M. J. Berger and R. J. LeVeque. A rotated difference scheme for Cartesian grids in complex geometries. Technical Report CP-91-1602, AIAA, 1991.

[26] A. C. Berkenbosch. *Capturing detonation waves for reactive Euler equations.* PhD thesis, Techn. Univ. Eindhoven, 1995.

[27] G. Berti. A calculus for stencils on arbitrary grids with applications to parallel PDE solution. In *Proc. of GAMM-Workshop - Discrete Modelling and discrete Algorithms in Continuum Mechanics*, Braunschweig, Nov 24-25 2000.

[28] G. Berti. *Generic software components for Scientific Computing.* PhD thesis, Brandenburgische Technische Universität Cottbus, 2000.

[29] G. Berti. A generic toolbox for the grid craftsman. In *Proc. of 17th GAMM-Seminar Construction of Grid Generation Algorithms*, Leipzig, Feb 1-3 2001.

[30] G. Booch. *Object oriented design.* Benjamin/Cummings, Redwood City, 1991.

[31] J. P. Boris and D. L. Book. Flux-corrected transport I. SHASTA, a fluid transport algorithm that works. *J. Comput. Phys.*, 11:38–69, 1973.

[32] J. P. Boris and D. L. Book. Flux-corrected transport III. Minimal-error FCT algorithms. *J. Comput. Phys.*, 20:397–431, 1976.

[33] J. P. Boris, D. L. Book, and K. Hain. Flux-corrected transport II. Generalizations of the method. *J. Comput. Phys.*, 18:248–283, 1975.

[34] A. Bourlioux and A. J. Majda. Theoretical and numerical structure for unstable two-dimensional detonations. *J. Combustion Flame*, 90:211–229, 1992.

[35] A. Bourlioux, A. J. Majda, and V. Roytburd. Theoretical and numerical structure for unstable one-dim. detonations. *SIAM J. Appl. Math.*, 51(2):303–343, April 1991.

[36] D. L. Brown, W. D. Henshaw, and D. J. Quinlan. Overture: An object oriented framework for solving partial differential equations. In *Proc. ISCOPE 1997, appeared in Scientific Computing in Object-Oriented Parallel Environments*, number 1343 in Springer Lecture Notes in Computer Science, 1997.

[37] J. D. Buckmaster. Pressure transients and the genesis of transverse shocks in unstable detonations. *Combustion Science and Technology*, 61:1–20, 1988.

[38] J. D. Buckmaster. A theory for triple point spacing in overdriven detonation waves. *J. Combustion Flame*, 77:219–228, 1989.

[39] J. D. Buckmaster and G. S. S. Ludford. The effect of structure on the stability of detonations I. Role of the induction zone. In *21th Int. Symposium on Combustion*, pages 1669–1676, Pittsburgh, 1987. The Combustion Institute.

[40] J. D. Buckmaster and J. Neves. One-dimensional detonation stability: The spectrum for infinite activation energy. *Phys. Fluids*, 31:3571–3576, 1988.

[41] D. L. Chapman. On the rate of explosion in gases. *Philos. Mag.*, 47:90–104, 1899.

[42] I.-L. Chern and P. Colella. A conservative front tracking method for hyperbolic systems of conservation laws. Technical Report UCRL-97200, Lawrence Livermore National Laboratory, Livermore, CA, 1987.

[43] T. Chiang and K. Hoffmann. Determination of computational time step for chemically reacting flows. In *AIAA 20th Fluid Dynamics, Plasma Dynamics and Lasers Conference*, volume 89-1855 of *AIAA*, 1989.

[44] P. Colella and P. Woodward. The piecewise parabolic method (PPM) for gas-dynamical simulations. *J. Comput. Phys.*, 54:174–201, 1984.

[45] R. Courant and K. O. Friedrichs. *Supersonic flow and shock waves.* Applied mathematical sciences, volume 21. Springer, New York, Berlin, 1976.

[46] M. G. Crandall and A. Majda. Monotone difference approximations for scalar conservation laws. *Math. Comp.*, 34:1–21, 1980.

[47] W. Crutchfield and M. L. Welcome. Object-oriented implementation of adaptive mesh refinement algorithms. *J. Scientific Programming*, 2:145–156, 1993.

[48] S. F. Davis. Simplified second-order Godunov-type methods. *SIAM J. Sci. Stat. Comp.*, 9:445–473, 1988.

[49] R. Deiterding. Accurate simulation of Rayleigh-Taylor instabilities. In P. Jonas and V. Uruba, editors, *Proc. of Colloquium on Fluid Dynamics*, pages 37–44, Prague, Oct 19-20 1999. Inst. of Thermodynamics, Academy of Sciences of Czech Republic.

[50] R. Deiterding. Object-oriented design of an AMR-algorithm for distributed memory computers. In *Book of abstracts 8th Int. Conf. on Hyperbolic Problems*, Magdeburg, Feb 2000.

[51] R. Deiterding. Simulation of a shock tube experiment with non-equilibirum chemistry. Technical Report NMWR-00-3, Brandenburgische Technische Universität Cottbus, Oct 2000.

[52] R. Deiterding. Efficient simulation of multi-dimensional detonation phenomena. In *Proc. of ALGORITMY 2002, Conf. on Scientific Computing*, pages 94–101. Dep. of Math. and Descriptive Geometry, Slovak Univ. of Techn., Bratislava, Slovakia, Sep 8-13 2002.

[53] R. Deiterding. AMROC - Blockstructured Adaptive Mesh Refinement in Object-oriented C++. Available at http://amroc.sourceforge.net, Jul 2003.

[54] T. J. Dekker. Finding a zero by means of successive linear interpolation. In *Proc. of Symposium on Constructive Aspects of fundamemtal Theoretical Algebra*, pages 37–48, Zürich - Rüschlikon 1967, 1969.

[55] Y. N. Denisov and Y. K. Troshin. Structura gazovoi detonatsii v trubakh (Structure of gaseous detonations in tubes). *Zh. Eksp. Teor. Fiz.*, 30(4):450–459, 1960.

[56] P. Deuflhard and F. Bornemann. *Numerische Mathematik II. Integration gewöhnlicher Differentialgleichungen.* Walter de Gruyter, Berlin, 1994.

[57] W. Doering. On detonation processes in gases. *Ann. Phys.*, 43:421–436, 1943.

[58] M. Dumbser and J.-M. Moschetta. The carbuncle phenomenon: A new stability analysis. In D. E. Zeitoun, J. Periaux, J. A. Désidéri, and M. Marini, editors, *Proc. West East High Speed Flow Fields, Barcelona*, CIMNE, 2002.

[59] C. A. Eckett. *Numerical and analytical studies of the dynamics of gaseous detonations.* PhD thesis, California Institute of Technology, Pasadena, California, September 2001.

[60] C. H. Edwards. *Advanced calculus of several variables*. Acad. Press, New York, 1973.

[61] D. H. Edwards, G. O. Thomas, and M. A. Nettleton. Diffraction of planar detonation in various fuel-oxygen mixtures at an area change. In *7th Int. Coll. on Gasdynamics of Explosions and Reactive Systems*, pages 341–357. AIAA, 1979.

[62] B. Einfeldt, C. D. Munz, P. L. Roe, and B. Sjögreen. On Godunov-type methods near low densities. *J. Comput. Phys.*, 92:273–295, 1991.

[63] B. Engquist and S. Osher. One sided difference approximations for nonlinear conservation laws. *Math. Comp.*, 36(154):321–351, 1981.

[64] J. J. Erpenbeck. Stability of steady-state equilibrium detonations. *Phys. Fluids*, 5:604–614, 1962.

[65] J. J. Erpenbeck. Stability of idealized one-reaction detonations. *Phys. Fluids*, 7:684–696, 1964.

[66] J. J. Erpenbeck. Nonlinear theory of unstable one-dimensional detonations. *Phys. Fluids*, 10:274–288, 1967.

[67] J. J. Erpenbeck. Theory of detonation stability. In *Twelfth Int. Symposium on Combustion*, pages 711–721, Pittsburgh, 1969. The Combustion Institute.

[68] J. J. Erpenbeck. Nonlinear theory of unstable two-dimensional detonation. *Phys. Fluids*, 13:2007–2026, 1970.

[69] R. P. Fedkiw, T. Aslam, B. Merriman, and S. Osher. A non-oscillatory Eulerian approach to interfaces in multimedial flows (the ghost fluid method). *J. Comput. Phys.*, 152:457–492, 1999.

[70] R. P. Fedkiw, T. Aslam, and S. Xu. The ghost fluid method for deflagration and detonation discontinuities. *J. Comput. Phys.*, 154:393–427, 1999.

[71] R. P. Fedkiw, B. Merriman, and S. Osher. Numerical methods for a mixture of thermally perfect and/or calorically perfect gaseous species with chemical reactions. UCLA CAM Report 96-1, Jul 1996.

[72] R. P. Fedkiw, B. Merriman, and S. Osher. High accuracy numerical methods for thermally perfect gas flows with chemistry. *J. Comput. Phys.*, 132:175–190, 1997.

[73] W. Fickett and W. C. Davis. *Detonation*. University of California Press, Berkeley and Los Angeles, California, 1979.

[74] W. Fickett and W. W. Wood. Flow calculations for pulsating one-dimensional detonation. *Phys. Fluids*, 9:903–916, 1966.

[75] H. Forrer and R. Jeltsch. A higher-order boundary treatment for Cartesian-grid methods. *J. Comput. Phys.*, 140:259–277, 1998.

[76] H. Friedel, R. Grauer, and C. Marliani. Adaptive mesh refinement for singular current sheets in incompressible magnetohydrodynamics flows. *J. Comput. Phys.*, 134(1):190–198, 1997.

[77] T. Fujiwara and K. V. Reddy. Memoirs of the faculty of engineering. Technical Report 1, Nagoya University, 1989.

[78] T. Geßner. *Dynamic mesh adaption for supersonic combustion waves modeled with detailed reaction mechanisms*. PhD thesis, Math. Fakultät, University Freiburg, 2001.

[79] T. Geßner and D. Kröner. Dynamic mesh adaption for detonations using detailed chemical reaction mechanisms. In *Proc. 8th Int. Conf. on Hyperbolic Problems: Theory, Numerics and Applications, Magdeburg, Feb/Mar 2000*, volume 140 of *ISNM*, pages 119–128, Basel, 2001. Birkhäuser Verlag.

[80] P. Glaister. An approximate linearized Riemann solver for the Euler equations for real gases. *J. Comput. Phys.*, 74:382–400, 1988.

[81] E. Godlewski and P.-A. Raviart. *Hyperbolic systems of conservation laws*. Mathématiques et Applications. Ellipses, Paries, 1991.

[82] E. Godlewski and P.-A. Raviart. *Numerical approximation of hyperbolic systems of conservation laws*. Springer Verlag, New York, 1996.

[83] J. Gressier, P. Villedieu, and J.-M. Moschetta. Positivity of flux vector splitting schemes. *J. Comput. Phys.*, 155:199–220, 1999.

[84] B. Grossmann and P. Cinella. Flux-split algorithms for flows with non-equilibrium chemistry and vibrational relaxation. *J. Comput. Phys.*, 88:131–168, 1990.

[85] E. Hairer and G. Wanner. *Solving ordinary differential equations II. Stiff and differential-algebraic problems*. Springer Verlag, Berlin, 1980.

[86] M. Hanana, M. H. Lefebvre, and P. J. Van Tiggelen. Pressure profiles in detonation cells with rectangular or diagonal structure. In *Proc. of 17th Int. Colloquium on the Dynamics of Explosive and Reactive Systems*, Heidelberg, Jul 1999.

[87] A. Harten. High resolution schemes for hyperbolic conservation laws. *J. Comput. Phys.*, 49:357–393, 1983.

[88] A. Harten. On a class of high resolution total variation stable finite difference schemes. *SIAM J. Numer. Anal.*, 21(1):1–23, 1984.

[89] A. Harten and J. M. Hyman. Self adjusting grid methods for one-dimensional hyperbolic conservation laws. *J. Comput. Phys.*, 50:235–269, 1983.

[90] A. Harten, J. M. Hyman, and P. D. Lax. On finite-difference approximations and entropy conditions for shocks. *Comm. Pure Appl. Math.*, 29:297–322, 1976.

[91] A. Harten, P. D. Lax, and B. Van Leer. On upstream differencing Godunov-type schemes for hyperbolic conservation laws. *SIAM Review*, 25(1):35–61, 1983.

[92] C. Helzel. *Numerical approximation of conservation laws with stiff source term for the modelling of detonation waves*. PhD thesis, Otto-von-Guericke-Univ. Magdeburg, 2000.

[93] R. Hillier. Computation of shock wave diffraction at a ninety degrees convex edge. *Shock Waves*, 1:89–98, 1991.

[94] C. Hirsch. *Numerical computation of internal and external flows.* John Wiley & Sons, Chichester, 1988.

[95] P. Hwang, R. P. Fedkiw, B. Merriman, T. D. Aslam, A. R. Karagozian, and S. Osher. Numerical resolution of pulsating detonation waves. *Combustion Theory and Modelling*, 4(3):217–240, 2000.

[96] N. N. Janenko. *Die Zwischenschrittmethode zur Lösung mehrdimensionaler Probleme der mathematischen Physik.* Springer-Verlag, Berlin, 1969.

[97] P. Jenny and B. Müller. Correction of conservative Euler solvers for gas mixtures. *J. Comput. Phys.*, 132:91–107, 1997.

[98] E. Jouguet. On the propagation of chemical reactions in gases. *J. de Mathematiques Pures et Appliquees*, 1:347–425, 1905. Continued in 2:5-85, 1906.

[99] K. Kailasanath, E. S. Oran, J. P. Boris, and T. R. Young. Determination of detonation cell size and the role of transverse waves in two-dimensional detonations. *J. Combustion Flame*, 61:199–209, 1985.

[100] P. Kaps and P. Rentrop. Generalized Runge-Kutta methods of order four with stepsize control for stiff ordinary differential equations. *Num. Math.*, 33:55–68, 1979.

[101] S. Karni. Hybrid multifluid algorithms. *SIAM J. Sci. Comp.*, 17(5):1019–1039, 1996.

[102] R. J. Kee, F. M. Rupley, and J. A. Miller. *Chemkin-II: A Fortran chemical kinetics package for the analysis of gas-phase chemical kinetics.* SAND89-8009, Sandia National Laboratories, Livermore, California, Sep 1989.

[103] R. J. Kee, F. M. Rupley, and J. A. Miller. *The Chemkin thermodynamic data base.* SAND87-8215B, Sandia National Laboratories, Livermore, California, Mar 1990.

[104] S. R. Kohn and S. B. Baden. A parallel software infrastructure for structured adaptive mesh methods. In *Proc. of the Conf. on Supercomputing '95*, December 1995.

[105] D. Kröner. *Numerical schemes for conservation laws.* John Wiley & Sons and B. G. Teubner, New York, Leipzig, 1997.

[106] J. D. Lambert. *Numerical methods for ordinary differential equations.* John Wiley & Sons, Chichester, 1991.

[107] J. Langseth and R. LeVeque. A wave propagation method for three dimensional conservation laws. *J. Comput. Phys.*, 165:126–166, 2000.

[108] B. Larrouturou. How to preserve the mass fractions positivity when computing compressible multi-component flows. *J. Comput. Phys.*, 95:59–84, 1991.

[109] B. Larrouturou and L. Fezoui. On the equations of multi-component perfect or real gas inviscid flow. In Carasso et al., editor, *Proc. of Second Int. Conf. on Nonlinear Hyperbolic Equations - Theory, Numerical Methods, and Applications, Aachen 1988*, Lecture Notes in Mathematics 1402, pages 69–98. Springer-Verlag Berlin, 1989.

[110] P. D. Lax and B. Wendroff. Systems of conservation laws. *Comm. Pure Appl. Math.*, 13:217–237, 1960.

[111] H. I. Lee and D. S. Stewart. Calculation of linear detonation stability: One-dimensional instability of plane detonation. *J. Fluid Mechanics*, 216:103–132, 1990.

[112] J. H. S. Lee. Dynamic parameters of gaseous detonations. *Ann. Rev. Fluid Mech.*, 16:311–336, 1984.

[113] M. H. Lefebvre and E. S. Oran. Analysis of the shock structures in a regular detonation. *Shock Waves*, 4:277–283, 1995.

[114] M. H. Lefebvre, E. S. Oran, K. Kailasanath, and P. J. van Tiggelen. The influence of the heat capacity and diluent on detonation structure. *J. Combustion Flame*, 95:206–218, 1993.

[115] M. H. Lefebvre, E. S. Oran, K. Kailasanath, and P. J. van Tiggelen. Simulation of cellular structure in a detonation wave. *Prog. Astronaut. Aeronaut.*, 153:64–77, 1993.

[116] M. Lemke, K. Witsch, and D. Quinlan. An object-oriented approach for parallel self adaptive mesh refinement on block structured grids. In W. Hackbuch and G. Wittum, editors, *Proc. Ninth GAMM-Seminar - Adaptive Methods-Algorithms, Theory and Applications*, pages 199–220, Braunschweig/Wiesbaden, 1994. Vieweg & Sohn.

[117] R. J. LeVeque. *Numerical methods for conservation laws*. Birkhäuser, Basel, 1992.

[118] R. J. LeVeque. Simplified multi-dimensional flux limiter methods. In M. J. Baines and K. W. Morton, editors, *Numerical Methods for Fluid Dynamics 4*, pages 175–190, Oxford, 1993. Clarendon Press.

[119] R. J. LeVeque. High-resolution conservative algorithms for advection in incompressible flow. *SIAM J. Numer. Anal.*, 33(2):627–665, 1996.

[120] R. J. LeVeque. Wave propagation algorithms for multidimensional hyperbolic systems. *J. Comput. Phys.*, 131(2):327–353, 1997.

[121] R. J. LeVeque. CLAWPACK software. Available at http://www.amath.washington.edu/~rjl/clawpack.html, Apr 2003.

[122] R. J. LeVeque and K. M. Shyue. One-dimensional front tracking based on high resolution wave propagation methods. *SIAM J. Sci. Comp.*, 16(2):348–377, 1995.

[123] R. J. LeVeque and H. C. Yee. A study of numerical methods for hyperbolic conservation laws with stiff source terms. *J. Comput. Phys.*, 86:187–210, 1990.

[124] M.-S. Liou. On a new class of flux splittings. *Lecture Notes Phys.*, 414:115–119, 1993.

[125] M.-S. Liou and C. J. Steffen. A new flux splitting scheme. *J. Comput. Phys.*, 107:23–39, 1993.

[126] M.-S. Liou, B. van Leer, and J.-S. Shuen. Splitting of inviscid fluxes for real gases. *J. Comput. Phys.*, 87:1–24, 1990.

[127] Y. Liu and M. Vinokur. Nonequilibrium flow computations. I. An analysis of numerical formulations of conservation laws. *J. Comput. Phys.*, 83:373–397, 1989.

[128] U. Maas and S. B. Pope. Simplifying chemical kinetics: Intrinsic low-dimensional manifolds in composition space. *J. Combustion Flame*, 88:239–264, 1992.

[129] P. MacNeice, K. M. Olson, C. Mobarry, R. deFainchtein, and C. Packer. PARAMESH: A parallel adaptive mesh refinement community toolkit. *Computer Physics Communications*, 126:330–354, 2000.

[130] A. Majda. *Compressible fluid flow and systems of conservation laws in several space variables.* Applied Mathematical Sciences Vol. 53. Springer-Verlag, New York, 1984.

[131] C. Morley. Gaseq: A chemical equilibrium program for Windows. Available at http://www.c.morley.ukgateway.net, Apr 2003.

[132] W. Mulder, S. Osher, and J. Sethian. Computing interface motion: The compressible Rayleigh-Taylor and Kelvin-Helmholtz instabilities. *J. Comput. Phys.*, 100:209, 1996.

[133] H. J. Neeman. *Autonomous Hierarchical Adaptive Mesh Refinement.* PhD thesis, University of Illinois at Urbana-Champaign, 1996.

[134] D. Nguyen, F. Gibou, and R. Fedkiw. A fully conservative ghost fluid method & stiff detonation waves. In *Proc. 12th International Detonation Symposium, San Diego, CA*, August 11 - 16th, 2002.

[135] S. Ohyagi, O. Tetsuro, N. Fusao, and H. Shintaro. A numerical simulation of reflection processes of a detonation wave on a wedge. In *Proc. of 17th Int. Colloquium on the Dynamics of Explosive and Reactive Systems*, Heidelberg, Jul 1999.

[136] E. S. Oran and J. P. Boris. Theoretical and computational approach to modelling flame ignition. *Prog. Aeronautics Astronautics*, 76:154–171, 1981.

[137] E. S. Oran and J. P. Boris. *Numerical simulation of reactive flow.* Cambridge Univ. Press, Cambridge, 2nd edition, 2001.

[138] E. S. Oran, J. W. Weber, E. I. Stefaniw, M. H. Lefebvre, and J. D. Anderson. A numerical study of a two-dimensional H_2-O_2-Ar detonation using a detailed chemical reaction model. *J. Combustion Flame*, 113:147–163, 1998.

[139] E. S. Oran, T. R. Young, J. P. Boris, and A. Cohen. Weak and strong ignition. I. Numerical simulation of shock tube experiments. *J. Combustion Flame*, 48:135–148, 1982.

[140] S. Osher and S. Chakravarty. Upwind schemes and boundary conditions with applications to Euler equations in general geometries. *J. Comput. Phys.*, 50:447–481, 1983.

[141] S. Osher and F. Solomon. Upwind difference schemes for hyperbolic conservation laws. *Math. Comp.*, 38(158):339–374, 1982.

[142] M. Pandolfi and D. D'Ambrosio. Upwind methods and carbuncle phenomenon. In *Proc. 4th ECCOMAS, Comp. Fluid Dynamics 98*, volume 1, pages 126–131, 1998.

[143] M. Pandolfi and D. D'Ambrosio. Numerical instabilities in upwind methods: Analysis and cures for the "Carbuncle" phenomenon. *J. Comput. Phys.*, 166:271–301, 2001.

[144] M. V. Papalexandris, A. Leonard, and P. E. Dimotakis. Unsplit schemes for hyperbolic conservation laws with source terms in one space dimension. *J. Comput. Phys.*, 134:31–61, 1997.

[145] M. Parashar and J. C. Browne. On partitioning dynamic adaptive grid hierarchies. In *Proc. of the 29th Annual Hawaii Int. Conf. on System Sciences*, Jan 1996.

[146] M. Parashar and J. C. Browne. System engineering for high performance computing software: The HDDA/DAGH infrastructure for implementation of parallel structured adaptive mesh refinement. In *Structured Adaptive Mesh Refinement Grid Methods*, IMA Volumes in Mathematics and its Applications. Springer, 1997.

[147] R. B. Pember, J. B. Bell, P. Colella, W. Y. Crutchfield, and M. L. Welcome. An adaptive Cartesian grid method for unsteady compressible flow in irregular regions. *J. Comput. Phys.*, 120:278–304, 1995.

[148] K. Perry and S. T. Imlay. Blunt body flow simulations. Technical Report 88-2924, AIAA, 1988.

[149] J. J. Quirk. An alternative to unstructured grids for computing gas dynamics flows around arbitrarily complex two-dimensional bodies. *Computers Fluids*, 23:125–142, 1994.

[150] J. J. Quirk. A contribution to the great Riemann solver debate. *Int. J. Numer. Meth. Fluids*, 18:555–574, 1994.

[151] J. J. Quirk. Godunov-type schemes applied to detonation flows. In J. Buckmaster, editor, *Combustion in high-speed flows: Proc. of a Workshop on Combustion, Oct 12-14, 1992, Hampton,*, pages 575–596, Dordrecht, 1994. Kluwer Acad. Publ.

[152] J. J. Quirk and S. Karni. On the dynamics of a shock-bubble interaction. *J. Fluid Mech.*, 318:129–163, 1996.

[153] C. A. Rendleman, V. E. Beckner, M. Lijewski, W. Crutchfield, and J. B. Bell. Parallelization of structured, hierarchical adaptive mesh refinement algorithms. *Computing and Visualization in Science*, 3, 2000.

[154] T. W. Roberts. The behaviour of flux difference splitting schemes near slowly moving shock waves. *J. Comput. Phys.*, 90:141–160, 1990.

[155] J.-C. Robinet, J. Gressier, G. Casalis, and J.-M. Moschetta. Shock wave instability and the carbuncle phenomenon: Same intrinsic origin? *J. Fluid Mech.*, 417:237–263, 2000.

[156] P. L. Roe. Approximate Riemann solvers, parameter vectors and difference schemes. *J. Comput. Phys.*, 43:357–372, 1981.

[157] P. L. Roe. Some contributions to the modelling of discontinous flows. In *Proc. of the SIAM/AMS Seminar*, San Diego, 1983.

[158] P. L. Roe and J. Pike. Efficient construction and utilisation of approximate Riemann solutions. In *Proc. of the 6th Int. Symposium on Computing Methods in Applied Science and Engineering*, pages 499–518. Elsevier North-Holland, 1984.

[159] H. Sagan. *Space-Filling Curves.* Springer-Verlag, New-York, 1994.

[160] R. Sanders, E. Morano, and M.-C. Druguett. Multidimensional dissipation for upwind schemes: Stability and applications to gas dynamics. *J. Comput. Phys.*, 145:511–537, 1998.

[161] K. Schenk. Hybrid formulations for multicomponent flow. In *Proc. Sem. Topical Prob. Fluid Mech.* Czech Technical University Prag, Februar 1999.

[162] S. Schöffel. *Berechnung der Dynamik zellularer Detonationsstrukturen ausgehend vom Zeldovich-Döring-v.Neumann-Modell.* VDI-Reihe 7 Nr. 142. VDI-Verlag, Düsseldorf, 1988.

[163] E. Schultz. *Detonation diffraction through an abrupt area expansion.* PhD thesis, California Institute of Technology, Pasadena, California, April 2000.

[164] G. J. Sharpe and S. A. E. G. Falle. Numerical simulation of pulsating detonations: I. Nonlinear stability of steady detonations. *Combust. Theory Modelling*, 4:557–574, 2000.

[165] K. I. Shchelkin and Y. K. Troshin. *Gasdynamics of Combustion.* Mono Book Corp., Baltimore, 1965.

[166] J. E. Shepherd. Chemical kinetics of hydrogen-air-diluent detonations. In J. B. Bowen, J.-C. Leyer, and R. I. Soloukin, editors, *Dynamics of Explosions*, volume 106 of *Progress in Astronautics and Aeronautics, AIAA*, 1986.

[167] J. E. Shepherd. Detonation waves and propulsion. In J. Buckmaster, editor, *Combustion in high-speed flows: Proc. of a Workshop on Combustion, Oct 12 - 14, 1992, Hampton*, pages 373–420, Dordrecht, 1994. Kluwer Acad. Publ.

[168] M. Short. Multidimensional linear stability of a detonation wave at high activation energy. *SIAM J. Appl. Math.*, 57:307–326, 1997.

[169] J.-S. Shuen, M.-S. Liou, and B. van Leer. Inviscid flux-splitting algorithms for real gases with non-equilibrium chemistry. *J. Comput. Phys.*, 90:371–395, 1990.

[170] K.-M. Shyue. An efficient shock-capturing algorithm for compressible multicomponent problems. *J. Comput. Phys.*, 142:208–242, 1998.

[171] J. Smoller. *Shock waves and reaction-diffusion equations.* Springer-Verlag, New-York, 1982.

[172] T. Sonar. *Mehrdimensional ENO-Verfahren.* Teubner Verlag, Stuttgart, 1997.

[173] D. S. Stewart and J. B. Bdzil. A lecture on detonation shock dynamics. In J. Buckmaster and T. Takeno, editors, *Mathematical Modeling in Combustion Sciences*, pages 17–30, New York, 1988. Springer.

[174] D. S. Stewart and J. B. Bdzil. The shock dynamics of stable multidimensional detonation. *J. Combustion Flame*, 72:311–323, 1988.

[175] G. Strang. On the construction and comparison of difference schemes. *SIAM J. Num. Anal.*, 5:506–517, 1968.

[176] R. A. Strehlow. Gas phase detonations: Recent developments. *J. Combustion Flame*, 12(2):81–101, 1968.

[177] R. A. Strehlow. The nature of transverse waves in detonations. *Astron. Acta*, 14:539–548, 1969.

[178] R. A. Strehlow. Multi-dimensional detonation wave structure. *Astron. Acta*, 15:345–357, 1970.

[179] R. A. Strehlow. *Combustion Fundamentals.* McGraw-Hill, New York, 1984.

[180] R. A. Strehlow. *Fundamentals of combustion.* Kreiger, Huntington, 1984.

[181] R. A. Strehlow and F. D. Fernandez. Transverse waves in detonations. *J. Combustion Flame*, 9:109–119, 1965.

[182] R. A. Strehlow, R. E. Maurer, and S. Rajan. Transverse waves in detonations: I. Spacing in the hydrogen-oxygen system. *AIAA*, 7:323–328, 1969.

[183] D. R. Stull and H. Prophet. JANAF thermodynamical tables. Technical report, U. S. Departement of Commerce, 1971.

[184] K. Takayama and O. Inoue. Shock wave diffraction over a 90 degree sharp corner. *Shock Waves*, 1:301–312, 1991.

[185] S. Taki and T. Fujiwara. In *18th Int. Symposium on Combustion*, pages 1671–1681, Pittsburgh, 1981. The Combustion Institute.

[186] V. T. Ton. Improved shock-capturing methods for multicomponent and reacting flows. *J. Comput. Phys.*, 128:237–253, 1996.

[187] E. F. Toro. *Riemann solvers and numerical methods for fluid dynamics.* Springer-Verlag, Berlin, Heidelberg, 2nd edition, 1999.

[188] E. F. Toro, M. Spruce, and W. Speares. Restoration of the contact surface in the HLL-Riemann solver. *Shock Waves*, 4:25–34, 1994.

[189] P. A. Urtiew and M. T. Craig. Effects of cellular structure on the behavior of gaseous detonation waves under transient conditions. In *7th Int. Coll. on Gasdynamics of Explosions and Reactive Systems*, pages 370–384. AIAA, 1979.

[190] G. D. van Albada, B. van Leer, and W. W. Roberts. A comparative study of computational methods in cosmic gas dynamics. *Astron. Astrophysics*, 108:76–84, 1982.

[191] B. van Leer. Towards the ultimate conservative difference scheme I. The quest of monotonicity. *Springer Lecture notes in Physics*, 18:163–168, 1973.

[192] B. van Leer. Towards the ultimate conservative difference scheme II. Monotonicity and conservation comb. in a second order scheme. *J. Comput. Phys.*, 14:361–370, 1974.

[193] B. van Leer. Towards the ultimate conservative difference scheme III. Upstream-centered finite-difference schemes for ideal compressible flows. *J. Comput. Phys.*, 23:263–275, 1974.

[194] B. van Leer. Towards the ultimate conservative difference scheme IV. A new approach to numerical convection. *J. Comput. Phys.*, 23:276–299, 1974.

[195] B. van Leer. Towards the ultimate conservative difference scheme V. A second order sequel to Godunov's method. *J. Comput. Phys.*, 32:101–136, 1979.

[196] B. van Leer. On the relation between the upwind-differencing schemes of Godunov, Enguist-Osher and Roe. *SIAM J. Sci. Stat. Comp.*, 5(1):1–20, 1985.

[197] A. A. Vasiliev and Y. Nikolaev. Closed theoretical model of a detonation cell. *Astron. Acta*, 5:983–996, 1978.

[198] M. Vinokur, , and J.-L. Montagné. Generalized flux-vector splitting and Roe average for an equilibirum real gas. *J. Comput. Phys.*, 89:276–300, 1990.

[199] B. V. Voitsekhovsky, V. V. Mitrofanov, and M. E. Topchian. Structure of a detonation front in gases. Technical report, Izd. Akad. Nauk SSSR, Novosibirsk, 1963.

[200] J. von Neumann. Theory of detonation waves. In *John von Neumann, Collected works*, volume 6, New York, 1942. Macmillan.

[201] Y. Wada and M.-S. Liou. An accurate and robust flux splitting scheme for shock and contact discontinuities. *SIAM J. Sci. Comp.*, 18(3):633–657, 1997.

[202] C. K. Westbrook. Chemical kinetics of hydrocarbon oxidation in gaseous detonations. *J. Combustion Flame*, 46:191–210, 1982.

[203] D. N. Williams, L. Bauwens, and E. S. Oran. Detailed structure and propagation of three-dimensional detonations. In *26th International Symposium on Combustion*, Naples, Apr. 1996.

[204] F. A. Williams. *Combustion theory.* Addison-Wesley, Reading, Massachusetts, 1985.

[205] P. Woodward and P. Colella. The numerical simulation of two-dimensional fluid flow with strong shocks. *J. Comput. Phys.*, 54:115–173, 1984.

[206] H. C. Yee. A class of high-resolution explicit and implicit shock-capturing methods. Technical Report Lecture Series 1989-4, Von Karman Inst. of Fluid Dynamics, 1989.

[207] H. C. Yee, R. F. Warming, and A. Harten. Implicit total variation diminishing (TVD) schemes for steady state problems. *J. Comput. Phys.*, 57:327–360, 1985.

[208] T. R. Young and J. P. Boris. A numerical technique for solving stiff ordinary differential equations associated with the chemical kinetics in reactive-flow problems. *J. Phys. Chem.*, 81:2424–2427, 1977.

[209] Y. B. Zel'dovich. On the theory of the propagation of detonations on gaseous systems. [Translation from Zh. Eksp. Teor. Fiz., 10:542-568, 1940] TM 1261, NACA, 1960.

Appendix

A.1 Properties of the Jacobians

In this section useful mathematical properties of the Jacobians of the Euler equations for mixtures of thermally perfect gaseous species (see Sec. 2.3) are supplied. The following derivation of the Jacobians and their properties is restricted to $\mathbf{f}_1(\mathbf{q})$, the flux function in the x_1-direction of the three-dimensional case. The Jacobians of $\mathbf{f}_2(\mathbf{q})$ and $\mathbf{f}_3(\mathbf{q})$ follow directly by interchanging the velocities $u_1, \ldots, u_d$ canonically and all results, which are derived for the Jacobian of $\mathbf{f}_1(\mathbf{q})$, carry over to the Jacobians of $\mathbf{f}_2(\mathbf{q})$ and $\mathbf{f}_3(\mathbf{q})$ immediately.

In order to compute $\mathbf{A}_1(\mathbf{q}) = \partial\mathbf{f}_1(\mathbf{q})/\partial\mathbf{q}$ the flux function $\mathbf{f}_1(\mathbf{q})$ has to be expressed in terms of the conserved variables, i.e.

$$\begin{aligned}\mathbf{f}_1(\mathbf{q}) &= \mathbf{f}_1(\rho_1, \ldots, \rho_K, \rho u_1, \rho u_2, \rho u_3, \rho E) = \mathbf{f}_1(\rho_1, \ldots, \rho_K, m_1, m_2, m_3, \bar{E}) \\ &= \left(\rho_1 \frac{m_1}{\rho}, \ldots, \rho_K \frac{m_1}{\rho}, \frac{m_1^2}{\rho} + p, \frac{m_1 m_2}{\rho}, \frac{m_1 m_3}{\rho}, \frac{m_1}{\rho}(\bar{E} + p)\right)\end{aligned} \tag{A.1}$$

Beside the evaluation of the partial derivatives of the hydrostatic pressure p in section 2.3.2 the derivation of the Jacobian is a straight-forward calculation. It reads

$$\mathbf{A}_1(\mathbf{q}) =$$

$$\begin{bmatrix} u_1(1-Y_1) & -u_1Y_1 & \ldots & -u_1Y_1 & Y_1 & 0 & 0 & 0 \\ -u_1Y_2 & u_1(1-Y_2) & \ldots & -u_1Y_2 & & & & \\ \vdots & & \ddots & \vdots & \vdots & \vdots & \vdots & \vdots \\ -u_1Y_{K-1} & \ldots & u_1(1-Y_{K-1}) & -u_1Y_{K-1} & & & & \\ -u_1Y_K & \ldots & -u_1Y_K & u_1(1-Y_K) & Y_K & 0 & 0 & 0 \\ \phi_1 - u_1^2 & & \ldots & \phi_K - u_1^2 & (3-\gamma)u_1 & -\bar{\gamma}u_2 & -\bar{\gamma}u_3 & \bar{\gamma} \\ -u_1u_2 & & \ldots & -u_1u_2 & u_2 & u_1 & 0 & 0 \\ -u_1u_3 & & \ldots & -u_1u_3 & u_3 & 0 & u_1 & 0 \\ u_1(\phi_1 - H) & & \ldots & u_1(\phi_K - H) & H - \bar{\gamma}u_1^2 & -\bar{\gamma}u_1u_2 & -\bar{\gamma}u_1u_3 & \gamma u_1 \end{bmatrix} \tag{A.2}$$

where ϕ_i is defined in expression (2.60).

Proposition 8 (Homogeneity Property). *The flux function* $\mathbf{f}_1(\mathbf{q})$ *defined in Eq. (A.1) and their Jacobian matrices* $\mathbf{A}_1(\mathbf{q})$ *satisfy the homogeneity property for all admissible states of* $\mathbf{q}$.

$$\mathbf{f}_1(\mathbf{q}) = \mathbf{A}_1(\mathbf{q})\,\mathbf{q}\ .$$

Proof. A direct computation proves the proposition. During the calculation the identity

$$\sum_{i=1}^{K} Y_i\,\phi_i - \bar{\gamma}\mathbf{u}^2 + \bar{\gamma}E = \frac{p}{\rho}\ ,$$

which is derived by setting Eq. (2.69) equal to Eq. (2.70), is applied to eliminate sums of ϕ_i. ■

Proposition 9 (Eigenvalues). *For all admissible states* $\mathbf{q}$ *the eigenvalues of* $\mathbf{A}_1(\mathbf{q})$ *are* $u_1 - c$, u_1 *and* $u_1 + c$. *The eigenvalue* u_1 *occurs* $K+2$ *times.*

Proof. The proof of the proposition requires the evaluation of the characteristic polynomial $|\mathbf{A}_1(\mathbf{q}) - \lambda\,\mathbf{I}|$ for all admissible states. The calculation can be simplified significantly, if column-wise algebraic manipulations are applied. After some simple modifications we obtain

$$|\mathbf{A}_1(\mathbf{q}) - \lambda\,\mathbf{I}| =$$

$$\frac{1}{\lambda - u_1}\begin{bmatrix} u_1-\lambda & 0 & \dots & 0 & 0 & 0 & 0 & 0 \\ 0 & & & & & & & \\ \vdots & & \ddots & \vdots & \vdots & \vdots & \vdots & \vdots \\ & & & 0 & & & & \\ 0 & \dots & 0 & u_1-\lambda & 0 & 0 & 0 & 0 \\ \phi_1-\xi & \dots & & \phi_K-\xi & \tau & -\bar{\gamma}u_2 & -\bar{\gamma}u_3 & \bar{\gamma} \\ 0 & \dots & & 0 & u_2 & u_1-\lambda & 0 & 0 \\ 0 & \dots & & 0 & u_3 & 0 & u_1-\lambda & 0 \\ u_1(\phi_1-\bar{\gamma}u_1^2) & \dots & & u_1(\phi_K-\bar{\gamma}u_1^2) & \delta & -\bar{\gamma}u_1u_2 & -\bar{\gamma}u_1u_3 & \gamma u_1-\lambda \end{bmatrix}$$

with

$$\begin{aligned} \tau &= (\lambda-u_1)\left[(2-\bar{\gamma})u_1-\lambda\right] + u_1(u_1-\lambda) - \bar{\gamma}u_1^2 + \sum_{i=1}^{K} Y_i\phi_i\ , \\ \delta &= (\lambda-u_1)\left[H-\bar{\gamma}u_1^2\right] - \bar{\gamma}u_1^3 + u_1\sum_{i=1}^{K} Y_i\phi_i\ , \\ \xi &= (\lambda-u_1)u_1 + \bar{\gamma}u_1^2\ . \end{aligned}$$

The eigenvalues are the roots of the characteristic polynomial, i.e.

$$
\begin{aligned}
|\mathbf{A}_1(\mathbf{q}) - \lambda\,\mathbf{I}| &= (\lambda - u_1)^K \left(\left[(\lambda - u_1)\tau - \bar{\gamma}(u_2^2 + u_3^2) \right] (\gamma u_1 - \lambda) - \right. \\
&\qquad \left. \bar{\gamma} \left[(\lambda - u_1)\delta - \bar{\gamma}(u_2^2 + u_3^2) \right] \right) \\
&= (\lambda - u_1)^{K+2} \left(\lambda^2 - 2\lambda u_1 + u_1^2 - \bar{\gamma} H - \sum_{i=1}^{K} Y_i \phi_i + \bar{\gamma}\mathbf{u}^2 \right) = 0.
\end{aligned}
\tag{A.3}
$$

After canceling the factor $(\lambda - u_1)^{K+2}$ of the multiple eigenvalue u_1 and applying relation (2.69) for the frozen speed of sound the remaining term reads

$$\lambda^2 - 2\lambda u_1 + u_1^2 - c^2 = 0\ .$$

Its real roots $\lambda_1 = u_1 - c$ and $\lambda_{K+4} = u_1 + c$ are the two remaining eigenvalues. ■

Proposition 10 (Complete set of eigenvectors). *The Jacobian matrix* $\mathbf{A}_1(\mathbf{q})$ *has a complete set of eigenvectors, hence it is diagonalizable with* $\mathbf{R}_1^{-1}(\mathbf{q})\,\mathbf{A}_1(\mathbf{q})\,\mathbf{R}_1(\mathbf{q}) = \mathbf{\Lambda}_1(\mathbf{q})$ *for all admissible states* $\mathbf{q}$ *with* $\mathbf{\Lambda}_1(\mathbf{q}) = \mathrm{diag}(u_1 - c, u_1, \ldots, u_1, u_1 + c)$.

Proof. Tedious but straight-forward linear algebra is necessary to derive three linear independent sets of basic vectors that span up the three vector spaces defined by $(\mathbf{A}_1(\mathbf{q}) - \lambda\mathbf{I})\,\mathbf{r} = \mathbf{0}$ corresponding to $\lambda = \{u_1 - c, u_1, u_1 + c\}$. In the matrix of right eigenvectors

$$
\mathbf{R}_1(\mathbf{q}) = \begin{bmatrix}
Y_1 & 1 & 0 & \ldots & & 0 & 0 & 0 & Y_1 \\
 & 0 & & & & & & & \\
\vdots & \vdots & & \ddots & & \vdots & \vdots & \vdots & \vdots \\
 & & & & & 0 & & & \\
Y_K & 0 & & \ldots & 0 & 1 & 0 & 0 & Y_K \\
u_1 - c & u_1 & & \ldots & & u_1 & 0 & 0 & u_1 + c \\
u_2 & u_2 & & \ldots & & u_2 & 1 & 0 & u_2 \\
u_3 & u_3 & & \ldots & & u_3 & 0 & 1 & u_3 \\
H - u_1 c & \mathbf{u}^2 - \dfrac{\phi_1}{\bar{\gamma}} & & \ldots & & \mathbf{u}^2 - \dfrac{\phi_K}{\bar{\gamma}} & u_2 & u_3 & H + u_1 c
\end{bmatrix}
\tag{A.4}
$$

the first and the last column are the vectors that span up the one-dimensional vector spaces corresponding to $u_1 - c$ and $u_1 + c$. The vectors of the columns 2 to $K+3$ span up the $K+2$-dimensional vector space for u_1. $\mathbf{R}_1(\mathbf{q})$ has full rank and is therefore invertible for all admissible states.

The inverse of $\mathbf{R}_1(\mathbf{q})$ reads

$$\mathbf{R}_1^{-1}(\mathbf{q}) = \frac{1}{c^2} \cdot$$

$$\begin{bmatrix}
\frac{\phi_1 + u_1 c}{2} & & \dots & \frac{\phi_K + u_1 c}{2} & -\frac{\bar{\gamma} u_1 + c}{2} & -\frac{\bar{\gamma}}{2} u_2 & -\frac{\bar{\gamma}}{2} u_3 & \frac{\bar{\gamma}}{2} \\
c^2 - Y_1 \phi_1 & -Y_1 \phi_2 & \dots & -Y_1 \phi_K & Y_1 \bar{\gamma} u_1 & Y_1 \bar{\gamma} u_2 & Y_1 \bar{\gamma} u_3 & -Y_1 \bar{\gamma} \\
-Y_2 \phi_1 & c^2 - Y_2 \phi_2 & \dots & -Y_2 \phi_K & & & & \\
\vdots & & \ddots & \vdots & \vdots & \vdots & \vdots & \vdots \\
-Y_{K-1} \phi_1 & \dots & c^2 - Y_{K-1} \phi_{K-1} & -Y_{K-1} \phi_K & & & & \\
-Y_K \phi_1 & \dots & -Y_K \phi_{K-1} & c^2 - Y_K \phi_K & Y_K \bar{\gamma} u_1 & Y_K \bar{\gamma} u_2 & Y_K \bar{\gamma} u_3 & -Y_K \bar{\gamma} \\
-u_2 c^2 & & \dots & -u_2 c^2 & 0 & c^2 & 0 & 0 \\
-u_3 c^2 & & \dots & -u_3 c^2 & 0 & 0 & c^2 & 0 \\
\frac{\phi_1 - u_1 c}{2} & & \dots & \frac{\phi_K - u_1 c}{2} & -\frac{\bar{\gamma} u_1 - c}{2} & -\frac{\bar{\gamma}}{2} u_2 & -\frac{\bar{\gamma}}{2} u_3 & \frac{\bar{\gamma}}{2}
\end{bmatrix}.$$

A.2 Mixture Properties

In this section useful relations for thermally perfect multi-component gas-mixtures are notated.

$$\rho = \sum_{i=1}^{K} \rho_i \qquad \sum_{i=1}^{K} Y_i = \sum_{i=1}^{K} X_i = 1 \qquad Y_i = \frac{\rho_i}{\rho} = \frac{X_i W_i}{W} \qquad X_i = \frac{Y_i W}{W_i}$$

$$c_v = \sum_{i=1}^{K} Y_i \, c_{vi} \qquad e_i = h_i^0 + \int_{T_0}^{T} c_{vi}(s) ds \qquad c_p = \sum_{i=1}^{K} Y_i \, c_{pi} \qquad h_i = h_i^0 + \int_{T_0}^{T} c_{pi}(s) ds$$

$$e = \sum_{i=1}^{K} Y_i \, e_i \qquad h^0 = \sum_{i=1}^{K} Y_i \, h_i^0 \qquad h = \sum_{i=1}^{K} Y_i \, h_i$$

$$E = e + \frac{\mathbf{u}^2}{2} \qquad H = h + \frac{\mathbf{u}^2}{2} \qquad \rho h - \rho e = p \qquad \rho H - \rho E = p$$

$$R = c_p - c_v = \frac{\mathcal{R}}{W} = \sum_{i=1}^{K} Y_i R_i \qquad R_i = c_{pi} - c_{vi} = \frac{\mathcal{R}}{W_i} \qquad W = \sum_{i=1}^{K} X_i \, W_i = \left(\sum_{i=1}^{K} \frac{Y_i}{W_i} \right)^{-1}$$

$$\gamma = \frac{c_p}{c_v} = \frac{c_p}{c_p - R} \qquad \gamma_i = \frac{c_{pi}}{c_{vi}} \qquad \gamma - 1 = \frac{R}{c_p - R} = \left(\sum_{i=1}^{K} \frac{X_i}{\gamma_i - 1} \right)^{-1}$$

$$p = \rho \, R \, T = \rho \frac{\mathcal{R}}{W} T = \sum_{i=1}^{K} p_i \qquad p_i = \rho_i \, R_i \, T = \rho \, Y_i \, \frac{\mathcal{R}}{W_i} T$$

A.3 Units of Reactive Flow Quantities

The computations in Chap. 7 utilize the Chemkin-II-library [102]. All simulations have been run in the unit system determined by Chemkin-II and have been converted into SI-units only for visualization subsequently. The two following tabulars display the conversion factors.

Symbol	Definition	Chemkin	SI	F†
$\dot{\omega}_i$	Chemical production rate of species i	mol cm^{-3} s^{-1}	mol m^{-3} s^{-1}	10^6
A_j^f, A_j^r	Pre-exponential factor for Arrhenius law of reaction j. Reaction j has order r_o.	$s^{-1}\left(\frac{\text{cm}^3}{\text{mol}}\right)^{r_o-1}$	$s^{-1}\left(\frac{\text{m}^3}{\text{mol}}\right)^{r_o-1}$	$(10^{-6})^{r_o-1}$
β_j^f, β_j^r	Temperature dependent exponent of reaction j	-	-	-
E_j^f, E_j^r	Activation energy of reaction j	cal mol^{-1}	J mol^{-1}	4.18392
k_j^f, k_j^r	Forward and backward reaction rate of reaction j	$s^{-1}\left(\frac{\text{cm}^3\,\text{K}}{\text{mol}}\right)^{r_o-1}$	$s^{-1}\left(\frac{\text{m}^3\,\text{K}}{\text{mol}}\right)^{r_o-1}$	$(10^{-6})^{r_o-1}$
ν_{ji}^f, ν_{ji}^r	Stoichiometric coefficient of species i as reactant and product in reaction j	-	-	-
$\dot{\varsigma}$	Thermicity. See Eq. (2.87).	m^{-2} s^{-1}	m^{-2} s^{-1}	10^{-4}
$\dot{\varsigma}_i$	Thermicity coefficients. See Eq. (2.88).	cm^{-2}	m^{-2}	10^{-4}
$\mathcal{R}$	Gas constant*=1.98723	cal mol^{-1} K^{-1}	$8.31441\ \frac{\text{J}}{\text{mol K}}$	4.18392

Subscripts

j	Reaction $j = 1, \ldots, J$

† Conversion factor from units used in Chemkin- into SI-units.
* used for activation energy within Chemkin.

$$1\ \text{J} = 1\ \text{kg m}^2\ \text{s}^{-2},\ 1\ \text{erg} = 1\ \text{g cm}^2\ \text{s}^{-2} = 10^{-7}\ \text{J} = 2.3901 \cdot 10^{-8}\ \text{cal}$$
$$1\ \text{Pa} = 1\ \text{Nm}^{-2} = 1\ \text{kg m}^{-1}\ \text{s}^{-2},\ 1\ \text{dyne} = \text{g cm s}^{-2} = 10^{-5}\ \text{kg m}^2\ \text{s}^{-2}$$
$$1\ \text{atm} = 1.01325 \cdot 10^5\ \text{Pa} = 1.01325 \cdot 10^6\ \text{dyne cm}^{-2}$$

Table A.1: Quantities for chemical reactions in the gas-phase and their units.

Symbol	Definition	Chemkin	SI	F†
c	Speed of sound for frozen mixture	cm s^{-1}	m s^{-1}	10^{-2}
c_p, c_{pi} c_v, c_{vi}	Heat capacity at constant pressure/volume of mixture and for species i	erg g^{-1} K^{-1}	J kg^{-1} K^{-1}	10^{-4}
C_i	Specific concentration of species i	mol cm^{-3}	mol m^{-3}	10^{6}
e, E	Specific internal and total energy	erg g^{-1}	J kg^{-1}	10^{-4}
γ, γ_i	Adiabatic coefficient of mixture and for species i	-	-	-
h, H	Specific internal and total enthalpy	erg g^{-1}	J kg^{-1}	10^{-4}
h_i	Specific enthalpy of species i	erg g^{-1}	J kg^{-1}	10^{-4}
h^0, h_i^0	Standard heat of formation of mixture and for species i at a reference temperature T_0	erg g^{-1}	J kg^{-1}	10^{-4}
m_n	Momentum density $m_n = \rho u_n$	g cm^{-2} s^{-1}	kg m^{-2} s^{-1}	10^{1}
p, p_i	Hydrostatic pressure of mixture and partial pressure of species i	dyne cm^{-2}	N m^{-2}	10^{-1}
$\mathcal{R}$	Gas constant $= 8.31441 \cdot 10^7$	erg mol^{-1} K^{-1}	J mol^{-1} K^{-1}	10^{-7}
R, R_i	Specific gas constant of mixture and for species i	erg g^{-1} K^{-1}	J kg^{-1} K^{-1}	10^{-4}
ρ, ρ_i	Density of mixture and partial density of species i	g cm^{-3}	kg m^{-3}	10^{3}
s	Specific entrophy	erg K^{-1}	J K^{-1}	10^{-7}
T	Temperature	K	K	-
u_n	n-th component of fluid velocity vector $\mathbf{u}$	cm s^{-1}	m s^{-1}	10^{-2}
W, W_i	Molecular weight of mixture and for species i	g mol^{-1}	kg mol^{-1}	10^{-3}
X_i	Mole fraction of species i	-	-	-
Y_i	Mass fraction of species i	-	-	-

Abbreviations

$\mathbf{u}^2$	$u_1^2 + \cdots + u_d^2$
$\mathbf{m}^2$	$m_1^2 + \cdots + m_d^2$
$\bar{\gamma}$	$\gamma - 1$

Subscripts

i	Indiviual species $i = 1, \ldots, K$
n	Space direction $n = 1, \ldots, d$

Table A.2: Hydrodynamic flow quantities for gas-mixtures and their units.

A.4 Reaction Mechanism

				A_j [cm, mol, s]	β_j	E_j [cal mol^{-1}]
1.	$H + O_2$	$\longrightarrow$	$O + OH$	1.86×10^{14}	0.00	16790.
2.	$O + OH$	$\longrightarrow$	$H + O_2$	1.48×10^{13}	0.00	680.
3.	$H_2 + O$	$\longrightarrow$	$H + OH$	1.82×10^{10}	1.00	8900.
4.	$H + OH$	$\longrightarrow$	$H_2 + O$	8.32×10^{09}	1.00	6950.
5.	$H_2O + O$	$\longrightarrow$	$OH + OH$	3.39×10^{13}	0.00	18350.
6.	$OH + OH$	$\longrightarrow$	$H_2O + O$	3.16×10^{12}	0.00	1100.
7.	$H_2O + H$	$\longrightarrow$	$H_2 + OH$	9.55×10^{13}	0.00	20300.
8.	$H_2 + OH$	$\longrightarrow$	$H_2O + H$	2.19×10^{13}	0.00	5150.
9.	$H_2O_2 + OH$	$\longrightarrow$	$H_2O + HO_2$	1.00×10^{13}	0.00	1800.
10.	$H_2O + HO_2$	$\longrightarrow$	$H_2O_2 + OH$	2.82×10^{13}	0.00	32790.
11.	$HO_2 + O$	$\longrightarrow$	$OH + O_2$	5.01×10^{13}	0.00	1000.
12.	$OH + O_2$	$\longrightarrow$	$HO_2 + O$	6.46×10^{13}	0.00	56160.
13.	$HO_2 + H$	$\longrightarrow$	$OH + OH$	2.51×10^{14}	0.00	1900.
14.	$OH + OH$	$\longrightarrow$	$HO_2 + H$	1.20×10^{13}	0.00	40100.
15.	$HO_2 + H$	$\longrightarrow$	$H_2 + O_2$	2.51×10^{13}	0.00	700.
16.	$H_2 + O_2$	$\longrightarrow$	$HO_2 + H$	5.50×10^{13}	0.00	57800.
17.	$HO_2 + OH$	$\longrightarrow$	$H_2O + O_2$	5.01×10^{13}	0.00	1000.
18.	$H_2O + O_2$	$\longrightarrow$	$HO_2 + OH$	6.31×10^{14}	0.00	73860.
19.	$H_2O_2 + O_2$	$\longrightarrow$	$HO_2 + HO_2$	3.98×10^{13}	0.00	42640.
20.	$HO_2 + HO_2$	$\longrightarrow$	$H_2O_2 + O_2$	1.00×10^{13}	0.00	1000.
21.	$H_2O_2 + H$	$\longrightarrow$	$HO_2 + H_2$	1.70×10^{12}	0.00	3750.
22.	$HO_2 + H_2$	$\longrightarrow$	$H_2O_2 + H$	7.24×10^{11}	0.00	18700.
23.	$H_2O + M$	$\longrightarrow$	$H + OH + M$	2.19×10^{16}	0.00	105000.
24.	$H + OH + M$	$\longrightarrow$	$H_2O + M$	1.41×10^{23}	-2.00	0.
25.	$H + O_2 + M$	$\longrightarrow$	$HO_2 + M$	1.66×10^{15}	0.00	$-1000.$
26.	$HO_2 + M$	$\longrightarrow$	$H + O_2 + M$	2.29×10^{15}	0.00	45900.
27.	$H_2O_2 + M$	$\longrightarrow$	$OH + OH + M$	1.20×10^{17}	0.00	45500.
28.	$OH + OH + M$	$\longrightarrow$	$H_2O_2 + M$	9.12×10^{14}	0.00	$-5070.$
29.	$O + H + M$	$\longrightarrow$	$OH + M$	1.00×10^{16}	0.00	0.
30.	$OH + M$	$\longrightarrow$	$O + H + M$	7.94×10^{19}	-1.00	103720.
31.	$O_2 + M$	$\longrightarrow$	$O + O + M$	5.13×10^{15}	0.00	115000.
32.	$O + O + M$	$\longrightarrow$	$O_2 + M$	4.68×10^{15}	-0.28	0.
33.	$H_2 + M$	$\longrightarrow$	$H + H + M$	2.19×10^{14}	0.00	96000.
34.	$H + H + M$	$\longrightarrow$	$H_2 + M$	3.02×10^{15}	0.00	0.

Third body efficiencies: $f(O_2) = 0.40$, $f(H_2O) = 6.50$

Table A.3: Mechanism 1. Hydrogen-oxygen mechanism extracted from the hydrocarbon mechanism of Westbrook [202].

A.5 Numerical Results

The last section of the appendix contains graphics of numerical simulations, especially from the Chaps. 6 and 7.

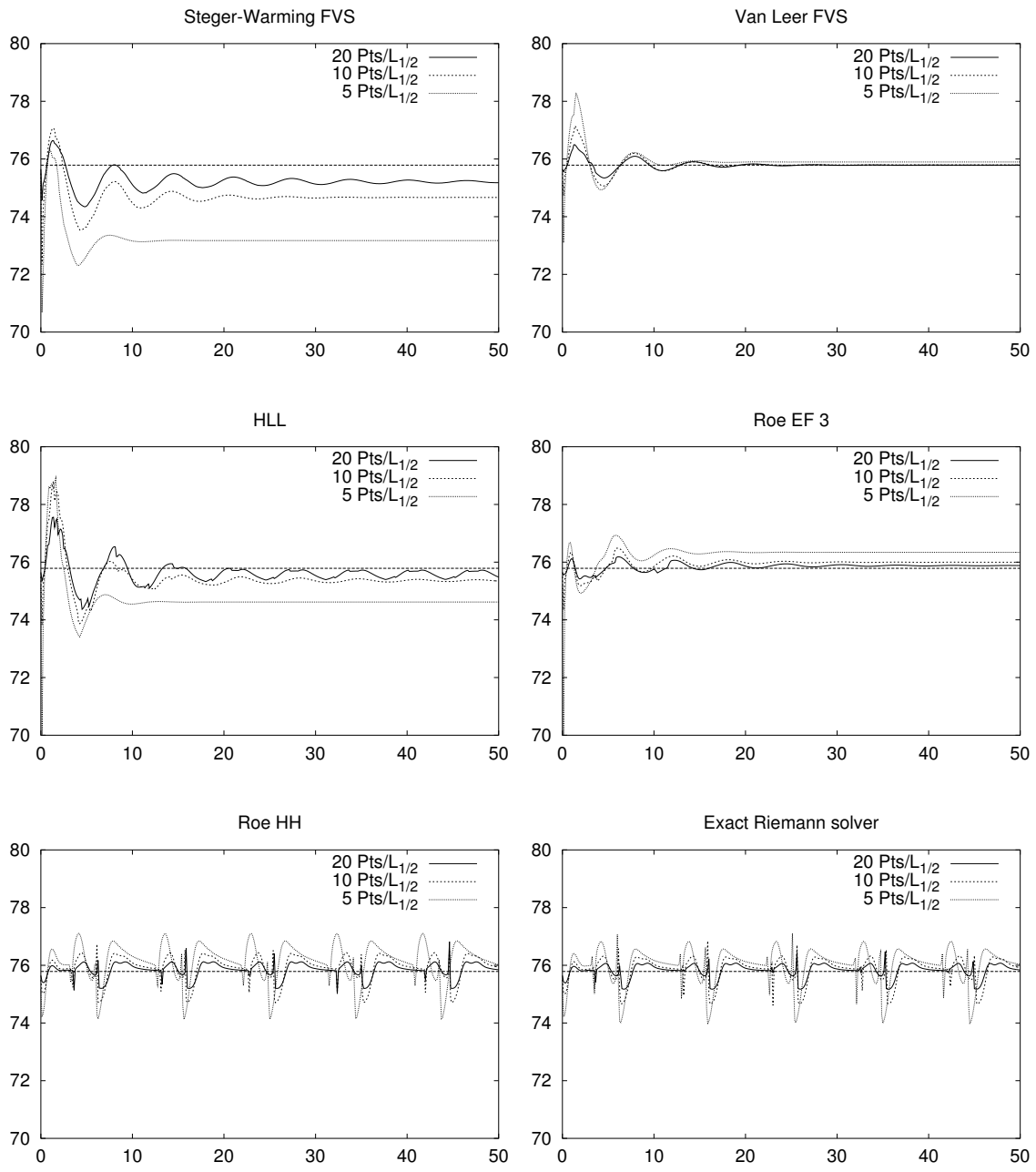

Figure A.1: Front pressure histories of ZND Test 1 for different first-order accurate FV upwind schemes. $C_{CFL} \approx 0.9$.

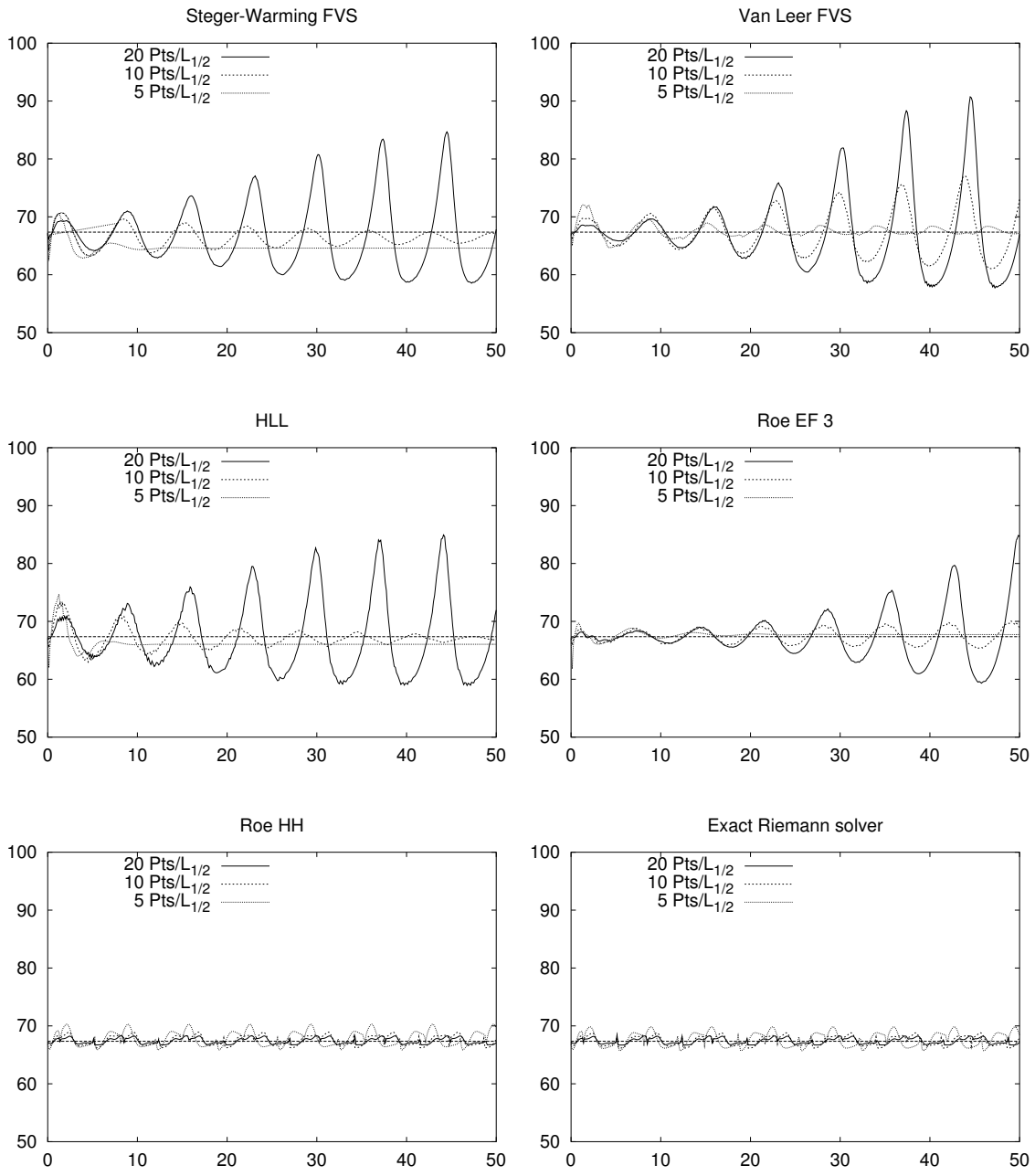

Figure A.2: Front pressure histories of ZND Test 2 for different first-order accurate FV upwind schemes. $C_{CFL} \approx 0.9$.

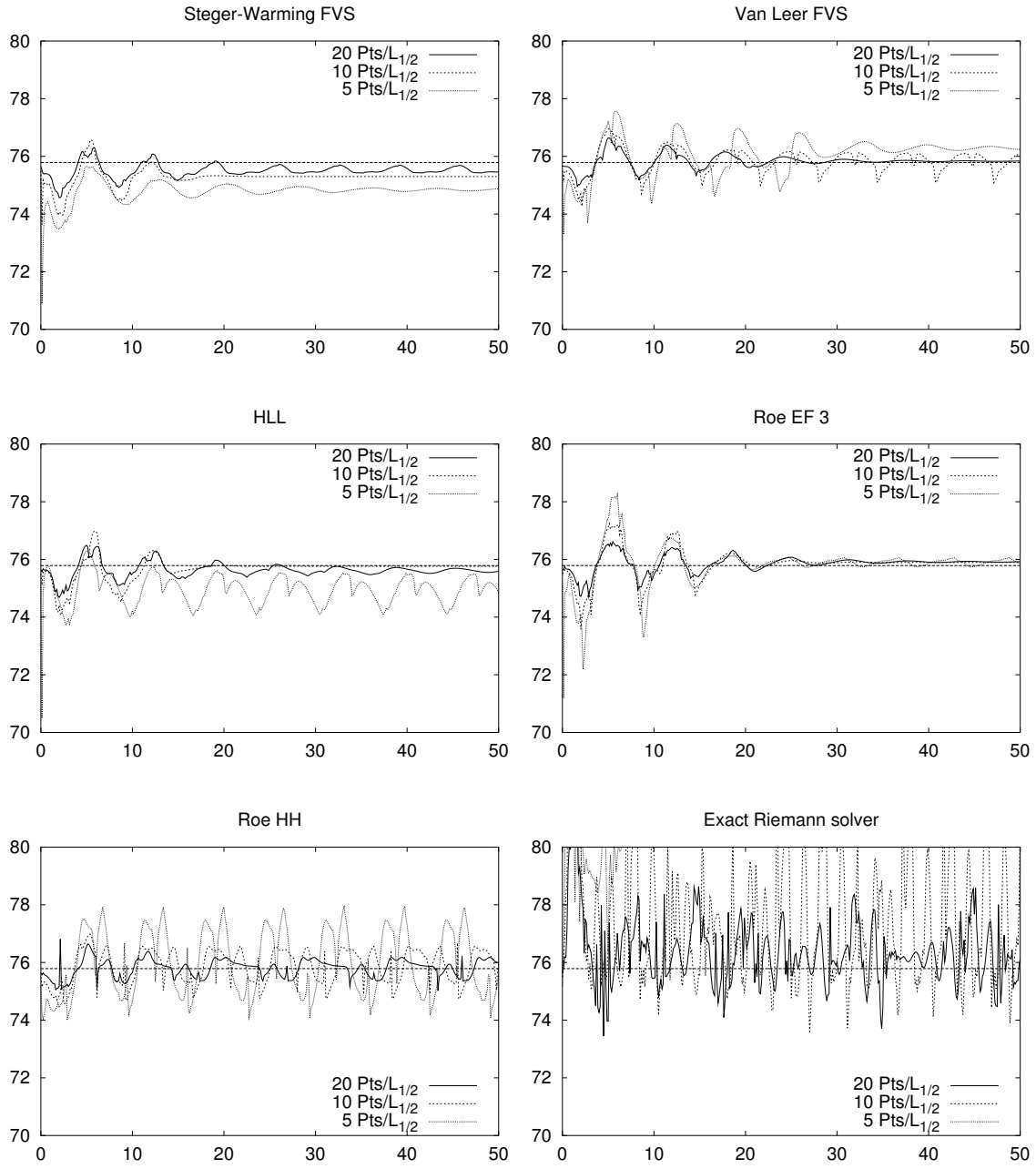

Figure A.3: Front pressure histories of ZND Test 1 for second-order MUSCL-Hancock method (Minmod limiter) with different upwind schemes. $C_{CFL} \approx 0.9$.

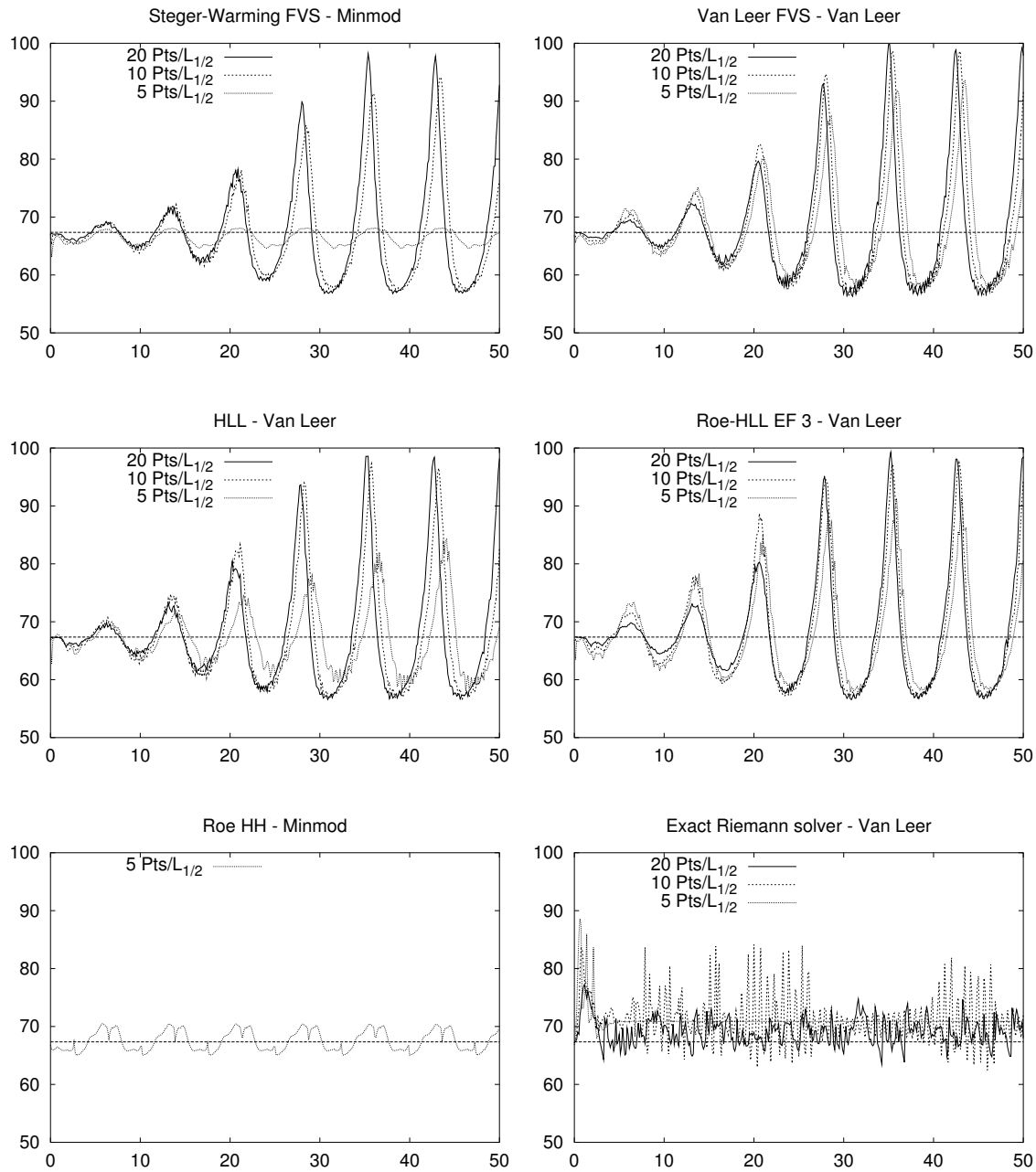

Figure A.4: Front pressure histories of ZND Test 2 for second-order MUSCL-Hancock method with different upwind schemes and limiters. $C_{CFL} \approx 0.9$. The Van Leer-limiter is used where possible. Steger-Warming FVS only works with Minmod. Roe HH gives a result only with Minmod for $5\,\mathrm{Pts}/L_{1/2}$.

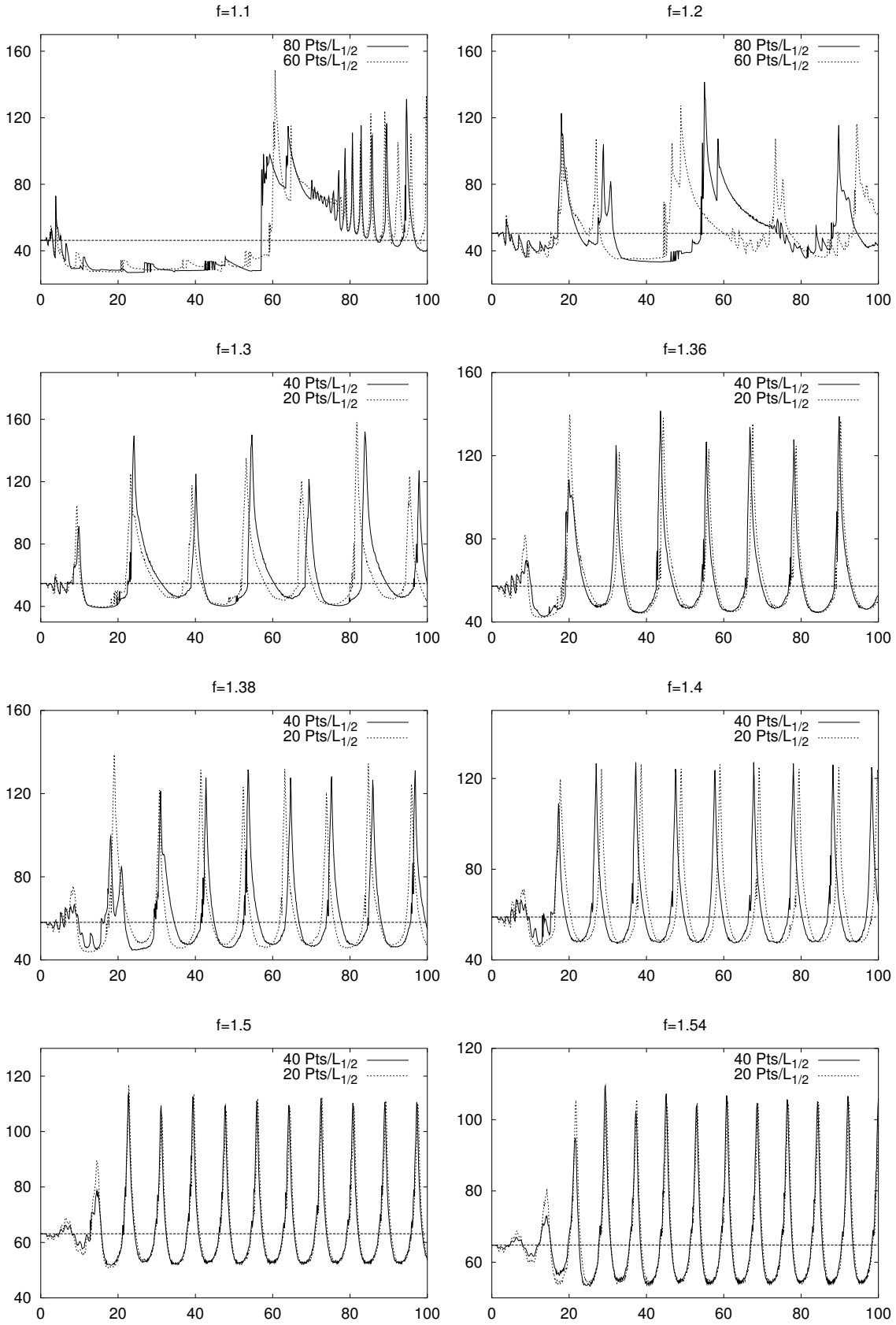

Figure A.5: Front pressure histories for overdrive factors $f = 1.1$ to $f = 1.54$, $\gamma = 1.2$, $E_0^\star = 50$, $Q_0 = 50$. MUSCL-Hancock method with Roe-HLL EF 3 and Van Leer-limiter. $C_{CFL} \approx 0.9$.

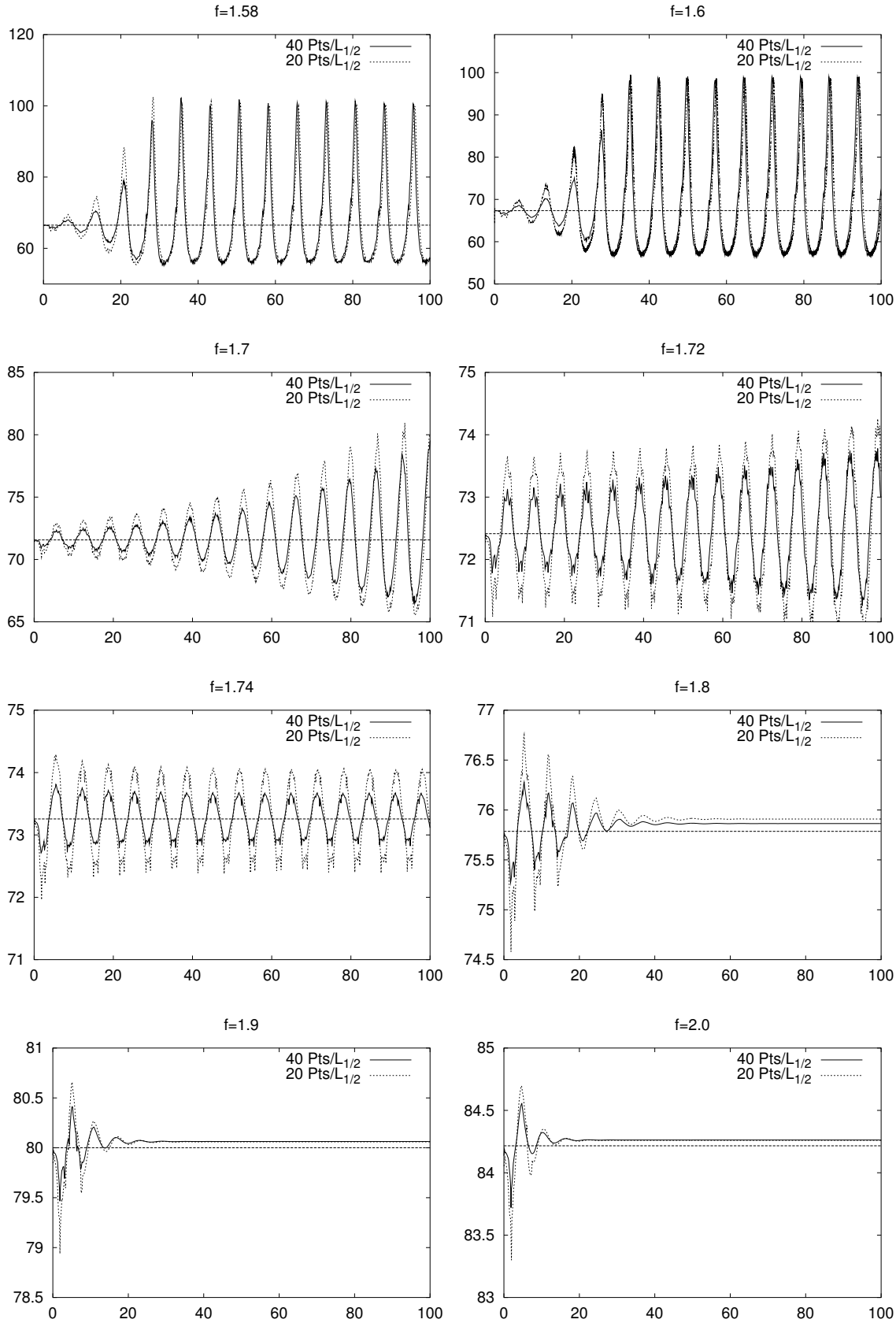

Figure A.6: Front pressure histories for overdrive factors $f = 1.56$ to $f = 2.0$, $\gamma = 1.2$, $E_0^\star = 50$, $Q_0 = 50$. MUSCL-Hancock method with Roe-HLL EF 3 and Van Leer-limiter. $C_{CFL} \approx 0.9$.

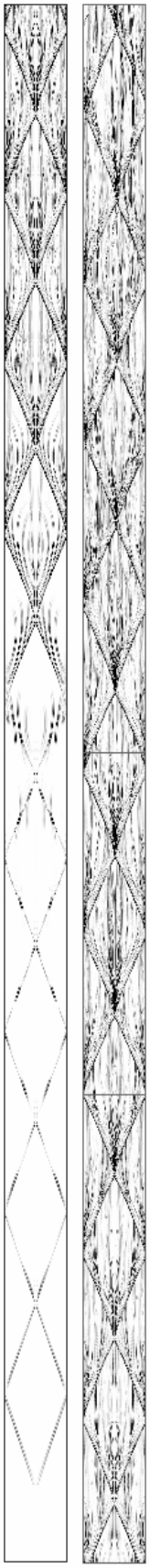

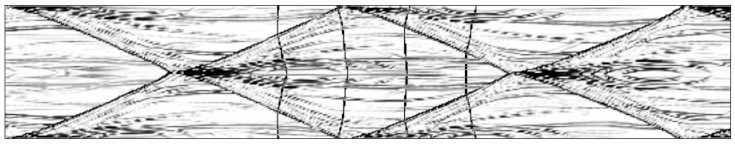

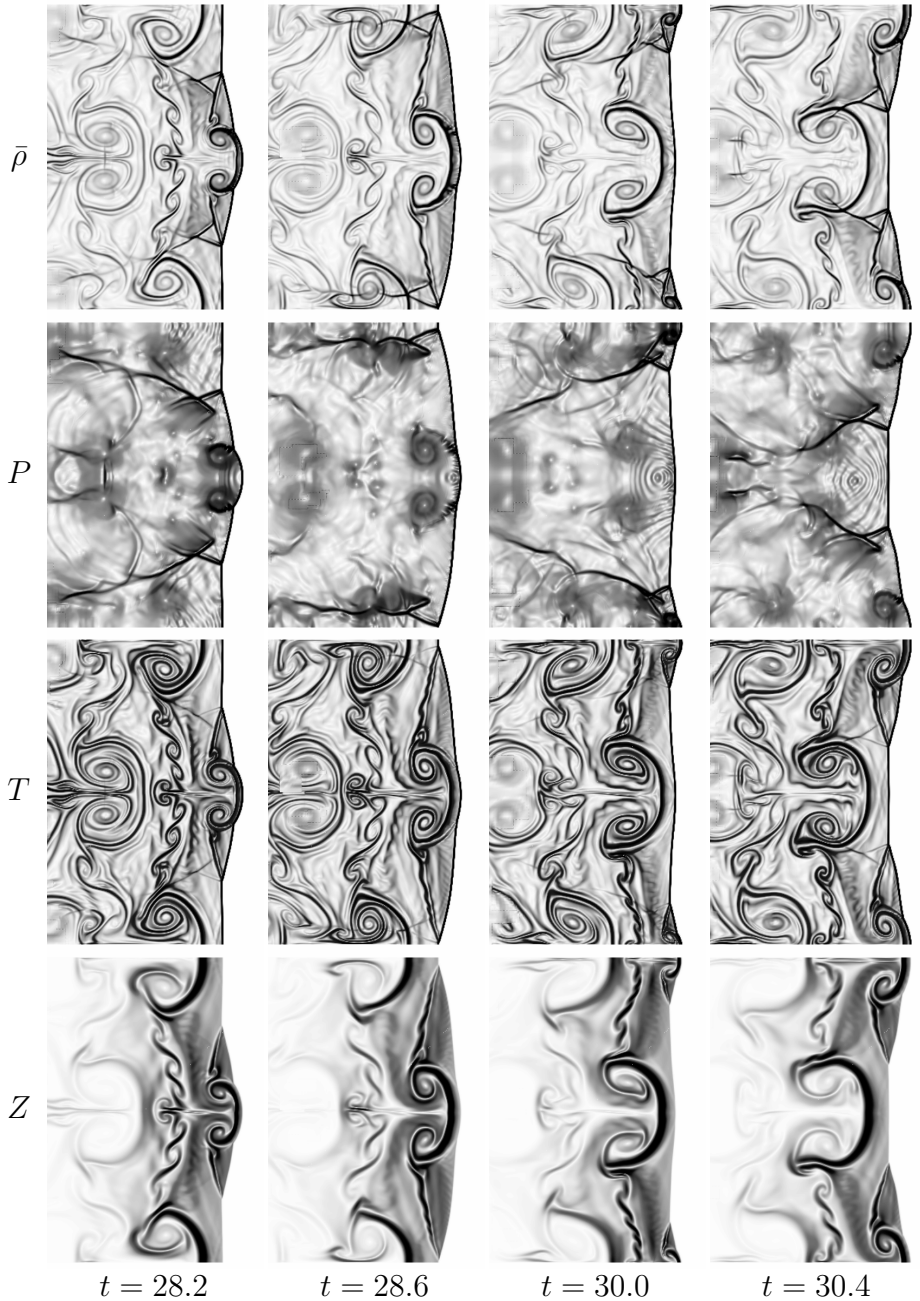

Figure A.7: Schlieren plots for ZND Test 4. Roe-HLL EF 3⋆-H with Wave Propagation Method, Van Albada-limiter, $40\,Pts/L_{1/2}$, $C_{CFL}^{Roe} \approx 0.95$.

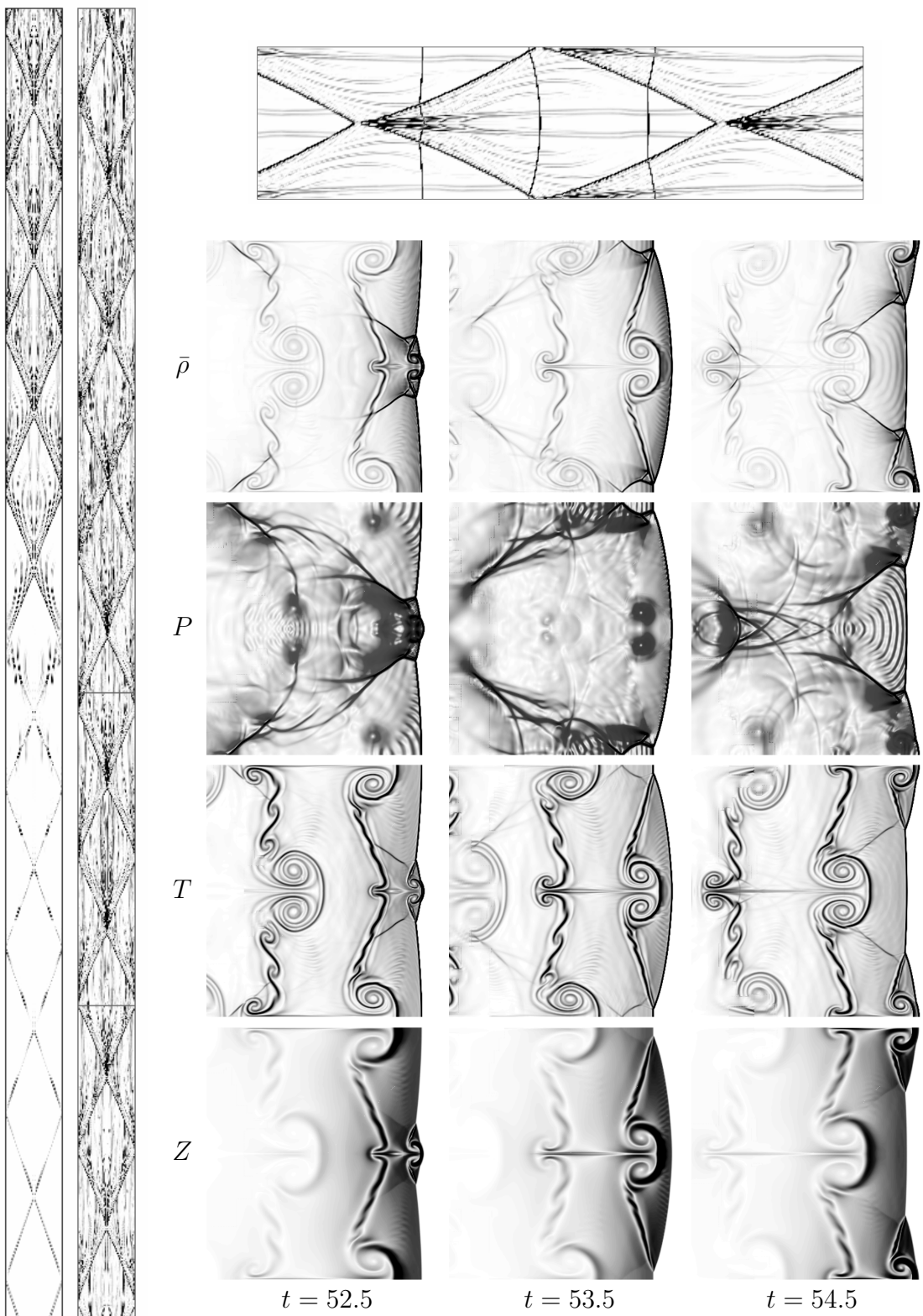

Figure A.8: Schlieren plots for ZND Test 5. Roe-HLL EF 3⋆-H with Wave Propagation Method, Van Albada-limiter, $40\,Pts/L_{1/2}$, $C_{CFL}^{Roe} \approx 0.95$.

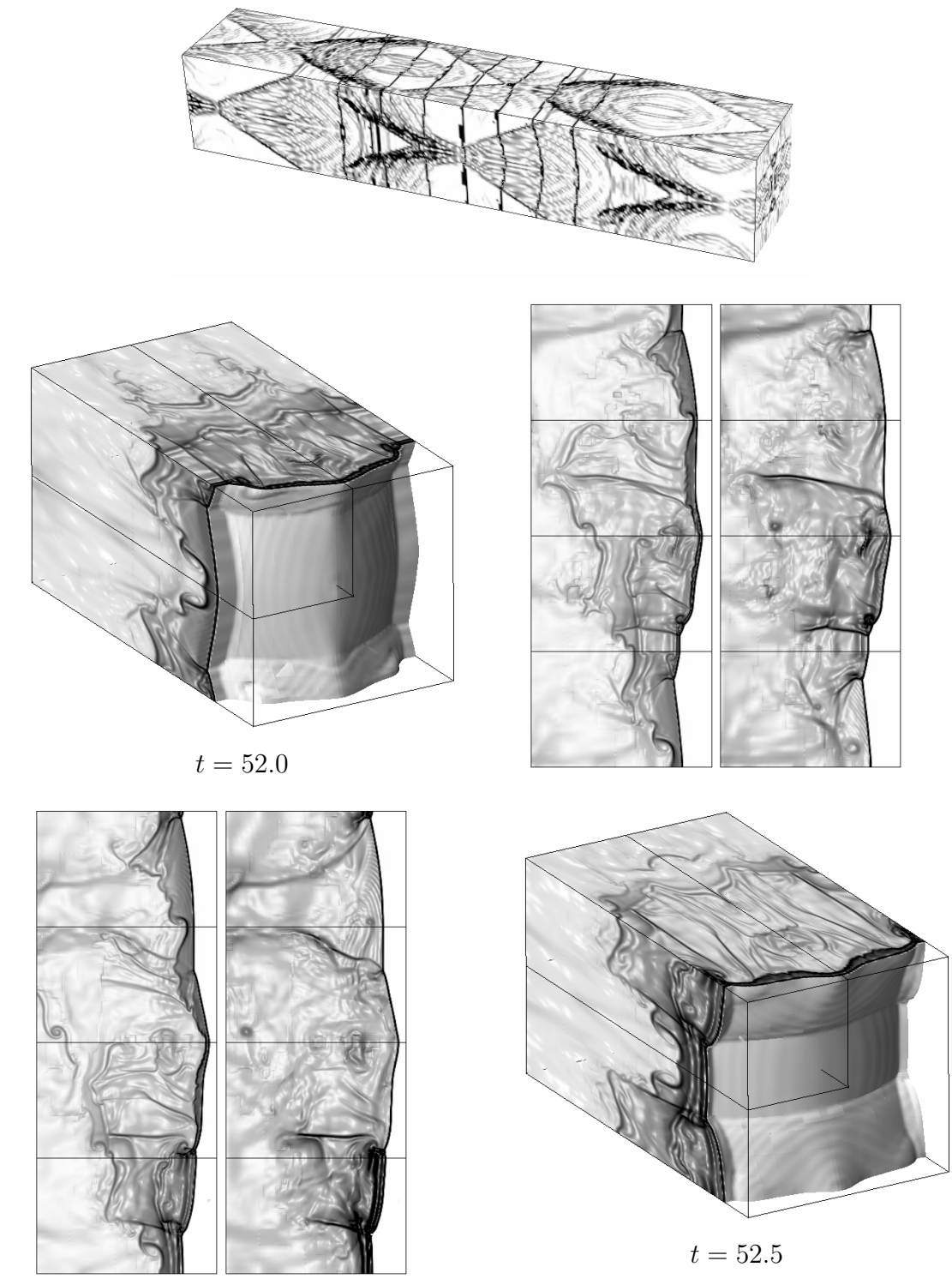

Figure A.9: Schlieren plots for ZND Test 6b. Displayed: $7.2 < X_1 < 14.5$. 3D graphics display $\bar{\rho}$, 2D roll-ups show $\bar{\rho}$ (left) and P (right). See Fig. A.11 for the location and orientation of the two-dimensional roll-ups.

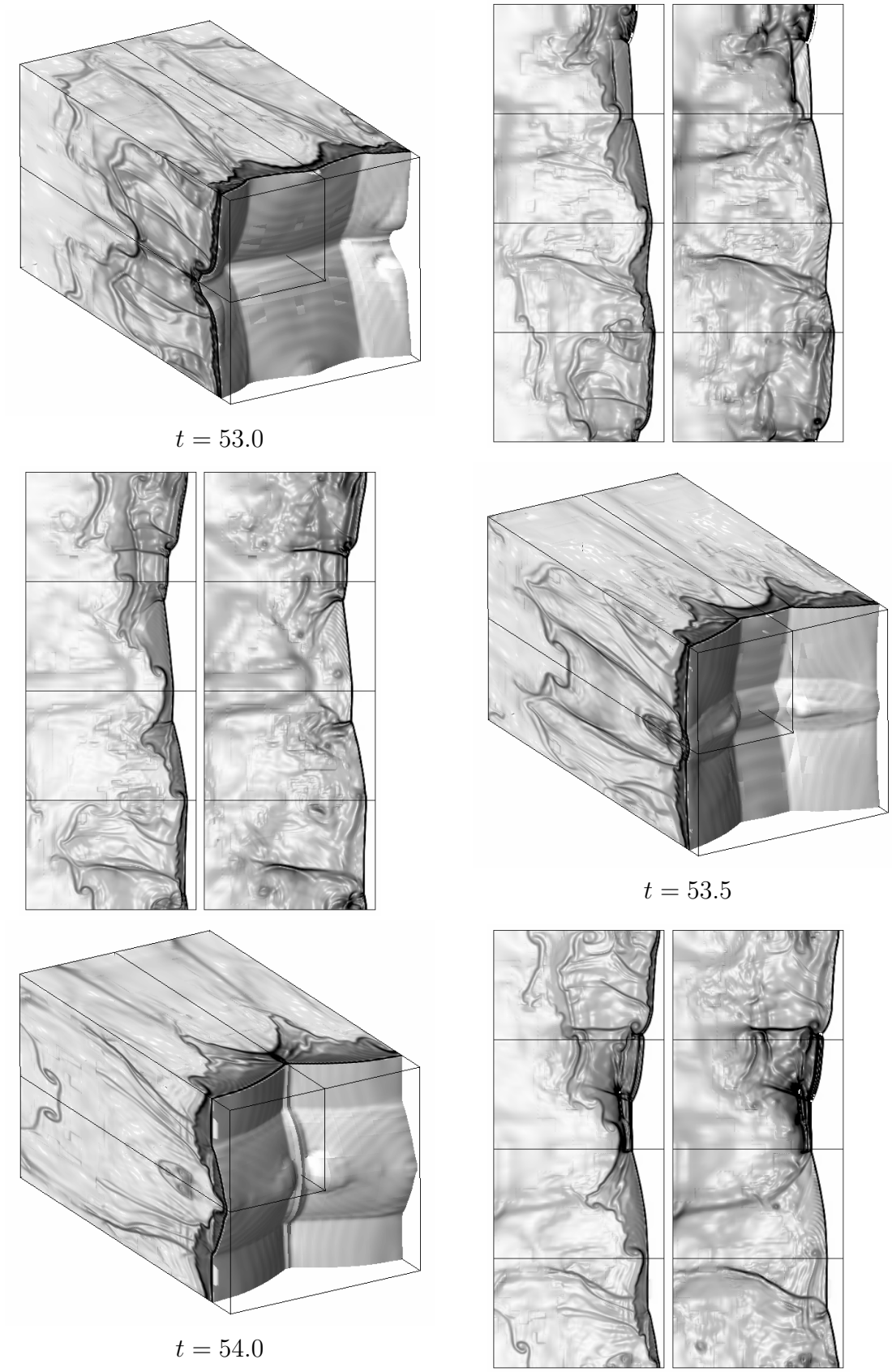

Figure A.10: Schlieren plots for ZND Test 6b. Displayed: $7.2 < X_1 < 14.5$. 3D graphics display $\bar{\rho}$, 2D roll-ups show $\bar{\rho}$ (left) and P (right). See Fig. A.11 for the location and orientation of the two-dimensional roll-ups.

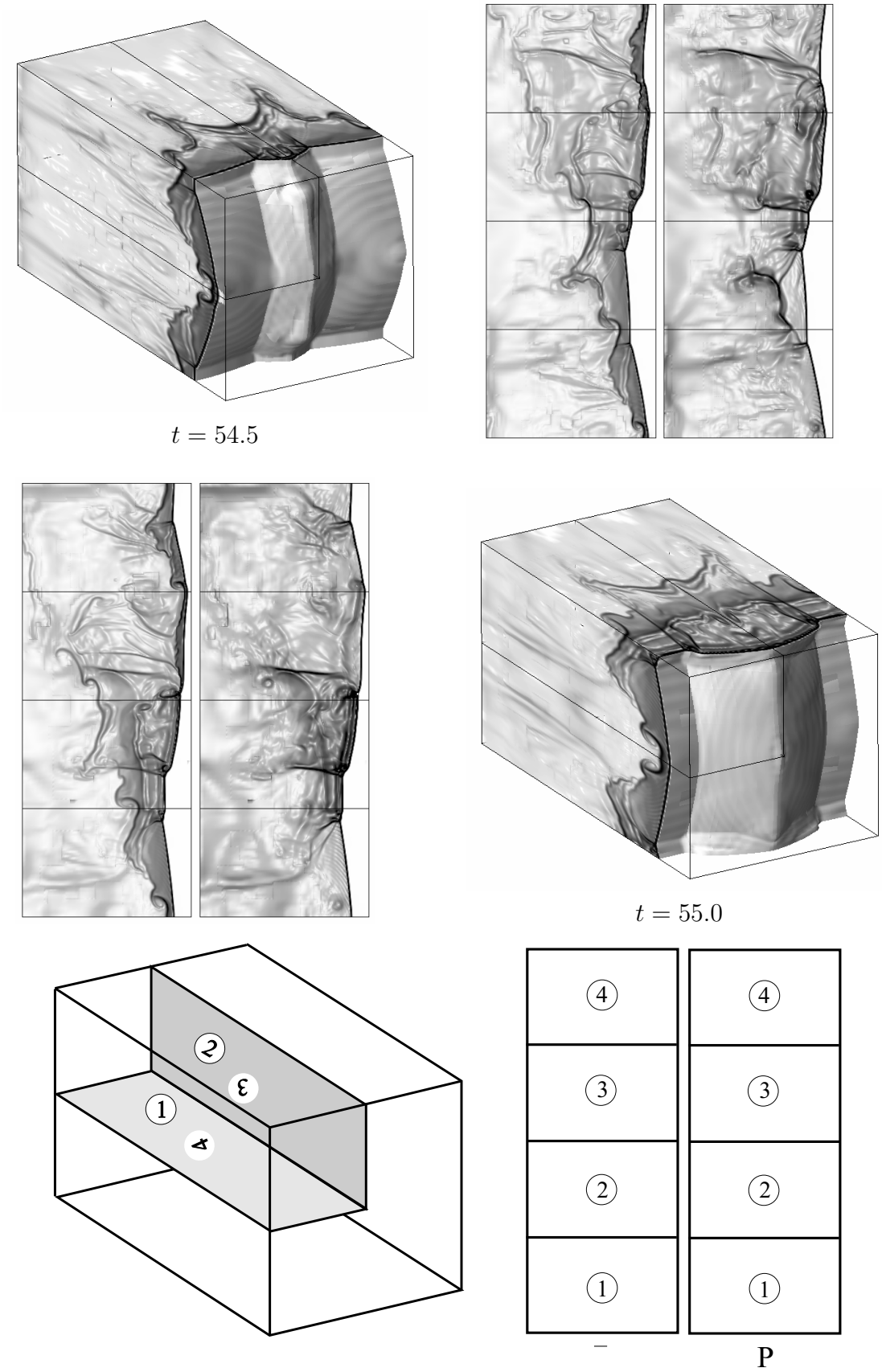

Figure A.11: Schlieren plots for ZND Test 6b. Displayed: $7.2 < X_1 < 14.5$. 3D graphics display $\bar{\rho}$, 2D roll-ups show $\bar{\rho}$ (left) and P (right). Bottom: location and orientation of the two-dimensional roll-ups.

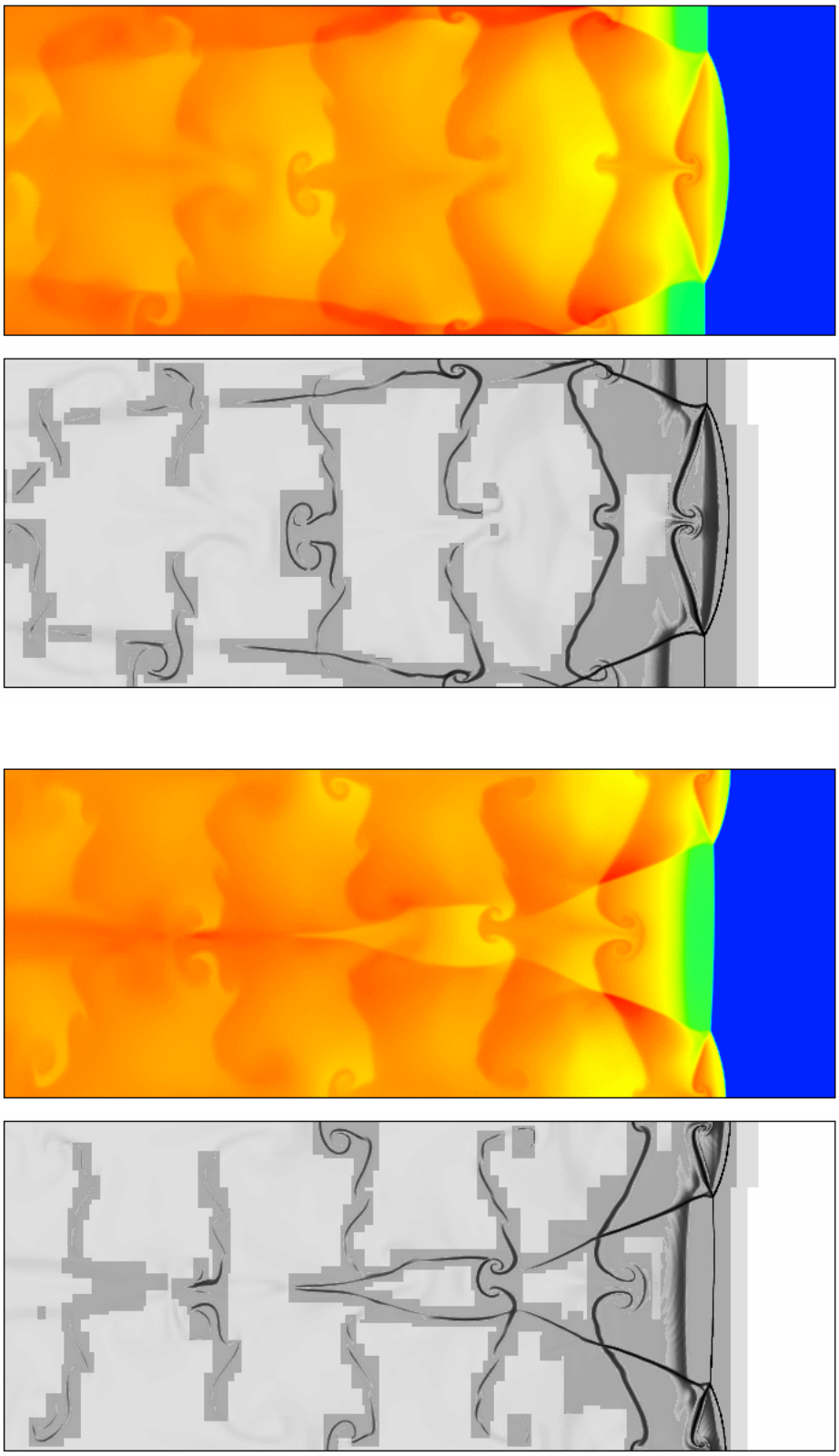

Figure A.12: Color plots of the temperature and schlieren plots of the density on refinement regions in the first (upper pictures) and second half (lower pictures) of a detonation cell, 22.4 Pts/l_{ig}.

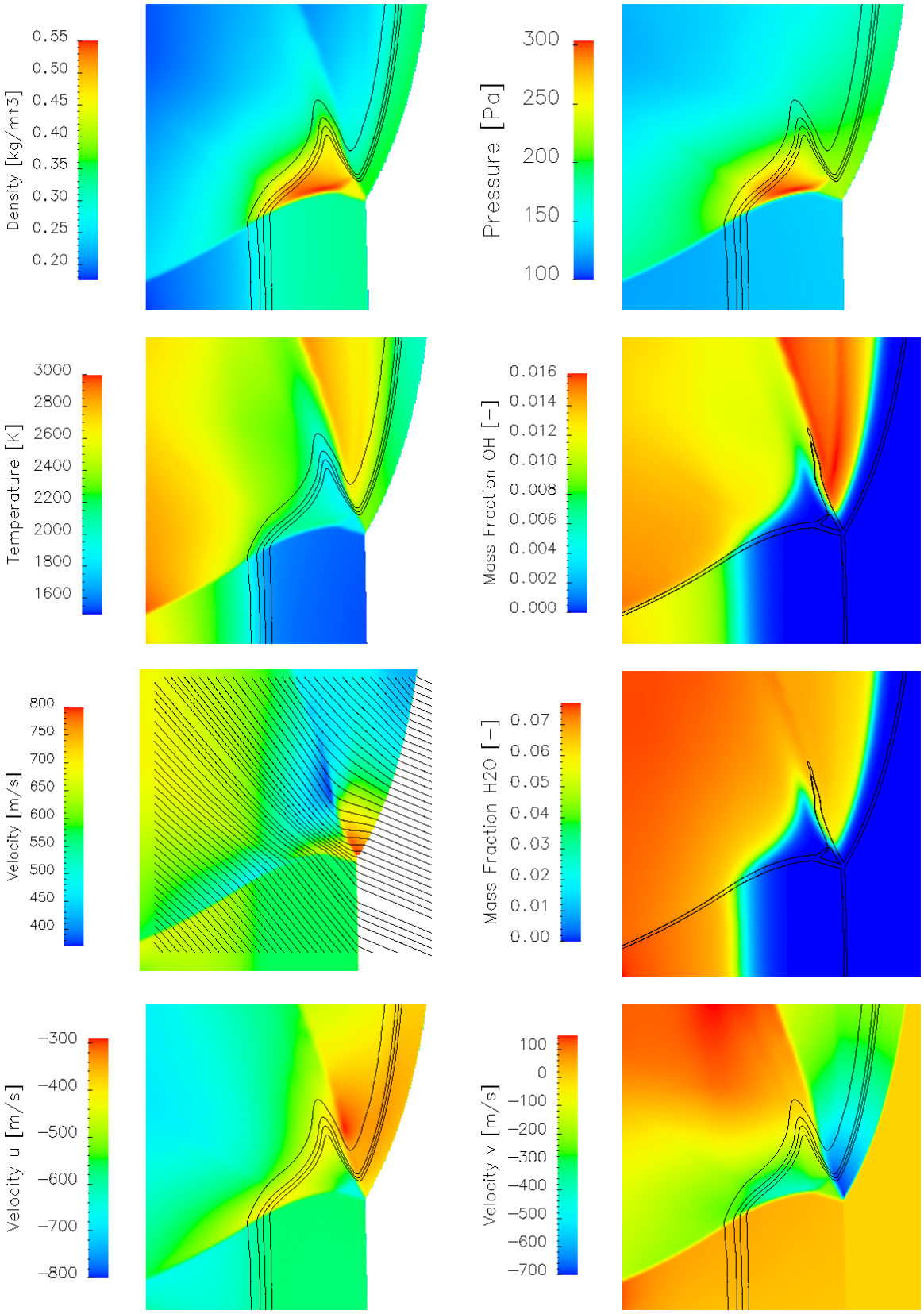

Figure A.13: Color plots of the triple point structure close to the end of a detonation cell at $t = 632\,\mu s$.

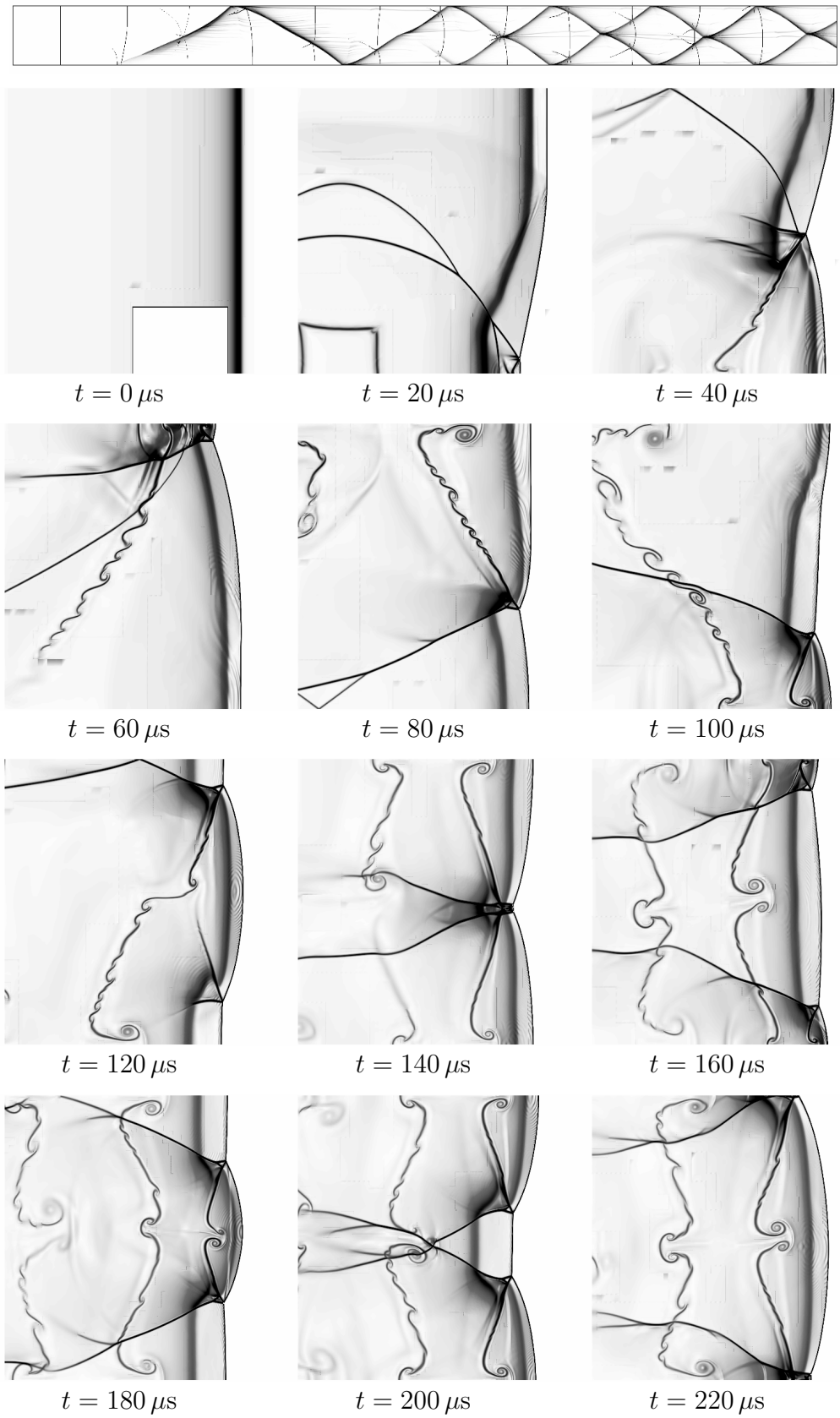

Figure A.14: Schlieren plot of ρ at the beginning of the computation. The oscillation becomes regular after $\approx 200\,\mu$s, $44.8\,\mathrm{Pts}/l_{ig}$.

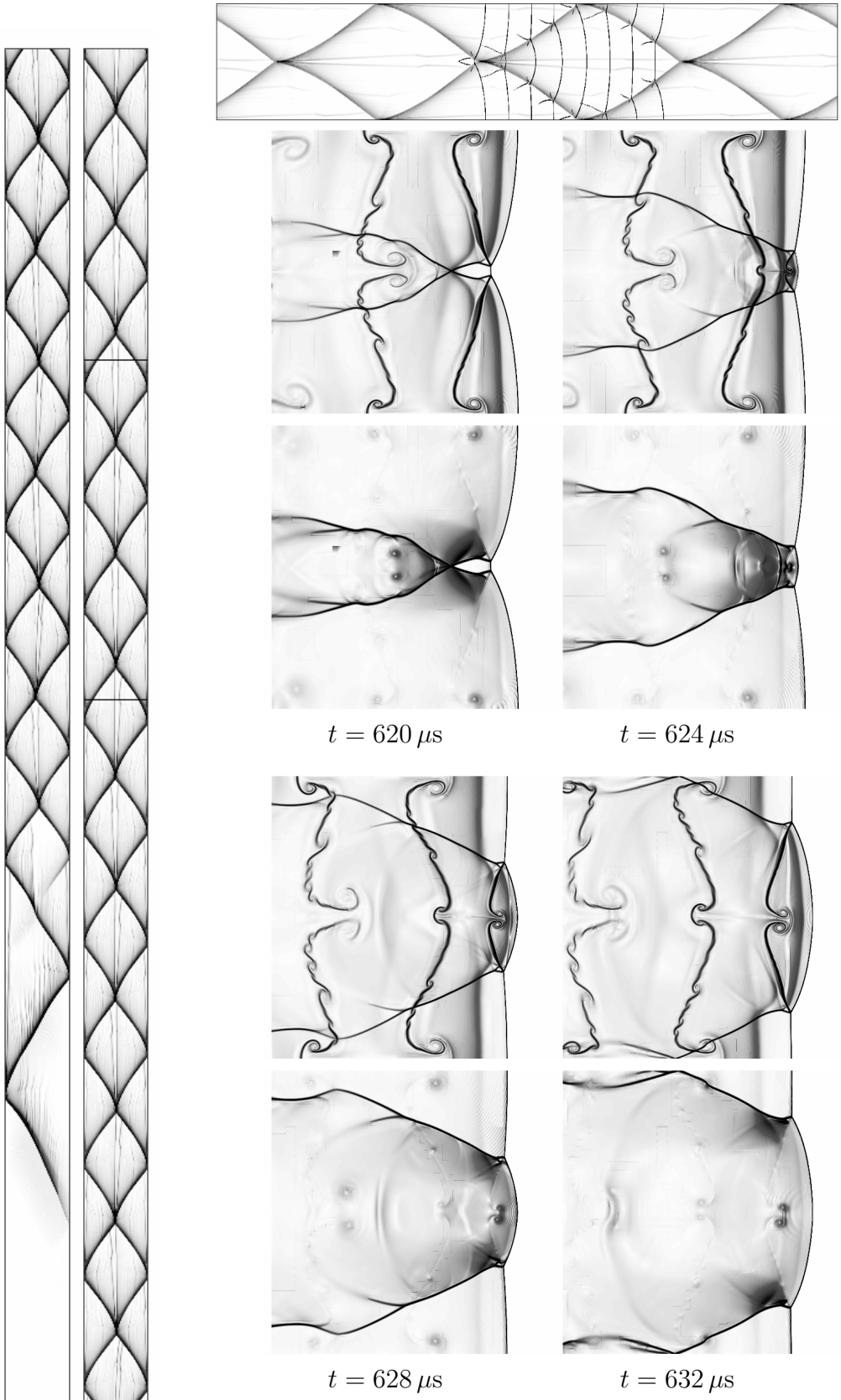

Figure A.15: Triple point tracks and schlieren plots of T (upper graphic for each time step) and p (lower graphic) for the reiniation and for the first half of a detonation cell, $44.8\,\mathrm{Pts}/l_{ig}$.

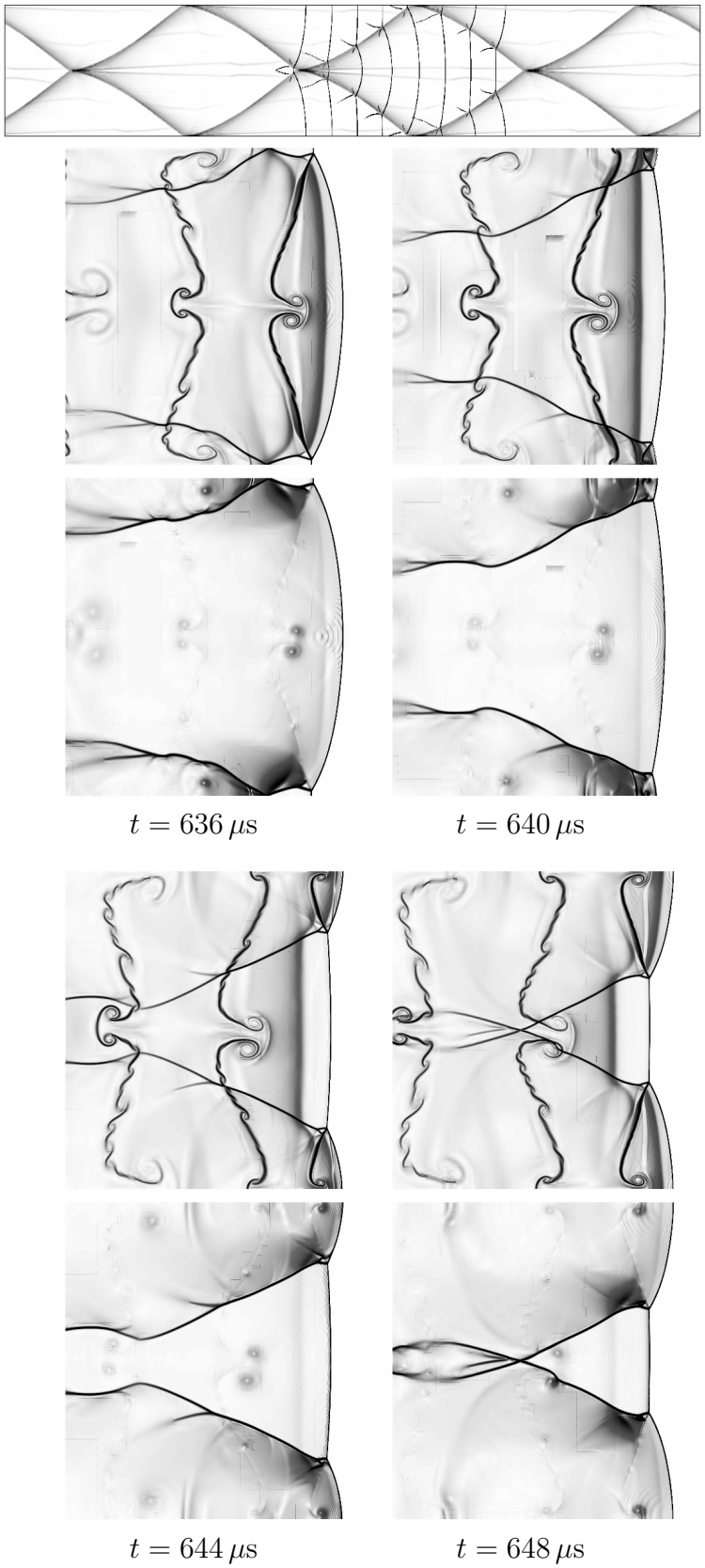

Figure A.16: Schlieren plots of T (upper graphic for each time step) and p (lower graphic) for the second half of a detonation cell, $44.8\,\mathrm{Pts}/l_{ig}$.

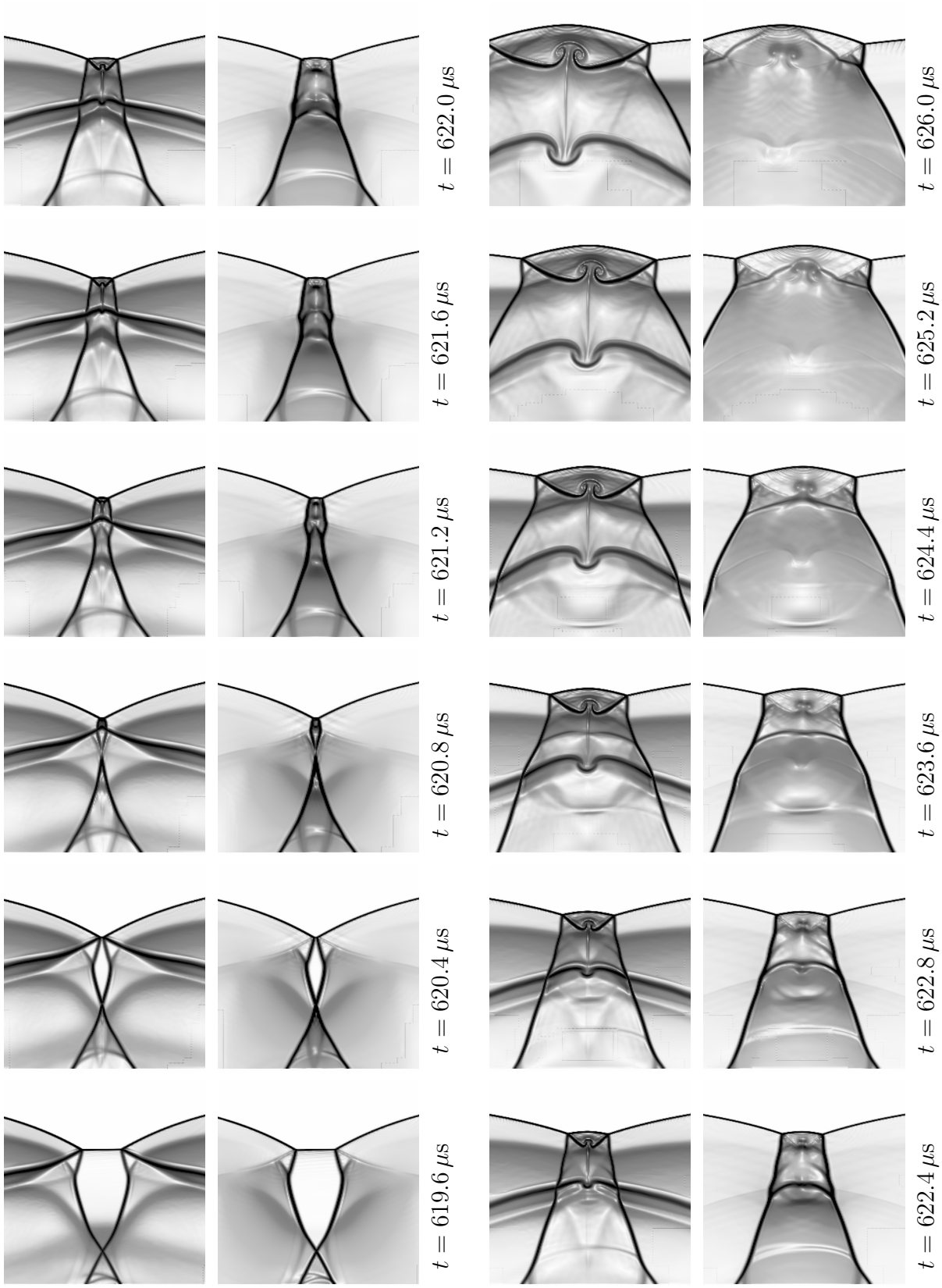

Figure A.17: Schlieren plots T (upper graphic for each time step) and p (lower graphic) of the reinitiation process at the end of an old and at the beginning of a new detonation cell $44.8\,\mathrm{Pts}/l_{ig}$.

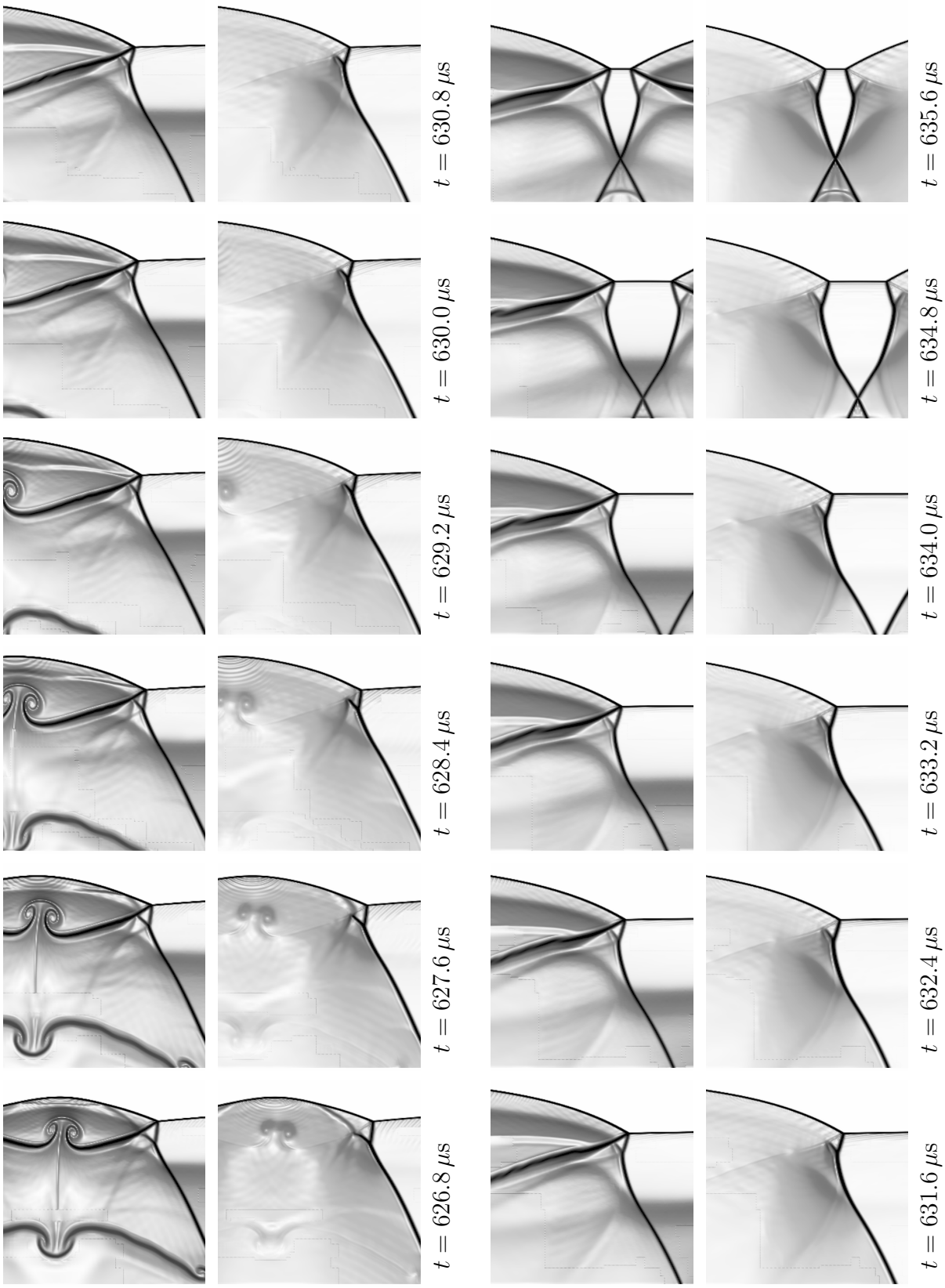

Figure A.18: Schlieren plots T (upper graphic for each time step) and p (lower graphic) before a triple point collision.

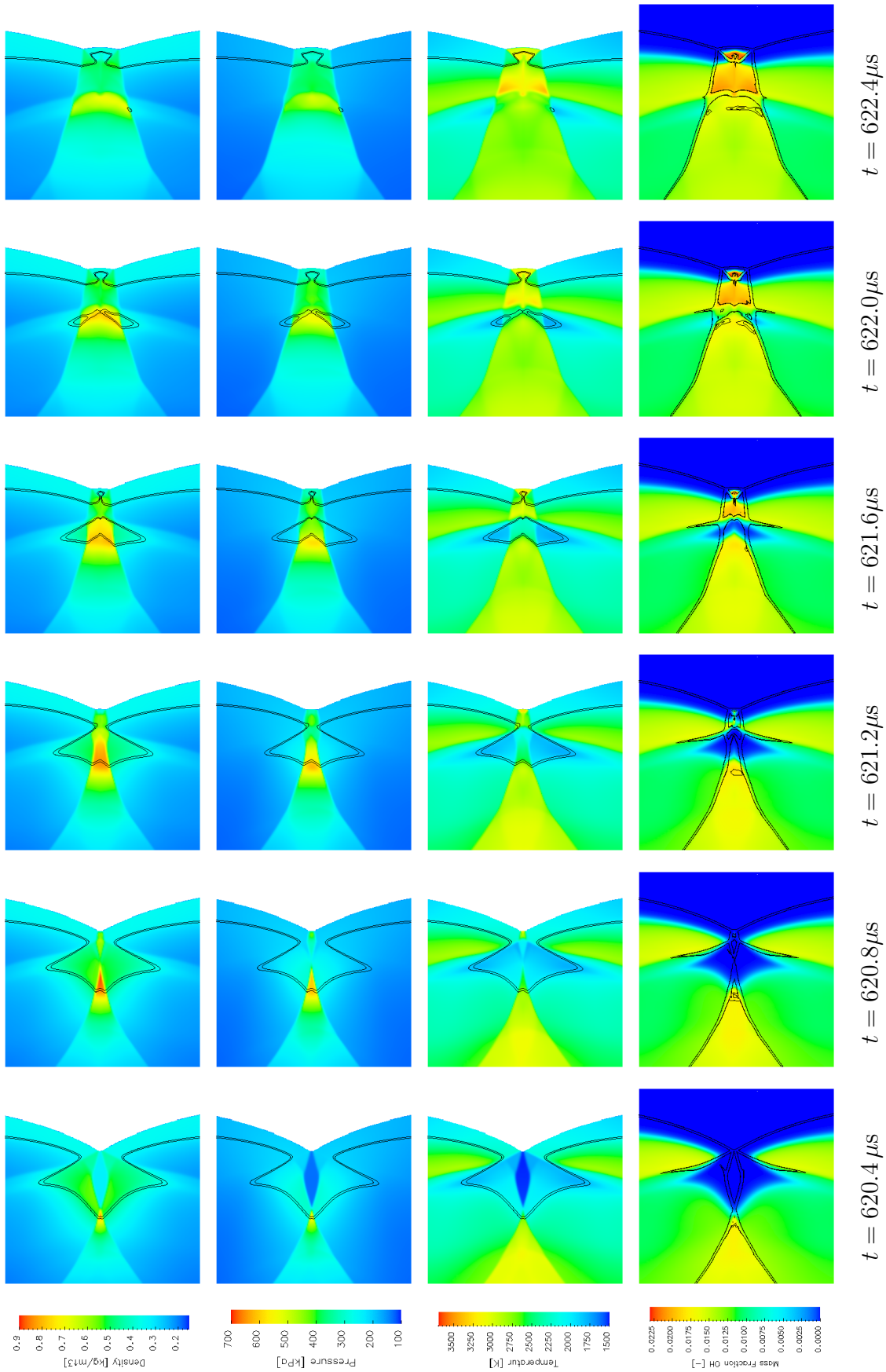

Figure A.19: Color plots of the reinitiation process at the end of a detonation cell, $44.8\,\mathrm{Pts}/l_{ig}$.

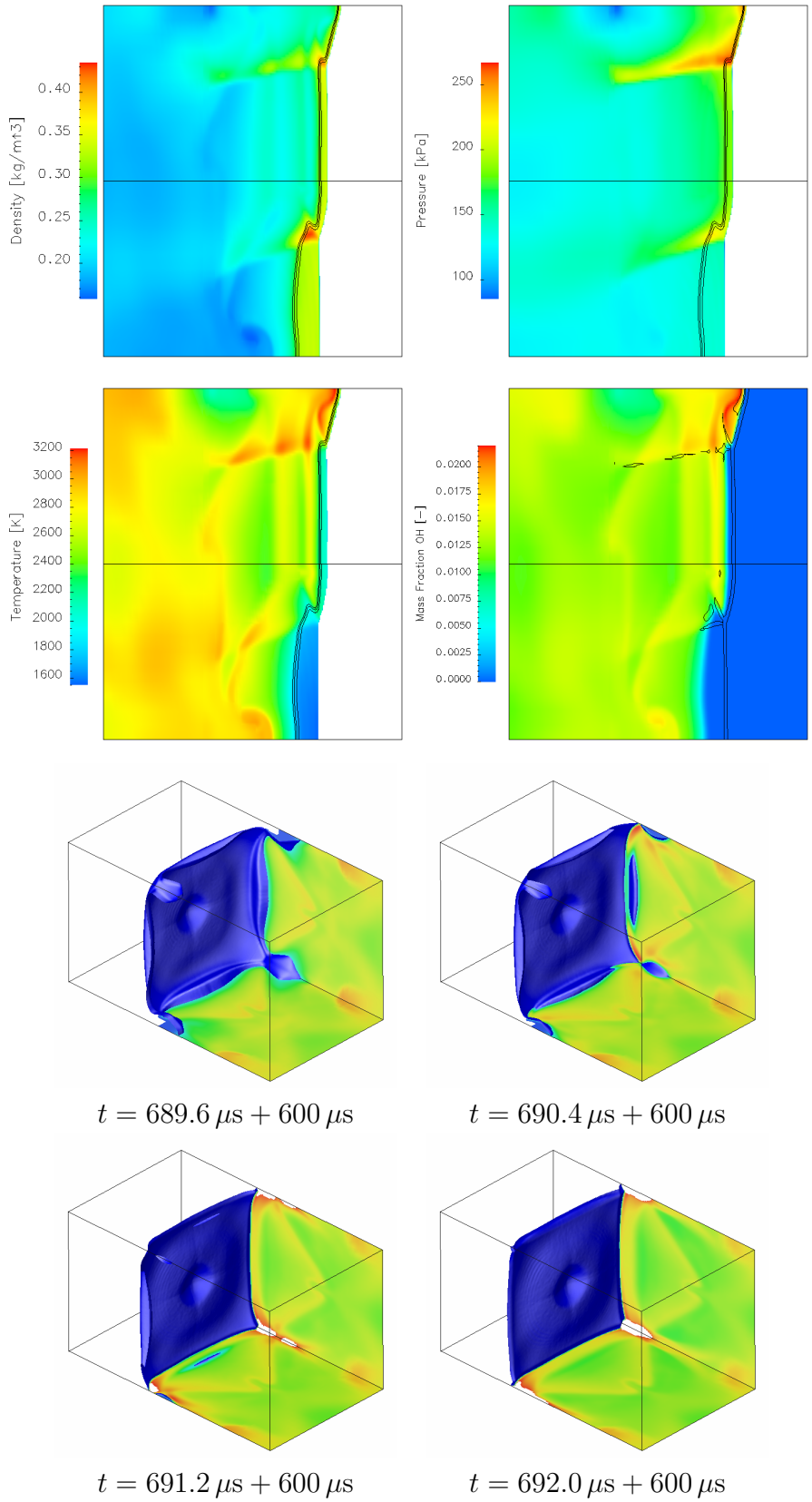

Figure A.20: Results of Setup 4a. Top: 2D color plots for the sides 2 and 3 (cf. Fig. 7.16) at $t = 680\,\mu s + 600\,\mu s$. Bottom: Color plots of Y_{OH} show the formation of unreacted regions during reinitiation. $5.0\,cm < x_1 < 7.0\,cm$

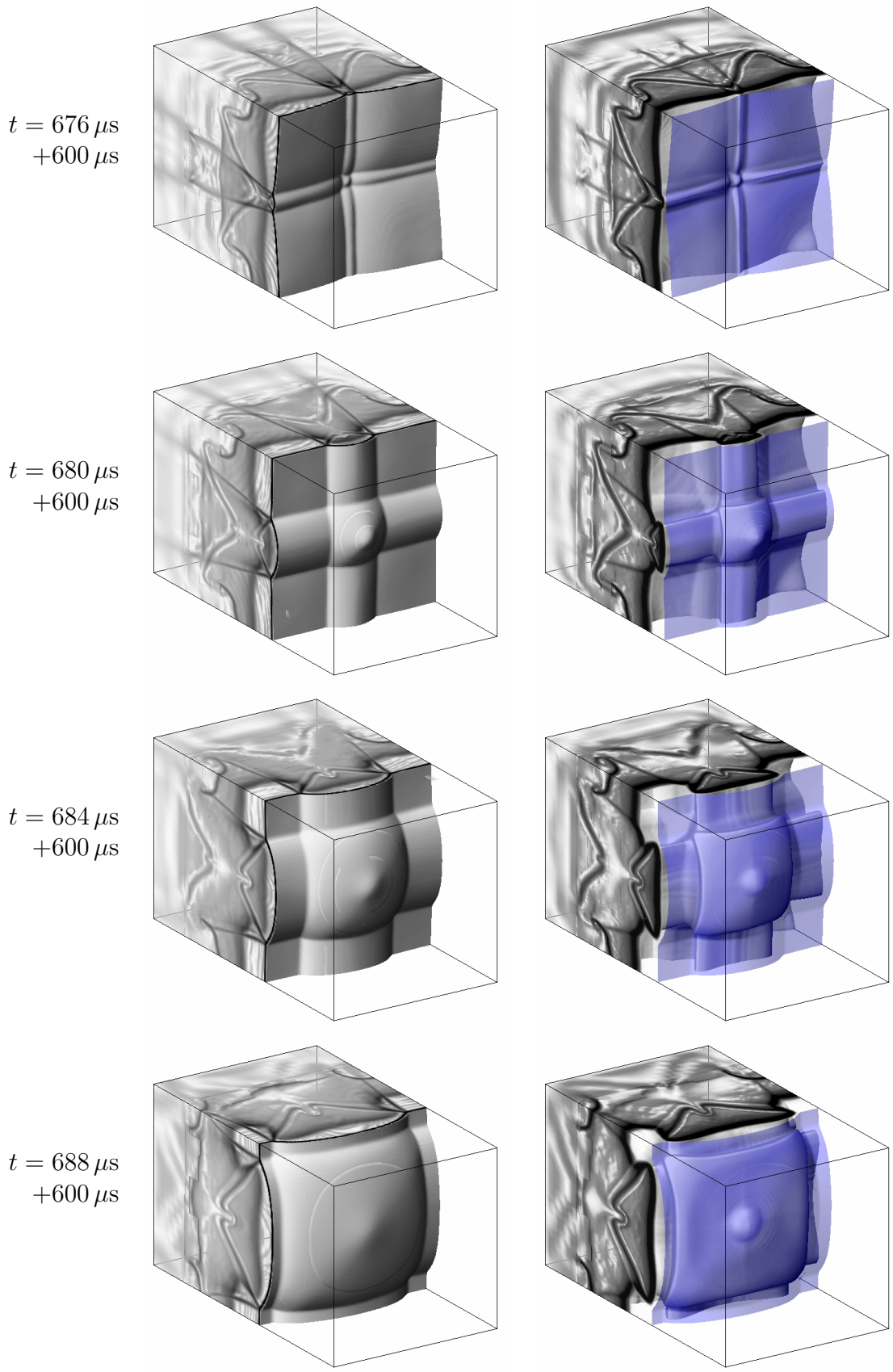

Figure A.21: Schlieren plots for Setup 4a of ρ (left) and Y_{OH} (right) in the first half of a detonation cell, mirrored at $x_2 = 0\,\mathrm{cm}$, $5.0\,\mathrm{cm} < x_1 < 7.0\,\mathrm{cm}$.

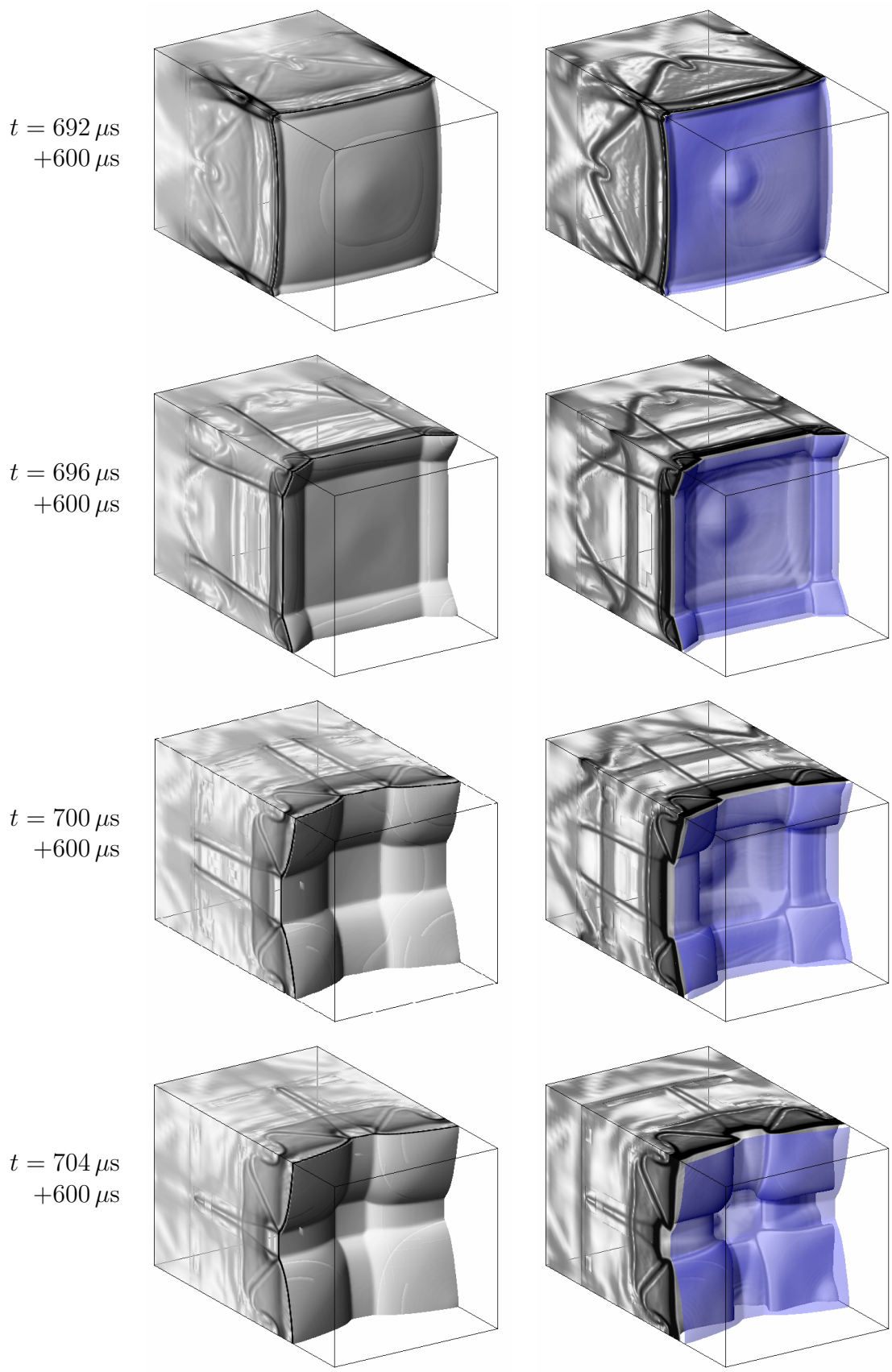

Figure A.22: Schlieren plots for Setup 4a of ρ (left) and Y_{OH} (right) in the second half of a detonation cell, mirrored at $x_2 = 0\,\mathrm{cm}$, $5.0\,\mathrm{cm} < x_1 < 7.0\,\mathrm{cm}$.

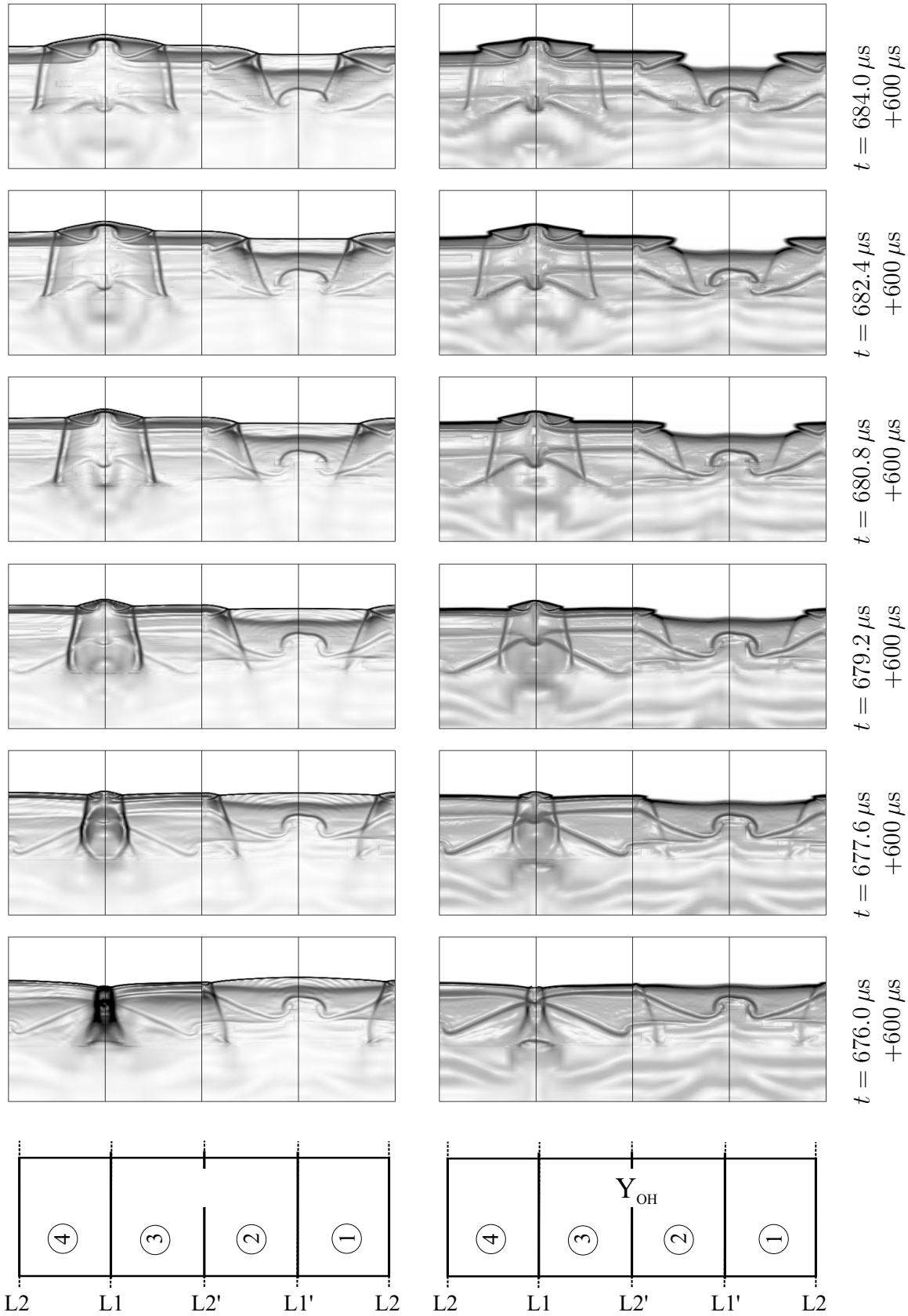

Figure A.23: Roll-ups of schlieren plots for ρ and Y_{OH} for Setup 4a. Compare Fig. 7.16 for orientation and location of 2D graphcis.

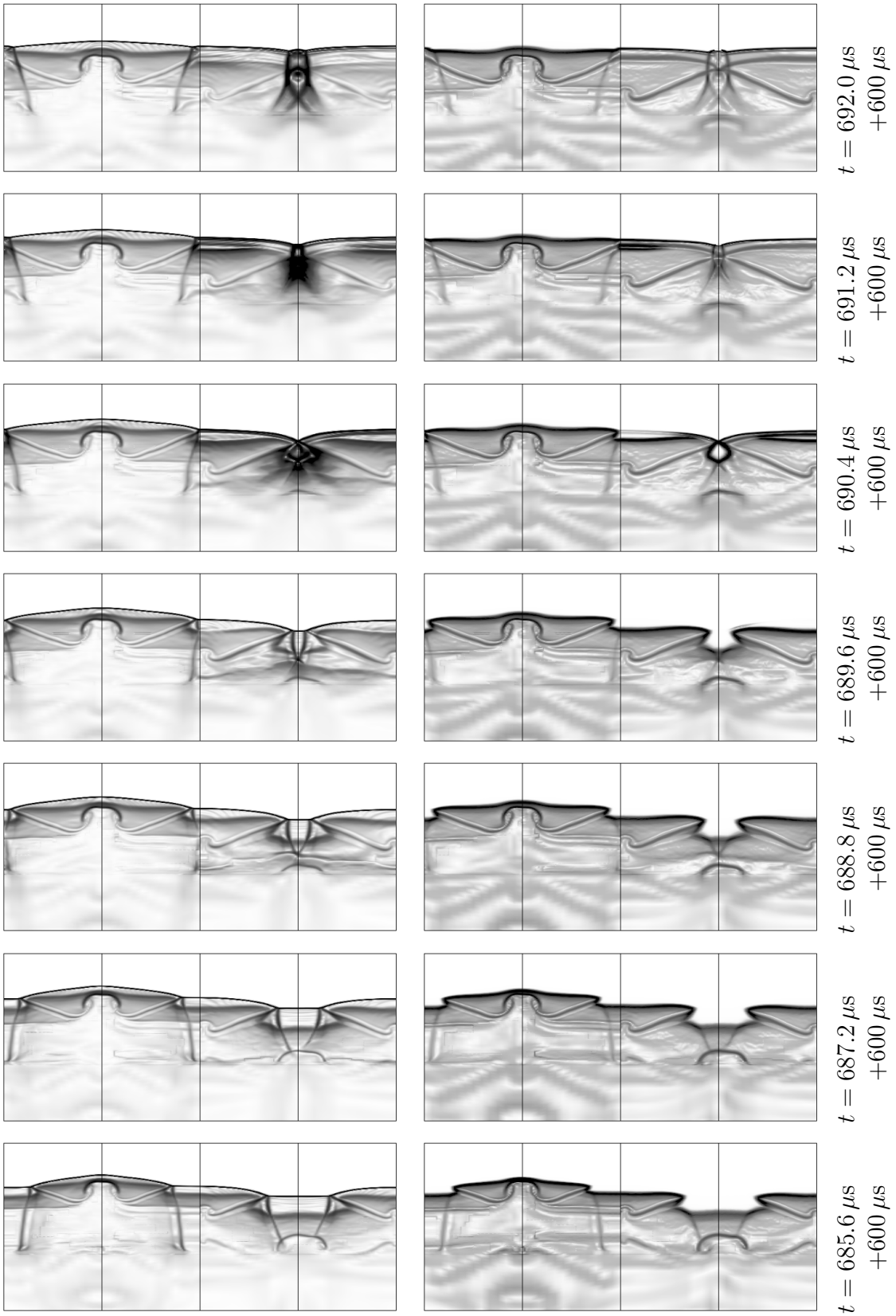

Figure A.24: Roll-ups of schlieren plots for ρ and Y_{OH} for Setup 4a. Compare Figs. 7.16 and A.23 for orientation and location of 2D graphcis.

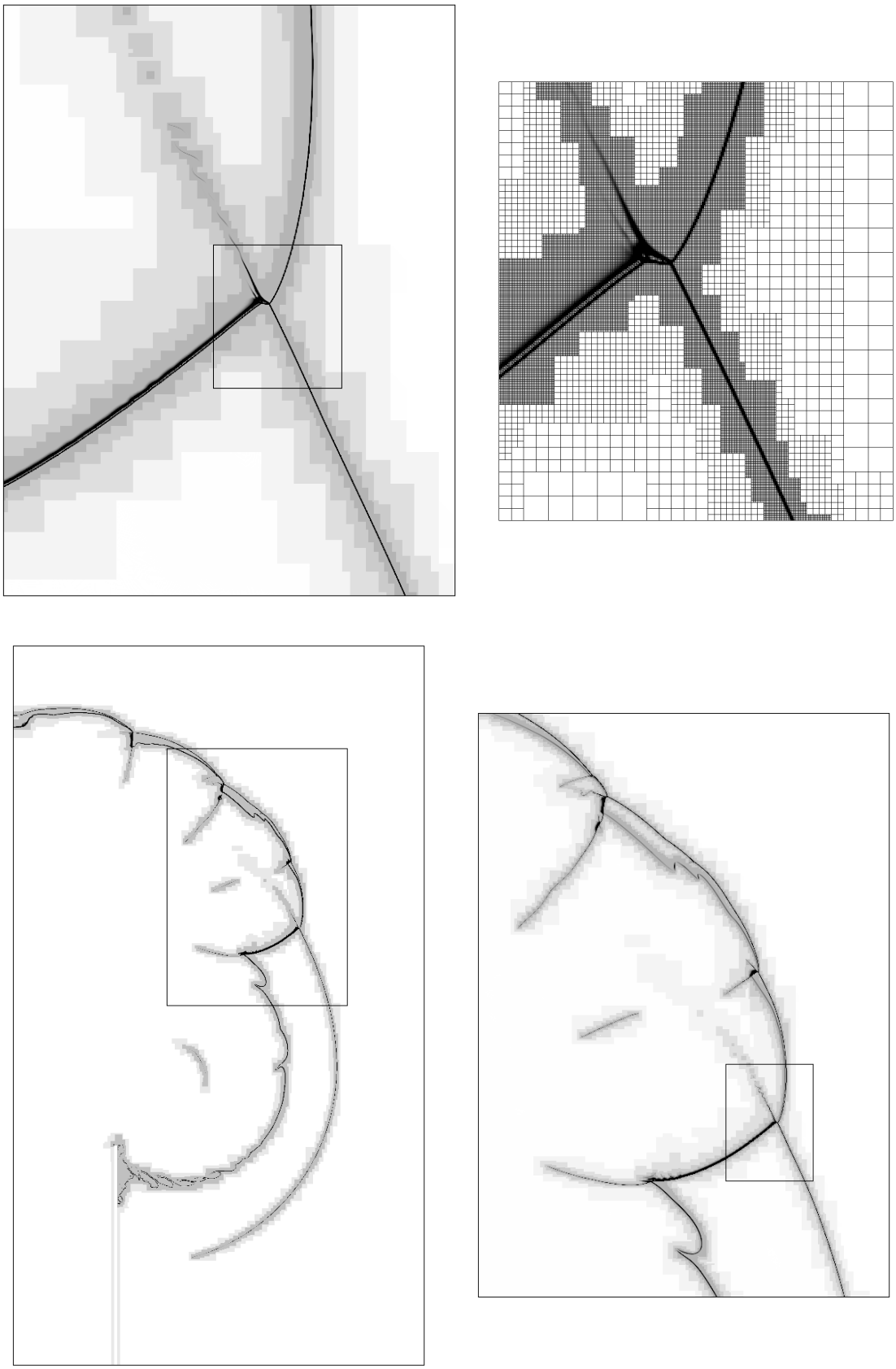

Figure A.25: Density distribution on four refinement levels at $t = 240\,\mu$s for Setup 6a.

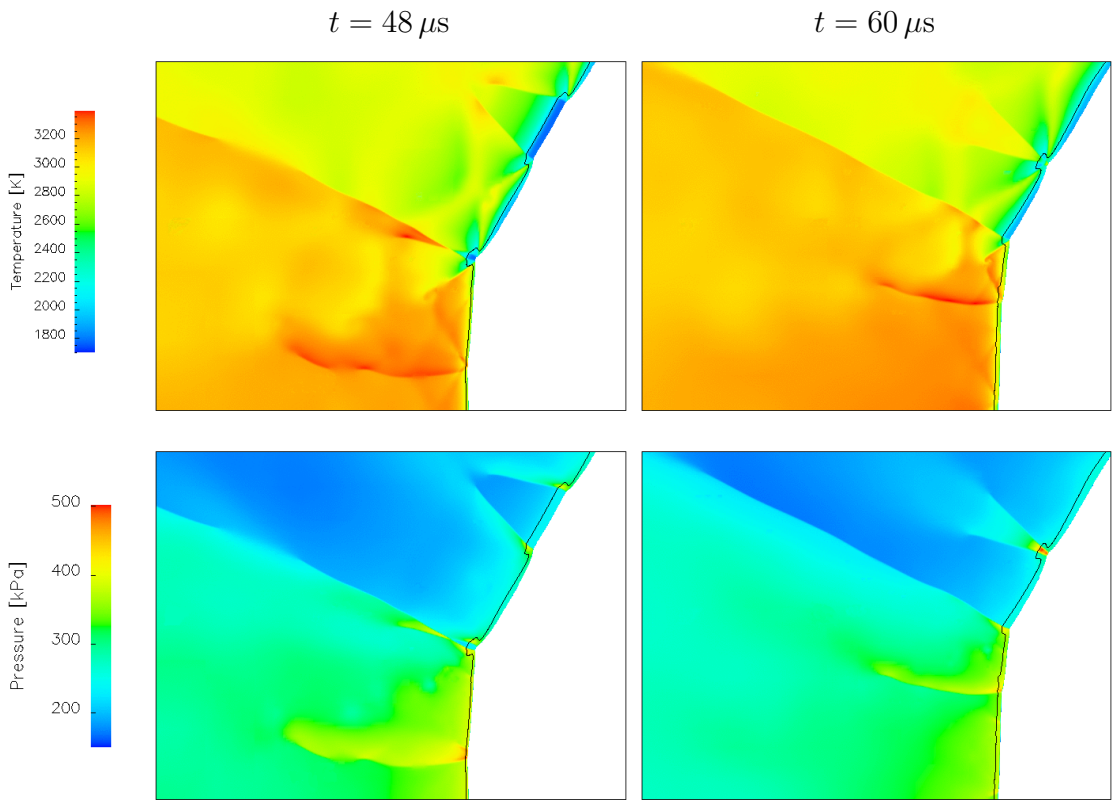

Figure A.26: Color plots of T and p for a Mach reflection with $\Theta = 30^{\circ}$ (Setup 5b).

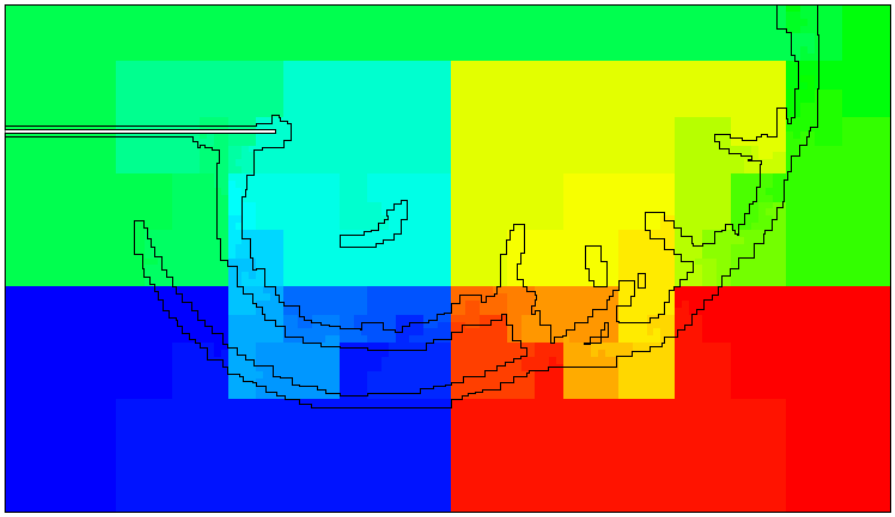

Figure A.27: Distribution of Setup 6a with $r_w = 5\lambda$ to 48 nodes at $t = 240\,\mu s$.

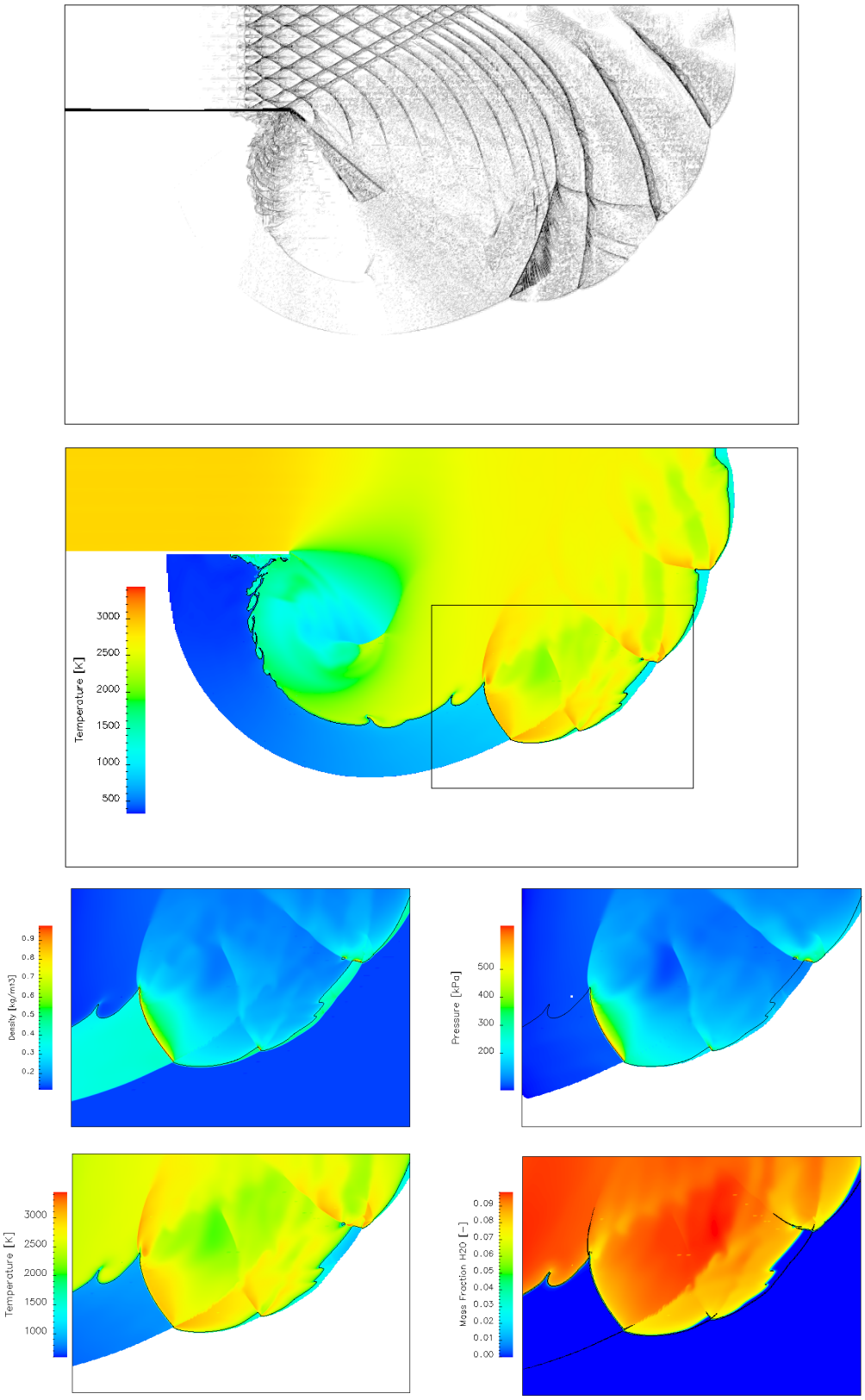

Figure A.28: Results of Setup 6a with $r_w = 5\lambda$ at $t = 240\,\mu s$. Top: triple point tracks, middle: color plot of T in the entire computational domain, bottom: color plots of important flow quantities.

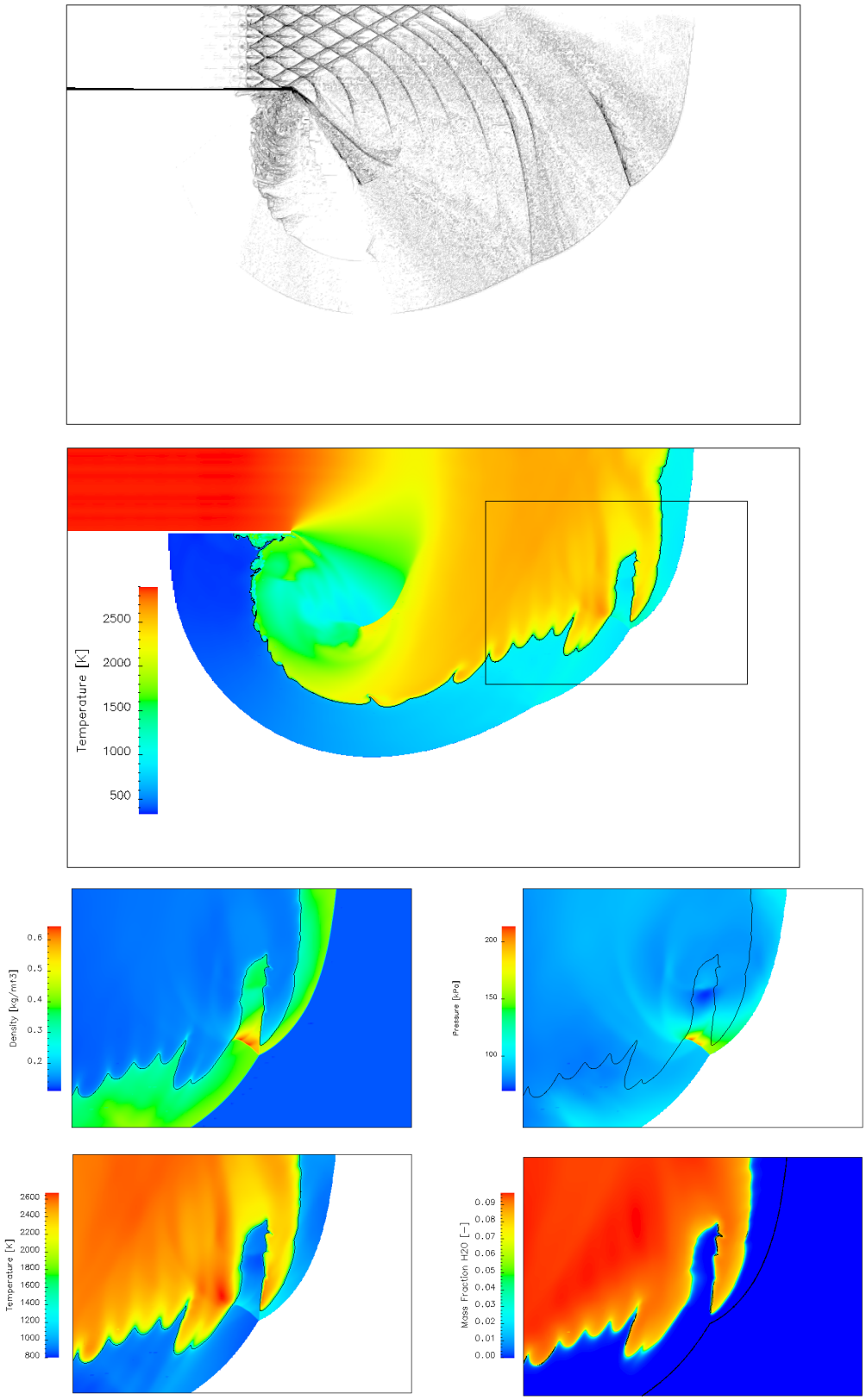

Figure A.29: Results of Setup 6b with $r_w = 4\lambda$ at $t = 240\,\mu s$. Top: triple point tracks, middle: color plot of T in the entire computational domain, bottom: color plots of important flow quantities.

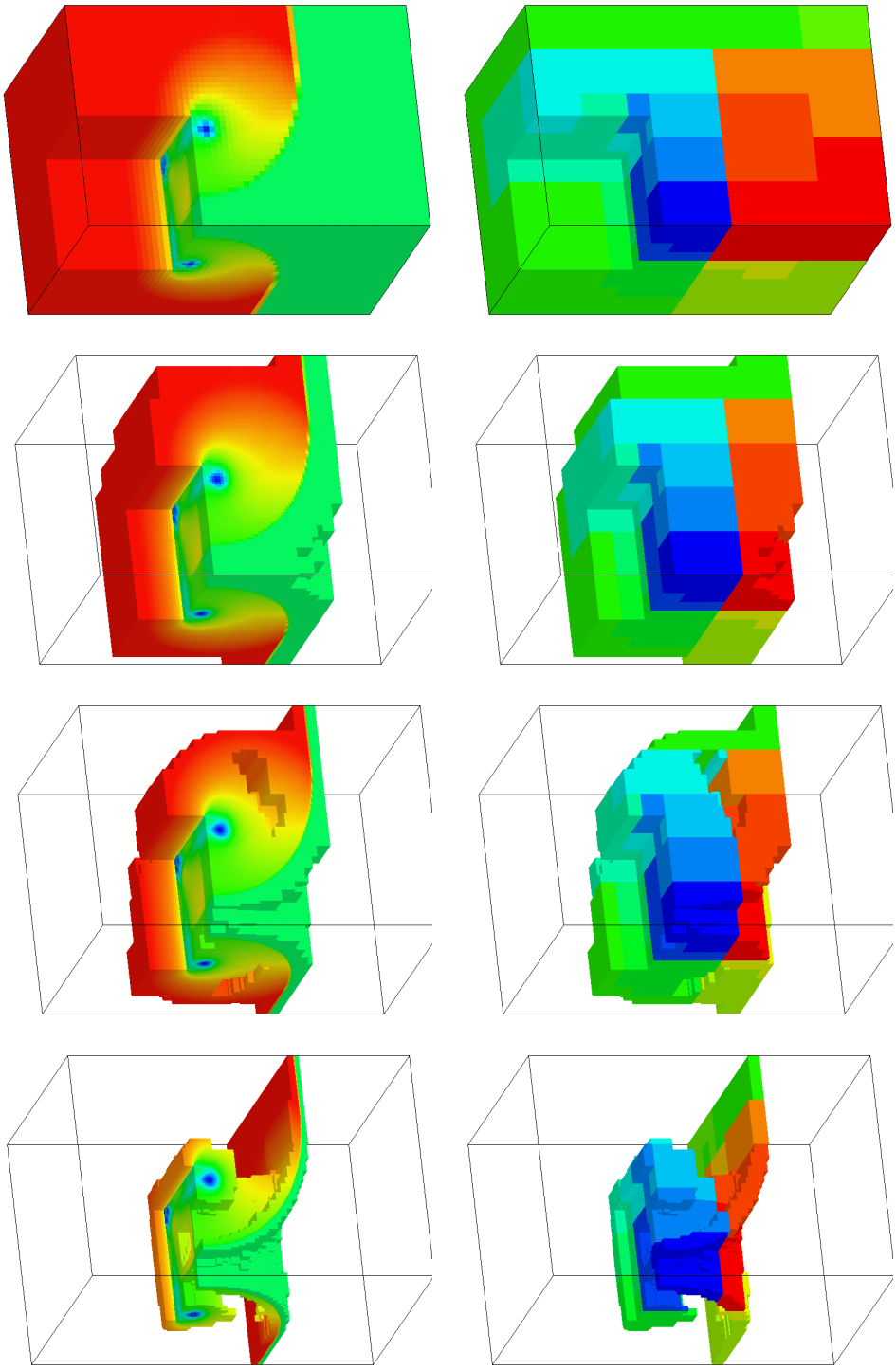

Figure A.30: Left column: color plot of ρ on three refinement levels at t_{end} for AMR Test 2. Right column: actual distribution at t_{end} to 16 nodes.

List of Figures

List of Tables

List of Algorithms

List of Definitions

List of Theorems

List of Propositions

List of Symbols

Roman Characters

a_m	wave strength in mth characteristic field, the coefficient for $\mathbf{r}_m$ in the solution of the linear RP, $a_m := \beta_m - \delta_m$ [cf. Eq. (2.19) on page 15]
A_j^f, A_j^r	pre-exponential factor for Arrhenius law of reaction j [see Eq. (2.82) on page 33]
$\mathbf{A}$	Jacobian matrix [cf. page 10]
$\mathbf{A}^{\pm}$	splitting of A [cf. page 60]
$\mathbf{A}_1$	Jacobian matrix of flux function $\mathbf{f}_1$ [see Eq. (A.2) on page 219]
$\mathbf{A}_n$	Jacobian matrix of flux function $\mathbf{f}_n$, $\mathbf{A}_n = \partial \mathbf{f}_n / \partial \mathbf{q}$ [see Def. 1 on page 10]
$\mathcal{A}^{\pm}\Delta$	fluctuations in x_1-direction used in Wave Propagation [see Eq. (4.44) on page 64]
b	number of buffer cells around flagged cells [cf. page 121]
$\mathbf{B}$	Jacobian matrix of $\mathbf{f}_2$ in Sec. 4.3.2, $\mathbf{B} \equiv \mathbf{A}_2$ [cf. page 69]
$\mathcal{B}^{\pm}\Delta$	fluctuations in x_2-direction in Sec. 4.3.2 [cf. page 69]
c	speed of sound in the frozen mixture [see Eqs. (2.69), (2.70) on page 26]
c_p, c_{pi}	heat capacity at constant pressure of mixture and species i [see Eqs. (2.46), (2.48) on page 22]
c_v, c_{vi}	heat capacity at constant volume of mixture and species i [see Eqs. (2.46), (2.48) on page 22]
C	dimensionless speed of sound [cf. page 38]
C_i	specific concentration of species i [see Eq. (2.40) on page 21]
C_{jk}	rectangular FV cell around (x_1^j, x_2^k) [cf. page 54]
C_{CFL}	CFL number, scheme-dependent [see Eqs. (4.67) on page 74, (4.70) on page 76, (4.84) on page 81, (4.98) on page 87]
C^1, C^2	space of (twice) continuously differentiable functions with $D \longrightarrow S$ [cf. page 10 ff]
d	spatial dimension [cf. page 10]
$d^\star$	detonation speed [cf. page 37]
D	domain in Chap. 2 [cf. page 10]
D	dimensionless detonation speed in Chaps. 3, 6 [see Eq. (3.18) on page 38]
e, e_i	Specific internal energy of mixture and species i [see Eqs. (2.45), (2.47) on page 22]
E	specific total energy [cf. page 19]
$\bar{E}$	total energy density, $\bar{E} = \rho E$ [cf. page 19]

$E_0^\star$	dimensionless activation energy [see Eq. (3.18) on page 38]
$E_A^\star$	activation energy in simplified model [cf. page 36]
E_j^f, E_j^r	activation energy of reaction j [see Eq. (2.82) on page 33]
f	overdrive parameter [see Eq. (3.26) on page 41]
$\mathbf{f}_n$	flux function $\mathbf{f}_n = \mathbf{f}_n(\mathbf{q})$ in x_n-direction, $\mathbf{f} \equiv \mathbf{f}_1$ [cf. page 10]
$\mathbf{f}^\pm$	FVS functions of $\mathbf{f}$ [see Eq. (4.30) on page 61]
$\mathbf{F}^n$	numerical flux approximation in x_n-direction [see Def. 12 on page 53]
$\mathbf{F}^{n,i}$	approximation $\mathbf{F}^n$ on level i, face-centered [see Eq. (5.6) on page 116]
$\delta\mathbf{F}^{n,i}$	flux correction terms for level $i-1$ stored on level i, face-centered [see Eq. (5.7) on page 116]
$\mathbf{F}_i$	numerical flux approximation for ρ_i [cf. page 100]
$\mathbf{F}_\rho$	numerical flux approximation for ρ [cf. page 100]
$\mathbf{F}_{jk}^{n,\pm 1/2}$	numerical fluxes at cell C_{jk}, $\mathbf{F}_{jk}^{1,\pm 1/2} := \mathbf{F}_{j\pm\frac{1}{2},k}^1$, $\mathbf{F}_{jk}^{2,\pm 1/2} := \mathbf{F}_{j,k\pm\frac{1}{2}}^2$ [cf. page 53]
$\mathbf{g}$	right side of ODE $\mathbf{y}' = \mathbf{g}(\mathbf{y})$ [see Def. 17 on 105]
G_i	domain of level i [see Eq. (5.2) on page 114]
$G_{i,m}$	domain of mth grid on level i [see Eq. (5.1) on page 114]
$\partial G_{i,m}$	boundary of $G_{i,m}$ [cf. page 114]
$\bar{G}_{i,m}$	hull of $G_{i,m}$, $\bar{G}_{i,m} = G_{i,m} \cup \partial G_{i,m}$ [cf. page 114]
G_i^p	portion of G_i on node p [see Eq. (5.17) on page 124]
G_i^s	domain G_i extended by s ghost cells as required by $\mathcal{H}^{(\Delta t)}$
$G_i^{s,p}$	portion of G_i^s on node p [cf. page 125]
G_i^ν	maximal domain for space interpolation on G_i [cf. page 120]
$G_{i,m}^\sigma$	$G_{i,m}$ extended by σ cells [see Eq. (5.3) on page 114]
$G_{i,m}^s$	$G_{i,m}$ extended by s ghost cells as required by $\mathcal{H}^{(\Delta t)}$ [cf. page 115]
$\tilde{G}_{i,m}^s$	ghost cell region of $G_{i,m}^s$, $\tilde{G}_{i,m}^s := G_{i,m}^s \backslash \bar{G}_{i,m}$ [cf. page 118]
$G_{i,m}^{s,p}$	domain of $G_{i,m}^s$ on node p [cf. page 125]
$\tilde{G}_{i,m}^{s,p}$	ghost cell region of $G_{i,m}^{s,p}$ [cf. page 125]
h, h_i	specific enthalpy of mixture and for species i [see Eqs. (2.45), (2.47) on page 22]
h^0, h_i^0	heat of formation of mixture and for species i [cf. page 21]
Δh	discrete step size in ODE approximation [cf. page 106]
H	specific total enthalpy [cf. page 19]
$\mathbf{H}^i$	auxiliary function on level i, cell-centered [cf. page 127]
I_{jk}	domain of cell C_{jk} [see Eq. (4.7) on page 54]
$\tilde{I}_{i,m}^s$	ghost cells in $G_{i,m}^s$ to be set with interpolated values [see Eq. (5.14) on page 119]
$\mathbf{I}$	identity matrix
J	total number of chemical reactions [cf. page 32]
k	frequency factor in Chap. 3 [cf. page 36]
k_j^f, k_j^r	forward and backward reaction rate of reaction j [see Eq. (2.82) on page 33]

K	total number of species [cf. page 18]
K	dimensionless frequency factor in Chap. 3 [see Eq. (3.18) on page 38]
l_{ig}	induction length [cf. page 46]
L	length of a detonation cell [cf. Fig. 3.6 on page 49]
$L_{1/2}$	half reaction length [see Eq. (3.20) on page 38]
L^1, L^∞	space of measurable functions $D \longrightarrow S$, norms $\|.\|_1$ [see Eq. (4.6) on page 53] and $\|.\|_{\mathrm{L}^\infty}$ [cf. page 11]
$\mathcal{L}^p$	load on processor p [see Eq. (5.19) on page 124]
m_n	n-th component of $\mathbf{m}$, $m_n = \rho u_n$ [cf. page 18]
$\mathbf{m}$	vector of momentum densities $\mathbf{m} = (m_1, \ldots, m_d)^T = \rho\mathbf{u}$ [cf. page 18]
M	number of components in vector of state $\mathbf{q}$ [cf. page 10]
M	Mach number in Chap. 3 [cf. page 45]
M_i	number of grids on level i [cf. page 114]
M_i^p	number of grids on level i on node p [cf. page 124]
$\mathbf{n}$	unit normal vector $\mathbf{n} := (\sigma_1, \ldots, \sigma_d)^T \in \mathbb{R}^d$ [cf. page 13]
N	number of finite volumes in one-dimensional scheme [cf. page 71]
N^ι	scalar refinement flags on level ι, cell-centered [cf. page 121]
o	order of accuracy of scheme $\mathcal{H}^{(\Delta t)}$ [see Def. 11 on page 53]
p, p_i	pressure of mixture and partial pressure of species i [see Eqs. (2.37), (2.38) on page 20]
$\acute{p}$	pressure of mixture from Eq. (2.53) on page 23
$\check{p}$	pressure of mixture from Eq. (2.55) on page 23
P	dimensionless pressure in Chaps. 3, 6 [see Eq. (3.18) on page 38]
P	number of parallel nodes in Chap. 5 [cf. page 124]
$\tilde{P}_{i,m}^s$	ghost cells in $G_{i,m}^s$ outside physical domain [see Eq. (5.12) on page 118]
q_0	heat release in simplified detonation model [cf. page 36]
Q_0	dimensionless heat release [see Eq. (3.18) on page 38]
Q_j^l	scalar discrete value in cell C_j and time step l [cf. page 66]
$\tilde{Q}_{j+1/2}^{L/R}$	MUSCL extrapolated values between cells C_j, C_{j+1} [see Eqs. (4.45), (4.46) on page 66]
$\mathbf{q}$	vector of state $\mathbf{q} = \mathbf{q}(\mathbf{x}, t) \in S$ [cf. page 10]
$\mathbf{q}_0$	initial condition $\mathbf{q}_0 = \mathbf{q}_0(\mathbf{x}) \in S$ [cf. page 10]
$\mathbf{q}_\varepsilon$	solution $\mathbf{q}_\varepsilon = \mathbf{q}_\varepsilon(\mathbf{x}, t) \in S$ of extended viscous system [cf. page 11]
$\mathbf{q}_L$, $\mathbf{q}_R$	Left and right state of a RP [cf. page 15]
$\mathbf{Q}$	approximation to the vector of state $\mathbf{Q} = \mathbf{Q}(\mathbf{x}, t) \in S$ [cf. page 52]
$\mathbf{Q}^i$	approximation $\mathbf{Q}$ on level i, cell-centered [see Eq. (5.5) on page 115]
$\mathbf{Q}_{jk}^l$, $\mathbf{Q}_j^l$	discrete value for vector of state in cell C_{jk}, C_j and time step l [cf. page 52]
r	spatial mass fraction change $r = r(Z)$ in Chap. 3 [see Eq. (3.19) on page 38]
r	argument for slope limiter in Chap. 4 [cf. page 67]
r_i	refinement factor from level $i-1$ to level i [cf. page 114]

r_w	half width of rectangular channel [cf. page 201]
$\mathbf{r}_m$	right eigenvector of $\mathbf{A}$ or $\mathbf{A}_n$ in mth characteristic field [see Def. 1 on page 10]
$\mathcal{R}$	gas constant $= 8.31441 \cdot 10^7 \frac{\mathrm{J}}{\mathrm{mol\,K}} = 1.98723$ cal mol^{-1} K^{-1}
R, R_i	specific gas constant of mixture and species i [see Eqs. (2.49), (2.50) on page 22]
$\mathbf{R}_1$	matrix of right eigenvectors of $\mathbf{A}_1$, $\mathbf{R}_1 = (r_1, \vert \ldots, \vert r_M)$ [see Eq. (A.4) on page 221]
s	specific entropy in Chap. 2 [cf. page 25]
s	radius of numerical stencil in Chaps. 4 and 5 [cf. page 52]
$\mathbf{s}$	source term function $\mathbf{s} = \mathbf{s}(\mathbf{q})$ [cf. page 10]
S	space of admissible states $S \subset \mathbb{R}^M$ [cf. page 10]
S_i	species i [cf. page 32]
S_L, S_R	smallest, largest eigenvalue or signal speed [cf. pages 63 and 86]
S_w	scaling factor for relative error of quantity w [see Eq. (5.26) on page 131]
S_m^{ODE}	scaling factor for mth component of $\mathbf{Y}^\iota$ in ODE solver [see Eq. (4.117) on page 107]
$\tilde{S}^s_{i,m}$	ghost cells in $G^s_{i,m}$ to be synchronized with G_i [see Eq. (5.13) on page 118]
$\tilde{S}^{s,p}_{i,m}$	local ghost cells in $G^{s,p}_{i,m}$ [cf. page 125]
$\tilde{S}^{s,q}_{i,m}$	ghost cells in $G^{s,p}_{i,m}$ that require parallel communication [cf. page 125]
t	time [cf. page 10]
t_{end}	final time for simulations
t_{ig}	induction time [cf. page 46]
t_l	discrete time step [cf. page 52]
t_p	time period for cellular oscillation [cf. page 159]
Δt	discrete time step [cf. page 52]
Δt_i	discrete time step on level i [cf. page 114]
T	temperature [cf. page 20]
$\mathbf{T}$	rotation matrix $\mathbf{T} = \mathbf{T}(\mathbf{n})$ [cf. page 13 and see Prop. 2 on page 27]
u_n	n-th component of $\mathbf{u}$ [cf. page 18]
$\mathbf{u}$	vector of flow velocity $\mathbf{u} = (u_1, \ldots, u_d)^T$ [cf. page 18]
U_n	dimensionless velocity in nth space direction, $U \equiv U_1$ [see Eq. (3.18) on page 38]
v	specific volume [cf. page 37]
$\mathbf{v}$	self-similar, one-dimensional solution $\mathbf{v}(x/t)$ [cf. page 16]
V	dimensionless specific volume [see Eq. (3.18) on page 38]
w	scalar quantity $w = w(\mathbf{q})$ derived from vector state [cf. page 130]
W, W_i	molecular weight of mixture and for species i [cf. page 21]
$\mathcal{W}$	work load function $\mathcal{W} = \mathcal{W}(\Omega)$ [see Eq. (5.18) on page 124]
$\mathcal{W}_m$	wave in mth characteristic field, $\mathcal{W}_m := a_m \mathbf{r}_m$ [cf. page 64]
x_n	coordinate in nth space direction, $x \equiv x_1$ [cf. page 10]
x_1^j, x_2^k	discrete grid points, (x_1^j, x_2^k) denotes a cell center [see Eq. (4.1) on page 52]

$x_1^{j-1/2}$, $x_2^{k-1/2}$	discrete mesh points, $(x_1^{j-1/2}, x_2^{k-1/2})$ denotes a vertex [see Eq. (4.2) on page 52]
Δx_n	mesh width in nth space direction [cf. page 52]
$\Delta x_{n,i}$	mesh width in nth space direction on level i [cf. page 114]
$\mathbf{x}$	point in space $\mathbf{x} = (x_1, \ldots, x_d)^T \in \mathbb{R}^d$ [cf. page 10]
X_n	dimensionless coordinate in nth space direction, $X \equiv X_1$ [see Eq. (3.20) on page 38]
X_i	mole fraction of species i [see Eq. (2.41) on page 21]
y	x_2-direction in Sec. 4.3.2 [cf. page 69]
$\mathbf{y}$	argument of ODE $\mathbf{y}' = \mathbf{g}(\mathbf{y})$ [see Def. 17 on page 105]
Y_i	mass fraction of species i [see Eq. (2.39) on page 21]
$\mathbf{Y}^\iota$	approximation to $\mathbf{y}$ [cf. page 106]
Z	mass fraction of product in simplified detonation model [cf. page 36]

Greek Characters

β_j^f, β_j^r	temperature dependent exponent of reaction j [see Eq. (2.82) on page 33]
β_m	coefficient for $\mathbf{r}_m$ in the eigenvector decomposition of $\mathbf{q}_R$ [cf. Eq. (2.19) on page 15]
γ, γ_i	adiabatic coefficient of mixture and for species i [see Eqs. (2.49), (2.51) on page 22]
$\bar{\gamma}$	$\bar{\gamma} := \gamma - 1$ [see Eq. (2.61) on page 25]
δ_m	coefficient for $\mathbf{r}_m$ in the eigenvector decomposition of $\mathbf{q}_L$ [cf. Eq. (2.19) on page 15]
δ_{jn}	Kronecker symbol [cf. page 19]
ϵ_w	refinement threshold for scalar gradient of quantity w [see Eq. (5.20) on page 130]
ε	viscosity parameter in extended viscous equation [cf. page 11]
ζ	parameter $\zeta = \rho_0/\rho$ in Chap. 3 [cf. page 43]
η	entropy function $\eta = \eta(\mathbf{q})$ in Chap. 2 [see Def. 3 on page 12]
η	numerical viscosity parameter in EF 1 to 3 in Chaps. 4, 6 [cf. page 82]
η_{tol}	clustering threshold [cf. page 121]
η_{ODE}	accuracy threshold in ODE solver [see Eq. (4.117) on page 107]
η_w^r	refinement threshold for relative error of quantity w [see Eq. (5.26) on page 131]
θ^y, θ^z	rotation angles [see Prop. 2 on page 27]
Θ	wedge angle in Chap. 7 [cf. Fig. 7.22 on page 196]
λ	width of a detonation cell [cf. Fig. 3.6 on page 49]
λ_m	eigenvalue of mth characteristic field [see Def. 1 on page 10]
Λ	$\Lambda := \Delta x/\Delta t$ on page 102

$\mathbf{\Lambda}_1$	diagonal matrix of eigenvalues, $\mathbf{\Lambda} \equiv \mathbf{\Lambda}_1$ [see Prop. 10 on page 221]
$\mathbf{\Lambda}^{\pm}$	splitting of $\mathbf{\Lambda}$ [cf. page 60]
μ_1, μ_2	number of cells in x_1-, x_2-direction in grid domain $G_{i,m}$ [see Eq. (5.1) on 114]
ν^f_{ji}, ν^r_{ji}	stoichiometric coefficient of species i as reactant, product in reaction j [see Eq. (2.80) on page 32]
ξ	scalar auxiliary variable, $\xi = x/t$ in Chap. 2 [cf. page 18]
ξ_m	eigenvalues of Jacobian of ODE in Chap. 4 [see Def. 17 on page 105]
ϖ	Riemann invariant $\varpi = \varpi(\mathbf{q})$ [see Def. 7 on page 18]
ρ, ρ_i	total density of mixture and partial density for species i [cf. page 18]
$\bar{\rho}$	dimensionless density [see Eq. (3.18) on page 38]
ϱ	auxiliary quantity in derivatives of c [see Eq. (2.72) on page 27]
σ_n	component of unit normal vector $\mathbf{n}$, $\sigma \equiv \sigma_1$ [cf. page 13]
Σ	magnitude of vorticity during simulation with respect to detonation velocity [cf. page 159]
$\dot{\varsigma}$	thermicity [see Eq. (2.87) on page 33]
ς_i	thermicity coefficients for species i [see Eq. (2.88) on page 34]
τ^w_{jk}	error estimation for quantity w in C_{jk} [see Eq. (5.24) on page 131]
τ^{ODE}_m	error estimation for mth component of $\mathbf{Y}^\iota$ in ODE solver [see Eq. (4.117) on page 107]
ϕ_i	$\phi_i := \partial p/\partial \rho_i$ [see. Eq. (2.60) on page 25]
Φ	slope limiter function $\Phi = \Phi(r)$ [cf. page 67]
$\Phi^{\pm}_{j+\frac{1}{2}}$	slope limiter values for MUSCL between cells C_j, C_{j+1} [see Eqs. (4.45), (4.46) on page 66]
φ	test function $\varphi = \varphi(\mathbf{q})$ [see Def. 2 on page 11]
φ	implicit temperature-equation $\varphi(\mathbf{q}, T) = 0$ [see. Prop. 1 on page 23]
ψ_n	entropy flux function $\psi_n = \psi_n(\mathbf{q})$ in x_n-direction [see Def. 3 on page 12]
ψ	implicit temperature-function $\psi(\mathbf{q}) = T$ [cf. Prop. 1 on page 23]
ω	vorticity in Chaps. 6, 7 [see Eqs. (6.3) on page 159, (6.6) on page 167]
$\dot{\omega}_i$	chemical production rate of species i [see Eq. (2.81) on page 32]
Ω	problem domain $\Omega \subset D$ [cf. page 10]
$\partial\Omega$	boundary of Ω [cf. page 19]

Operators

Δ	difference between right and left state [cf. page 15]
∂	geometric boundary
C	geometric complement [cf. page 121]
$\mathcal{H}^{(\Delta t)}$	one step of scheme (4.4) [cf. page 53] with time step Δt
$\mathcal{S}^{(\Delta t)}$	one time step Δt of discrete operator for Eq. (4.18) [cf. page 58]
$\mathcal{X}^{(\Delta t)}_n$	update step in nth space direction in dimensional splitting [cf. page 59]

Subscripts

0	unburned or initial gas state [cf. page 37]
CJ	values in the CJ point [cf. page 39]
i	species index, $i = 1, \ldots, K$ [cf. page 18]
i	level index in Chap. 5, $i = 1, \ldots, i_{\max}$ [cf. page 114]
j	cell index [cf. page 52]
j	reaction index in Chap. 2, $j = 1, \ldots, J$ [cf. page 32]
k	cell index [cf. page 52]
l	time step index [cf. page 52]
L	left state [cf. page 15]
m	mth component of vector of state or flux function [e.g. page 71]
m	mth grid $G_{i,m}$ on level i in Chap. 5, $m = 1, \ldots, M_i$ [cf. page 114]
n	space direction index, $n = 1, \ldots, d$ [cf. page 10]
R	right state [cf. page 15]
vN	values in the von Neumann point [cf. page 45]
ι	auxiliary index, in Chap. 5 new level index [cf. page 121]
ν, κ	auxiliary indices

Superscripts

$\pm$	splitting in positive and negative parts in FVS [cf. page 60]
0	unburned or initial gas state [cf. page 42]
$\star$	intermediate state in RP
f	forward reaction [cf. page 32]
i	level index, $i = 1, \ldots, i_{\max}$ [cf. page 114]
j	cell index [cf. page 52]
k	cell index [cf. page 52]
l	time step index [cf. page 52]
L	left state
p	node index [cf. page 124]
q	node index [cf. page 124]
r	backward reaction [cf. page 32]
R	right state
s	simple wave
T	transpose
ι	auxiliary index

Accents

$\grave{}$	Galilean transformation, $\grave{x} = t\, d^\star - x$ [cf. page 37]
$\hat{}$	Roe average [cf. page 77 ff]
$\tilde{}$	rotated coordinates in quasi-one-dimensional RP in Chap. 2 [cf. page 14]

$\tilde{}$	MUSCL extrapolated variables in Chap. 4 [cf. page 65 ff]
$\breve{}$	new grids [cf. page 121]

Acronyms

AMR	Adaptive Mesh Refinement
AMROC	Adaptive Mesh Refinement in Object-oriented C++
CFL	Courant-Friedrichs-Levy
CJ	Chapman-Jouguet
CPU	Central Processing Unit
EF	Entropy Enforcement
ENO	Essentially Non-Oscillating
FCT	Flux-Corrected Transport
FDS	Flux-Difference Splitting
FV	Finite Volume
FVS	Flux-Vector Splitting
HH	Harten-Hyman
ODE	Ordinary Differential Equation
HLL	Harten-Lax-Van Leer
IC	Initial Condition
II	Incident shock - Incident shock [cf. page 169]
ILDM	Intrinsic Low-Dimensional Manifold
MI	Mach stem - Incident shock [cf. page 169]
MM	Mach stem - Mach stem [cf. page 169]
MUSCL	Monotone Upwind Schemes for Conservation Laws
PC	Personal Computer
PDE	Partial Differential Equation
RH	Rankine-Hugoniot
RP	Riemann Problem
RS	Riemann Solver
SW	Steger-Warming
TVD	Total Variation Diminishing
VL	Van Leer
ZND	Zel'dovich-von Neumann-Döring